EFFECT OF GEOMETRY, COMPOSITION AND THERMOMECHANICAL TREATMENT ON THE TYPE IV CRACKING DURING CREEP IN ADVANCED 9Cr FERRITIC STEELS WELD JOINT

By

T. SAKTHIVEL

Enrolment No.: **ENGG02201304008**

Indira Gandhi Centre for Atomic Research,

Kalpakkam 603102, India

A thesis submitted to the

Board of Studies in Engineering Sciences

In partial fulfillment of requirements

for the Degree of

DOCTOR OF PHILOSOPHY

of

HOMI BHABHA NATIONAL INSTITUTE

July, 2019

Homi Bhabha National Institute

Recommendations of the Viva Voce Committee

As members of the Viva Voce Committee, we certify that we have read the dissertation prepared by Mr. T. Sakthivel entitled **"Effect of geometry, composition and thermomechanical treatment on the Type IV cracking during creep in advanced 9Cr ferritic steels weld joint"** and recommend that it may be accepted as fulfilling the thesis requirement for the award of Degree of Doctor of Philosophy.

Chairman - Prof. Shaju K Albert		Date: 9.02.2021
Guide / Convener - Prof. G. Sasikala		Date: 09.02.2021
External Examiner- Dr. D.V.V. Satyanarayana		Date 09.02.2021
Member 1- Prof. S. Murugan	S. Murugan	Date: 09.02.2021
Member 2- Prof. M. Kamaraj	M. Kamaraj	Date: 09.02.2021
Member 3- Prof. S. Amirthapandian		Date: 09/2/21

Final approval and acceptance of this thesis is contingent upon the candidate's submission of the final copies of the thesis to HBNI.

I/We hereby certify that I/we have read this thesis prepared under my/our direction and recommend that it may be accepted as fulfilling the thesis requirement.

Date: 09.02.2021

Place: IGCAR, Kalpakkam

Signature of Guide

STATEMENT BY AUTHOR

This dissertation has been submitted in partial fulfillment of requirements for an advanced degree at Homi Bhabha National Institute (HBNI) and is deposited in the Library to be made available to borrowers under rules of the HBNI.

Brief quotations from this dissertation are allowable without special permission, provided that accurate acknowledgement of source is made. Requests for permission for extended quotation from or reproduction of this manuscript in whole or in part may be granted by the Competent Authority of HBNI when in his or her judgment the proposed use of the material is in the interests of scholarship. In all other instances, however, permission must be obtained from the author.

T. Sakthivel

DECLARATION

I, hereby declare that the investigation presented in the thesis has been carried out by me. The work is original and has not been submitted earlier as a whole or in part for a degree / diploma at this or any other Institution / University.

T. Sakthivel

LIST OF PUBLICATIONS ARISING FROM THESIS

Journal

1. Creep deformation and rupture behavior of P92 steel weld joint fabricated by NG-TIG welding process, T. Sakthivel, G. Sasikala, M. K. Dash, P. Syamala Rao, Journal of Materials Engineering and Performance, 2019, 28(7), 4364-4378.
2. An improvement in creep strength of thermo-mechanical treated modified 9Cr-1Mo steel weld joint, T. Sakthivel, S. M. Nandeswarudu, P. Shruti, G. V. S. Nageswara Rao, K. Laha, G. Sasikala, T. Srinivasa Rao, Materials at High Temperatures, 2019, 36:1, 76-86.
3. An assessment of creep deformation and rupture behaviour of 9Cr-1.8W-0.5Mo-VNb (ASME Grade 92) steel, T. Sakthivel, S. Panneer Selvi, K. Laha, Materials Science and Engineering: A, 2015, 640, 61-71.
4. Integrity assessment of grade 92 welded joint under creep condition, T. Sakthivel, K. Laha, M. Vasudevan, P. Parameswaran, K.S. Chandravathi, M.D. Mathew, Procedia Engineering, 2014, 86, 215-222.
5. Creep deformation behavior of intercritical heat treated boron added modified 9Cr-1Mo steel, T. Sakthivel, C.R. Das, K. Laha, G. Sasikala, Metals and Materials International, 2019, Doi.org/10.1007/s12540-019-00377-1.
6. Role of microstructures on heterogeneous creep behavior across P91 steel weld joint assessed by impression creep testing, T. Sakthivel, G. Sasikala, M. Vasudevan, Materials Characterization 159 (2020) 109988.
7. An enhancement in mechanical properties of grade 91 steel on microalloying with boron and nitrogen, T. Sakthivel, G. Sasikala, P. Parameswaran and K. Laha, Materials at High Temperatures (2020), DOI: 10.1080/09603409.2020.1836743.
8. Creep deformation and rupture behavior of boron added P91 Steel, T. Sakthivel, G. Sasikala, P. Shyamala Rao, P. Parameswaran, K. Laha, Materials Science and Technology (under review).
9. Influence of thermo-mechanical treatment (TMT) on microstructure and tensile and creep properties of modified 9Cr-1Mo Steel, T. Sakthivel, V. Sony Priya, P. Parameswaran, P. Shruti, S. Panneer Selvi, G.V.S.Nageswara Rao, T. Srinivasa Rao, K. Laha, G. Sasikala, Materials Science and Technology (communicated).

Conferences

1. Type IV Creep Failure in P92 Steel Weld Joint, T. Sakthivel, G. Sasikala and K. Laha International Institute of Welding Congress (IWC), Paper No: 121, Dec 7-9, 2017 Chennai, India
2. Creep behaviour of boron added modified 9Cr-1Mo steel weld joint, T. Sakthivel, K. Laha, National Welding Meet-2017, Indian Institute of Welding, May 12-13, 2017, Bengaluru.
3. Enhancement in mechanical strength of modified 9Cr-1Mo Steel on microalloying of Boron, T. Sakthivel, K. Laha, P. Parameshwaran, S. Panneerselvi, International Conference on Advances in Materials, Manufacturing and Applications (AMMA 2015), National Institute of Technology, Apr 9-11, 2015, Tiruchirapalli.

(T. Sakthivel)

Dedicated

To

My Grandparents

ACKNOWLEDGEMENTS

I am extremely grateful to my research supervisor Dr. G. Sasikala, Head, Materials Technology and Development Division, IGCAR for her guidance, inspiration and encouragement, useful suggestions and good wishes throughout this project. I also thank her for critically reviewing my thesis.

I am delighted to record my gratitude to my doctoral committee Chairman Dr. Shaju K. Albert, and members- Dr. S. Murugan, Dr. M. Kamaraj, IIT Madras, and Dr. S. Amirthapandian for their kind advice and valuable suggestions at various stages during the course of the work. I sincerely thank former doctoral committee Chairman Dr. U. Kamachi Mudali and convener Dr. K. Laha for their valuable suggestions at various stages during the course of the work.

I sincerely thank Dr. A. K. Bhaduri, Director, IGCAR, Dr. G. Amarendra, Director, Metallurgy and Materials Group, Dr. Shaju K. Albert, Associate Director, Materials Engineering Group, for their motivation during the entire course of this work.

I would like to sincerely thank for Dr. Anish Kumar, Dean Academic, Engineering Sciences, HBNI, IGCAR for the encouragement, support and good wishes.

The help extended by Dr. S. Raju for DSC experimentation is sincerely acknowledged.

I would like to sincerely thank Dr. Parameswaran and Dr. M. Vasudevan for their vital experimental support throughout this work.

I would like to sincerely acknowledge the constant support provided by Dr. P. Shyamal Rao and Dr. Kishan Singh from MSG. Also special thanks to Mr. M. Shanmugavel, Mr. M. Muthuganesh, Mr. A. Anthuvan Clement from FRTG for their support during the course of this work. The help extended by Dr. Manmath Kumar Dash, Mr. K. Mariappan, Dr. Haraprasanna Tripathy, Dr. R.N. Hajra, Mr. P. Vasantharaja, Ms. S. Paneerselvi, Ms. Srividya, Mr. M. Govindasamy, Mr. D. Manokaran, Mr. K. C. Sahoo, Mr. M. Ragavendra, Mr. M. Arul from MMG, Mr. T. Saravanan from CWD for experimentation work is sincerely acknowledged.

I would like to sincerely thank my friend Cdr. Dr. Rishi Pamnani for the valuable suggestions and encouragement throughout the work. The motivation by Dr. Vani Shankar, Dr. R. Ramaseshan, Dr. Sunil Goyal and Dr. S. Latha are duly acknowledged. I would like to express my thanks to all my friends at DAE (OCES 51st batch) and IGCAR who helped me directly or indirectly during this work.

Most importantly, the unconditional love, support and care of my wife, grandmother, uncles, parents, sisters and brothers have been unsurpassed at all times; for this I am eternally indebted.

CONTENTS

List of Figures

List of Table

List of Abbreviations and General Symbols

A	Austenite
AC	Air Cooled
A-TIG	Activated-Tungsten Inert Gas
BM	Base Metal
BSE	Back Scattered Electrons
CGHAZ	Coarse Grained Heat Affected Zone
CCT	Continuous Cooling Transformation
CSL	Coincident Site Lattice
DSC	Differential Scanning Calorimetry
EBSD	Electron Backscatter Diffraction
EBW	Electron Beam Welding
EDS	Energy Dispersive x-ray Spectroscopy
FEM	Finite Element Method
FGHAZ	Fine Grained Heat Affected Zone
FCC	Face Center Cubic
FL/FB	Fusion Line/Fusion Boundary
HAZ	Heat Affected Zone
HAGB	High Angle Grain Boundary
HT	Heat Treatment
ICHT	Intercritical Heat Treated
ICHAZ	Intercritical Heat Affected Zone
ICP	Inductively Coupled Plasma
IPF	Inverse Pole Figure
KAM	Kernel Average Misorientation
LAGB	Low Angle Grain Boundary
LW	Laser Welding
LMP	Larson-Miller Parameter
NT	Normalized and Tempered
NG-TIG	Narrow Gap Tungsten Inert Gas

OES	Optical Emission Spectroscopy
OM	Optical Microscopy
PWHT	Post Weld Heat Treatment
SADP	Selected Area Diffraction Pattern
SE	Secondary Electrons
SEM	Scanning Electron Microscopy
SMAW	Shielded Metal Arc Welding
TIG	Tungsten Inert Gas
TMT	Thermomechanical Treatment
TEM	Transmission Electron Microscopy
T_p	Peak Temperature
VHN	Vickers Hardness Number
WM	Weld Metal
wt %	Weight Percent
WSF	Weld Strength Factor
XRD	X-ray Diffractometer
Ac_1	Lower critical temperature on heating
Ac_3	Upper critical temperature on heating
T_m	Melting Point
T	Temperature
σ_a	Applied Stress
ρ_f	Free Dislocation Density
M	Taylor factor
G or μ	Shear Modulus,
b	Burgers Vector
λ_p	Mean Interparticle Spacing
D_0	Frequency Factor
k	Boltzmann Constant
n	Stress Exponent
ρ_b	Boundary Dislocation Density
$\dot{\varepsilon}$	Strain Rate
α	Ferrite

α'	Martensite
γ	Austenite
M_s	Martensite Transformation Start
M_f	Martensite Transformation Finish
Q	Activation Energy
T_c	Curie temperatures
R	Universal Gas Constant
t_r	Rupture Time
σ_{th}	Threshold stress
λ	Creep Damage Tolerance Factor
t_{ot}	Time to Onset of Tertiary
ε_f	Strain to Fracture
$\dot{\epsilon}_{min}$	Minimum Creep Rate
Q_C	Activation Energy for Creep
Q_D	Lattice Self Diffusion

CHAPTER 8

Summary and Scope for Future Work

This chapter summarizes the findings from the investigations on the type IV cracking behaviour of P91 and P92 steel weld joints. Effects of microstructural heterogeneity across the weld joint as influenced by different welding processes, boron + nitrogen content and thermo-mechanical treatment in P91 joint are examined. Influence of joint geometry (bevel angle) in P91 steel, and specimen orientation in P92 steel weld joint have been studied in connection with the stress triaxiality in the HAZ (type IV cracking region) which modifies the cavity nucleation and growth. Also, some suggestions for future work in these directions have been made.

8.1 Summary

The factors leading to higher rate of deformation in the ICHAZ region than the other regions in the single-pass A-TIG weld jointare the following: (i) lower content of low misorientation angle and coincidence site lattice (CSL) boundaries, (ii) finer grain size, (iii) enhanced heterogeneity in microstructures by a combination of recovered and deformed structure in the martensite, (iv) coarser $M_{23}C_6$ precipitates, and (v) boundaries devoid of precipitates. Creep rupture strength at 923 K for 10^4 h for the single-pass activated-TIG weld joint is lower by about 26% than the base metal. Heterogeneous microstructure and variations in high temperature strength of the different regions across the joint has led to reduction in rupture strength. Although the geometry of both TIG and SMAW joints are similar, weld strength reduction factor (WSRF) is low for SMAW than the TIG joint, and the difference decreased under long-term exposure. Activated TIG (A-TIG) welding is preferred to fabricate the components in order to achieve resistance against Type IV cracking; TIG welding is preferred to SMAW in the case of thick components requiring multi-pass welding.

P91BN steels containing boron with controlled nitrogen content resulted in finer martensite lath width and higher dislocation density than in the P91 steel. The time spent in each creep regime increased significantly in P91BN steels as compared to P91 steel. P91BN steels possessed significantly enhanced creep rupture life as compared to P91 steel under similar test conditions associated with comparable ductility. Sluggish coarsening of $M_{23}C_6$ and finer MX precipitates significantly delayed the recovery of dislocation structure and migration of boundaries in P91BN steel than in P91 steel. From the point of view of rupture life of P91BN steel and its weld joint, the combination of 60 ppm boron with controlled (110 ppm) nitrogen content is optimum at 873 K as compared to other combinations of B and N examined in this study. The joint of steel with higher boron (0.010 wt.%) and nitrogen (0.0047 wt.%) exhibited higher type IV cracking resistance at 923 K. The reduction in heterogeneous mechanical properties across the weld joint enhances the type IV cracking resistance as observed in the P91BN steel.

Thermo-mechanical treatment (TMT) processing of modified 9Cr-1Mo steel (P91) leads to refined microstructure of the steel with more uniform precipitation of fine MX particles, finer martensite lath structure, and fine $M_{23}C_6$ precipitation than NT steel. The degree of TMT deformation is important since high levels of deformation leads to ferrite formation. Creep deformation resistance and rupture strength of the steel improved remarkably up to 25%TMT processing than NT steel. TMT processing for 40 and 50% deformation precludes the benefit of TMT due to presence of ferrite phase. The enhanced MX precipitation through TMT processing and reduction in coarsening of $M_{23}C_6$ precipitates under thermal cycle resulted in improved creep rupture life of TMT joint than NT weld joint. The thermo-mechanical processing of modified 9Cr-1Mo steel led to enhanced type IV cracking resistance significantly.

Creep damage tolerance factor ($\dot{\varepsilon_{min}} \cdot t_r / \varepsilon_f$) of 6 in the P92 steel demonstrates that the microstructural degradation such as coarsening of precipitates and subgrain structure is the dominant creep damaging mechanism in the steel. Creep rupture life of the NG-TIG weld joint was lower than the base metal; the difference in creep rupture life between the base metal and weld joint increased significantly with decrease in applied stress. The failure location in the NG-TIG weld joint with applied stress changes from the base metal at high stress regime to the fine grain (FG) HAZ (Type IV cracking) under lower stress level. Extensive Laves phase formation accompanied by significant loss of solution strengthening from tungsten under creep exposure led to premature type IV failure of the weld joint in the FGHAZ. A weld strength reduction factor about 0.59 has been evaluated for 10^5 hour at 923 K.

A bevel angle of 35° is found to be better than higher bevel angles from the point of view of longer life for the P91 weld joint due to the less number of weld thermal cycles/passes. At the same time, there will be the beneficial effect for reducing the maximum principle stress in the ICHAZ. 0° bevel single pass A-TIG weld joint exhibited significantly higher creep rupture life due to reduction in maximum principle stress and microstructural damage than the V-groove TIG joints in the ICHAZ. Increase in maximum principle stress in the ICHAZ and increase in triaxiality in the base metal with increase in bevel angle led to premature failure of the joint by shifting the fracture across the outer edge of HAZ to base metal region. The weld joint having lower bevel angle is preferred to have better creep rupture strength of the components associated with weld joints.

Specimen orientation influenced the creep rupture life of the P92 NG-TIG joint significantly. Creep cavitation damage in the FGHAZ of weld joint decreased with decrease in the angle between stress axis of the specimen and the weld fusion line/HAZ. The weld strength reduction factor is found to increase with decreasing orientation angle due to decrease in constraint effect on the FGHAZ/ICHAZ. Hence, minimization of the orientation angle between stress axis and weld joint fusion line/HAZ is recommended for improved life of the components of this steel with multi-pass joints operating at high temperature.

Apart from refinement of microstructural constituents (reduction in coarsening of $M_{23}C_6$ and enhanced MX precipitation) favorable for long term stability of microstructure to obtain better creep life of the base and weld joint, enhancement of the type IV cracking resistance of the steel joint can be obtained from joint having lower bevel angle, less heterogeneity across the weld joint, moving the orientation of stress axis in a joint to reduce the angle between HAZ and stress axis.

8.2 Scope for future work

Based on the study on the microstructural heterogeneity across the weld joint and type IV cracking behaviour of P91 steel and P91 steel thermo-mechanical treated, and alloyed with boron and nitrogen, P92 steel weld joints, following are the suggestions for further investigations.

1. Creep deformation and rupture behaviour of base metals and weld joints for longer duration (long term creep tests). Long term creep data provides more reliability of the component in the power plants.

2. Effect of notch acuity on simulated regions of HAZs in 9 wt.% Cr steels. Creep specimen length (L)/ diameter (D) ratio influence on weld joint, and thermo-mechanical treatment effects on joint of other steels.

3. Creep tests on thick specimen having actual size of the components to correlate creep data obtained from small specimens. Thickness of the joint led to alter the constrains in the joint.

4. Influence of weld joint geometry on type IV cracking behaviour under fatigue loading conditions needs to be studied. Since, type IV cracking also been observed under fatigue studies.

5. Atom probe tomography studies on processed and creep exposed materials to assess its microstructural constituents.

ABSTRACT

Ferritic-Martensitic (F/M) 9 wt.% Cr steel is an important member of the Cr-Mo F/M family of steels. Fusion welding technique is generally employed to fabricate the power plant components using grade 91 and 92 steels. The weld joint consists of weld metal (WM), heat affected zone (HAZ), and base metal. The HAZ consists of coarse prior-austenite grain (CGHAZ), fine prior-austenite grain (FGHAZ), and intercritical (ICHAZ) region. The premature creep failure of the weld joint is a life-limiting factor for the high-temperature power plant components that experience high temperature and low stress by predominantly localized creep cavitation and deformation at the ICHAZ/FGHAZ (Type-IV cracking). Mechanism pertaining to type IV cracking is not fully understood. Effects of heterogeneous microstructure and creep behaviour have been assessed to understand the loss of creep strength of the weld joint and premature failure by type IV cracking as compared to its base metal.

Addition of boron to 9 wt.% Cr steel is known to improve the creep rupture strength of the steel. However, controlling the nitrogen content is important to avoid the formation of boron nitride (BN) during normalizing heat treatment so that free form of boron is available in the matrix. The steel with different combinations of boron and nitrogen content have been developed. The tensile and creep deformation behaviour on base metal and weld joints have been studied over a wide range of temperatures. TMT processing in austenite phase field is generally introduced to influence the martensite transformation on subsequent cooling. Ageing followed by TMT in the austenite phase enhances the MX precipitation in presence of deformation-induced dislocations, which in turn along with the high dislocation density influences the martensite transformation upon cooling. Such an approach has been carried out in modified 9Cr-1Mo steel (P91 steel) to assess its influence on type IV cracking behaviour. The creep rupture behaviour of P92 steel weld joint fabricated by Narrow Gap-TIG (NG-TIG) welding process has been studied at 923 K. Detailed metallography on the creep ruptured weld joint has been performed to gain an insight into the operating failure mechanism based on the evolution of precipitates and cavitation under creep. In addition, creep studies on the effect of geometry of weld joint, i.e., bevel angles and orientation of the joint, have been carried out to assess its influence on type IV cracking.

INTRODUCTION

Materials suitable to sustain aggressive environmental conditions (high temperature and pressure, corrosion/oxidation, and irradiation) are needed to enhance energy efficiency and safety for advanced nuclear reactors as well as for the fossil fuel power plants. Ferritic-Martensitic (F/M) steels containing 9-12 wt.% Cr are used extensively in fossil-fired power plants and steam generators of the nuclear power plant. The F/M steels are also considered for in-core application in sodium-cooled fast reactors (SFR) because of their inherent outstanding void swelling resistance. These materials have adequate high temperature creep strength, less transmutation issues on irradiation, adequate oxidation/corrosion and stress corrosion cracking resistance, good weldability combined with low thermal expansion coefficient and high thermal conductivity as compared to austenitic stainless steels.

9 wt.% Cr steel is an important member of the Cr-Mo F/M family of steels and is used extensively in power plants as re-heater and super-heater tubes and headers and fuel cladding in the nuclear power plants. These steels (Grade 91 and Grade 92) derive their high temperature creep strength from the tempered martensitic lath structure, phase transformation induced high dislocation density, presence of $M_{23}C_6$ precipitates on prior austenite grain boundaries (PAGB) and martensite interfaces, and MX type of carbonitride precipitates in intra-lath regions and from solid solution hardening. The MX particles are quite resistant to coarsening against creep exposure, but their replacement by coarse Z-phase on long-term creep exposure is a concern. Fortunately MX precipitates in 9 wt.% Cr (Gr.91 and Gr.92) steel are not as much prone to replacement by Z-phase as in the relatively higher chromium steels. The $M_{23}C_6$ carbides coarsen appreciably on creep exposure, which triggers microstructural instability through the

transformation of fine lath structure into sub-grains, with consequent reduction in dislocation density. Development of steels with enhanced high temperature strength by extra low carbon content to reduce the $M_{23}C_6$ precipitation, addition of boron to reduce the coarsening of $M_{23}C_6$ precipitates, and enhancement of MX precipitation through thermo-mechanical treatment are being explored. Fusion welding technique is generally employed to fabricate the power plant components using grade 91 and 92 steels. The weld thermal cycles lead to microstructural changes across different regions that experience different peak temperatures. 9 wt.% Cr F/M steels weld joint consists of weld metal (WM), heat affected zone (HAZ), and base metal. The HAZ consists of coarse prior-austenite grain (CGHAZ) region adjacent to weld metal, fine prior-austenite grain (FGHAZ) region, and intercritical (ICHAZ) region that merges with the unaffected base metal (BM) in the order away from weld metal. The premature creep failure of the weld joint is a life-limiting factor for the high-temperature power plant components that experience high temperature and low stress by predominantly localized creep cavitation and deformation at the ICHAZ/FGHAZ. Based on the location of cracking in the weld joint, failure in the weld joint has been classified as Type-I (cracking in weld metal), Type-II (across weld metal and HAZ), Type-III (CGHAZ) and Type-IV (either in FGHAZ/ICHAZ). Detailed studies are available in literature on the microstructural variations across the HAZ in the as-welded, post-weld heat treated and exposed (to service or creep test) conditions in multi-pass joints. Worldwide, there are efforts to develop steels that are resistant to type IV cracking. Mechanism pertaining to type IV cracking is not fully understood. Effects of heterogeneous microstructure and creep behaviour have been assessed to understand the loss of creep strength of the weld joint and premature failure by type IV cracking as compared to its base metal. The geometry of the weld joint and orientation of the joint and its influence on type IV cracking are also focus of some studies.

Addition of boron to 9 wt.% Cr steel is known to improve the creep rupture strength of the steel. However, controlling the nitrogen content is important to avoid the formation of boron nitride (BN) during normalizing heat treatment so that free form of boron is available in the matrix. The steel with different combinations of boron and nitrogen content have been developed. The tensile and creep deformation behaviour on base metal and weld joints have been studied over a wide range of temperatures.

Reports are available on increase in creep strength of the steel by enhanced MX precipitation upon subjecting to thermo-mechanical treatment. The high dislocation density in the thermo-mechanically processed steel in austenite phase field leads to accelerated diffusion of elements like carbon. The dislocations act as nucleation sites for the precipitates too. TMT processing in austenite phase field is generally introduced to influence the martensite transformation on subsequent cooling. Ageing followed by TMT in the austenite phase enhances the MX precipitation in presence of deformation-induced dislocations, which in turn along with the high dislocation density influences the martensite transformation upon cooling. Such an approach has been carried out in modified 9Cr-1Mo steel (P91 steel) to assess its influence on type IV cracking behaviour.

Narrow gap welding is extensively used to join thick-walled components because this process offers, low distortion and lower thermal stresses than the conventional arc welding processes. The process involves small included angles in the weld edge preparation, less weld metal, and welding time. In the present investigation, the creep rupture behaviour of P92 steel weld joint fabricated by Narrow Gap-TIG (NG-TIG) welding process has been studied at 923 K. Detailed metallography on the creep ruptured weld joint has been performed to gain an insight into the operating failure mechanism based on the evolution of precipitates and cavitation under creep. In addition, creep studies on the effect of geometry of weld joint, i.e., bevel angles and orientation of the joint, have been carried out to assess its influence on type IV cracking.

The thesis consists of eight chapters. Chapter 1 gives the general introduction and detailed literature reviews pertaining to the present investigations, i.e., development of F/M steels and its type IV cracking behaviour. Chapter 2 gives the details related to composition of steels, heat treatments, weld joint fabrication, experimental procedure and finite element (FE) analysis. In chapter 3, microstructural heterogeneity across the weld joint and its influence on creep deformation and high temperature strength of P91 steel are presented. Influence of boron and nitrogen content combination on tensile and creep behaviour of base metal and weld joints of P91 steel have been presented and discussed in chapter 4. In chapter 5, the effect of thermo-mechanical treatment of P91 base metal to improve the creep resistance of weld joints has been explored. Creep deformation and rupture behaviour of base and weld joints of P92 steel have been discussed to understand the influence of tungsten in the steel in chapter 6. The influence of different weld joint geometries and orientation of the weld joint on type IV cracking have been carried out and discussed in chapter 7 with reference to P91 and P92 steels. In chapter 8, findings and conclusions are summarized along with scope for future work.

CHAPTER 1

Literature Review

1.1 Introduction

This chapter discusses the development of 9-12 wt.% Cr ferritic-martensitic steels for the nuclear and fossil-fired power plants, physical metallurgy of ferritic-martensitic steel, strengthening mechanisms, thermo-mechanical treatment, welding metallurgy, creep behaviour, and issues during long-term service at high temperatures. Various types of cracking in the weld joint of these steels during creep and long-term service exposure are discussed with special emphasis on type IV cracking. Several important factors responsible for the deterioration of creep properties of welded joints and methods to reduce type IV cracking susceptibility are reviewed in this chapter, thus bringing out the impetus for the work taken up in the scope of the present thesis.

1.2 Development of 9-12 wt.% Cr ferritic-martensitic steels

The development of 9-12% Cr steels has originated from the manufacture of 12%Cr steel for steam turbine blades in 1912 [1]. The 9-12% Cr steels with additions of C, Mo, W, V, Nb and N elements possessing higher creep strength combined with good oxidation and corrosion resistance at elevated temperatures have subsequently been developed for petrochemical and chemical plants, and nuclear fission and fusion reactor components [2-8]. The 9Cr-1Mo (T9 or Grade 9) type steel possessing moderate creep strength was initially developed for high temperature applications [2, 9]. This steel was further alloyed with Nb and V to obtain higher strength. 9Cr-2Mo (EM12) steel consisted of duplex microstructure structure containing delta ferrite that led to poor impact toughness. 12Cr-1Mo steel developed around the same time, possessed lesser creep strength than EM12 at higher temperature >520°C due to high carbon content and it is difficult to weld. Between 1975 and 1980, Grade 91 steel possessing excellent mechanical properties was developed together by the Oak Ridge National Laboratory (ORNL) and Combustion Engineering (currently named as Alstom Power Inc.) by optimizing the V, Nb, and N content [2, 9-11]. This steel has superseded both EM12 and 12Cr-1Mo (X20CrMoV12-1) steels. The evolution of grade 91 steel has attracted the attention for the choice of material for boilers and pressure vessels. In 1983, Grade 91 steel gained an initial acceptance in the ASME Boiler and Pressure Vessel Code for tubing in Section I construction in Code Case 1943. The steel in the succeeding years has seen broad applications in both the power and petrochemical industries. Further research on these steels have led to the development of other advanced 9-12Cr ferritic steels, that led to the introduction of new alloys by addition of tungsten that claims to have modest strength advantages over Grade 91 steel, *viz.,* Grade 122, Grade 92 and Grade 911 [2,9-12]. Advanced steels having tungsten, cobalt and boron content, and low carbon content are being developed with the aim of achieving creep rupture strength of 150 MPa at 873 K for 10^5 h [9]. Different 9-12 wt.% Cr ferritic-martensitic steels have been summarized in Fig. 1.1, along with their creep rupture strength for 10^5 h at 873 K. The typical chemical compositions of 9-12 wt.% Cr steels are given in Table 1.1 [9,11-12]. Figure 1.2 shows the allowable stress for various steels obtained by extrapolating the data 2/3rd of rupture stress with time to 10^5 h [12].

1.3 Physical metallurgy of 9-12 wt.% Cr steels

The 9-12 wt.% Cr ferritic-martensitic steels are austenized to obtain fully austenite phase or it forms duplex structure (austenite and δ-ferrite) upon heating. The austenite transforms to martensite upon normalizing, i.e., cooling in the air environment or rapid quenching in liquid media. The normalized steels are further tempered to obtain good

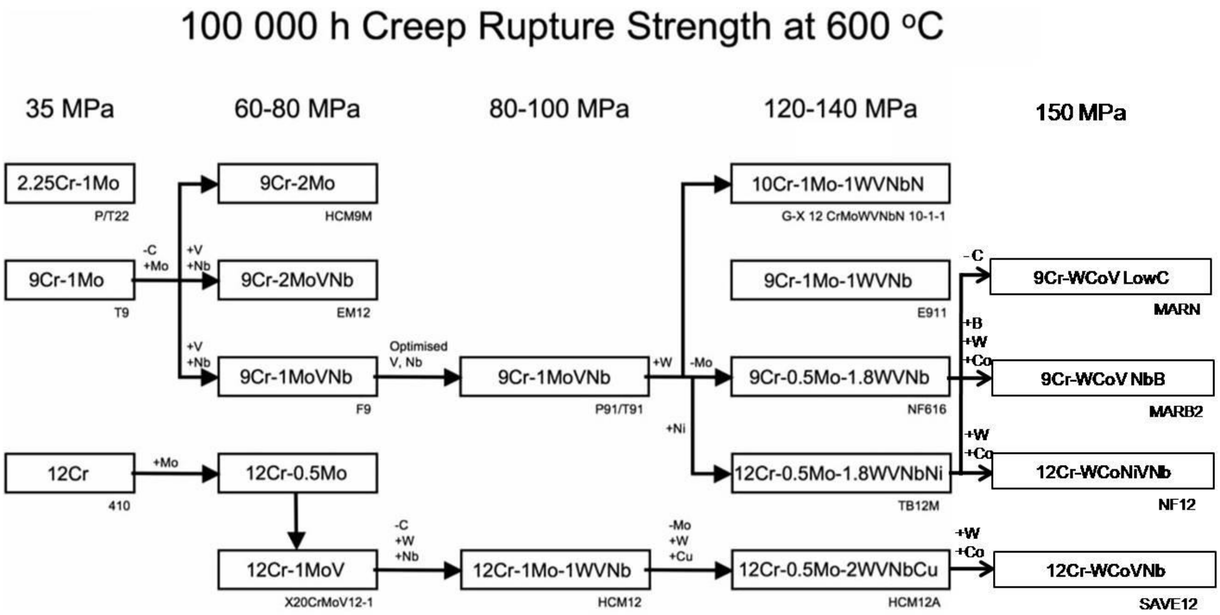

Fig. 1.1 Creep rupture strength of different 9-12 wt.% Cr steels for 10^5 h at 873 K [9,11].

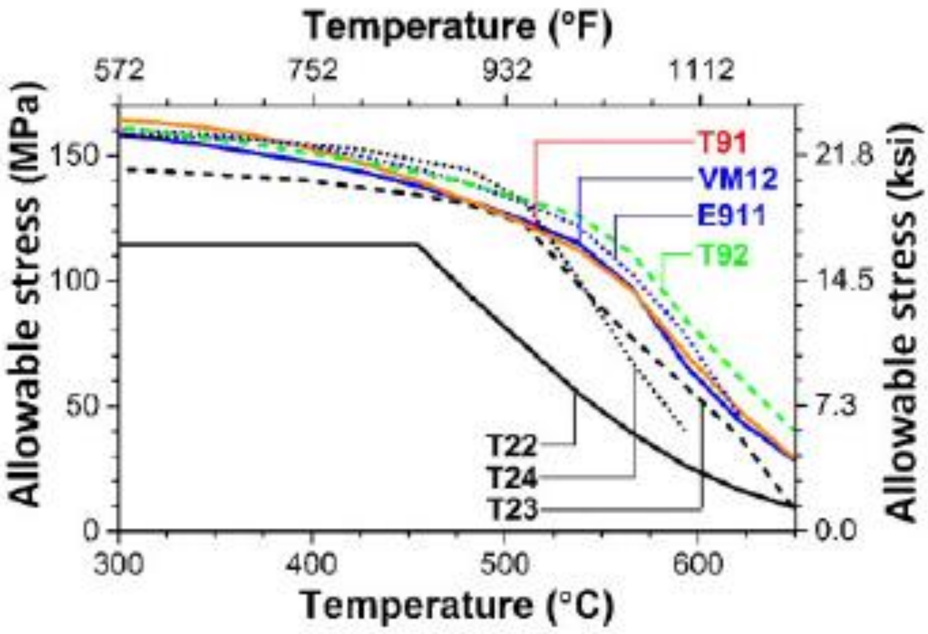

Fig. 1.2 Allowable stress for various alloys with temperature capabilities [12].

Table 1.1: Typical chemical composition of 9-12 wt.% Cr steels, and rupture stress (MPa) for 10^5 h at 873 K for various steels [9,11,12].

Elements / Steels	**C**	**Mn**	**Si**	**Cr**	**Mo**	**V**	**Nb**	**N**	**W**	**Co**	**Cu**	**Ni**	**B**	**S**	**P**	**Rupture stress for 10^5 h / 873 K (MPa)**
ASME T9	0.12	0.45	0.6	9.0	1.0	-	-	-								
HCM9M	0.07	0.45	0.3	9.0	2.0	-	-	-								
EM12	0.10	0.10	0.4	9.0	2.0	0.30	0.40	-								
X20CrMoV-12-1	0.20	0.60	0.4	12.0	1.0	0.25	-	-								59
ASMEP/T91	0.10	0.45	0.4	9.0	1.0	0.20	0.08	0.05						≤0.010	≤0.020	94
HCM 12	0.10	0.55	0.3	12.0	1.0	0.25	0.05	0.03	1.0					≤0.010	≤0.020	75
GX12CrMoWVNbN-10-1-1	0.13	0.60	0.3	10.5	1.0	0.23	0.08	0.05	1.0					≤0.010	≤0.020	115 *
NF616 (ASME P/T92)	0.07	0.45	0.1	9.0	0.5	0.22	0.05	0.06	1.8	-	-	-	0.004	≤0.010	≤0.020	113
HCM12A (ASME P/T122)	0.11	0.60	0.1	12	0.4	0.20	0.05	0.06	2.0	-	1.0	0.25	0.003	≤0.010	≤0.020	101
SAVE12	0.10	0.20	0.3	11.0	-	0.20	0.07	0.04	3.0	3.0				≤0.010	≤0.020	

*estimated

combination of strength, ductility, and toughness by tempering the martensite. The Fe-Cr equilibrium phase diagram is shown in Fig. 1.3 [1]. The austenite (γ-Fe) loop is present up to 12 wt.% Cr. Beyond this ferrite phase (α) is present up to high temperature. However, additions of austenite and ferrite stabilizing elements lead to expansion and contraction the γ-Fe loop respectively. Austenite stabilizing elements are C, N, Ni, Mn, Cu, and Co. The ferrite forming elements are Cr, Mo, Si, V, W, Nb, Al, and Ti. Ferrite forming elements increases the tempering resistance of the steel, addition of more ferrite elements alloying in the steel may lead to formation of δ-ferrite. Presence of δ-ferrite phase leads to restricting the growth of austenite grains but it decreases the strength and toughness of the steel. Influence of addition of austenite and ferrite forming elements on the δ-ferrite content is given in Table 1.2.

The 9-12 wt.% Cr ferritic-martensitic steels are used in the normalized and tempered condition (Fig. 1.4) [13,14]. The steels are used in the high temperature components of nuclear and fossil fired power plants industries. The choice is based on its (i) good high temperature creep strength, (ii) higher thermal conductivity and lower thermal expansion coefficient than austenitic stainless steels, (iii) immunity to stress corrosion cracking in aqueous and chloride environment and (iv) relatively good weldability [15-40]. 9-12 wt.% Cr ferritic-martensitic steels are normalized at 1313-1353 K and tempered below 1073 K. Microstructure constituents in the steels, i.e., fully martensite (M) or martensite + δ-ferrite duplex structure is predicted using Ni and Cr equivalents in Schaeffler-Schneider diagram (Fig.1.5) [10]. δ-ferrite formation in high chromium martensitic steel is avoided by maintaining Cr equivalent to less than 9 (wt.%) [10]. Ni and Cr equivalents are given below.

Ni *equivalent* (wt.%) = (%Ni) + (%Co) + 0.5(%Mn) + 0.3(%Cu) + 30(%C) + 25(%N)

Cr *equivalent* (wt.%) = (%Cr) + 2(%Si) + 1.5(%Mo) + 5(%V) + 1.75(%Nb) + 0.75(%W) + 1.5(%Ti) + 5.5(%Al)

Table 1.2 Effect of alloying elements on change in the δ-ferrite (%) content in microstructure constituents of the 9-12 wt.% Cr steels [1].

Element	N	C	Ni	Co	Cu	Mn	W	Mo	Si	Cr	V	Al
Change in δ-ferrite (%) content, by alloying (wt.%)	-220	-210	-20	-7	-7	-6	+3	+5	+6	+14	+18	+54

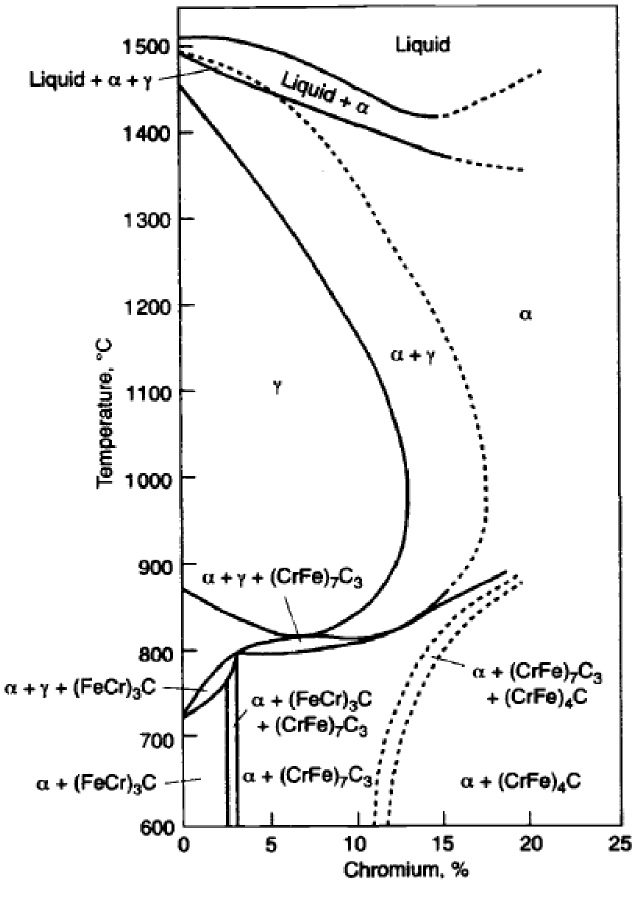

Fig. 1.3 Effect of chromium content on the Fe-Cr-C (0.1 wt.%) alloy [1].

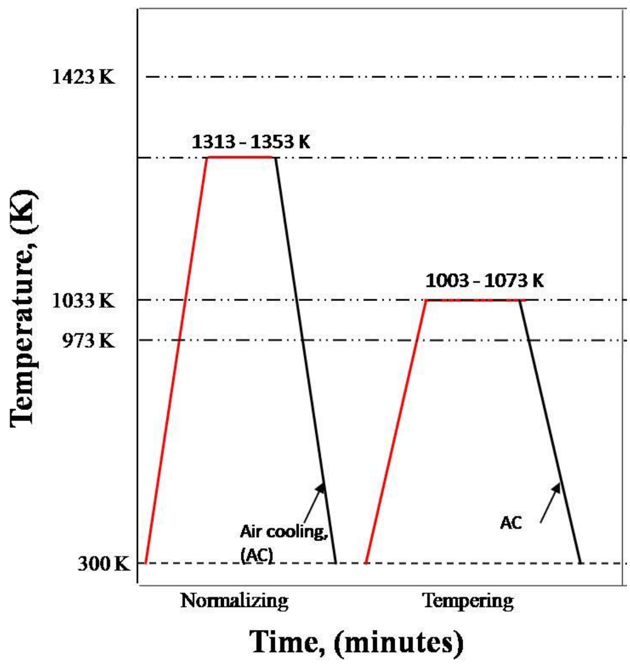

Fig. 1.4 Normalizing and tempering treatment of 9-12 wt.% Cr steels [14].

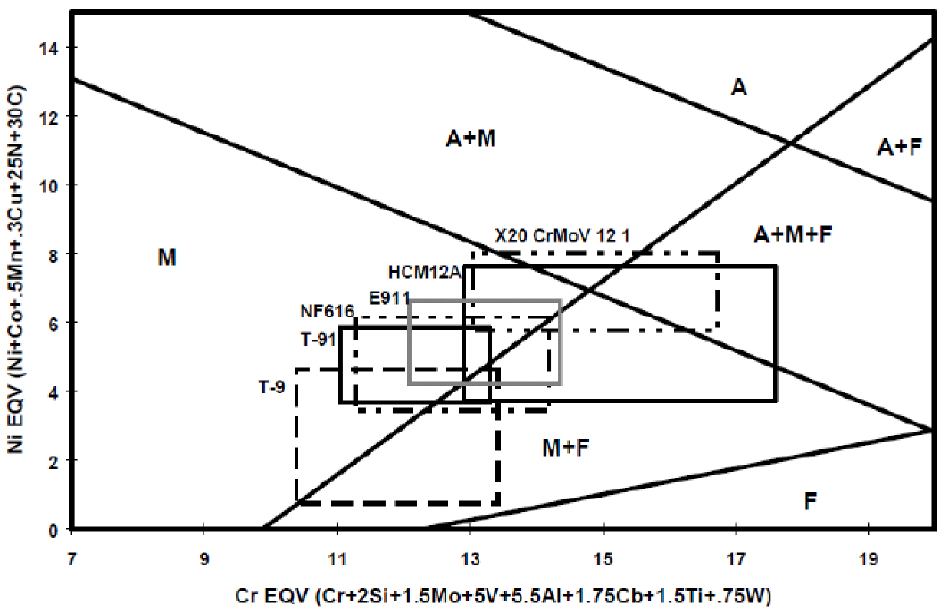

Fig. 1.5 Modified Schaeffler diagram showing the presence of martensite (M), ferrite (F) and austenite (A) phase changes with Ni and Cr equivalent for selected 9-12 wt.% Cr steels [10].

1.3.1 Effects of alloying elements

Alloying elements present in 9-12 wt.% Cr steels and their roles in the physical metallurgy and high temperature creep strength of these steels are given in Table 1.3 [1-7,40].

Chromium is the main alloying element that provides solid solution hardening, and it forms carbides that restrict the movement of dislocations and boundaries. Molybdenum and tungsten are added to impart solid solution strengthening in the steel. Their content is limited by the Mo equivalent, i.e., Mo+0.5W (wt.%), which if > 1%, results in precipitation of Laves phase. Vanadium and Niobium are added to obtain MX carbide/nitride/carbonitride precipitates; these are more resistant to coarsening than higher carbides and contribute to strengthening by impeding the movement of dislocations and sub-boundaries. Nitrogen is added to form VN precipitates, however the ratio of Al:N is to be maintained (below 4) to avoid formation of AlN which results in premature failure of the components. Boron and phosphorus segregate at the interfaces. Boron is added in small quantity, at ppm level, which decreases the coarsening of $M_{23}C_6$ precipitates by combining with vacancies to reduce the self-diffusion coefficients of matrix. It forms Cottrell atmosphere that decreases the creep deformation resistance. Nickel and manganese are added to ensure 100% austenite phase formation during the austenisation treatment without δ-ferrite formation. Ni improves the toughness but degrades the creep strength by acceleration of $M_{23}C_6$ precipitates coarsening. Copper is added to replace Ni partially and enhances the creep strength. Addition of C, N, W, V, Nb, Ti provides precipitation hardening. The precipitation of Laves and Z-phase causes loss of long-term creep strength of the steel. This is due to reduced solid solution strengthening effects resulting from removal of solutes from the solution. Large particles of Z-phase also form at the expense of finely dispersed VN, it has largely been associated with the degradation of 10-12 wt.% Cr steels such as P122. This leads to the formation of a VN free zone around the prior austenite boundaries by the Ostwald coarsening mechanism and leads to loss of creep strength under long-term exposure.

Table 1.3 Roles of alloying elements in creep strength of 9-12 wt.% Cr ferritic steels [1-7,40].

Element	Merit	Demerit
C	Necessary to produce $M_{23}C_6$ and NbC; Increase hardenability.	
Cr	Improve oxidation resistance; lower M_s; Raise Ac_1; Main element in $M_{23}C_6$.	Increase *D**
Mo	Lower M_s. Raise Ac_1; Solid solution hardening.	Accelerate growth of $M_{23}C_6$. Laves phase
W	Lower M_s; Raise Ac_1; Delays coarsening of $M_{23}C_6$ particles; solid solution hardening.	Laves phase
V	Form MX and contribute to strengthening.	
Nb	Form MX and contribute to strengthening, grain refinement.	Promote precipitation of Z Phase.
Mn	Ensure full austenisation, Suppress δ-ferrite formation	Increase *D** and reduce creep strength; Lower Ac_1; Promote M_6C precipitation.
N	Necessary to produce VN.	
Si	Improve oxidation resistance.	Increase *D** and reduce creep strength.
Ni	Improve toughness.	Increase *D** and reduce creep strength; lower Ac_1.
Re	Prevent loss of creep rupture strength; Lower M_s.	Lower Ac_1.
Cu	Suppress δ-ferrite formation.	Promote precipitation of Fe_2M (Laves phase).
B	Improve creep strength and quench hardenability; Stabilize $M_{23}C_6$ particles and delay their coarsening.	Reduce impact toughness.
Al		Formation of AlN; deprive the steel of MX precipitate.
Co	Suppress δ-ferrite formation; Decrease *D**.	
*D** - diffusion coefficient of carbon in ferrite matrix.		

1.3.2 Continuous cooling transformation for modified 9Cr-1Mo steel

Fig. 1.6 shows the continuous cooling transformation (CCT) diagram for modified 9Cr-1Mo steel [15]. The Ac_1 and Ac_3 temperatures are found to be around 1113 and 1193 K respectively. Alloying additions are also adjusted in order to obtain martensite starts (M_s) [1] and finish (M_f) temperature above room temperature, in order to avoid retained austenite. M_s and M_f temperatures ranges are from 523-643 K and 353-463 K respectively. Martensite transformation occurs in a wide range of cooling rates and corresponding microhardness range of 420 to 380 HV. The equilibrium transformation products are ferrite and carbides.

$$M_s(°C) = 550 - 450\,(\%C) - 11\,(\%Si) - 33(\%Mn) - 20(\%Cr) - 17(\%Ni) - 15(\%Mo) - 20(\%V) - 11(\%Nb) - 10(\%W) - 10(\%Cu) + 15(\%Co)$$

Martensite transformation is the diffusionless, shear-dominant, lattice distortive solid state transformation, which is also called as military transformation as the atoms move in an organized manner relative to their neighbor in contrast to diffusion transformations. The strain energy arising from shear displacement decides the morphology and kinetics. Morphology of ferrous martensite is characterized by lath and plate forms. In general, plate martensite forms in high carbon and high alloy steels, which is characterized by internal structure consisting of a single set of twins that extend completely across the plate to the interfaces. Lath martensite found in low carbon steels (typically <0.4 wt.%) are not twinned internally but contain high dislocation density estimated to be $\sim10^{15}$ m/m^3, which implies considerable plastic accommodation during growth. Tempering treatment is essential for martensite formed from austenite at below Ac_1 temperature to avoid re-austenisation as well as to achieve tailored combination of strength and toughness. Ni, Mn, Co decrease Ac_1 temperature and Si, Mo, Al, V increase the Ac_1 temperature (Table 1.4). During tempering $M_{23}C_6$ and MX precipitates grows at the interfaces and intra-lath regions, and the dislocation density comes down. The precipitates observed generally in the normalized and tempered, aged and creep rupture high chromium martensite steels are given in Table 1.5 [1,6].

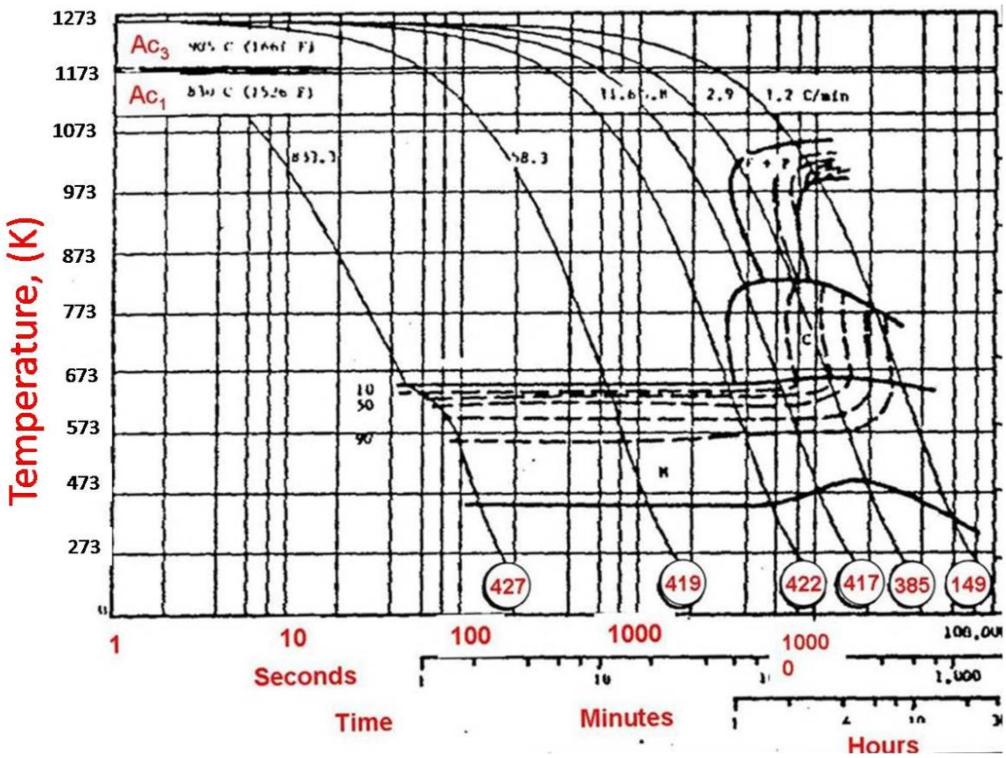

Fig. 1.6 Continuous cooling transformation diagram of modified 9Cr-1Mo steel [15].

Table 1.4 Effect of alloying elements on Ac_1 temperature of 12 wt.% Cr steels [1].

Elements	Ni	Mn	Co	Si	Mo	Al	V
Change in Ac_1 (°C) per mass (%)	–30	–25	–5	+25	+25	+30	+50

Table 1.5 Precipitates observed in the normalized and tempered, aged and creep rupture tested high chromium ferritic-martensite steels [1,6].

Precipitate phase	Typical composition	Distribution of precipitates
$M_{23}C_6$	$(Cr_{16}Fe_6Mo)C_6$ $(Cr_4Fe_{12}Mo_4Si_2WV)C_6$	Coarser particles at prior austenite grain and martensite lath boundaries and fine intra lath particles
MX	NbC, NbN, VN, (CrV)N, Nb(CN) and (NbV)C	Undisolved particles and fine precipitates at martensite lath boundaries
M_2X	Cr_2N, Mo_2C and W_2C	Martensite lath boundaries (Cr_2N and Mo_2C); prior austenite grain boundaries (Mo_2C), intra-lath (Mo_2C, W_2C); ferrite in duplex steels [(Cr_2(CN) and $(Cr,Mo)_2$(CN)]
Z-phase	(Cr,V,Nb)N	Large plate-like particles in the matrix after creep straining
Laves	Fe_2Mo, Fe_2W and $Fe_2(Mo,W)$	Prior austenite grain and martensite lath boundaries and intra-lath; δ-ferrite in duplex steels
η-carbide	M_6C $(Fe_{39}Cr_6Mo_4Si_{10})C$	Prior austenite grain, martensite lath boundaries and intra-lath region

1.4 Strengthening mechanisms in 9-12 wt.% Cr steels

Microstructure of 9-12 wt.% Cr steel in the normalized and tempered condition exhibiting tempered martensite structure is shown in Fig. 1.7 [6,41]. The microstructure is hierarchical consisting of prior-austenite grain boundaries, packet boundaries within the prior-austenite grain boundaries (PAGB), martensite block boundaries within packet boundaries, parallel lath boundaries (sub-boundaries) and transformation induced dislocations within the martensite blocks (Fig. 1.7 (b)). $M_{23}C_6$ precipitates decorate the prior austenite grain boundaries, and MX precipitates are mainly in the intra-lath regions. Schematic of ferritic-martensitic steel microstructure is shown in Fig.1.8. The high temperature strength of the steel arises from the tempered martensitic lath structure, phase transformation induced high dislocation density, presence of $M_{23}C_6$ precipitates on prior austenite grain boundaries and martensite interfaces and MX type of carbonitride precipitates in intra-lath regions and from solid solution hardening from molybdenum, tungsten [6,7,14-41]. Thus, the contributing strengthening mechanisms in the 9-12 wt.% Cr steels are solute hardening, dislocation hardening, precipitation hardening and boundaries hardening [2,12]. However, quantification of contributions from each mechanism for the enhancement in strength is difficult.

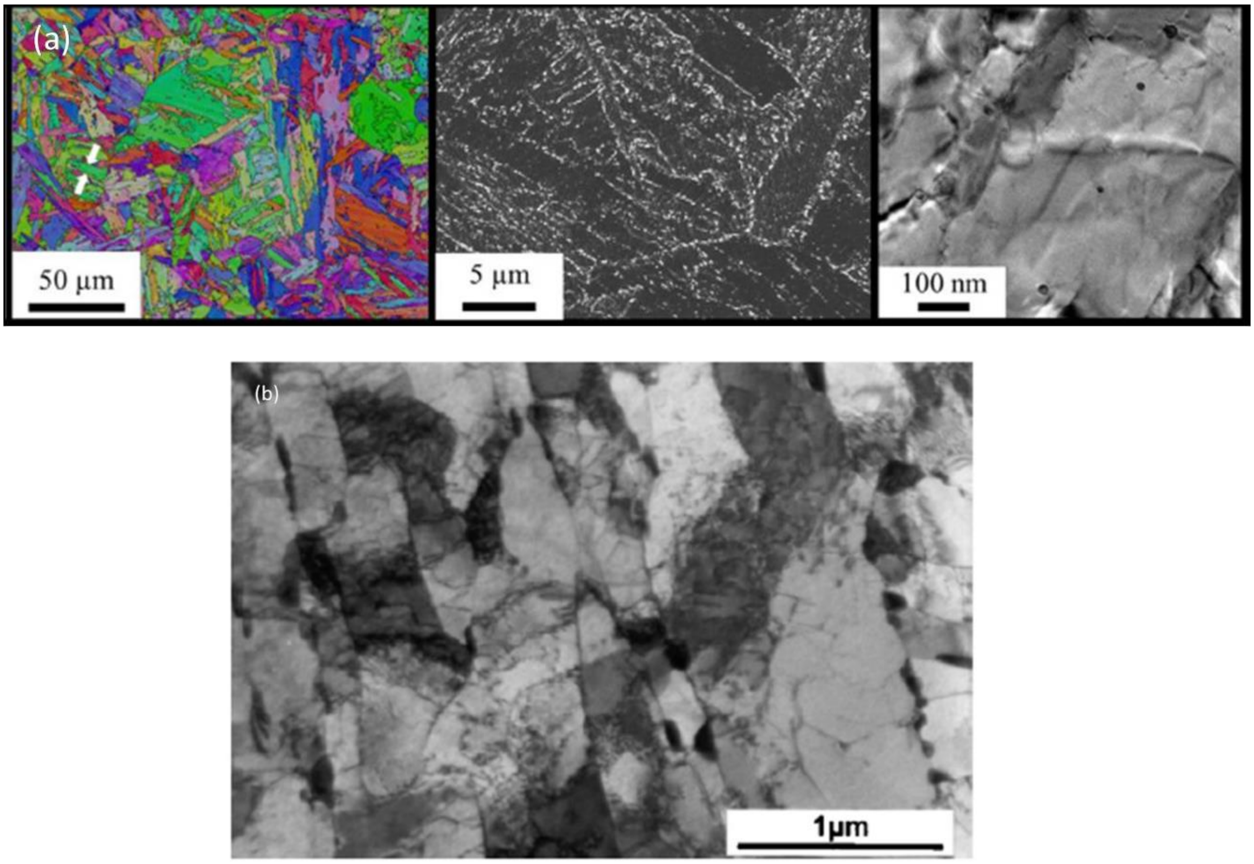

Fig. 1.7 (a) SEM-EBSD and TEM micrographs [41], (b) TEM micrograph [6] in the normalized and tempered 9-12 wt.% Cr steel shows the prior austenite grain, packet and block boundaries, precipitates and dislocations.

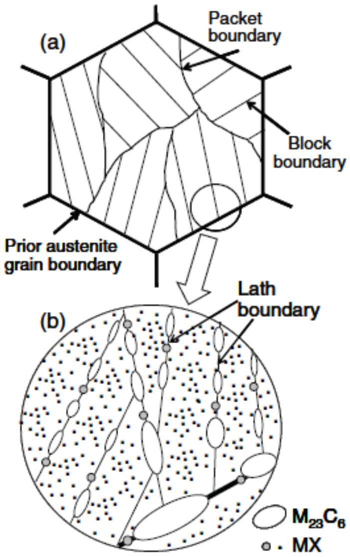

Fig. 1.8 Schematic of tempered martensitic microstructure of 9-12 wt.% Cr steels [4].

Solid solution strengthening based on Hume-Rothery size effect is employed for obtaining the higher strength that arises due to restricting the easy motion of atoms and dislocations. Substitutional solute atoms such as Mo and W have been favored as robust solution hardeners for 9-12 wt.% Cr steels because of its larger atomic sizes in comparison with the solvent iron atom (size difference effect). In the 9-12 wt.% Cr steel, Mo and W are added to impart substantial solution strengthening [4,6].

Dislocation strengthening occurs due to the interaction of dislocations with each other that impede the subsequent movement of dislocations. Dislocation strengthening can be estimated in general from the overall dislocation density that is the length (l) of dislocation per unit volume (l^3). It is an important strengthening mechanism in steel at ambient temperatures. Dislocation hardening is given by

$$\sigma_p = 0.5\ MGb(\rho_f)^{1/2}$$

Where ρ_f is the free dislocation density in the matrix, M is the Taylor factor, G is the shear modulus, b is the magnitude of Burgers vector. 9-12 wt.% Cr ferritic-martensitic steels usually contain high dislocation density in the normalized condition as well as after tempering treatment; it is in the range of 1 to 10×10^{14} m^{-2} in the matrix [4, 6]. At elevated temperatures, recovery of dislocations and recrystallisation of deformed structures occurs leading to softening of the matrix. This causes loss of creep strength significantly at long duration. Hence, dislocation hardening is useful for short-term creep strengthening but it is not useful for increasing the long-term creep strength without particles at elevated temperatures [4, 6].

Precipitate hardening is a strengthening of one phase by another phase finely dispersed in it. On quenching excess solute should be available in the solution, so that the precipitation occurs on heating at the elevated temperature (tempering temperature). 9-12 wt.% Cr creep resistant steels usually contain different types of precipitates i.e., carbides and carbonitride as $M_{23}C_6$, M_6C, M_7C_3, MX and M_2X, where M denotes a metallic element and X is carbon and/or nitrogen atoms, and intermetallic compounds of Fe_2(Mo,W) Laves phase, $Fe_7W_6\chi$ phase, or χ phase. The MX type of precipitate stabilizes the free dislocations by impeding it for dislocation hardening and the $M_{23}C_6$ type of precipitate stabilize the subgrain structure to minimize the preferential recovery around the prior austenite grain boundary (sub boundary hardening) (Figs. 1.7 and 1.8) [4,6,40]. Several mechanisms have been proposed for the stress required (threshold stress) for a dislocation to pass through precipitate particles, such as the Orowan mechanism, local climb mechanism, general climb mechanism [4,6]. The Orowan stress σ_{or} is given by

$$\sigma_{or} = 0.8\ MGb/\lambda_p$$

where, λ_p is the mean interparticle spacing. The major precipitates present in the tempered martensite 9-12 wt.% Cr steels, and the corresponding Orowan stress estimated from the values of interparticle spacing are listed in Table 1.6 [4].

Table 1.6 Volume percent, diameter and inter particle spacing of different precipitate in 9-12 wt.% Cr steel, and Orowan stress estimated from the value of interparticle spacing [4].

Particle	**Volume percent, V (%)**	**Diameter, d_p (nm)**	**Spacing, λ_p(nm)**	**Orowan stress, σ_{or} (MPa)**
Fe_2(W, Mo)	1.5	70	410	95
$M_{23}C_6$	2	50	260	150
MX	0.2	20	320	120

In general, $M_{23}C_6$ (face centre cubic) carbide is the major precipitate found in 9-12 wt.% Cr steels in the normalized and tempered conditions mainly on prior austenite grain boundaries and sub grain boundaries, and smaller in size and quantity has been found in the martensite lath interiors (Fig. 1.8). $M_{23}C_6$ carbides completely dissolve at 1243 K and above (Fig. 1.9). It forms very rapidly during tempering which is about 50 nm in size [3-7,40]. $M_{23}C_6$ are rich in chromium with iron and molybdenum in modified 9Cr-1Mo steel, nickel has been substituted partially for chromium. $M_{23}C_6$ carbides increase the strength of the steel by retarding the sub-grain growth.

The most important precipitate strengtheners in the interior of the subgrains are the MX (NaCl face centred cubic structure) type that forms inside the lath boundaries. These are generally finer and more stable than $M_{23}C_6$ carbides. MX precipitates form during both austenisation and tempering. Secondary MX precipitates form during tempering as fine (about 20 nm in size) spherical NbX and platelet VX particles distributed uniformly inside the sub-grains and on sub-grain boundaries. The primary precipitates are NbX, which remain undissolved during austenisation. These act as the nucleation sites for the plate-like V-rich nitrides (V-wing complexes) that form during creep on the fine primary NbX particles [3]. The secondary MX precipitates are vanadium rich. Primary MX precipitates retard the growth of austenite grain boundaries during austenisation as well as ensure the creep strength by retarding the recovery of martensite lath during tempering. These precipitates not only increase the strength due to the pinning of free dislocations retarding the movement of dislocations but also slow down the recovery of the dislocation substructure, thus retaining the dislocation hardening for longer durations (Fig.1.10). M_2X and M_6X believed to be undesirable phases found in modified 9Cr-1Mo steel. These particles may dissolve or be replaced by the more stable MX type precipitates.

The Z-phase {Cr(Nb,V)N} precipitation occurs during long-term creep exposure. Precipitation of Z-phase causes loss of long-term creep strength because it consumes MX cabonitrides which are important strengtheners [16-19]. Z-phase in 9-12%Cr martensitic steels was first properly described in 1996 [42] stating that the Z-phase was the thermodynamically stable nitride in 11-12 wt.% Cr martensitic steels. It has been reported that the formation of Z-phase occurs around prior austenite grain boundaries/packet boundaries. It is important to note that the Z-phase formation in the gauge portion of the crept specimens is two to four times higher than that in the grip portion. Stress/strain accelerates the Z-phase precipitation during creep exposure. In general, mean metallic composition of Z-phase in steels are V=32 to 36 wt.%, Cr= 44 to 49 wt.%, Nb= 11 to 19 wt. %, Fe=4 to 5 wt.% [16-19].

Boundary hardening Boundaries are the regions of disturbed lattice. Normalized and tempered 9 wt.% Cr steel microstructure consists of martensite lath and blocks decorated with fine carbonitride precipitates on the boundaries and also in the matrix. Creep strength of 9%Cr steels is inversely correlated with martensite lath width. The lath and block boundaries (considered as elongated subgrains) result in sub boundary hardening given by [4].

$$\sigma_{sg} = 10\ Gb/\lambda_{sg}$$

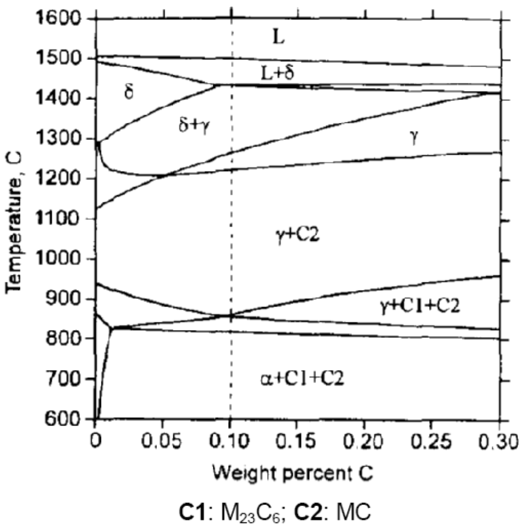

Fig. 1.9 Isopleth phase diagram of P91 steel [41].

Where λ_{sg} is the short width of the subgrains. Here, λ_{sg} corresponds to the width of the lath, which is generally in the range of 0.3 to 1 μm in the normalized and tempered 9-12 wt.% Cr steels. σ_{sg} has been estimated to impart 320 to 530 MPa strength using the values of G = 64 GPa at 923 K, b = 0.25 nm and λ_{sg} = 0.3 to 0.5 μm, which is higher than the Orowan stress (Table 1.6) due to Fe_2(W, Mo), $M_{23}C_6$ and MX. Sub boundary hardening enhanced the creep strength of 9 wt.% Cr steel in the long term, by the distribution of fine precipitates along the boundaries [4].

Another method by which boundary strengthening can be achieved is the thermo-mechanical treatment (TMT) process [43]; the studies are focusing towards improvement of creep resistance by grain boundary engineering [43]. The fraction of coincident site lattice (CSL) or special boundaries led to strengthen the grain boundaries against sliding and deformation, which improves the creep resistance. Enhancement of CSL boundaries by thermo mechanical treatment process has been established for modified 9Cr-1Mo steel resulting in creep rates lower by a factor of 3-4 than the as-received condition in the stress range of 200-235 MPa at 773-823 K [43]. However, fabrication of components using this material without deterioration in its properties is a difficult issue.

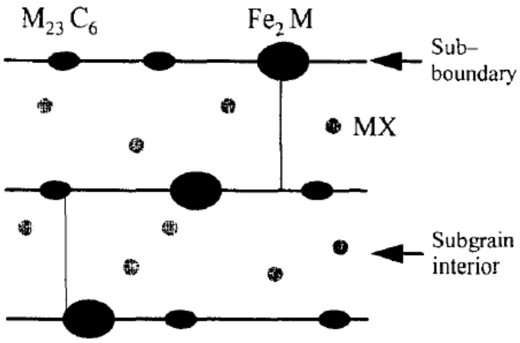

Fig. 1.10 Schematic illustrations of precipitates in high chromium ferritic steel [40].

1.5 Welding metallurgy of 9-12 wt.% Cr ferritic-martensitic steels

Fusion welding is the technique generally employed to fabricate the nuclear and fossil power plants components from 9-12 wt.% Cr ferritic-martensitic steels in the normalized and tempered condition. In general, the arc welding techniques such as tungsten inert gas welding (TIGW), manual metal arc welding (MMAW) or shielded metal arc welding (SMAW), flux cored arc welding (FCAW), submerged arc welding (SAW), electron beam welding (EBW) and laser beam welding (LBW) processes are used to join 9-12 wt.% Cr steels [9,11,12,23-33]. However, in arc welding processes in the case of thick plate/pipe weld joint fabrication, the root pass of the joint is usually carried out by using TIG welding technique (Fig.1.11). Filler metals for welding are to match the creep strength of the base or parent material in the service. The work piece is preheated to avoid cracking on cooling after welding. Welding procedure for 9-12 wt.% Cr steels weld joint fabrication is shown in Fig. 1.11. The choice of welding process depends on whether the component is to be fabricated in workshop or in situ [9,11,12]. Post weld heat treatment (PWHT) is recommended after welding for tempering of martensitic microstructure and to reduce the stress induced by welding.

Although significant improvements in development of ferritic steels for high temperature applications have been achieved by alloy modification, precipitation and boundaries hardening, these weld joints are inferior to the base metals at high temperature

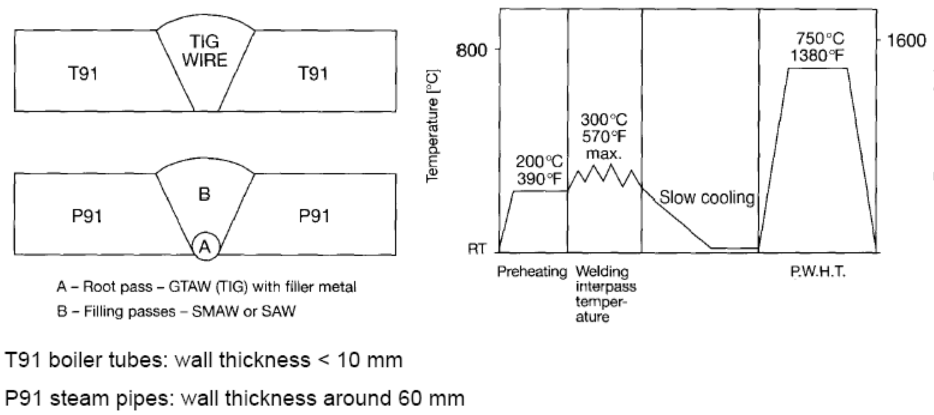

Fig. 1.11 Schematic representation of weld joint and thermal cycles for T/P91 steel joint fabrication [11,12].

service condition, which leads to premature creep failure in the HAZ (Type IV cracking) especially in thick welded components. Although the base metal loses the creep strength due to preferential recovery around the prior austenite grain boundary and Z-phase formation (Fig.1.12), majority of the creep failures in pressurized components are associated with the weld joints, which is one of the serious problems for the 9-12 wt.% Cr ferritic steels of thick section of boiler components [4]. At present, the mechanisms responsible for the premature failure in HAZ of the joints are not clearly understood. It is essential to investigate the relationship between the microstructural characteristics of the HAZ and creep deformation behaviour in order to clarify the mechanisms responsible for premature creep failure at the HAZ especially in the thick welded joints and for the further development of advanced heat resistant ferritic steels.

Thermal cycles during welding introduce changes in the microstructure of the adjacent base metal and the weld deposit. The peak temperature experienced by different regions across the weld joint changes with the distance from the fusion line, and this has significant influence on the microstructure of these regions. According to the welding peak temperature and microstructure, the typical 9-12 wt.% Cr steels weld joint consists of weld

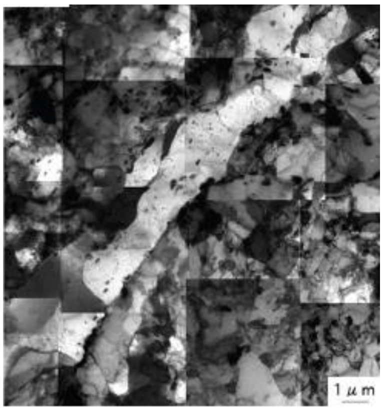

Fig. 1.12 TEM micrograph of T91 steel crept for 34141 h at 873 K and 100 MPa [4].

metal (WM), heat affected zone (HAZ) and base metal as shown in Fig. 1.13 [12]. The HAZ is a transition region between weld and base metals, which can be further subdivided into different zones, namely coarse prior-austenite grain zone (CGHAZ) adjacent to the weld metal, fine prior-austenite grain zone (FGHAZ) and intercritical (ICHAZ) zone. The FGHAZ lies between the CGHAZ and ICHAZ zones. The ICHAZ occurs next to the base metal and is furthest from the weld boundary [9,11,12,25]. The peak temperature reaches well above Ac_3 during welding in the material near to the fusion boundary. The carbides, which constitute the main obstacle to growth of the austenite grains, dissolve during welding resulting in formation of coarse grain austenite. The austenite transforms to martensite on cooling. In the FGHAZ, which is further away from the fusion boundary the peak temperature is lower, but still above Ac_3. Austenite grain growth is limited by the incomplete dissolution of carbides. Hence fine grained austenite is produced, this is subsequently transformed into martensite. In the ICHAZ, peak temperature lies between Ac_3 to Ac_1, resulting in partial reversion to austenite on heating and insignificant dissolution of carbides. The new austenite nucleates during heating at the prior austenite grain boundaries and martensite lath boundaries, where the remainder of the microstructure is simply over tempered. This austenite is transformed into untempered martensite on cooling. Further, away from fusion boundary where the peak temperature is below Ac_1 the original microstructure of the base metal undergoes further tempering. Hence, different peak temperatures experienced by different regions during welding results in different microstructures, grain size, precipitate distribution and its growth rate, which ultimately result in strength heterogeneity across the weld joint and results in premature failure during service at high temperature and stress conditions [25].

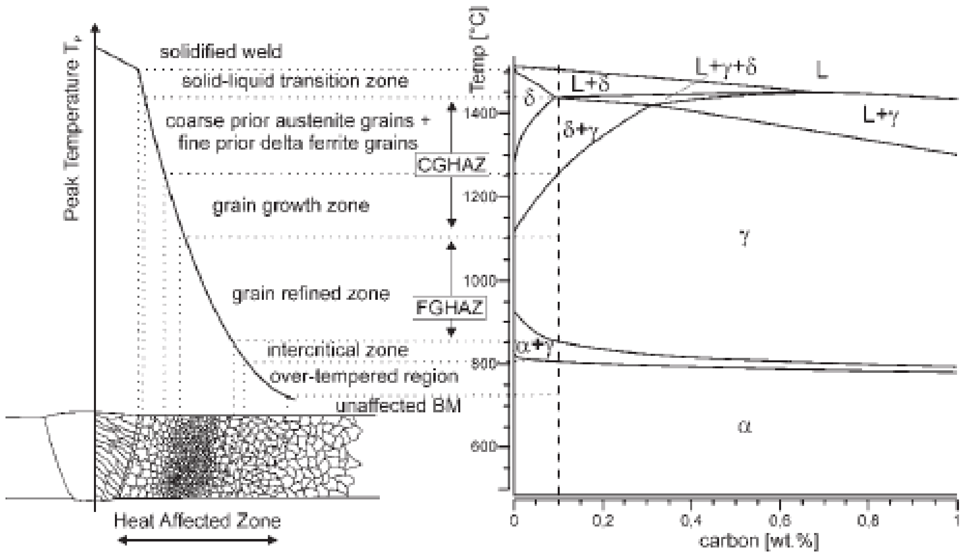

Fig. 1.13 Schematic representation of the HAZ subzones microstructure developed as a function of peak temperature (T_p) during welding and corresponding phase diagram for grade 91 steel [12].

1.6 Creep deformation

Creep of materials is classically associated with time-dependent plasticity under constant stress or load at an elevated temperature generally higher than roughly $0.3T_m$ in a given environment, where T_m is the melting temperature in K. The typical creep curve for constant stress conditions is shown in Fig. 1.14 [44,45]. This consists of three regions: Stage I, or primary creep, which denotes that portion where the creep rate decreases with increasing time or plastic strain due to work hardening. However, with some types of creep such as solute drag, an ‘‘inverted’’ primary occurs leading to increase in the strain rate with strain. At high temperature, another mechanism, viz., recovery, operates which leads to softening of the material. A balance between work hardening and softening due to recovery leads to a constant strain rate. Often, in pure metals, the strain rate is constant over a range of strain. This phenomenon is termed Stage II, secondary, or steady-state creep. However, in engineering alloys, microstructural degradation occurs at high temperatures resulting in absence of steady state creep. Eventually, progressive accumulation of creep damage results in an increase in the apparent strain rate and leads to fracture. This regime is termed Stage III, or tertiary creep. Generally, engineering materials for high temperature are characterized by the steady state (or minimum) creep rate $\dot{\varepsilon}_{min}$ and time to fracture t_r [44,45].

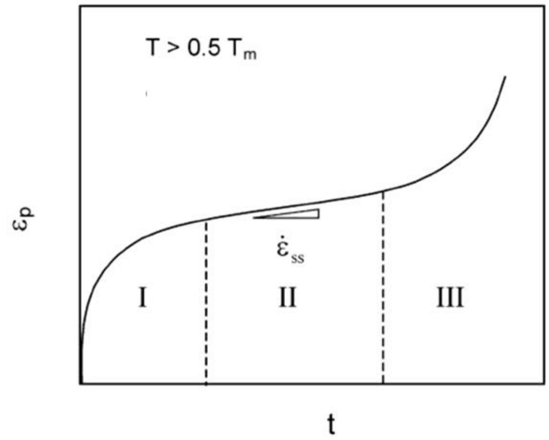

Fig. 1.14 Typical creep curve for constant nominal stress conditions [46].

1.6.1 Deformation mechanisms

Crystalline solid materials deform plastically by various competitive mechanisms depending on the variables of deformation such as stress (σ), temperature (T), and strain rate ($\dot{\varepsilon}$). The deformation mechanisms are described through a deformation mechanism map that summarizes the range of domains consisting of different mechanisms of deformation. The deformation mechanism map, i.e., normalized stress σ/G (where G is the shear modulus) plotted against homologous temperature T/T_m (where T_m is the melting point in Kelvin) is shown in Fig. 1.15. In figure 1.15, H.T. and L.T mean high and low temperature respectively. The deformation mechanism map describes the different dominance domains of rate controlling deformation mechanism [47]. The upper limit of the diagram is described by the ideal shear strength above which deformation becomes elastic and further led to catastrophic.

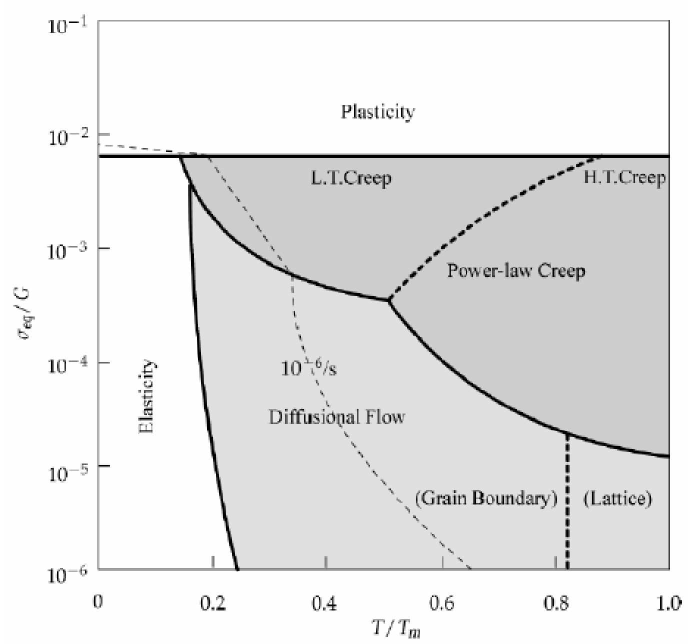

Fig. 1.15 Typical creep deformation mechanism map [47].

Plastic deformation or flow occurs by dislocation glide in the regime below the ideal shear strength. The time dependent deformation, i.e., creep deformation regime is divided into dislocation and diffusion creep regimes. Dislocation creep deformation regime is further divided based on temperature such as high (H-T creep) and low temperature creep (L-T creep) regimes. The creep deformation that occurs by the diffusion is divided into Nabarrow-Herring creep (N-H creep) and Coble creep regions [47].

In the range of intermediate temperatures (*T*) and stresses (*σ*), the creep rate becomes sensitive to stress. This exhibits a power law form as $\dot{\epsilon}_{min}= A\sigma^n$, where *A* is a constant, *n* is the stress exponent, $\dot{\epsilon}_{min}$ is the minimum/steady-state creep rate. In the power law creep deformation regime, dislocations acquire a new degree of freedom at high temperatures, in which the thermal activation assists climb and glide process of dislocation. The glide step is responsible for almost all the creep strain, but the rate-controlling process is the diffusive motion of vacancy or climbing dislocation rather than thermally activated glide.

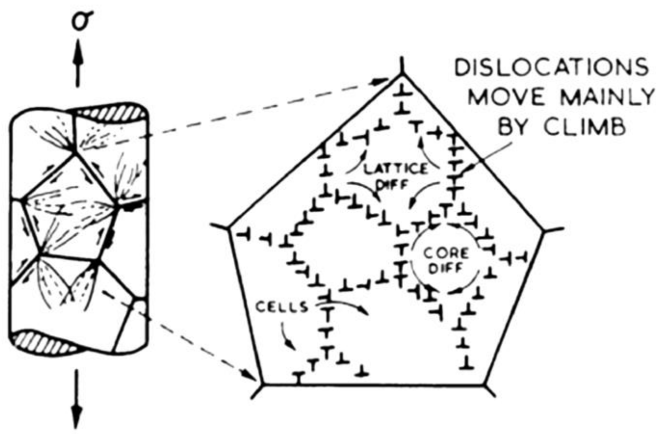

Fig.1.16 Schematic representation of power law creep involving cell formation by climb [47].

Creep in the H-T regime is controlled by lattice diffusion, and the activation energy for creep deformation is close to that of activation energy for self-diffusion. At low temperatures and high stresses, the transport of substance through dislocation core contributes to the overall diffusive transport of the matter (Fig. 1.16) [47].

At high stresses ($\sigma > 10^{-3}$ G), the power-law breaks down, and dependence of strain rate on stress varies exponentially. This region is known as power-law breakdown (PLB), and the plastic flow is glide controlled. At high temperatures and low stresses, creep occurs by diffusion processes and does not involve dislocation movement to generate strain. Creep results from stress directed diffusional transport of matter (Fig. 1.17). At high temperatures, lattice diffusion (N-H creep) controls the rate, while at relatively lower temperatures, grain boundary diffusion (Coble creep) takes over. In both the diffusional creep regimes, creep rate exhibits a linear stress dependency but varies as $D1/d^2$ for N-H creep and Dgb/d^3 for Coble creep. At lower stresses, another creep mechanism known as Harper-Dorn (H-D) creep was observed for larger grain size. In H-D creep, the creep rate exhibits a linear stress dependence but is independent of grain size, and the creep rate is much higher than those possible by the diffusional flow. The mechanism underlying H-D creep is complex, and the most plausible explanation is that of climb controlled dislocation process under conditions such that the dislocation density does not change with stress. Also, at high temperatures, grain boundary sliding takes place to provide plastic strain. Thus, the deformation mechanism map is useful in the following ways: (1) to identify the dominant mechanism by which a structure deforms in service, (2) to determine the constitutive law that can be used in the design, (3) to give inputs for alloy design and selection.

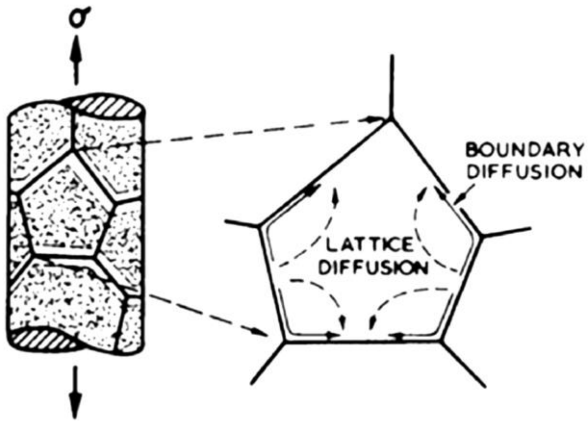

Fig. 1.17 Schematic representation of diffusion flow through and around the grains [47].

The stress is applied in the specimen when it overcomes the inter-atomic forces in a perfect crystal, and it causes the specimen to fracture on a plane normal to the stress axis. The fracture mechanism map illustrating the dominant domains of different fracture mechanism is shown in Fig. 1.18. Almost all crystalline solids fail by cleavage or intergranular brittle fracture if the temperature is sufficiently low [48]; certain FCC metals and alloys appear to be the exceptions. Cracks nucleated by slip, twinning or grain boundary sliding, can propagate catastrophically to give this type of failure.

1.6.2 Creep cavitation during creep

Creep at high temperatures always terminates in fracture by the nucleation, growth and coalescence of cavities [46-51].

Nucleation of creep cavity:

The cavities nucleate at grain boundaries perpendicular to the applied stress, so that failure

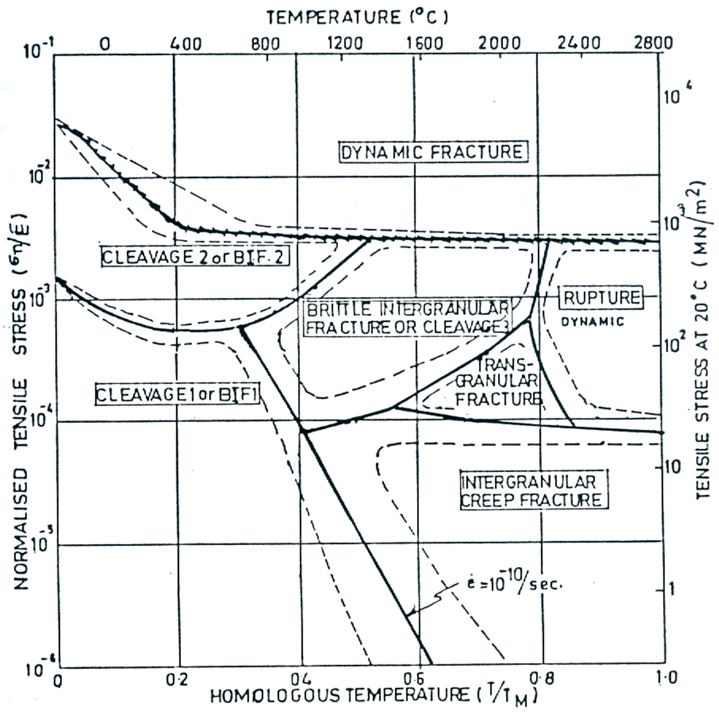

Fig. 1.18 Schematic fracture mechanism map illustrating the dominant domains of different fracture mechanism [48].

occurs in an intergranular manner. Two forms of intergranular cracking are commonly observed. Wedge (or w-type) crack formed at the triple junctions in association with grain boundary sliding (Fig. 1.19); this type of cavities form most easily at higher stresses (lower temperatures) and larger grain sizes when grain boundary sliding is not accommodated [46]. Another mode of fracture associated with grain boundary irregularities such as precipitates, ledges etc, r-type cavities is illustrated in Fig. 1.20. The stress and strain concentration at grain boundary particles due to grain boundary sliding nucleates ‘r’ type of cavities.

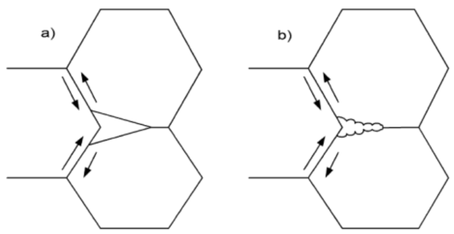

Fig. 1.19 (a) Wedge (or w-type) crack formed at the triple junctions in association with grain boundary sliding; (b) illustrates a wedge crack as an accumulation of spherical cavities [46].

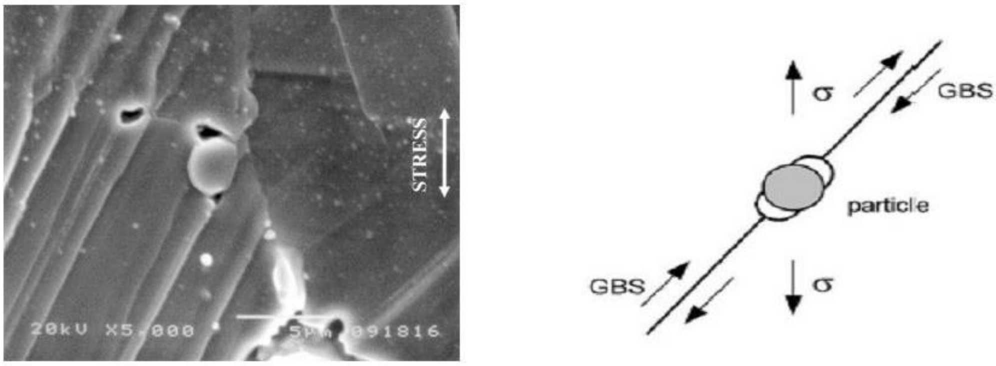

Fig. 1.20 Cavitation (r-type) or voids at a transverse grain boundary, associated with boundary particle [46].

Creep cavity growth (by diffusion)

Once the cavities reach a critical size, growth can occur by absorption of vacancies from the surrounding grain boundaries. Under stress, atoms from cavity surface diffuse and deposit on the grain boundary (Fig. 1.21). Both the grain boundary and cavity surface diffusion and normal stress result in the growth of the nucleated cavity. Macro cracks were found to form by coalescence of these cavities.

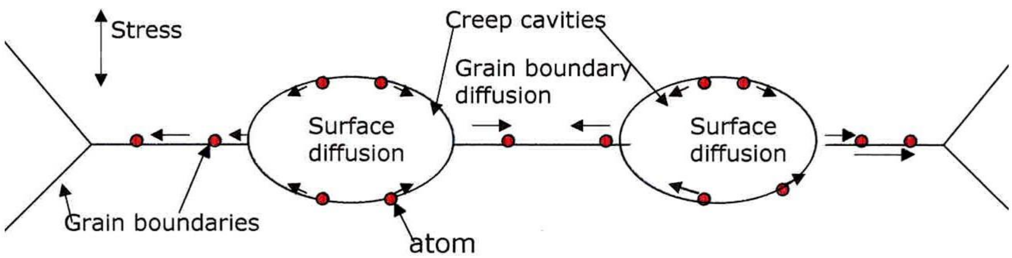

Fig. 1.21 Growth of creep cavities by diffusive transfer of atoms from cavity surface to grain boundary under normal stress [46].

1.7 Creep cracking in the weld joint

Creep cracking in the welded joints of ferritic steels is generally classified according to the location of the crack as Type-I, Type-II, Type-III, and Type-IV [25]. Fig.1.22 schematically illustrates the types of crack in a weld joint on creep exposure.

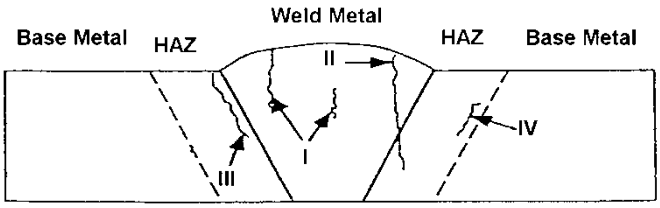

Fig. 1.22 Schematic representation of the classification of cracking in weldments [25].

Cracking occurs in the (i) weld metal along longitudinal or transverse direction Type I), weld metal and ends in the HAZ (Type II), coarse-grained region of the HAZ (Type III), and fine-grained HAZ or intercritical HAZ (Type IV).

Type IV cracking is a serious problem, which occurs at relatively high temperatures and low stresses. This location lies in the partially austenizing region with peak temperature during welding from Ac_1 to Ac_3 or completely austenizing region with peak weld temperature slightly above Ac_3. There is an urgent need to clarify the mechanisms responsible for the Type IV cracking and to mitigate or minimize the Type IV cracking problem.

1.8 Comparison of creep studies on 9-12 wt.% Cr ferritic steel weld joints

Watanabe et al. [23] investigated the creep rupture properties of P91 (9Cr-1Mo-V-Nb) steel weld joints. It has been noticed that the rupture location across the weld joint were found to change from weld metal to fine grained region in the HAZ (adjacent to the base metal) for high stress and low stress conditions respectively (Fig. 1.23). Decrease in dislocation density, growth of $M_{23}C_6$ precipitates, sub-grain formation in the vicinity of prior austenite grain boundaries and Laves phase formation during creep has been observed in the vicinity of the fine grained region. It has been reported that the specimen tested at 823 K, 160 MPa (13748.5 h) fractured in the weld metal. The specimen tested at 873 K, 80 MPa (12414.8 h) failed in the intercritical HAZ, however, specimen tested at 923 K, 40 MPa

(7687.7 h) displayed larger deformation in the weld metal although it failed in the ICHAZ of the weld joint. Type IV cracking occurred in the fine grained HAZ about 400-500 µm away from base metal and HAZ interface, the location where the hardness values were minimum. It is important to note that type IV crack in the weld joint is assumed to initiate in the curved part of the groove angle and propagate towards the top part of the V-groove. It has been clearly shown that the creep voids and cracks in the HAZ nucleated well inside the plate thickness rather than on the surface of the specimen. The stress triaxiality factor is higher in the fine-grained HAZ adjacent to base metal than the other regions; and specifically it was higher in the curved part of the groove angle [23].

Laha et al. [25] investigated the variation of microstructures across the heat affected zone in P91 steel weld joint to understand its role in promoting Type IV cracking. Formation

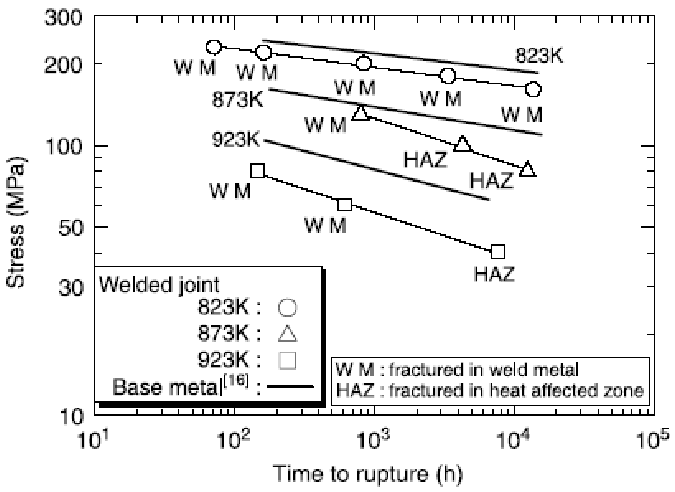

Fig. 1.23 Time to rupture with stress curves for the P91 welded joint and base metal [23].

of soft zone at the outer edge of the HAZ in the base metal side of ICHAZ has been identified. Preferential accumulation of creep deformation, coupled with extensive creep cavitation in the intercritical region of HAZ led to the premature failure of the weld joint in the ICHAZ. The softer matrix and fine grain size aiding deformation, coarse precipitate particles providing damage nucleation sites, and constraint effect by stronger surrounding constituents enhancing the cavity growth resulted in the extensive creep cavitation in the ICHAZ [25].

Spigarelli et al. [26] investigated the creep behaviour of P91 steel welds. The HAZ exhibiting a fine grained structure shows the lowest creep strength by localized deformation in the ICHAZ of the weld joint (Fig. 1.24).

Albert et al. [28] investigated the effect of post weld heat treatment (PWHT) (at 1013 K for varying duration from 15 to 240 minutes) on Type IV cracking in P122 steel weld joint. The duration of PWHT (15 to 240 minutes) did not influence the t_r and all the specimens failed in a Type IV manner. The t_r increased with the decrease in the width of the HAZ and the weld groove angle [28, 29].

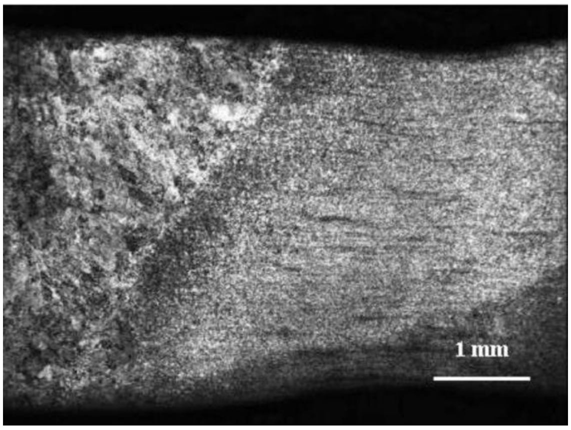

Fig. 1.24 Macrostructure of a cross-weld sample (CW) crept at 650°C and 115 MPa. The necking reflecting the localized deformation at the intercritical zone in the fine-grained HAZ region is clearly visible [26].

Cerjak et al [53] have reported a type IV failure in a long-term creep test of cross-weld E911 specimen (Fig. 1.25). This depicts that the damage and failure are clearly in the HAZ, specifically in a region consistent with the FGHAZ.

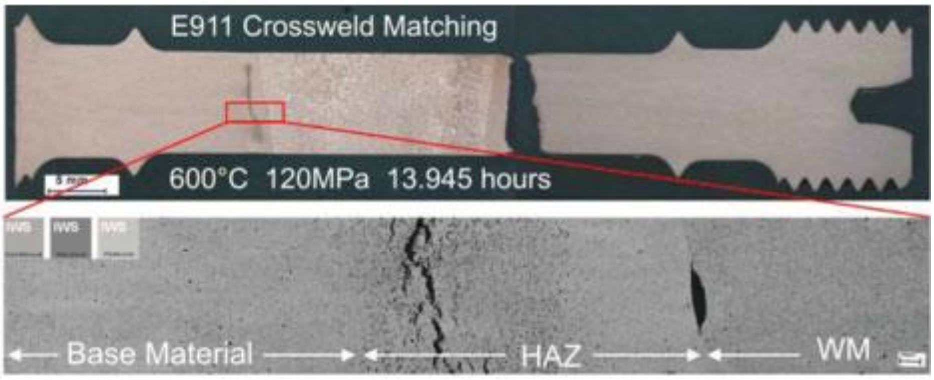

Fig. 1.25 Type IV failure location in a cross-weld creep specimen from E911 after 13945 h at 873 K and 120 MPa [53].

Abe et al. [29] investigated on Type IV fracture and improvement in creep rupture strength of 9Cr-3W-3Co-VNb-B steel weld joint by addition of boron. Addition of about 100 ppm boron combined with about 10-20 ppm nitrogen suppressed the Type IV fracture and improved the long term creep rupture strength of weld joints (Fig. 1.26). Reducing the width of the HAZ by employing EB welding process is effective for the extension of creep life of weld joint [28,29].

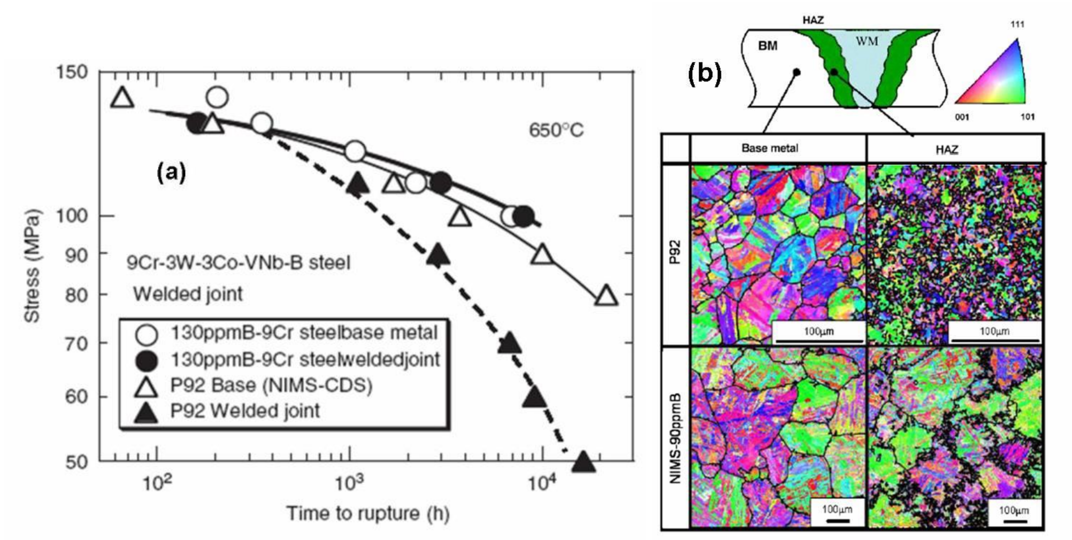

Fig. 1.26 (a) Comparison of creep rupture data at 650°C for welded joints of 130 ppm B-9Cr steel and P92, with those for their base metals; (b) microstructure of base metal and HAZ of 90 ppm B-9Cr steel and P92 [29].

C.R. Das et al, studied the role of boron and heat-treatment temperature in improving the type IV cracking resistance of modified 9Cr-1Mo steel (0.002 wt.% N; 0.010 wt.% B) weldment. The addition of boron to modified 9Cr-1Mo steel has increased the resistance against softening in fine-grained heat-affected zones (FGHAZ) and intercritical heat-affected zones (ICHAZ) of the weldment. Transition of crack from type IV to type II failure in P91 steel weldment by effective utilization of boron at a higher normalizing temperature has been reported [54].

Baral et al [55] studied the creep damage evolution in P91B steel (B:0.01 and N:0.0021 wt.%) over a range of temperatures (873-923 K) and stresses (50-180 MPa). Weld joint fabricated by MMAW process has exhibited creep rupture time of 4083 hat 873 K/120 MPa (as against ~10000 h for the base metal), and about 3000 h at 923 K/50 MPa (as against higher than 10000 h for the base metal) (Fig.1.27).

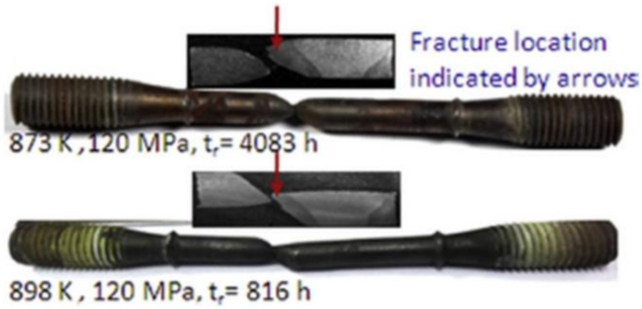

Fig. 1.27 P91B steel weld joint specimens after creep exposure [55].

Fujio Abe [4,29,56] has carried out extensive studies towards suppression of particle coarsening and maintaining a homogeneous distribution of $M_{23}C_6$ carbides near prior austenite grain boundaries during creep in tungsten and cobalt bearing 9Cr steel. Boron content is higher in $M_{23}C_6$ precipitates, which are near the PAG boundaries. Abe has stated that boron retards the diffusive α/γ transformation during heating, because the grain boundary segregation of boron reduces grain boundary energy and makes the boundaries less effective as heterogeneous nucleation sites for γ phase. Soluble boron is essential for the change in α/γ transformation behaviour during heating and for the suppression of grain refinement. The combination of boron and nitrogen contents to avoid the formation of boron-nitride (BN) is shown in Fig.1.28. In Gr.92N steel subjected to only normalizing but no tempering before the thermal cycle, the grain morphology is approximately the same as the base metal after the AC_3 thermal cycle. This results from the mechanism of austenite memory effect [56].

Using 3-D atom maps of the as-quenched martensitic steel (low-carbon steel; Fe-0.19C-0.35Si-1.20Mn-0.20Cr-0.50Mo-0.06Al-0.03Nb-0.03V-0.00124B in wt.%), Li et al [57] have showed significant segregation of B, C and Mo and no segregation of Cr at the PAGB (Fig. 1.29). The steel was austenitized at 1023 K for 15 min and subjected to water quenching prior to Atom Probe Tomography (APT) analysis.

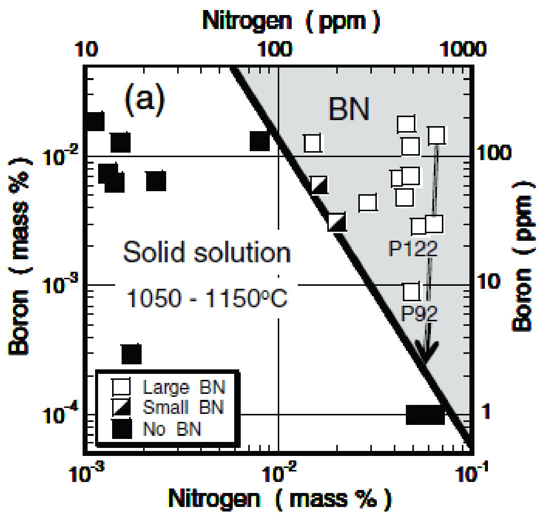

Fig.1.28 Composition diagram for boron and nitrogen showing formation of solid solution or boron nitride (BN) [56].

Several investigations are available in literature on thermo-mechanical treatments of grade 91 steel through forging with and without ausageing treatment to obtain refined microstructure to impart better high temperature mechanical properties, Klueh [58], S.

Hollner et al,[59] L. Tan et al [60-62], Benjamin et al [63], M. Song et al [64], and J. Visva et al [41] (Fig.1.30).

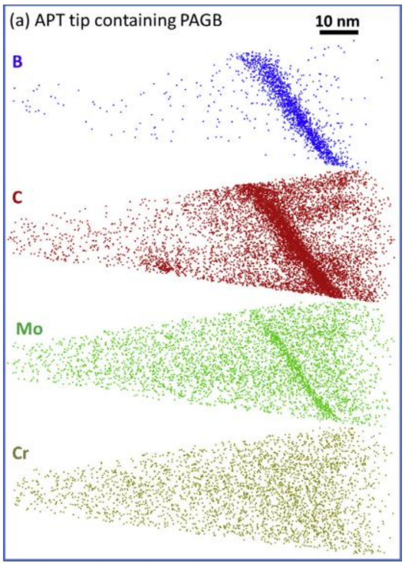

Fig. 1.29 APT 3-D atom maps of the as-quenched martensitic steel distributions of atoms in the probed volume containing a PAGB [57].

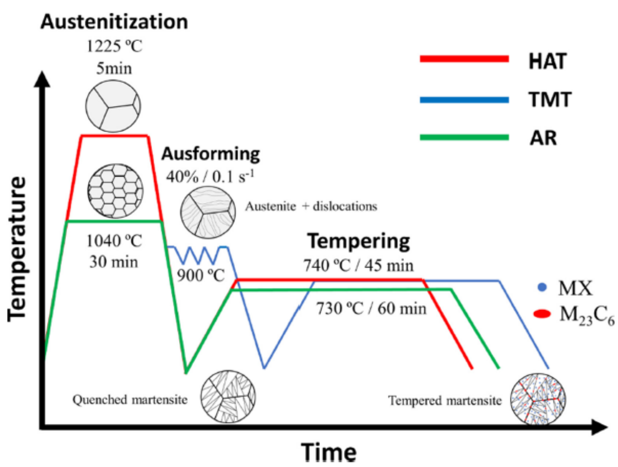

Fig. 1.30 Scheme of the different thermo-mechanical and heat treatment [65]

Yongkui et al. [24] carried out interrupted creep tests on 21 mm thick weld joint of P91 steel. Quantitative investigations on creep damage were carried out using laser microscope. It has been found that the creep voids initiate at early stage of creep life (0.2 of life) and these voids size and number increases up to 0.7 of creep life and coalesce into macro crack at the stage of (0.8 of rupture life). The creep damages concentrated at a quarter depths of the plate thickness in the fine grained HAZ. It has been noticed that the high level stress triaxiality factor combined with large creep strain accumulation in the fine grained HAZ accelerated the formation of voids in this location.

El-Desoky et al [65] studied the creep behaviour of weld joints fabricated using manual metal arc welding (MMAW) from 85 mm thick tubes of P91 steel at 873 K. The fine grained region of HAZ limited the creep rupture strength of weld joint, and recovery of martensite lath by annihilation of dislocation within the sub-grains is the rate controlling creep deformation mechanism in the low stress region in the weld joint [65] .

Takashi Ogata et al. [27] have characterized the damage of P91 steel weldments under uniaxial and multi axial creep conditions. They observed that the creep rupture time of the cross weld joints reduced to one fifth of t_r of the base metal due to type IV cracking. Creep voids were observed around 0.32 t_r and the number of voids was larger at the mid-thickness of the specimen as compared to the surface of the specimens (Fig. 1.31).

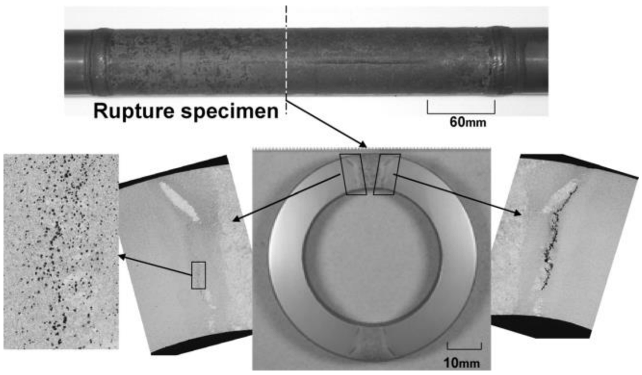

Fig. 1.31 Appearance of failure surface of the welded tube specimen (t_r: 6740 h) [27].

Gaffard et al. [30] investigated the creep flow and damage properties of 9Cr1MoNbV steel and its weldment and showed that the loss of creep strength is due to carbide coarsening and extensive lath recovery during welding. Effect of HAZ width on creep behaviour has been studied on round specimens using the power-law flow rules and Monkman-Grant life assessments. Results of these models were in contradiction to the numerical analysis (FE) results, which indicated that decrease in width of HAZ leads to increase in creep rupture life.

Jonathan Parker et al. [68] investigated the factors affecting the type IV creep damage in grade 91 steel welds prepared from SMAW (50 mm thick pipe weld joint) and gas metal arc welding (GMAW) (38 mm thick plate weld joint). The effects of variation in N/Al ratio (ranging 1.05-13.5) and bevel angles of the joint (10°, 15°, and 30°) were studied. Three-dimensional finite element (FE) analyses of weld joints with different weld angles were carried out. Increase in N/Al ratio led to increase in creep life. The bevel angle of the weld preparation influenced the creep life of cross-weld specimens. Results of FE analysis indicated decrease in creep failure time with weld bevel angle up to 27.5°, and increase in creep life with further increase in weld angle (Fig.1.32) [68]. Siefert et al [8] have reported an increase in creep cavitation damage resulting from increase in angle within a weld joint.

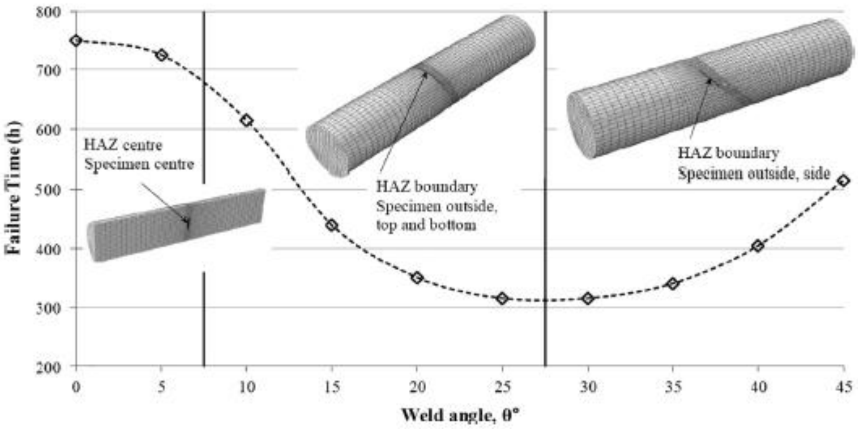

Fig. 1.32 Change in calculated creep rupture life with weld angle for cross weld test on grade 91 steel [68]

Parker et al [69] have studied the creep performance of a grade 91 header installed on a 500 MW unit in 1992, after service about 58000 h operations at 568°C and close to the design pressure at 17.58 MPa (Fig.1.33). In 2004 extensive Type IV cracking was found on branch welds. It has been reported that the most vulnerable welds are those containing Type IV zones perpendicular to the hoop stress, primarily large branches or seam welds.

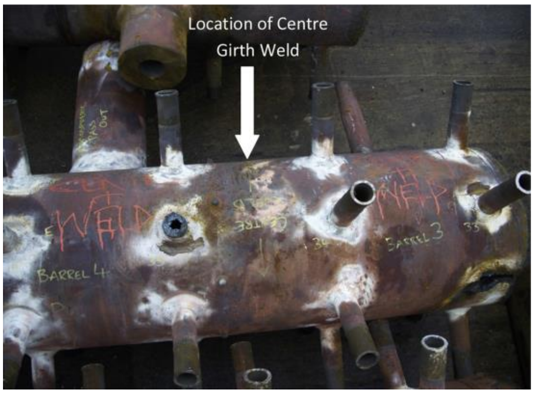

Fig. 1.33 Photograph of central portion of header after removal from the power plant [69].

Francis et al [70] have studied the effects of weld preheat temperature, weld groove preparation and heat input on type IV failure. They observed that the narrow-gap welding configurations and U groove preparations offer significant benefits to creep performance, since these configurations are often associated with joint preparation angles of zero (Fig.1.34). Increases in the weld preheat temperature significantly improves the rupture life

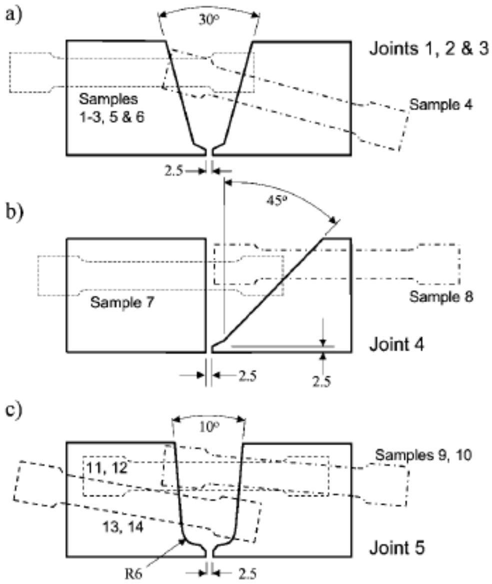

Fig. 1.34 Schematic representation of joint preparations and locations of extracted creep specimens [70].

limited by type IV failure. It would be beneficial to specify the highest practical preheat temperature. It has been stated that in situations where the principal loading direction is transverse to the weld and it is not possible to use a joint preparation angle of zero, an increase in the preheat temperature may substantially compensate for any penalty in rupture life associated with the non-zero joint preparation angle.

Xue et al [70, 71] investigated the type IV cracking behaviour of P92 steel weldments fabricated using SAW process. An occurrence of type IV fracture in the FGHAZ with low ductility and laves phase formation at 923 K and 120 MPa have been reported.

From the literature survey presented above, regarding the reasons for type IV cracking or its mitigation. Different attempts results are available in literature, which vary with the steels, temperatures and welding procedures. Also, the mechanisms of improvements, if any, are also not unequivocally established. Therefore, there is a need to carry out studies specific to the steels and the welding procedures at temperatures in consideration.

The objective of the present investigation involves the study of creep deformation and rupture behaviour of (i) modified 9Cr-1Mo steel (P91), (ii) controlled nitrogen P91 with boron addition (P91BN) and (iii) tungsten bearing P92 steels and their welds in order to understand the effects of heterogeneity in mechanical properties across the joint, influence of boron and nitrogen combination on creep strength of base and weld joints to assess its type IV cracking resistance, and P92 weld joint to understand the influence of tungsten in the steel. The thermo-mechanical treatment of the P91 base metal to improve the creep resistance of weld joints has been explored. This thesis also examines the influence of different weld geometries and orientation of the weld joint on type IV cracking.

CHAPTER 2

Experimental Details

2.1 Introduction

In this chapter, the details of the materials, various steps in preparation of test specimens, the mechanical tests, data analysis, microstructural analysis and other analytical techniques employed in this study are presented. Specifically, the chemical compositions, heat treatment and thermo-mechanical treatment of the materials used in this study, bevel preparation and weld joint fabrication, mechanical tests (hardness, tensile, impact and creep), microstructural characterization techniques (OM, SEM, EBSD and TEM), Differential Scanning Calorimetry, X-ray diffraction, phase stability prediction by Thermo-Calc, and Finite Element Analysis studies have been described.

2.2 Materials

Chemical composition (wt. %) of the steels used in this study have been analyzed by inductively coupled plasma (ICP) and optical emission spectroscopy (OES) techniques. Chemical composition of the 9Cr ferritic martensitic steels used in this study are given in Table 2.1. Modified 9Cr-1Mo steel (P91), P91 steel with controlled addition of boron and nitrogen (P91BN), and tungsten bearing P92 steel were investigated. The chemical compositions of the matching electrode and filler materials used for joining of P91 and P92 steels are given in Table 2.2. P91 and P92 steels plate dimensions of 12 mm (T) x 250 mm (w) x 500 mm (L) were used in this investigation. Thermo-mechanical treatment of P91 steel was performed using 25 mm thick plates.

Table 2.1: Chemical composition of various 9Cr steels employed in this study (wt.%).

Elements	C	Mn	Si	Cr	Mo	W	S	P	Ni	Al	V	Nb	B	N	Fe
P91 steel	0.10	0.46	0.32	8.80	0.90	-	0.01	0.004	0.10	0.001	0.22	0.08	-	0.05	Bal.
P91BN-1	0.10	0.50	0.48	9.20	1.0	-	0.004	0.004	0.010	0.003	0.21	0.07	0.006	0.011	Bal.
P91BN-2	0.092	0.40	0.35	9.00	1.0	-	0.005	0.004	0.010	0.001	0.20	0.07	0.010	0.0047	Bal.
P91BN-3	0.104	0.40	0.36	9.00	1.0	-	0.004	0.004	0.010	0.003	0.21	0.07	0.009	0.010	Bal.
P91BN-4	0.10	0.30	0.40	8.50	1.04	-	0.002	0.005	0.020	0.03	0.23	0.09	0.0100	0.0021	Bal.
P92 steel	0.10	0.36	0.27	9.20	0.51	1.90	0.002	0.010	0.060	0.010	0.22	0.07	0.001	0.050	Bal.

Table 2.2: Chemical composition (wt.%) of electrode and filler materials used to fabricate the joints.

Elements	C	Mn	Si	Cr	Mo	W	S	P	Ni	Al	V	Nb	B	N	Fe
P91 steel SMAW	0.098	0.58	0.35	8.63	1.00	-	0.008	0.01	0.63	0.004	0.20	0.06	-	0.055	Bal.
P91 steel TIG filler metal	0.10	0.50	0.36	8.90	1.00	-	0.007	0.009	0.10	0.005	0.21	0.07	-	0.050	Bal.
P92 steel filler metal	0.10	0.80	0.25	8.50	0.40	1.60	0.002	0.010	0.070	0.010	0.20	0.06	0.001	0.040	Bal.

2.3 Heat treatment

All the 9 wt.% Cr ferritic martensitic steels used in this study were initially normalized, air-cooled (AC) to room temperature, then tempered followed by air-cooling to room temperature. The temperature and duration of normalizing and tempering (NT) treatment differed for the different steels, the details are given in Table 2.3 and Fig. 2.1. Other heat treatments employed in this study are post-weld heat treatment (PWHT) of weld pads, and for simulation of heat-affected zone (HAZ) microstructures. Electrical resistance heating box type furnace was used for normalizing, tempering, PWHT and HAZ simulation. The temperature of the furnace was controlled within ±2 K.

2.3.1 Thermo-mechanical treatment (TMT)

Also, a study on the effect of thermo-mechanical treatment (TMT) on the microstructure and mechanical properties of P91 steel. TMT was carried out in order to refine the microstructure of the steel. The P91 steel in normalized and tempered condition was taken as the starting material for TMT. This steel was heated to 1423 K and held for 10 minutes to dissolve the precipitates present in the steel, the temperature of the steel was reduced to 983±10 K from 1423 K in the austenite phase field. The ausforming was performed at 983 K for different degrees of deformation (15, 25, 40 and 50%), subsequently aged at the ausforming temperature for 30 minutes prior to cooling to room temperature (Fig. 2.1(a) and (b)) [72]. The reduction in thickness was obtained by multiple passes. The duration of rolling was kept limited to 10 minutes to avoid undesirable γ to α phase transformation. This ausformed steel was further subjected to tempering treatment 1033 K for 150 minutes and then cooled to room temperature. The box type electrical resistance heat treatment furnace, hot-rolling mill and non-contact (pyrometer) temperature measurement equipments were used for the TMT.

Table 2.3: Normalizing, tempering treatment and post-weld heat treatments (PWHT) for different steels employed in the study.

Material	Normalizing	Tempering	Pre-& post-heating	PWHT
P91 steel	1313 K 30 min. / AC	1033 K 150 min. / AC	523 K	1033 K 60 min. / AC
P91, P91BN steels	1373 K 30 min. / AC	1033 K 180 min. / AC	523 K	1033 K 60 min. / AC
P92 steel	1323 K 30 min. / AC	1053 K 120 min. / AC	523 K	1053 K 120 min. / AC

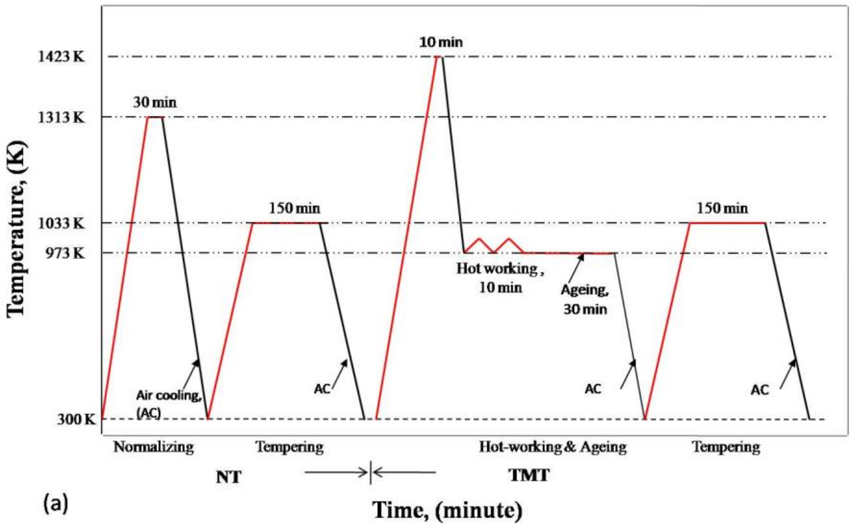

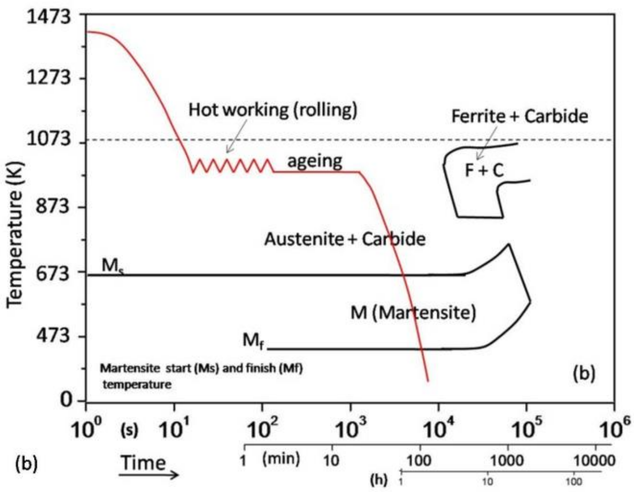

Fig. 2.1 Process diagram for (a) normalizing and tempering (NT), and thermo-mechanical treatment (TMT) and (b) TMT and schematic of CCT of modified 9Cr-1Mo steel (P91 steel).

2.3.2 Furnace simulation of HAZ microstructures

The different microstructural regions of HAZ of the P91 steel weld joint such as prior-austenite coarse grain, prior-austenite fine grain and intercritical HAZ were simulated by heat treatment. For this, P91 steel blanks of dimensions 12 mm x 12 mm x 120 mm were held for 5 minutes at 1453, 1200, and 1140 K respectively to obtain coarse grain, fine grain and intercritical HAZ, followed by oil quenching until to reach room temperature. These steel blanks were tempered at 1033 K for 1 hour and then air cooled. This heat treatment is in line with PWHT of the weld pads (Table 2.3). The temperature to simulate the different regions of HAZ was chosen based on the study conducted by Chandravathi et al [31]. Similarly, P92 steel HAZ microstructures were simulated at different temperatures such 1473, 1323, 1203, 1173 and 1153 K followed by oil quenching until to reach room temperature. These steel blanks were tempered at 1053 K for 2 hours and then air cooled in line with PWHT of P92 steel weld joint (Table 2.3).

2.4 Groove and weld joint fabrication

Different welding processes employed to fabricate the weld joints in this work are activated-TIG, Tungsten Inert Gas (TIG), Narrow-Gap TIG (NG-TIG), Shielded Metal Arc Welding (SMAW) and Electron Beam Welding (EBW). The V-groove butt joint configuration for TIG was prepared with different weld bevel angles using conventional workshop machining methodology (Fig.2.2). V-groove butt joint configuration is shown in Fig. 2.3. The joints having bevel angles of 45° and 60° were fabricated by 34 and 56 passes respectively. Square butt joint configuration was prepared to fabricate autogenous (A-TIG and EB) weld joints (Fig. 2.4). Activated-TIG welding process involves employing of thin coating of multi-component flux in the form of paste on the surface of the joint prior to welding (Fig. 2.5(a)). The weld pad fabricated from different welding techniques were heated to about 523 K prior to and after welding (Fig. 2.5(b)). Single and double-pass A-TIG weld joints of P91 and P91BN steels were fabricated to study the creep behaviour (Fig. 2.4 and 2.5(c)). The weld pads were post-weld heat-treated at 1033 K for 1 hour for P91 steel and 1053 K for 2 hour for P92 steel (12 mm thickness) as already given in Table 2.3. The welding process parameters for P91, P91BN and P92 steels weld joints are given in Table 2.4, 2.5 and 2.6. Weld pads were subjected to X-ray radiography for verifying their soundness.

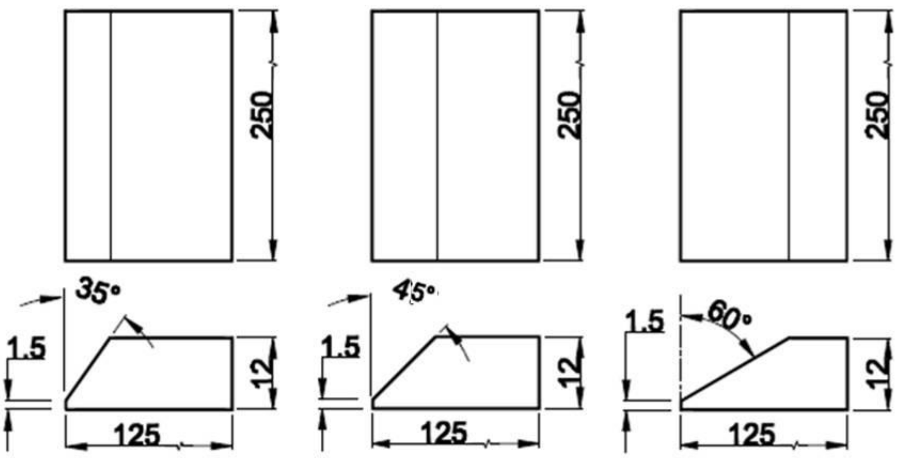

Fig.2.2 Edge preparion of plates with different bevel angles (35°,45°, 60°), (all dimensions are in mm).

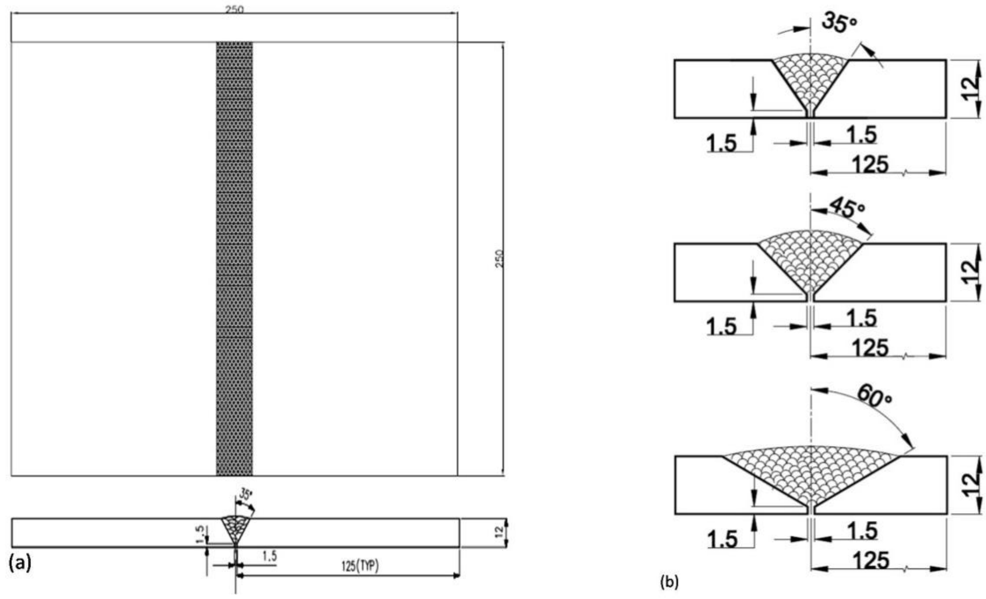

Fig. 2.3 (a) V-groove weld pad line diagram for 35° bevel angle, (b) different bevel angles of weld joint, (all dimensions are in mm).

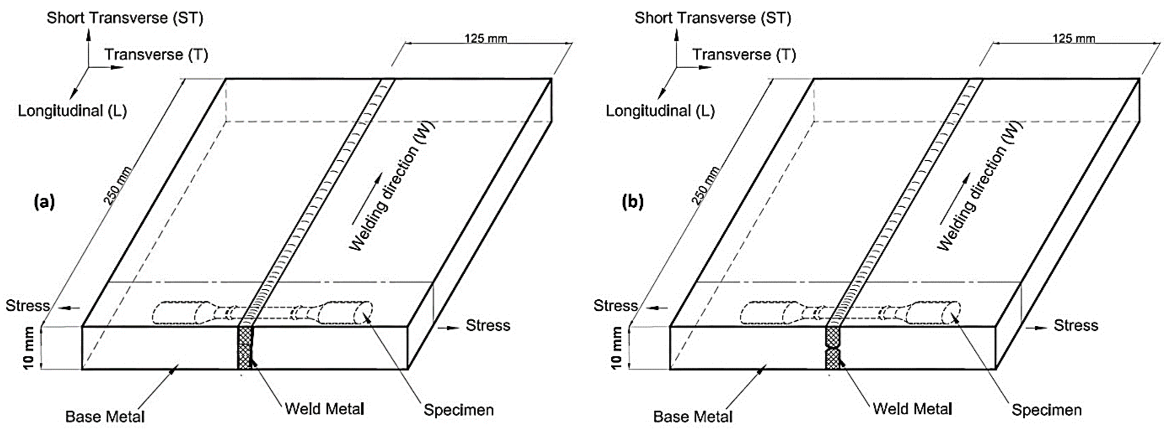

Fig. 2.4 Schematic diagram of the square butt (a) single-pass by A-TIG and EBW, and (b) double -pass weld joint fabricated by A-TIG process.

Table 2.4: Welding process parameters employed for P91 steel.

Welding Parameters	A-TIG	TIG	SMAW	EBW
Current, (A)	297	110	115	80 mA
Voltage, (V)	21	22	24	55 kV
Welding speed (mm/min)	60	~75	~90	800
No. of passes	1	18	9	1
Shielding gas size of filler / electrode	Ar	Ar root-pass 1.6 mm Φ; fill-pass 2.4 mm Φ	Ar root 1.6 mm TIG; electrode 3.12 mm	Vacuum, 278 mm work distance

Table 2.5: Welding process parameters employed for P91 and P91BN steels.

Welding Parameters	A-TIG weld joint	
	Double-pass	Single-pass
Current, (A)	225	290
Voltage, (V)	16.7	17.5
Welding speed (mm/min)	100	60
Shielding gas	Ar	Ar

Table 2.6: Welding process parameters employed for P92 steel.

Welding Parameters	NG-TIG
Current (A)	230
Voltage (V)	10
Travel Speed (mm/min)	80
Heat input (kJ/mm)	1.72
Pre-heating and inter-pass temperature (K)	473-573
Dwell time (left and right) (s)	0.4
Oscillation speed (rpm)	40

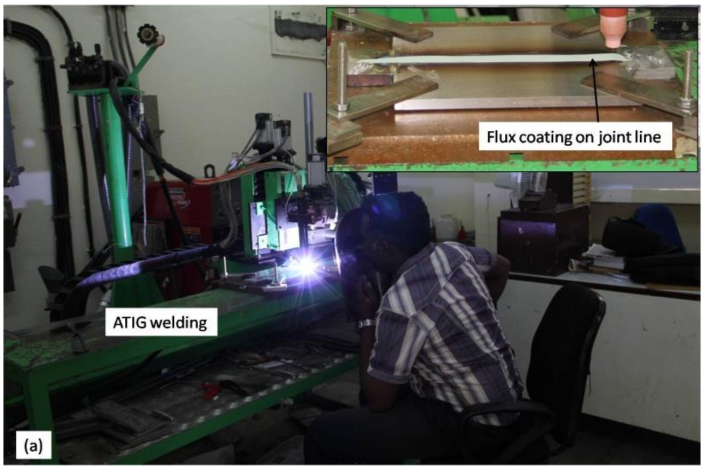

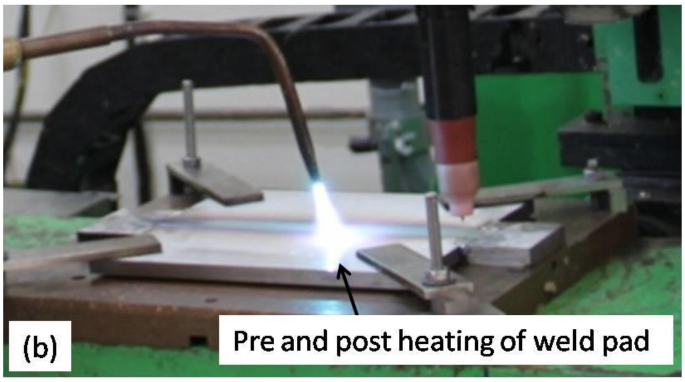

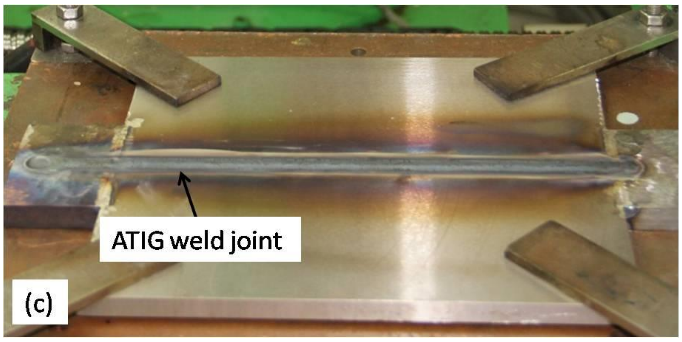

Fig. 2.5 (a) Flux coating on joint line and weld joint fabrication by A-TIG, (b) pre and post-heating of weld pad and (c) as-welded A-TIG joint.

2.5 Fabrication of specimens

Standard as well as miniature specimens to perform mechanical tests, and characterization specimens were extracted using conventional workshop and electrical discharge machining (EDM) machines. Specimens extracted in different orientations with respect to weld fusion line/ welding direction in P92 steel NG-TIG weld joint (Fig. 2.6(a)) and schematic of weld joint flat creep specimens are shown in Fig. 2.6(b). The miniature flat tensile specimens extracted from different regions across the single-pass weld joint and test set-up consisting of specimen holders and pins are shown in Fig. 2.7.

The schematic diagram of cylindrical tensile specimen is shown in Fig. 2.8. The flat tensile specimen is shown in Fig. 2.9. Schematic of Charpy impact V-notch specimen used in this study is shown in Fig. 2.10. Schematic of cylindrical (Fig. 2.11(a)) and square creep specimens are shown in Fig. 2.11.

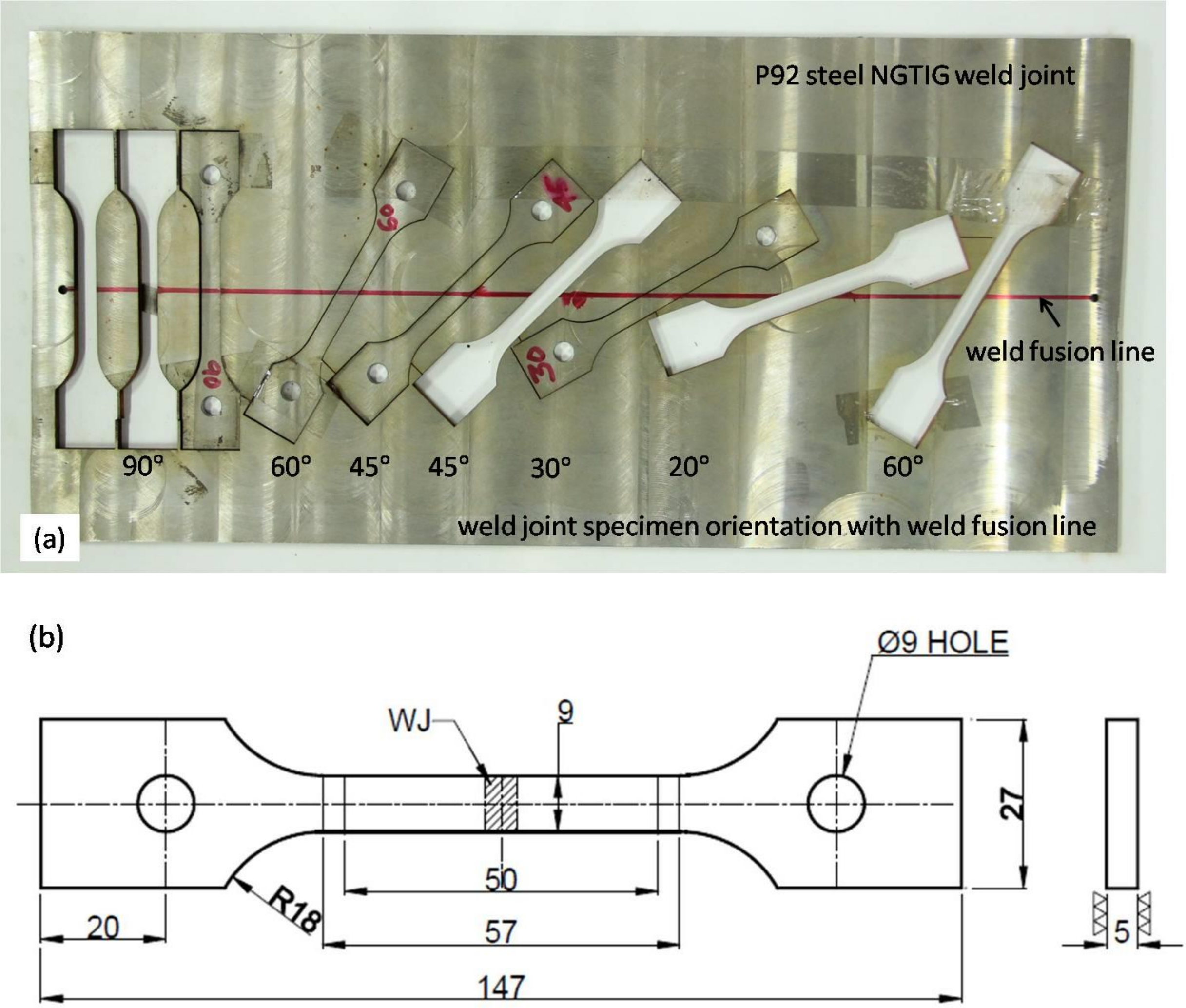

Fig. 2.6 (a) Extraction of weld joint specimen in the different orientation with respect to welding fusion line/welding direction, (b) schematic of weld joint flat specimen (all dimensions are in mm).

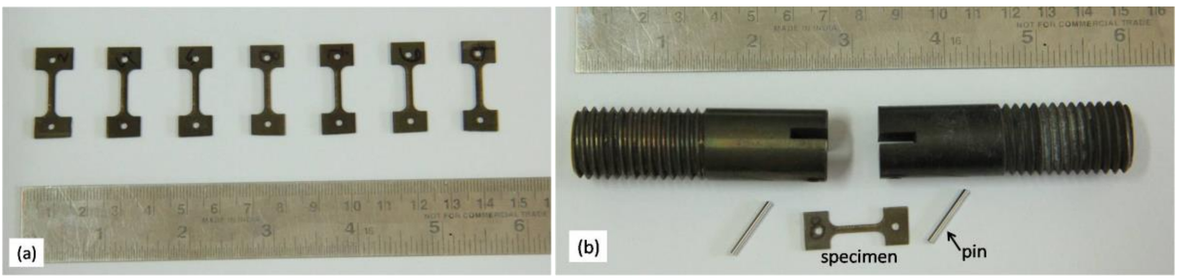

Fig. 2.7 (a) Miniature flat tensile specimens and (b) testing set-up consisting of speicmen holders and pins.

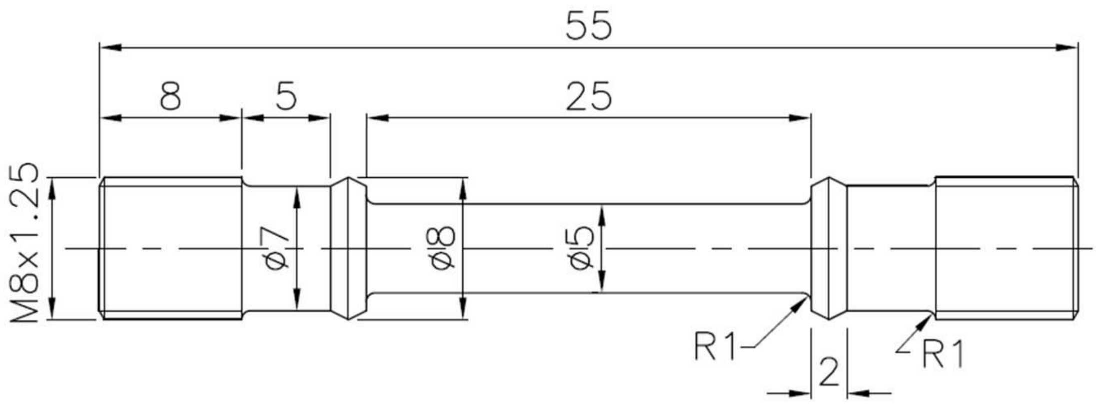

Fig. 2.8 Schematic diagram of cylindrical tensile specimen (all dimensions are in mm).

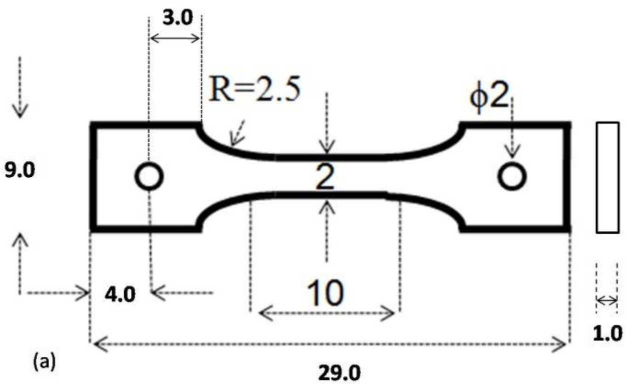

Fig. 2.9 Schematic of flat tensile specimen (all dimensions are in mm).

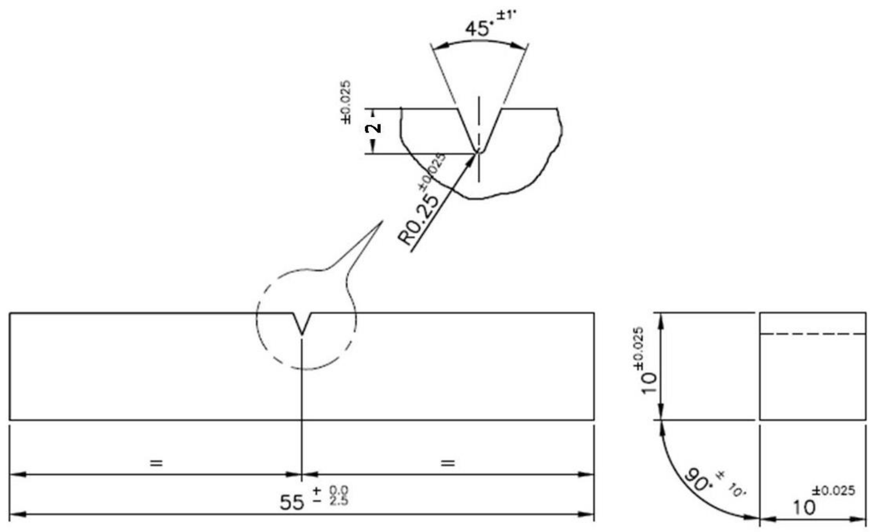

Fig. 2.10 Schematic of Charpy impact V-notch specimen (all dimensions are in mm).

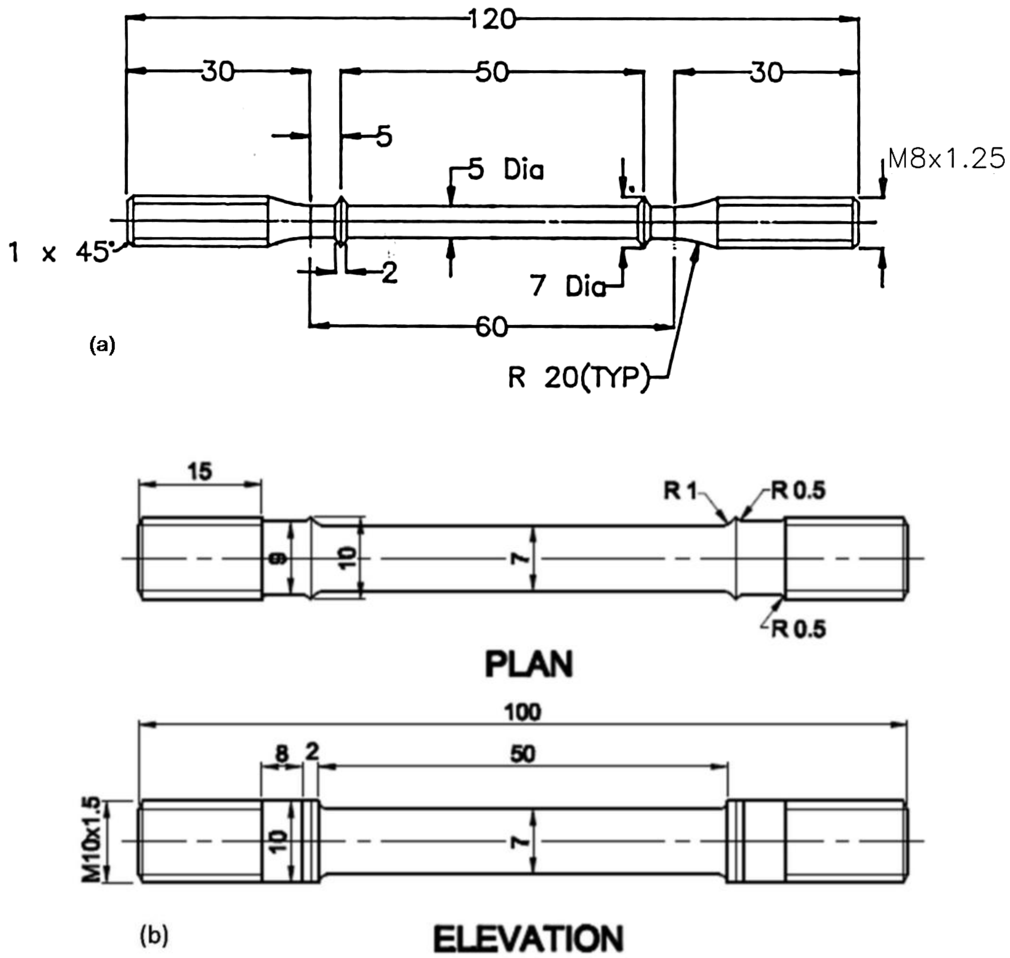

Fig. 2.11 Schematic of (a) cylindrical and (b) square creep specimens used in this study (all dimensions are in mm).

2.6 Mechanical tests

The different mechanical tests conducted in this study are hardness, tensile, impact and creep. Details of these tests are given in the following sections

2.6.1 Hardness, tensile and impact tests

(a) Hardness measurements: Macro and micro - Vickers hardness measurements were made on base steels as well as across the weld joint in the as-weld, PWHT and creep exposed conditions. The indentation load value 10 kgf in the macro-Vickers (FIE make VM-50) and 50 to 300 gf in the micro-Vickers (Walter UHL make VMH-I04M) were used. Dwell time 15

seconds was used in all conditions of the measurements. The diagonal length of the indentation was measured to obtain the hardness values, ten indentations were taken to arrive at the average value of hardness in the base steels. Hardness measurements across the weld joint were performed at three different locations to confirm the hardness variations across the joints. The Vickers hardness values were obtained in the materials using the following equation,

$$HV = 1.854\, P / d^2$$

where HV is the Vickers hardness in kgf/mm^2, P is the load in kgf, d is the mean of two diagonals of the indentation made on the specimens in mm.

(b) Tensile testing: HungTa make 100 kN Universal Testing Machine (UTM) was used to carry out tensile testing. Cylindrical tensile specimens (Fig. 2.8) were used to carry out tests on base metal, and different furnace-simulated HAZ regions at different temperatures (300 - 1073 K) over a range of strain rates from $3x10^{-5}$ to $3x10^{-3}$ s^{-1} as per the ASTM E8 and E21 standards. The stress relaxation tests were carried out by interrupting the cross-head motion in tensile tests at 2% engineering strain and monitoring the variation of load with time. In addition, specimens with rectangular cross sections (Fig. 2.9) were fabricated from the different locations in the single-pass cross weld joints for evaluation of tensile properties. Prior to tensile test, the specimen was heated to test temperatures using electrical resistance split type of furnace having three heating zones. Separate temperature controllers were used to maintain constant temperature across the different zones of the furnace. K-type thermocouples have been used to monitor the temperature of the testing specimen. The specimen was held for 15 minutes at test temperature to ensure uniform temperature along the specimen within ±2 K. Load-elongation data were recorded using digital data logger. The

yield stress (YS), ultimate tensile strength (UTS) and ductility were calculated as per the equations given below,

$YS_{0.2}$ (MPa) = $P_{0.2}/A_o$

UTS (MPa) = P_u/A_o

Reduction in area (%) = $[(A_o – A_f)/A_o] \times 100$

Elongation (%) = $[(L_f – L_o)/L_o] \times 100$

where, $YS_{0.2}$ and $P_{0.2}$ are yield stress and load in N at 0.2% strain, P_u is the ultimate tensile load in N, A_o and A_f are the original and final areas of the specimen in mm^2, L_o and L_f are the original and final lengths of the specimen in mm.

(c) Impact test: Charpy impact tests were carried out as per ASTM E23 at different temperatures. Standard Charpy specimens having dimensions of 10x10x55 mm^3 with V-notch at the middle of the block were used. The schematic of impact specimen is shown in Fig. 2.10.

2.6.2 Creep tests

Constant load uniaxial creep tests at different temperatures over a wide range of applied stresses on the base metals and weld joints were carried out using single lever arm type creep machine in air environment as per ASTM E139 standard. The creep tests on base metal and weld joints of various steels were performed over a wider range of temperatures 823 - 973 K (550-700 °C) and applied stresses (60 to 350 MPa). Schematic of cylindrical and square creep specimens are shown in Fig. 2.11. The lever ratio of the loading arms were either 1:10 or 1:20 for the different machines employed in the study. The machine consists of three-zone temperature controlled resistant type split furnace. Three K-type thermocouples were attached with the specimen, one each for each zone, to monitor and maintain the test temperature. The temperature of the specimen across the gauge length was maintained within ±1 K of the set temperature. Elongation of the specimen during creep test was measured using four-rod mechanical extensometer attached with digimatic dial indicator with a measuring resolution of ± 0.001 mm. The data was acquired by an automated data logger. The percentage reduction in area and percentage elongation of the creep exposed specimens were determined. Impression creep tests were performed under vacuum (10^{-6} mbar) on specimens extracted from different regions of the P91 steel single pass A-TIG weld joint. Vacuum chambers consisting of high temperature heating facility were used to perform these tests using cylindrical indenter having 1 mm diameter. Test blocks having dimensions 20x20x10 mm^3 extracted from the A-TIG weld joint of P91 steel were used in this study. Size of individual regions such as CGHAZ, FGHAZ and ICHAZ in the A-TIG joint were 3.0 mm, 3.5 mm and 1.8 mm respectively. The weld metal region was about 8-10 mm. Lever arm type uniaxial creep and impression creep machines used for investigation are shown in Fig. 2.12.

2.7 Microstructural characterization

The different features of the microstructure of the steels at different length scales were characterized using optical metallography (OM), and field emission gun scanning electron microscopy (FEG-SEM) and TEM equipped with energy dispersive spectroscopy (EDS) measurement techniques.

Specimens were extracted from base metal, cross weld joint and the simulated HAZ regions before and after creep exposure for metallographic preparation. The location of the fracture vis-à-vis different regions of the weld joints was identified based on microstructural and hardness profile studies close to the fracture surface. Metallography samples from cross-

Fig. 2.12 (a) Photograph of lever arm type uniaxial creep machines, (b) creep machine with creep specimen, thermocouple, extensometer and digimatic indicator and (c) impression creep machine.

weld specimens before and after creep test were obtained from sections normal to the welding direction. The metallographic specimens were prepared using conventional mechanical polishing using SiC emery papers (up to 4000 grit) and subsequently polished using 1 and 0.1 μm alumina suspension. The finely polished specimens were immersion etched for 12 to 15 seconds using Villela's reagent (Picric acid 5 gm, HCl 25 ml, Ethyl alcohol 500 ml) to reveal the microstructures in the steels. Optical microscope of inverted type Carl-Xeiss (Axio Vert.A1) was used for examination of microstructure at 50, 500 and 1000X magnifications. Higher magnification examination of the microstructure was done using metallography samples under SEM.

Specimens for EBSD study were prepared using standard metallographic procedure up to 0.1 µm alumina suspension under low rotational speed ~80 rpm in order to avoid introducing additional strain in the material. Specimens were thinned down to 70 µm thickness by mechanical polishing with emery paper under flowing water, followed by electrolytic double jet thinning (Struers make TenuPol) using 20 % perchloric acid and ethanol solution at 238 K and 20 V for transmission electron microscopic (TEM) investigation. Cross-weld joint specimens were thinned to 100 µm then etched for 5 seconds (etched lightly) using Villela's reagent then subsequently 3 mm discs were punched out at the region of interest, these discs were again polished to 70 µm then electrolytic double jet thinned as above. Fractography was carried out on tensile and creep tested specimens at various conditions to study the features and identify the damage mechanisms. For this, samples were obtained by cutting the fracture end of the specimens to about 10 mm along the gage length; the specimens were ultrasonically cleaned in methanol for 1 minute before examining under SEM.

SEM secondary electron (SE) and backscattered electron (BSE) images were employed to reveal various features. BSE image is obtained based on the contrast governed by the difference in atomic number (Z) of the elements in the region. Higher Z elements lead to higher backscattered electrons than the lighter elements. Characteristics X-ray emitted from the alloying elements in the steel and qualitative composition of the precipitates and matrix were obtained. Electron Backscatter Diffraction (EBSD) Analysis technique available with SEM was extensively used in this study. EBSD scanning on different conditions of the steels was performed in 0.2 mm step size over an area of 102 x 77 µm^2. Mostly eight numbers of Kikuchi diffraction pattern were obtained for indexing bcc ferrite phase. EBSD data were analyzed using HKL® channel-5 software; and inverse pole figure (IPF) map coupled with grain boundary maps, Kernel average misorientation (KAM) map with misorientations 0.1 to 2°, coincidence site lattice (CSL) boundary and dislocation density were obtained. Photograph of SEM (Zeiss SUPRA 55) used in this study is shown in Fig. 2.13.


Fig. 2.13 Photograph of FEG-SEM SUPRA 55.

Transmission electron microscopy was performed for the study of microstructure at small length scales and substructural studies. TEM work has been performed using Philips CM200 TEM with EDX facility attached; LaB_6 cathode is operated at an accelerating voltage of 200 kV with a sample tilt of ± 60°. Prior austenite grain and subgrain structure size were measured by linear intercept method. Microstructural constituents (precipitates, lath, and grain size) were analyzed using image analysis Image-J software.

2.8 DSC, XRD and phase prediction

Differential scanning calorimetry was performed to identify the temperatures for different transformations in the various steels in this study. Setaram Setsys 1600 DSC with heat flux compensated under continuous Argon flow was used. The specimen dimensions and mass were 2 x 2 x 2 mm^3 and 100 to 120 mg respectively. The calibration was carried out using pure Iron. The specimens were heated to 1323 K and held for 15 minutes then cooled to room temperature. The temperature uncertainty is ± 2 K. The heating and cooling rates were between 3 to 99 K/minute in nine discrete steps. Each scan rate experiment was repeated three times with a fresh sample of nominally the same mass. Critical cooling rate for 100% martensite is 5 K/minute and above. The Ac_1, Ac_3, M_s, and M_f temperatures were obtained from the average of eight samples for each composition. The accuracy of determination of these temperatures are ±5 K for Ac_1 and Ac_3, and ±8 K for M_s and M_f.

The structural phase characterization of the specimen was performed in a Bruker D8 Discover X-ray diffractometer (XRD) with CuKα radiation (λ = 1.5406 Å) in Bragg Brentano (θ-2θ) geometry at room temperature. The step size was 0.02° and scan speed was 15 seconds per step. The peak positions were estimated by fitting the XRD patterns using X'PertHighScore Plus software and indexed by matching it with standard powder diffraction data (PDF). The pattern matches with ICDD Card No. 00-006-0696 (Fe: BCC) and 00-035-0783 ($Cr_{23}C_6$). Phase fractions in the P91 and P92 steels as a function of temperature were obtained from equilibrium calculations in the temperature range of 673 to 1873 K using Thermo-Calc software (TCFE8: steel/Fe-alloys v8.0).

2.9 Finite element analysis

Finite element analysis of stress distribution across the weld joint during creep exposure was carried out to understand creep deformation and rupture behaviour of the weld joint. 2D planer geometry considering ½th of the actual geometry was created, and meshing was performed using 4 nodded quadrilateral elements employing ABAQUS 6.14 finite element solver [73]. The elastic behaviour was incorporated in the model using Young's modulus and Poisson's ratio, and creep behaviour using Norton's creep law relating the minimum creep rate with applied stress ($\dot{\epsilon}_{min} = A\sigma^n$). Von-Mises yield criterion has been used for occurrence of yielding across the weld joint. The element size was reduced at the inter-critical region of the joint and elastic analysis was used to ensure that the mesh configuration was sufficiently refined across the weld joint. Elastic-creep steady state analysis of the weld joint specimens was carried out under plane strain condition. The analysis was carried out until the creep strain reaches the elastic strain of the material [74].

CHAPTER 3

Effect of Microstructural Heterogeneity and Welding Process on Type IV Cracking of P91 Steel Weld Joint

3.1 Introduction

In this chapter, variations in microstructural constituents across the modified 9Cr-1Mo (P91) steel weld joints generated during weld thermal cycles for fabrication using different welding processes *viz* A-TIG, TIG, SMAW and EBW and its influence on high temperature tensile strength and creep deformation across different regions in the joint have been discussed. Impression creep on A-TIG weld joint for assessing different regions in the weld joint, and conventional uniaxial creep tests on different weld joints to assess its type IV cracking behaviour have been carried out.

3.2 Microstructure, hardness across the weld joint

P91 steel in the NT condition exhibited prior austenite grain size (PAG), lath width and $M_{23}C_6$ precipitates size about 20 μm, 700 nm and 100 nm respectively (Fig. 3.1). MX precipitates predominantly exist in the intra lath region and are thermally more stable as compared to $M_{23}C_6$ precipitates [3,5,11,23,65,75-79]. $M_{23}C_6$ precipitates were observed along the PAG and sub-grain boundaries, which strengthen the boundaries through restricting their migration by pinning. EDS spectrum of $M_{23}C_6$ precipitates is given in Fig. 3.1(c). Weld thermal cycle leads to alteration of the microstructural constituents of the base metal in the heat affected zone (HAZ) depending upon the weld peak temperature experienced in that particular region

(Fig. 3.2). The single pass A-TIG weld joint comprises the weld metal (WM), heat affected zone (HAZ) and base metal (BM) (Fig. 3.2(g)). The HAZ consists of distinct regions of coarse prior-austenite grain (CGHAZ) adjacent to weld metal, fine prior-austenite grain (FGHAZ) and intercritical region (ICHAZ) which merges with unaffected base metal (BM) in that order, away from weld metal (Fig. 3.2(b-f)). In the ICHAZ, partial transformation of α to γ upon heating, and γ to α' on cooling (un-tempered) and dissolution of $M_{23}C_6$ precipitates were observed (Fig. 3.3). The average size of $M_{23}C_6$ precipitates in the ICHAZ in as-welded condition was 80 nm. The microstructural features, *viz* PAG size, $M_{23}C_6$ precipitates size (estimated from SEM images) in different regions across the joint varied significantly (Fig. 3.4 and 3.5). Prior-austenite grain sizes of the CGHAZ, FGHAZ, ICHAZ and base metal across the PWHT A-TIG weld joint were around 40 μm, 14 μm, 8 μm and 20 μm respectively. The prior-austenite grain sizes of the A-TIG, EB, TIG and SMAW joint HAZs were comparable. However, the HAZs were much narrower in the EB, TIG (~3.3 mm) and SMAW (~3.5 mm) joints than in the A-TIG (~8.3 mm) joint. The HAZ of EB weld joint was 200-350 μm in width and only a few grains composed different regions in the HAZ. Finer grain size, coarser $M_{23}C_6$ precipitates, and more extensive subgrain formation with reduction in dislocation density were observed in the ICHAZ of PWHT A-TIG joint as compared to other regions in the joint. Dissolution of $M_{23}C_6$ precipitates was observed in the FGHAZ region of weld joint [80]. Partial α to γ transformation upon heating during welding and γ to α' on cooling led to introduce high dislocation density. This assisted to coarsening of existing undissolved precipitates in the ICHAZ during welding were further coarsened during the PWHT. The extent of coarsening of $M_{23}C_6$ precipitates after PWHT was higher in the ICHAZ than that in the base metal region (Fig. 3.5). $M_{23}C_6$ precipitates size in the ICHAZ of as-welded joint was lower (80 nm) as compared to base metal (100 nm). Relatively finer $M_{23}C_6$ precipitates were observed in the WM. In addition to significant coarsening of precipitates during welding in the ICHAZ, boundaries decorated by the particles were lost due to α to γ transformation and migration of boundaries under the very high temperatures experienced (~ 1112 to 1144 K) (Fig. 3.3). In the A-TIG joint [81-84], $M_{23}C_6$ precipitates in the PWHT ICHAZ had an average size of 140 nm and area fraction of 6.5 %, while in the SMAW joint these were 140 nm and 14.4 % respectively (Fig. 3.6). In the EB weld joint, these were 88 nm and 4.0 % respectively (Fig. 3.6). Coarser precipitates in the A-TIG and SMAW joint were due to higher heat input as compared to EB joint. Precipitates size were comparable in the A-TIG, TIG and SMAW joint. Area fraction of $M_{23}C_6$ precipitates were higher in the TIG and SMAW joint is due to re-heating effect on the previous HAZ by the subsequent pass. A-TIG and EB are single-pass joints. Reduction in strength (Table 1) has been noticed in the ICHAZ as compared to other regions in the weld joint due to increase in distance between the barriers to the movement of dislocations such as lath/subgrain boundaries, $M_{23}C_6$ precipitates, and subgrain formation with reduction in dislocation density [65,77,85,86].

SEM EBSD investigation has been performed on single pass A-TIG joint that consists of unmixed regions in the HAZ. EBSD inverse pole figure (IPF) Z-map superimposed with low and high angle grain boundary map revealed the presence of significantly finer grain structure in the ICHAZ than in the WM, CGHAZ, FGHAZ and BM (Fig. 3.7(a-e)). IPF color legend is shown in Fig. 3.7(f). Uniformity of IPF color shade within the packet boundary (packet consists of sub-blocks and lath) depicted the nearly single orientation in it. The packet size decreased from WM to ICHAZ. The subgrain structure size of 1.79, 2.29, 1.93, 1.32 and 1.91 μm were observed in the WM, CGHAZ, FGHAZ, ICHAZ and BM respectively. Low angle grain boundaries (LAGB) ($2<\theta<15°$; red) and high angle grain boundaries (HAGB) ($\theta >15°$; black) distribution in the WM, CGHAZ, FGHAZ, ICHAZ and BM are shown in Fig. 3.8(a-e). The fraction of HAGBs were higher in the ICHAZ and were comparable with base metal. Smaller grains (~1.5 µm) having HAGBs around the bigger grains were observed in the ICHAZ (Fig. 3.8). The ratios of HAGB to LAGBs fraction in different regions across the joint are summarized in Table 2 and Fig. 3.8(f). The ratio was lower in the WM, CGHAZ, and FGHAZ regions, 0.26, 0.20 and 0.30 respectively, which depicted the significant existence of block/lath structure. The ratio of HAGB to LAGBs in the ICHAZ was comparable to the BM region. The variation of misorientation angle in different regions in the joint are shown in Fig. 3.9. Fraction of low misorientation angle (MOA) boundaries (at ≤ 1.5°) was higher in the WM, CGHAZ and FGHAZ. MOA in the ICHAZ and BM regions were comparable. Relatively less low MOA boundaries in the ICHAZ depict the less lath structure. This led to contribute for faster deformation of the zone as compared to other regions. The CSL boundary map (colour lines) and distribution in frequencies (%) in different regions of P91 steel joint are shown in Fig. 3.10. The CSL map overlapped with the boundary map depicting existence of CSL character predominantly in the block boundaries. The fractions of CSL boundaries ($\Sigma 3$, $\Sigma 11$ and $\Sigma 25b$) were noticed to be relatively lower in the ICHAZ region (Fig. 3.10(h)) than in other regions (WM, CGHAZ, BM and FGHAZ) in the joint (Fig. 3.10). CSL boundaries in the CGHAZ and ICHAZ were comparable. The presence of finer precipitates and predominant lath structure in the CGHAZ led to prevent the faster deformation observed in the ICHAZ. The partial transformation to austenite and over tempering of untransformed martensite during weld thermal heating cycle in the ICHAZ region resulted in coarsening of subgrain structure and reduction in CSL boundaries. CSL boundaries improve the creep strength by minimizing the boundary sliding in the steel [75,85].

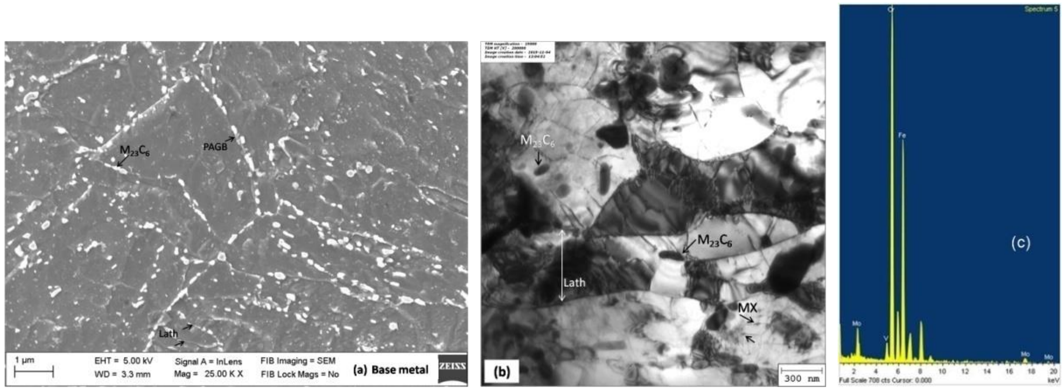

Fig. 3.1 (a) SEM and (b) TEM micrographs of P91 steel in the normalised and tempered (NT) condition, (c) EDS spectrum of $M_{23}C_6$ precipitate.

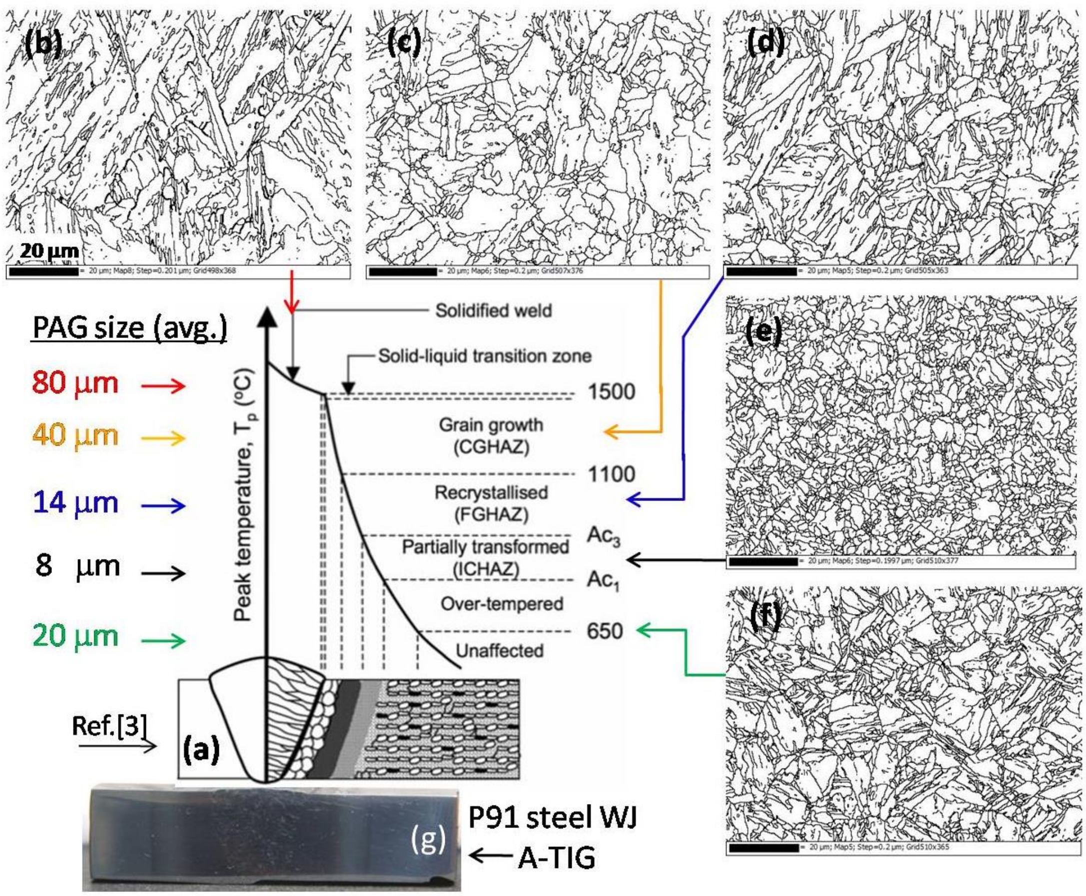

Fig. 3.2 (a) diagram depicting the peak temperature across the joint [3], P91 steel grain boundary map of (b) weld metal, (c) coarge grain, (d) fine grain, (e) inter-critical region, (f) base metal and (g) activated-TIG single-pass joint.

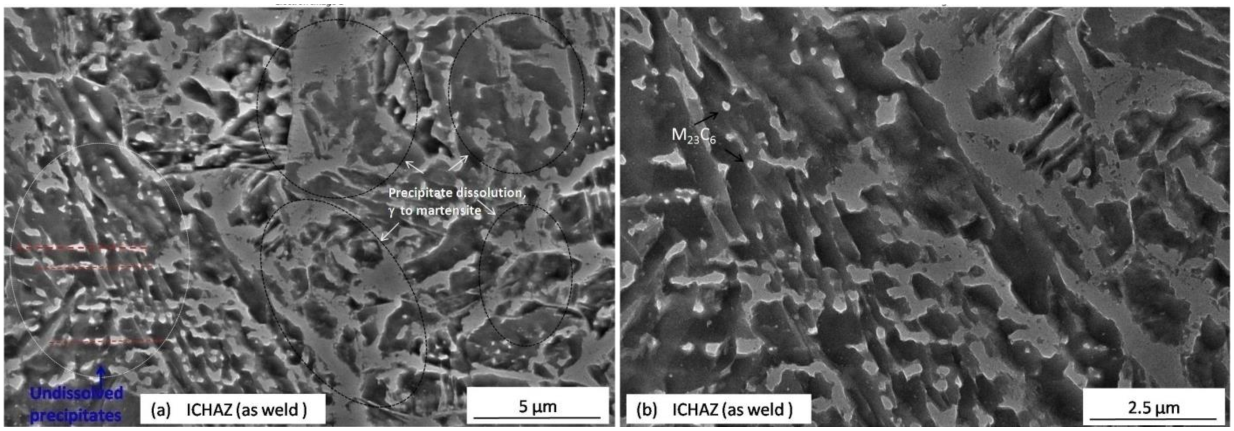

Fig. 3.3 Microstructure of ICHAZ ((a) and (b)) in the as-weld condition depicting the partial transformation to austenite and untransformed martensite upon heating during weld thermal cycle (precipitates without prior boundaries - red line).

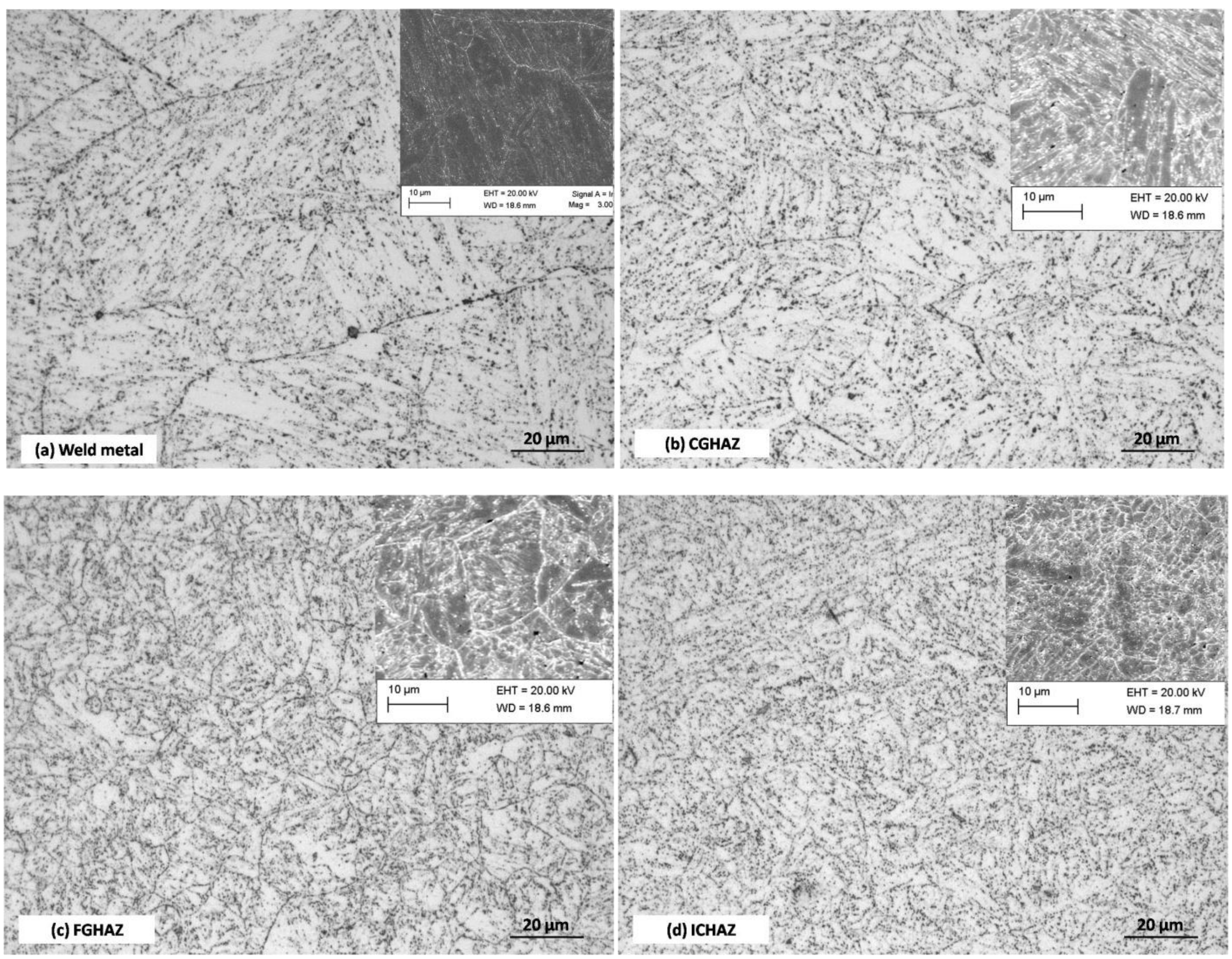

Fig. 3.4 Micrographs across the PWHT A-TIG weld joint of P91 steel, (a) weld metal, (b) CGHAZ, (c) FGHAZ, and (d) ICHAZ.

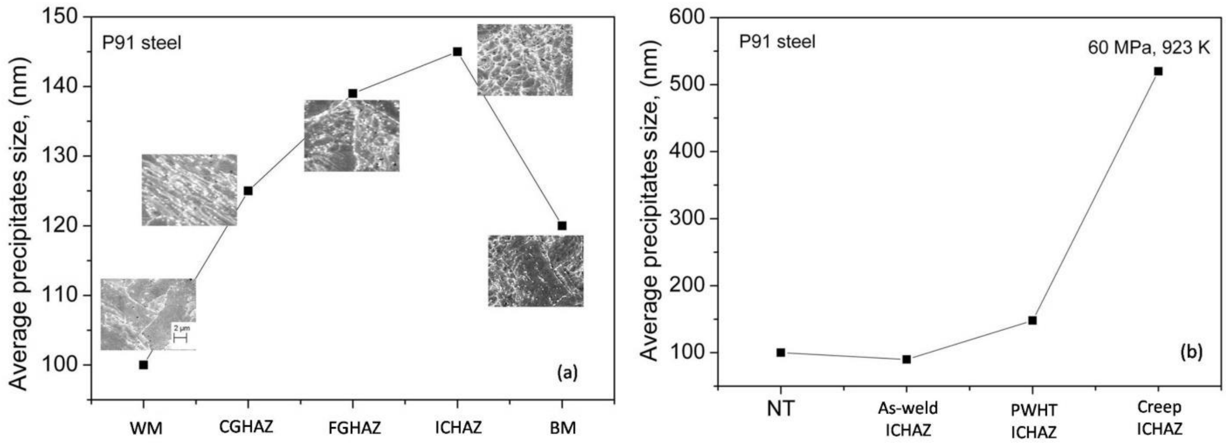

Fig. 3.5 (a) Variation of $M_{23}C_6$ precipitates size across the PWHT A-TIG weld joint and (b) ICHAZ at different condition in the P91 steel joint.

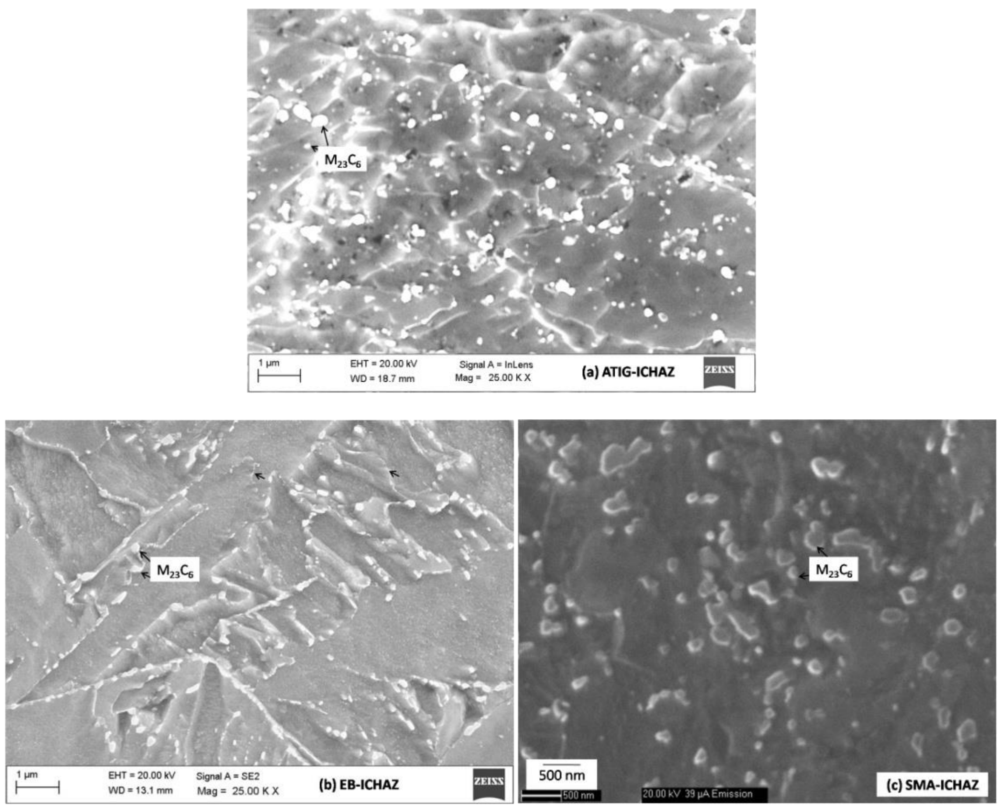

Fig. 3.6 Micrographs of intercritical region in the P91 steel weld joint (a) A-TIG ICHAZ, (b) EB ICHAZ and (c) SMAW ICHAZ

Microstructure of this steel can be considered to consist of these types; (i) recovered (recovery of dislocation structure), (ii) substructure (lath and block) and (iii) deformed structure (consisting of more dislocations at intra-lath region or at interfaces). Relative amounts of these structures vary in different regions of the joint (Fig. 3.11). Substructure frequency (%) in the WM and CGHAZ region was relatively higher than in the other regions, whereas recovered and deformed structure frequencies were lower in the WM and CGHAZ regions (Fig. 3.11(a, b)). In the case of FGHAZ, ICHAZ and BM regions, recovered and substructure frequencies were comparable; but the deformed structure in the ICHAZ region was relatively higher than in the FGHAZ and BM region (Fig. 3.11). Higher deformed structure in the ICHAZ is presumably due to more interfaces (grain boundaries, precipitates/matrix interface). It may be noted that the presence of softer (recovered) and harder (deformed structure) regions in the ICHAZ leads to significant heterogeneity in the microstructure. Under short term creep and at lower test temperature, softer regions might contribute to strengthening by work hardening under the applied stress. Increase in temperature and reduction in applied stress restricts the advantage of work hardening of soft regions of the ICHAZ, concurrently harder regions containing dislocation structure tend to recover, which ultimately leads to loss in strength at high temperature and low stresses. Kernel average misorientations (KAM) maps across the different regions in the weld joint are shown in Fig. 3.12. The color legend for KAM distribution is given in Fig. 3.12(f). The non-uniform color distribution depicts the variations in strain distribution within the blocks and packets. Formation of equiaxed subgrain structure from elongated substructure is predominantly existent in the ICHAZ region (Fig. 3.12(d)).

The KAM value was used to evaluate the dislocation density from the following relationship i.e, $\boldsymbol{\rho_b = \theta_{KAM\,(avg)} . r_{avg}/2b}$, where ρ_b is grain boundary dislocation density, $\boldsymbol{\theta_{KAM\,(avg)}}$ is the average KAM angle in radian, r_{avg} is the ratio of surface area to volume of substructure (misorientations > 0.1°) [87]. Evaluated boundary dislocation density in the WM, CGHAZ, FGHAZ, ICHAZ and BM were about 0.32 x 10^{14}, 0.34 x 10^{14}, 0.25 x 10^{14}, 0.59 x 10^{14} and 0.30 x 10^{14} m^{-2} respectively. Dislocation density estimated in the WM, CGHAZ, FGHAZ and BM were lower than that observed in the ICHAZ. FGHAZ has shown the lowest dislocation density as observed in the KAM map (Fig. 3.12(c)). However, dislocation density of WM, CGHAZ and BM were comparable.

Heterogeneity in strain distribution increased in the order WM, FGHAZ, BM, CGHAZ and ICHAZ region (Fig. 3.12). In addition to the heterogeneous combination of softer and high strain regions, the boundary dislocation density and coarse precipitates are higher in the ICHAZ region. However, the boundaries decorated by the precipitates prior to welding were lost due to reverse transformation to austenite during welding. The presence of more precipitates without pinning the boundary is not much useful for long term creep resistance. Also, presence of more dislocations due to lower martensite start (M_s) temperature contributed by local increase in chromium due to dissolution of precipitates and smaller prior austenite grain size in the ICHAZ region. The low contents of chromium and carbon near the undissolved precipitates results in martensite structure with low dislocation density, which further softened during post weld heat treatment. ICHAZ region exhibited low yield stress-YS and ultimate tensile strength-UTS as compared to other regions in the HAZ (Table 1).

Variation of hardness across the A-TIG weld joint in the as-weld and PWHT conditions are shown in Fig. 3.13(a). The hardness values obtained across the as-weld condition in the weld metal, CGHAZ and FGHAZ regions were comparable. However, a decrease in hardness from the outer edge of the FGHAZ to the base metal with a dip in the ICHAZ was observed. The similar hardness values (400 VHN) observed for weld metal, CGHAZ and FGHAZ in the as-welded condition is due to the similar dislocation density obtained by martensite transformation during

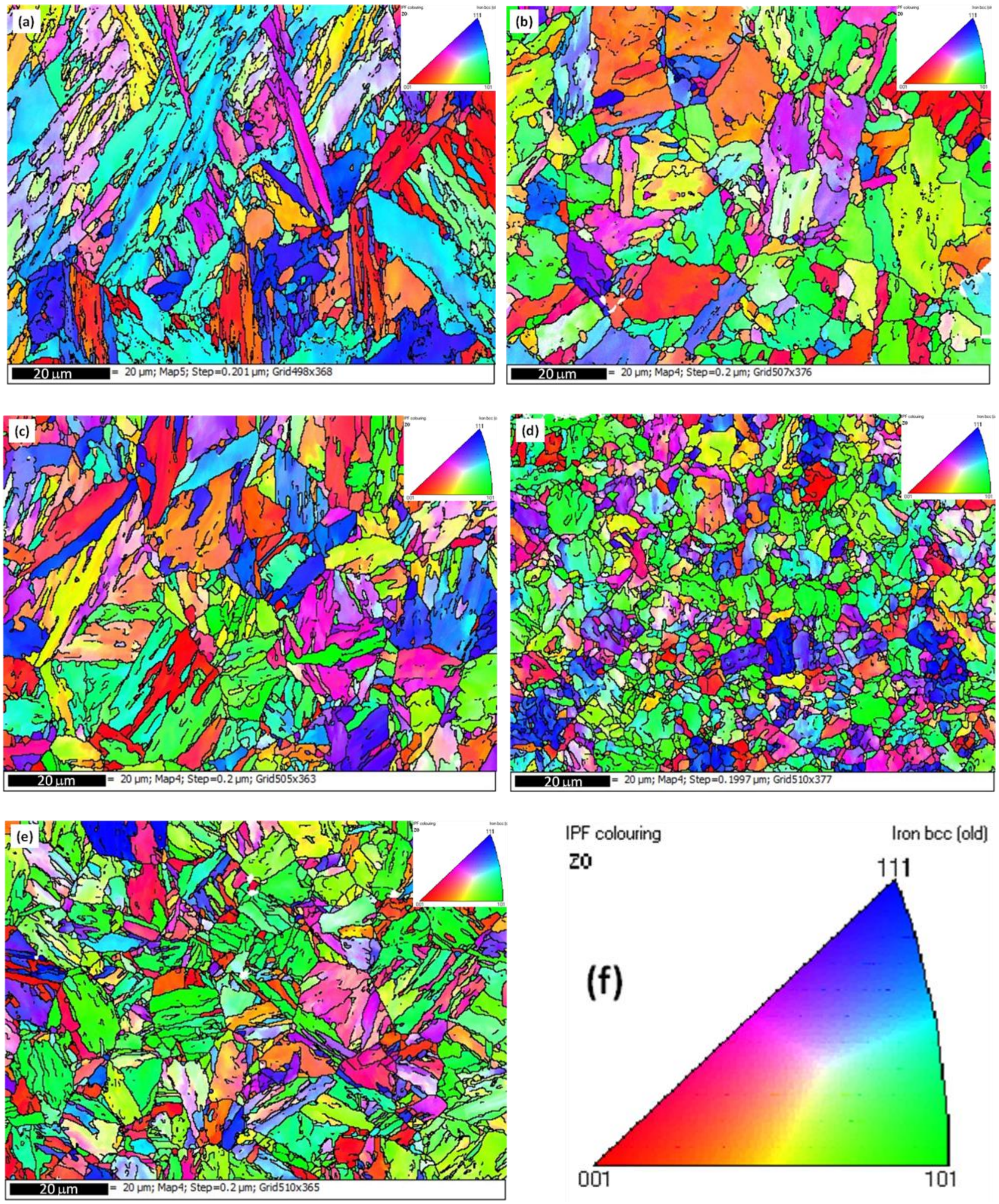

Fig. 3.7 EBSD-IPF map across the A-TIG weld joint of P91 steel, (a) weld metal, (b) CGHAZ, (c) FGHAZ, (d) ICHAZ, (e) base metal and (f) IPF colour legend.

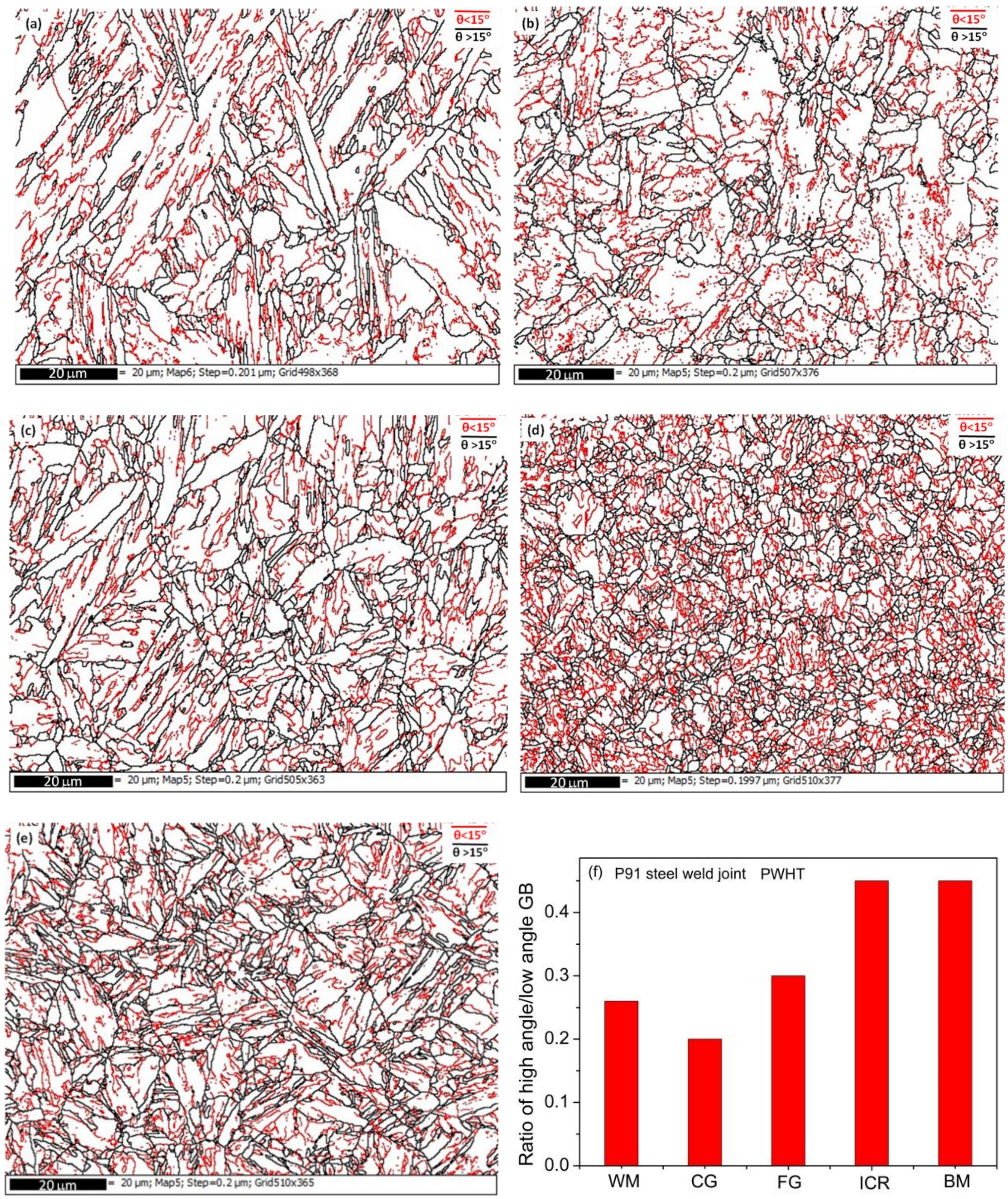

Fig. 3.8 EBSD grain boundary map depicting low angle boundaries (2<θ<15°; red) and high angle boundaries (θ >15°; black) (a) weld metal, (b) CGHAZ, (c) FGHAZ, (d) ICHAZ, (e) base metal and (f) ratio of HAGB/LAGB in the P91 steel A-TIG joint.

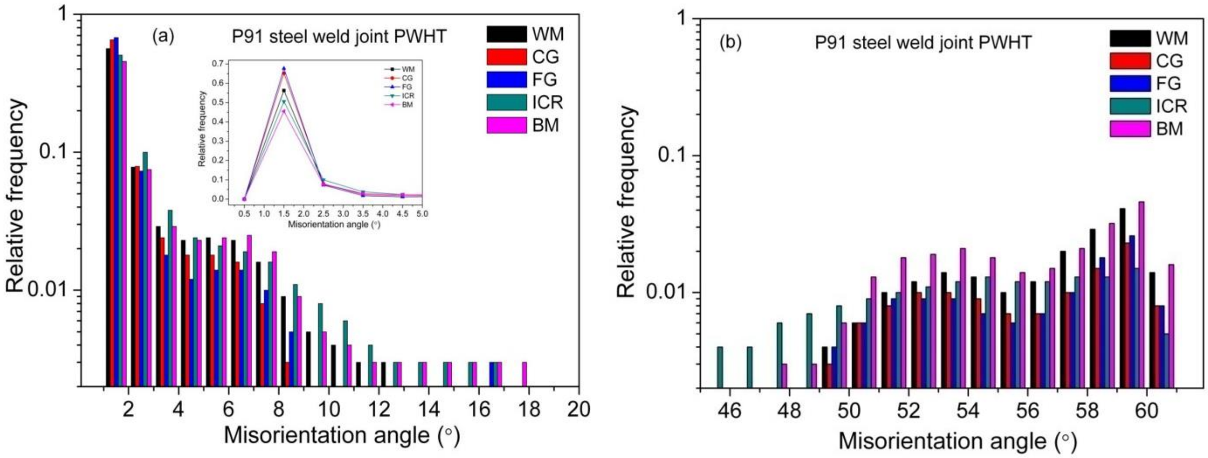

Fig. 3.9 Misorientation angle distribution at different regions in the P91 steel A-TIG joint (a) up to 20°, (b) 45 t o 62° (refer colour picture for interpretation).

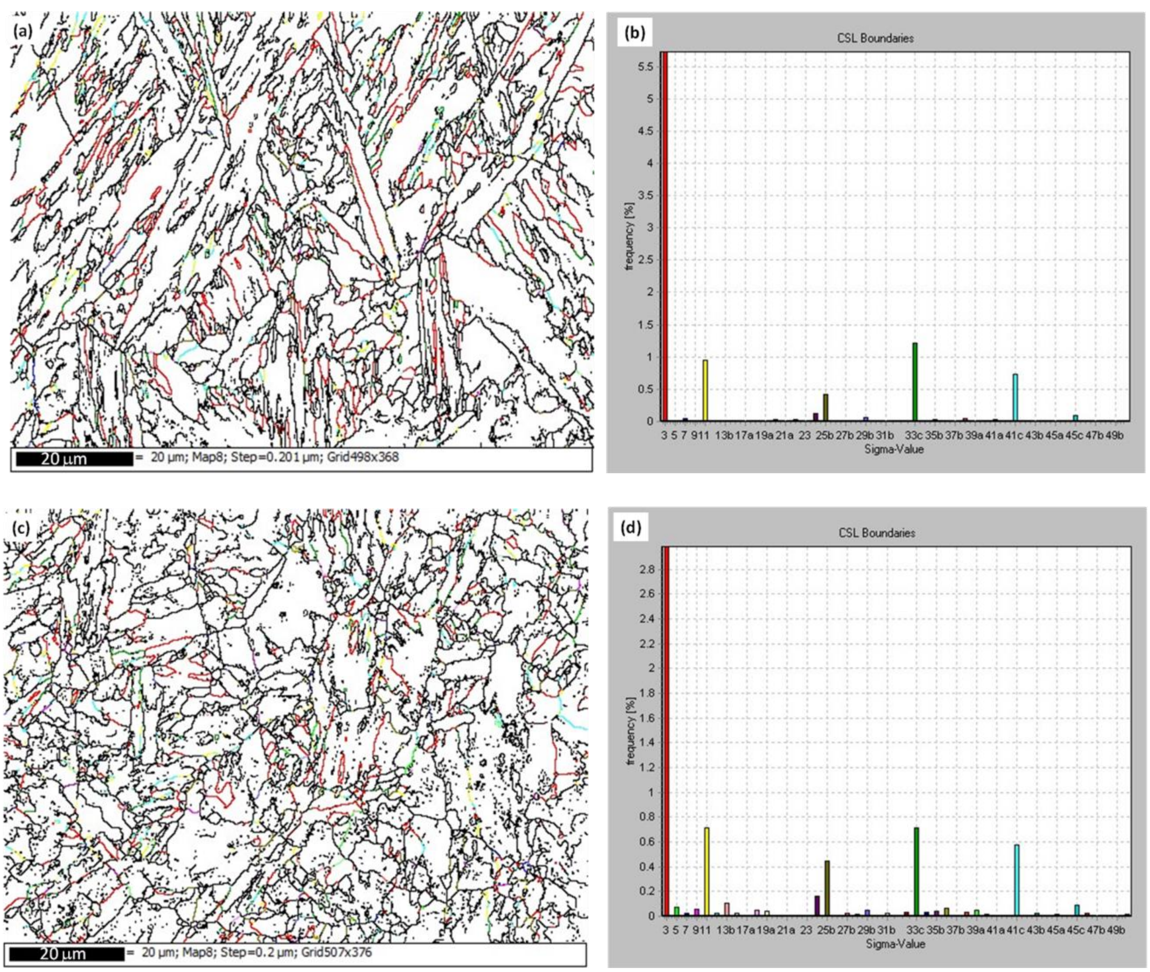

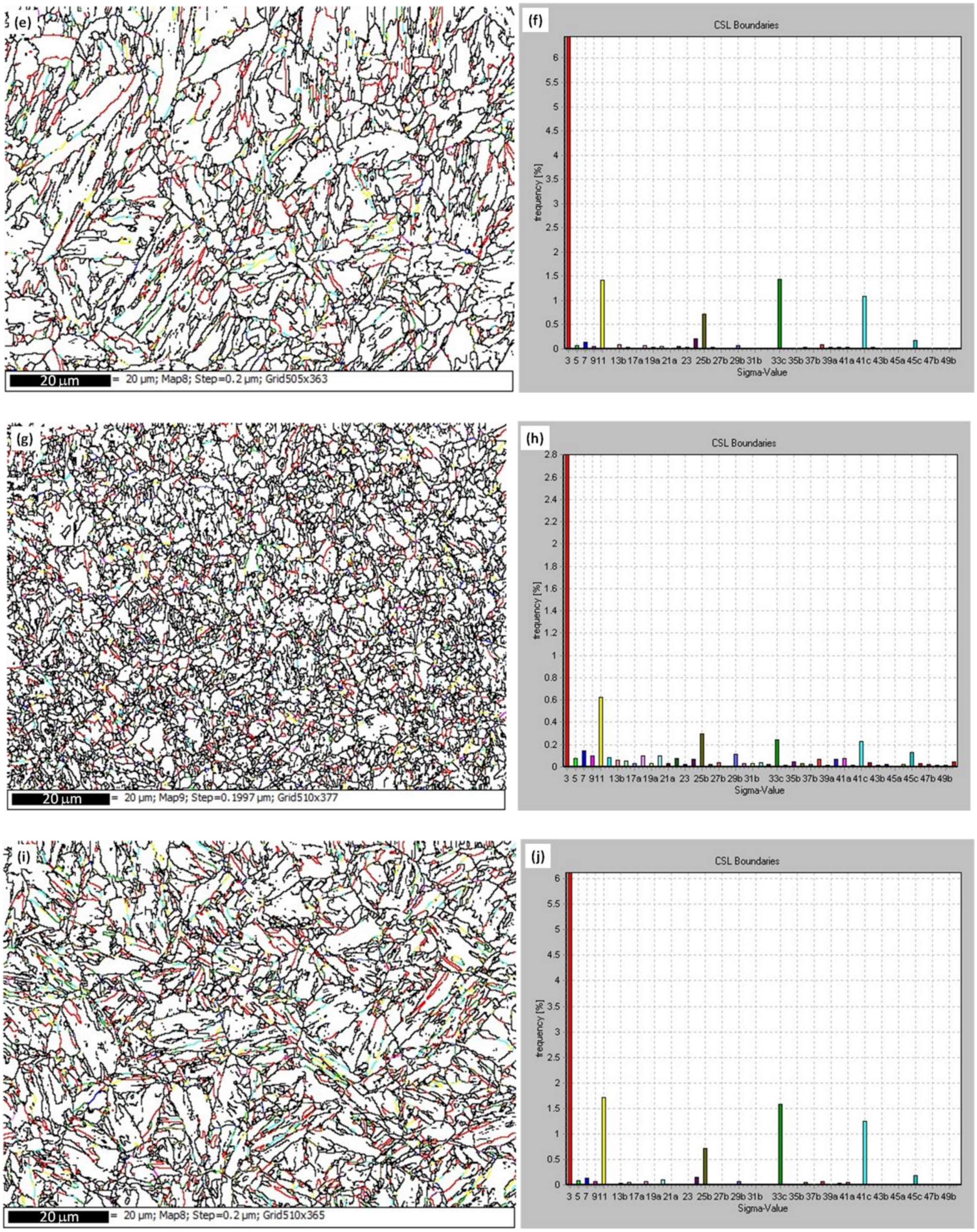

Fig. 3.10 CSL boundary map (colour lines) in different regions of P91 steel A-TIG joint (a,b) weld metal, (c,d) CGHAZ, (e,f) FGHAZ, (g,h) ICHAZ and (i,j) base metal.

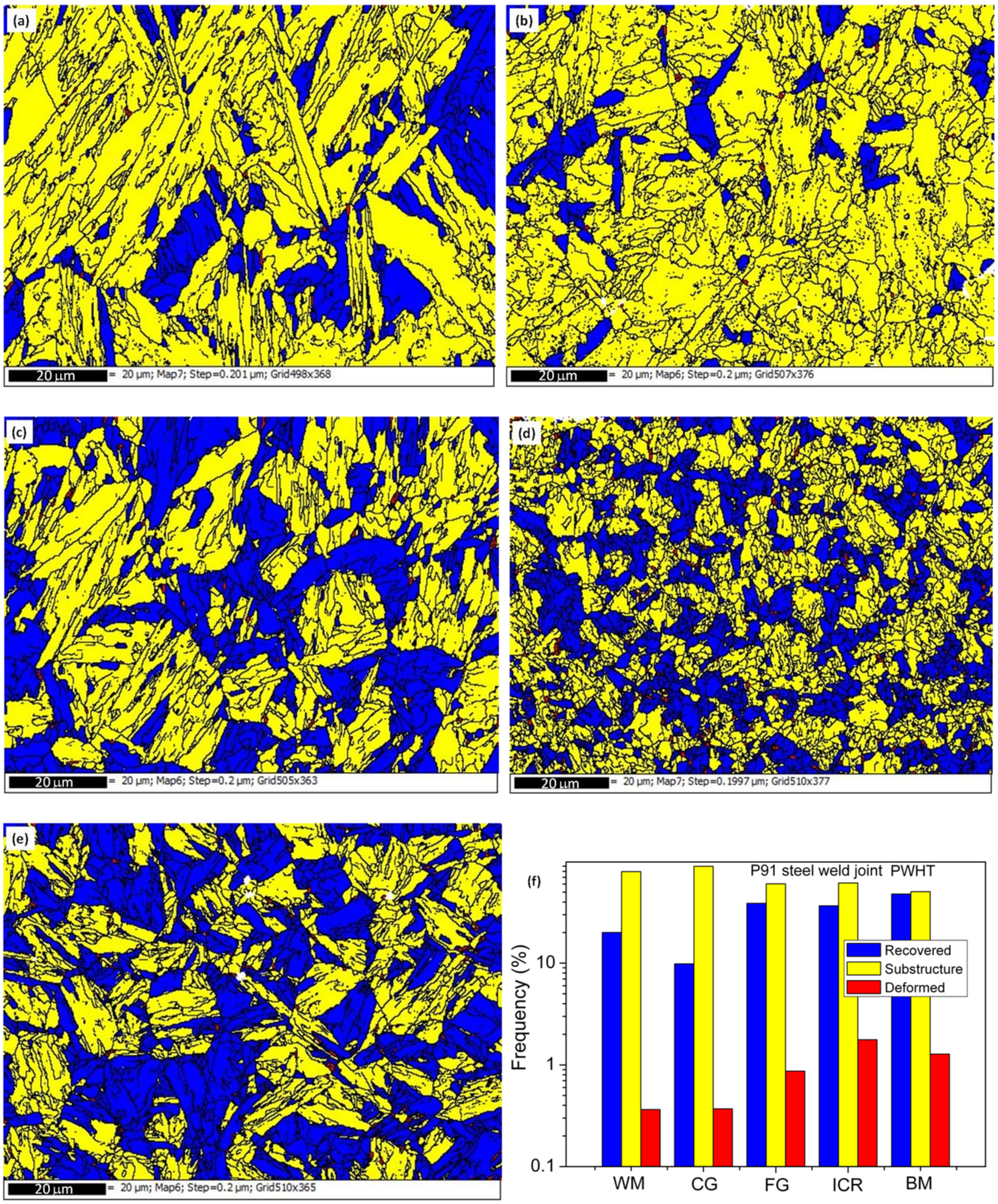

Fig. 3.11 Recovery of substructure (blue), substructure (yellow) and deformed (red) regions in the (a) weld metal, (b) CGHAZ, (c) FGHAZ, (d) ICHAZ, (e) base metal and (f) frequency (%) of microstructural conditions in different regions of P91 steel A-TIG joint.

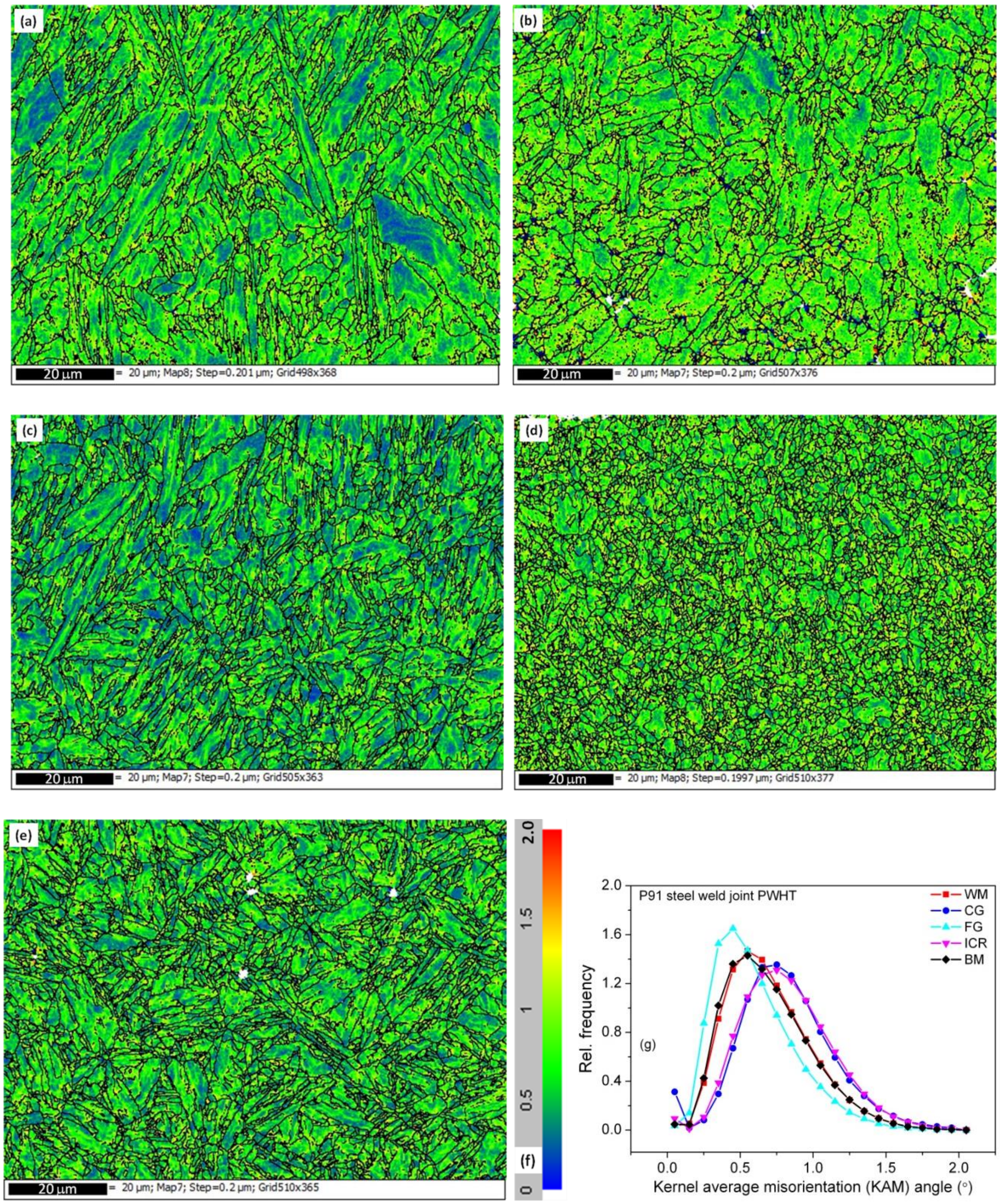

Fig. 3.12 EBSD KAM map depicting the strain distribution in the P91 steel A-TIG joint regions of (a) weld metal, (b) CGHAZ, (c) FGHAZ, (d) ICHAZ, (e) base metal, (f) colour legend for KAM distribution and (g) frequency of KAM angle for different regions in the joint.

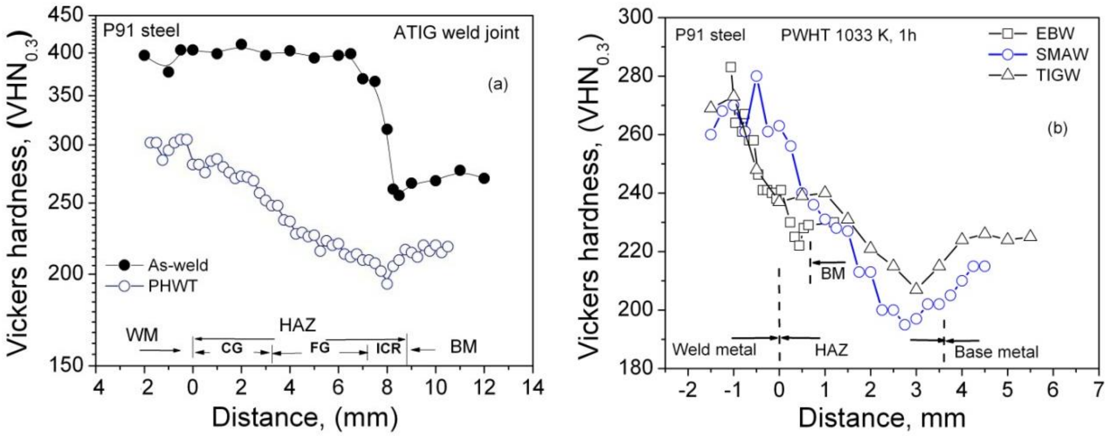

Fig. 3.13 Variation of hardness across the weld joint in the (a) as-weld and PWHT conditions of A-TIG and (b) PWHT condition of EB, TIG and SMA weld joints.

the weld thermal cycle. The A-TIG, EB, TIG and SMAW weld joints subjected to PWHT exhibited a decrease in hardness from the fusion zone (300 VHN) to the base metal (216 VHN) with a hardness trough in the ICHAZ (Fig. 3.13(b)). The formation of subgrain structure with decreased dislocation density and coarser precipitates observed in the ICHAZ are responsible for the lower hardness as compared to other regions in the weld joints. ICHAZ of the EB, TIG and SMAW joints possessed higher hardness as compared to A-TIG weld joint. The increased number density of precipitates in the ICHAZ of TIG and SMAW (~17/μm^2) joint than the A-TIG joint (~6/μm^2) resulted in their higher hardness. Higher number density (~10/μm^2) of finer $M_{23}C_6$ precipitates in the EB joint resulted in its higher hardness than the other weld joints. Although, ICHAZ exhibits the lowest hardness, the synergistic effect of strain hardening of softer regions restricted by the harder regions within the ICHAZ resulted in its increased strength as compared to base metal in the short term creep exposure (high stress), and low temperature condition, leading to failure in the base metal [23,77,80]. However, ICHAZ failure in the joint is evidently seen at high temperature (923 K) even at short durations due to decreased strain hardening capability and recovery dominant in the region containing fine grains and coarser precipitates. Elimination or reduction of heterogeneity in microstructural constituents across the weld joint and restricting the sliding of boundaries in the ICHAZ would enhance the creep rupture strength of the weld joint as compared to the base metal.

3.3 Impression creep

The creep deformation assessed at WM, CGHAZ, FGHAZ, ICHAZ and BM using impression creep test at 923 K under a punching stress of 300 MPa on single pass A-TIG joint is presented in Fig. 3.14(a). ICHAZ has exhibited higher depth of penetration/deformation (Fig. 3.14). CGHAZ region experienced significantly less creep deformation in comparison with other regions. BM and FGHAZ deformation were comparable, whereas ICHAZ region deformed at faster rate than the BM, FGHAZ, CGHAZ and WM (Fig. 3.14(b)). Presence of soft ferrite in the weld metal leads to deformation at higher rate than the BM, FGHAZ and CGHAZ. The creep deformation rate of CGHAZ was the lowest. The impression punch stress (300 MPa) in different regions of the joint is equivalent to uniaxial applied stress about 99 MPa with a correlation factor of 0.33 reported by H.Y. Yu et al [88]. Distinct heterogeneity in the shorter creep exposure would further enhance the difference in deformation behaviour between the regions, which would ultimately result in the premature failure of the joint by localized deformation and creep cavitation in the ICHAZ due to microstructural heterogeneity within the ICHAZ. Creep deformation (depth of penetration) with time for ICHAZ at 923 K at applied punch stresses over a range of 180-330 MPa (equivalent uniaxial stresses 59-109 MPa) are shown in Fig. 3.15. Lower creep strength of the ICHAZ than the other regions in the joint is evident, about 120 MPa loss of strength in ICHAZ compared to the CGHAZ (at a given depth of penetration and exposure duration). Minimum creep rates obtained from impression creep and uniaxial tensile creep for ICHAZ at 923 K have been given in Fig. 3.15(b). Minimum creep rate of ICHAZ in the weld joint obtained from impression creep has shown relatively higher as compared to the uniaxial tensile creep rate evaluated from simulated ICHAZ.

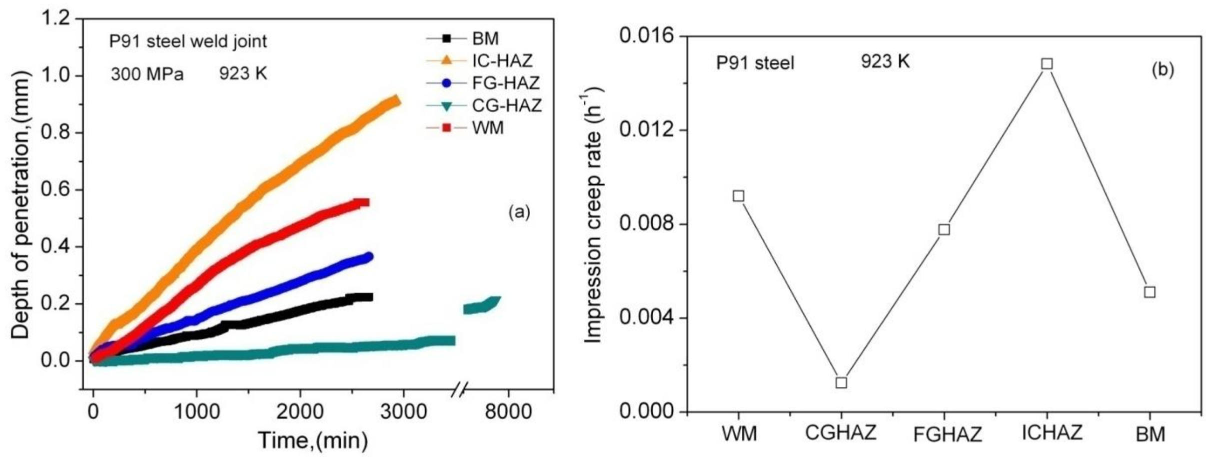

Fig. 3.14 (a) Depth of penetration with time and (b) impression creep rate for weld metal, CGHAZ, FGHAZ, ICHAZ and base metal in P91 steel weld joint at 923 K and 300 MPa punch stress.

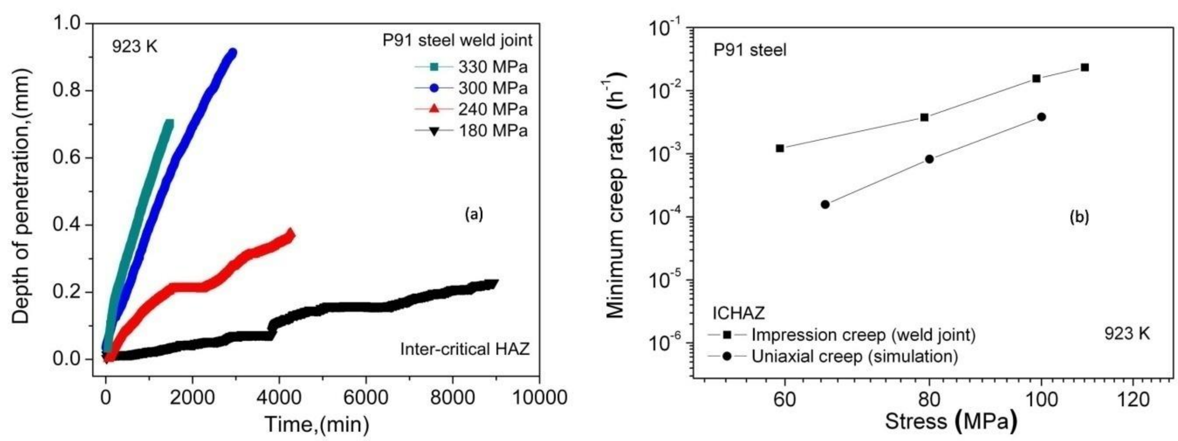

Fig. 3.15 (a) Depth of penetration with time for ICHAZ in P91 steel A-TIG weld joint at 923 K and different punch stress levels, (b) minimum creep rate for ICHAZ at 923 K from simulation and A-TIG weld joint of P91 steel at different stress levels.

3.4 Uniaxial creep behaviour of weld joints

A comparison of the creep curves of A-TIG and SMA weld joints of P91 steel with the base metal at 923 K and 80 MPa is shown in Fig. 3.16(a). Both the joints exhibited primary creep regime followed by an apparent steady state creep deformation and an accelerating tertiary creep regime as observed in the base metal. The SMAW joint has the lowest life a factor of 20 lower than the base metal, whereas the A-TIG weld joint has a life lower by a factor of 10. The variations of creep rate with creep exposure for the base metal and weld joints are compared in Fig. 3.16(b). The creep rate decreased from initial deformation with creep exposure to a minimum value followed by increase with no considerable secondary stage of creep deformation. The tertiary stage of creep deformation in the weld joint was found to initiate much early than the base metal. Extensive microstructural changes (higher rate of recovery of dislocations and coarsening of subgrain boundaries in the ICHAZ) and localized creep deformation in the selected constituents of the joints have been considered responsible for the early onset of tertiary stage of creep deformation in the steel weld joints in comparison with base metal. The early initiation of tertiary creep deformation in the SMAW joint is attributed to the higher deformation constraint (generated by mixed HAZ regions due to multi-pass process) imposed on the soft ICHAZ by adjacent regions. The delayed initiation of tertiary creep deformation in the A-TIG weld joint is attributed to lesser deformation constraint in ICHAZ caused by adjacent unmixed HAZ regions (Fig. 3.2(g)). The variations of rupture life (t_r) with applied stress (σ_a) for the base metal, A-TIG, EB, TIG and SMAW joints of the P91 steel at 923 K are shown in Fig. 3.17. The weld joints had significantly lower creep rupture life than the base metal at all the stress levels. Difference in the rupture life (t_r) between the weld joints and base metal increased with decrease in applied stress. The A-TIG and EB weld joints show higher t_r in comparison with TIG and SMAW joints. TIG weld joint possessed higher t_r than the SMAW joint. The differences in rupture life between A-TIG and TIG weld joints were increasingly evident with decrease in σ_a.

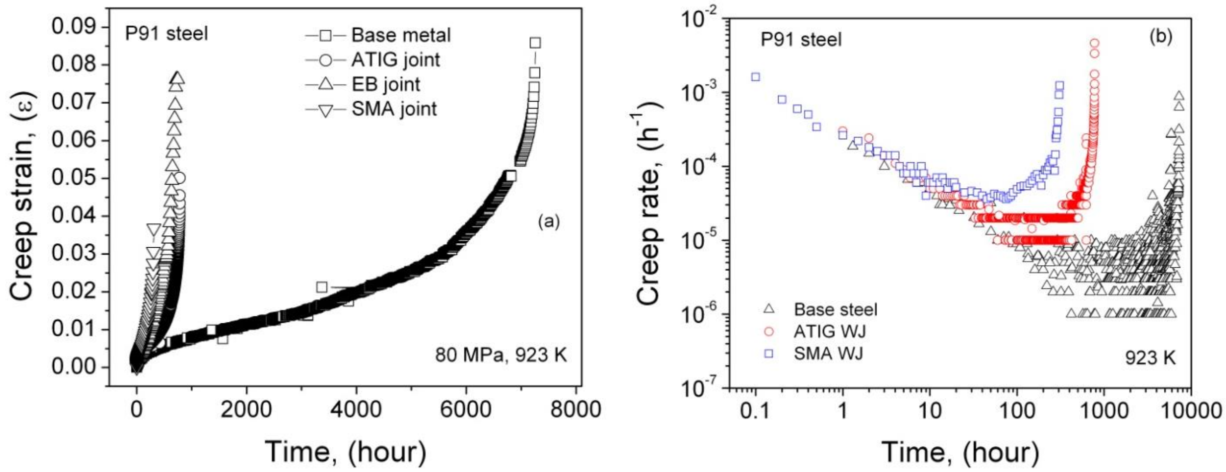

Fig. 3.16 (a) Creep curves and (b) Creep rate with time curves of base metal, joints of P91 steel at 923 K.

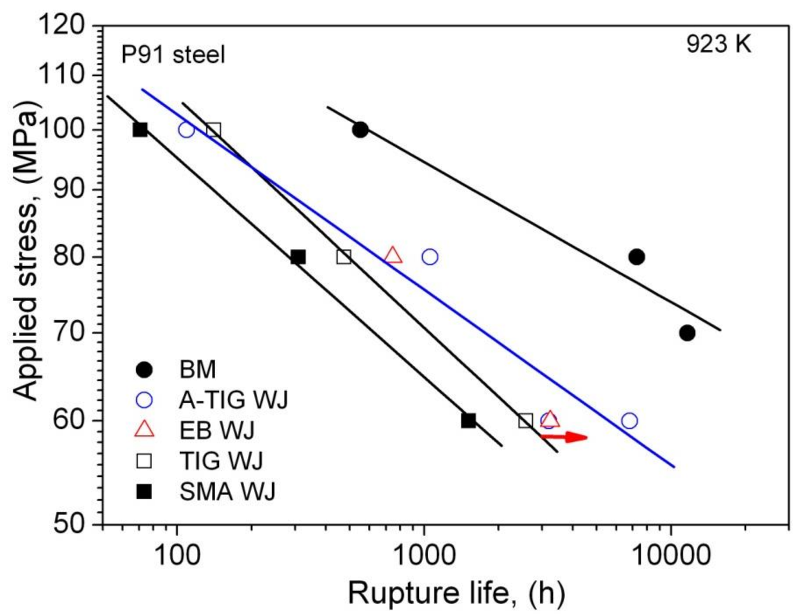

Fig. 3.17 Variations of creep rupture life with applied stress for base metal and weld joints of P91 steel at 923 K.

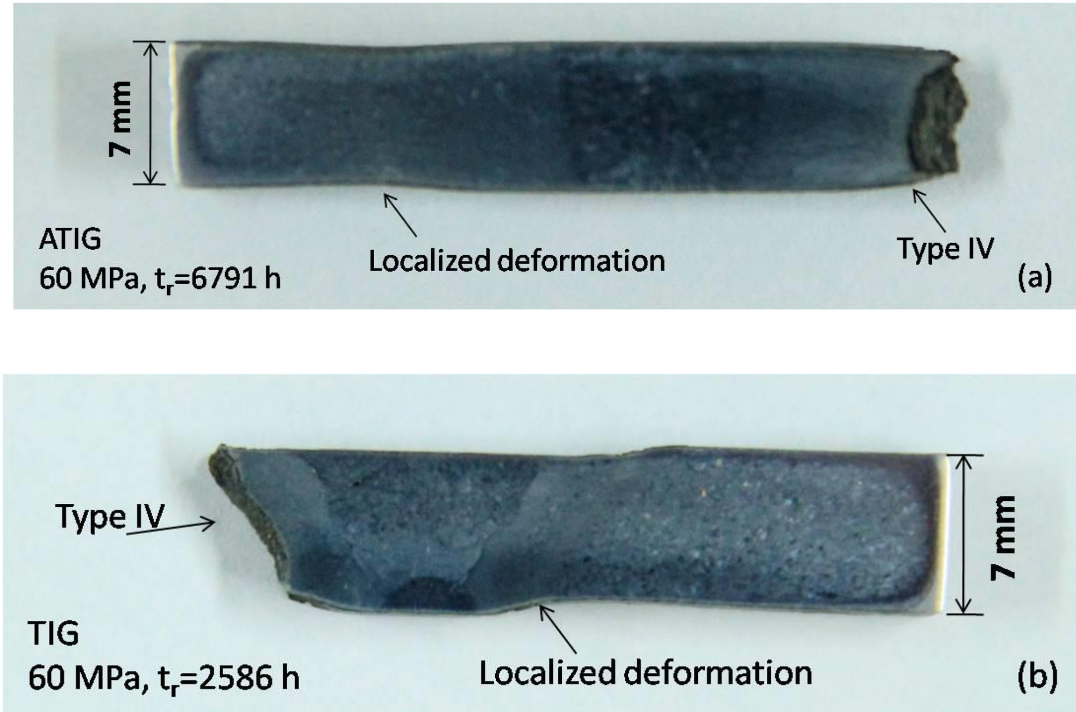

Fig. 3.18 A-TIG and TIG weld joints creep ruptured specimens at 60 MPa stress and 923 K.

3.5 Rupture behaviour and microstructure of crept weld joints

The creep ruptured A-TIG and TIG weld joints specimens at 60 MPa are shown in Fig. 3.18. Localized creep deformation was observed in the outer edge of HAZ in both the joints. The base metal, weld metal, CGHAZ and FGHAZ regions were found to be more or less damage free. A drastic reduction in rupture ductility occurred in the weld joints as compared to the base metal (Fig. 3.16) indicating localized deformation. Since the creep specimen consists of different regions with widely varying microstructure and mechanical properties, the deformation is highly heterogeneous and the rupture ductility calculated on the entire gauge length has less meaning. However, the reduction in rupture ductility was relatively lower in the A-TIG joint as compared to the TIG joint. Nondestructive measurement of local reduction of dimension in the ICHAZ has been reported to be one of the life predicting variable incase of difficulties to acquire the volumetric information (voids) [80,86]. However, the weld joint exposed to high temperatures for long duration may not provide considerable indication of outer dimensional change (which decreases with decrease in applied stress) in the ICHAZ of the weld joint. Since, the creep damage accumulates in the interior. The mixed mode of failure (ductile and brittle) has been observed in the A-TIG joint specimen tested at 60 MPa (Fig. 3.19). A relatively brittle mode of failure occurred in TIG joint in comparison with A-TIG joint under similar test conditions. Microstructural investigations on the intact side of the creep exposed joint revealed that creep failure of the joint occurred in the ICHAZ which had exhibited lowest hardness prior to creep testing. Fracture in the EB joint has occurred in the base metal region at 80 MPa. In the present study, at 923 K, type IV failure has been observed in the ICHAZ of the A-TIG, TIG and SMAW joints 80 MPa and below. However, the localized creep deformation and reduction in ductility became increasingly prominent with decrease in σ_a.

Microstructures of the weld metal, base metal and different HAZ constituents of A-TIG weld joint creep exposed at 60 MPa are shown in Fig. 3.20. Localized creep cavitation was observed in the ICHAZ as compared to other regions in the joint. SEM micrographs of ICHAZ in the A-TIG and SMAW weld joints depicting $M_{23}C_6$ precipitates are shown in Fig. 3.21. Extensive coarsening of $M_{23}C_6$ precipitates with sub-grain formation has been observed in the ICHAZ. The localized plastic flow in the ICHAZ might have enhanced the coarsening of $M_{23}C_6$ precipitates on creep exposure than other regions of the HAZ by enhanced diffusion by providing easy paths. The coarsening of $M_{23}C_6$ precipitates led to accelerate the recovery process of the steel, which led to decrease its strength drastically. The $M_{23}C_6$ precipitates size about 520 nm and area fraction of 3.0% have been observed in the ICHAZ A-TIG crept at 923 K and 60 MPa stress (Fig.3.21). Coarser and higher area fraction of $M_{23}C_6$ precipitates have been observed in the ICHAZ of creep tested TIG and SMAW weld joints.

Creep cavitation was localized in the ICHAZ, and was associated with $M_{23}C_6$ precipitates. Extensive creep cavitation was observed in the ICHAZ of TIG and SMAW joints than the A-TIG joint (Fig. 3.22). The flow of the low creep resistance region is restricted by the surrounding stronger creep resistance region resulting in the development of greater triaxial state of stress in the soft ICHAZ. Creep damage accumulation due to strain incompatibility between the creep strong and creep weak regions was reported in the P91 welds [3,24,89-91]. However, in the present investigation, the lower deformation constraint imposed on the soft intercritical region due to existence of systematic unmixed regions across the HAZ of the A-TIG weld joint resulted in decrease in triaxial state of stress (which causes predominant creep cavitations assisting the premature Type IV failure). This led to lower creep cavitations in the ICHAZ of A-TIG joint. TIG and SMAW joints exhibited lower creep rupture life due to coarsening of $M_{23}C_6$ precipitates and enhanced creep cavitation. Coarsening of precipitates lowers the strength locally by depletion of alloying elements from solid solution leading to increased plasticity. Nucleation of cavities is easier at the coarse precipitates and their growth is aided by increased plasticity.

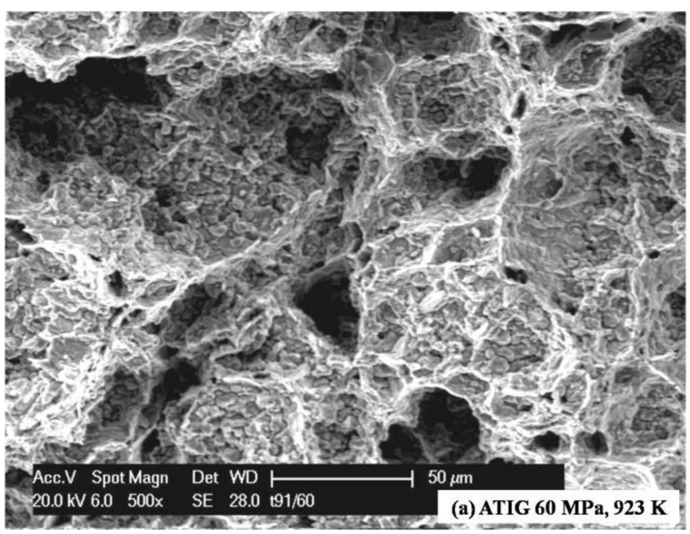

Fig. 3.19 Fracture surface of the crept joint of P91 steel at 923 K, 60 MPa A-TIG.

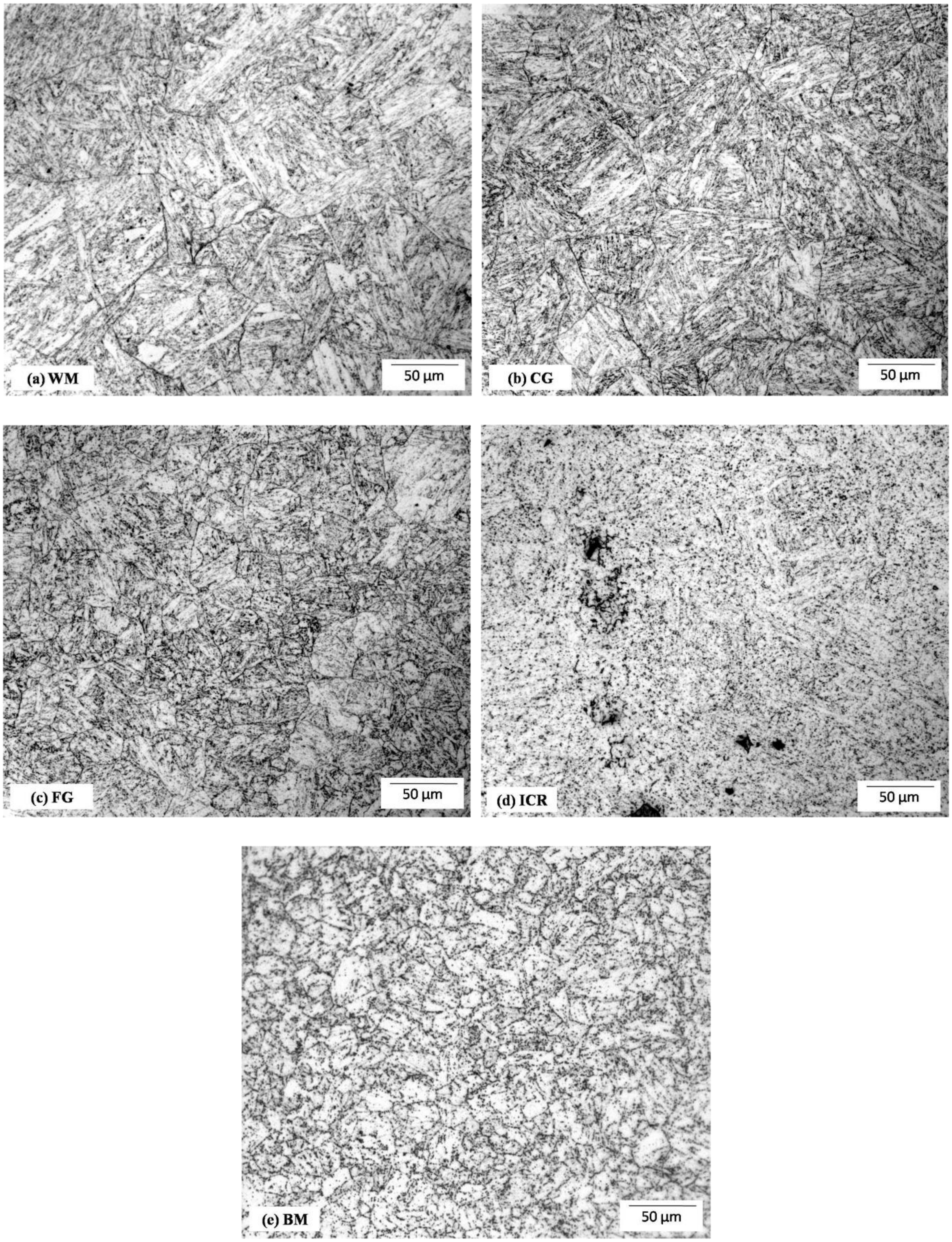

Fig. 3.20 Microstructure across the crept A-TIG joint of P91 steel at 923 K, 60 MPa (a) WM, (b) CGHAZ, (c) FGHAZ, (d) ICHAZ and (e) BM.

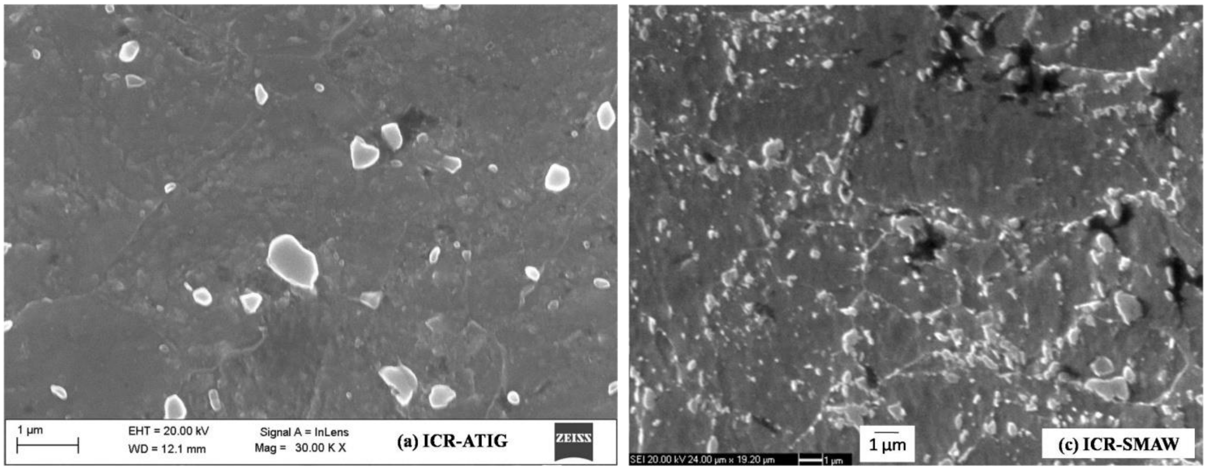

Fig. 3.21 SEM micrographs of ICHAZ in the (a) A-TIG, (c) SMAW weld joints at 923 K, 60 MPa.

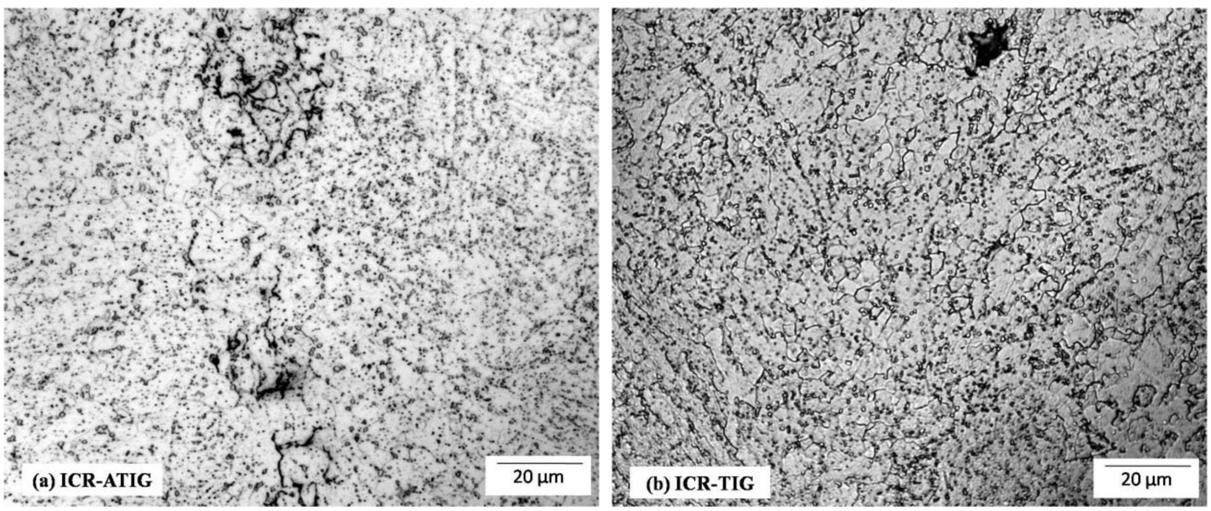

Fig. 3.22 Creep cavitation in the ICHAZ observed at 923 K, 60 MPa in (a) A-TIG and (b) TIG and (c) SMAW.

3.6 Weld strength factor

The creep strength of a welded component is decided by that of the weld. Therefore, creep design of welded components introduces a weld strength factor (WSF), which is defined as the ratio of the uniaxial creep rupture strength of the weld joint (σ_{WJ}) to the uniaxial creep rupture strength of the base metal (σ_{BM}) at the same rupture life, temperature and environment,

$\sigma_{WSF} = (\sigma_{WJ}/\sigma_{BM})$ [68, 83]. Weld strength factor (WSF) has been used with base metal data to calculate allowable design stress for the welded components [68]. The variation of WSF A-TIG, EB, TIG and SMAW weld joints of P91 steel with creep rupture life at 923 K presented in Fig. 3.19 clearly shows the loss of creep rupture strength of the steel joint with increase in creep exposure time. A 26% loss of creep rupture strength of the joint (WSF about 0.74) compared to the base metal (at 923 K for $t_r = 10^4$ h) in the A-TIG joint has been obtained by extrapolation in this investigation. The HAZ width of SMAW and A-TIG weld joints were ~3.5 and 8.3 mm respectively. WSRF values in the range 0.79 to 0.65 under long term creep at 923 K have been reported by Parker et al in the P91 steel weld joint [68] from conventional creep tests. The higher deformation constraint in the TIG and SMAW joints results in higher loss of strength as compared to the base metal and A-TIG joint (Fig. 3.23). Extensive creep cavitation in the ICHAZ of TIG and SMAW cross weld joints confirms the presence of higher levels of constraint in it than in the ICHAZ of A-TIG joint. WSF for SMAW joint is lower than the TIG joint. Although the geometry of both TIG and SMAW joints are similar, less microstructural degradation in TIG joint during weld thermal cycle led to cause this difference. However, WSF difference between TIG and SMAW joints decreased under long term exposure. Further, the creep rupture strength of the joint would depend on the geometry of the joint. Hence, a reduction of about 0.10-0.14 in WSF value in the TIG and SMAW joints compared to the A-TIG joint is observed (Fig. 3.23).

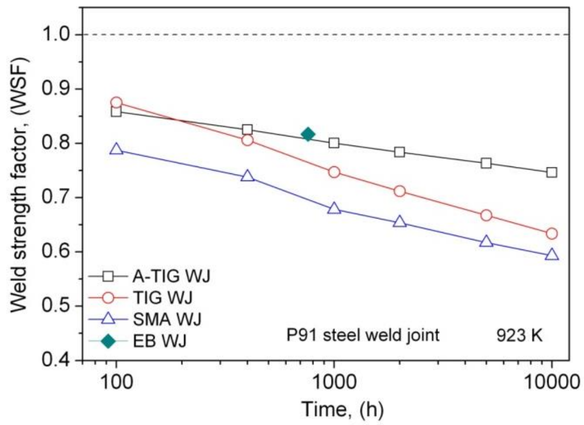

Fig. 3.23 Weld strength factor for P91 steel weld joints prepared using different process at 923K.

Table 3.1 Tensile properties of P91 steel HAZ simulated microstructures at 923 K.

P91 steel	923 K			PAG size (µm)
	Y. S (MPa)	U.T.S (MPa)	Total elongation, (%)	
CGHAZ	234	242	29.9	40
FGHAZ	195	210	27.2	18
ICHAZ	132	139	36.4	9
BM	209	215	35.0	20

Table 3.2 EBSD analysis and hardness of different constituents of P91 steel PWHT A-TIG joint.

P91 steel	Grain boundary frequency			Vickers Hardness, ($VHN_{0.3}$)
	LAGB $\theta < 15^o$	HAGB $\theta > 15^o$	Ratio of HAGB/LAGB	
WM	0.79	0.21	0.26	291
CGHAZ	0.83	0.17	0.20	268
FGHAZ	0.77	0.23	0.30	220
ICHAZ	0.69	0.31	0.45	195
BM	0.69	0.31	0.45	218

3.7 Conclusions

Based on the detailed microstructural investigations across the single-pass A-TIG weld joint, and assessment of welding process influence on type-IV cracking behaviour of P91 steel joint, following conclusions have been drawn:

1. The lower content of low misorientation angle and coincidence site lattice (CSL) boundaries, coarser substructure, finer grain size, predominant heterogeneous combination of more recovered and deformed structure, coarser $M_{23}C_6$ precipitates, and boundaries devoid of precipitates have been identified as the factors leading to higher rate of deformation in the ICHAZ region as compared to other regions in the joint.

2. The more heterogeneous microstructure of the ICHAZ than the other regions, contributed to significant damage under creep in addition to the constraint imposed by adjacent regions in the weld joint.

3. Heterogeneous microstructure and variations in high temperature strength of the different regions across the joint has led to reduction in creep rupture strength of the single-pass activated-TIG weld joint by about 26% as compared to the base metal at 923 K for a rupture life of 10^4 h.

4. Although geometry of both TIG and SMAW joints are similar, less microstructural degradation in TIG joint during weld thermal cycle led to lower SRF for SMAW than the TIG joint. However, WSF difference between the WSFs of TIG and SMAW joints decreased under long term exposure. Reduction of about 0.10-0.14 in WSF value in the TIG and SMAW joints vis-á-vis that of A-TIG joint has occurred due to mixed microstructural regions and more repeated thermal cycle in HAZ.

5. A-TIG welding is preferred to fabricate the components against Type IV cracking resistance; TIG welding is recommended than the SMAW in the case of component required manufacturing from multi-pass welding technique.

CHAPTER 4

Influence of Boron with Controlled Nitrogen Content on Creep Deformation and Rupture Behaviour of P91BN Steels and Weld Joints

4.1 Introduction

In this chapter, P91 steels having different combination of boron and nitrogen contents (P91BN) and the steel without boron (P91) have been investigated. The studies pertaining to microstructure, differential scanning calorimetry, tensile properties, creep deformation and rupture behaviour of base metals and weld joints were carried out. The creep behaviour of simulated ICHAZ of P91 and P91BN-4 (B=0.010, N=0.0021) steels has been presented in this chapter. Creep tests were carried out at different temperatures (823 - 923 K) over a wider range of applied stress (50-350 MPa).

4.2 Base metals

4.2.1 Optical microstructure

Optical microstructures of the steels having boron (P91BN) and without boron (P91) in the normalized and tempered (NT) conditions are given in Fig. 4.1. The tempered martensitic microstructure was observed in the steels with prior austenite grain (PAG) size of 45 ± 10 µm, 55 ± 10 µm, 60 ± 15 µm and 48 ± 10 µm in P91 (N=0.050), P91BN-1 (B=0.006, N=0.011), P91BN-2 (B=0.010, N=0.0047) and P91BN-3 (B=0.009, N=0.010) steels respectively under similar heat-treated conditions (Fig. 4.1 (a-d)). The PAG size relatively decreased with increase in nitrogen content. Comparatively similar PAG size has been reported in the 9Cr-W steel with and without boron [92]. PAG size of about 30-50 μm in 9Cr-3W steel and ~100 μm in the 10Cr steel were observed under similar normalizing temperature [93,94]. In general, boron containing steel with lower nitrogen (<0.003% N) content exhibits higher PAG size [94].

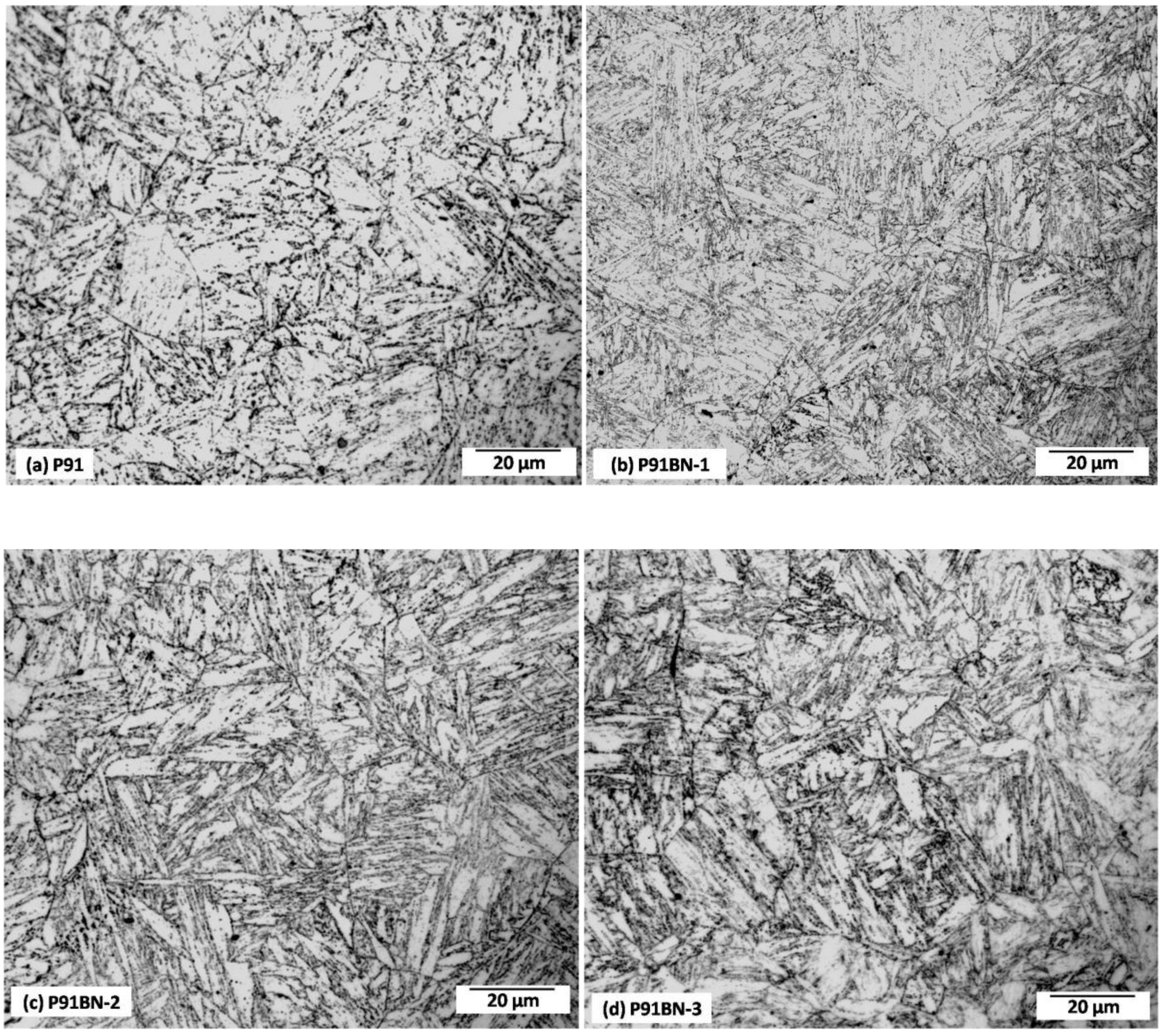

Fig. 4.1 OM micrographs of (a) P91, (b) P91BN-1, (c) P91BN-2 and (d) P91BN-3 steels in the normalized and tempered condition.

4.2.2 Phase transformations

The differential scanning calorimetry (DSC) thermograms for P91 and P91BN steels are shown in Fig. 4.2 in which α to γ phase transformation occurs during heating. The temperature at which α to γ transformation starts is commonly referred to as Ac_1, and the finish temperature (complete transformation to γ phase) is called as Ac_3. This phase transformation occurs over a range of temperatures, and the region between these critical temperatures (Ac_1 and Ac_3) is known as intercritical region. The Ac_1, Ac_3, and Curie temperatures for P91 and P91BN steels at a heating rate of 10 K min^{-1} are given in Table 4.1. P91BN steels containing boron have exhibited about 20 K higher Ac_1 and Ac_3 transformation temperatures than the P91 steel. These transformation temperatures among the P91BN steels were comparable.

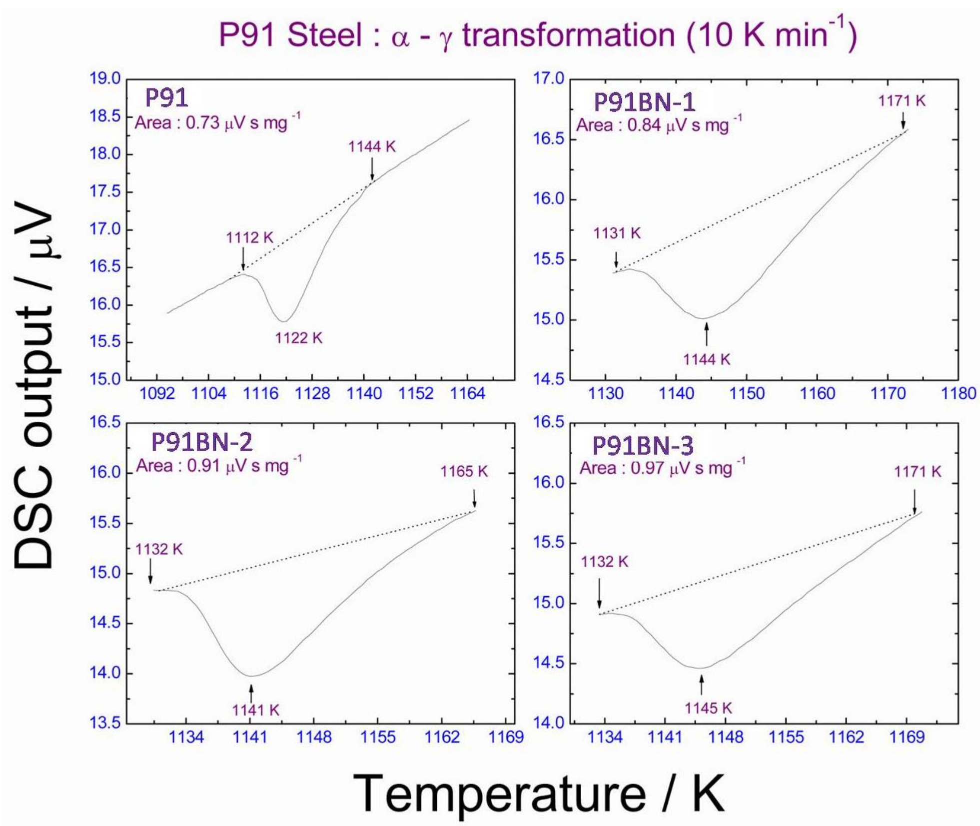

Fig. 4.2 DSC thermograms for P91, P91BN-1, P91BN-2 and P91BN-3 steels during heating at the rate of 10 K min^{-1}.

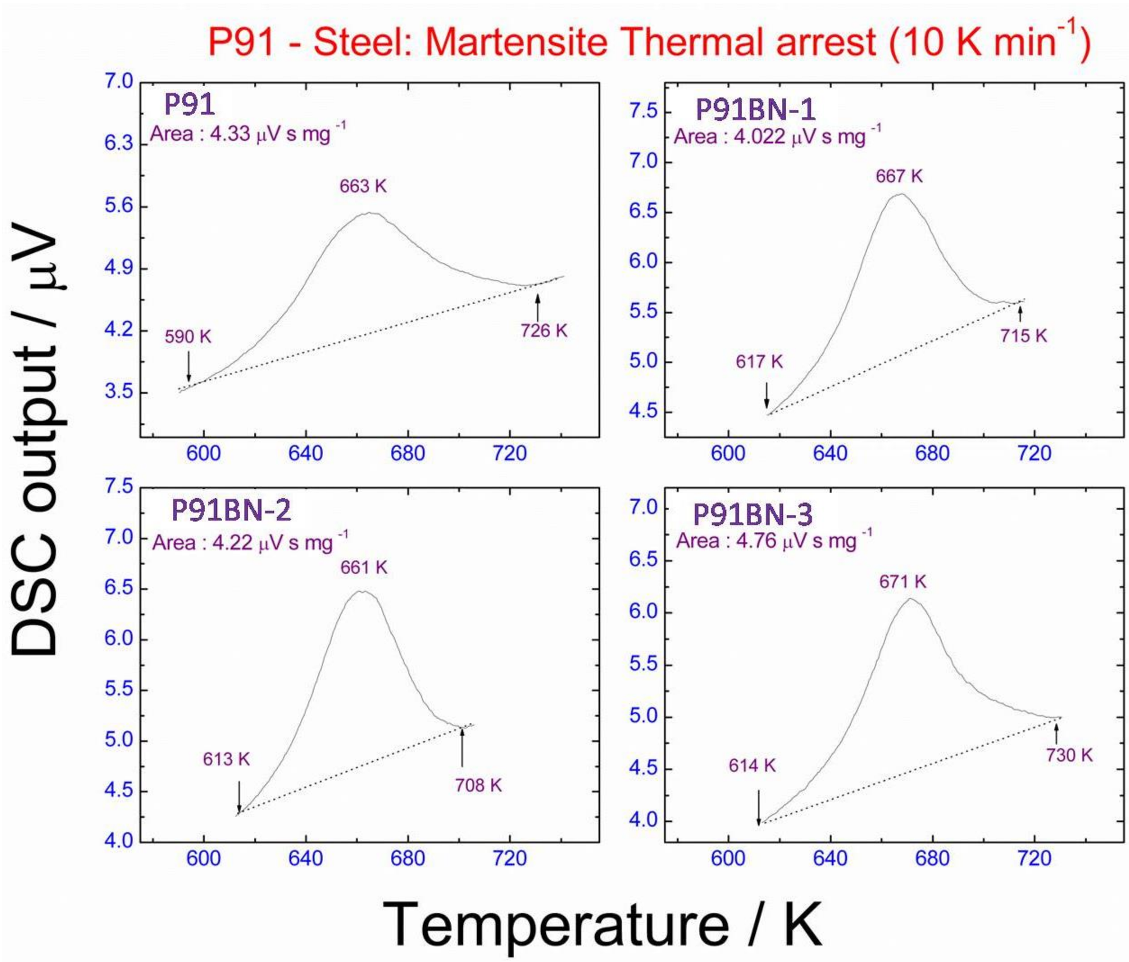

Fig. 4.3 DSC thermograms for P91, P91BN-1, P91BN-2 and P91BN-3 steels for martensite thermal arrest at 10 K min^{-1}.

The DSC thermograms for P91 and P91BN steels are shown in Fig. 4.3 where γ to α' phase transformations occurs during cooling. The temperature at which martensite starts forming is referred to as M_s temperature, and the finish temperature is called as M_f temperature. The M_s temperature was low in the P91BN-1 and P91BN-2 steels as compared to P91 steel. Boron addition leads to decrease the M_s temperature in P91BN steels. However, the difference in M_s temperature between the P91BN-3 steel and P91 steel is less. The M_s and M_f temperatures for P91 and P91BN steels at a cooling rate of 10 K min^{-1} are given in Table 4.1.

Table 4.1 The Ac_1, Ac_3,M_s, M_f, and Curie temperatures for P91 and P91BN steels at the heating and cooling rate of 10 K min^{-1}.

Steel	**On - heating**				**On-Cooling**	
	T_c K	**α+ carbide $\rightarrow \gamma$**			**Martensite Transformation**	
		Ac_1 K	**Ac_3 K**		**M_s K**	**M_f K**
P91 steel	1008	1112 ±5	1144 ±5		726 ±8	590 ±8
P91BN-1	1008	1131 ±5	1171 ±5		715 ±8	617 ±8
P91BN-2	1008	1132 ±5	1165 ±5		708 ±8	613 ±8
P91BN-3	1008	1132 ±5	1171 ±5		730 ±8	614 ±8

4.2.3 SEM, EBSD, and TEM microstructures

SEM micrographs of the P91 and P91BN-1 steels in the NT condition are given in Fig. 4.4. The PAG, packet, block and lath boundaries were decorated by $M_{23}C_6$ precipitates (Fig.4.4). The δ-ferrite was not observed in the P91 and P91BN steels. MX precipitates were predominantly observed in the intra-lath regions (Fig. 4.5). The energy dispersive spectroscopy (EDS) spectrum of $M_{23}C_6$ precipitates in P91 and P91BN steel are given in Fig. 4.6. Finer $M_{23}C_6$ and MX precipitates, and lath structure having higher dislocation density were present in P91BN-1 steel as compared to P91 steel (Fig. 4.7). Boron nitride (BN) formation was not observed in the present steel, which is generally observed in steels containing higher levels of nitrogen and boron [92,95,96]. Formation of borides would lead to ineffective utilization of boron in providing creep strength [92]. The increased concentration of vacancy at high temperature is thermodynamically introduced, the complex of vacancy-boron is formed due to their attractive interaction; under lower cooling rate tend to vacancy-boron complex segregate at the prior-austenite grain boundaries, which acts as sink to the vacancies. Hence, boron atoms are segregated at the grain boundaries [97]. Higher normalizing temperature in addition to compositional control has generally been employed to avoid formation of boron enriched compounds so that free boron is available in the matrix. Boron enriches into $M_{23}C_6$ precipitates during tempering treatment, which stabilizes the boundaries against migration. The $M_{23}C_6$ precipitates which are near to boundaries have higher boron content as compared to those which are far from the boundaries [4,97]. Phases present in P91BN (Fig. 4.8) and P91 (Fig. 5.2) steels are predicted by Thermo-Calc. $M_{23}C_6$ precipitates are in general less stable than MX precipitates. The size of $M_{23}C_6$, MX precipitates, and lath width were respectively 125, 30 and 700 nm in P91 steel while in P91BN-1 steel these were 115, 25 and 500 nm respectively. Finer precipitates pin the dislocation structure and boundary more effectively, which led to delay in recovery of dislocation structure and migration of boundaries against deformation. $M_{23}C_6$ precipitates size about 70 nm has been reported in boron added 9Cr-W steel [98]. Boron addition in P91 steel resulted in finer $M_{23}C_6$ precipitates and consequent increase in stability of various boundaries. The decrease in M_s temperature due to presence of boron in P91BN steels (Fig. 4.3 and Table 4.1) resulted in higher transformation induced dislocation density. Relatively higher dislocation density in the P91BN steels presumably enhanced the MX precipitation during tempering at intra-lath region, which contribute to strengthening through stabilization of dislocation networks against recovery of dislocation structure. These led to increase in hardness in P91BN steels (220±5 HV_{10} in P91BN-1; 230±5 HV_{10} in P91BN-2; 212±5 HV_{10} in P91BN-3; 210±5 HV_{10} in P91) (Fig. 4.9). Researchers have reported that relatively higher hardness in the boron containing 9Cr-3W steel normalized at 1323 K [92].

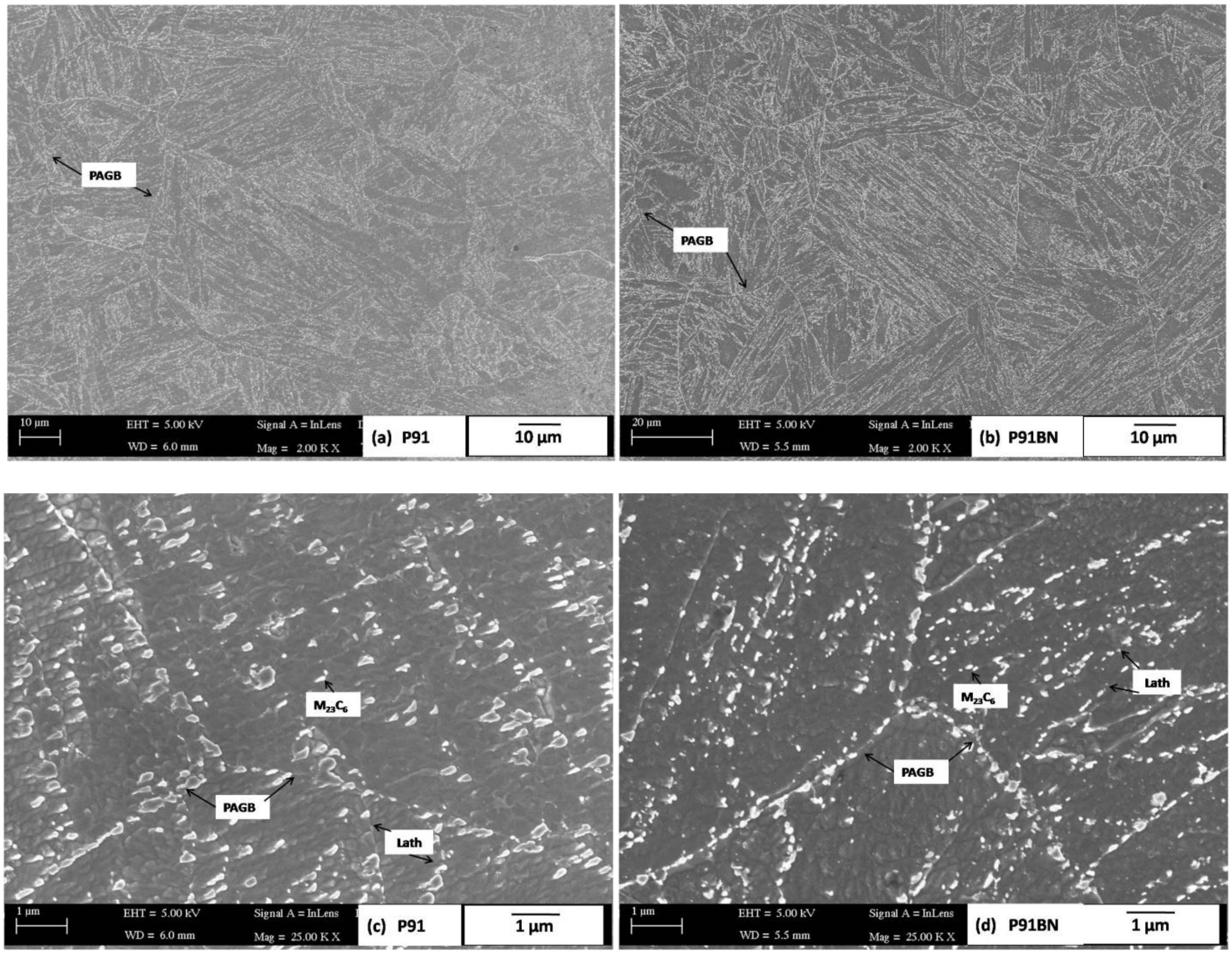

Fig. 4.4 SEM SE micrographs of (a, c) P91 and (b, d) P91BN-1 steels in the NT condition.

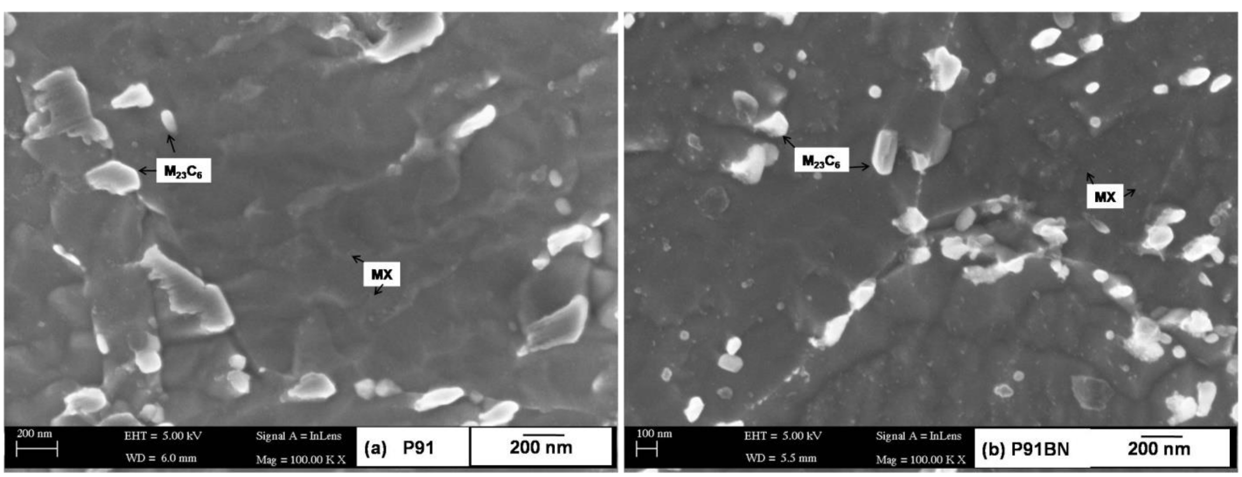

Fig. 4.5 SEM SE high magnification micrographs of (a) P91 and (b) P91BN-1 steels in the NT condition depicts the presence of $M_{23}C_6$ and MX precipitates.

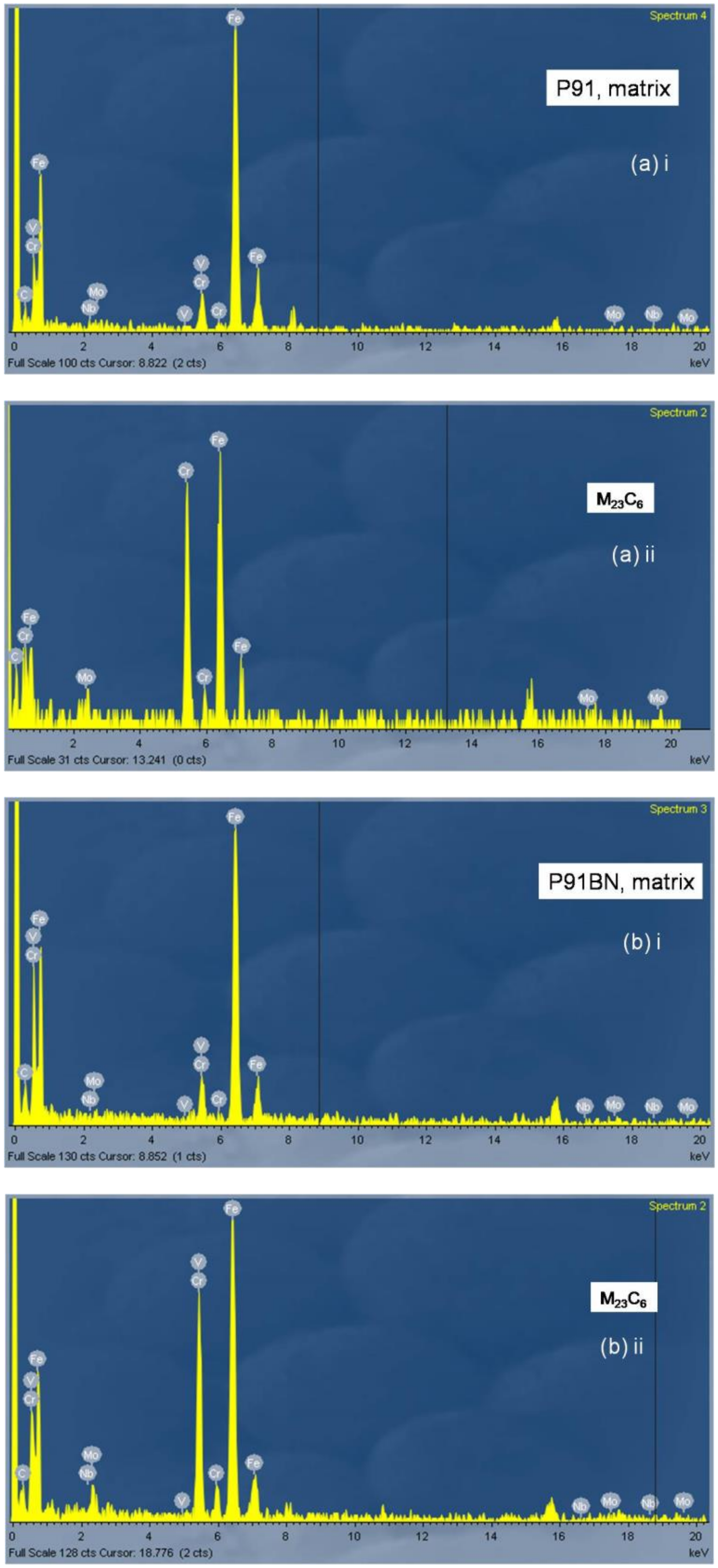

Fig. 4.6(a) EDS spectrum of (i) matrix and (ii) $M_{23}C_6$ precipitates in the P91 steel, (b) EDS spectrum of (i) matrix and (ii) $M_{23}C_6$ precipitates in the P91BN-1 steel.

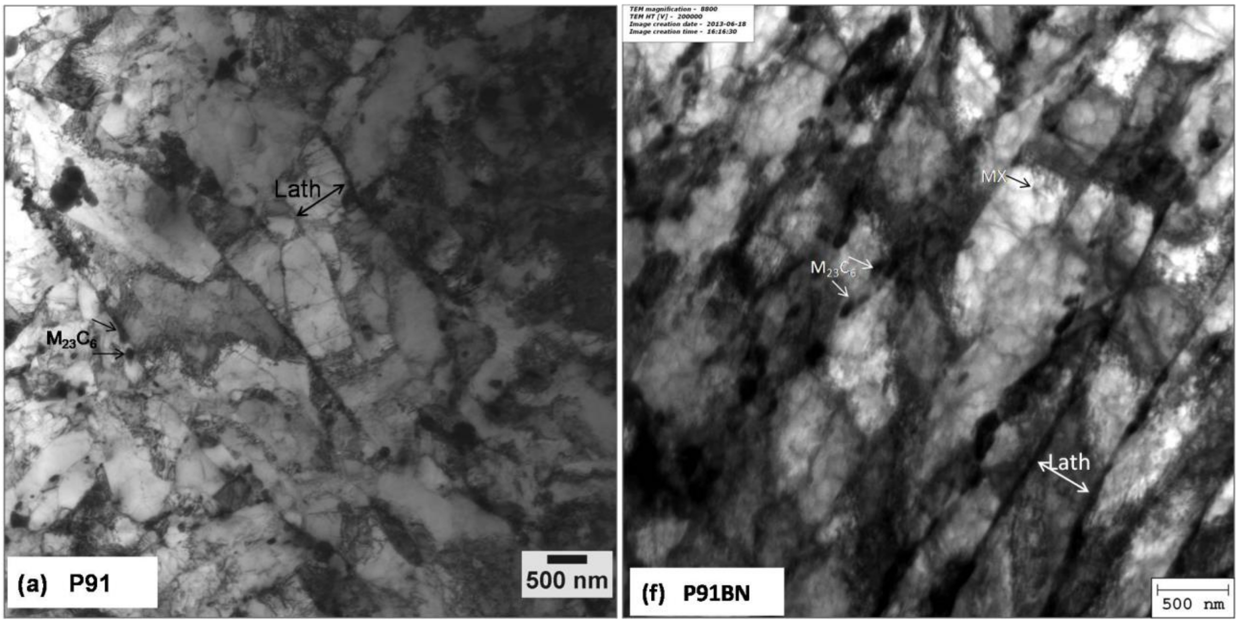

Fig. 4.7 TEM micrographs of (a) P91 and (b) P91BN-1steels in the NT condition.

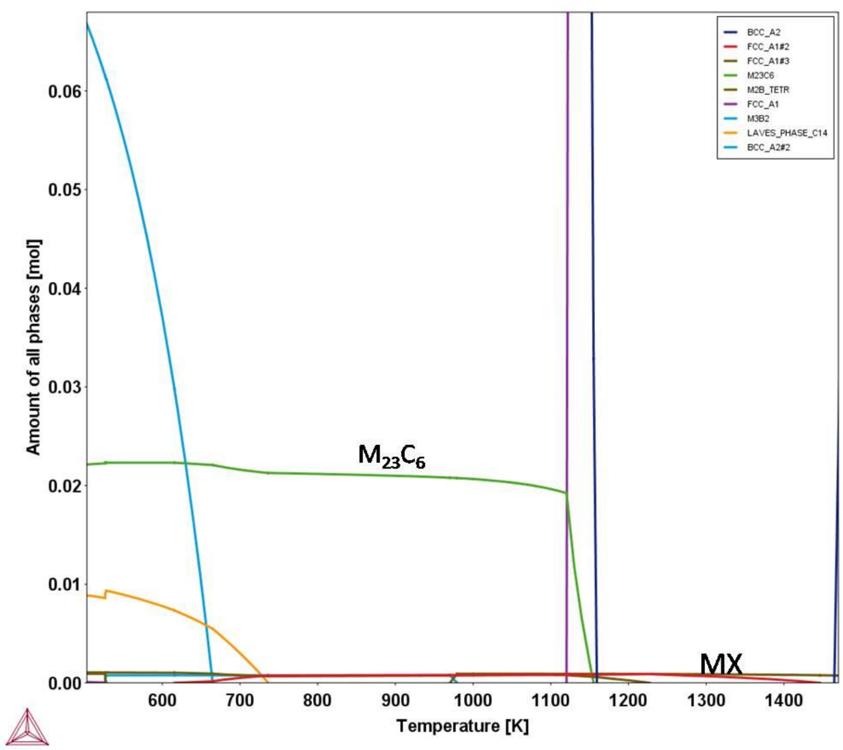

Fig. 4.8 Predicted equilibrium phases in P91BN-1 steel with temperature using Thermo-Calc program.

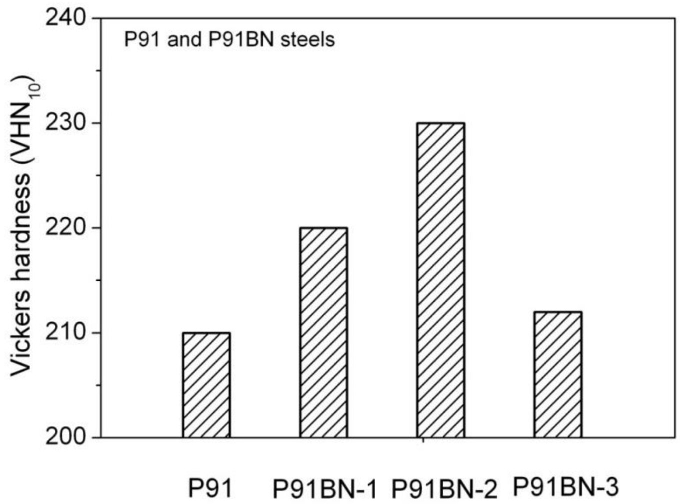

Fig. 4.9 Vickers hardness in P91 and P91BN steels in the NT condition.

SEM-EBSD study:

EBSD inverse pole figure (IPF) Z-map superimposed with grain boundary map revealed the presence of significantly finer lath structure in the P91BN steels (Fig. 4.10(a-c)). IPF color legend is shown in Fig. 4.10(d). The PAG and packet size increased in the P91BN steels as compared to P91 steel. The subgrain structure size of 1.64, 1.69, 1.87 and 1.91 μm were observed in the P91BN-1, P91BN-2, P91BN-3, and P91 steels respectively. P91BN steels possess finer lath width as compared to P91 steel (Figs. 4.10 and 4.7). The HAGBs were higher in the P91 steel, and were comparable within P91BN steels. The ratio of HAGB to LAGBs was lower in the P91BN steels, which depicted the significant existence of block/lath structure. Fraction of low misorientation angle (MOA) boundaries (at 1.5°) was higher in the P91BN-1 and P91BN-2. MOA in the P91BN-3 and P91 steels were comparable. Relatively less low MOA boundaries in the P91 steel depict the less lath structure (Fig. 4.11(a)). This leads to contribute less resistance against creep deformation of the steel as compared to P91BN steels. The CSL boundary map (colour lines) and distribution in frequencies (%) for P91BN steels are shown in

Fig. 4.12. CSL map overlapped with boundary map depicted existence of CSL character predominantly in the block and lath boundaries. The fractions of CSL boundaries (Σ3, Σ11 and Σ25b) were noticed to be relatively higher in the P91BN-1 and P91BN-3 steels (Fig. 4.12) than in P91BN-2 steel. CSL boundaries in the P91 and P91BN-2 steels were comparable. The presence of finer precipitates, lath structure and higher CSL boundaries in the P91BN steels leads to provide better resistance against deformation in the steel.

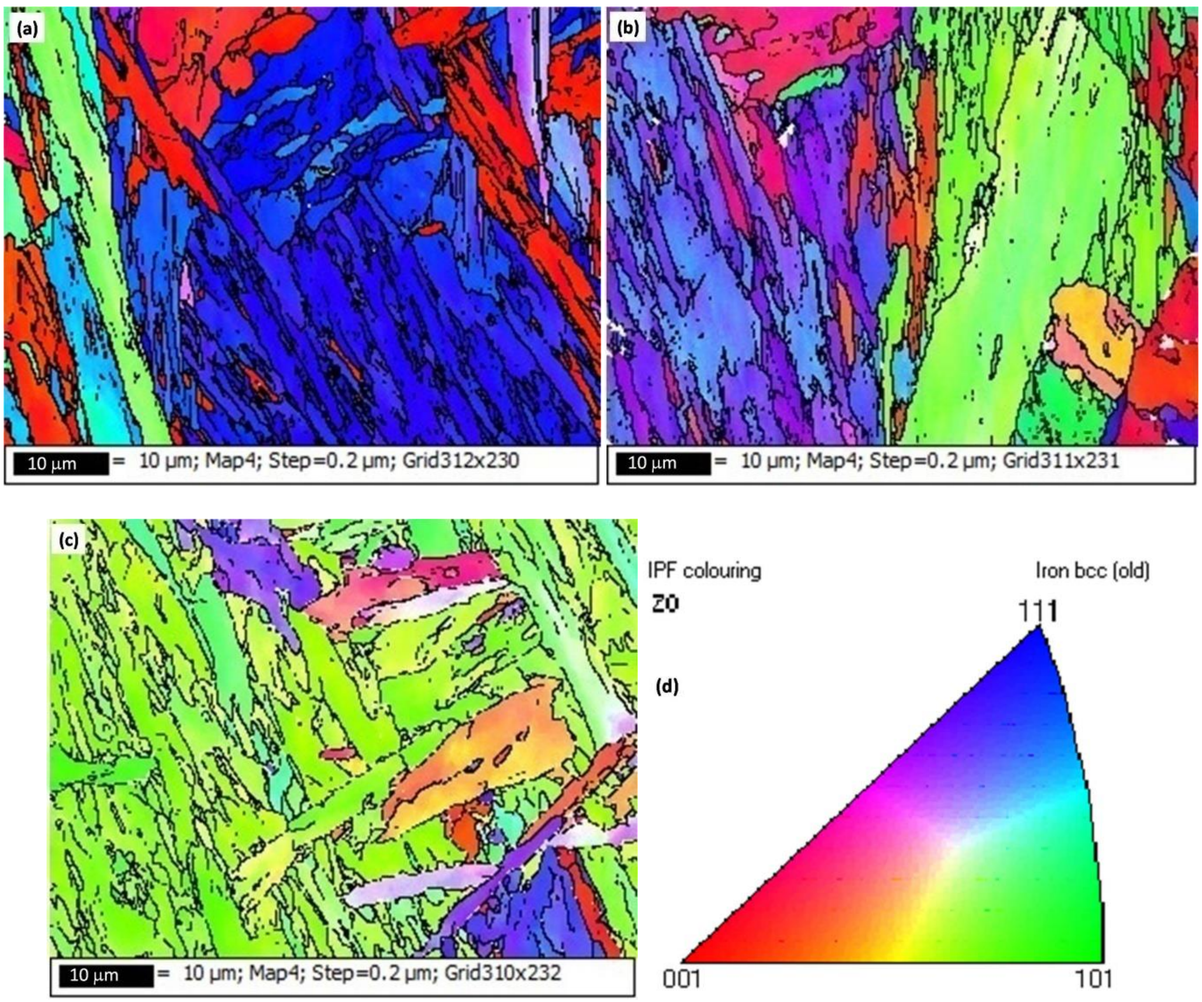

Fig. 4.10 EBSD-IPF map for (a) P91BN-1, (b) P91BN-2, (c) P91BN-3 steels, and (d) IPF colour legend.

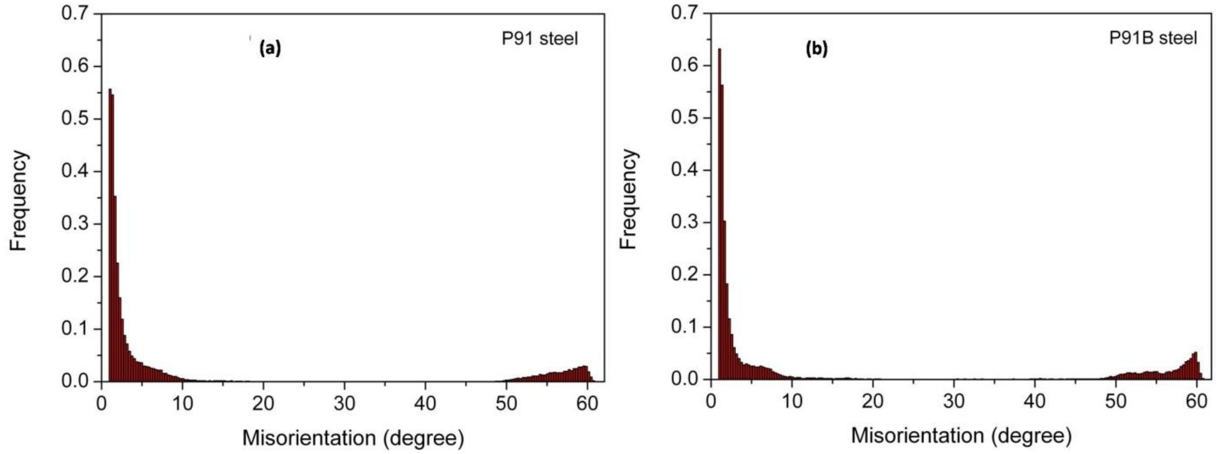

Fig. 4.11 EBSD misorientation angle from (a) P91 and (b) P91BN-1 steels in the NT condition.

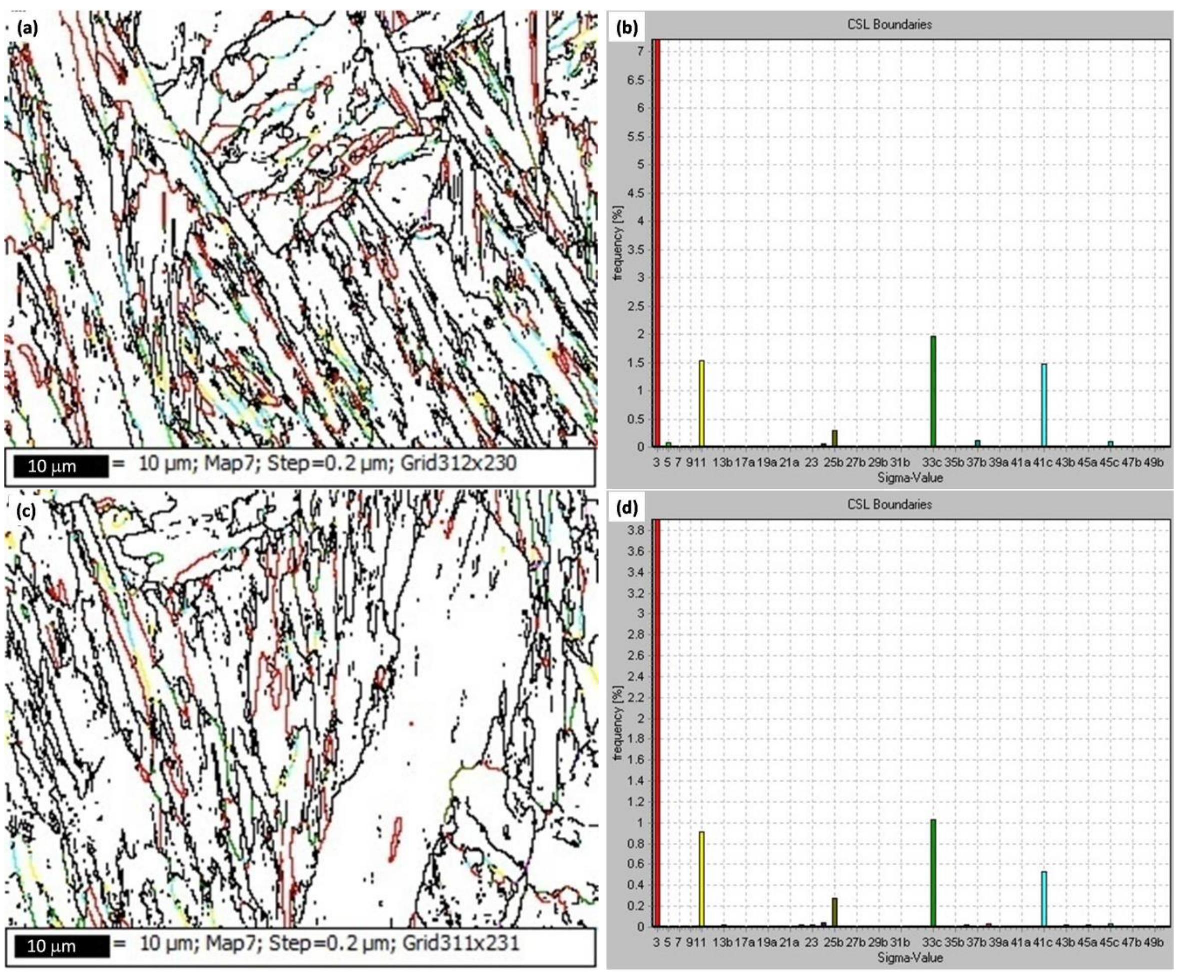

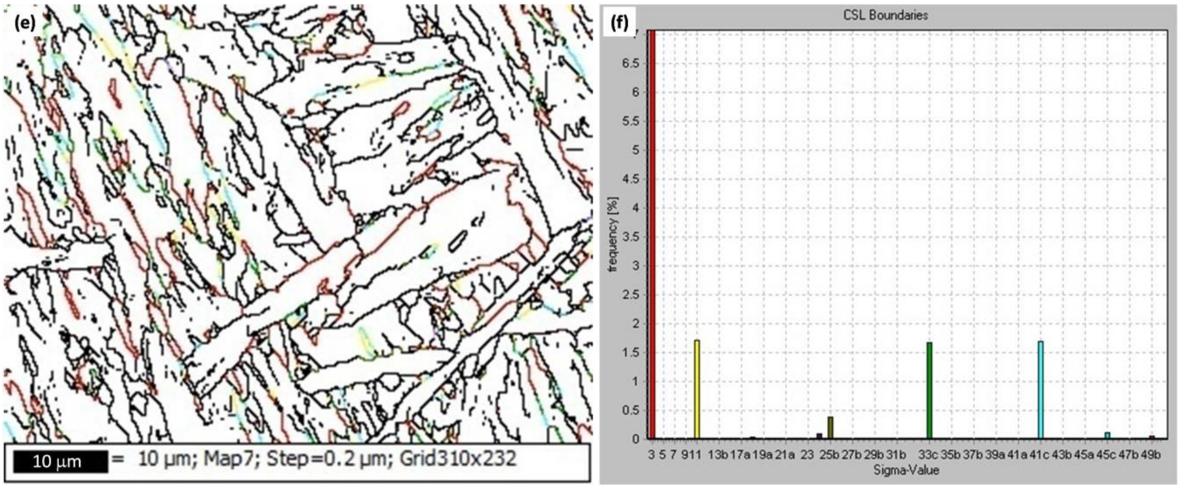

Fig.4.12 CSL boundary map (colour lines) for (a,b) P91BN-1, (c,d) P91BN-2 & (e,f) P91BN-3 steels.

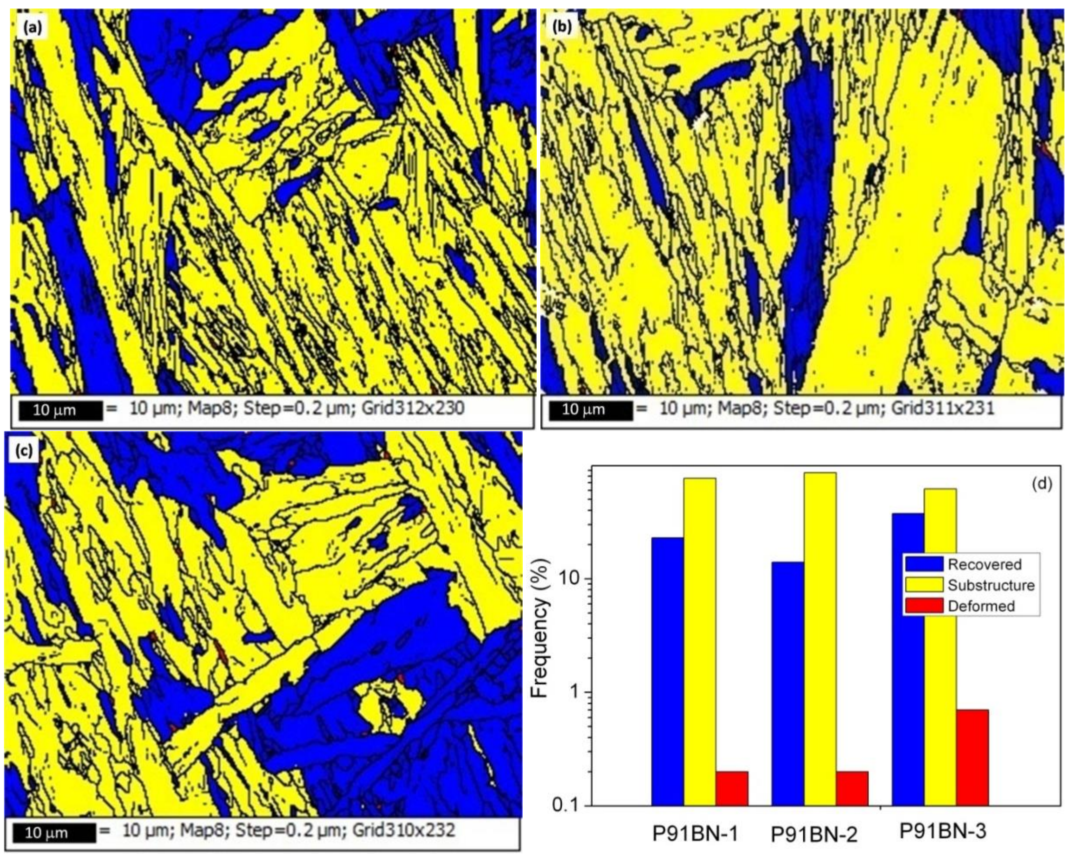

Fig. 4.13 Recovery of substructure (blue), substructure (yellow) and deformed (red) regions in the (a) P91BN-1, (b) P91BN-2, (c) P91BN-3 steels, and (d) frequency (%) of microstructural conditions in the steels.

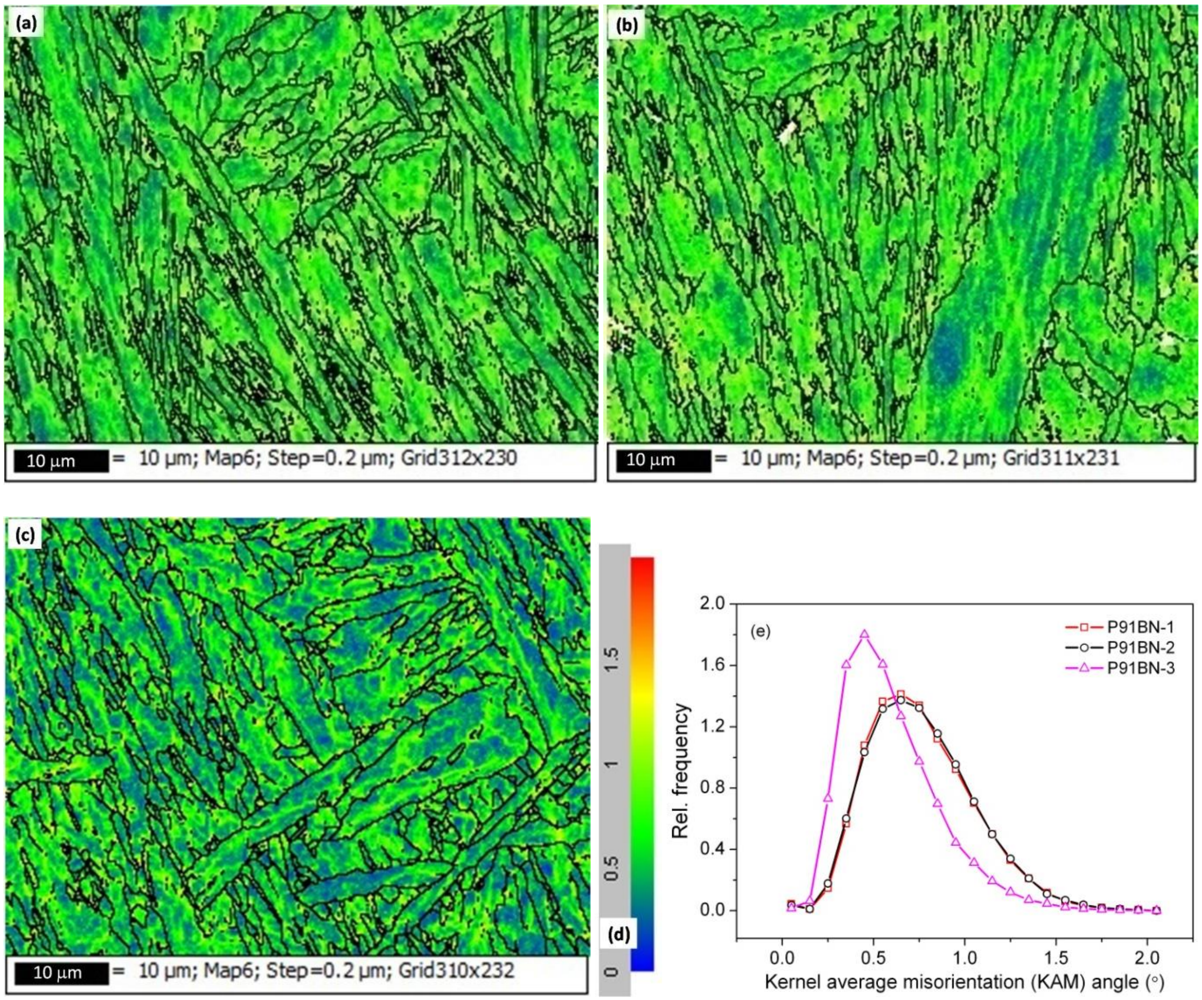

Fig. 4.14 EBSD KAM map depicting the strain distribution in the (a) P91BN-1, (b) P91BN-2, (c) P91BN-3 steels, (d) colour legend for KAM, and (e) frequency of KAM angle in the steels.

Microstructure conditions of the steel such as (i) recovered (recovery of dislocation structure), (ii) substructure (lath and block) and (iii) deformed structure (consisting of more dislocations at intra-lath region or at interfaces) vary in P91 and P91BN steels. Substructure frequency (%) in the P91BN-1 and P91BN-2 steels was higher than the P91BN-3 steel, whereas recovered and deformed structure was relatively lower in the P91BN-1 and P91BN-2 steels (Fig.4.13(a, b)). In the case of P91 and P91BN-3 steels recovered and substructure and deformed structure frequencies were comparable. Kernel average misorientations maps for P91BN steels are shown in Fig.5.14. The color legend for KAM distribution is given in Fig.4.14(d), and this depicts the variations in strain distribution within the blocks and packets. The more recovered structure possessing less strain is evident in the P91BN-3 steel (Fig.4.14(c)). The average KAM value was used to evaluate the dislocation density from the following relationship i.e, $\boldsymbol{\rho_b} = \boldsymbol{\theta_{KAM\,(avg)}}.\boldsymbol{r_{avg}/2b}$. Evaluated boundary dislocation density in the P91BN-1, P91BN-2 and P91BN-3 steels were about 0.427 x 10^{14}, 0.405 x 10^{14}, and 0.255 x 10^{14} m^{-2} respectively. The dislocation density of P91BN-3 steel is relatively comparable with the P91 steel. Higher dislocation density evaluated through EBSD study is in line with the reported lower M_s temperature in the DSC study, where the decrease in M_s temperature lead to increase in the dislocation density, and consequent increase in hardness (Fig. 4.7).

4.2.4 Tensile properties

Tensile tests were carried on the P91 and P91BN steels over the temperature range 300 - 923 K. Engineering stress-strain curves of the steels tested at the selected characteristic temperatures of 300 K, 573 K and 923 K are shown in Fig.4.15. At 300 K, classical tensile curves of tempered martensitic ferritic steels with smooth transition from elastic to plastic deformation are observed with P91BN steel having higher work-hardening capability than the P91 steel. The increase in testing temperature to intermediate temperatures around 573 K, decreased the deformation capability of the steel probably due to the occurrence of dynamic strain ageing (DSA), even though no serrated flow except a few jerks, a manifestation of DSA, was observed. Serrated flow behaviour due to DSA in grade 91 steel having different microstructures was reported by Chandravathi et al [99], showing reduced DSA activity with increase in strength of the steel. Enhanced interaction between dislocations and solute atoms during DSA restrict the motion of the dislocations in planer manner to reduce the plastic deformation capability [100]. On increasing the testing temperature above around 773 K, enhanced recovery of dislocation substructure decreased the tensile strength quite drastically. In this temperature zone, even though the total elongation of the steel increased, the uniform elongation decreased significantly with yield stress and UTS values are close to each other. The post necking elongation was more in the P91BN steel than in the P91 steel, showing higher resistance against strain concentration during necking in the P91BN steel.

Variations of 0.2% off-set yield stress (YS) and ultimate tensile strength (UTS) of the P91 and P91BN-1 steels with temperature are shown in Figs.4.16 (a) and (b), respectively. In both the steels, the tensile strength variation with temperature exhibited three distinct regimes such as lower temperature at around 300-473 K, intermediate temperature at around 473-723 K and high temperature regime at around 773-923 K. The deformation over the temperatures around 300 to 473 K is dominated by planar slip of dislocation at low strain and cross slip of dislocation at high strain and the increase in temperature, facilitates the deformation processes resulting in decrease in tensile strength with increase in temperature [101]. A shallow-decrease or plateau in the variation of tensile strength with temperature was observed in the intermediate temperature range (473 to 723 K). The occurrence dynamic strain aging due to enhanced interaction of dislocations with solute atoms during tensile deformation in the intermediate temperature leads to the shallow-decrease in tensile strength with temperature in the regime [101]. However, clear serrations were not observed in tensile flow curve in the present investigation except mild appearance at 573 K. The negative strain rate sensitivity in a tempered martensitic steel even in the absence of serrated flow to establish the occurrence of DSA has been reported by researchers [99], probably this is applicable in the present case also. Further increase in test temperature (> 723 K) led to rapid decrease in strengths due to the dominance of dynamic recovery of dislocation structure over the strain hardening [101]. The yield stress (YS) of the P91 and P91BN steels were comparable up to around 823 K where recovery was not so dominant. The P91BN steel possessed quite higher yield stress than the P91 steel at temperatures beyond 823 K. The P91BN steel has 30-40 MPa more yield stress at temperatures above 823 K than the P91 steel (Fig.4.16(a)), indicating high recovery resistant characteristic of the P91BN steel over the P91 steel. Similarly, the P91BN steel has higher ultimate tensile strength than the P91 steel. Significant increase in UTS of the P91BN steel (~30MPa) at temperatures above 823 K was observed (Fig. 4.16(b)). Work-hardening capability of the steels at three characteristic temperatures of 300, 573 and 923 K are compared in Fig.4.17. At temperatures around in the range 300 - 423 K, work-hardening capability of the P91BN steel is slightly more than the P91 steel (Fig.4.17(a)). Refined martensitic microstructure of the P91BN steel than that in the P91 steel (Figs.4.5, 4.7 and 4.10) probably has increased the work-hardening capability in P91BN steel over the P91 steel. In the DSA temperature range around 573 K, work-hardening capability of the steels are comparable (Fig.4.17(b)) as in the tensile strength (Fig. 4.16). Generally, DSA activity is more pronounced in the relatively softer structure [99] and the enhancement in work-hardening and tensile strength of the P91 steel to the levels of P91BN steel probably had occurred. Above the temperature domain (more than around 823 K) where the recovery is dominant, the work-hardening capability of the P91BN steel is much more than that of the P91 steel (Fig. 4.17(c)). This clearly indicates that the P91BN steel has remarkably higher resistance against recovery than in the P91 steel. The phenomenon like creep deformation in ferritic steels where recovery takes a dominant role than the hardening, creep behaviour is expected to be better in P91BN steel than in the P91 steel, as discussed subsequently. Studies have been carried out on the relaxation behaviour of the steels on tensile deformation. Relaxation of stress (straining up to 2.3 % at 873 K, relaxed stress is normalized by the peak stress) is much more sluggish in the P91BN steel than in the P91steel (Fig.4.18), once again indicating higher recovery resistance capability in the steel on microalloying with boron particular at high temperatures where creep is important.

The elongation (%) and reduction in area (%) for both the steels are shown in Fig.4.19. The elongation (%) decreased marginally with increase in temperature from 300 K to intermediate temperature, and increases with further increase in temperature with a minimum in the intermediate temperature (473 to 723 K) regime. It may be noted that the increase in elongation (%) in P91BN steel is relatively more significant than the P91 steel especially at higher test temperature. The reduction in area (%) increased with increase in temperature with a plateau in the intermediate temperature range. The P91BN steel has shown lower reduction in area up to intermediate temperature range than the P91 steel, while both the steels show comparable reduction in area with further increase in temperatures. The P91BN steel exhibited slightly higher uniform elongation (UE) than P91 steel at lower test temperature and comparable UE at higher temperature.

In materials, fracture toughness is a property which describes the ability of a material to resist fracture, and is considered as one of the most important properties of any material for design. The area under the stress-strain curve is considered as a measure of the energy required to fracture a material by tensile deformation and provides an indication of fracture toughness of the material. Variations of the fracture energy (area under the stress-strain curve) of the P91 and P91BN steels with test temperature are shown in Fig.4.19(c). Boron microalloying of the P91 steel increased its tensile strength (Fig. 4.16) along with ductility (Figs.4.19(a) and (b)), which is reflected in the increase in fracture energy. Refined martensite microstructural features of fine lath size along with fine distribution of precipitate particles on boron micro alloying in-spite of higher dislocation density (Figs.4.7 and 4.14) increased its fracture toughness.

Fractographic investigation of the tensile specimens tested at 300 K and 923 K are shown in Figs.4.20 and 4.21, respectively. Relatively lesser ductile dimple mode of failure and lower reduction in area with distinct radial cracks has been observed in P91BN steel at 300 K (Fig.4.21(b)). However, at higher test temperature (923 K) both P91 and P91BN steels exhibited ductile mode of failure. Impact toughness value of 200 J at 300 K were obtained in the P91BN steels and were comparable with the P91 steel.

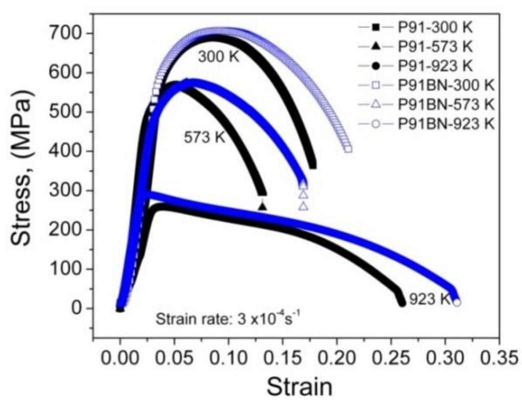

Fig.4.15 Typical tensile stress-strain curves of P91 and P91BN-1 steels at 300 K, 573 K and 923K.

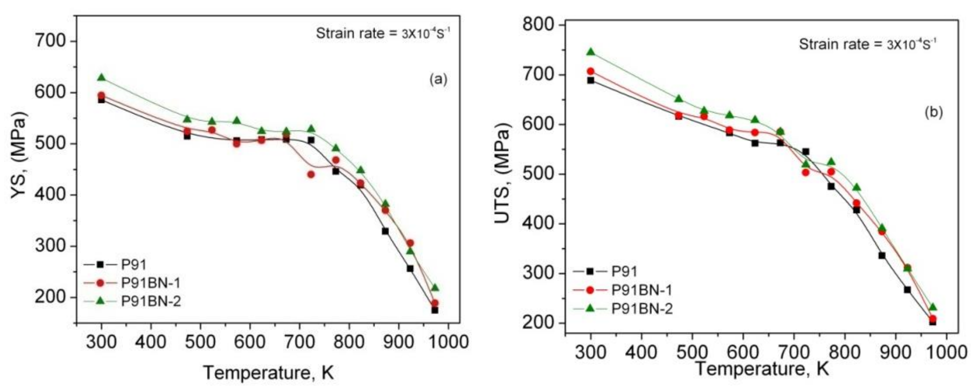

Fig. 4.16 Variation of (a) yield stress and (b) ultimate tensile strength with test temperatures for P91, P91BN-1 and P91BN-2 steels.

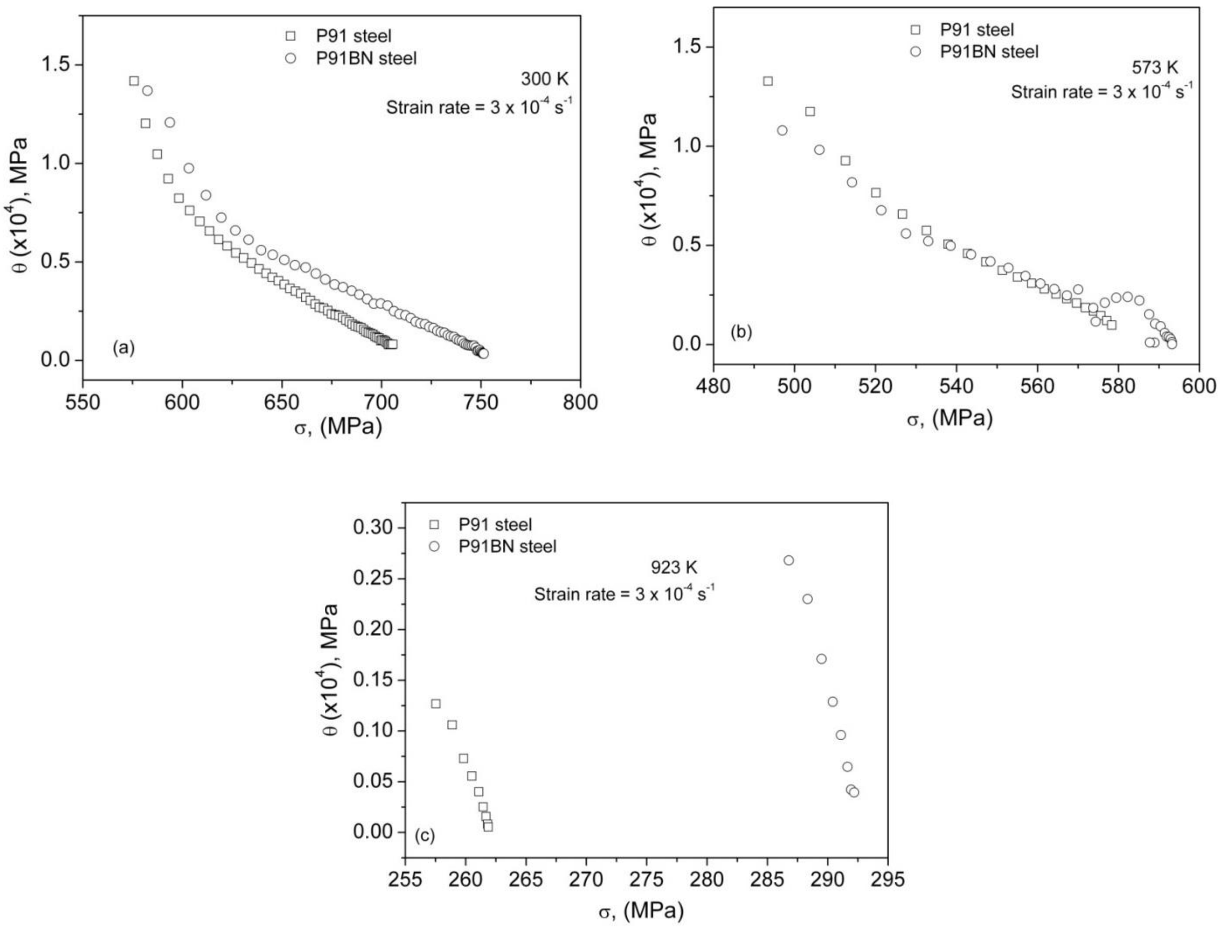

Fig. 4.17 Work hardening (θ) behaviour of P91 and P91BN-1 steels at (a) 300, (b) 573 and (c) 923 K.

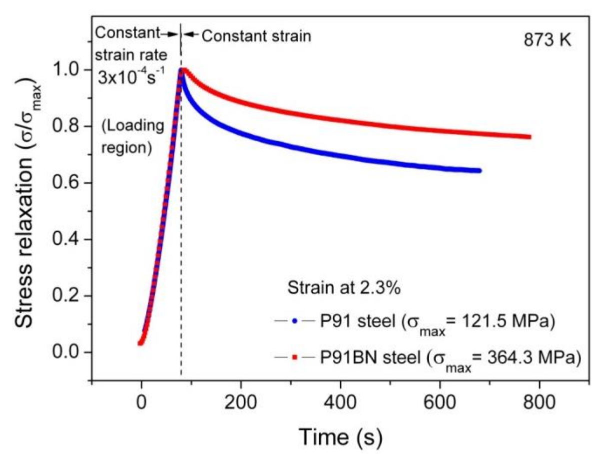

Fig. 4.18 Stress relaxation behaviour of P91 and P91BN-1 steels at 873 K.

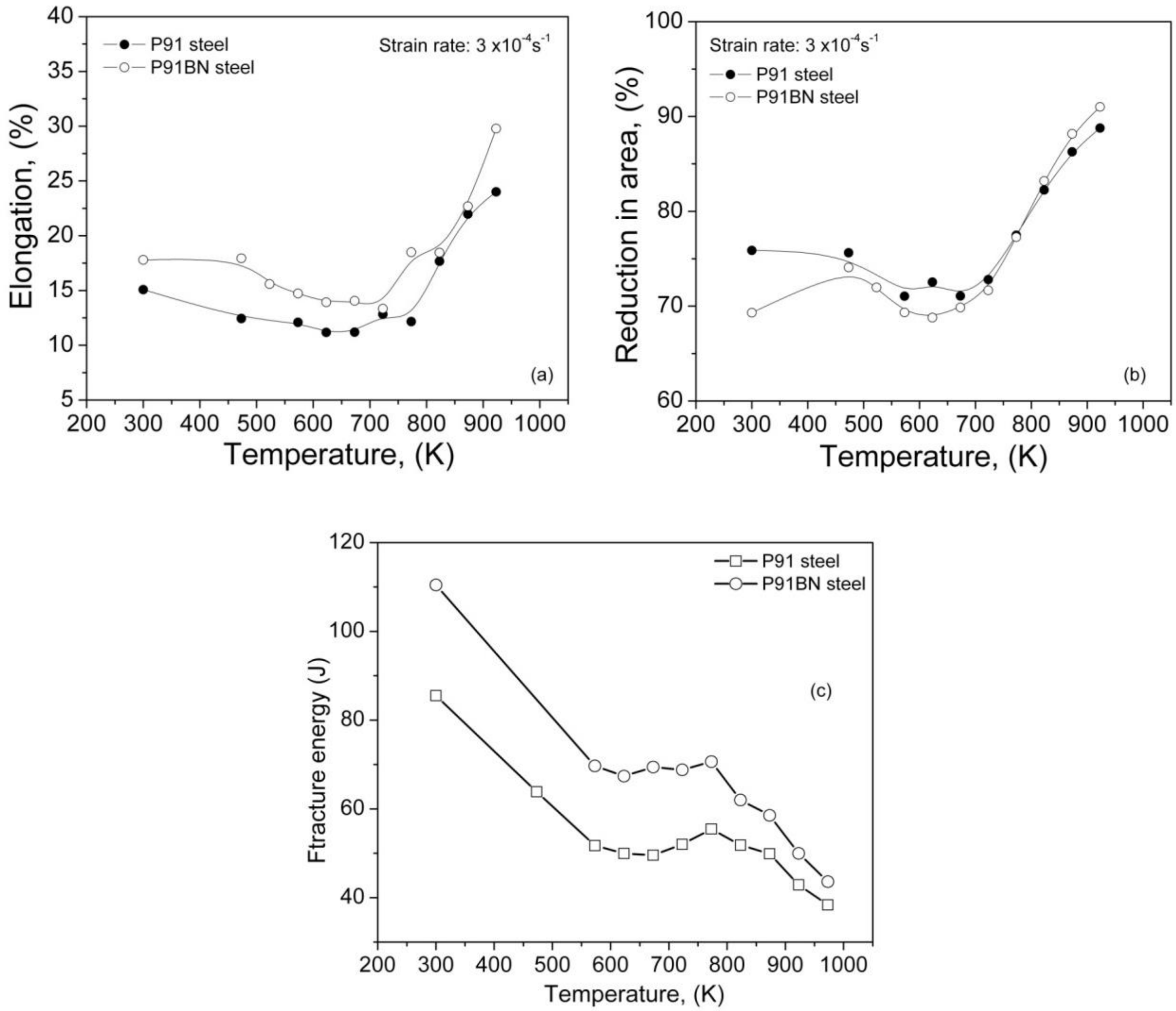

Fig. 4.19 Variation of (a) elongation (%), (b) reduction in area (%), (c) fracture energy with test temperatures for P91 and P91BN-1 steels.

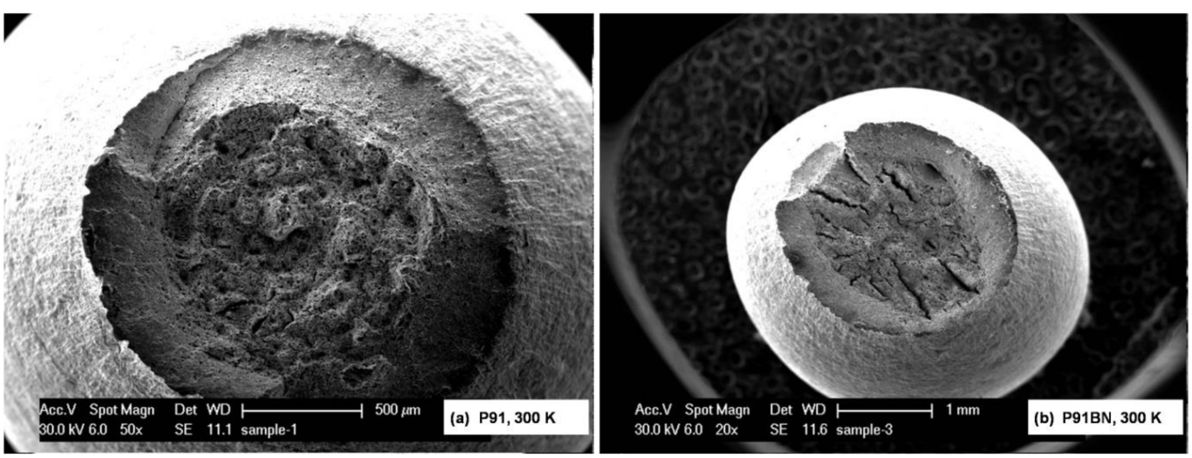

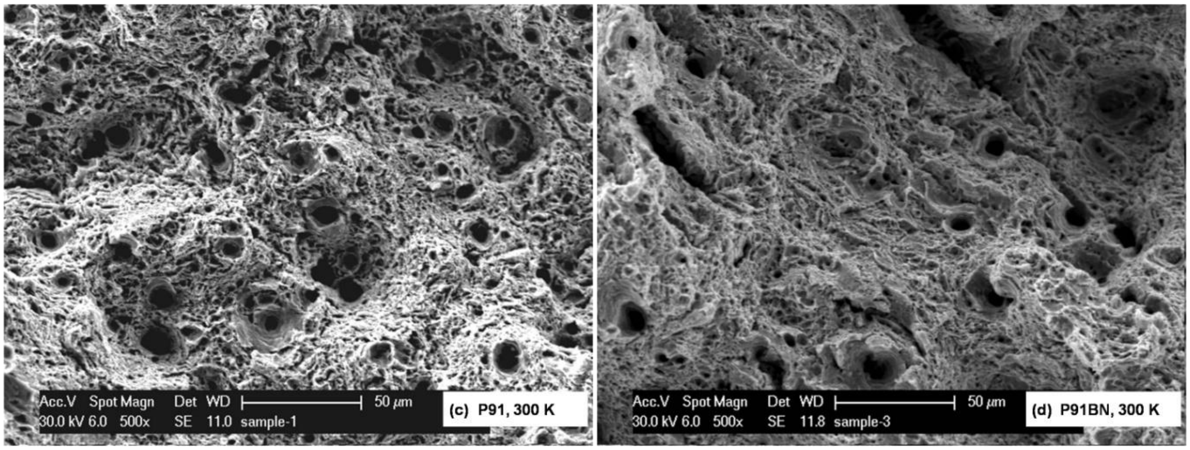

Fig. 4.20 Fracture surface of specimens tensile tested at 300 K of P91 steel [(a),(c)] and P91BN-1 steel [(b),(d)].

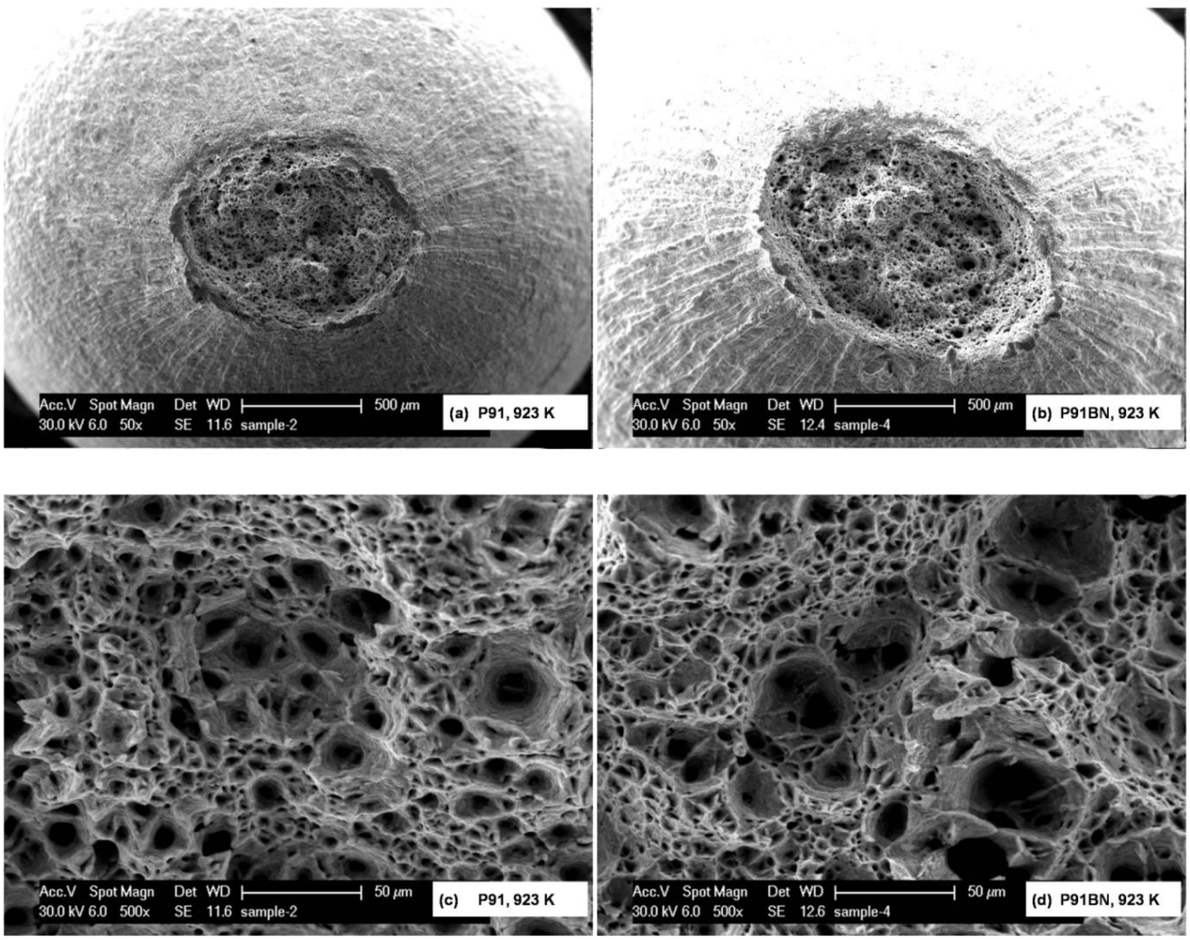

Fig. 4.21 Fracture surface of specimens tensile tested at 923 K of P91 steel [(a),(c)] and P91BN-1 steel [(b),(d)].

4.2.5 Creep deformation behaviour

The creep curves of P91 and P91BN-1 steels at 823, 873 and 923 K are shown in Fig. 4.22. The creep curves were characterized by well defined primary, secondary and accelerating tertiary creep regimes in both the steels at the investigated temperature and stress regimes. Creep ductility in both the steels was comparable. P91BN steel has experienced longer creep exposure period as compared to P91 steel under similar test conditions. Variation of creep rate with time at different test conditions (stress and temperature) are shown in Fig. 4.23 for P91 and P91BN-1 steels. The creep rate decreases with time and reaches minimum value followed by accelerated creep rate regime. Significant decrement in creep rate occurred in the transient creep regime in P91BN-1 steel due to contribution of predominant hardening by finer lath width, $M_{23}C_6$ and MX precipitates, and higher dislocation density than in P91 steel. Subsequently, the difference in creep rate between P91 and P91BN steels increased extensively in the secondary creep regime. Although, significant decrease in creep rate in P91BN steels occurred at high temperature due to addition of boron in the steel, the influence of boron in the steel is predominantly realized with decreasing temperature and applied stress. The secondary creep rate in P91BN-1 steel were lower by about two orders of magnitude at 823 and 873 K, and one order at 923 K have been noticed as compared to P91 steel. Remarkable decrement in minimum creep rate under lower stress level has been reported in the boron containing 9Cr-W steel [92]. The work hardening contribution is counter-balanced by recovery mechanisms such as annihilation and rearrangement of dislocations in the secondary creep regime [98]. The delay in onset of tertiary creep deformation in P91BN steels occurred due to stabilization of various boundaries predominantly by finer $M_{23}C_6$ precipitates, in addition to the contribution of MX precipitates against recovery of intra-lath dislocation structure. Accelerated onset of tertiary creep has been reported in 9Cr-3W-3CoVNb steel with boron, but excess nitrogen content leading to formation of BN, thus limiting the availability of free boron [92]. Stabilization of subgrain structure and boundaries by finer and stable pinning particles plays a vital role in delaying the creep damage in tertiary creep regime [2,4,6,7,102,103]. The creep strain to reach minimum creep rate was found to decrease with decrease in applied stress and increase in temperature (Fig. 4.24). The creep strain to reach minimum creep rate was more or less same in both the steels. Creep strain accumulations up to onset of tertiary creep regime in both the steels were about 0.5 to 3.5% (Fig. 4.25(a)). Relatively U-type creep curve at lower temperature and changes towards V-type creep behaviour at higher test temperature were exhibited in both the steels. This demonstrate the microstructural instability with increase in temperature. Researchers have reported similar behaviour in the 9Cr-ferritic steel [103,109,111]. The time spent in each creep regime was significantly higher in P91BN-1 steel than the P91 steel (Fig. 4.25 (b, c)). This is due to enhanced microstructural stability in P91BN-1 steel.

4.2.5.1 Stress and temperature dependencies of minimum creep rate

The minimum creep rate with applied stress for P91 and P91BN-1 steels at different temperatures are shown in Fig. 4.26. The reduction in minimum creep rate in P91BN-1 steel about two orders of magnitude at 823 and 873 K, and one order of magnitude at 923 K have been observed as compared to P91 steel. The minimum creep rate ($\dot{\epsilon}$) with applied stress (σ) variation followed Norton's power law of creep as $\dot{\epsilon}=A\sigma^{n}$, where A is a constant and n is the stress exponent of the matrix. The stress exponent values about 16.3, 14.6 and 12.9 for P91 steel and 20.6, 15.7 and 15.1 for P91BN-1 steel at 823, 873 and 923 K respectively were obtained, indicating dislocation creep to be operative in the investigated conditions (Table 4.2). Stress exponent (n) over the investigated range of applied stress was not changed in both the steels.

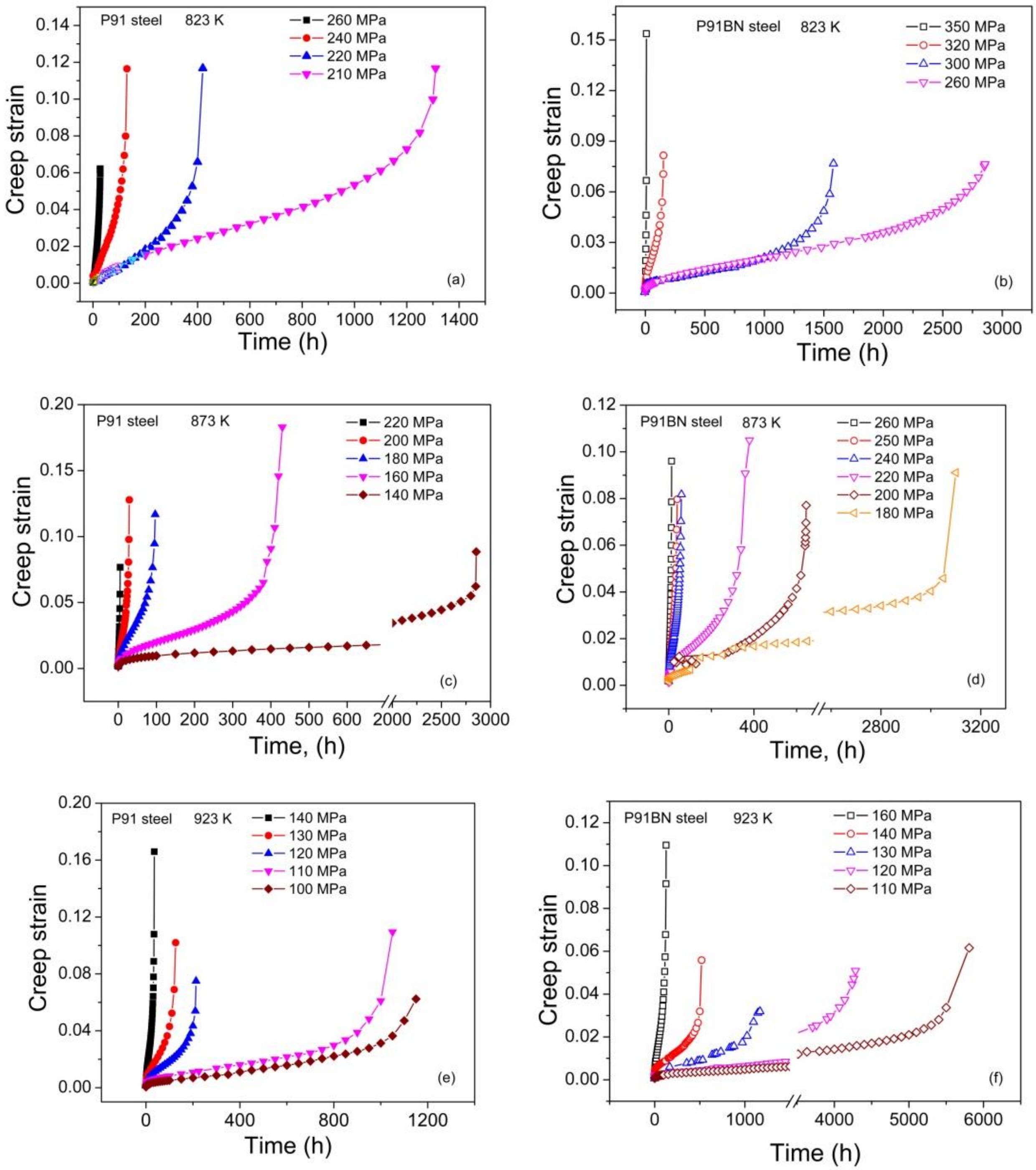

Fig. 4.22 Creep curves of P91 (a,c,e) and P91BN-1 (b,d,f) steels at 823 K (550 °C), 873 K (600 °C) and 923 K (650 °C).

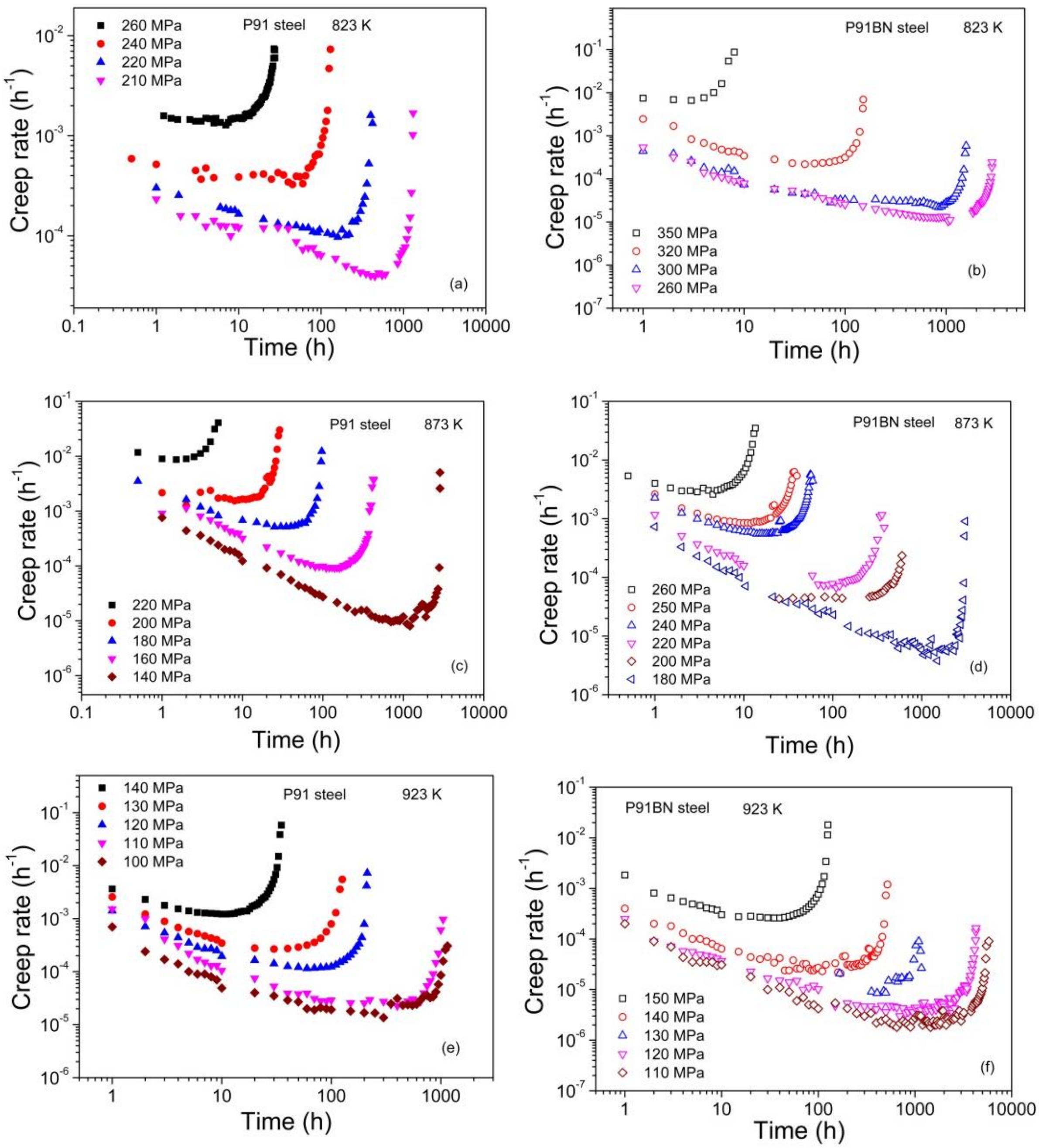

Fig. 4.23 Creep rate with time curves of P91 (a,c,e) and P91BN-1 (b,d,f) steels at 823 K (550 °C), 873 K (600 °C) and 923 K (650 °C).

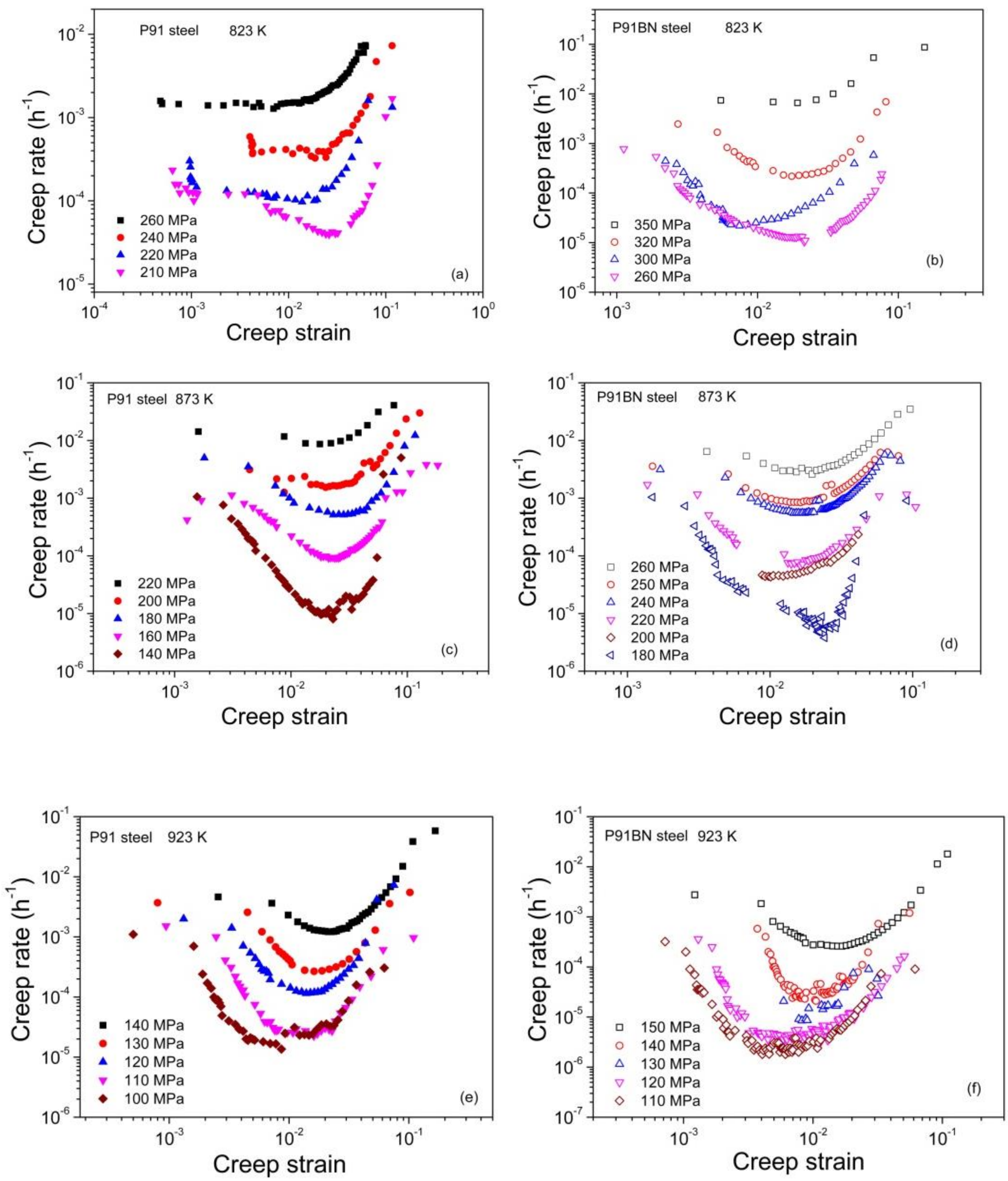

Fig. 4.24 Creep rate with creep strain curves of P91 (a,c,e) and P91BN-1 (b,d,f) steels at 823 K (550 °C), 873 K (600 °C) and 923 K (650 °C).

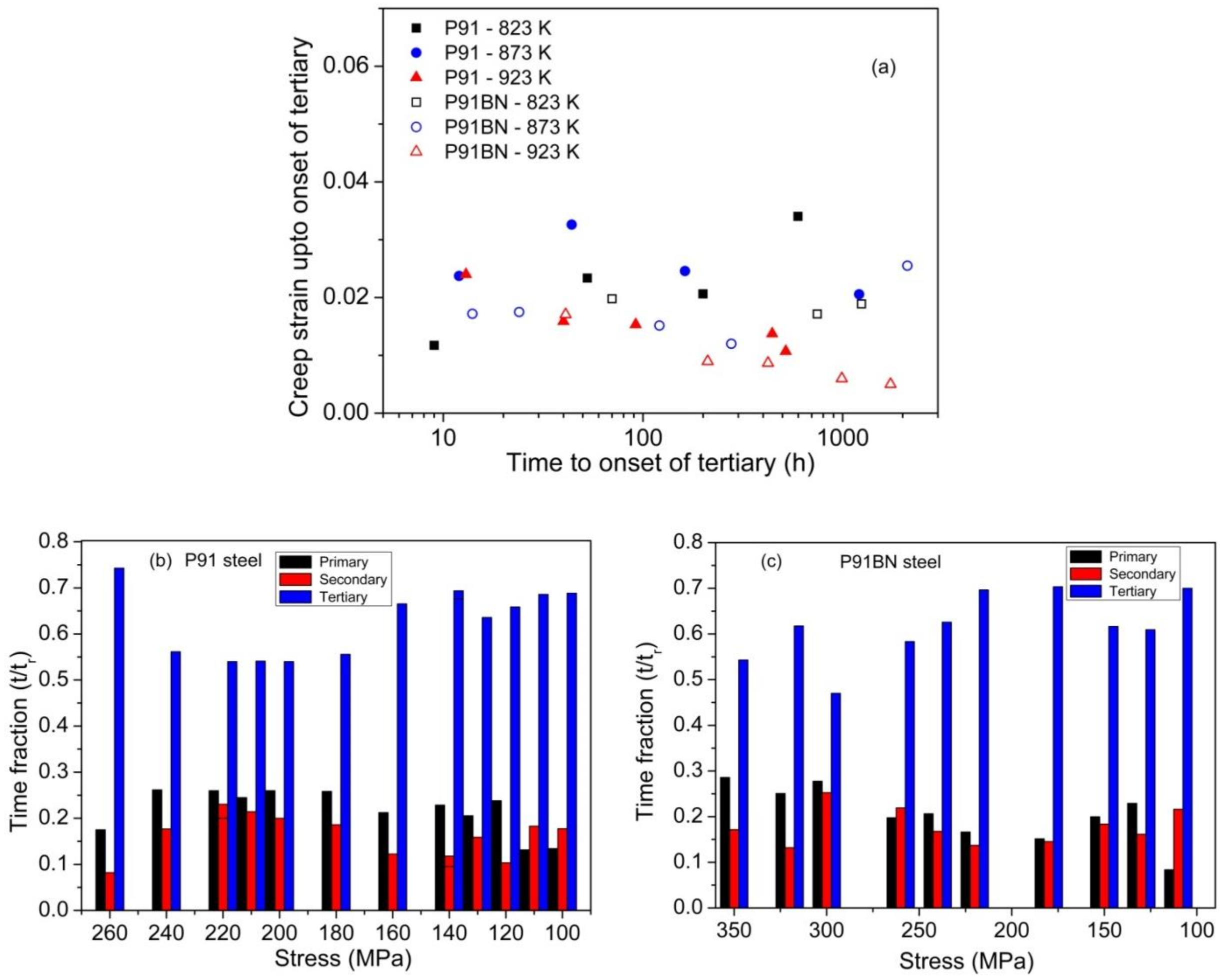

Fig. 4.25 (a) Variation of creep strain up to onset of tertiary with time to onset of tertiary creep of P91 and P91BN-1 steels; Time spent in primary, secondary and tertiary creep regimes of (b) P91 and (c) P91BN-1 steels at 823 K (550 °C), 873 K (600 °C) and 923 K (650 °C).

Higher *n* values were observed in P91BN-1 steel than in P91 steel at all temperatures due to finer microstructural constituents in the former. A change in *n* with decreasing stress level (high and low stress regimes) has been reported by researchers in Grade 91 steel [5,104], indicating a shift in creep deformation mechanism [16]. Value of *n*=3 to 5 for dislocation creep and 1 for diffusion creep are generally observed. However, higher *n* values have been reported in particle strengthened materials. Higher *n* values in the range about 9 to 18 for modified 9Cr-1Mo steel, 5.8 to 15 for P92 steel and 13 to 38 for 9Cr-3W-3Co steel have been reported [5,93].

The stress (σ) and temperature (T) dependence of creep rate for pure metals and single phase alloys are described by Bird-Mukherjee-Dorn (BMD) as [1,26],

$$\frac{\dot{\epsilon} kT}{D_o \mu b} = A\left(\frac{\sigma}{\mu}\right)^n \exp(-\frac{Q_C}{RT})$$

where, $D = D_0 \exp(-Q_c/RT))$ is the diffusion coefficient, D_0 is the frequency factor, Q_c is the activation energy for creep deformation, R is the gas constant, T is the temperature in Kelvin, μ is the shear modulus, b is the burgers vector, k is the Boltzmann constant, n is the stress exponent, A is a dimensionless constant. Q_c was evaluated from slope of the Arrhenius ($\ln(\dot{\epsilon}_{\min})$ versus $1/T$) plot at two constant applied stress values, namely 150 and 200 MPa (Fig. 4.27). For P91 steel these values were 571 and 519 kJ/mole for 150 and 200 MPa respectively, while for P91BN-1 steel 919 and 828 at 150 and 200 MPa stress respectively. The Q_c value obtained for P91 steel is comparable to the reported values of 510 kJ/mole [105] and 510 to 545 kJ/mole [27,28] for P91 steels, and for Fe-with various Cr concentrations [106]. The Q_c value about 678 kJ/mole has been reported for P91B steel containing 0.01 wt.% B and 0.0021 wt.% N [30], which is lower than the present study. The n and Q_c values obtained for P91BN-1 steel are higher than those for P91 steel. Higher Q_c values observed for both the steels in comparison with those reported for solid solution Fe-based single phase alloys can be attributed to strong interaction between precipitates and mobile dislocations, grain and subgrain boundaries, which is generally described by threshold stress [107].

Threshold stress (σ_{th}) values have been determined for P91 and P91BN-1 steels at different temperatures in order to assess the influence of boron on the stability of precipitates and therefore on interactions between precipitates and mobile dislocations. Threshold stress for a specific creep mechanism is described as the stress below which creep deformation does not occur by that mechanism. Hence, the effective stress rather than the applied stress is considered as responsible for creep deformation where the alloy is strengthened by particles or precipitates [5]. The modified version of Mukherjee-Bird-Dorn creep equation can be used to evaluate the threshold stress (σ_{th}) as [1,26-32],

$$\dot{\epsilon}_{min} = A\left(\frac{\sigma_a - \sigma_{th}}{\mu}\right)^n \exp\left(-\frac{Q_c}{kT}\right)$$

where, A is a constant, n is the matrix stress exponent, σ_a is the applied stress, Q_c is the creep activation energy, T is the temperature in Kelvin, μ is the shear modulus, k is the Boltzmann's constant. For pure metals, n value of about 4, and $Q_C = Q_D$ (the activation energy for lattice self diffusion) have generally been reported [107]. The threshold stress is evaluated from plots of $\dot{\epsilon}^{1/4}$ versus σ_a applied stress, assuming n=4 (Fig. 4.28). The intercept on the stress axis at zero strain rate provides σ_{th}threshold stress at various temperatures. These are presented in Table 4.3. Threshold stress decreased with increase in temperature in both P91 and P91BN-1 steels. The evaluated threshold stress for P91 steel in the present work is comparable with the values reported for P91 steel in literature [5,105,108]. The increase in threshold stress (about 31 MPa at 823 and 873 K; 17 MPa at 923 K) in P91BN-1 steel as compared to P91 steel is due to presence of fine microstructural constituents, and increased resistance to coarsening of precipitates, recovery of dislocation structure, and migration of sub-grain and grain boundaries in P91BN steel under creep exposure. The threshold stress obtained at 923 K for P91BN-1 steel is comparable with the reported value for 9Cr-3W-3Co-CuVNbBN steel in literature [93].

The variation of minimum strain rate ($\dot{\epsilon}_{\text{min}}$) with effective stress normalized by shear modulus ((σ_a -σ_{th})/μ) for P91 and P91BN-1 steels are shown in Fig. 4.29(a) and (b). The stress exponent value ~4 in P91 and P91BN steels have been obtained at different temperatures (4.0, 3.6 and 3.5 in P91 steel; and 4.2, 4.0 and 4.0 in P91BN steel at 823, 873 and 923 K respectively). The true creep activation energy (Q_c) for P91 and P91BN-1 steels have been evaluated from $\ln(\dot{\epsilon}_{min})$ versus 1/T plot at constant normalized stress ($(\sigma_a - \sigma_{th})/\mu$) of 9.86x10^{-4}. Creep activation energy (Q_c) about ~ 250 kJ/mole in P91 and P91BN-1 steels has been obtained from the slope of the Arrhenius plot, these values are similar to the activation energy for self diffusion of α - iron, 241 kJ/mole [5]. The true creep activation energy value of 244 kJ/mole for precipitation strengthened Fe-19Cr steel has been reported by researchers [55]. The variation of minimum creep rate normalised by creep activation energy with effective stress normalised by shear modulus values at different temperatures fall into a single line and slope, which is generally rationalized with matrix stress exponent of 4 and creep activation energy 244.1 kJ/mole [5, 93].

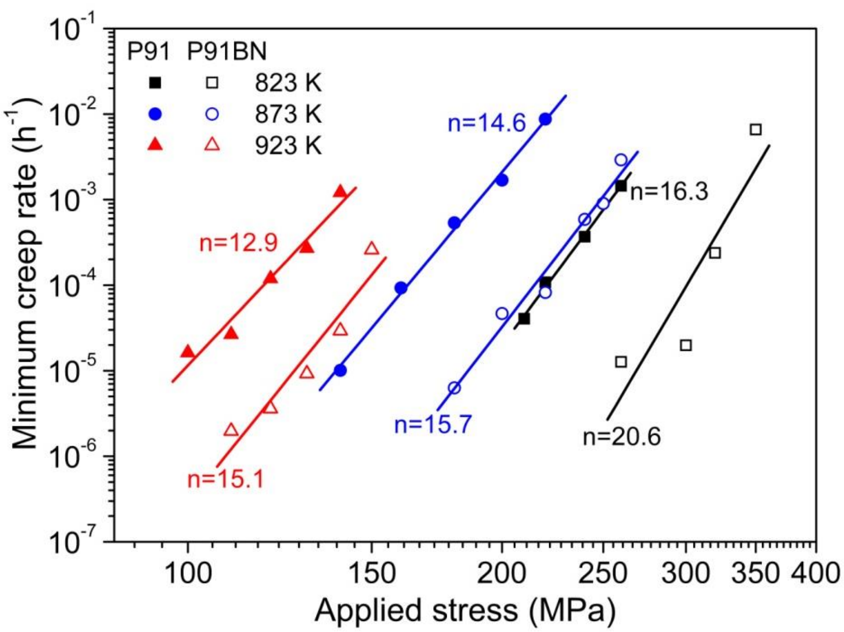

Fig. 4.26 Variation of minimum creep rate with applied stress of P91 and P91BN-1 steels at 823 K (550 °C), 873 K (600 °C) and 923 K (650 °C).

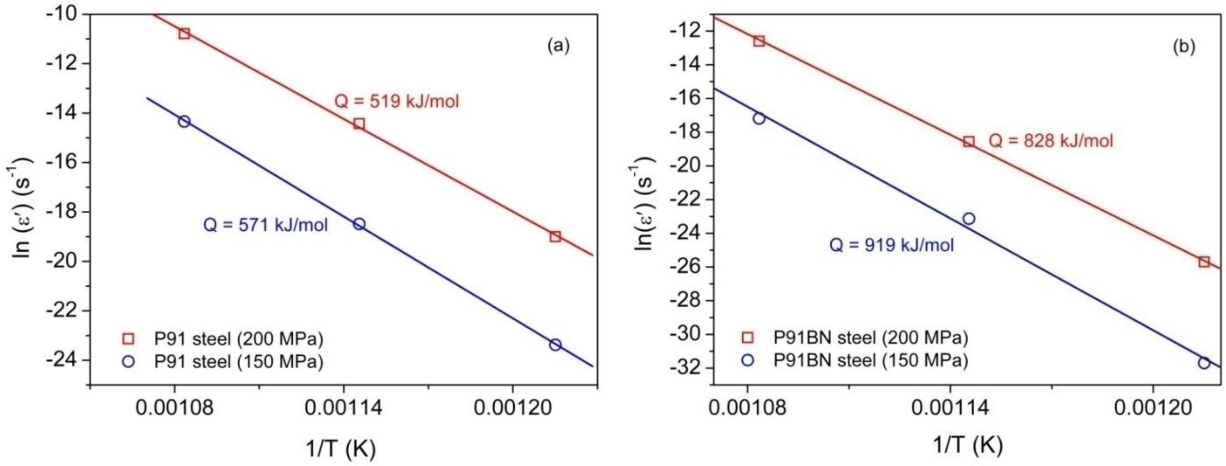

Fig. 4.27 Evaluation of creep activation energy from strain rate vs (1/T) for (a) P91 and (b) P91BN-1 steels.

Table 4.2 Stress exponent (*n* and n_1) for P91 and P91BN-1 steels at different temperature.

Temperature (K)	$\dot{\epsilon}=A\sigma^{n}$		$t_r = A_1\sigma^{-n1}$	
	P91	P91BN-1	P91	P91BN-1
823	16.3	20.6	17.3	19.9
873	14.6	15.7	13.7	14.5
923	12.9	15.1	10.3	10.1

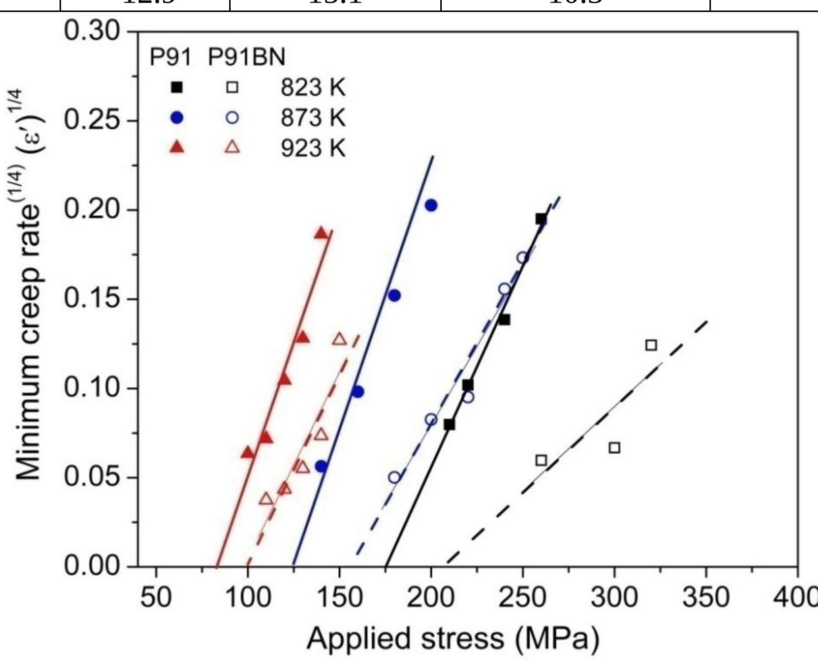

Fig. 4.28 Evaluation of threshold stress of P91 and P91BN-1 steels at 823 K (550 °C), 873 K (600 °C) and 923 K (650 °C).

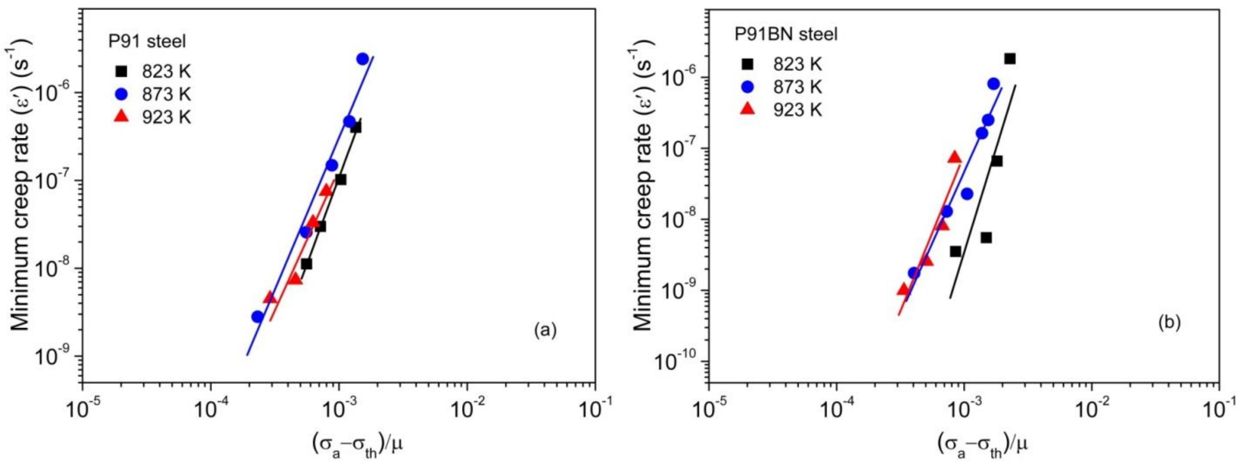

Fig. 4.29 Variation of creep rate with shear modulus compensated effective stress (a) P91 and (b) P91BN-1 steel.

Table 4.3 Threshold stress (σ_{th}) for P91 and P91BN-1 steels at different temperature.

Temperature (K)	σ_{th} (MPa)	
	P91	P91BN-1
823	175	206
873	124	155
923	83	100

4.2.5.2 Creep rupture behaviour

The variation of creep rupture life (t_r) with σ_a at 823, 873 and 923 K for P91 and P91BN-1 steels are shown in Fig. 4.30. P91BN-1 steel possessed higher creep rupture life in comparison with P91 steel over the investigated temperature and applied stress range. Creep rupture life of P91 steel evaluated at different temperatures in the present study is comparable with rupture life of this steel reported by researchers [5,105,106,108,110]. The differences in creep rupture life between P91BN and P91 steels increased with decreasing test temperature. The enhancement in creep rupture life by one order at 923 K and more than one order at 873 and 823 K in P91BN steel under similar test conditions has been observed. Addition of boron with controlled nitrogen content led to improvement of about 70, 40 and 20 MPa in the creep rupture strength of P91BN steel at 823, 873 and 923 K respectively as compared to P91 steel. Creep rupture life of P91B steel at 873 K and 120 MPa applied stress reported in literature is comparable with the steel without boron, this might be due to lower normalizing temperature, which precludes the boron benefit by forming boron-nitride and lower nitrogen content [54,55]. The variation of creep rupture life (t_r) with σ_a at 873 K for P91, P91BN-1, P91BN-2 and P91BN-3 steels are shown in Fig. 4.31. The P91BN-1 to 3 steels has shown significantly higher creep rupture life than the P91 steel. The difference in creep rupture life between P91 steel and P91BN steels increases under longer creep exposure. The differences in creep rupture life between P91BN steels are relatively less as compared to that of P91 steel. However, P91BN-1 has exhibited higher rupture life (optimum boron and nitrogen combination) (creep test >20000 h duration was conducted), and P91BN-2 and P91BN-3 steels possessed comparable rupture life at 873 K. The variation of nitrogen content in the steels having same content of boron (P91BN-2 and P91BN-3) has not influenced the creep rupture life significantly at 873 K. P91BN-1 steel containing 0.006 wt.% B and 0.011 wt.% N has exhibited an improvement in creep rupture strength about 40 MPa at 873 K for 10^4 h as compared to the P91 steel and P91B [30] steel. Creep rupture life variation in both the steels with applied stress followed linear trend, within the investigated stress regime. A change in slope of t_r-σ plots reported to occur in P91 steel under long-term creep exposure around 50000 h at 923 K [110]. Where the coarsening of $M_{23}C_6$ precipitates and lath width, formation of Z-phase, loss of solute elements in the matrix and recover of dislocation structure predominantly observed under long-term creep exposure. The creep rupture strength of P91BN steel is comparable with the Fe-9Cr-3Co-1.8WVNb steel containing boron and nitrogen [111] at 923 K.

The variation of rupture life with applied stress obeyed the power law as $t_r = A_1\ \sigma^{-n_1}$, where A_1 is the stress coefficient and n_1 is the stress exponent. The n_1 values of 17.3, 13.7, 10.3

in P91 steel and 19.9, 14.6, 10.1 in P91BN-1 steel at 823, 873, 923 K respectively were obtained (Table 4.2). The stress exponent decreased with increase in temperature in both the steels. The relationship between creep rupture life, applied stress and temperature is expressed as $t_r = A_1\sigma^{-n1}$ exp (Q_{c1}/RT), where Q_{c1} is the apparent activation energy for creep rupture, R is the gas constant, T is the temperature in K. Q_{c1} values of 570 kJ/mole in P91 steel and 728 kJ/mole in P91BN-1 steel have been obtained (Fig. 4.32(a)). Q_{c1} values for various 9% Cr ferritic steels in the range 599-624 kJ/mole have been reported [105,106,108]. The comparable values of n and n_1, and Q_c and Q_{c1} for P91 and P91BN-1 steels indicate that the similar operating mechanisms of creep deformation and rupture are same for both the steels. However, the addition of boron with controlled nitrogen in P91BN steel led to relatively finer microstructural constituents that lead to enhanced creep rupture strength as compared to P91 steel.

The variation of reduction in area (%) and elongation percentage (%) for P91 and P91BN-1 steels at different temperatures and applied stresses are shown in Fig. 4.32(b). Although P91BN-1 steel experienced longer creep exposure than the P91 steel, reduction in area and elongation observed in P91BN-1 steel were comparable with P91 steel except for the creep test at 823 K. The elongation (%) in both P91 and P91BN-1 steels varied between 15 to 20 % with a marginal increase in elongation with increase in temperature and stress. The reduction in area (%) and elongation (%) for P91 steel were comparable with the values reported by other researchers [5,105]. At 823 K, the P91BN-1 steel exhibits relatively lower reduction in area as compared to P91 steel. This may be attributed to the higher resistance to recovery of dislocation lath structure offered by stable fine $M_{23}C_6$ precipitates. The reduction in area increased with increase in temperature in both the steels due to increased recovery of dislocation structure and coarsening of precipitates, which led to softening of the matrix. The loss of load bearing capacity due to reduction in cross section through external surface (oxidation) and internal cross section due to formation, growth and coalescence of cavity in addition to microstructural degradation at high temperature lead to fracture in 9Cr-1Mo steel [5,105].

4.2.5.3 Creep rate-rupture life relationships

The variation of t_r with $\dot{\epsilon}_{min}$ minimum creep rate at different temperatures are given in Fig. 4.33(a) and (b) respectively for P91 and P91BN-1 steels. The relationships between $\dot{\epsilon}_{\mathrm{min}}$ minimum creep rate and t_r can be expressed by the Monkman-Grant (MG) equation as [5,55,105-108,112],

$$\dot{\epsilon}_{min}^{\alpha} \cdot t_r = C_{\mathrm{MG}}$$

where α is the constant close to unity and C_{MG} is the MG constant. The value of constant (α) in P91 and P91BN-1 steels are found to be 0.95 ± 0.06 and 0.91 ± 0.03 respectively, which exhibits

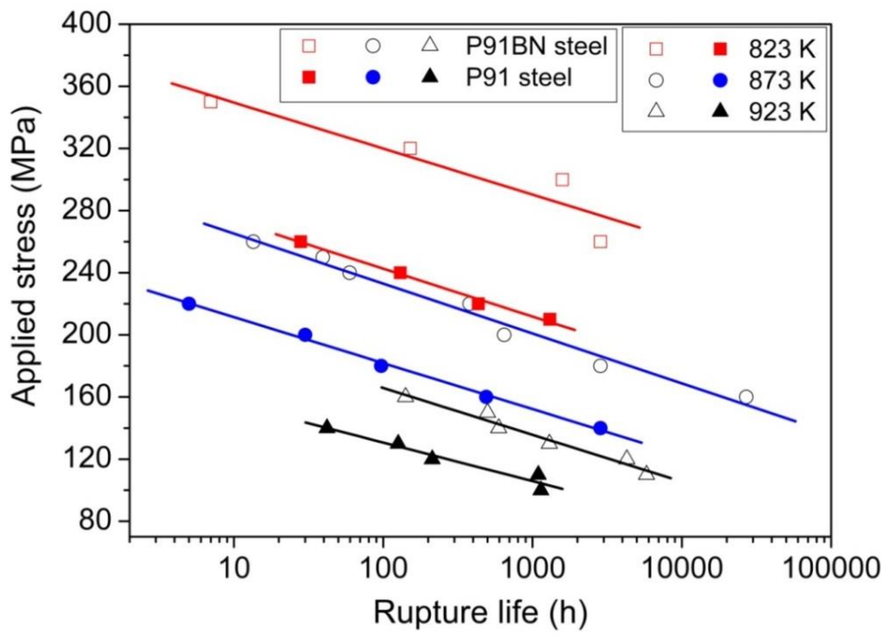

Fig. 4.30 Variation of creep rupture life with applied stress of P91 and P91BN-1 steels at 823 K (550 °C), 873 K (600 °C) and 923 K (650 °C).

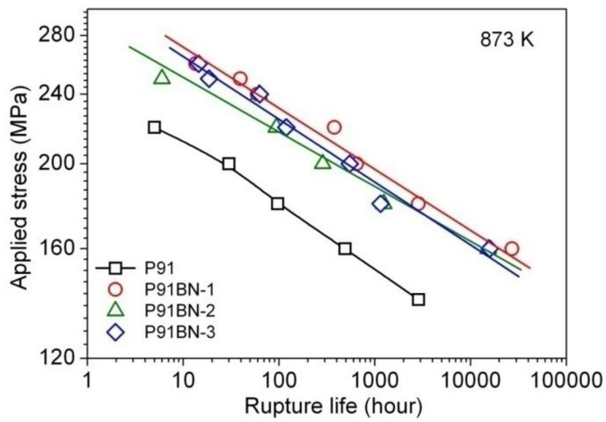

Fig. 4.31 Variation of creep rupture life with applied stress of P91, P91BN-1, P91BN-2 and P91BN-3 steels at 873 K (600 °C).

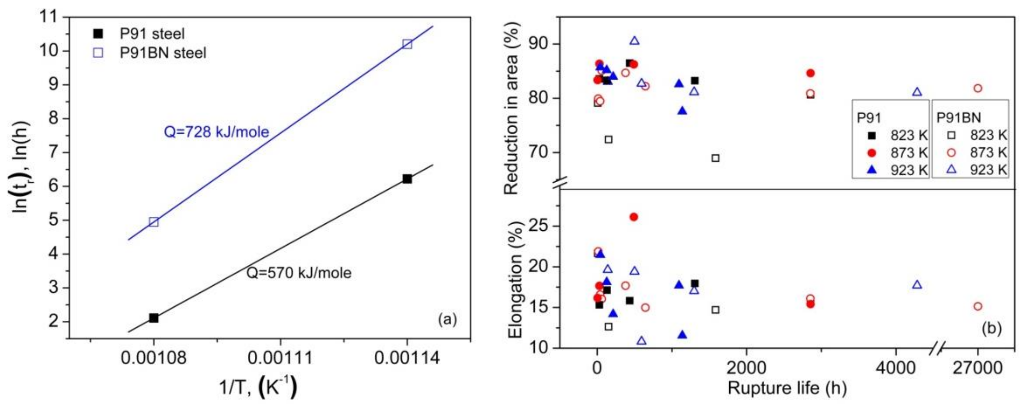

Fig. 4.32 (a) Arrhenius plot of temperature dependence of creep rupture life for P91 and P91BN-1 steels; and (b) variation of reduction in area (%) and elongation (%) with rupture life of P91 and P91BN steels at 823 K (550 °C), 873 K (600 °C) and 923 K (650 °C).

the validity of MG relation. Several single-phase materials and precipitation hardened alloys have been found to obey MG relationship [5,55,105-108,112]. C_{MG} values of 0.037 ± 0.01 and 0.028 ± 0.01 were obtained in P91 and P91BN-1 steels respectively. The lower values of C_{MG} depicted the lower creep strain accumulation in the secondary creep as compared to tertiary creep regime. P91BN-1 steel exhibited lower value of C_{MG} as compared to P91 steel, which depicted the relatively lower creep strain accumulation in P91BN steel. C_{MG} values ~0.04 in P91 steel has been reported by researchers [5]. For materials that exhibiting shorter secondary creep deformation regime and larger tertiary creep deformation regime modified Monkman-Grant relationship has been proposed as [5,55,105-108,112],

$$\dot{\epsilon}_{min}^{\alpha'} . \frac{t_r}{\varepsilon_f} = C_{\mathrm{MMG}}$$

where ϵ_f is the strain to failure, α' is a constant close to unity, and C_{MMG} is the modified Monkman-Grant constant. The plots of t_r/ϵ_f against $\dot{\epsilon}_{\min}$ for P91 and P91BN-1 steels are given in Fig. 4.34(a) and (b) respectively. The value of constant α' for P91 and P91BN-1 steels are similar (about 0.96 ± 0.05 and 0.95 ± 0.05 respectively), which is close to 1. The C_{MMG} value is ~ 0.338 ± 0.06 in P91 and 0.298 ± 0.06 in P91BN-1 demonstrating the higher creep strain accumulation in the tertiary creep regime in the steels. However, for P91BN-1 steel, the creep strain accumulation was relatively lower than the P91 steel. Both P91 and P91BN-1 steels obeyed the Monkman-Grant and modified Monkman-Grant relationship. Values of C_{MMG} ranging from 0.1 to 0.83 have been reported for various ferrous and non-ferrous alloys [112].

Plots of variation of time to onset of tertiary creep (t_{ot}) (initiation of accelerated creep rate regime) with t_r for P91 and P91BN-1 steels have been shown in Fig. 4.35, this variation followed a linear relationship as $t_{ot} = f.t_r$, where f is a constant. The f value about 0.299 ± 0.08 in P91 steel and 0.289 ± 0.06 in P91BN-1 steel demonstrated that both steels spent more than 70% of the creep exposure time in the tertiary creep regime as generally observed in various 9-12% Cr steels [2,105,106]. A creep damage tolerance factor (λ) based on continuum damage mechanics has been defined as inverse of modified Monkman-Grant ductility as $\lambda = \frac{\varepsilon_f}{\dot{\epsilon}\, t_r} = 1/C_{MMG}$ [1,26-31]. The value of λ for various alloys ranges from 1 to 20. Low value of λ indicates brittle mode of fracture with low tertiary creep strain and higher values indicate ductile fracture accommodating higher creep strain in tertiary without local cracking [1,26]. Creep damage by cavity growth when λ lies in the range from 1 to 2.5. Necking dominant damage is exhibited when the value of λ ranges from 2.5 to 5, and values higher than 5 corresponds to fracture caused by coarsening of precipitates, subgrains and decrease in dislocation density [1,26]. In this investigation, value of λ about 3.5 to 5.5 and 4.4 to 8.4 were obtained in P91 and P91BN-1 steels, which demonstrates necking and dominant microstructural instability caused fracture in the steels. Damage tolerance factor about ~4 to 5 for grade 91 steel and about 6 for P92 steel have been reported [5]. Ashby and Dyson have proposed a creep failure diagnostic diagram [5,110]. Creep failure diagnostic diagram constructed for P91 and P91BN-1 steels (($\dot{\epsilon}_{min} \,.\, t_r$ *x 100) vs* ε_f) are shown in Fig. 4.36. Loss of section and necking dominant creep failure predominantly observed at 823 K in P91 and P91BN-1 steels. Modification in microstructural constituents such as coarsening of precipitates and subgrain, reduction in dislocation density influenced the creep fracture in P91 and P91BN-1 steels at higher temperature. Shrestha et al have reported that the dominant microstructural degradation in grade 91 steel and void growth based dominant creep fracture in iron resulted in creep fracture (creep tested at 873-973 K) [5,105].

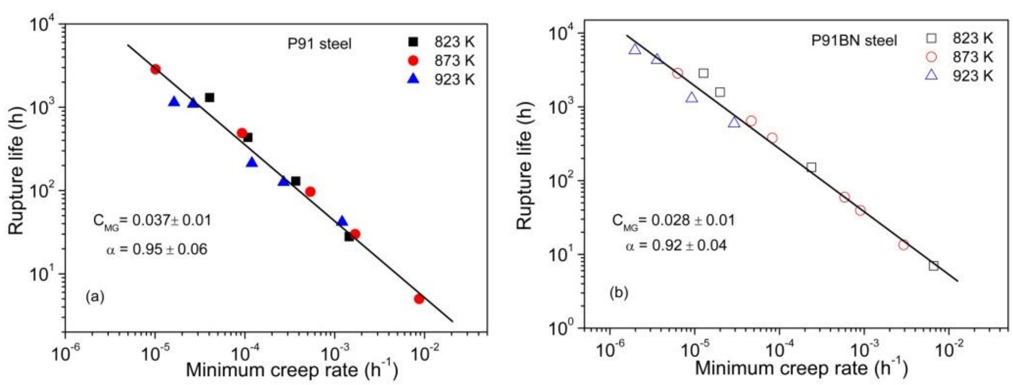

Fig. 4.33 Variation of rupture life with minimum creep rate of (a) P91 and (b) P91BN-1 steel at 823 K (550 °C), 873 K (600 °C) and 923 K (650 °C).

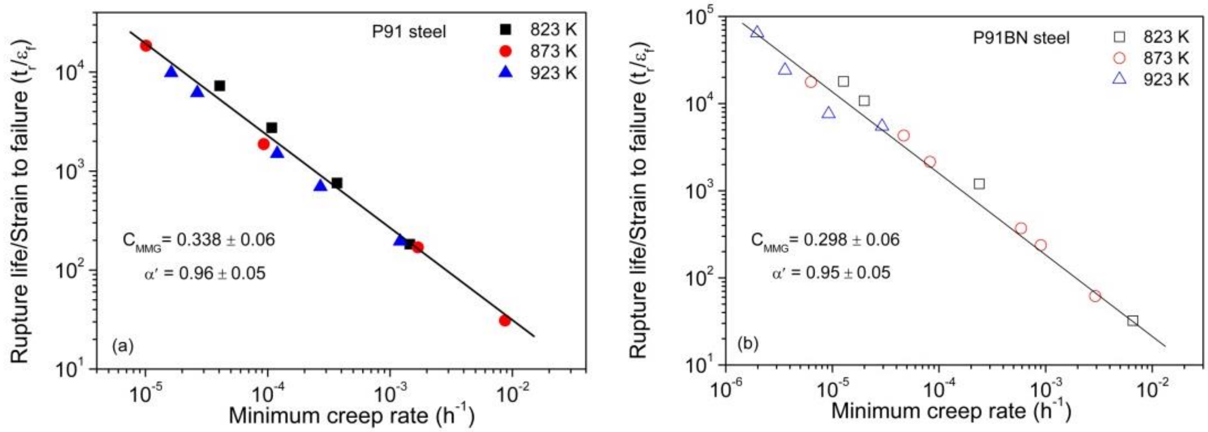

Fig. 4.34 Variation of normalized rupture life by strain to failure with minimum creep rate of (a) P91 and (b) P91BN-1 steels at 823 K (550 °C), 873 K (600 °C) and 923 K (650 °C).

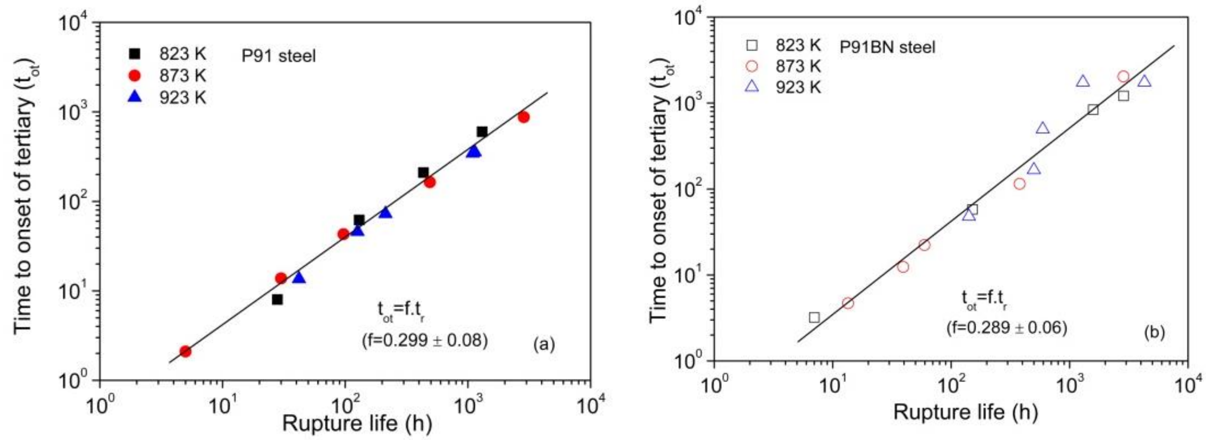

Fig. 4.35 Variation of time to onset of tertiary with rupture life of (a) P91 and (b) P91BN-1 steels at 823 K (550 °C), 873 K (600 °C) and 923 K (650 °C).

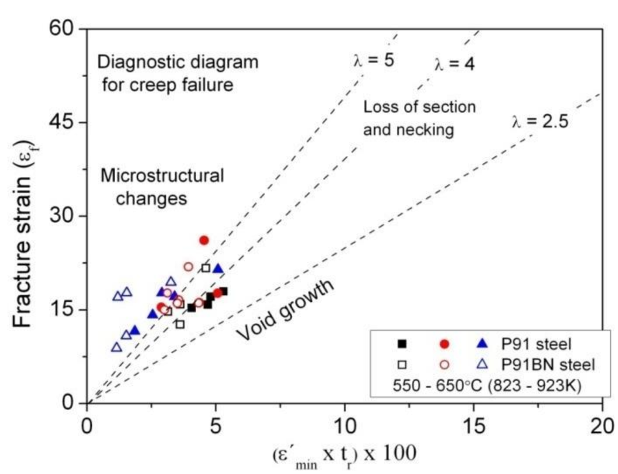

Fig. 4.36 Diagnostic diagram for creep failure of P91 and P91BN-1 steels.

4.2.5.4 Creep rupture life prediction

Larson-Miller parameter method is used in order to predict the creep rupture strength of the steels under longer creep exposure. Larson-Miller parameter has been expressed as, $LMP = T(\log(t_r) + C)$, where T is in K, t_r is in h and C is a constant. For this class of steels C=31 has been widely used. The applied stress with *LMP* (Larson-Miller parameter) for P91 and P91BN-1 steels are shown in Fig. 4.37(a). The creep data of P91 steel presented in the present study was comparable with the creep rupture data reported in the literature [5,105,106,113-116]. The creep strength of P91BN-1 steel was significantly higher than the strength of P91 steel reported in the present study and literature. The prediction of creep rupture strength at different temperatures for 10^5 h duration was performed based on LMP plot and given in Table 4.4 and Fig. 4.37(b). The predicted creep rupture strength of P91 steel for 10^5 h duration at different temperatures were compared favorably with the values reported by RCC-MR code [114]. An improvement in the 10^5 h creep rupture strength about 16, 25, 33 and 37 (%) at 773, 823, 873 and 898 K respectively were observed in P91BN-1 steel as compared to P91 steel. However, microstructural stability over the longer creep duration is required for both the steels to avoid error in the predicted creep rupture strength value.

4.2.5.5 Fractography and microstructural investigation of creep exposed steels

Fracture surface of P91 and P91BN-1 steels creep tested at 823, 873 and 923 K are shown in Figs. 4.38 and 4.39. Ductile mode of fracture with dimple features was observed in both the steels over the investigated temperature region. Number of dimples in the P91BN-1 steel was higher as compared to P91 steel. The dimple size increased with increase in test temperature in P91 steel, which demonstrates the dominance of recovery of dislocation structure in P91 steel. However, dimple size in P91BN-1 steel has not changed significantly with test temperature over the investigated duration, which confirms the stable microstructural constituents and less straining during creep as compared to P91 steel.

P91 steel derives its high temperature strength from (i) transformation induced dislocation density, (ii) PAG, packet, block and lath/subgrain boundaries stabilized by (iii) MX and $M_{23}C_6$ precipitates predominantly at the intra-lath region and boundaries respectively and (iv) solid solution strengthening from Mo. The stability of dislocation network and boundaries against mobility depends on the stability of precipitates pinning at them. MX carbonitride precipitates that are rich in V and Nb is thermally more stable as compared to $M_{23}C_6$ precipitates [97,98,117]. The reliability of creep rupture strength of 9Cr ferritic-martensitic steel under long term exposure is important, as this class of steel has been widely used in harsh environments (high temperature and neutron flux), which relies on the stability of microstructure [97,117]. Researchers [117] have reported the increased Cr/Fe ratio in coarser $M_{23}C_6$ precipitates that are near to PAG boundaries under creep. Coarsening of precipitates is depends on the diffusion of solute elements, energy at the precipitate-matrix interface and strain/dislocation density in the steel. An addition of boron with controlled nitrogen in P91BN-1 steel led to finer lath width, $M_{23}C_6$ precipitates and higher number of precipitates per unit area. The incorporation of boron in the $M_{23}(CB)_6$ [97,118] and segregation of boron at the interfaces led to reduce the diffusivity of elements required for coarsening of precipitates [97,118]. Microstructure of P91 and P91BN-1 steel creep exposed are shown in Figs. 4.40 and 4.41. The coarsening of $M_{23}C_6$ precipitates was reduced in P91BN-1 steel as compared to the P91 steel; it is imperative to note that the fine precipitates presence in the P91BN-1 steel effectively resist the movement of boundaries under complex stress state (necked region) (Fig. 4.40(e,f)). The coarsening of $M_{23}C_6$ precipitates was reduced significantly in P91BN-1 steel as compared to the P91 steel under long term creep exposure at 873 K and 160 MPa stress (Fig. 4.42). In the case of P91 steel boundaries were almost parallel to the stress direction near the fracture region, while in the case of P91BN-1 steel distinct impingement of boundaries by fine precipitates exerting higher pinning pressure has been noticed (Fig. 4.40(e,f)). Segregation of boron at the interfaces/boundaries led to reduces the energy at interfaces/boundaries [97]. Hence, coarsening resistance of $M_{23}(CB)_6$ phase is more as compared to $M_{23}C_6$ because of decreased energy at the Fe{110}// $M_{23}(CB)_6$ {111} interfaces [98,119-122]. An addition of boron in P91BN steels with controlled nitrogen lead to increase the stability of microstructural constituents as compared to P91 steel, thus results in significant enhancement of creep rupture strength (P91BN-1 steel - optimum combination of boron and nitrogen).

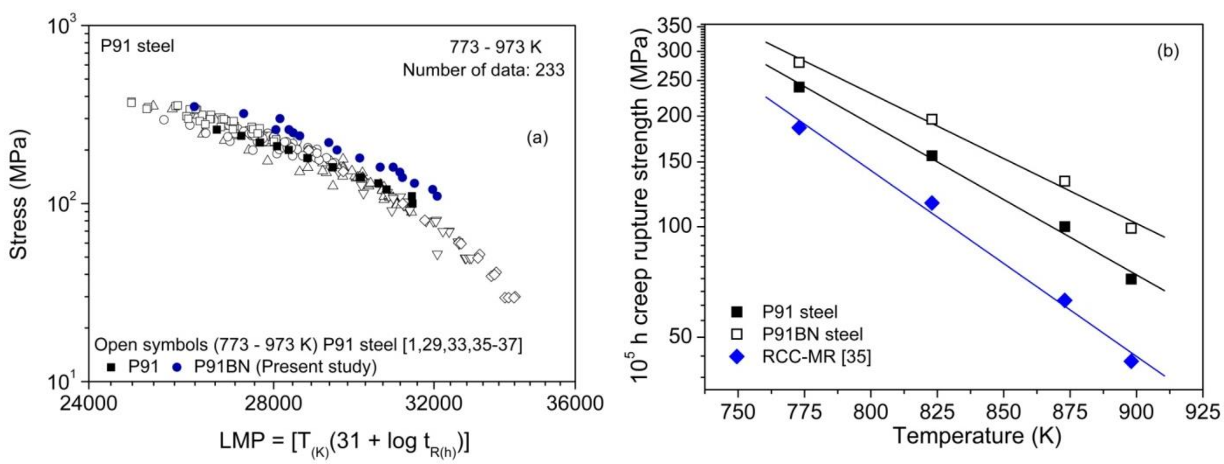

Fig. 4.37 (a) Larson–Miller creep parameter plot of P91 and P91BN-1 steels, (b) 10^5 h creep rupture strength estimated from LMP at different temperature for P91 and P91BN-1 steels.

<table>
<tr><td>Temperature (K) / stress (MPa)</td><td colspan="2">P91 steel</td></tr>
<tr><td>823 K

(210 MPa; t_r=1307.2 h)</td><td>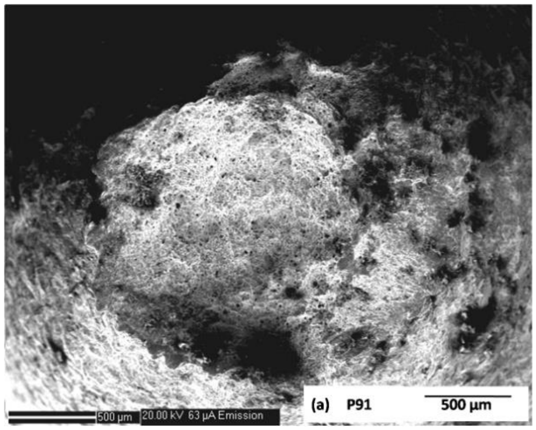
</td><td>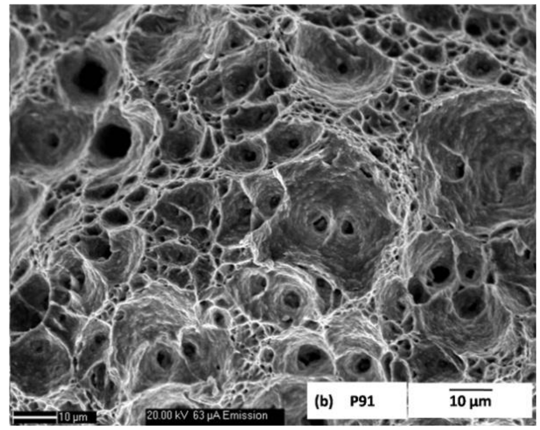
</td></tr>
<tr><td>873 K

(180 MPa; t_r=96.8 h)</td><td>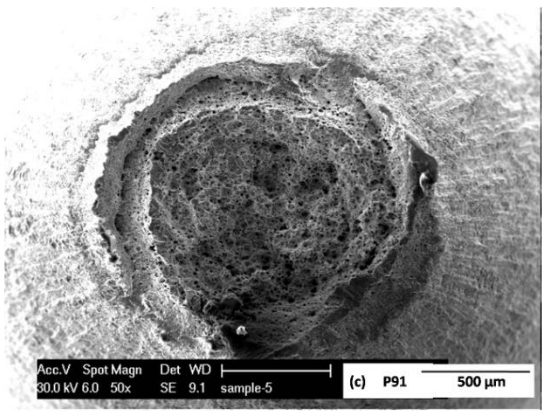
</td><td>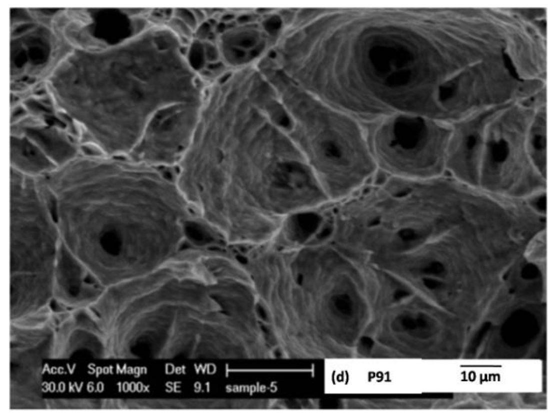
</td></tr>
<tr><td>923 K

(100 MPa; t_r=1139.2 h)</td><td>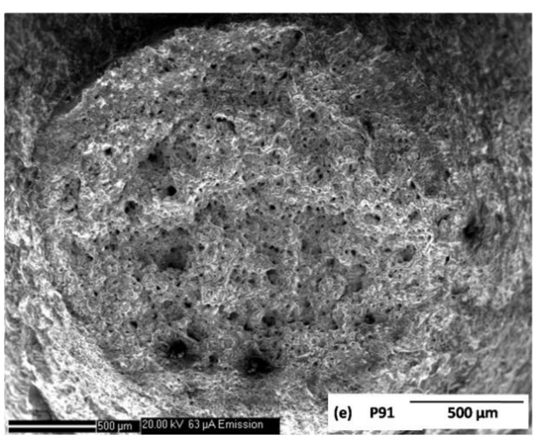
</td><td>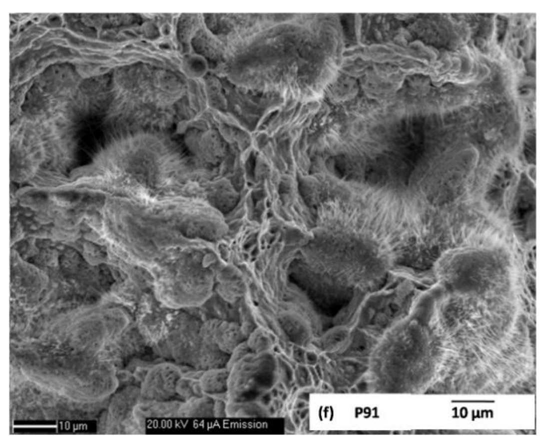
</td></tr>
</table>

Fig. 4.38 Fracture surface of crept P91 steel at (a, b) 823 K, (c, d) 873 K and (d, e) 973 K.

Temperature (K) / stress (MPa)	P91BN-1 steel	
823 K (260 MPa; t_r=2855.0 h)	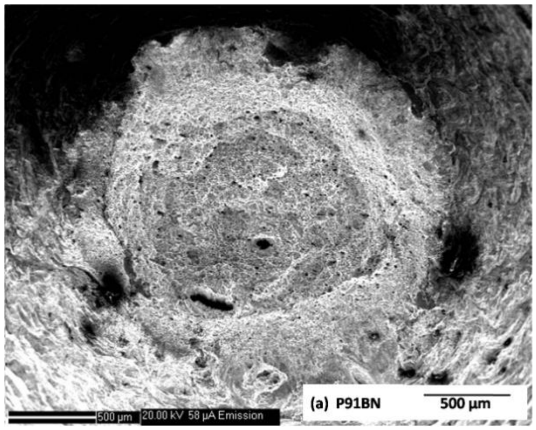	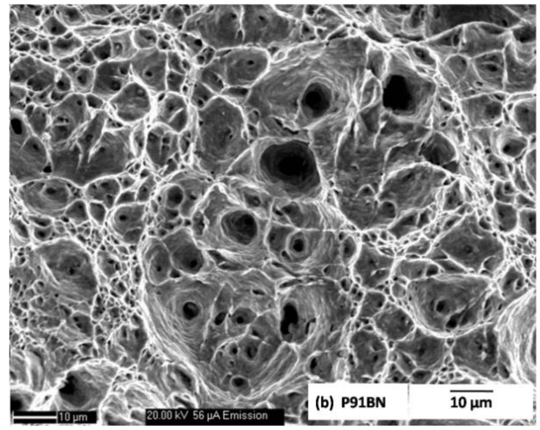
873 K (180 MPa; t_r=3100.1 h)	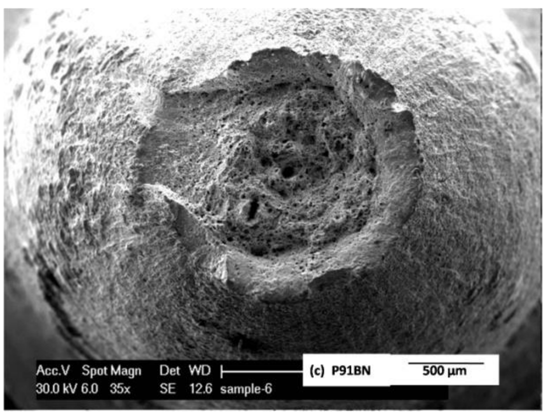	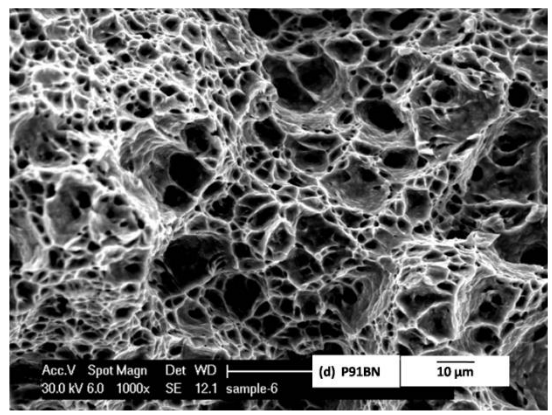
923 K (110 MPa; t_r=5808.4 h)	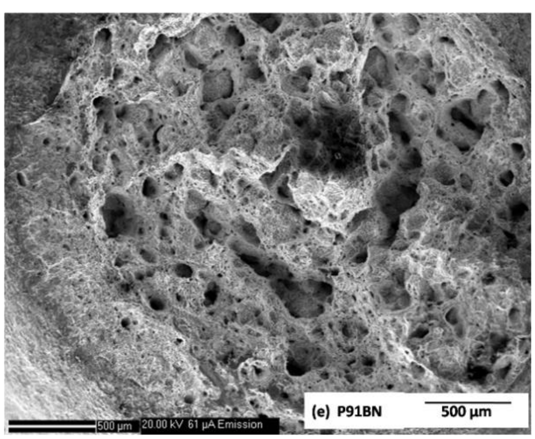	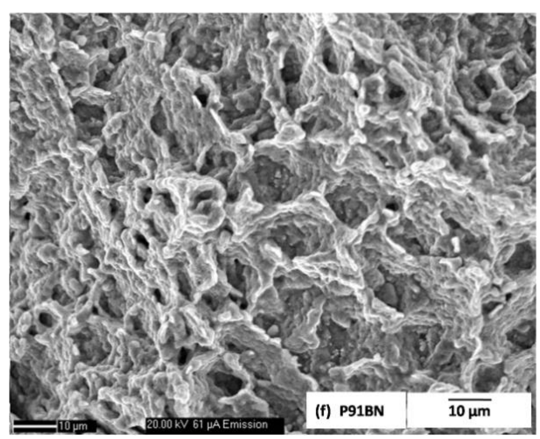

Fig. 4.39 Fracture surface of creep exposed P91BN-1 steel at (a, b) 823 K, (c, d) 873 K and (d, e) 973 K.

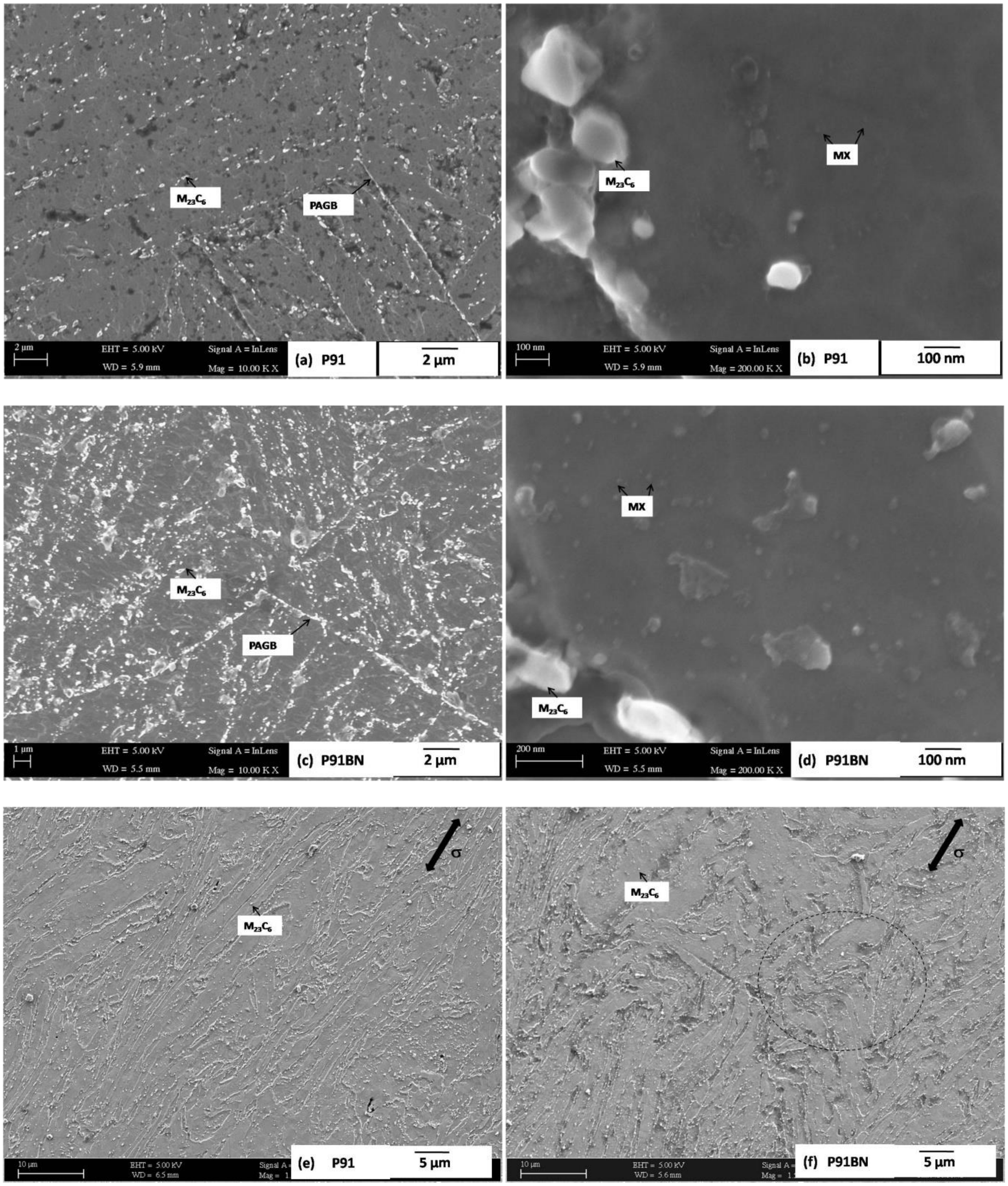

Fig. 4.40 SEM micrographs of creep exposed (a, b) P91 [t_r=96.8 h] and (c, d) P91BN-1 [t_r=3100.1 h] steels at 873 K and 180 MPa stress in the gauge region. Boundaries pinned by precipitates against migration at the necked region (e) P91 (160 MPa) and (f) P91BN-1 (200 MPa) steels at 873 K.

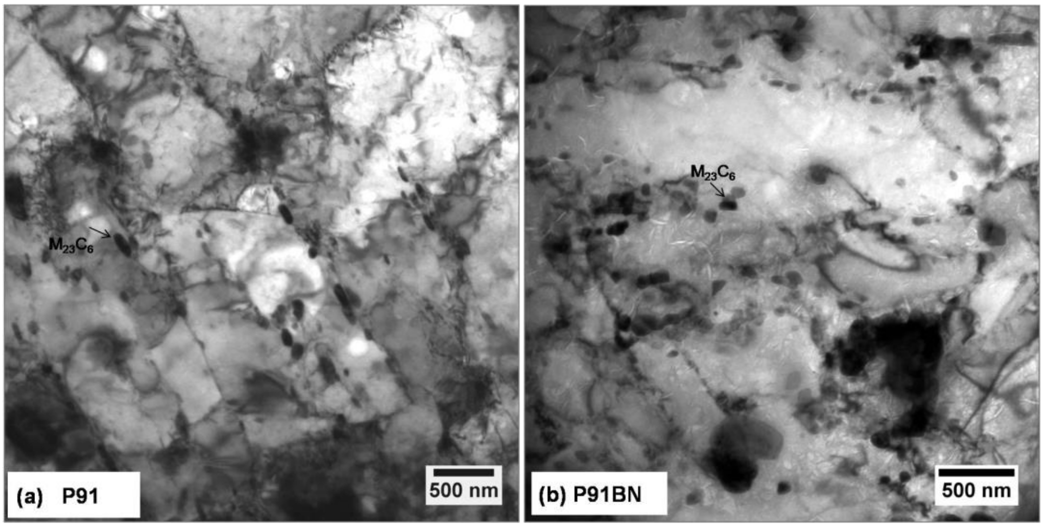

Fig. 4.41 TEM micrographs of creep exposed at 873 K and 180 MPa stress in the gauge region of P91 (a) and P91BN-1 (b) steels.

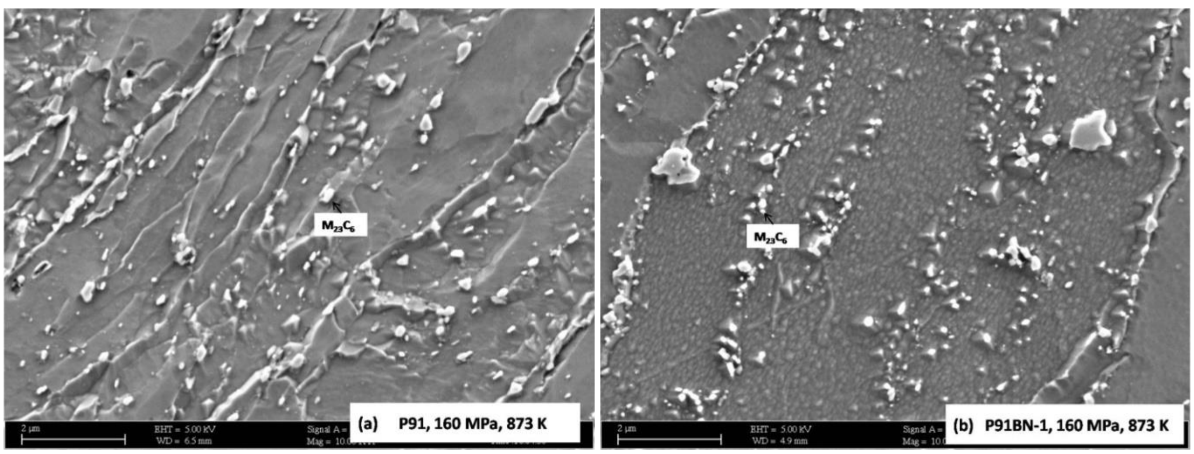

Fig. 4.42 SEM micrographs of creep exposed at 873 K and 160 MPa stress in the necked region of (a) P91 and (b) P91BN-1 steels.

Table 4.4 RCC-MR minimum creep rupture stress for 10^5h, and predicted creep rupture stress for 10^5h life for P91 and P91BN-1 steels by LMP.

Temperature (K)	Predicted creep rupture stress (MPa)			Minimum creep rupture stress (MPa) for P91
	P91	P91BN-1	Strength enhancement in P91BN-1 than P91 steel (%)	RCC-MR
773	240	280	16.6	186
823	156	196	25.6	116
873	100	133	33	63
898	72	99	37.5	43
923	51			28

4.3 Weld joints

In this section, creep deformation and rupture behaviour of P91, P91BN-1, P91BN-2 and P91BN-3 steels weld joints fabricated by A-TIG welding processes have been presented. The microstructural and hardness investigations across the joints in the pre-creep and creep exposed conditions have been carried out.

4.3.1 Microstructure and hardness variations across the weld joints

Optical micrographs across the A-TIG weld joint of P91 and P91BN-1 steels after PWHT are shown in Fig. 4.43 and 4.44. Three distinct macro-region of the weld joint are BM, weld fusion zone (WM) and HAZ between the base metal and fusion zone. Weld metal exhibited the significantly lengthy martensitic structure. In both the joints, microstructure in HAZ was found to consist of CGHAZ, FGHAZ and ICHAZ region in an order away from fusion zone to unaffected base metal. In the weld fusion zone and fusion boundary (FB) close to the CGHAZ, δ-ferrite was observed in the P91BN steels weld joints. However, δ-ferrite was not observed in the HAZ and BM of P91BN steels. δ-ferrite was not observed in the P91 steel weld joint. Prior-austenite grain size of the BM, CGHAZ, FGHAZ and ICHAZ of the P91 steel A-TIG weld joint was found to vary significantly across it. Whereas in the case of P91BN steels joints, the regions having coarse grains were higher than the regions of FGHAZ and ICHAZ in it. The boundaries in the ICHAZ region were not clearly evident in both the steel joints as compared to other regions across the weld joints. However, ICHAZ of P91BN steels weld joints possessed higher PAG size in comparison with that of ICHAZ of P91 steel joint.

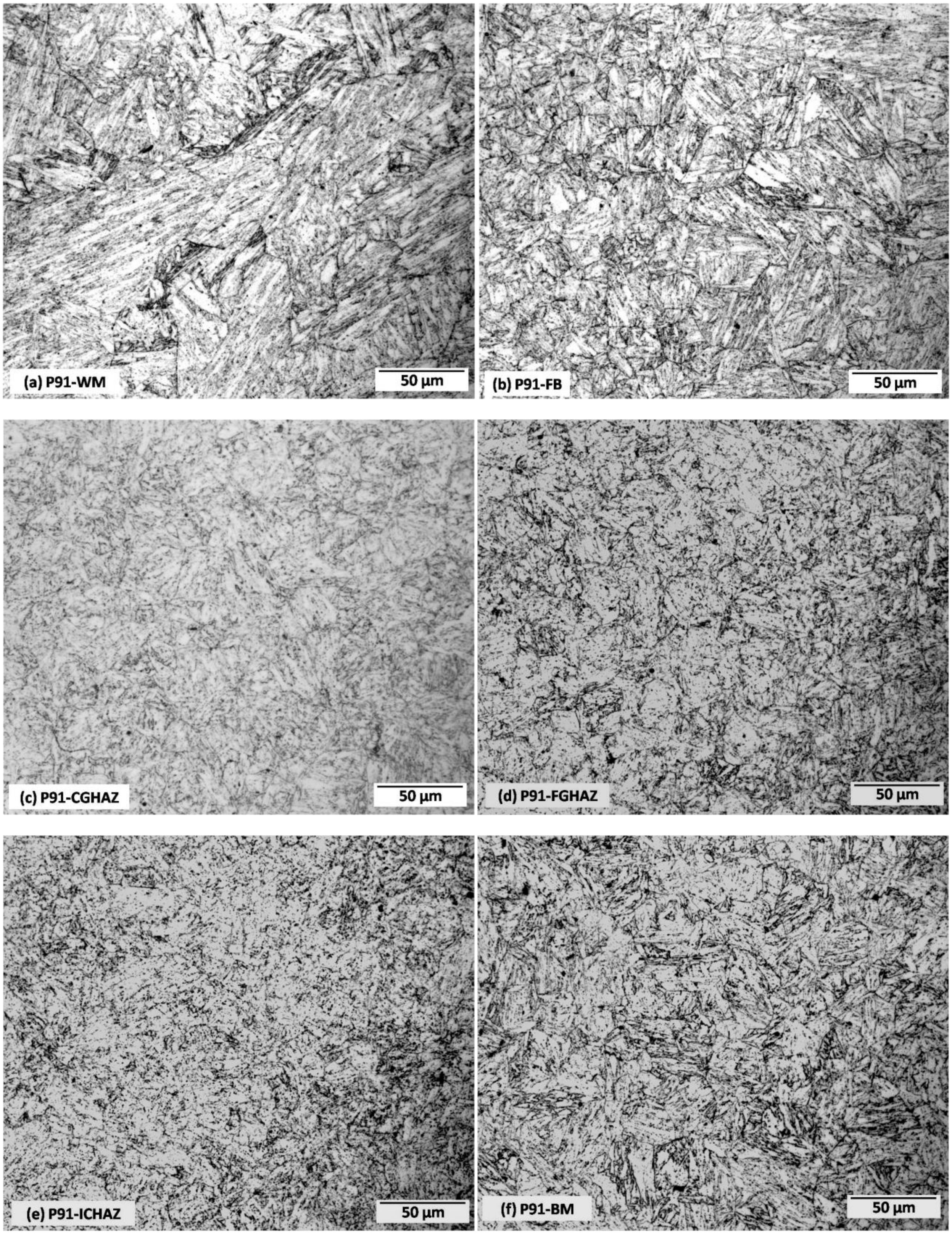

Fig. 4.43 Optical micrographs across the weld joint of P91 steel (a) WM, (b) fusion boundary (FB), (c) CGHAZ, (d) FGHAZ, (e) ICHAZ and (f) BM.

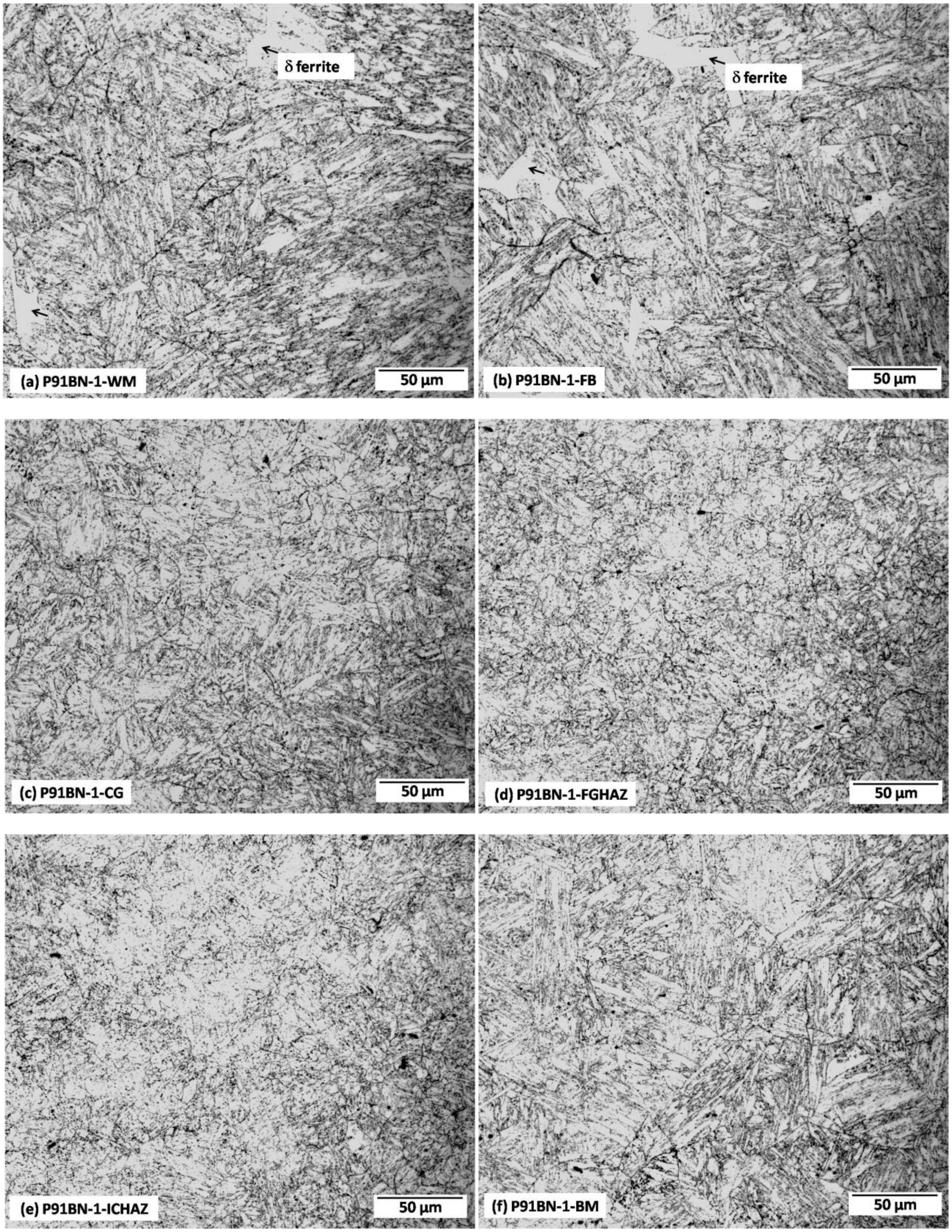

Fig. 4.44 Optical micrographs across the weld joint of P91BN-1 steel (a) WM, (b) FB, (c) CGHAZ, (d) FGHAZ, (e) ICHAZ and (f) BM.

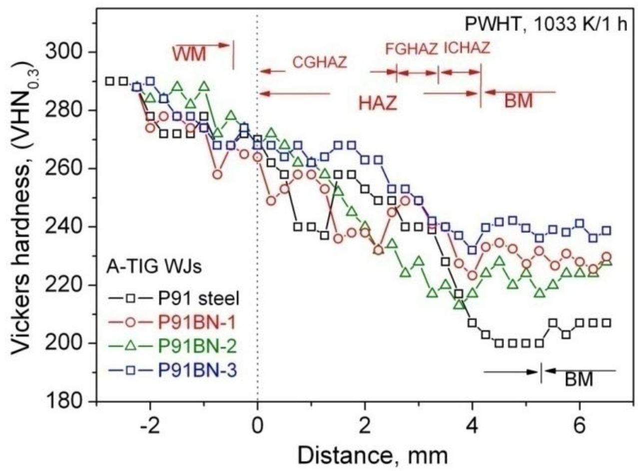

Fig.4.45 Variations of hardness across the P91, P91BN-1, P91BN-2 and P91BN-3 steels weld joint in the PWHT conditions.

Variation of hardness across the P91, P91BN-1, P91BN-2 and P91BN-3 steels weld joint in the PWHT conditions are shown in Fig. 4.45. The hardness values obtained across the as-welded condition in the WM, CGHAZ and FGHAZ regions were comparable. However, the decrease in hardness from outer edge of the FGHAZ to BM with a dip in the ICHAZ was observed. The similar hardness values of WM, CGHAZ and FGHAZ in the as-welded condition might be due to the similar dislocation density obtained by martensite transformation during weld thermal cooling cycle. The variation of hardness across the PWHT weld joint were exhibited the decrease in hardness from WM to BM about 300 VHN to 210 VHN with hardness trough in the ICHAZ about 199 VHN in the P91 steel weld joint (Fig.4.45). The variation of hardness across the P91BN steels weld joints were exhibited the decrease in hardness from WM to BM about 300 VHN to 219 VHN with hardness trough in the ICHAZ about 214-229 VHN. The hardness variation across the P91 steel joint is significantly higher as compared to P91BN steels joints. The considerable softening in the ICHAZ of the PWHT weld joint has been attributed to the coarsening of $M_{23}C_6$ precipitates, and the replacement of martensite laths structure with high dislocation density by formation of sub-grains with decreased dislocation density. These effects are relatively less in the P91BN steels, which led to show higher hardness than the ICHAZ of P91 steel joint. The formation of soft ICHAZ has been expressed by other investigators in different 9-12 % Cr-ferritic steels weld joint [25,55,65,77,85,86].

4.3.2 Tensile properties across the weld joint

Tensile tests were carried on the specimens extracted across the weld joints of P91BN steels at a strain rate of 3 x 10^{-4} s^{-1}. Engineering stress-strain curves of different regions in the P91BN-1 and P91BN-3 steels joints at 300 K and 873 K are shown in Fig. 4.46. ICHAZ of the joints possessed lower tensile strengths with higher ductility as compared to other regions in the joint. Variations of 0.2% off-set yield stress (YS) and ultimate tensile strength (UTS) of different regions of the P91, P91BN-1, P91BN-2 and P91BN-3 steels joints are shown in Figs. 4.47. Tensile strengths (YS and UTS) and ductility were found to vary significantly across the weld joints. P91BN steels have shown relatively higher tensile strengths with comparable ductility. The variation of tensile strengths across the P91 steel weld joint was higher as compared to that of P91BN steels weld joints. The ICHAZ region has shown lower strengths and higher ductility than the other regions in the weld joints. CGHAZ has shown higher strength in the P91 steel. FGHAZ and BM strengths were comparable in the P91 steel. However, in the case of P91BN steels joints, tensile strengths of CGHAZ, FGHAZ and BM were relatively comparable. In P91BN steels, WM has shown lower tensile strengths and ductility than the CGHAZ, FGHAZ and BM, might be due to presence of δ-ferrite in the region. In comparison with ICHAZ, WM possessed higher tensile strengths and lower ductility. Boron addition in the steel led to reduce the heterogeneity in tensile strengths across the weld joints. The reduction in heterogeneity across the joint led to reduce the constraint in different region across the weld joint by adjacent regions.

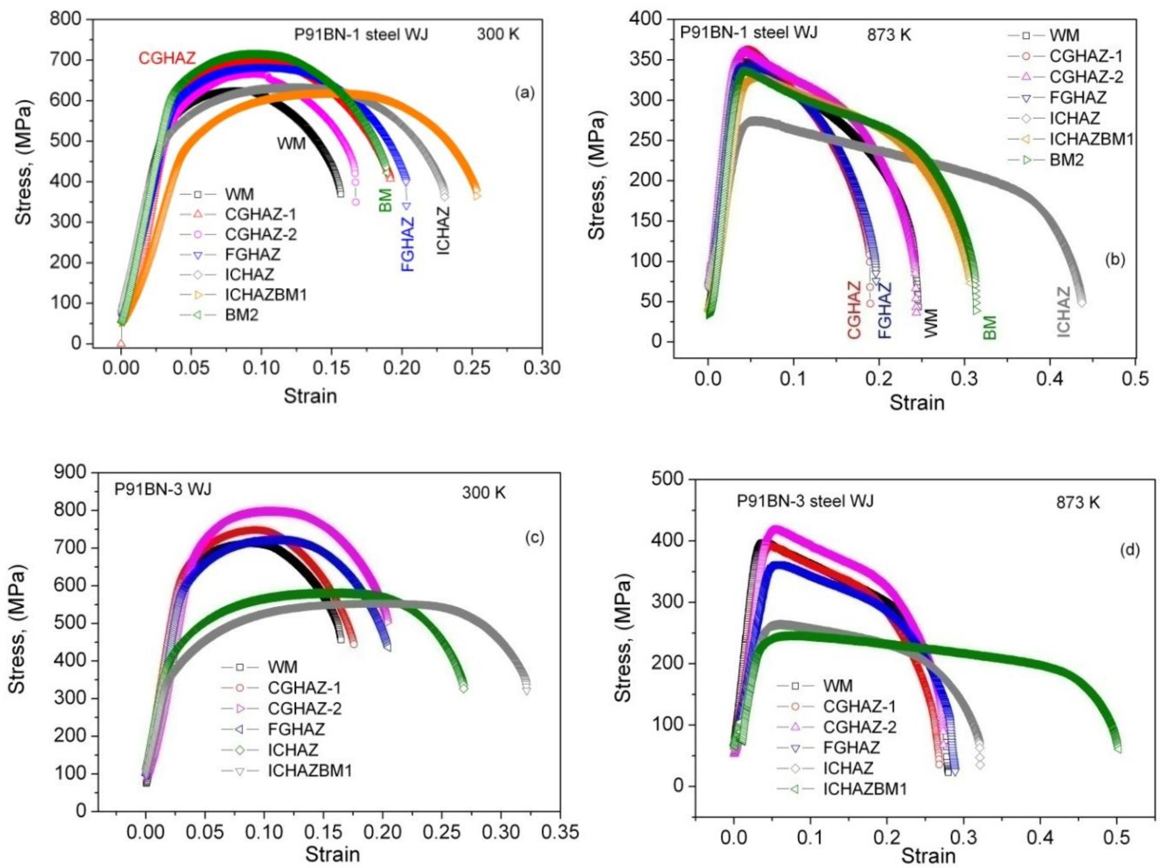

Fig. 4.46 Tensile stress-strain curves of (a,b) P91BN-1 and (c,d) P91BN-3 steels weld joints regions at 300 K and 873 K.

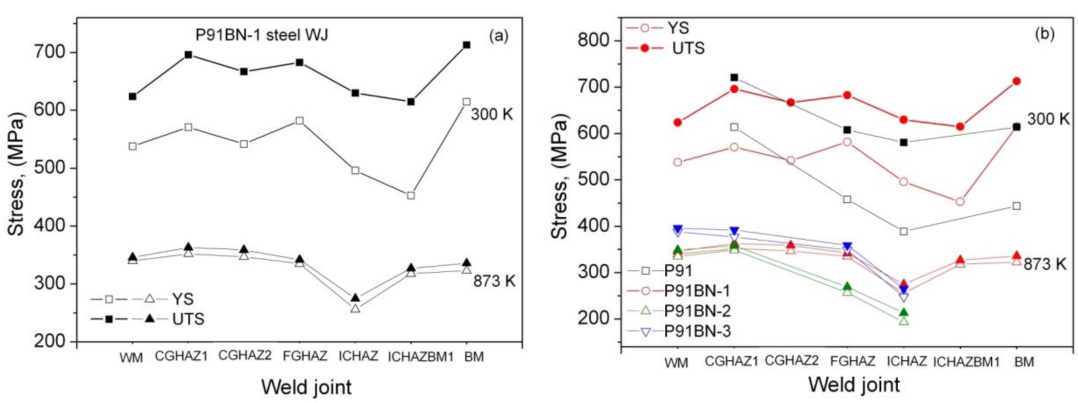

Fig. 4.47 Variation of tensile strength across the (a) P91BN-1, (b) P91, P91BN-1, P91BN-2 and P91BN-3 steels weld joint in the PWHT conditions at 300 and 873 K at a strain rate of $3x10^{-4}s^{-1}$.

4.3.3 Creep deformation

The creep curves of the weld joints have even though little practical relevance since the joint is composed of the different microstructural gradient, the creep curves exhibited primary creep regime followed by an apparent steady state creep deformation and an accelerating tertiary creep regime as observed in the base metals. The tertiary stage of creep deformation in the weld joints was found to initiate much early than the base metals. Extensive microstructural changes (higher rate of recovery of dislocations and coarsening of subgrain boundaries in the ICHAZ) and localized creep deformation in the selected constituents of the joints have been considered for the early onset of tertiary stage of creep deformation in the steel weld joints in comparison with the base metal. The early initiation of tertiary creep deformation in the P91 steel joint is attributed to the higher deformation constraint imposed on the soft ICHAZ by adjacent region. Boron in the P91BN steels leads to delayed initiation of tertiary creep deformation in the weld joints. This is attributed to lesser deformation constraints in ICHAZ caused by relatively less heterogeneity in mechanical properties across the weld joint. The variations of rupture life with applied stress for the P91 and P91BN steels base metal and weld joints of P91BN steels at 873 K are shown in Fig. 4.48. The P91BN steels weld joints possessed comparable rupture life with its base metals. However, the difference in the rupture life between the weld joints and base metal was increased at lower applied stress [54,55]. The P91BN-1 and P91BN-2 steels weld joints have shown higher rupture life in comparison with P91BN-3 weld joint. The P91BN-1 steel weld joint has exhibited higher rupture life at 873 K, but the difference in rupture life between P91BN-1 and P91BN-2 weld joints is relatively less. The variations of rupture life with applied stress for weld joints of P91, P91BN-1, P91BN-2, P91BN-3 steels at 923 K are shown in Fig. 4.49. P91 steel weld joint has shown a significantly lower rupture life than the P91BN steels weld joints.

P91BN-2 steel weld joint possessed a higher rupture life as compared to P91BN-1 and P91BN-3 joints. The P91BN steels weld joint creep rupture life is comparable with the creep rupture strength of P91 steel base metal at 923 K (Fig. 4.50).Higher content of boron with controlled nitrogen content in the P91BN steel (P91BN-2) led to provide better resistance against type IV cracking in the weld joint at the higher temperature (923 K) (Fig. 4.49).

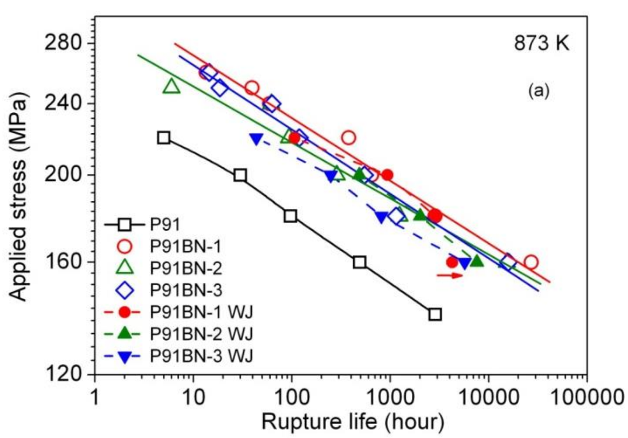

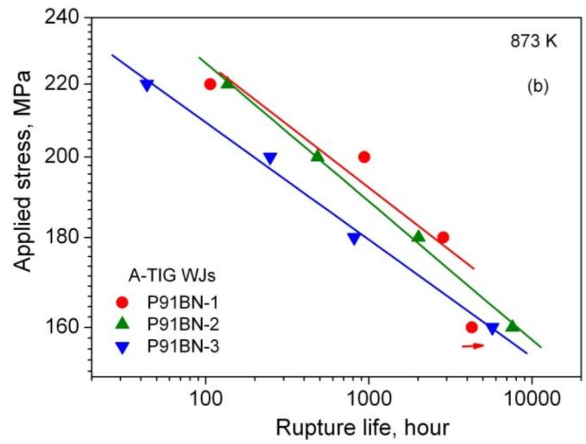

Fig. 4.48 Variations of rupture life with applied stress for (a) P91, P91BN-1, P91BN-2 and P91BN-3 steels base metals and weld joints, (b) P91BN steels weld joints at 873 K.

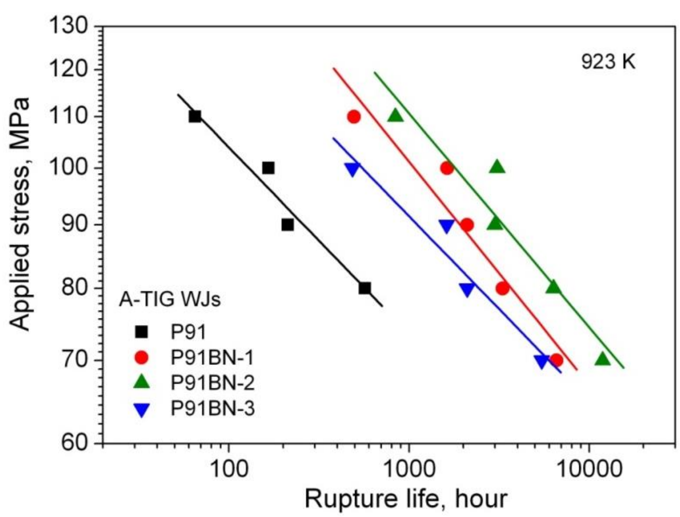

Fig. 4.49 Variations of creep rupture life with applied stress for the weld joints of P91, P91BN-1, P91BN-2, P91BN-3 steels at 923 K.

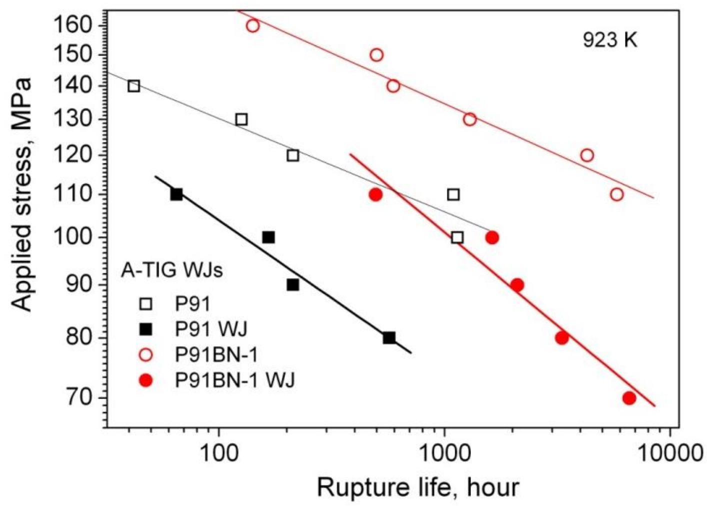

Fig. 4.50 Variations of creep rupture life with applied stress for P91 and P91BN-1 steels and its weld joints at 923 K.

4.3.4 Creep ductility and fracture

The P91BN steels weld joints creep ruptured specimens at 923 K and 80 MPa stress is shown in Fig. 4.51. The failure location of the weld joint has not changed with applied stress in the investigated regime. However, the reduction in creep ductility has been evidenced with the decrease in applied stress. The localized creep deformation was observed in the ICHAZ. The variation of reduction in the area of the weld joints at 923 K and 80 MPa is shown in Fig. 4.52. The weld joint possessed lower reduction in area as compared to its base metal. The drastic reduction in rupture ductility occurred in the weld joints as compared to the base metal with decrease in applied stress. P91 steel possessed relatively higher reduction in area as compared to the P91BN steels weld joints (Fig. 4.52), which experienced significantly shorter creep exposure than P91BN steel joints. Very low ductile intercritical HAZ failures were reported on the P91 steel weld joint by Rui Wu et al. [123]. The fracture surfaces of the P91 and P91BN steels weld joints creep tested at 923 K, 80 MPa stress is shown in Fig. 4.53. The fracture surface observation of the creep tested specimens revealed the existence of a mixed mode of fracture (ductile and brittle) with the predominant ductile mode of fracture in the ICHAZ of P91 steel (Fig. 4.53 (a)). The mixed mode of failure in the P91BN steels joint have been observed with the relatively predominant brittle fracture. The brittle mode of failure was higher in the P91BN-2 joint, the joint that has sustained the longer creep exposure (Fig.4.53(c)).

Fig. 4.51 P91BN steels weld joints creep ruptured specimens at 923 K and 80 MPa stress.

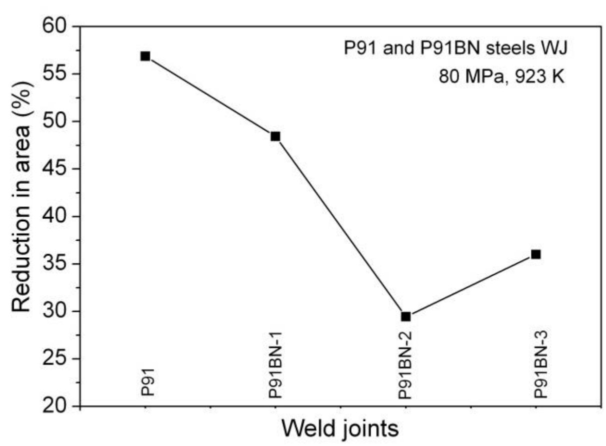

Fig. 4.52 Reduction in area (%) of P91 and P91BN steels joints creep exposed at 923 K, 80MPa.

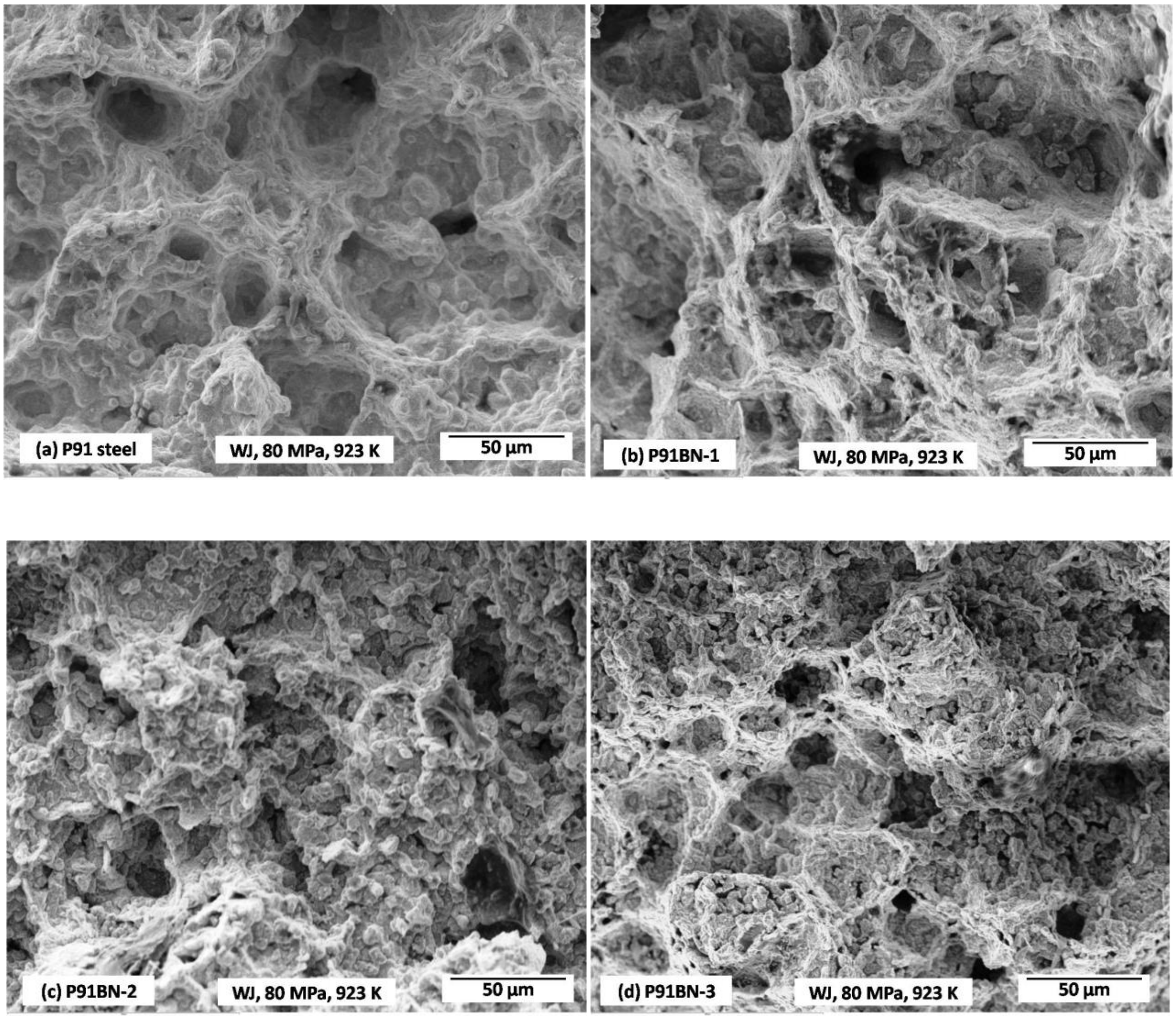

Fig. 4.53. Fracture surfaces of the creep tested weld joints of (a) P91, (b) P91BN-1, (c) P91BN-2 and (d) P91BN-3 steels at 923 K, 80 MPa stress.

4.3.5 Microstructure and hardness of crept weld joints

Microstructural investigation at the intact side of the creep exposed joint revealed that creep failure of the weld joint occurred in the ICHAZ, and that exhibited lower hardness before creep testing (Fig. 4.54 and 4.55). The type IV failure in the ICHAZ at 873 K and 923 K have been observed in the all investigated stress level. However, the localization of creep deformation and reduction in ductility were predominantly increased with decrease in applied stress. P91BN steels weld joints (Fig. 4.55 (g)) experienced more prolonged creep exposure have exhibited relatively lower localized creep deformation as compared to the P91 steel weld joint (Fig. 4.54 (a)). The preferential creep cavitation in the ICHAZ was observed in the P91 and P91BN steels weld joints (Fig. 4.54, 4.55 and 4.56). The type IV cracking observed in the P91BN-2 steel weld joint is shown in Fig. 4.55(e), which undergone longer creep exposure. The flow of the low creep resistance region is restricted by the surrounding stronger creep resistance region results in the development of higher triaxial state of stress in the soft ICHAZ. The creep damage accumulation due to strain incompatibility between the creep strong and creep weak regions was reported in the P91 welds [68,79,123].

The hardness measurement across the weld joints on creep exposed at 80 MPa and 923 K specimens exhibited the reduction of hardness in comparison with the pre-creep test condition of the weld joints (Fig. 4.57). ICHAZ has shown lower hardness as compared to other regions in the weld joints. Hardness across the P91BN steels weld joints exhibited relatively higher hardness as compared to the P91 steel weld joint. ICHAZ of P91 steel weld joint has displayed lowest hardness (where the weld joint experienced shorter creep exposure) as compared to ICHAZ of P91BN steels weld joints. The extensive coarsening of $M_{23}C_6$ precipitates was observed in the ICHAZ of P91 steel (Fig. 4.56(a)). The pinning of dislocation subgrain and network by the chromium rich $M_{23}C_6$, and V, Nb-carbonitides respectively, is very important for stabilizing the dislocation subgrain and network against long-term creep exposure and unavoidable high temperature exposures during welding. The coarsening of $M_{23}C_6$precipitates led to accelerating the recovery process of the steel, which led to a decrease in its strength drastically [25]. Finer $M_{23}C_6$ precipitates were observed in the ICHAZ of P91BN steels weld joints (Fig. 4.56), which has experienced significantly longer creep exposure as compared to the P91 steel weld joint.

Boron in the P91BN steels leads to finer $M_{23}C_6$ precipitates and more MX precipitates (due to higher dislocation density on martensite transformation). The decreased $M_{23}C_6$ precipitates coarsening, which stabilizes the martensitic lath structure, and relatively lesser extent of heterogeneity in mechanical properties across the weld joints of the P91BN steels led to higher creep rupture life as compared to that the steel having without boron (P91 steel).

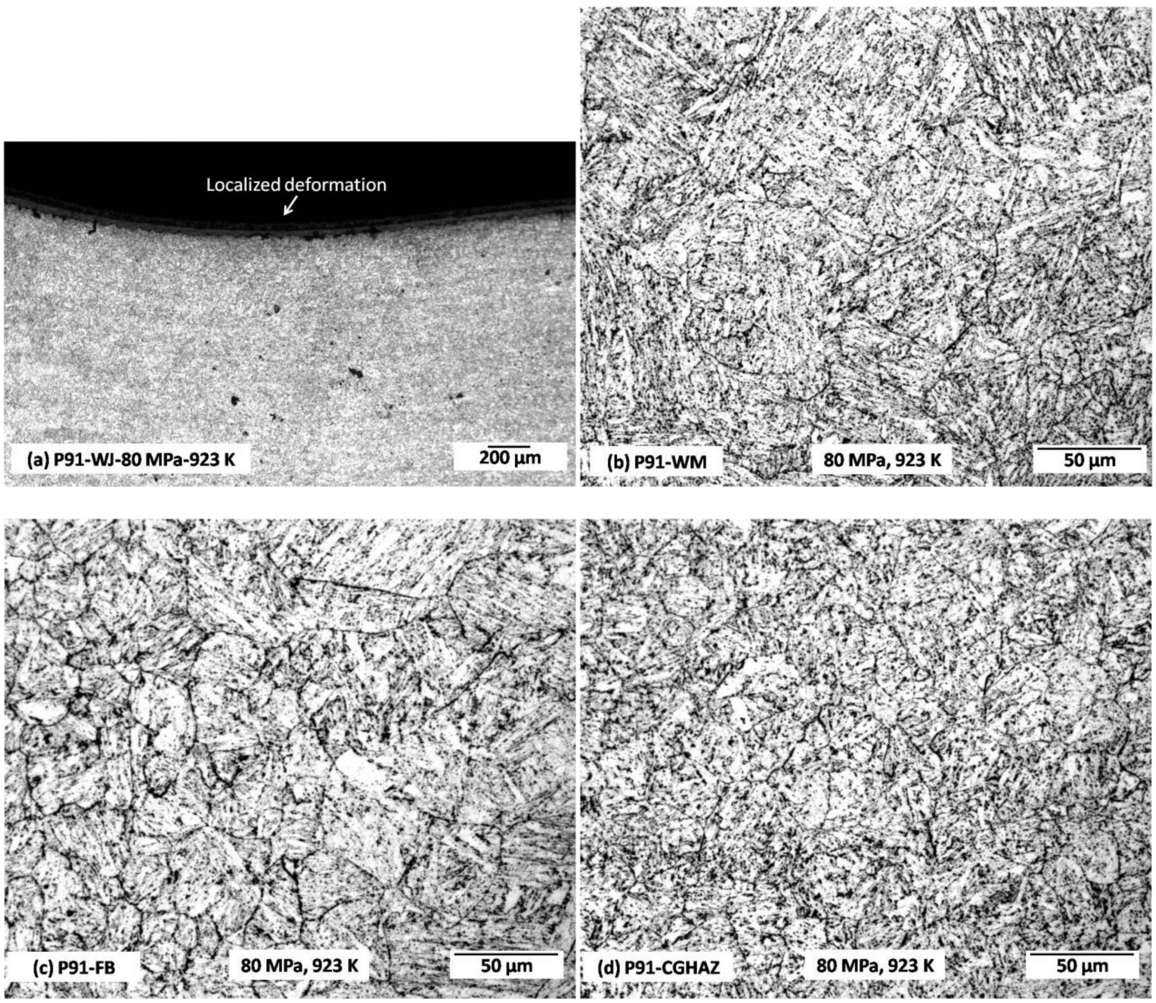

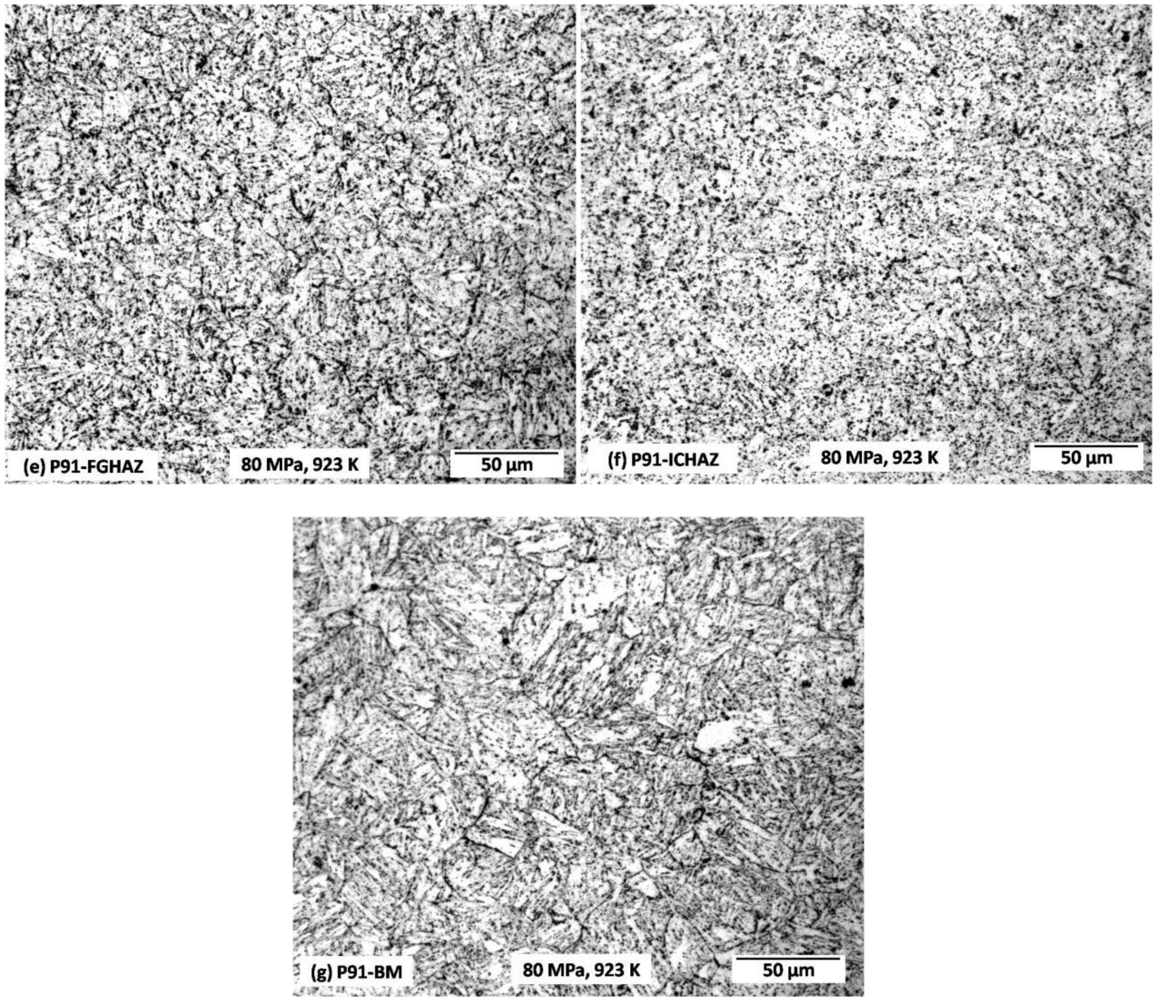

Fig. 4.54 Optical micrographs across the P91 steel weld joint at 923 K, 80 MPa stress, (a) localised deformation in the ICHAZ, (b) WM, (c) FB, (d) CGHAZ, (e) FGHAZ, (f) ICHAZ, and (g) BM.

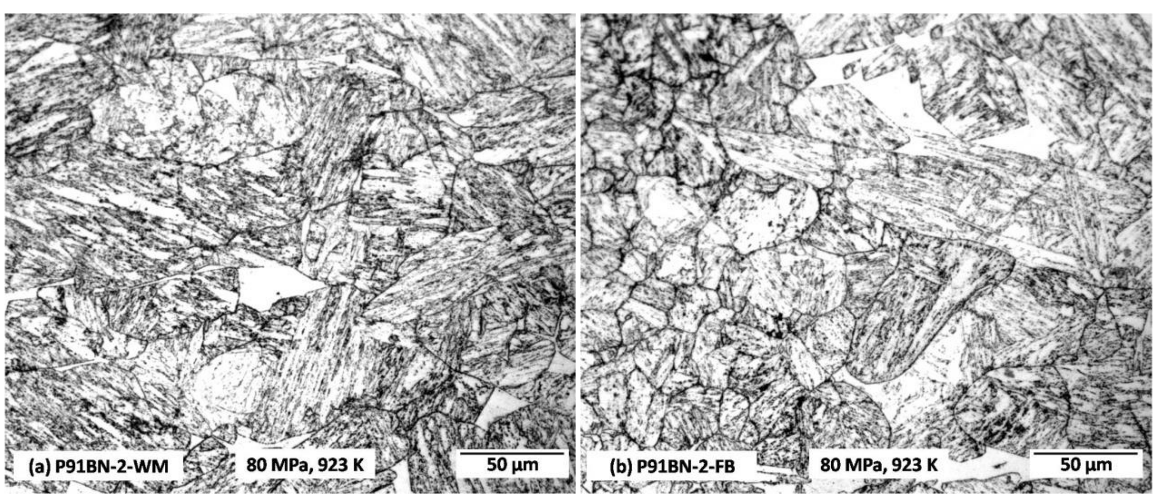

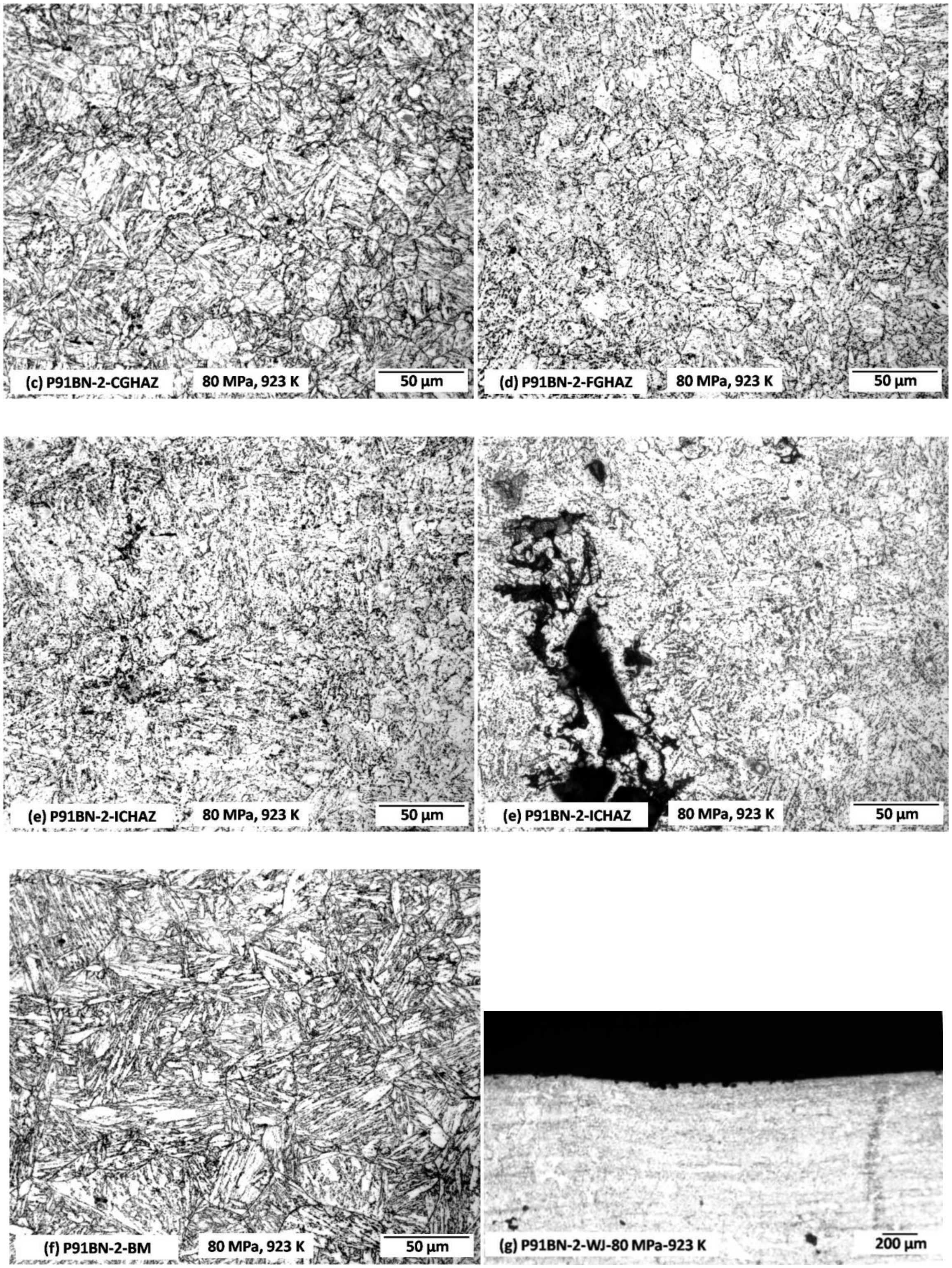

Fig. 4.55. Optical micrographs across the P91BN-2 steel weld joint at 923 K, 80 MPa stress, (a) WM, (b) FB, (c) CGHAZ, (d) FGHAZ, (e) ICHAZ, (f) BM, and (g) localised deformation in the ICHAZ (localised deformation is less as comapred to P91 steel).

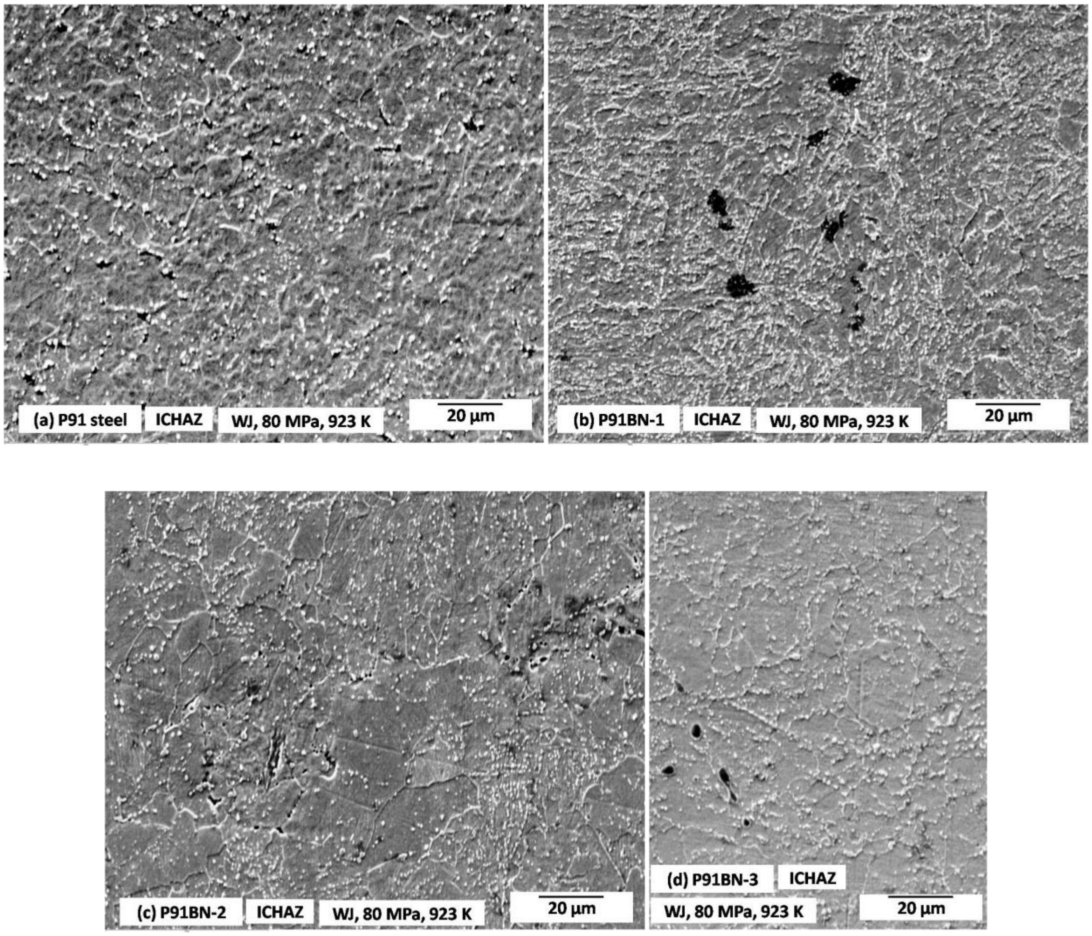

Fig. 4.56 SEM micrographs of ICHAZ in the weld joints of (a) P91, (b) P91BN-1, (c) P91BN-2 and (d) P91BN-3 steels at 923 K, 80 MPa stress.

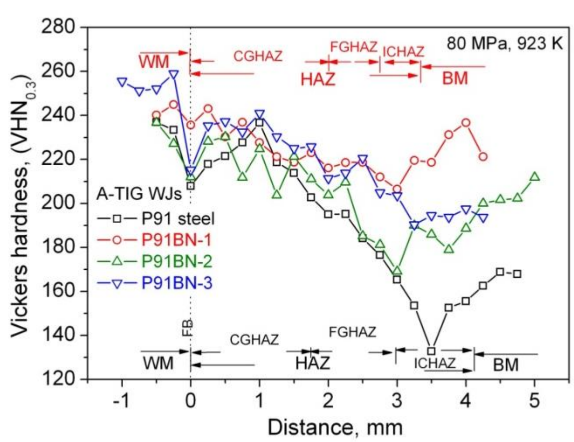

Fig. 4.57 Variations of hardness across the P91, P91BN-1, P91BN-2 and P91BN-3 steels weld joints in the creep exposed at 923 K, 80 MPa stress conditions.

4.4 Intercritical heat treated P91 and P91BN-4 Steels

In the present section, creep properties of the intercritically heat-treated (ICHT) boron free (P91) steel and boron containing P91 steel (P91BN-4) were investigated at 923 K. The normalized and tempered P91 and P91BN-4 steels (Table 4.5) were subjected to ICHT at 1148 K for 5 minutes followed by water quenching. Subsequently, these heat-treated steels were tempered at 1033 K for 1 hour in a similar line to that of PWHT commonly performed on P91 weld joints. This heat treatment has been carried out to reproduce the microstructure of the ICHAZ of the weld joint. The steels in this condition are referred to as P91-IC and P91BN-4-IC.

4.4.1 Microstructure and hardness of the steels

The optical and secondary electron (SEM-SE) micrographs of P91 and P91BN-4 steels base metal are shown in Fig. 4.58(a, c) and (b, d) respectively. The microstructure of both the steels consist of tempered lath martensite, and $M_{23}C_6$ precipitates decorating the prior-austenite grain boundaries and lath-boundaries. P91BN-4 steel has exhibited finer lath width and $M_{23}C_6$ precipitates than the P91 steel (Fig. 4.59). Energy dispersive spectroscopy (EDS) spectrum of $M_{23}C_6$ observed from TEM in P91BN-4 steel is shown in Fig. 4.59(c). For quantification, low atomic number elements are rejected to avoid error in the estimation. Quantified values are given in as an insert on the Fig. 5.59(c). Similar results are seen in the $M_{23}C_6$ precipitate present in P91 steel. SEM-SE micrograph of the P91-IC and P91BN-4-IC steels are shown in Fig. 4.60 (a, c) and (b, d) respectively. The prior austenite grain size of P91 and P91BN-4 base metals are comparable. After ICHT, substructure size about 5-7 μm in P91-IC steel and 10-15 μm in P91BN-4-IC steel were observed. However, it was predominantly observed in P91-IC steel as compared to P91BN-4-IC steel. The features of the two steels after ICHT are given in Table 4.5.

The hardness value (500 gf load and 15 seconds dwell time) of the intercritical heat-treated steels was comparable with the intercritical region (ICHAZ) of the actual weld joints fabricated from the P91 and P91BN-4 steels [54].

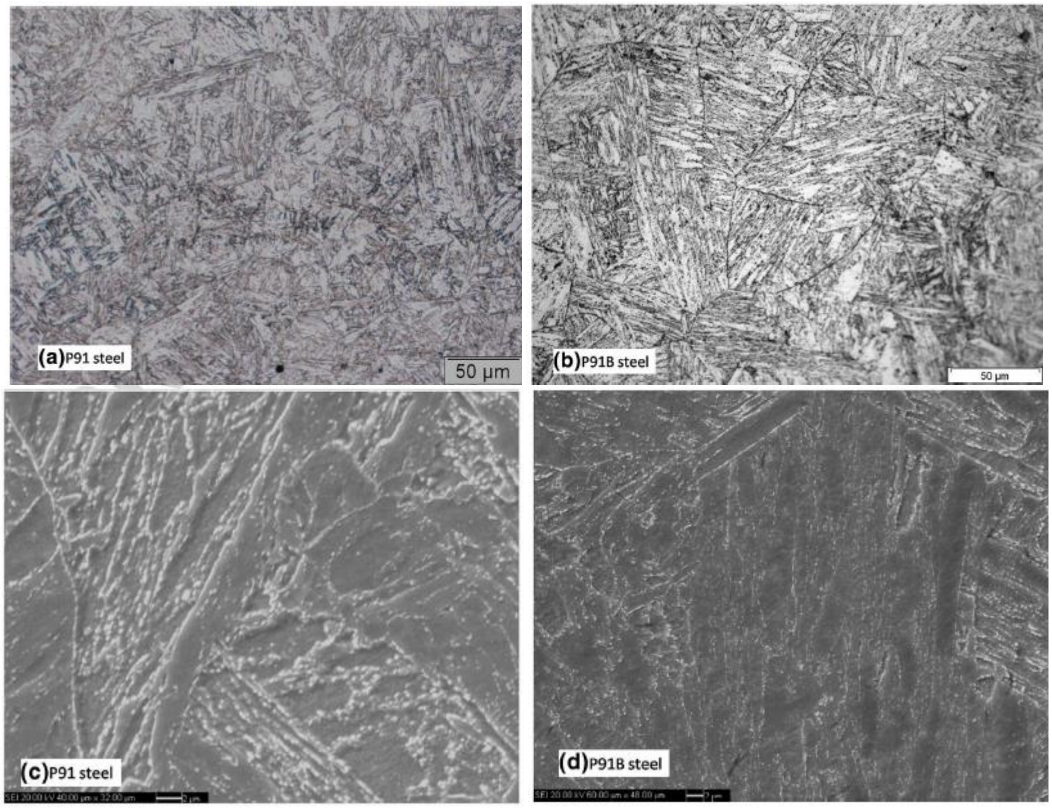

Fig. 4.58 SEM micrograph of (a) P91 and (b) P91BN-4 steels base metal in the normalized and tempered condition.

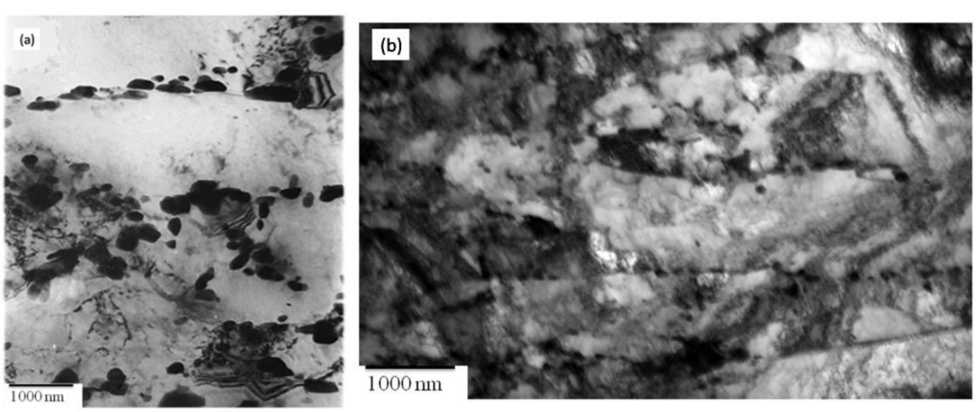

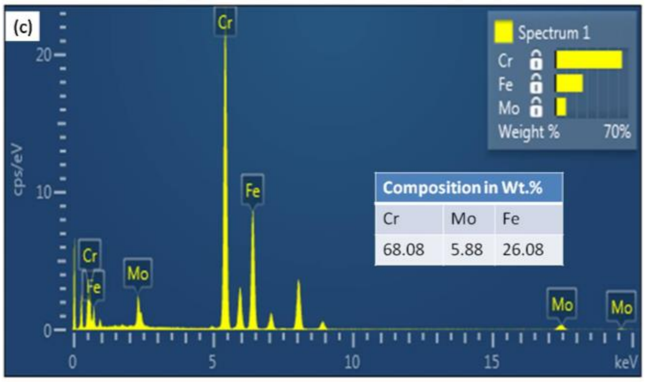

Fig. 4.59 TEM micrograph of (a) P91 and (b) P91BN-4 steels base metal in the normalized and tempered condition and (c) EDS spectrum of $M_{23}C_6$ precipitate.

Table 4.5 The features of the P91-IC and P91BN-4-IC steels after ICHT.

Steel	P91-IC	P91BN-4-IC
Substructure size (µm)	5-7	10-15
Size of $M_{23}C_6$ (µm)	0.090	0.090
Area fraction of precipitates (%)	14.1	8.9
Hardness, $HV_{0.5}$	180	207

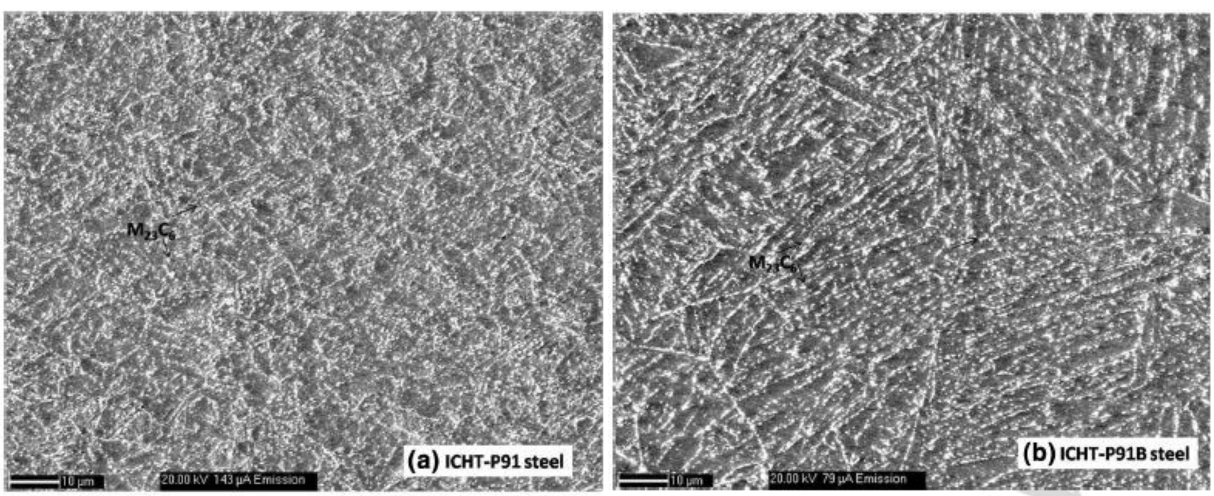

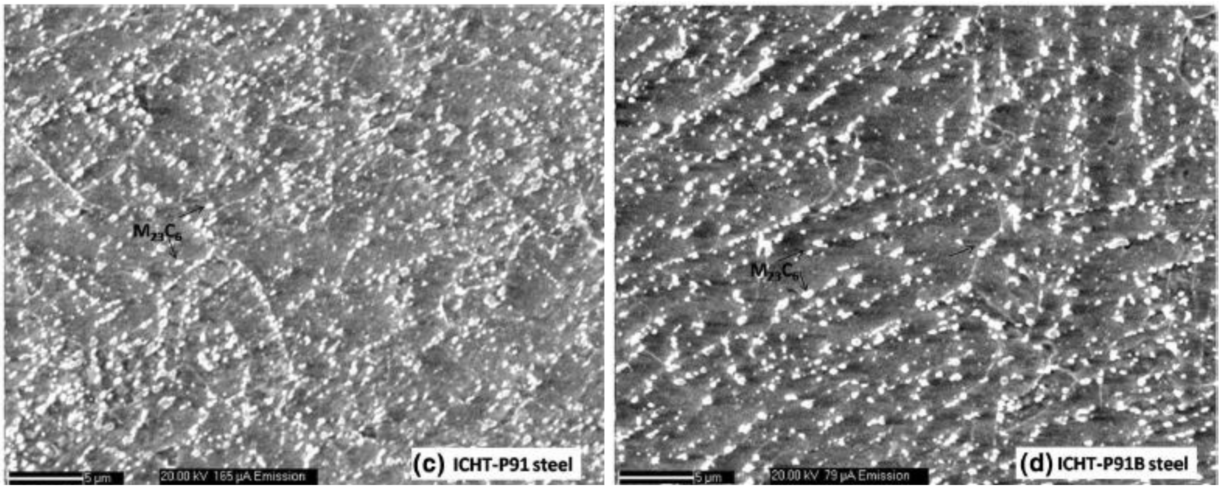

Fig. 4.60 SEM micrographs of ICHT (a, c) P91-IC and (b, d) P91BN-4-IC steels.

4.4.2 Creep deformation behaviour

The creep curves of P91-IC and P91BN-4-IC steels are shown in Fig. 4.61 (a) and (b). Creep strain accumulation in the P91-IC steel is higher than in P91BN-4-IC steel. The creep curves normalized by the respective rupture life at different stress levels are shown in Fig. 4.62. Figure indicates lower creep strain accumulation in P91BN-4-IC steel than P91-IC steel. The variations in creep rate with time at different stress levels are shown in Fig. 4.63. The decrease in creep rate with time has been observed in the primary creep regime followed by shorter steady state and longer accelerating creep rate regime. Longer tertiary creep regime has been generally observed in the 9% Cr ferritic steels [115]. The microstructure of NT P91 steel is ever evolving; dislocation density, size of precipitates and lath size changes continuously during creep [3,25]. Creep rate of both ICHT steels is higher as compared to their respective base metal. The variation in minimum creep rate ($\acute{\varepsilon}_s$) with applied stress (σ) for P91-IC and P91BN-4-IC steels are shown in Fig. 4.64. The variation in minimum/steady state creep rate with applied stress for both the steels obeyed Norton's power law relation as $\acute{\varepsilon}_s = A\ \sigma^n$. The stress exponent values of P91-IC and P91BN-4-IC steels are 6.5 and 8.7 respectively. The formation and growth of substructure and coarsening of $M_{23}C_6$ precipitates in the inter-critical region are known to enhance creep deformation rate in boron free P91 steel. Presence of boron in P91BN-4 steel increased the resistance against formation and coarsening of sub-structure, and coarsening of $M_{23}C_6$ precipitate resulting stabilization of lath martensite [25].

In order to understand the influence of precipitates in the P91-IC and P91BN-4-IC steels, the threshold stress (σ_{th}) has been evaluated, which arises due to the interaction of dislocations and precipitates. The effective stress (σ_a-σ_{th}) has been considered to be more appropriate than the applied stress in describing the stress dependence of creep deformation in precipitate strengthened 9-12 wt.% Cr steels [105,107]. The threshold stress (σ_{th}) can be calculated using the modified version of Mukherjee-Bird-Dorn creep equation [14,15],

$$\dot{\epsilon}_{min} = A\left(\frac{\sigma_a - \sigma_{th}}{\mu}\right)^n \exp(-\frac{Q_c}{kT})$$

Stress exponent value about 4, and similar activation energy for creep (Q_C) and lattice self diffusion (Q_D) have been observed in pure metals [14,15]. The threshold stress is evaluated from minimum creep rate ($\dot{\epsilon}_{\min}^{1/4}$) versus applied stress plot, where the value of stress exponent of the matrix was chosen as 4 (Fig. 4.65). The intercept of stress line values at zero strain rate provides threshold stress. Threshold stress values of 28 MPa and 38 MPa were obtained for P91-IC and P91BN-4-IC steels respectively. The higher threshold stress in the P91BN-4-IC steel than the P91-IC steel has been attributed to the relatively stable $M_{23}C_6$ precipitates and lath structure in P91BN-4-IC steel on high temperature exposure.

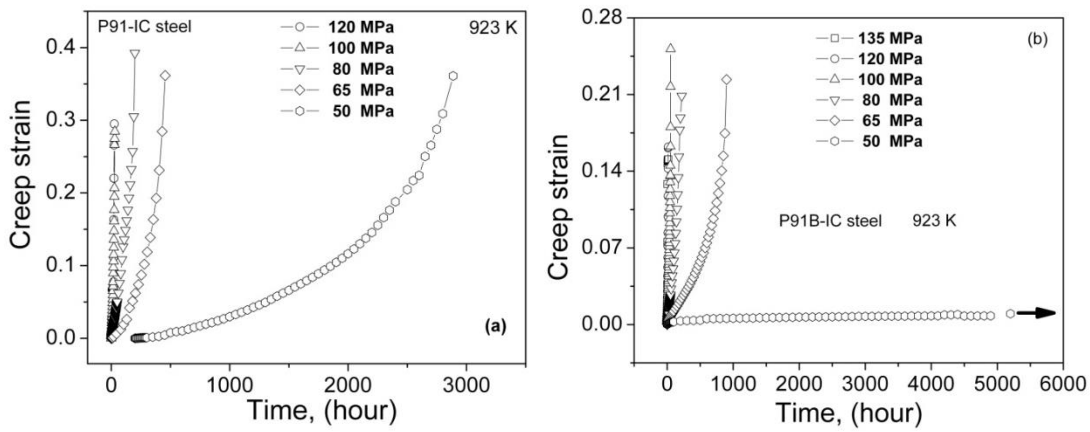

Fig. 4.61 Creep curves of (a) P91-IC and (b) P91BN-4-IC steels at 923 K.

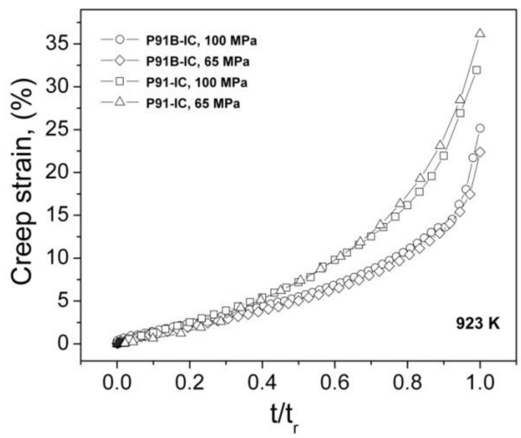

Fig. 4.62 Variation of creep strain (%) with normalized time to rupture (t/t_r) of P91-IC and P91BN-4-IC steels at 923 K.

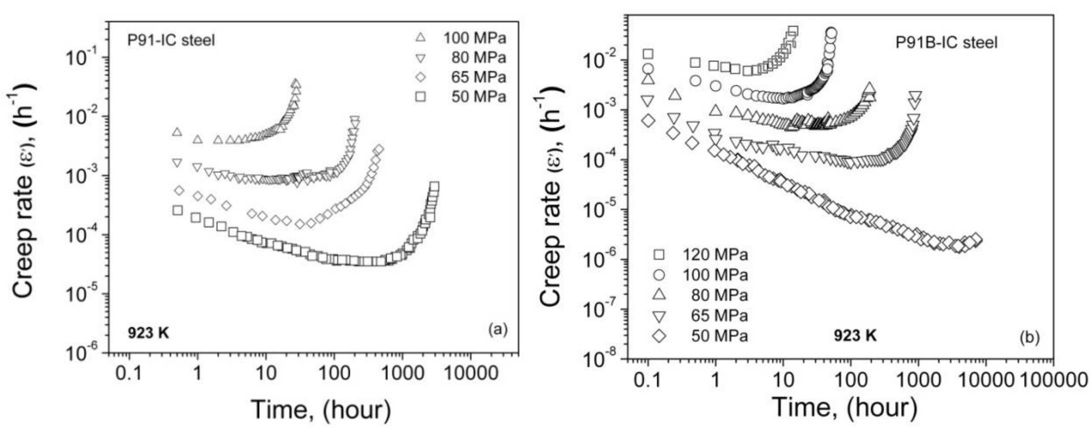

Fig. 4.63 Variation of creep rate with time for (a) P91-IC and (b) P91BN-4-IC steels at 923 K.

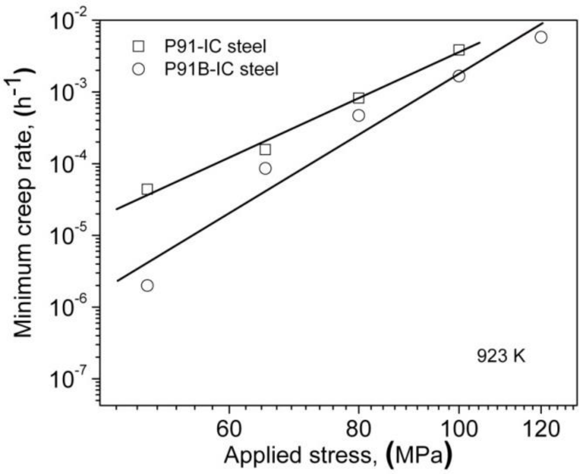

Fig. 4.64 Variation of minimum creep rate with applied stress of P91-IC and P91BN-4-IC steels at 923 K.

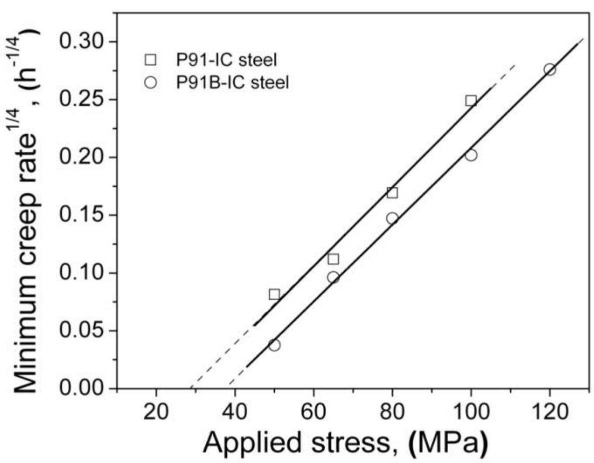

Fig. 4.65 Variation of minimum creep rate with applied stress of P91-IC and P91BN-4-IC steels at 923 K.

4.4.3 Creep rupture behaviour

The variations of creep rupture life with applied stress for intercritical heat treated steels are shown in Fig. 4.66. The creep rupture life with applied stress variation obeyed an inverse power law relation ($t_r=A'\sigma^{-n'}$) with n' value of P91-IC and P91BN-4-IC steels are 6.1 and 7.1 respectively as observed in the relation between minimum creep rate and applied stress (Fig. 4.64). The P91-IC steel possessed lower rupture life as compared to P91BN-4-IC steel. For stress levels above 65 MPa, the rupture life of P91BN-4-IC were higher by a factor of 2, whereas at 50 MPa this factor increased (>4). The higher stability of $M_{23}C_6$ precipitates in P91BN-4-IC steel arises due to the incorporation of boron in these precipitates. The boron effect would be pronounced at lower stress levels as seen in the large divergence in the rupture life between P91-IC and P91BN-4-IC steels.

Creep rupture life of P91-IC is 2800 h at 50 MPa. Under similar stress condition, the creep test of P91BN-4-IC steel progressed up to 11500 h (test interrupted) (Fig. 4.66). This shows a significant improvement in creep rupture life at a lower stress level. The variations in elongation (%) and reduction in area (%) with rupture life have been shown in Fig. 4.67(a) and (b). The elongation has been observed to be lower in the P91BN-4-IC steel as compared to P91-IC steel, indicating that the P91BN-4-IC steel is resistant against deformation at high temperature. Similar observation has been made in accumulation of creep strain in the steels (Fig. 4.62). The increased elongation in the P91 steel has been attributed to the coarsening of $M_{23}C_6$ precipitates and coarsening of sub-structure resulting in decrease in dislocation density. Interestingly reduction in area in both steels remains similar. The fractographs of crept specimens tested at different stress levels are shown in Figs. 4.68 and 4.69. From the fractographs, it is apparent that both the steels possessed ductile mode of failure in the investigated applied stress range.

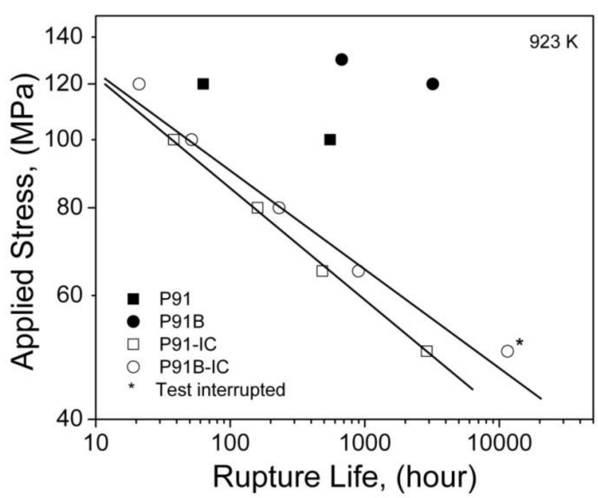

Fig. 4.66 Variation of rupture life with applied stress of P91-IC and P91BN-4-IC steels and its base metal at 923 K.

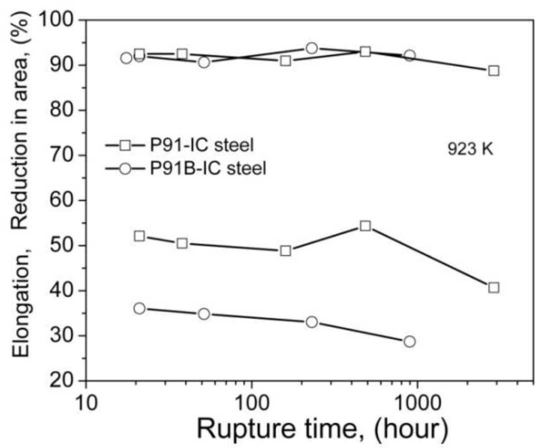

Fig. 4.67 Variation of % elongation and % reduction in area with rupture time of P91-IC and P91BN-4-IC steels at 923 K.

ICHT	P91-IC	P91BN-4-IC
100 MPa	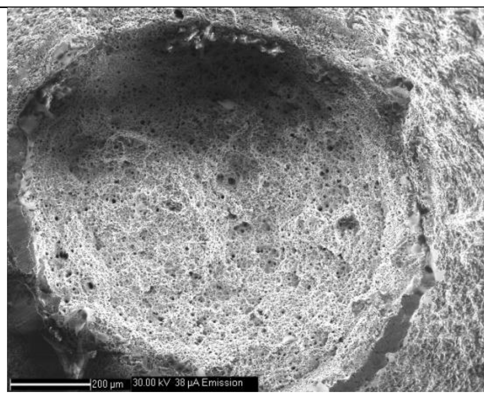	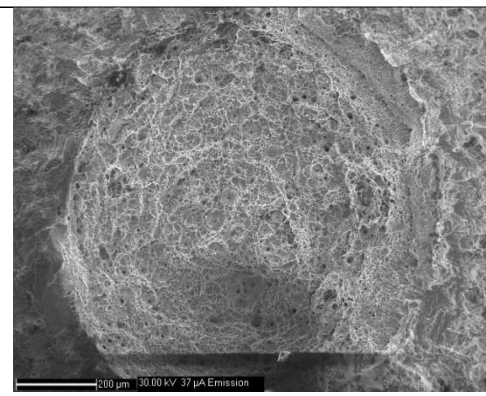
65 MPa	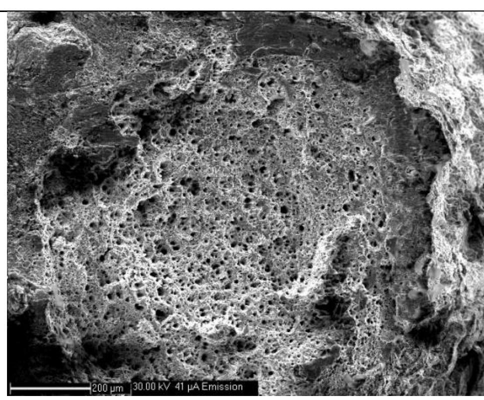	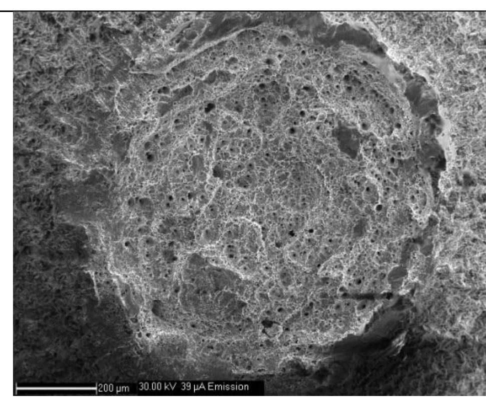

Fig. 4.68 Fractography of creep ruptured P91-IC and P91BN-4-IC steels in different applied stress conditions at 923 K.

ICHT	P91-IC	P91BN-4-IC
65 MPa	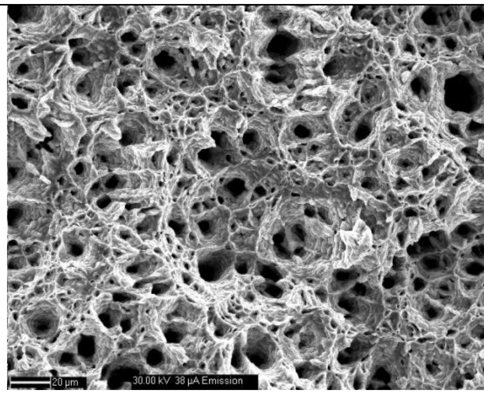	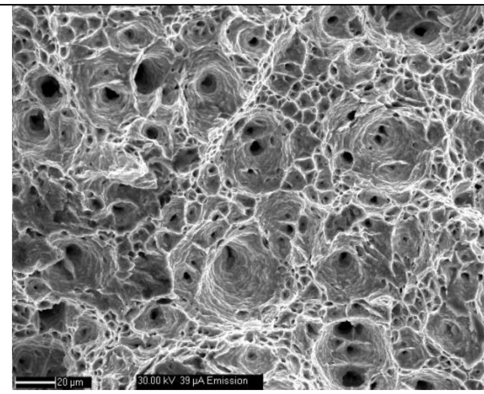

Fig. 4.69 Fracture surface appearance of P91-IC and P91BN-4-IC steels at 923 K and 65 MPa.

4.4.4 Precipitation strengthening

SE micrographs of crept specimens of P91-IC and P91BN-4-IC steels are shown in Fig. 4.70(a). It is evident that precipitate size increases with decrease in stress levels, and it is more pronounced in P91-IC steel. In addition to the size of precipitate, size of sub-structure is significantly bigger in P91-IC steel compared to P91BN-4-IC steel at 50 MPa (Fig. 4.70). Fig. 4.70(b) shows variation in precipitate size with creep rupture time. The size of the precipitates has been varied from 0.30 to 0.44 µm and 0.28 to 0.33 µm size in P91-IC and P91BN-4-IC steels respectively. It is evident that precipitate size increases monotonically in P91-IC steel whereas it has reached saturation in P91BN-4-IC steel at 200 h. No significant coarsening of precipitate has been observed for the 11500 h duration in P91BN-4-IC steel. These precipitates were of Cr rich $M_{23}C_6$ type. Arrows in the figure marks those precipitates. The presence of finer precipitates delays the onset of accelerating creep in P91BN-4-IC steel than P91-IC steel at a given stress level. It can be concluded that presence of fine and stable precipitates in the boundaries in P91BN-4-IC steel led to enhance the stability of martensite lath structure, which has been attributed to higher sub-boundaries hardening in P91BN-4-IC steel. Thus, the addition of boron in P91 steel enhances the creep rupture strength of the intercritical (ICHT) region of the weld joint in comparison with boron free P91 steel.

<table>
<tr><td>(a)</td><td>P91-IC</td><td>P91BN-4-IC</td></tr>
<tr><td rowspan="2">50 MPa</td><td>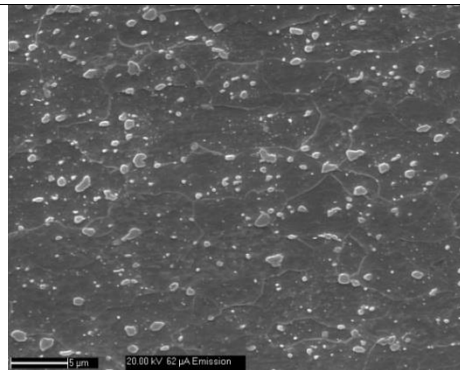
</td><td>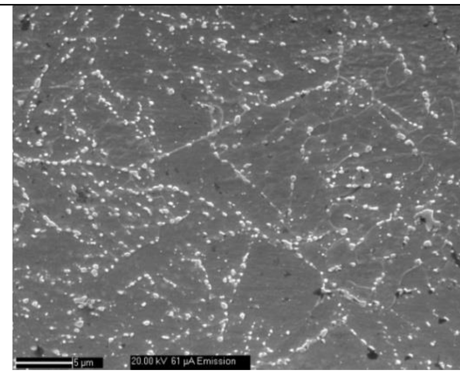
</td></tr>
<tr><td>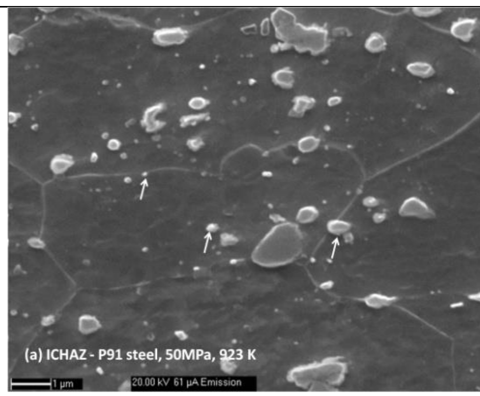
</td><td>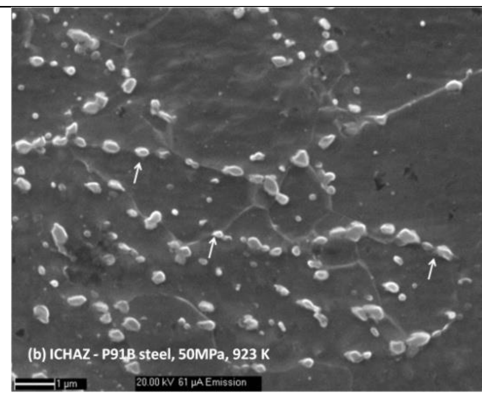
</td></tr>
</table>

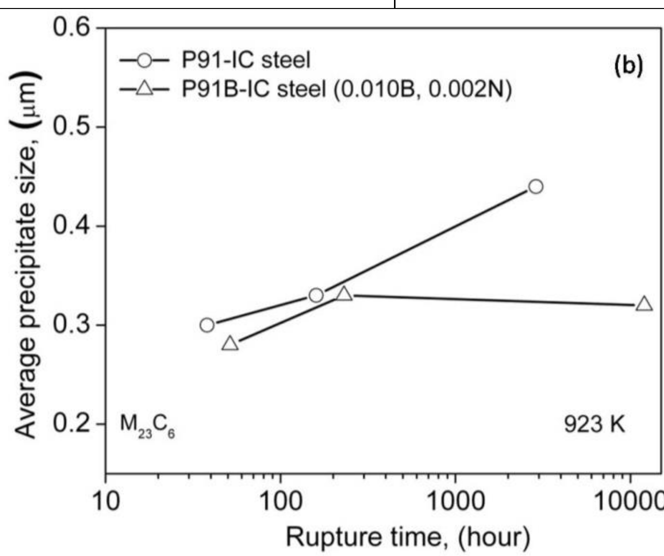

Fig. 4.70(a) SEM micrographs of crept P91-IC and P91BN-4-IC steels at 923 K and 50 MPa, and (b) precipitates size variation with rupture life of P91-IC and P91BN-4-IC steels at 923K.

4.5 Conclusions

Based on the studies on microstructure, tensile, creep deformation and rupture behaviour of base metal and weld joints of P91 steel and P91BN steels (boron along with controlled nitrogen content), following conclusions have been drawn.

a) P91BN steel containing boron (0.0060 wt.%) with controlled nitrogen content (0.0100 wt.%) resulted in finer martensite lath width, enhanced number density of finer $M_{23}C_6$ and MX precipitates, and higher dislocation density than in the P91 steel.

b) Tensile strength of the P91BN-1, P91BN-2 and P91BN-3 steels was higher than the P91 steel, which became more significant at higher temperature and was associated with higher ductility, fracture energy (area under stress-strain curve) and stress relaxation resistance.

c) The time spent in each creep regime was increased significantly in P91BN steels as compared to P91 steel.

d) The presence of boron in P91BN steels decreased the minimum creep rate predominantly with decrease in temperature and applied stress. P91BN steel exhibited higher threshold stress than the P91 steel.

e) P91BN-1, P91BN-2 and P91BN-3 steels possessed significantly enhanced creep rupture life at 823, 873 and 923 K as compared to P91 steel under similar test conditions associated with comparable ductility. Both P91 and P91BN-1 steels obeyed Monkman and modified Monkman-Grant relationships.

f) Sluggish coarsening of $M_{23}C_6$ and finer MX precipitates significantly delayed the recovery of dislocation structure and migration of boundaries in P91BN steels than in P91 steel. An improvement in the 10^5 h creep rupture strength about 16, 25, 33 and 37

(%) at 773, 823, 873 and 898 K respectively in P91BN-1 steel as compared to P91 steel were evaluated using Larson-Miller parametric method.

g) P91BN-1 steel base metal and weld joint has shown higher creep rupture life as compared other P91BN steels base and weld joints at 873 K.

h) P91BN-1, P91BN-2 and P91BN-3 steels weld joints has exhibited significantly higher creep rupture strength than the P91 steel weld joint. The loss of creep rupture strength of P91BN-1, P91BN-2 and P91BN-3 steels weld joint is relatively less as compared its base metals at 873 K.

i) The P91BN-2 steel weld joint having higher boron with controlled nitrogen possessed higher creep rupture life than the other P91BN steels weld joints at 923 K. The P91BN steels weld joints creep rupture life is comparable with the creep rupture strength of P91 steel base metal at 923 K. The reduction in heterogeneous mechanical properties across the weld joint enhances the type IV cracking resistance of P91BN steels as observed in the weld joint in the P91BN-1 steel.

j) Minimum creep rate in P91B-IC steel is lower as compared to P91-IC steel.

k) The size of $M_{23}C_6$ precipitate reached saturation value at 200 h in P91B-IC whereas it increased monotonically in P91-IC steel.

l) P91B-IC steel has exhibited higher creep rupture life. The differences in creep rupture life between P91-IC and P91B-IC steels increased with decrease in applied stress. Presence of boron in the P91B-IC steel led to stable precipitates and lath structure results in higher creep rupture strength than P91-IC steel.

CHAPTER 5

Thermomechanical Treatment of Modified 9Cr-1Mo Steel and its Influence on Type IV Cracking

5.1 Introduction

In this chapter, thermomechanical treatment (TMT) *viz.* deforming in the austenite phase field of modified 9Cr-1Mo steel is explored in order to enhance the long term creep resistance of base metal and weld joints. This refines the microstructure and increases MX precipitation. The extent of deformation in TMT is optimized based on the microstructure, hardness and creep resistance (at 923 K). Detailed studies have been carried out on TMT steel with 15, 25, 40 and 50% deformation. The influence of TMT processing on type IV cracking in the joint was evaluated by comparing the behaviours of joint prepared using 25% TMT steels with that of joint fabricated from conventionally heat treated normalized and tempered (NT) steel. Process diagrams for NT and TMT of modified 9Cr-1Mo steel details are given in chapter 3.3.

5.2 TMT processing of modified 9Cr-1Mo steel

5.2.1 Microstructure

Optical micrographs of the modified 9Cr-1Mo (P91) steel in the NT condition and after TMT processing with different degrees of deformation *viz.* 15, 25, 40 and 50% are shown in Fig. 5.1. The NT as well as 15 and 25% TMT steels show typical martensite microstructure, but in the 40 and 50% TMT steels martensite structure with some amount of ferrite was observed. Ferrite formation was extensive in 50% TMT steel. Prior-austenite grain (PAG) size of the NT steel was

18±3 μm (Fig. 5.1(a)). Coarser PAGs were observed in the TMT processed steel in comparison with the NT steel. PAG sizes of the 15, 25, 40 and 50 % TMT processed steel were about 61±5, 105±15, 59±10 and 43±10 μm, respectively (Fig. 5.1(b-e)). Increase in PAG size with normalization temperature and coarser PAG size in the TMT processed steel have been reported in 9Cr-steels [99,124]. PAG size increases up to 25% TMT and then decreases with further increase in TMT deformation. The equilibrium phases present in modified 9Cr-1Mo steel is predicted using Thermo-Calc program (Fig. 5.2). $M_{23}C_6$ precipitates are present up to 1173 K, whereas VNb(C,N) carbonitride precipitates are present up to 1373 K. Almost complete dissolution of primary niobium carbonitride (Nb(C,N)) precipitates during normalization at temperatures above 1423 K leads to enhanced grain growth. Lengthy blocks were predominantly observed in the TMT steel as compared to NT steel, it was higher in the 25% TMT steel. Fine lath structure in the 50% TMT steel as well was observed, in those regions in the steel that has not transformed to ferrite (Fig. 5.3(e)). Normalization at 1423 K in TMT processing (Fig. 2.1) was chosen with an intension of dissolving all the prior existing (V,Nb)(C,N) particles so as to precipitate them during ageing after deformation in TMT process as secondary particles to offer resistance to subsequent martensite transformation. Formation of ferrite along the prior austenite grain boundary is evident from Fig. 5.1(e). Formation of δ-ferrite on normalization at high temperature in modified 9Cr-1Mo steel has been reported by Chandravathi et al. [99], leading to grain refinement. In 40%TMT and 50%TMT steels, the grain refinement is due to the formation of ferrite. The absence of such ferrite in the 15%TMT and 25%TMT steels indicates that it is not δ-ferrite and forms during the deformation/ageing parts of 40 and 50%TMT processing as α-ferrite. The CCT diagram of modified 9Cr-1Mso steel (Fig.2.1(b)) [72] indicates that hold time of 40 minutes (10 minutes deformation + 30 minutes ageing) should not lead to the formation of pro-eutectoid ferrite provided the induced deformation has little effect. Evidence of no ferrite formation up to 25% TMT steel supports the view expressed in the CCT diagram of modified 9Cr-1Mo steel. The extensive formation of ferrite in the 50%TMT steel is due to the effect of deformation in enhancing ferrite formation on holding in the austenite phase.

SEM microstructures of the NT and TMT steels are shown in Fig. 5.4. The TMT processed steel exhibited enhanced precipitation, which is homogeneously distributed. The ferrite phase in the 40 and 50%TMT processed steel is found almost free of $M_{23}C_6$ precipitates due to lack of interfaces (Fig. 5.3(c)). High resolution FEG-SEM micrographs reveal more detailed precipitation of the NT and 25% TMT steels (Fig. 5.4). Energy dispersive spectroscopy (EDS) spectrum reveals that the precipitates are chromium rich $M_{23}C_6$ on interfaces, and V and Nb-rich MX precipitates (Fig. 5.5) in the intragranular regions, as reported in these steels earlier by many investigators [3,4,58-64]. More importantly, the SEM micrographs reveal that the $M_{23}C_6$ particles on the grain boundaries and martensite interfaces are much less in area fraction as well as in size in the 25% TMT steel. The sizes of the $M_{23}C_6$ precipitates in the 25%TMT and NT steels were 80±10 nm and 93±10 nm, respectively. The area fraction of $M_{23}C_6$ precipitates about 7.4% and 8.6% are observed in the 25%TMT and NT steel, respectively. This clearly indicates that the TMT processing of the steel reduces the precipitation of $M_{23}C_6$ since these require interfaces for nucleation. In TMT processing, the austenite offers lesser interfaces, namely only the PAG boundaries as opposed to numerous martensite transformation induced interfaces in normalized steel, which enhances precipitation of MX and therefore, the strength of the steel. MX precipitates observed in the TMT steels were finer than NT steel. The stored dislocation energy in the austenite matrix due to deformation prior to ageing plays a major role on strain enhanced precipitation of MX [68]. The dislocations generated during hot deformation in the austenitic regime provides nucleation sites for precipitates and channels for the diffusion of carbon and nitrogen atoms assisting in predominant nucleation of MX precipitates in the steel. In the present study, the MX precipitates are significantly finer in the TMT processed steel (20 ± 5 nm) than those in NT (30±5 nm) steel (Fig. 5.5). Also, the number of MX precipitates per unit area is relatively higher in the TMT processed steel (13/μm^2) than in the NT (9/μm^2) steel. MX particles were observed also on the interfaces in the TMT processed steel (Fig. 5.5). Further, a detailed examination of the grain structure in the steels was carried out by EBSD.

The inverse pole figure (IPF) Z-map superimposed with grain boundary map revealed the presence of significantly coarser prior austenite grain structure composed of finer substructure (elongated lath structure) in the TMT steels than in the NT steel (Fig. 5.6). Lath width in the TMT steels decreased with increase in degree of deformation in the austenite phase field, although ferrite phase was extensively present in the 50%TMT steel (Fig. 5.6(e)). IPF color legend is shown in Fig. 5.6(f). Uniformity of IPF color shade within the packet boundary (packet consists of sub-blocks and lath) depicts the nearly single grain orientation within packets. Distribution of grain boundary angles in the NT and 15%, 25%, 40% and 50%TMT steels are shown in Fig. 5.7(a-e). Grain boundary angles ranging from 1 to 5° shown in green mainly consist of lath boundaries, 5 to 10° shown in red mainly consist of packet and block boundaries, and high angle grain boundaries (HAGB) (θ >10°; black). The HAGBs were higher in the 50%TMT steel than in other conditions. The ratios of HAGB to LAGBs in different regions across the joint are summarized in Fig. 5.7(f). The ratio was lower in the 15-25% TMT steel than in the 50%TMT, indicating the significant existence of block/lath structure in the steel up to 25%TMT steel. The variation of misorientation angle (MOA) in different conditions of the steel are shown in Fig. 5.8(a-e). Fraction of low MOA boundaries (at 1-2°) was higher in the 15%, 25% and 40%TMT steels than in the NT and 50%TMT steels which were comparable.

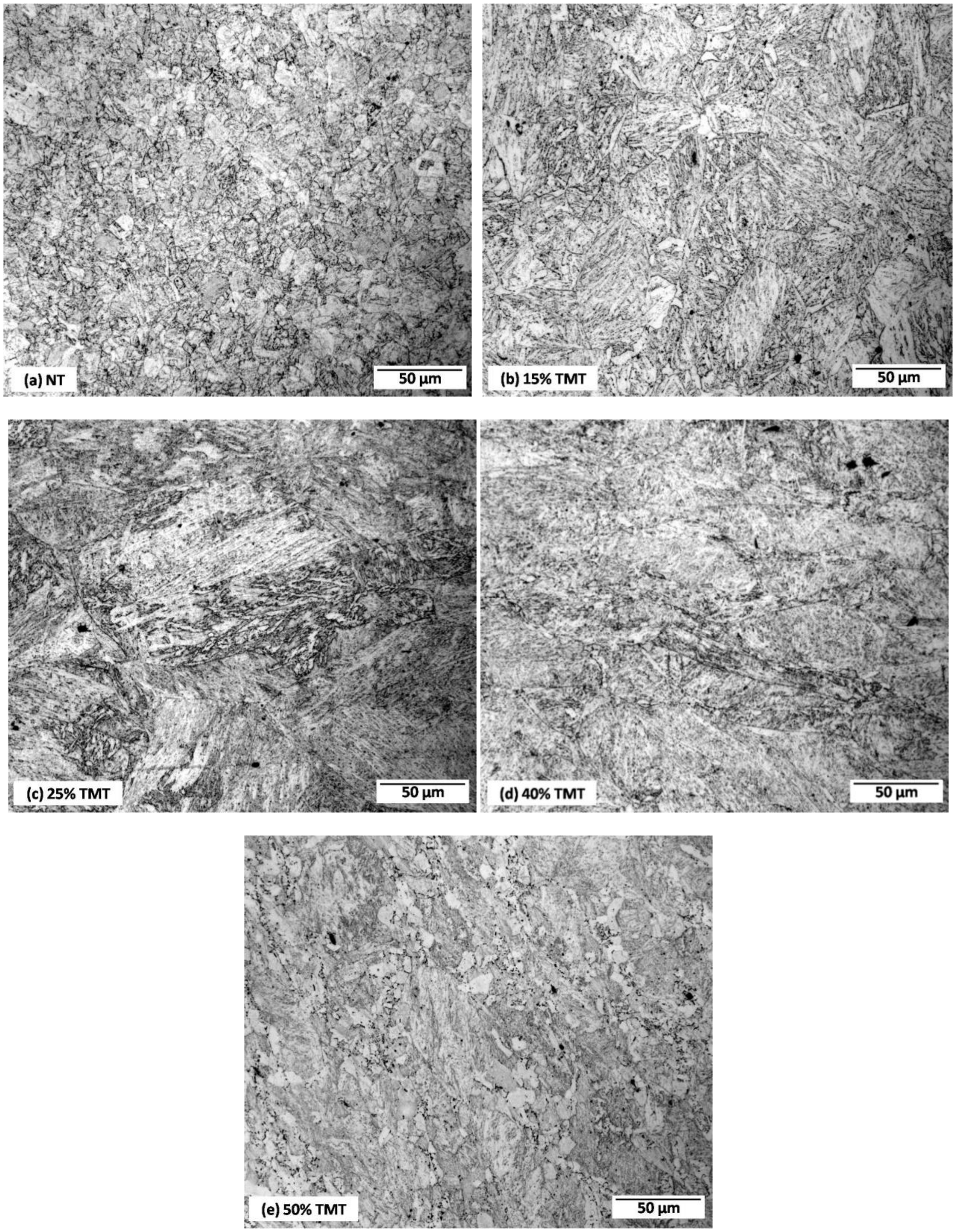

Fig. 5.1 Optical micrographs of the modified 9Cr-1Mo steel in the (a) NT, (b) 15%, (c) 25%, (d) 40% and (e) 50%TMT processed conditions.

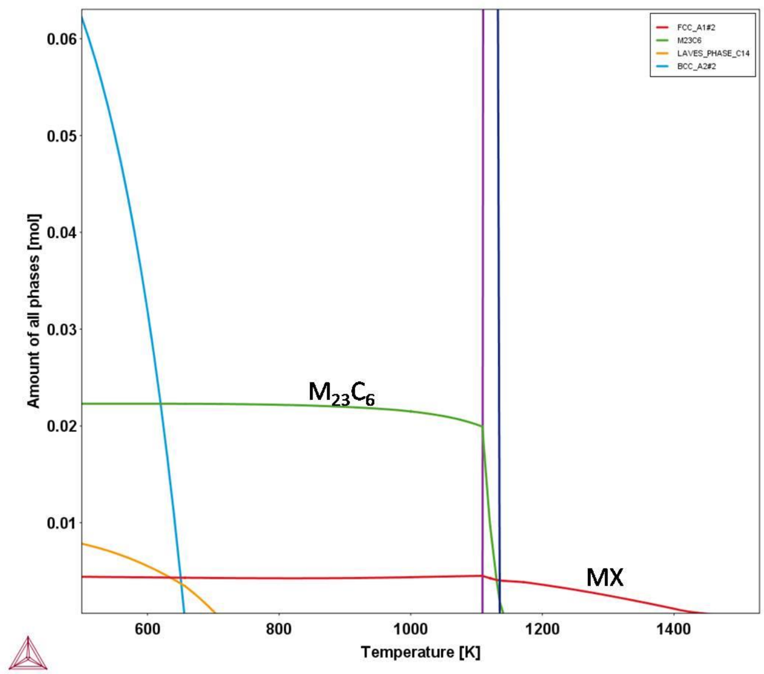

Fig. 5.2 Predicted equilibrium phases in modified 9Cr-1Mo steel with the temperature using Thermo-Calc program.

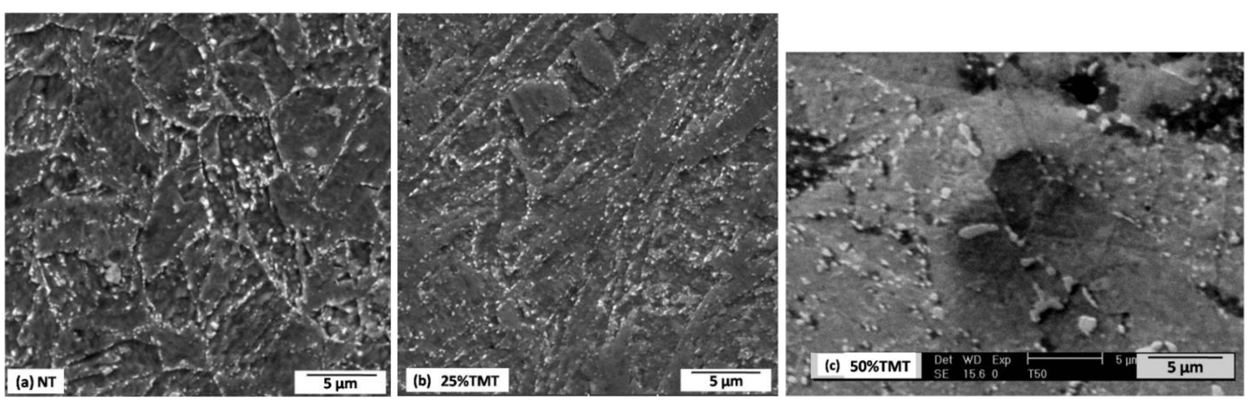

Fig. 5.3 SEM-SE micrographs of the modified 9Cr-1Mo steel in the (a) NT, (b) 25% and (c) 50%TMT processed conditions.

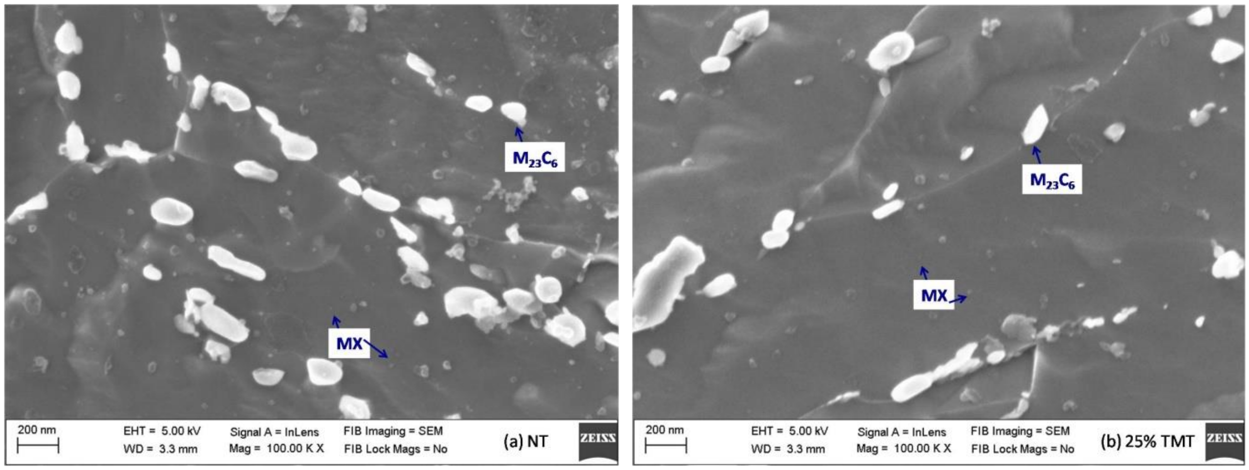

Fig. 5.4 FEG-SEM micrographs of the modified 9Cr-1Mo steel in the (a) NT and (b) 25%TMT conditions.

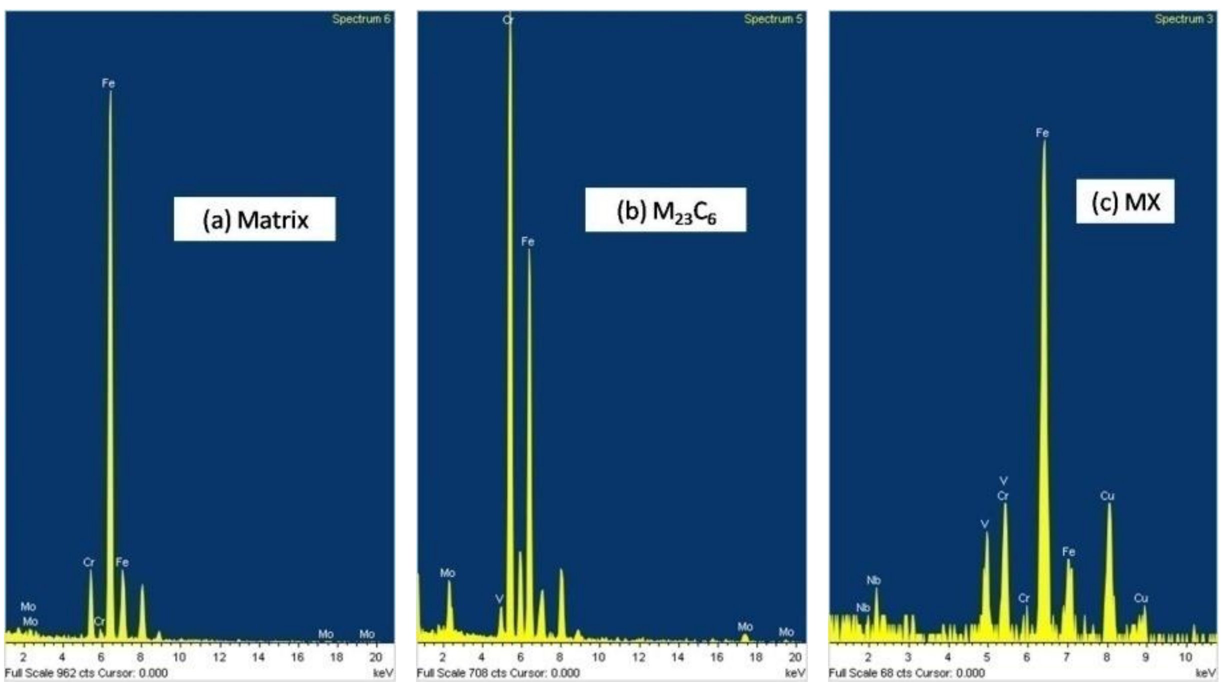

Fig. 5.5 Energy dispersive spectroscopy (EDS) spectrum of (a) matrix, (b) $M_{23}C_6$ and (c) MX (VC) precipitates.

The CSL boundary map (colour lines) and distribution in frequencies (%) in NT and TMT steels are shown in Fig. 5.9(a-e). CSL map overlapped with boundary map depicting the existence of CSL character predominantly in the block and lath boundaries. The fractions of CSL boundaries

(Σ3, Σ11 and Σ25b) were noticed to be lower in the NT and 50%TMT (boundary length is relatively low in the steel) steels (Fig. 5.9(a and e)) than in other TMT steels. Higher fractions of CSL boundaries in the 15%, 25% and 40%TMT steels are expected to increase the creep strength as compared to NT and 50%TMT steels. It has been reported in P91 steel that CSL boundaries improve the creep strength by minimizing the boundary sliding [62,125].

Microstructure of this steel can be considered to consist of the following types; (i) recovered (recovery of dislocation structure), (ii) substructure (lath and block) and (iii) deformed structure (consisting of more dislocations at intra-lath region and at interfaces). Relative amounts of these structures vary in the steel in different conditions (Fig. 5.10). Substructure and deformed structure frequency (%) in the TMT steels are relatively higher than NT steel except for 50%TMT steel due to formation of ferrite in the 50%TMT condition, whereas recovered structure was found to be lesser in the 15%, 25% and 40%TMT steels. (Fig. 5.10(b,c,d)). Higher substructure content was observed in the 25%TMT steel than in other conditions. More deformed structure in the 40%TMT steel results from more precipitates and less lath width in the steel (though the steel suffers from ferrite phase formation). In the case of NT and 40%TMT steels, recovered and substructure frequencies were comparable; but the deformed structure in the 40%TMT steel was relatively higher than in the NT (Fig. 5.10(a,d)). It may be noted that the presence of softer (recovered) structure in the 50%TMT steel leads to significant loss of creep strength as compared to other TMT conditions and NT steel in short term creep. Presence of MX precipitates, however, may contribute to higher strength in the long term creep exposure than the NT steel. On the other hand, presence of extensive ferrite in the 50%TMT steel excludes the advantage of TMT process in the steel. Kernel average misorientation (KAM) maps in the NT and TMT steels are shown in Fig. 5.11(a-e). The color legend for KAM distribution is given in

Fig. 5.11(f). The nonuniform color distribution depicts the variations in strain distribution within the blocks and packets. Formation of equiaxed ferrite structure during TMT processing is predominantly existent in the 50%TMT steel (Fig. 5.11(e)). The 25% and 40%TMT steels exhibited higher strain than the NT and other TMT conditions. The strain in the NT and 15%TMT steels were comparable with that in the untransformed martensite region in the 50%TMT steels (Fig. 5.11(a, b, e)).

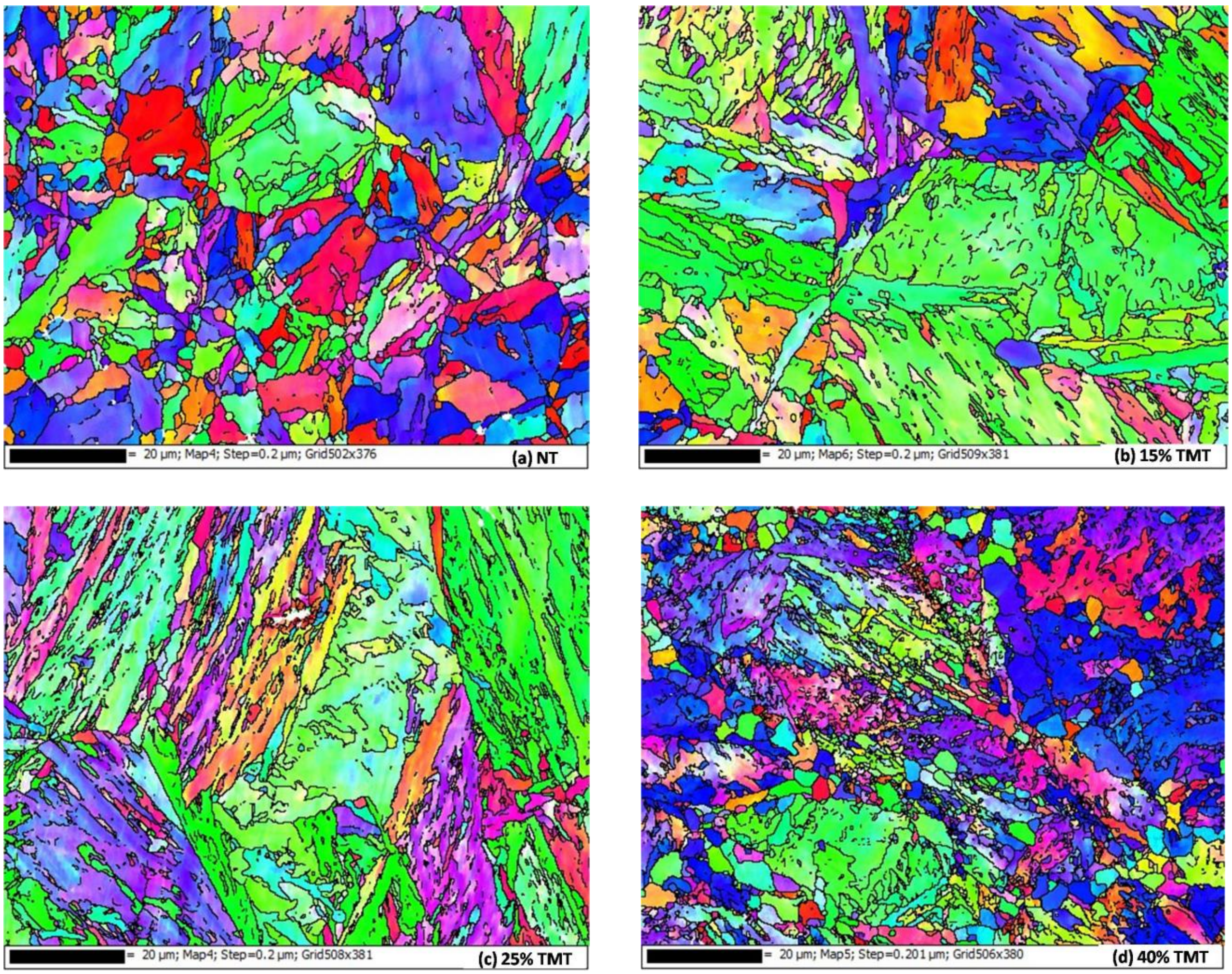

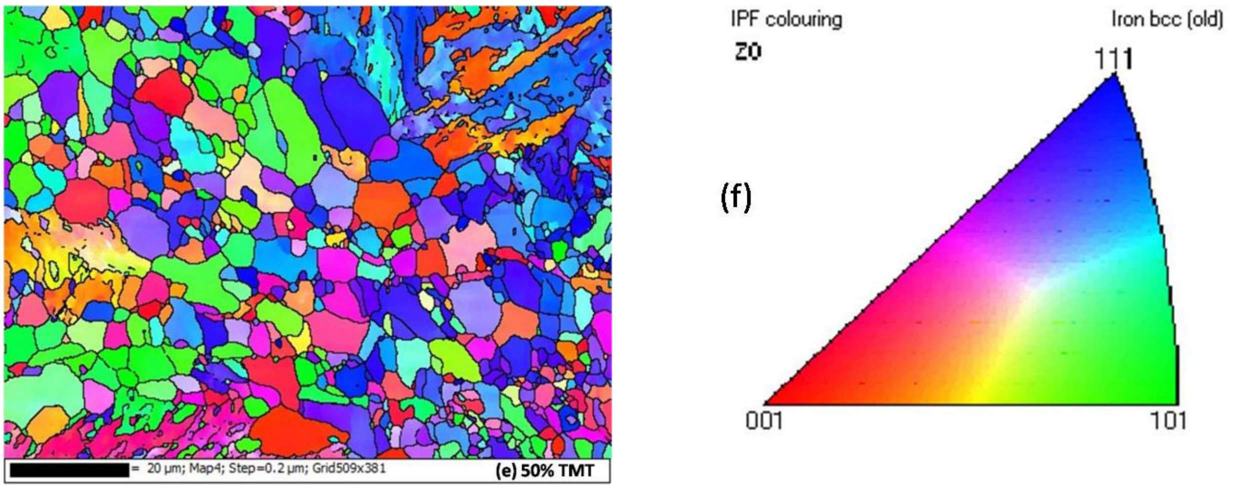

Fig. 5.6 EBSD-IPF map of modified 9Cr-1Mo steel in the (a) NT, (b) 15%, (c) 25%, (d) 40% and (e) 50% TMT conditions. (f) IPF colour legend.

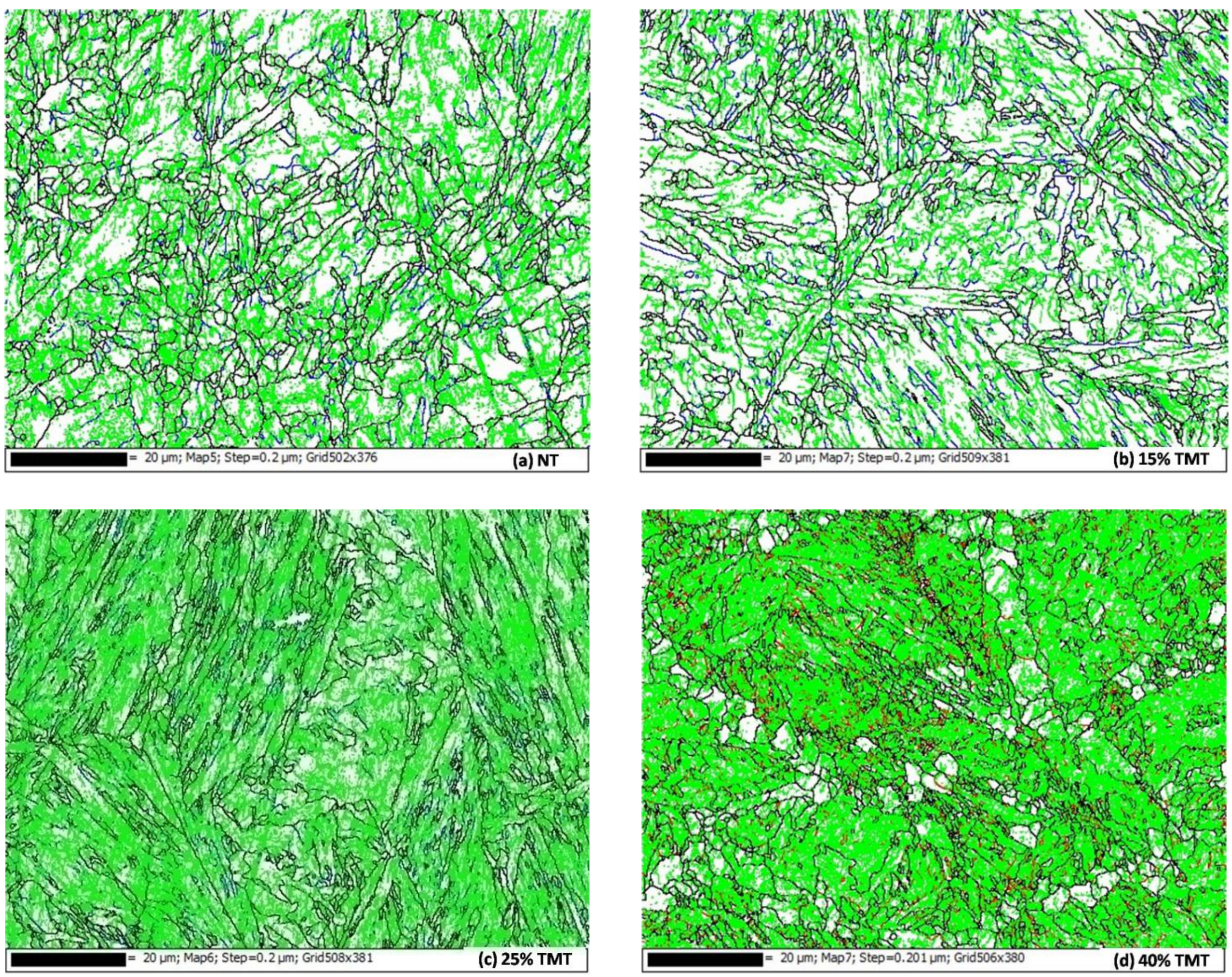

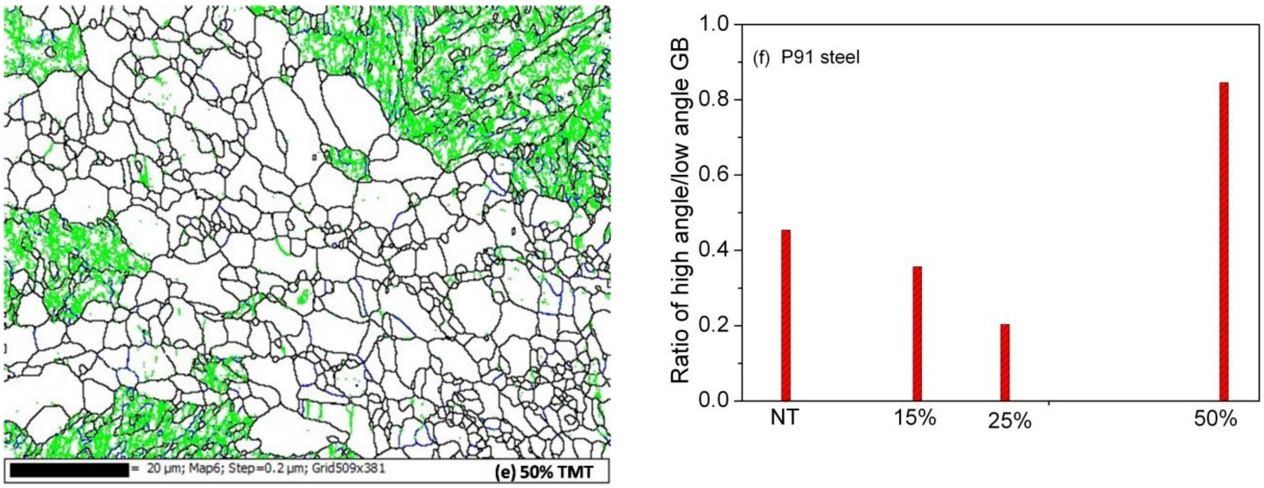

Fig. 5.7 Boundary map of P91 steel (**1 < θ > 5 Green; 5 < θ > 10 Blue; 10 < θ Black)** in the (a) NT, (b) 15%, (c) 25%, (d) 40% and (e) 50% TMT conditions, and (f) ratio of HAGB/LAGB in the P91 steel in NT and TMTs conditions.

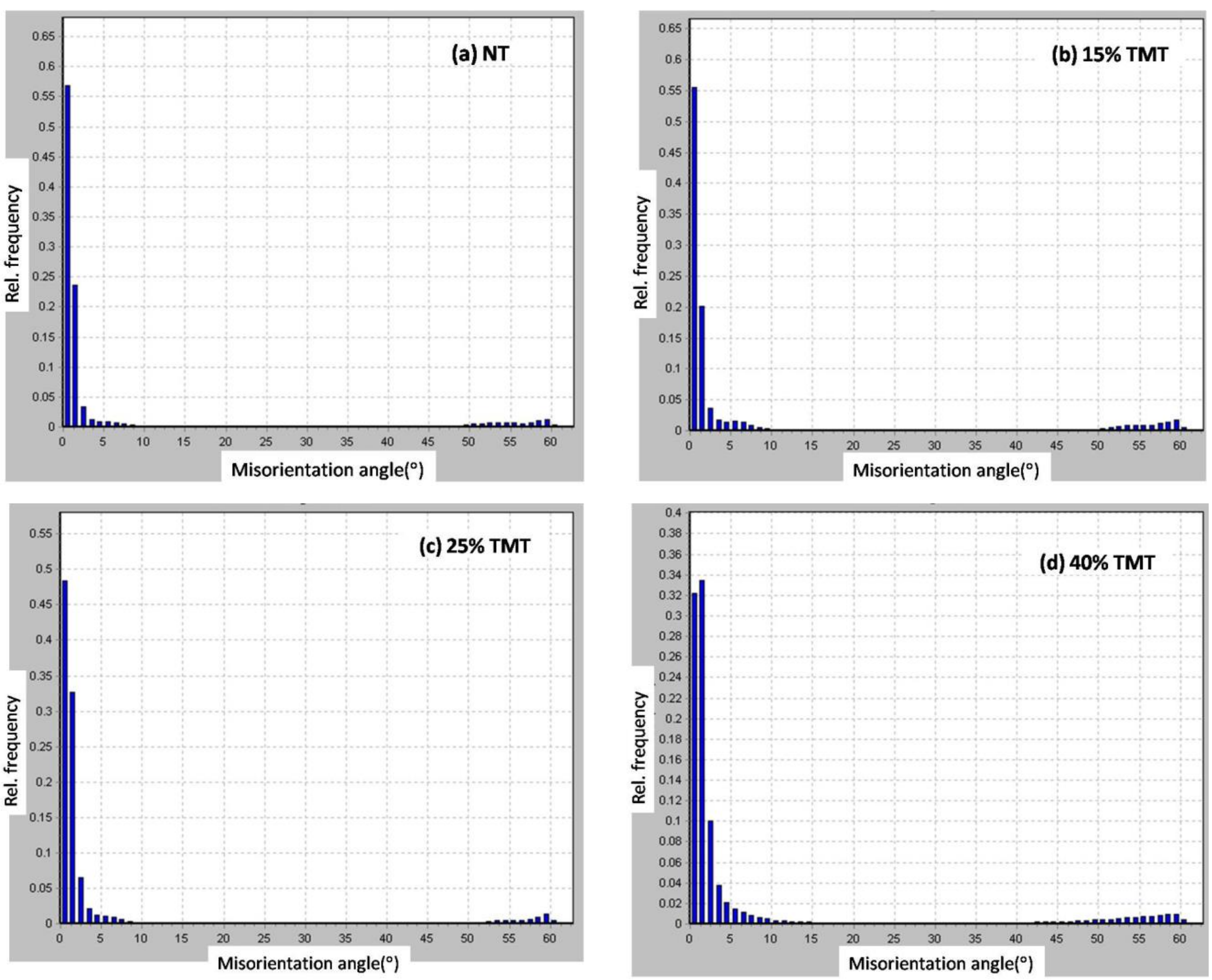

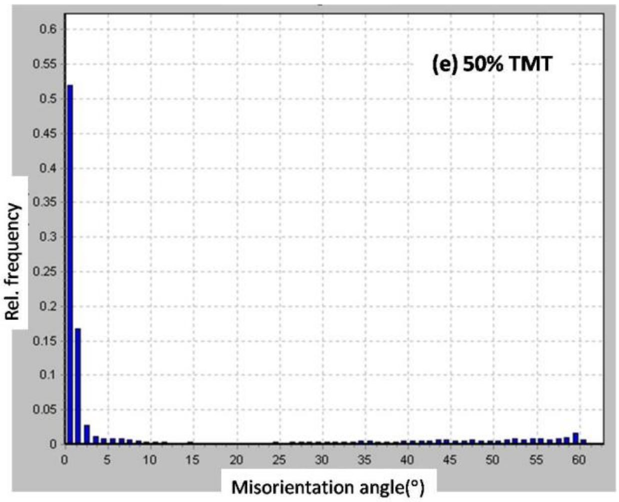

Fig. 5.8 Misorientations angle distribution of modified 9Cr-1Mo steel in the (a) NT, (b) 15%, (c) 25%, (d) 40% and (e) 50% TMT conditions.

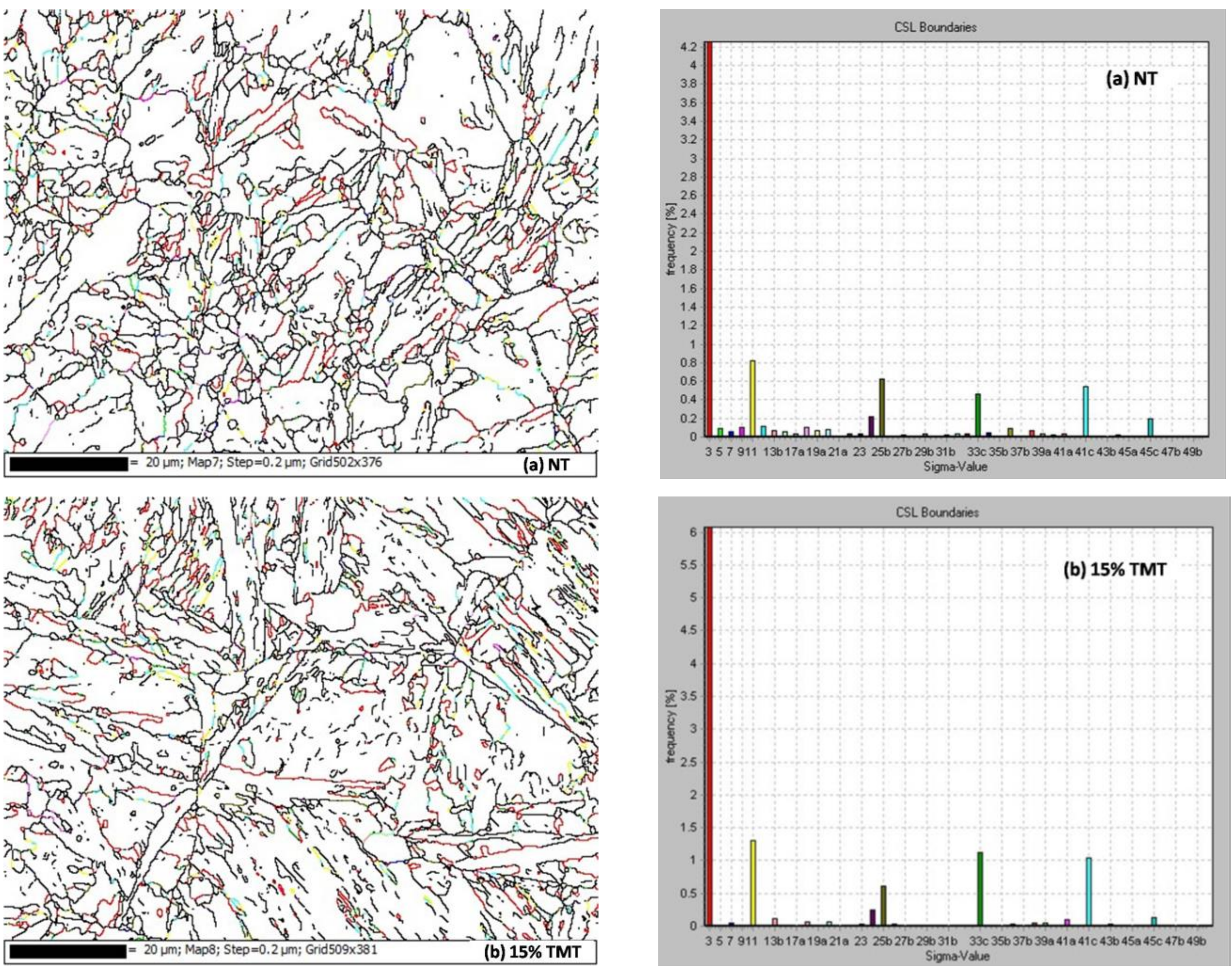

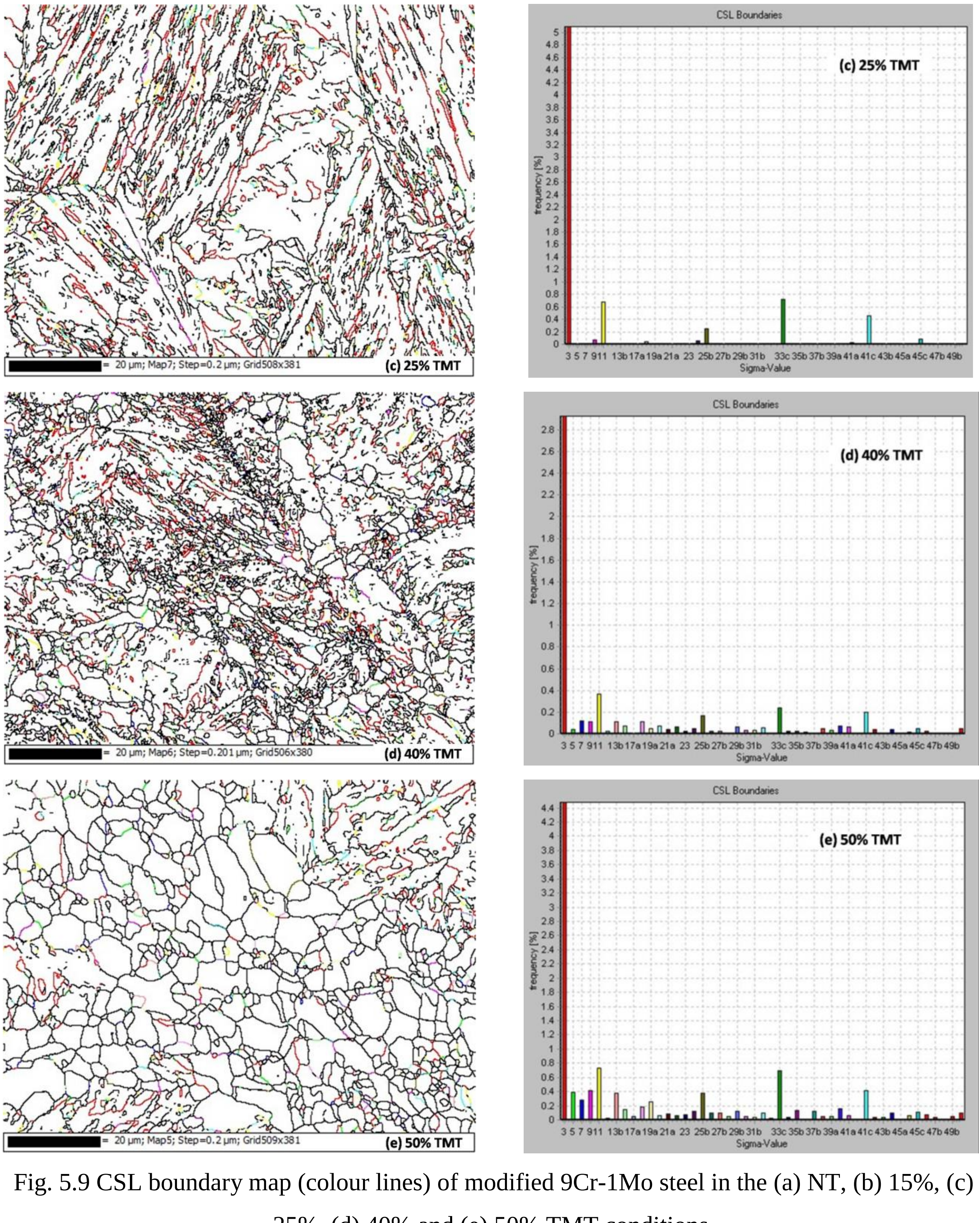

Fig. 5.9 CSL boundary map (colour lines) of modified 9Cr-1Mo steel in the (a) NT, (b) 15%, (c) 25%, (d) 40% and (e) 50% TMT conditions.

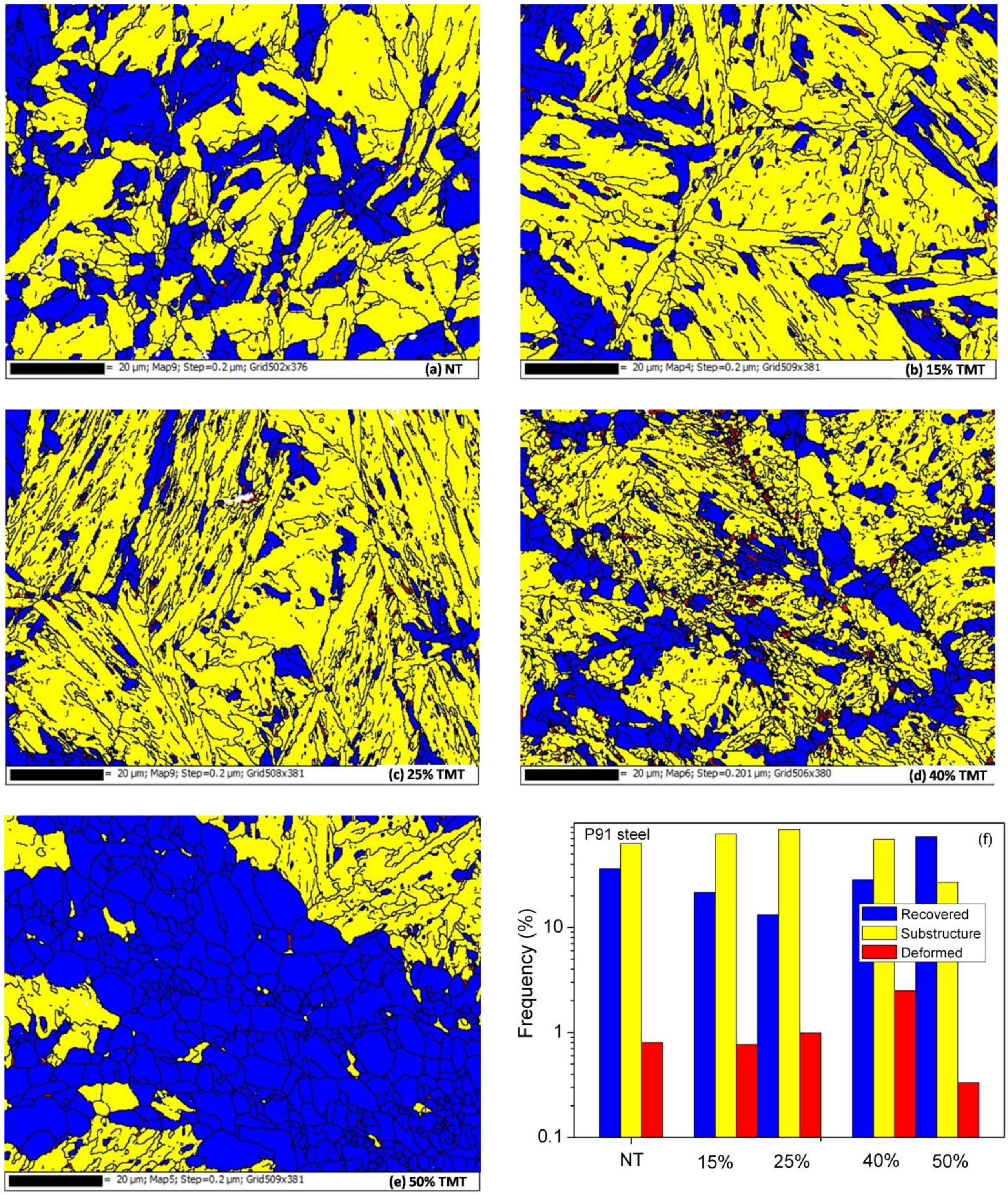

Fig. 5.10 Recovery of substructure (blue), substructure (yellow) and deformed (red) regions of modified 9Cr-1Mo steel in the (a) NT, (b) 15%, (c) 25%, (d) 40%, and (e) 50% TMT conditions. (f) frequency (%) of microstructural conditions in NT and TMT steels.

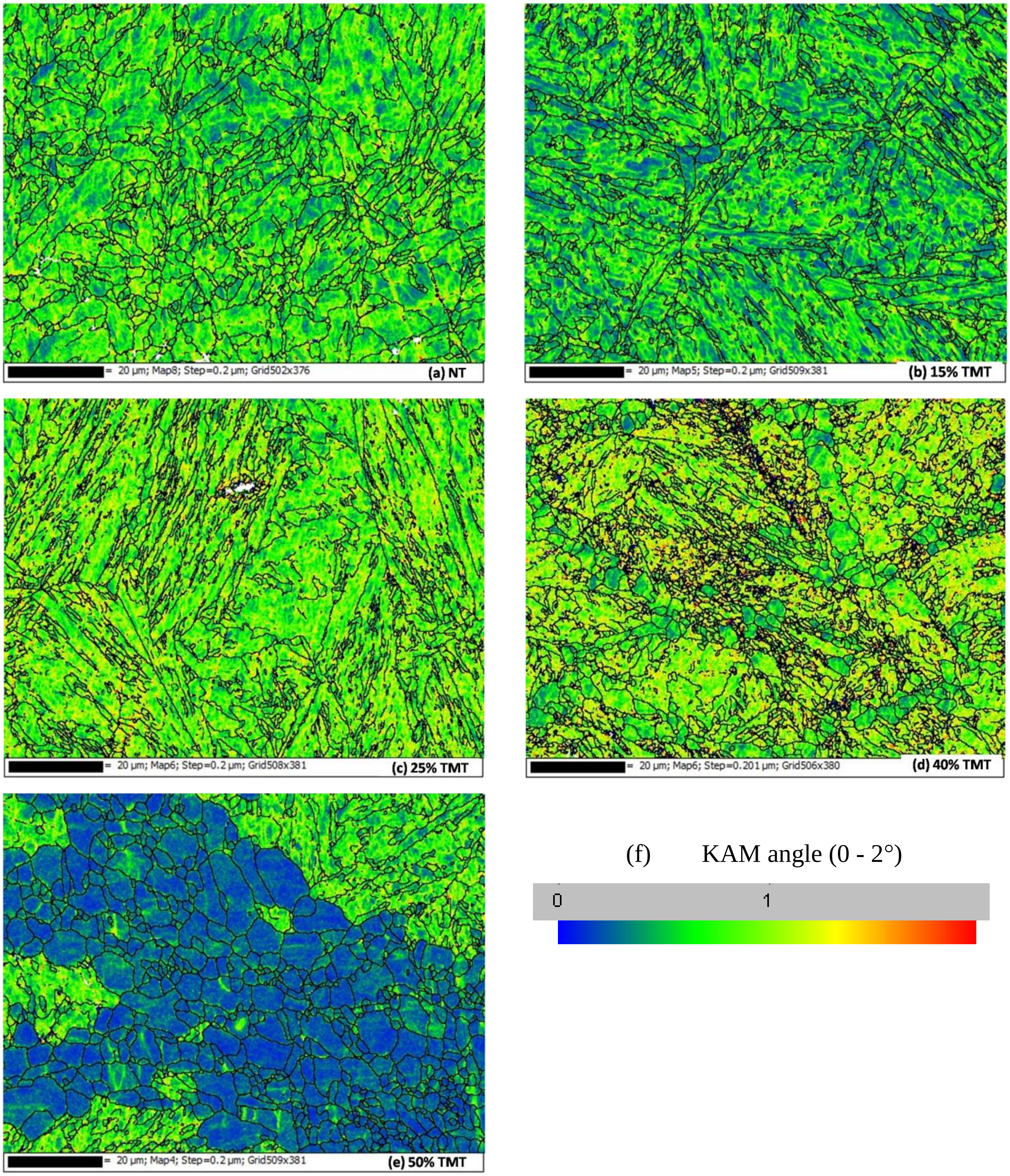

Fig. 5.11 EBSD KAM map depicting the strain distribution in the modified 9Cr-1Mo steel in the (a) NT, (b) 15%, (c) 25%, (d) 40% and (e) 50% TMT conditions. (f) KAM colour legend

TEM micrographs of NT, and 25% and 50% TMT processed steels are given in Fig. 5.12. The microstructure of the NT and 25%TMT steel consists of tempered martensitic lath structure. The lath boundaries and intra-lath regions are decorated with $M_{23}C_6$ and intragranular MX precipitates. The TMT processed steel has finer lath structure as compared to those in the NT steel as shown in Figs. 5.12 and 5.6. TMT 50% steel possessed lower dislocation density as compared to TMT 25% and NT steel (Fig. 5.12(c)). Selected area diffraction (SAD) pattern of $M_{23}C_6$ and MX precipitates are given in Fig. 5.12((d) and (e)), indicating their identification. The lath width was about 558±10 nm in the NT steel (Fig. 5.12(a)) and 460±10 nm in the 25%TMT steel (Fig. 5.12(b)). It is known that the strength of austenite affects the nucleation of martensite by providing resistance to the motion of dislocations involved in the martensite transformation process [126]. The increase in volume accompanied with the transformation of FCC austenite to body centred tetragonal (BCT) martensite creates stress in the austenite, which is accommodated by deformation. Stronger austenite leads to finer martensite lath size as counter force opposing driving force for martensite formation will be realized with reduced growth of the lath, which stops further martensite formation unless the temperature is decreased to increase the driving force. In the austenite phase of the TMT processed steel, change in the lath size on subsequent cooling can result from (i) coarse austenite grains due to higher normalization temperature, (ii) enhanced dislocation density due to deformation (which may also recover substantially at 973 K), (iii) precipitation of MX and $M_{23}C_6$ (possibly) on ageing and (iv) reduction in carbon, niobium, vanadium and chromium contents due to precipitation. Since precipitation and deformation induced dislocations provide higher strengthening against the loss of strength due to increase in grain size and reduction in solute elements, the reduction in martensite lath size on TMT processing over the NT process as observed (Fig. 5.6) is expected. The increase in alloy content in the solution at high normalizing temperatures leads to decrease in M_s temperature, resulting in finer lath width. It has been reported that [3,4] lath size decreases with increase in tungsten content, apparently due to increase in strength of austenite. Decrease in M_s temperature due to deformation in the austenite phase field was reported by Zang et al. [125]. Also, increase in PAG size leads to increases in M_s temperature [127]. Larger PAG size imposes less plastic constraint on martensite transformation resulting in longer martensite lath structure [125]. An increase in M_s temperature and low carbon content in the matrix thus leads to low dislocation density. Austenite in the TMT processed steel is stronger due to the precipitation of MX and can accommodate the stresses generated by nucleation and growth of martensite with less deformation, leading to decrease in M_s temperature. In the present investigation, it is evident that the TMT processing of modified 9Cr-1Mo steel produced finer lath structure, $M_{23}C_6$ and MX precipitates, and enhanced MX precipitation homogeneously distributed in matrix as well as on interface than those in NT steel. XRD patterns in different degrees of TMT conditions of the P91 steel is shown in Fig. 5.13. The presence of $M_{23}C_6$ precipitates in all the conditions of the steel, and enhanced Nb-rich precipitates in 25%TMT steel has been noticed.

Vickers hardness of the steel in the NT, 15%, 25%, 40% and 50% TMT conditions are shown in Fig. 5.14. Hardness increased on TMT processing, and increase in deformation from 40 to 50 % decreased it further. Lower hardness of 50% TMT steel (~200 HV_{10}) than that of 15, 25 and 40% TMT steel is considered to be due to the presence of ferrite predominantly. TMT processing up to 25% imparted in avoiding the ferrite formation to attain enhanced high temperature strength.

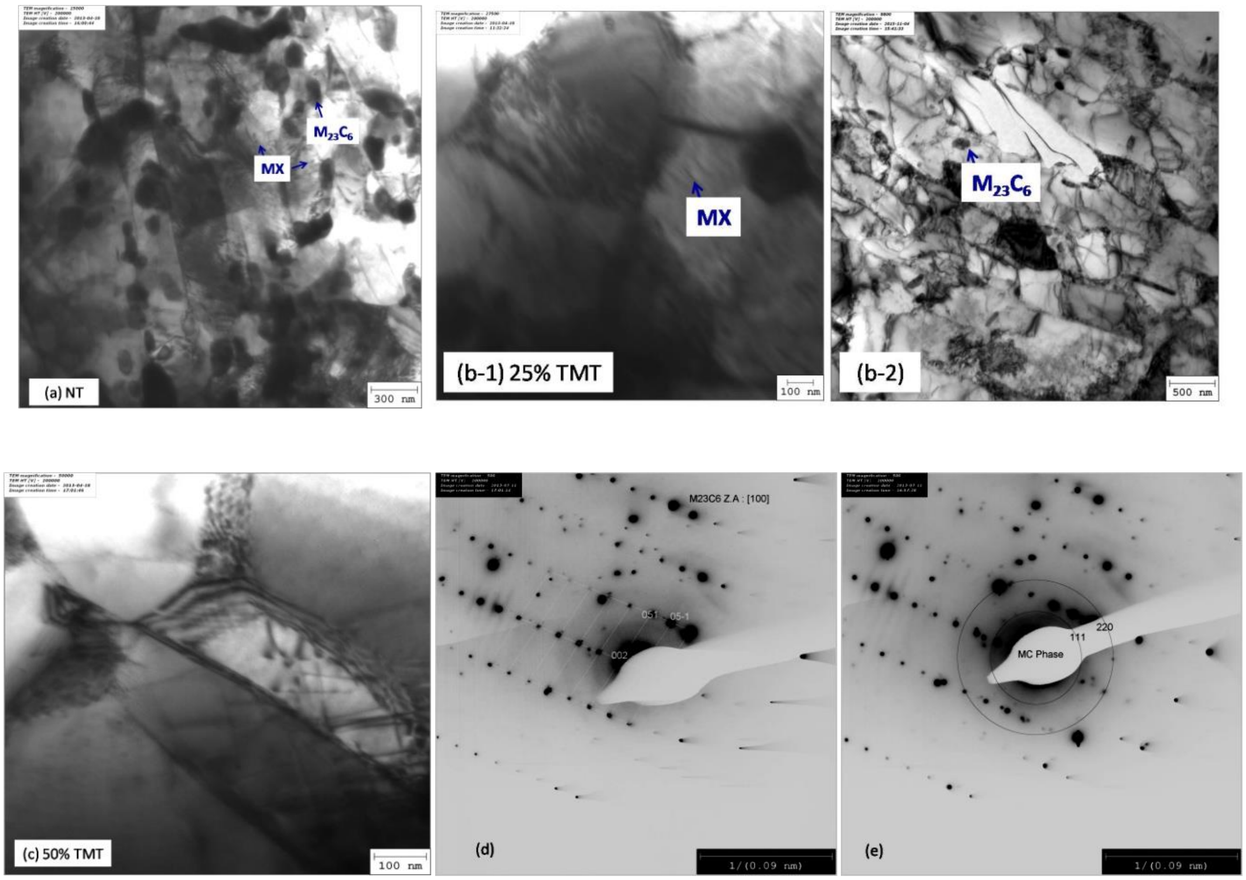

Fig. 5.12 TEM micrographs of (a) (NT), and (b) 25%TMT and (c) 50%TMT processed steels. SAD patterns of (d) $M_{23}C_6$ and (e) MX precipitates.

5.2.2 Creep deformation and rupture behaviour

In order to study the effect of TMT on the creep behaviour, tests were carried out on NT and all the TMT steels at 923 K and 100 MPa. The creep curves of the modified 9Cr-1Mo steel in the NT, 15%, 25%, 40% and 50%TMT conditions at 923 K and 100 MPa are shown in Fig. 5.15. The creep curves for the material in all the conditions exhibited primary, secondary and tertiary creep regimes. Creep strain accumulation in the all the TMT steels was comparable except for the 50%TMT steel which shows relatively lower strain accumulation than the other TMT steels. NT exhibits relatively higher creep strain accumulation than the TMT steels.

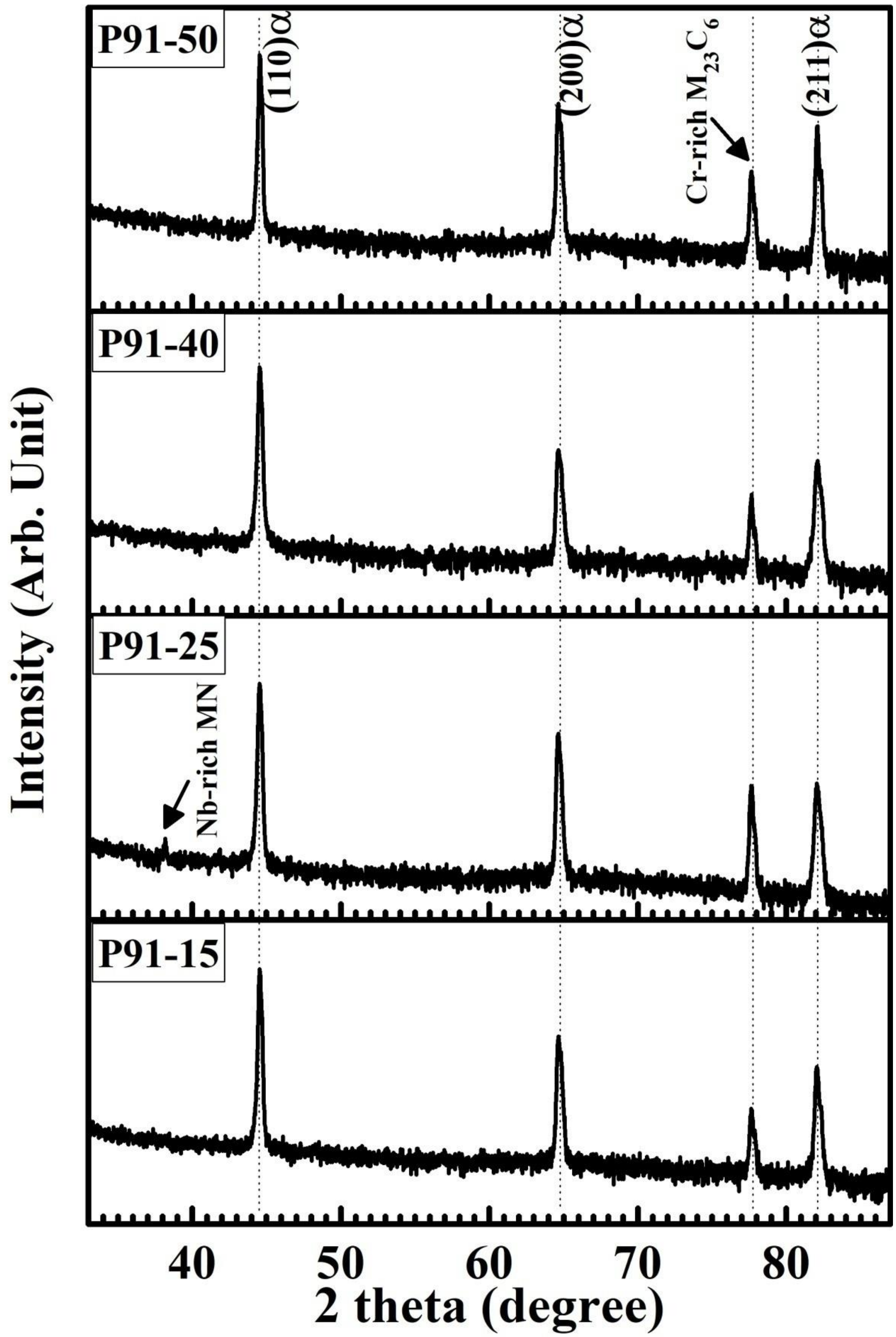

Fig. 5.13 XRD patterns in different conditions of the P91 steel (TMTs) depicting the presence of $M_{23}C_6$ precipitates, and enhanced Nb-rich precipitates in 25%TMT steel.

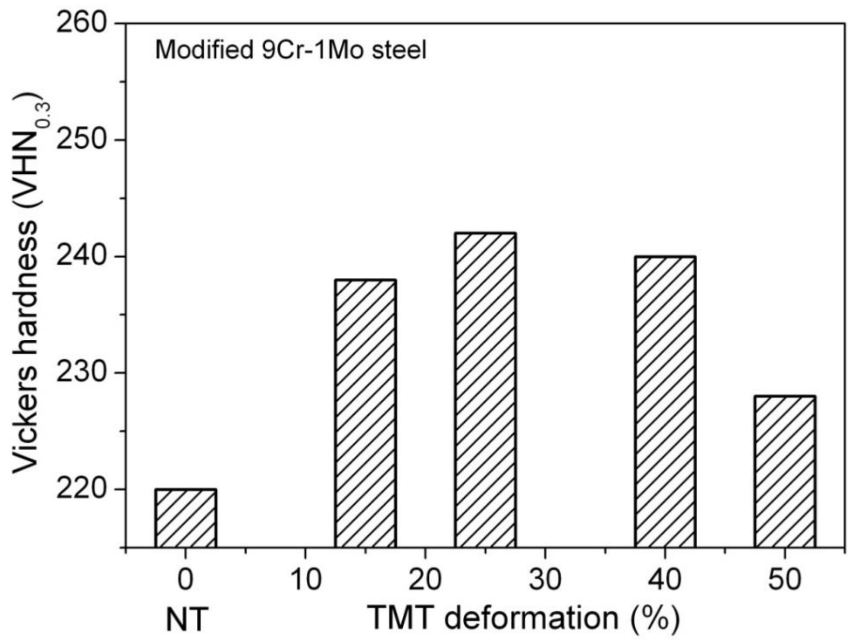

Fig. 5.14 Hardness values at different conditions of the steel.

Secondary creep regime was longer in the 15, 25 and 40 %TMT steels than NT and 50%TMT steels. Creep deformation regimes in the NT and 50% TMT steels were comparable. The variation of creep rate with time for the NT and TMT steels are shown in Fig. 5.15. The creep rate decreased with time and reached a minimum value, depicting less secondary stage of creep deformation and subsequently accelerated creep rate in the tertiary creep regime leading to failure. The initial creep rate was higher in the NT and 50%TMT steel than other TMT conditions. The transient creep rates in the 15%, 25% and 40%TMT steels were comparable, and it was lower than that of NT and 50%TMT steel. The 15%, 25% and 40%TMT steels exhibit relatively extended secondary creep regimes in comparison with the NT and 50%TMT steels. The presence of fine and higher number of MX precipitates in the 15%, 25% and 40%TMT steel leads to extended secondary creep regime with lower minimum creep rate (Fig. 5.15(b)). Minimum creep rates in the NT and 50%TMT steels were comparable and higher than in the other TMT conditions. However, onset of tertiary creep deformation was early in the 15 and 40%TMT steels; it was significantly early in the 40%TMT steel. Presence of α-ferrite phase in the 40 and 50%TMT steels precludes the possible benefit of TMT in these conditions. The variations of creep rate with creep strain of the steels at 923 K and 100 MPa are shown in Fig. 5.15(c). The creep rate decreased with increase in creep strain up to onset of tertiary creep in all conditions of the steel, this decrement in creep rate was profoundly observed in the 15%, 25% and 40%TMT steels. The minimum in creep rate occurred between 1 to 2% of creep strain at all TMT levels and in NT steel. The creep rate variations with creep strain in the NT and 50%TMT steels were comparable as expected from creep curves. TMT processing of the steel with up to 25% deformation led to a quite appreciable decrease in the minimum creep rate. However, presumably due to the presence of ferrite further increase in deformation reduced this beneficial effect of TMT on the minimum creep rate compared to that of the NT steel. This clearly emphasized the need for avoidance of ferrite formation in the TMT processing. The presence of coarser PAG, fine lath width, and fine $M_{23}C_6$ and MX precipitates and higher number density of MX precipitates in the 15%, 25% and 40%TMT steels led to increase in creep deformation resistance by delaying the recovery of dislocation substructure, and 25%TMT is optimum. The enhanced resistance to deformation has also been confirmed by the tensile stress relaxation behaviour. The deformation behaviour of the NT and 25% TMT steel has been studied at 873 K by subjecting the steel to 2% tensile deformation and observing the stress relaxation behaviour by holding cross-head of the testing machine. The deformation behaviour observed from the stress relaxation tests showed that the 25%TMT steel has greater resistance to creep deformation than the NT (Fig. 5.16).

The variation of minimum creep rate ($\dot{\epsilon}_{min}$) with applied stress (σ_a) for NT and 25%TMT steels (Fig. 5.17) followed Norton's power law of creep as $\dot{\epsilon}_{min}= A\sigma^n$, where A is a constant, n is the stress exponent. As already mentioned TMT processing with 25% deformation leads to a significant decrease in the creep rate compared to the NT steel; the difference increased with decrease in applied stress. This indicates better microstructural stability of the 25% TMT steel over the NT steel on high temperature creep exposure. The stress exponent values are 18 and 25 for NT and 25%TMT steels, respectively. Classically, dislocation creep results in 'n' value of 4 or 5, whereas for diffusional creep it is 1. However, no change in deformation mechanism is expected under the presently investigated stress and temperature ranges. The higher values of 'n' in precipitation-hardened alloys could not be interpreted by conventional creep theories. The creep deformation of precipitation hardened alloys can be rationalized by conventional dislocation creep theories by expressing creep rate in terms of the effective stress (σ_{eff}) i.e., the difference between the applied stress (σ_a) and the threshold stress (σ_{th}), ($\sigma_a - \sigma_{th}$) rather than applied stress. The threshold stress is associated with the mechanism by which the dislocations bypass the particles to cause creep deformation [5,107]. Considering the threshold stress (σ_{th}), the creep rate according to Mukherjee-Bird-Dorn [5,107] can be expressed as,

$$\dot{\epsilon}_{min} = A'\left(\frac{\sigma_a - \sigma_{th}}{\mu}\right)^{n'} \exp(-\frac{Q_c}{kT})$$

where A' is a constant, n' is the matrix stress exponent, σ_a is the applied stress, Q_c is the creep activation energy, T is the temperature in Kelvin, μ is the shear modulus, and k is the Boltzmann's constant. Stress exponent value of about 4, and activation energy for creep (Q_c) similar to that for lattice self-diffusion (Q_d) have been observed in pure metals [5,107]. Lagneborg and Bergman [128] proposed a graphical method to estimate the threshold stress σ_{th}

by plotting $(\dot{\varepsilon}_{min})^{1/4}$ against applied stress σ_a (Fig. 5.18). The stress intercept by extrapolating the straight-line $(\dot{\varepsilon}_{min})^{1/4}$ against applied stress σ_a plot to zero-creep rate gives σ_{th} values. In the present study, σ_{th} values of 87 MPa for NT and 98 MPa for 25%TMT steel were obtained. The higher resistive stress in the 25%TMT steel in comparison with NT steel has been attributed to the presence of finer and higher number density of MX precipitates along with finer martensite lath structure, which more effectively pin the dislocations.

The variation of creep rupture life at 923 K and 100MPa with extent of deformation is shown in Fig. 5.19. Rupture life increased with increase in TMT deformation up to 25%, further increase in deformation resulted in decrease in creep rupture life due to formation of ferrite in the steel. Creep rupture life of NT, 40% and 50%TMT steels were comparable. The variation of t_r with σ_a for NT, 25% and 50%TMT steels at 923 K are shown in Fig. 5.20. Significant increase in creep rupture life (t_r) of the 25%TMT processed steel in comparison with the NT was observed; however 50%TMT had lower t_r than NT though the difference decreased with decreasing stress. The difference in t_r between the 25%TMT steel and NT steel increased with decreasing σ_a, due to enhanced contribution of the precipitates under lower stress level by pinning of dislocations and the subsequent delay in the climbing event to overcome from barrier (Fig.5.16) also delaying the recovery process.

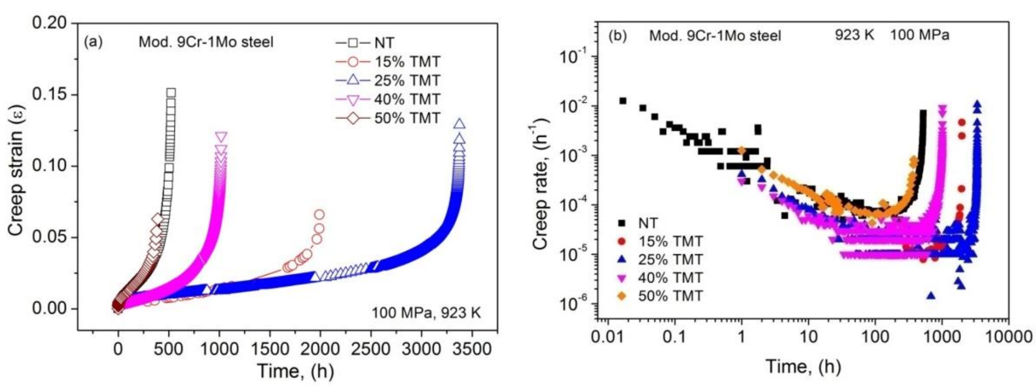

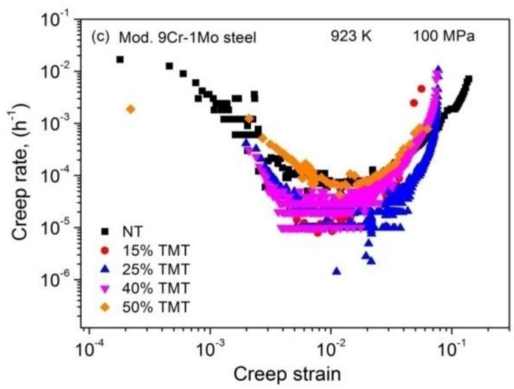

Fig. 5.15 (a) creep curves, creep rate with (b) time and (c) creep strain curves of modified 9Cr-1Mo steel in NT and TMT (15, 25, 40 and 50%) conditions at 923 K and 100 MPa.

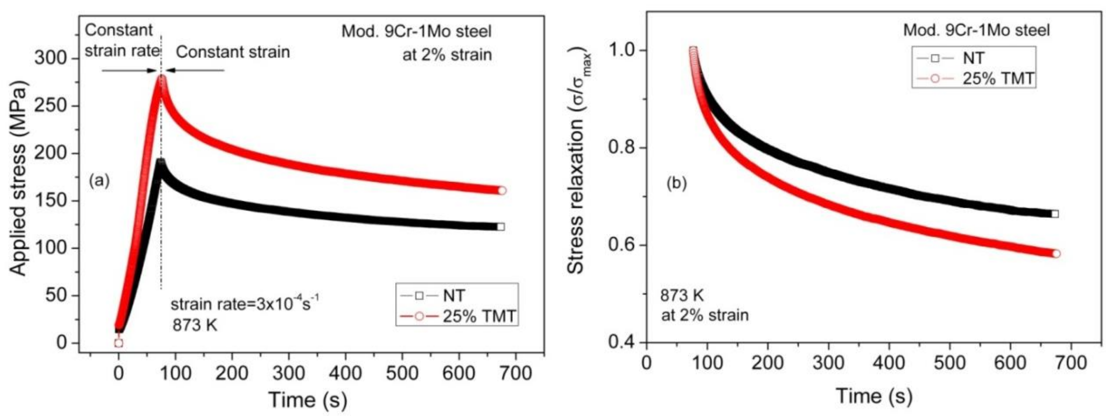

Fig. 5.16 (a) Stress relaxation test graph of NT and 25%TMT steels at 873 K and (b) stress relaxation behaviour of NT and 25% TMT steels at 873 K.

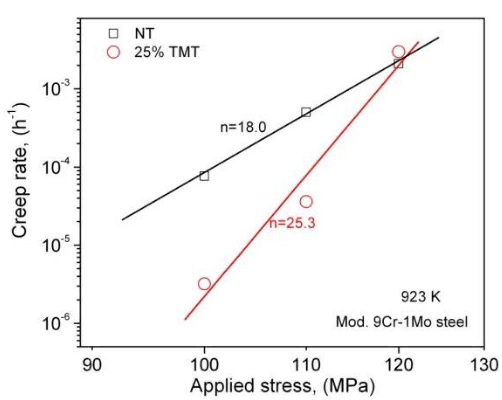

Fig. 5.17 Variation of minimum creep rate with applied stress of modified 9Cr-1Mo steel in the NT and 25%TMT processed conditions at 923 K.

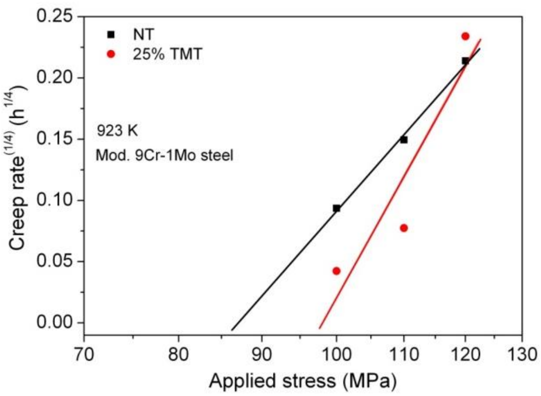

Fig. 5.18 Variation of strain rate ($\dot{\epsilon}^{1/4}$) versus applied stress plot for NT steel and 25%TMT conditions at 923 K.

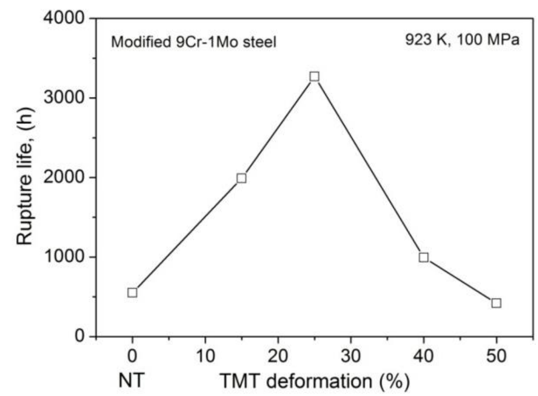

Fig. 5.19 Creep rupture life with different conditions of modified 9Cr-1Mo steel at 923 K and 100 MPa.

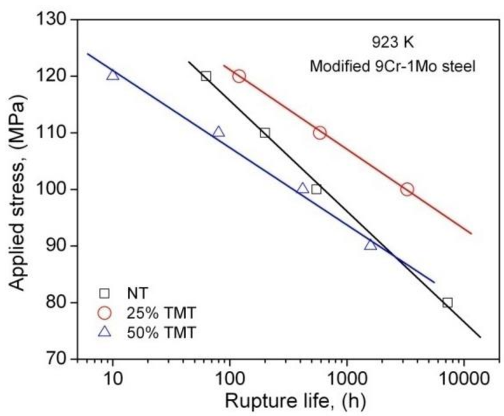

Fig. 5.20 Variation of creep rupture life with applied stress plot for NT and TMT (25% and 50%) steels at 923 K.

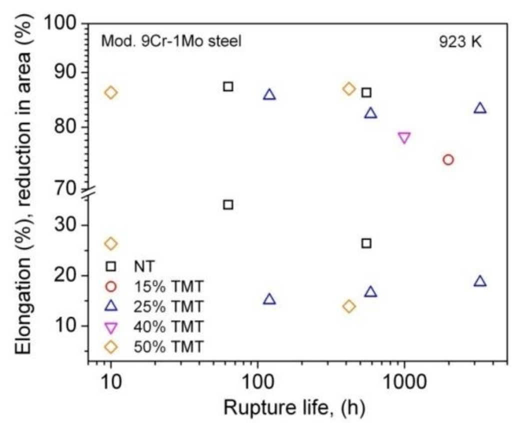

Fig. 5.21 Variation of elongation (%) and reduction in area (%) with rupture life of NT and TMT (25% and 50%) steels at 923 K.

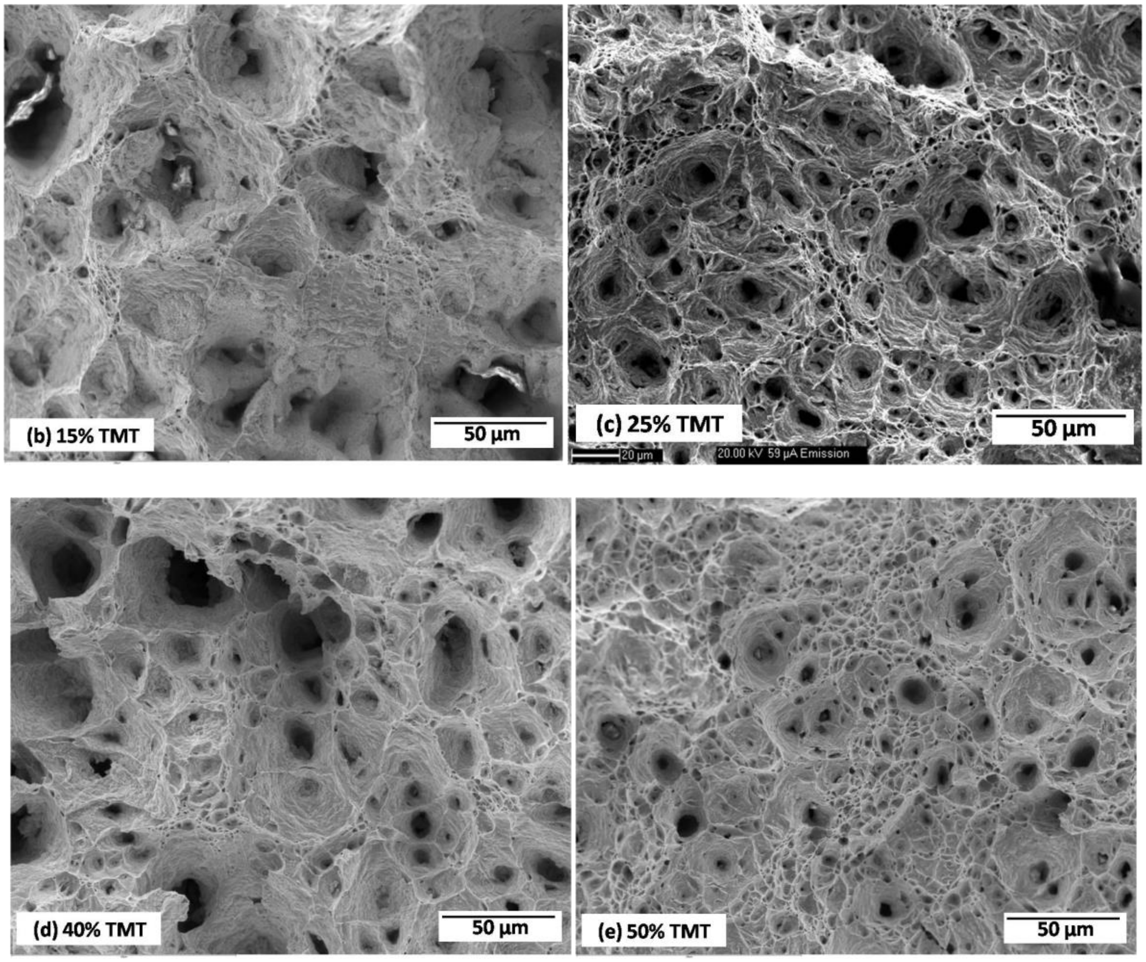

Fig. 5.22 Fracture surfaces of creep ruptured (b) 15%, (c) 25%, (d) 40% and (e) 50% TMT steels at 923 K and 100 MPa.

The variations of elongation (%) and reduction in area (%) with t_r are shown in Fig. 5.21. Both the TMT processed steels exhibited lower strain accumulation in comparison to NT steel. The reduction in area was comparable in the NT and TMT processed steels. However, the reduction in area of all the steels did not change significantly in the investigated creep duration in NT and 25%TMT steels. Relatively lower elongation in the 25%TMT steel has been attributed to reduction in rates of recovery and coarsening of precipitates with creep exposure than the NT steel. Examination of the fractured surfaces of creep ruptured 15%, 25%, 40% and 50%TMT processed steels revealed ductile mode of failure (Fig. 5.22).

5.2.3 Microstructure evolution under creep

Microstructural features of tempered martensite F/M steels and their role in strengthening against creep deformation have been discussed by many investigators [3-5]. From their detailed analysis pertaining to the effect of volume fraction and diameter of each kind of precipitates, dislocation density and subgrain size on Orowan stress Maruyama et al. [3] concluded that dislocation substructure is the major obstacle controlling the creep deformation, if it does not recover significantly during creep. Similar view has been expressed by many investigators [41,78,129,130]. The mobile dislocation density within subgrain/lath decreases and the subgrain/lath width increases with creep exposure [3,4], leading to a decrease in their strengthening role with creep exposure. For relatively long-term creep strength, the material should have high dislocation density and fine substructure, and more importantly they must be stable at high temperature. The precipitates, both on subgrain boundaries and inside grains, play an important role in stabilizing the microstructural features by pinning them against recovery. The $M_{23}C_6$ and MX precipitates on the subgrain boundaries and intragranular MX provide stability of the respective microstructural features [3,4]. It has been shown that $M_{23}C_6$ provides the highest pinning force on subgrain boundaries whereas MX on dislocations are most effective in pinning them [3]. However, stability is reduced because of the coarsening of $M_{23}C_6$ precipitates and the replacement of fine MX with coarser Z-phase on long term creep exposure [3,4]. Fortunately, the modified 9Cr-1Mo steel is not much prone to Z-phase formation. Naturally, much attention has been paid to increase the coarsening resistance of $M_{23}C_6$ precipitates by alloying with tungsten, boron etc. [3,4]. Alternatively, it has been thought to replace $M_{23}C_6$ on the subgrain with more stable MX precipitates. A schematic microstructural view of such steel is shown in Fig. 5.23, as conceived by Abe in ferritic steel [4]. Reduction in carbon content with appropriate increase in nitrogen content has been reported to increase creep strength of F/M steel by elimination of $M_{23}C_6$ precipitates by MX precipitates. However, in high nitrogen steels, the replacement of MX with Z-phase on long exposure is a concern. Attempts to reduce $M_{23}C_6$ and increase MX in the microstructure through TMT processing has been studied in order enhance creep strength [131-133]. Microstructures of the NT, and 25% and 50%TMT steels creep fractured at 923 K and 100 MPa are shown in Fig. 5.24. Extensive pinning of the dislocations and substructure precipitate particles are seen in the gauge section (Fig. 5.24(b)). At the neck region (*i.e.,* near fracture surface), which has undergone extensive recovery under tri-axial state of stress, many of the microstructural features remain. Presence of ferrite on TMT processing (40 and 50%), however, is a concern, and optimization of TMT parameters needs to be considered to avoid it. Optimum creep strength has been observed in the 25% processed TMT steel.

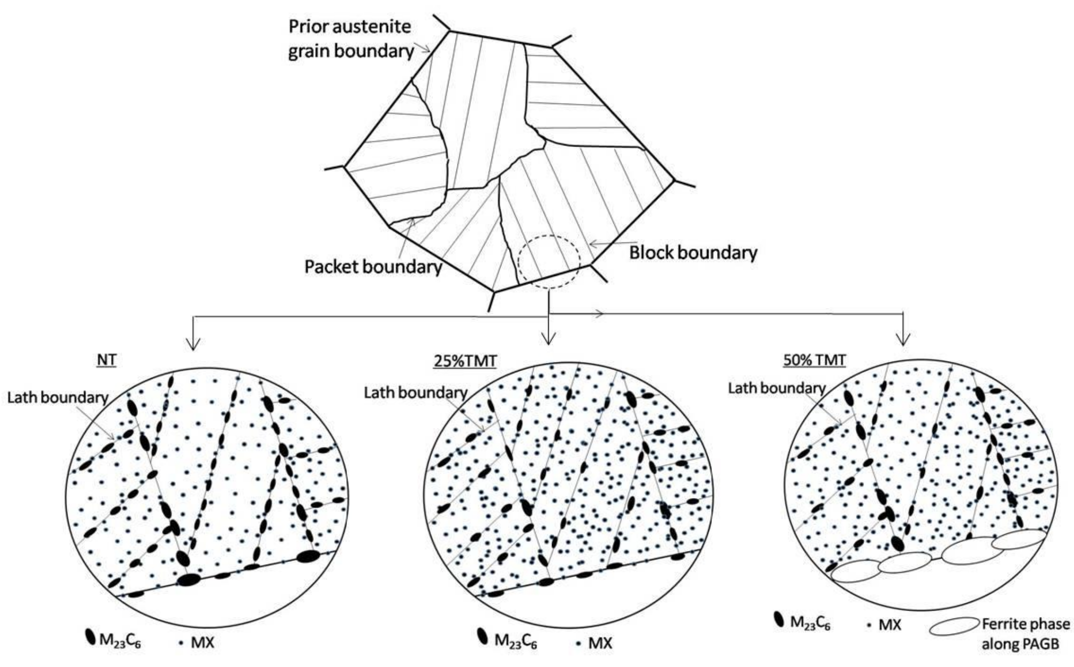

Fig. 5.23 Schematic of microstructural constituents of modified 9Cr-1Mo steel in the NT, 25%TMT and 50%TMT conditions.

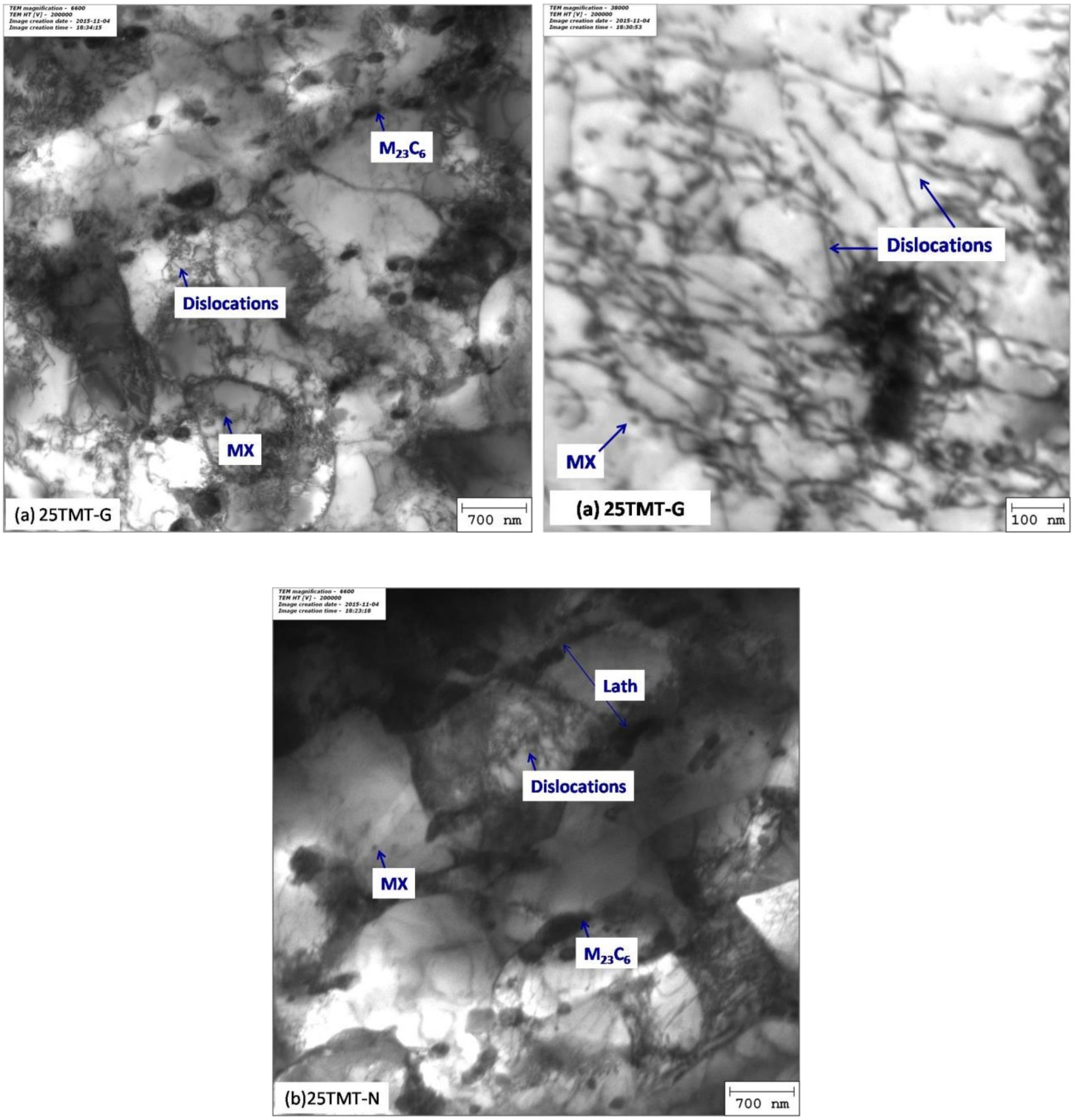

Fig. 5.24 TEM microstructures of (a) gauge region and (b) necked regions of 25%TMT processed steel creep exposed at 923 K and 100 MPa depicted the dislocation structure pinned by finer MX precipitates.

5.3 Creep behaviour of NT and TMT steels weld joints

Macrostructure of electron beam weld joint (EB) of modified 9Cr-1Mo steel fabricated from normalized and tempered (NT), and optimized 25%TMT steel are shown in Fig. 5.25.

5.3.1 Microstructure and hardness variations across the weld joints

The weld joint consists of weld metal, narrow heat affected zone (HAZ) of ~250 to 300 μm width and base metal. SEM micrographs observed across both the weld joints are shown in Fig. 5.26. The prior-austenite grain (PAG) size was found to vary significantly across the weld joint; In the NT steel weld joint, CGHAZ, FGHAZ, ICHAZ and base metal regions these were 32 μm, 21 μm, 13 μm and 30 μm respectively. In TMT steel weld joint, the PAG size of CGHAZ, FGHAZ, ICHAZ and base metal regions were 24 μm, 13 μm, 7 μm and 60 μm respectively. The dissolution and stability of precipitates, transformation kinetics of the steel with weld peak temperature resulted in significant variations in PAG size in the HAZ. The PAG sizes in the HAZ regions of TMT steel joint were relatively small in comparison with those in NT steel joint. Specifically, the PAG size of ICHAZ was significantly lower than its adjacent regions in the weld joint. The ICHAZ region of TMT steel joint possessed lower PAG size (7 μm) than that in the NT steel joint (13 μm) (Fig. 5.27). The presence of more MX precipitates is expected to lead to finer PAG size across the TMT joint by suppressing grain growth upon heating during weld thermal cycle. The steel derives its high temperature strength predominantly from tempered martensite lath structure, dislocations, $M_{23}C_6$ and MX carbonitrides, solute atoms, grain and sub-grain boundaries. The SEM microstructure observed at different regions of the NT and TMT weld joints are shown in Fig. 5.28. The microstructure consists of tempered martensitic lath structure, and decoration of PAG and sub-boundaries by $M_{23}C_6$ precipitate, and MX precipitates in the intra lath regions. MX precipitates possess relatively higher thermal stability in comparison with the $M_{23}C_6$ precipitate [6]. Hence, the $M_{23}C_6$ precipitate size has been examined at different zones in the weld joint (Fig. 5.28). Energy dispersive spectroscopy (EDS) spectrum of $M_{23}C_6$ precipitate observed in the steel is given in Fig. 5.29. $M_{23}C_6$ precipitate size and tempered martensite lath width across the different regions of both the weld joints reveals significant variations. The variation in size of $M_{23}C_6$ precipitate between the weld metal, CGHAZ and base metal regions was relatively less as compared to ICHAZ (Fig. 5.30). In both the weld joints, coarser $M_{23}C_6$ precipitate, and coarser lath width accompanied by subgrain formation has been noticed in the ICHAZ than in the adjacent regions. However, the extent of coarsening of $M_{23}C_6$ precipitates and lath width in the ICHAZ were relatively lesser in TMT joint as compared to NT steel joint (Figs. 5.28 and 5.30).

The average size of $M_{23}C_6$ precipitates in the weld metal, CGHAZ, FGHAZ, ICHAZ and base metal are 118, 133, 139, 143 and 127 nm in NT joint whereas these are 104, 116, 128, 137 and 110 nm in TMT joint respectively. In general, the average size of $M_{23}C_6$ precipitates in different regions of the weld joint was lower in the TMT steel than in the NT steel. Presence of these fine precipitates in TMT steel leads to effective pinning of the boundaries. Pinning of dislocations by MX precipitates delays the recovery of dislocation structure at the high creep temperature. The average size of $M_{23}C_6$ precipitates observed in the ICHAZ region of EB joint of the NT steel 137 µm was comparable with that in the joint made using shielded metal arc welding process. Presumably the lesser availability of carbon in the TMT steel matrix due to consumption of carbon for formation of MX (MCN) precipitates leads to reduced coarsening of $M_{23}C_6$ precipitates during subsequent weld thermal cycles. Enhanced MX precipitation (increased number density and finer size) through TMT processing and its influence on the improvement of creep strength of modified 9Cr-1Mo steel have been reported by researchers [58,62,63,133]. The variations in hardness across both the NT and TMT weld joints are given in

Fig. 5.31. A decrease in hardness values from weld metal to base metal with a hardness trough in the ICHAZ has been observed in both the weld joints. The lowest hardness has been observed in the ICHAZ in both NT and TMT steel joints. Formation of soft ICHAZ has been reported by other researchers in different 9-12Cr steel weld joints [81, 133]. This softening is due to coarsening of $M_{23}C_6$ precipitates and sub-grain formation with decreased dislocation density in the ICHAZ of the weld joint during weld thermal cycle (Fig. 5.28). Dislocation cell structure formation which causes dip in the hardness has been reported in the HAZ of electron beam PWHT weld joint of T91 steel [134]. The hardness values in the ICHAZ region of weld joints were about 227±2 VHN in TMT steel and about 222±2 VHN in NT steel. The observed higher hardness in ICHAZ of TMT steel joint than in the ICHAZ of NT steel joint is consistent with the presence of finer $M_{23}C_6$ and MX precipitates, and more number of MX precipitates in the TMT steel.

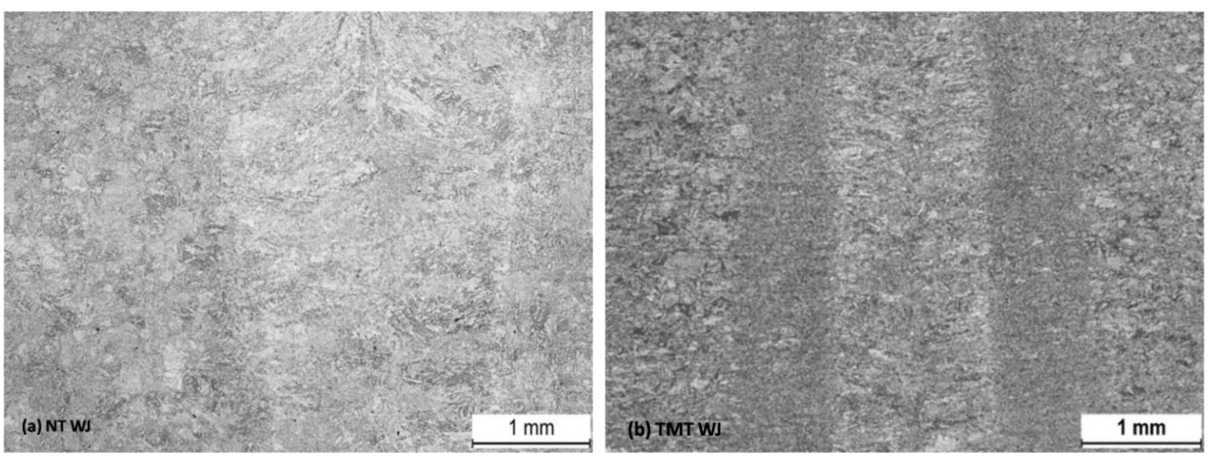

Fig. 5.25 Macrographs of (a) NT and (b) 25%TMT steels weld joints.

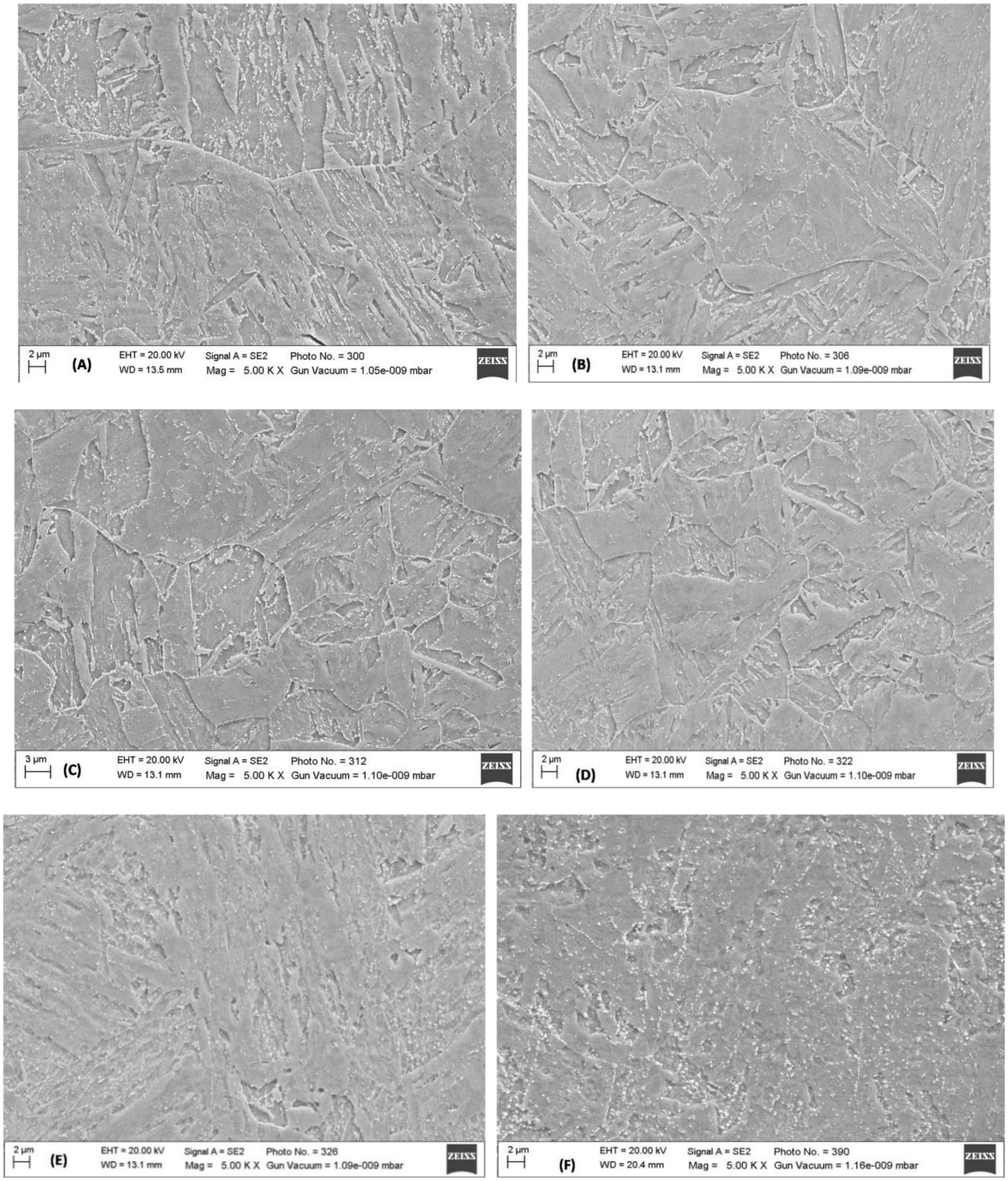
2 µm
(A)
EHT = 20.00 kV
WD = 13.5 mm
Signal A = SE2
Mag = 5.00 K X
Photo No. = 300
Gun Vacuum = 1.05e-009 mbar
ZEISS
2 µm
(B)
EHT = 20.00 kV
WD = 13.1 mm
Signal A = SE2
Mag = 5.00 K X
Photo No. = 306
Gun Vacuum = 1.09e-009 mbar
ZEISS
3 µm
(C)
EHT = 20.00 kV
WD = 13.1 mm
Signal A = SE2
Mag = 5.00 K X
Photo No. = 312
Gun Vacuum = 1.10e-009 mbar
ZEISS
2 µm
(D)
EHT = 20.00 kV
WD = 13.1 mm
Signal A = SE2
Mag = 5.00 K X
Photo No. = 322
Gun Vacuum = 1.10e-009 mbar
ZEISS
2 µm
(E)
EHT = 20.00 kV
WD = 13.1 mm
Signal A = SE2
Mag = 5.00 K X
Photo No. = 326
Gun Vacuum = 1.09e-009 mbar
ZEISS
2 µm
(F)
EHT = 20.00 kV
WD = 20.4 mm
Signal A = SE2
Mag = 5.00 K X
Photo No. = 390
Gun Vacuum = 1.16e-009 mbar
ZEISS

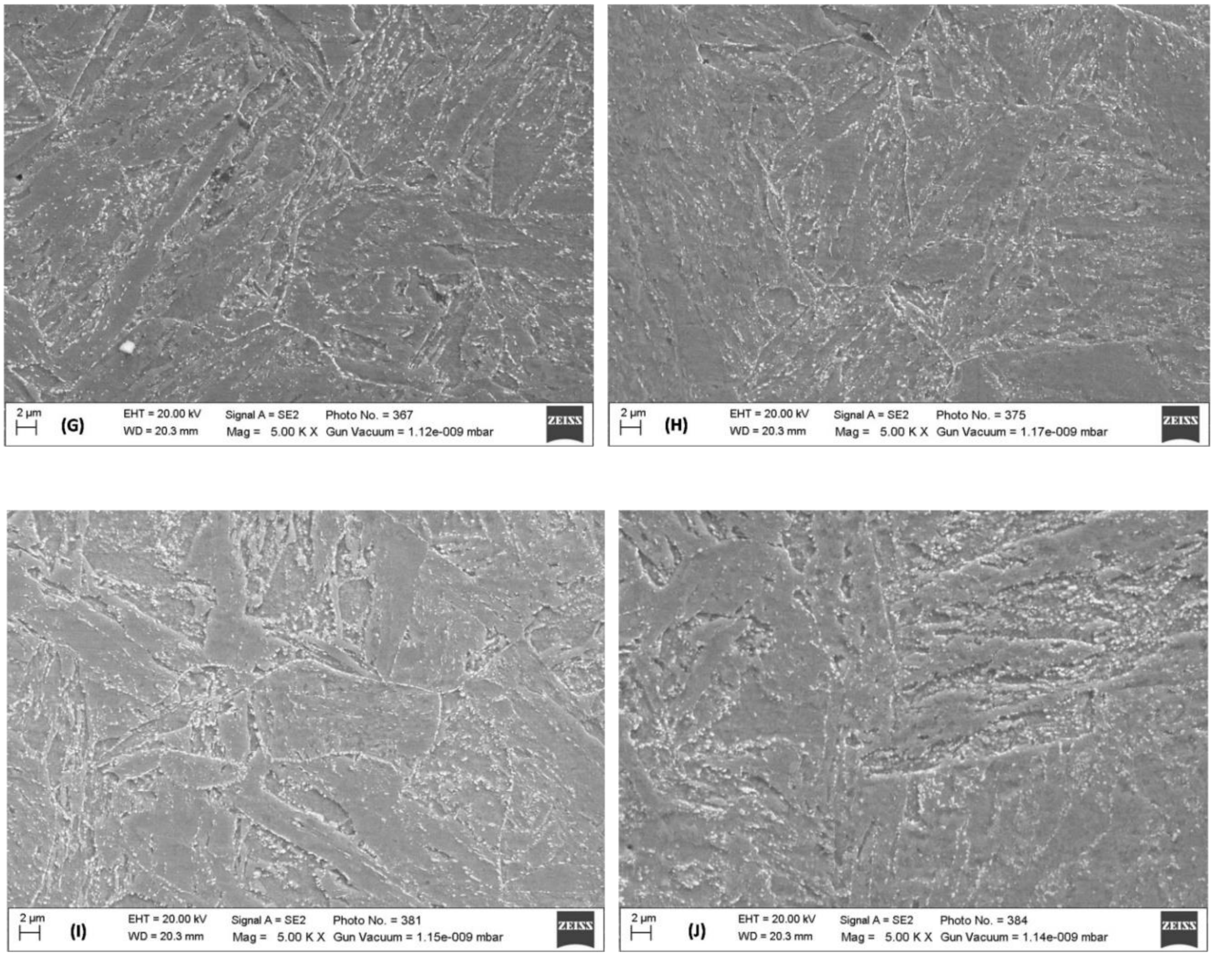

Fig. 5.26 SEM microstructures across the NT (a,b,c,d,e) and 25%TMT (f,g,h,i,j) steel weld joints depicting the different regions (WM, CGHAZ, FGHAZ, ICHAZ and BM).

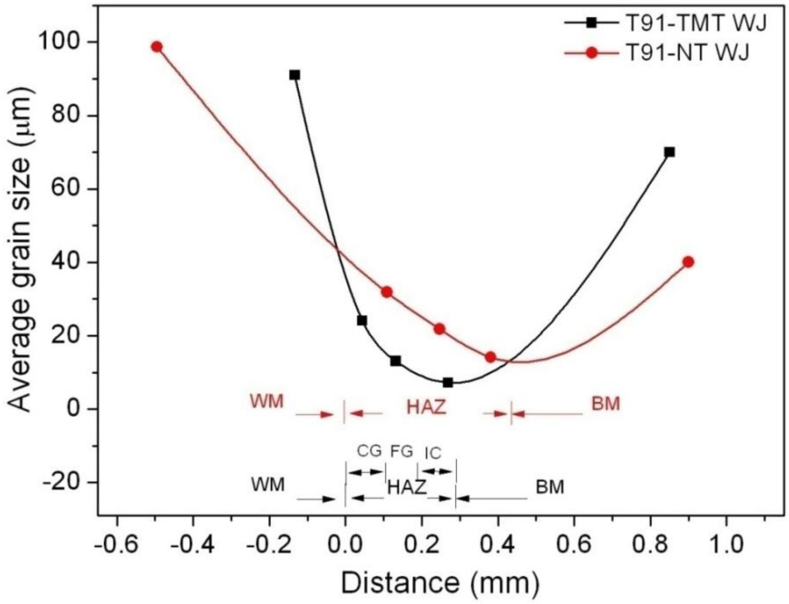

Fig. 5.27 Variation of grain size across the NT and 25%TMT steel weld joints.

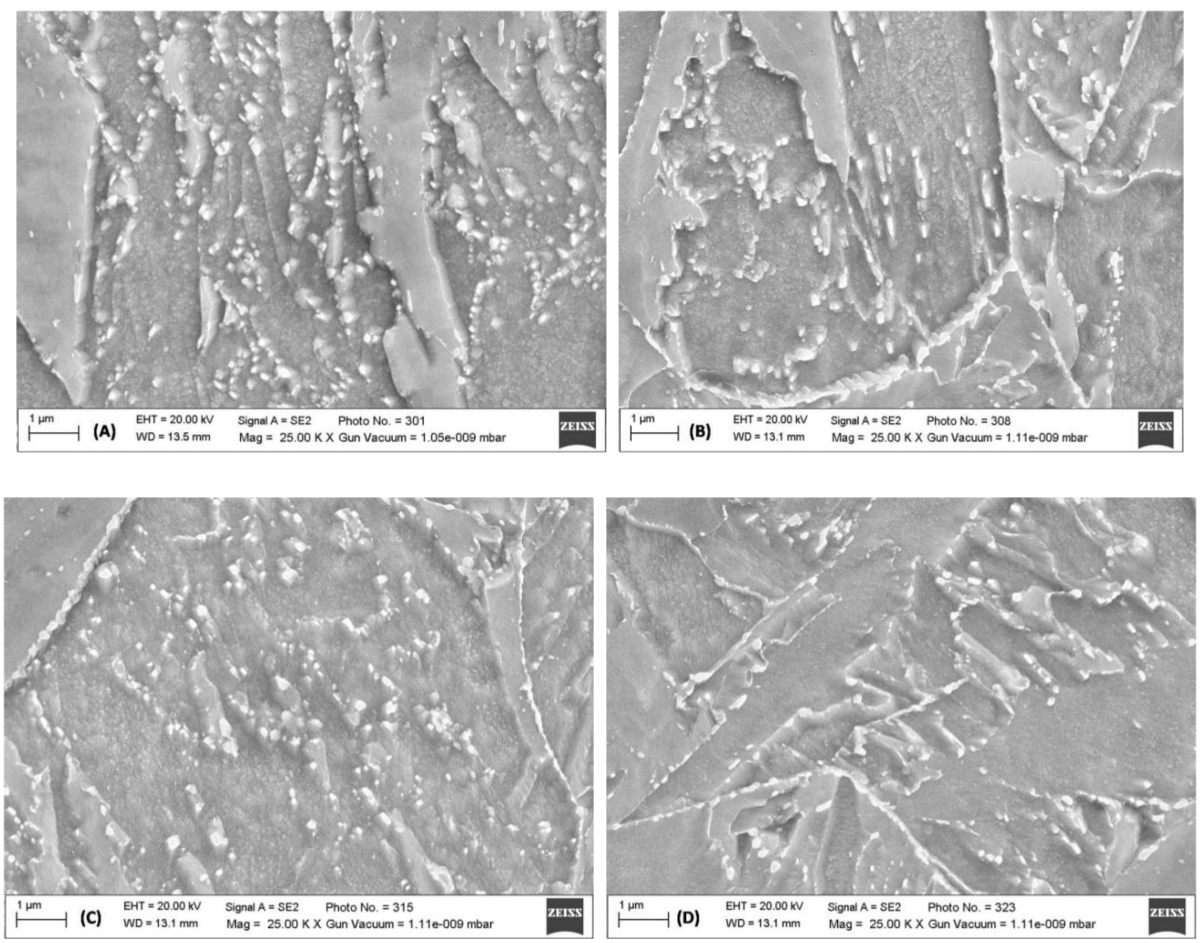

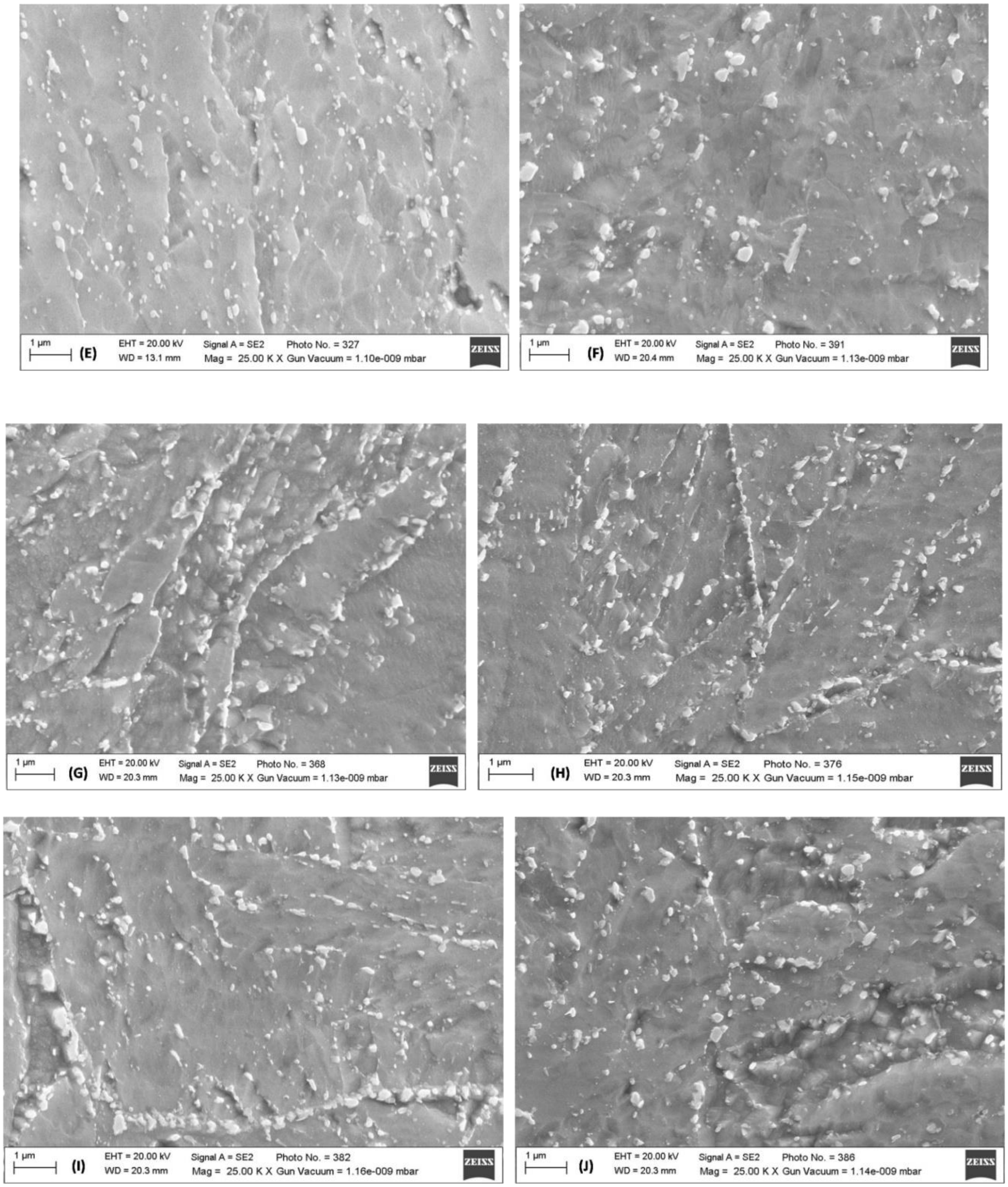

Fig. 5.28 SEM microstructures across the NT (a,b,c,d,e) and 25%TMT (f,g,h,i,j) steel weld joints depicting the different regions (WM, CGHAZ, FGHAZ, ICHAZ and BM).

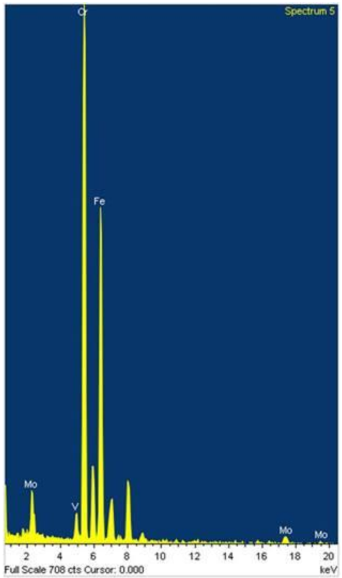

Fig. 5.29 EDS spectrum of $M_{23}C_6$ precipitates.

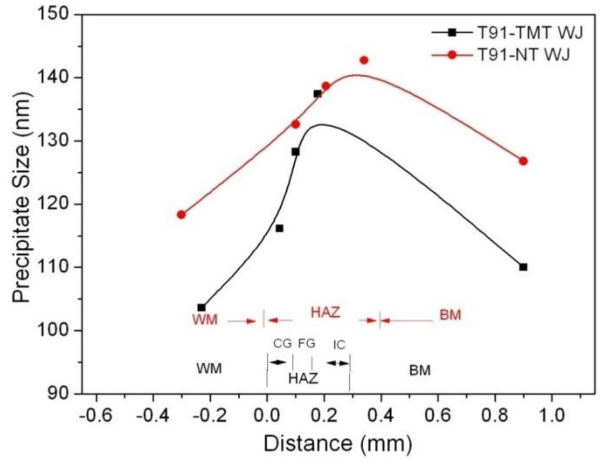

Fig. 5.30 Variation of $M_{23}C_6$ precipitates size across the NT and 25%TMT steel weld joints.

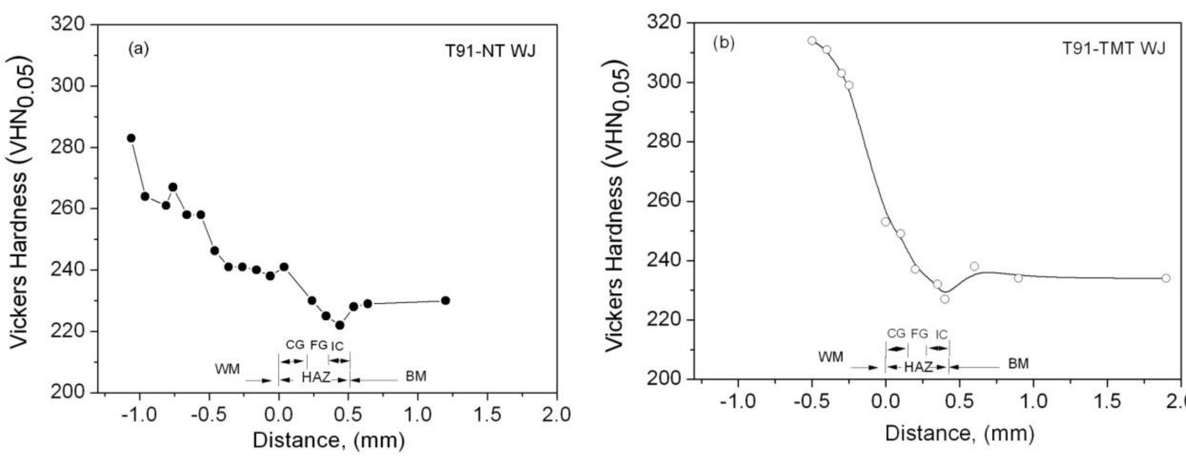

Fig. 5.31 Variation of hardness across the (a) NT and (b) 25%TMT steel weld joints.

5.3.2 Creep deformation and rupture behaviour of the weld joints

The creep curves of base metal and weld joints are shown in Fig. 5.32. The base metal and weld joints exhibited clear primary creep regimes followed by secondary creep and an accelerating tertiary creep regime. The weld joint of NT steel has exhibited higher creep strain with a failure at the BM region, and shown lower rupture life as compared to TMT weld joint (Fig. 5.32(a)). The TMT weld joint exhibited lower creep strain in comparison with its base steel (Fig. 5.32(b)). The creep rate curves of TMT base metal and its weld joints are shown in Fig.5.33. The creep rates of both base metal and weld joint decreased with time and reached a minimum in the secondary creep regime and exhibited the accelerated creep rate in the tertiary creep regime. The microstructural instability of the tempered martensitic steels under creep exposure has generally been considered as the reason for the absence of predominant steady state creep regime in this class of steels [25]. The base metals and the weld joints show similar creep rates in the primary and secondary regimes. However, the tertiary creep regime was initiated early weld joints in comparison with base steel (Fig. 5.33). The significant microstructural changes (enhanced rate of recovery of dislocation structure and coarsening of precipitates in the ICHAZ) and localized creep deformation in the selected constituents of the joints because of deformation constraints imposed on the soft zone by the adjacent stronger regions have been considered responsible for the early initiation of tertiary stage of creep deformation in the weld joints in comparison with the base steel. Comparison of the variations of creep strain with time for TMT and NT weld joints at 100 MPa and 923 K shows that the creep deformation of TMT weld joint was significantly lower in comparison with the NT steel weld joint. However, under lower stress levels, NT weld joint is expected to accumulate lower creep strain. Lower creep strain than the base metal has been observed in the modified 9Cr-1Mo steel weld joint made from SMAW and TIG welding process under lower stress levels [134]. The enhanced number density and smaller size MX precipitation obtained through TMT processing resulted in effective pinning of the dislocations or formation of dislocation networks leading to delayed the recovery of dislocation structure in the ICHAZ of TMT joint than in the ICHAZ of NT joint. Although higher number of fine MX precipitates is present in the TMT steel joint (ICHAZ), the heterogeneity in mechanical properties across the joints led to accelerated localized damage/deformation which ultimately resulted in the early initiation of tertiary creep regime as well in the TMT weld joint. However, TMT weld joint possessed higher creep rupture time than the NT base steel.

The variation of creep rupture life (t_r) with applied stress (σ_a) for the base metal and weld joint of NT and 25%TMT steels at 923 K is shown in Fig. 5.34. The base metals or weld joints do not exhibit significant difference in t_r between NT and TMT steels at 923 K at a stress of 110 MPa. At lower stress levels, the difference in creep strength between the two weld joints was significantly higher than that between the two base metals. This has generally been observed at high temperature and low stress levels in the 9-12 %Cr ferritic steel weld joints [81,134]. A reduction in creep strength of TMT weld joint in comparison with its base metal has been noticed at 100 MPa. The t_r of NT steel weld joint was comparable with its base steel at 100 MPa; under low stress level it is expected to reduce drastically. Drastic reduction in t_r of NT modified 9Cr-1Mo steel weld joint made from SMAW and TIG welding process has been observed under stress level < 80 MPa [134]. It is interesting to note that although TMT weld joint failed prematurely in comparison with its base metal at 100 and 80 MPa in the outer edge of HAZ accompanied with localized deformation, the t_r of the TMT weld joint was significantly higher than that of the NT base metal by about a factor of 2. This clearly depicts the importance of TMT processing of ferritic steel leading to significant increases in number density of fine MX precipitates in improving the creep strength by providing relatively stable microstructures thereby delaying the recovery of dislocation structure through pinning. Thus, TMT processing of modified 9Cr-1Mo steel led to enhanced creep strength of not only the steel but also for the weld joints prepared from it.

Fracture location in the weld joint was found to change with applied stress. At high stress regime (110 MPa), fracture of the weld joint took place in the base metal, whereas in the case of low stress regime (at 100 MPa or lower) failure occurs in the ICHAZ, where the lowest hardness has been observed in the pre-creep test condition (Fig. 5.31 and 5.35). The creep ductility is, in general higher in the specimen fractured at base metal region under high stress regime (>100 MPa). However, under low stress regime, significant reduction in ductility coupled with localized deformation in the ICHAZ was observed. This clearly demonstrates that type IV cracking occurs predominantly by brittle mode. The Type IV cracking in the TMT weld joint has been identified based on change in fracture location (at high stress - the base metal region of the weld joint failed exhibiting cup-cone ductile failure; at low stress - weld joint failed in the ICHAZ exhibiting significantly lower reduction in area and localized deformation in the outer HAZ) and distance of the fractured region identified by the hardness measurement on the unbroken HAZ side of tested specimen. Weld joint of the NT steel failed in the base metal at 923 K under 100 MPa; Type IV cracking in this joint may possibly be observed under even still lower stress level. TMT weld joint has shown type IV failure under similar testing conditions; however the rupture life of the TMT weld joint was higher than the NT steel joint which fractured in the base metal region. SEM investigations on the fracture surface of the creep tested specimens revealed that the specimens those fractured in base metal region displayed ductile mode of failure. The specimens fractured in the ICHAZ displayed lesser dimple features (predominantly brittle mode of failure) (Fig. 5.36). At higher stress level, the deformation was found to occur with gradual reduction in area across the gauge length of the specimen, whereas under lower stress level it occurred in a localized manner in the soft ICHAZ. Type IV cracking is found to occur in TMT steel weld joint at higher stress levels than in NT steel weld joint because of the longer rupture life of TMT joint.

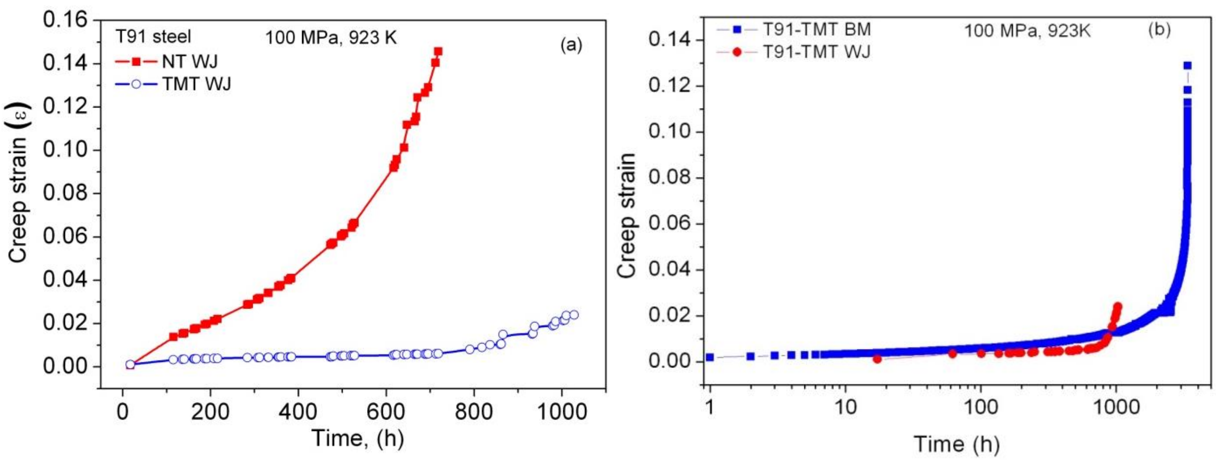

Fig. 5.32 Creep strain versus time curves of (a) NT and 25%TMT steel weld joints, and (b) 25%TMT steel base metal and weld joint at 923 K.

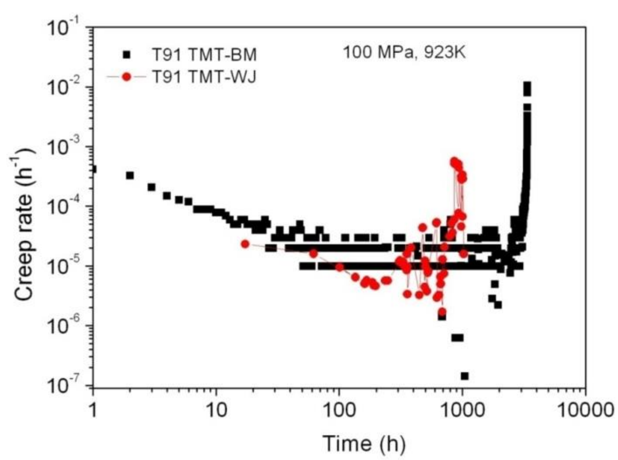

Fig. 5.33 Creep rate versus time curves of 25%TMT base metal and weld joint at 923 K.

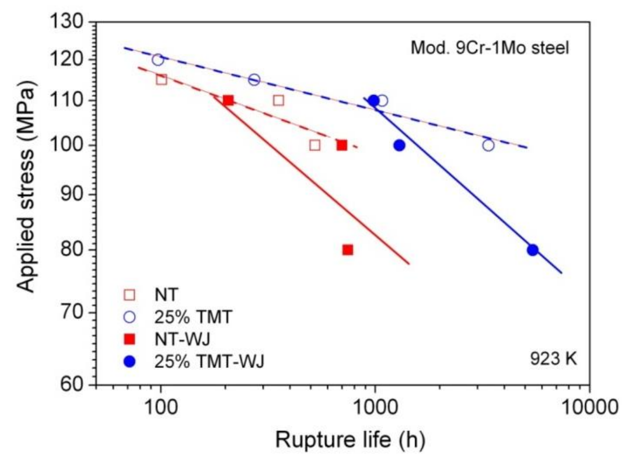

Fig. 5.34 Creep rupture life as a function of applied stress of NT and 25%TMT steels and their weld joints at 923 K.

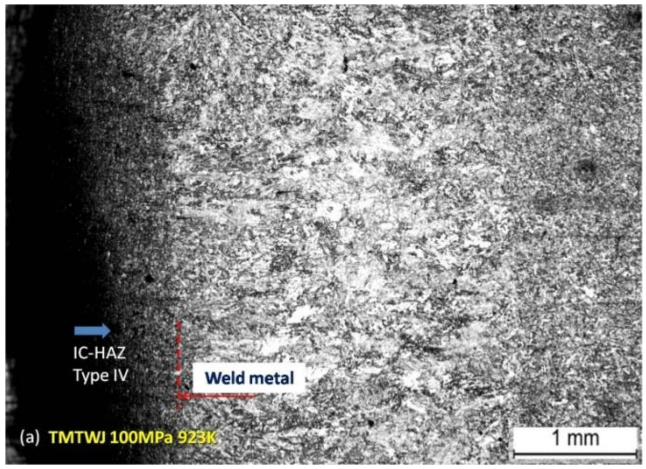

Fig. 5.35 Optical macrostructure creep exposed at 923 K and 100 MPa 25%TMT steel weld joint.

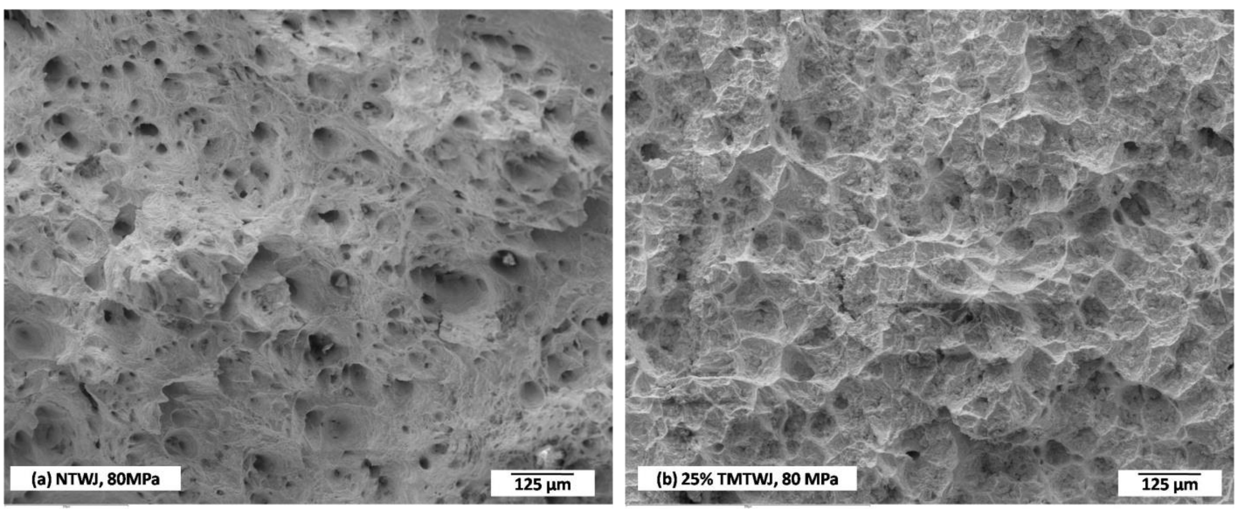

Fig. 5.36 Fracture surface of creep exposed (a) NT and (b) 25%TMT steel weld joints at 923 K and 80 MPa applied stress.

5.3.3 Microstructure evolution under creep

SEM observations of the microstructure across the weld joint of creep exposed TMT specimen are shown in Fig. 5.37. Coarser precipitates have been observed in the ICHAZ (Fig. 5.37(a)) and FGHAZ (Fig. 5.37(b)) regions of the HAZ than in the BM, WM and CGHAZ, Figs.

5.37 (c), (d) and (e) respectively. Size of the $M_{23}C_6$ precipitates across the weld joint after creep test at 923 K and 100 MPa is shown in Fig. 5.37(f). It may be noted that significant coarsening of $M_{23}C_6$ precipitates occurred in the ICHAZ of the joint in comparison with the pre-creep condition. The variation in the size of the precipitates across the different regions of the weld joint follows more or less the same pattern as that in PWHT condition (Fig. 5.30). Predominant coarsening of $M_{23}C_6$ precipitate in the ICHAZ of modified 9Cr-1Mo steel (NT) weld joint under creep condition has been reported earlier [134]. The coarser $M_{23}C_6$ precipitates in the ICHAZ region of NT joint led to accelerated recovery process by loss of effective pinning of dislocations, which results in lower creep strength of (reduction in precipitation strengthening). The mechanical constraint imposed on the soft ICHAZ by adjacent stronger region resulted in predominant coarsening of $M_{23}C_6$ precipitate subsequent recovery of dislocation structure and localized deformation. The deformation constraint on the ICHAZ led to predominant cavitation. The presence of less carbon in the matrix of the TMT steel joint resulted in lower extent of $M_{23}C_6$ precipitate coarsening. Hardness variations across crept TMT weld joint Fig. 5.38 indicates a lower hardness in comparison with pre-creep condition and a dip at the ICHAZ (Fig. 5.31(b)). The coarsening of $M_{23}C_6$ precipitate, and recovery of dislocation structure in the ICHAZ under creep exposure accompanied with deformation constraint imposed by adjacent stronger regions resulted in its further weakening. The enhanced MX precipitation through TMT processing of modified 9Cr-1Mo steel and consequent reduction in coarsening of $M_{23}C_6$ precipitates under weld thermal cycle as well as during creep led to improvement in type IV cracking resistance of TMT steel weld joint significantly.

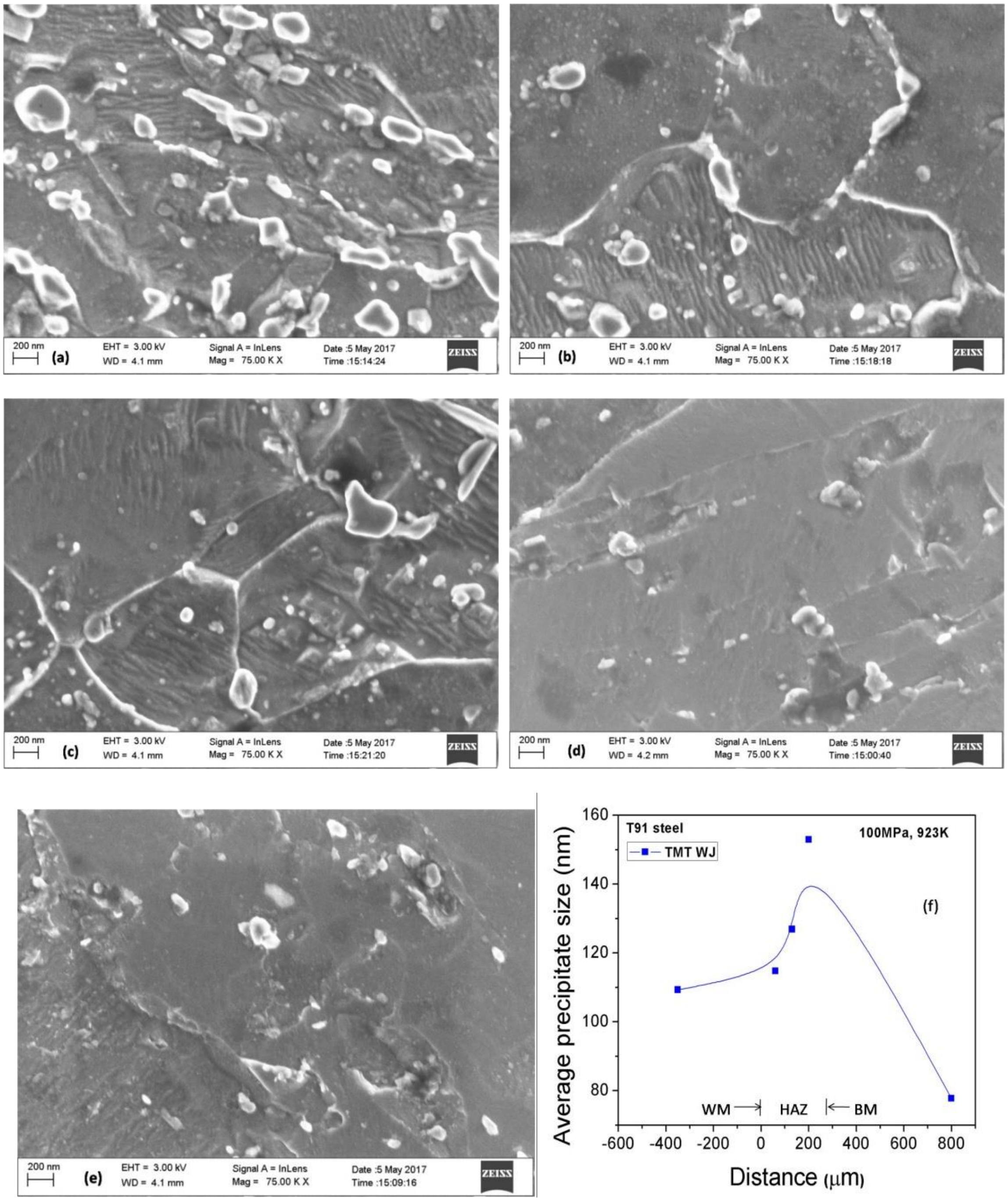

Fig. 5.37 SEM microstructures of (a) ICHAZ, (b) FGHAZ, (c) BM, (d) WM, (e) CGHAZ and (f) variation of precipitate size of creep exposed 25%TMT steel weld joint, creep tested at 923 K and 100 MPa.

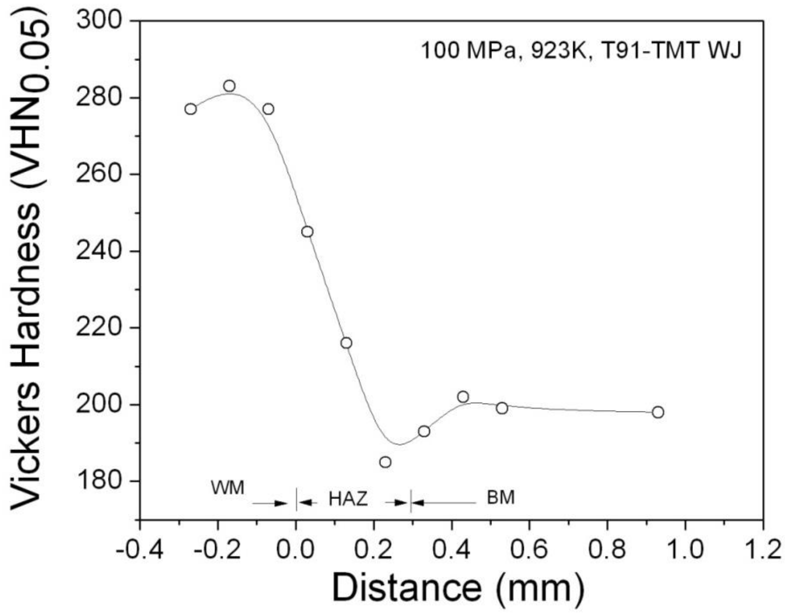

Fig. 5.38 Variation of hardness across the creep exposed 25%TMT steel weld joint, creep tested at 923K and 100 MPa.

5.4 Conclusions

Based on the detailed investigation on the effect of the extent of deformation in austenite phase field during TMT processing of modified 9Cr-1Mo steel on the microstructure and creep behaviour (Type IV cracking behaviour), the following conclusions have been drawn:

(i) TMT processing leads to a refinement of the microstructure of modified 9Cr-1Mo steel with more uniform precipitation of fine MX particles with finer martensite lath structure along with uniform and fine $M_{23}C_6$ precipitation. High degree of TMT deformation ($\geq$ 40%) led to ferrite formation.

(ii) The deformation behaviour assessed by stress relaxation testing revealed less relaxation indicating better microstructural stability on high temperature exposure for the TMT processed steel.

(iii) Creep deformation resistance and rupture strength of the steel improved remarkably with extend of deformation up to 25% compared to NT steel due to sluggish recovery of the dislocation substructure pinned more effectively by the stable MX particles. TMT processing for 40 and 50% deformation precludes the benefits of TMT due to presence of ferrite phase.

(iv) Extent of deformation in the austenite phase field during TMT processing is important. It is shown that 25%TMT is optimum to ensure that there is no ferrite phase formation, which decreases creep resistance.

(v) The enhanced MX precipitation through TMT processing and reduction in coarsening of $M_{23}C_6$ precipitates under thermal cycle resulted in improved creep rupture life of TMT joint than the NT joint. Thermo-mechanical processing led to significant enhancement of type IV cracking resistance of modified 9Cr-1Mo steel.

CHAPTER 6

Type IV Cracking Behaviour in P92 Steel

6.1 Introduction

In this chapter, creep deformation and rupture behaviour of 9Cr-1.8W-0.5Mo-VNb steel (P92), and weld joints of this steel fabricated by employing NG-TIG and TIG welding processes have been studied in order to understand the influence of solid solution strengthener W in this steel. Creep tests were carried out on the base steel in the applied stress range of 80 - 220 MPa at 873, 923 and 973 K, weld joints (80 - 150 MPa stress at 923 K) and HAZ constituents (120 - 170 MPa stress at 923 K). Tensile tests at 300 and 923 K at a strain rate of 3 x 10^{-3} s^{-1} have been carried out on different constituents of HAZ. The microstructural evolution was assessed by performing detailed metallography on base steel and weld joints to have insight of the creep deformation and damage/failure mechanism. Creep rupture life of base steel and weld joint, tensile strengths and creep rupture life of the various HAZ regions in the joint and WSRF for the weld joint have been discussed in this chapter.

6.2 P92 steel base metal

6.2.1 Microstructure of the steel

Microstructure of the P92 steel in the normalized and tempered condition is shown in Fig. 6.1(a). The prior-austenite grain size of the steel was around 20 µm. Microstructure of the steel consists of tempered martensitic lath structure (Fig. 6.1(b) and (c)) with transformation-induced high dislocation density of about 7 x 10^{14} m^{-2} [135]. The width of the martensitic lath structure was ~ 400 nm. Prior-austenite grain boundaries and sub-grain boundaries were decorated with $M_{23}C_6$ precipitates. Average size of the $M_{23}C_6$ precipitate measured from TEM micrograph was ~ 90 nm. The energy dispersive spectroscopy (EDS) spectrum analysis of the precipitates depicted the enrichment of tungsten about 7 - 8 wt. % (Fig. 6.1(d)). Presence of tungsten in the steel reduces the coarsening rate of $M_{23}C_6$ precipitates at high temperatures [136]. The MX type of V and Nb-rich carbide and carbo-nitride precipitates (around 30 nm as measured from FEG-SEM micrograph) in the intra-laths regions were observed in the steel. The presence of $M_{23}C_6$ and MX precipitates in the prior-austenite, sub-grain boundaries and intra-lath regions resists the movement of boundaries and dislocations respectively.

6.2.2 Creep deformation behaviour of the steel

Creep curves of P92 steel at 923 K over a stress range of 110 to 170 MPa are shown in Fig. 6.2(a). The variations of creep strain with creep exposure exhibited the instantaneous strain on loading, distinct primary creep, narrow region of secondary creep and prolonged tertiary creep regimes at 923 K. Similar creep deformation behaviour has been noticed at 873 and 973 K too. Narrow region of secondary and prolonged tertiary creep regimes have generally been observed in 9% Cr ferritic-martensitic steels [78,115,130,137,138]. However, clear primary creep regime was not observed under lower stress levels at 973 K (Fig. 6.2(b) and (c)). Longer secondary creep regime observed at 973 K under low stress level in the steel might be due to increase in solid solution strengthening contribution from tungsten by not forming Laves phase (Fe_2W) particles. The variations of creep rate with creep exposure at 873 and 923 K over a stress range of 110 to 220 MPa are given in Fig. 6.3. Creep rate of the steel with creep exposure decreases significantly in the primary creep regime, and subsequently shows the minimum creep rate regime followed by a faster rate of creep deformation in tertiary stage till the time of fracture. Maximum duration was spent in the tertiary state of creep deformation at all test conditions except under the low stress level at

973 K. Variation of creep rate with creep strain at various temperatures and stresses are given in Fig. 6.4. The creep rate decreases with increase in creep strain in the primary regime due to work hardening by dislocation multiplication and their interactions. Stabilized creep rate occurs in the short secondary strain regime where the work hardening effect is counter balanced by the recovery process such as dislocation annihilation and rearrangement. Rapid increase in creep rate in the tertiary creep strain is attributed to enhancement in recovery process, growth of precipitates and cavities [78,130,138]. However, the decreasing creep rate behaviour from initial deformation was not clearly observed under lower stress level at 973 K (Fig. 6.4(c)). This might be due to faster annihilation of dislocations generated in the primary creep region or increase in remobilization of immobile dislocations due to higher temperature. Strain to reach onset of tertiary creep varied with applied stress and test temperatures (Fig. 6.4 and 6.5); onset of tertiary creep deformation occurred at ~ 2 % creep strain at 873 K. However, strain to reach onset of tertiary creep decreases from 2% to 1% with decrease in stress level at 923 K. The change (decrease) in dislocation density up to secondary stage of deformation is relatively higher as compared to tertiary creep regime, where change in precipitation behaviour and boundary dimensions were considerably lower up to ~1% of creep strain or minimum creep rate regime [130,139]. Creep strain accumulation of about 1% for the onset of tertiary creep has been reported in W strengthened steels at 923 K [130,138]. Creep strain for onset of tertiary creep in the range of 0.5 to 2.5 % has been observed at 973 K (Fig. 6.5). The decrease and increase in creep strain accumulation to onset of tertiary creep (ε_t) at 923 K and 973 K respectively under lower stress level might be due to decrease in recovery rate of dislocation structure at 923 K, increase in recovery rate of dislocation structure and solid solution strengthening by tungsten at 973 K.

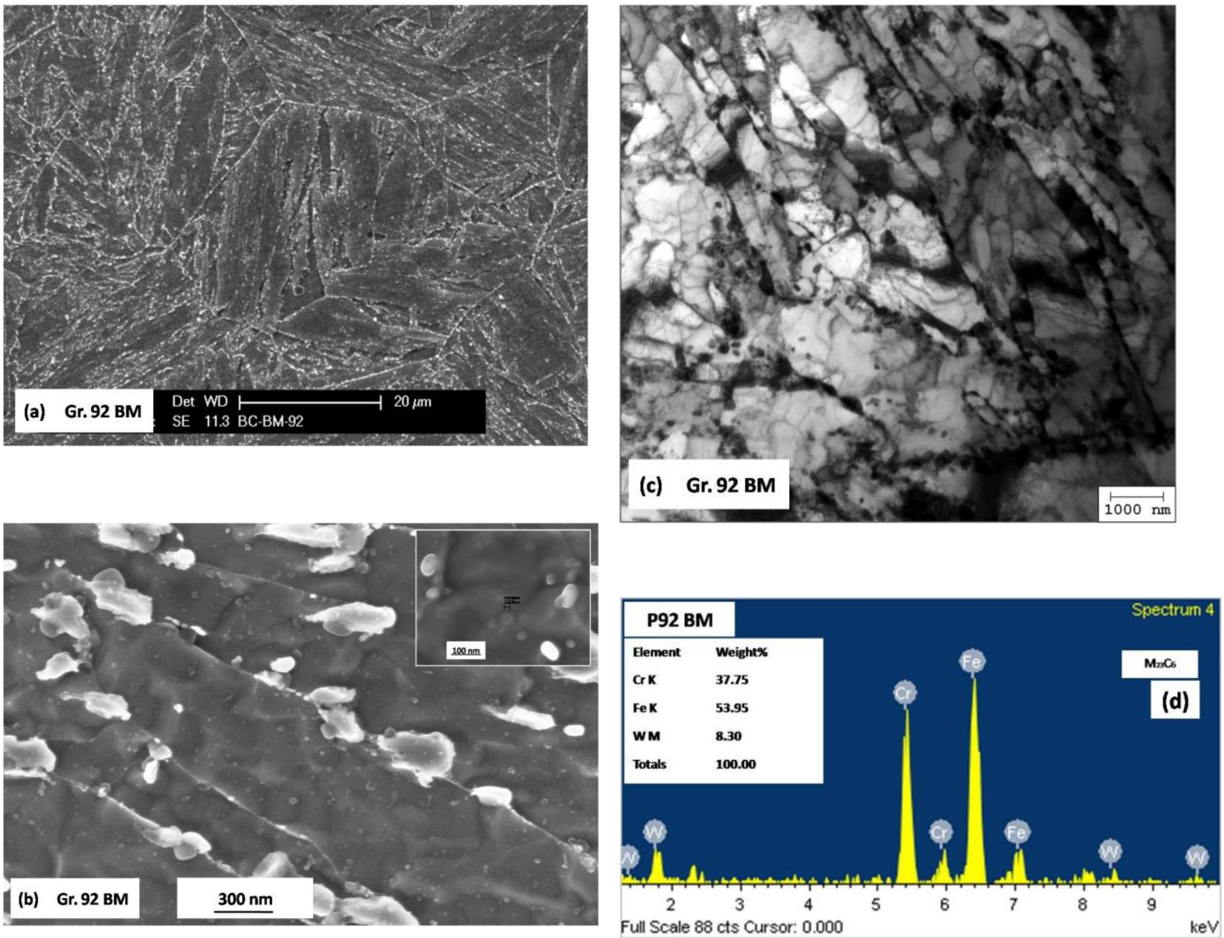

Fig. 6.1. P92 steel in the normalized and tempered condition (a) SE-SEM, (b) FEG-SEM and (c) TEM micrographs depicts the prior-austenite boundaries and lath regions decorated by $M_{23}C_6$ and MX precipitates, and (d) EDS spectra obtained from the $M_{23}C_6$ precipitate.

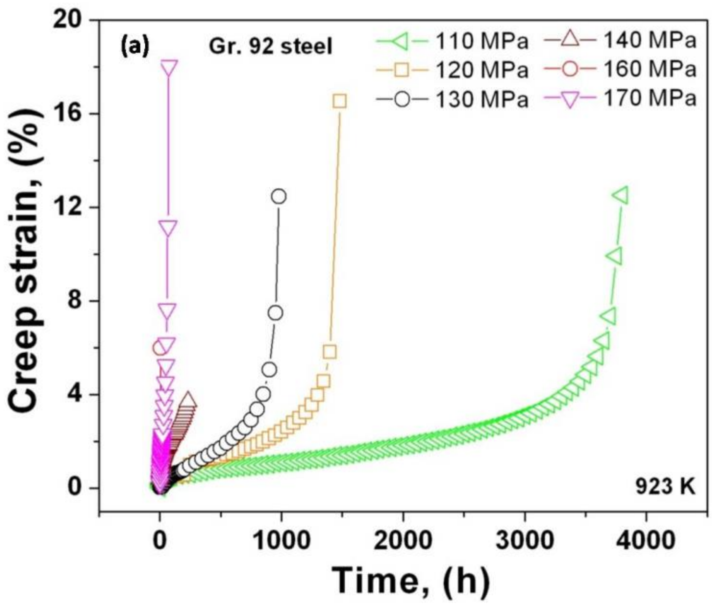

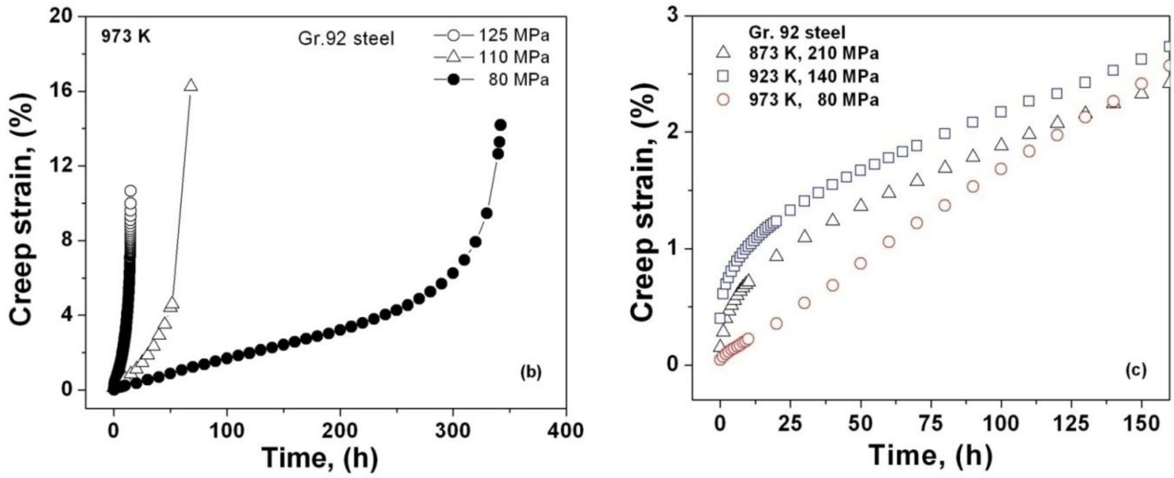

Fig. 6.2 Variation of creep strain (%) with time of Gr.92 steel at (a) 873 K (600 °C) and (b) 973 K (650 °C) over stress range of 80 MPa to 170 MPa, and (c) magnified primary creep regime at 873 K (600 °C), 923 K (650 °C) and 973 K (700 °C).

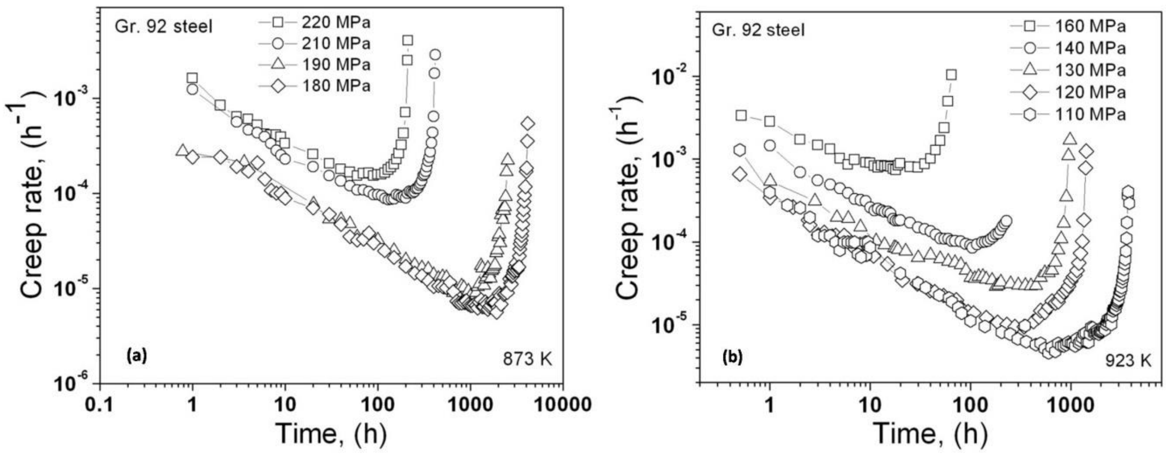

Fig. 6.3 Variation of creep rate with time of Gr. 92 steel at (a) 873 K (600 °C) and (b) 923 K (650 °C) over stress range of 110 MPa to 220 MPa.

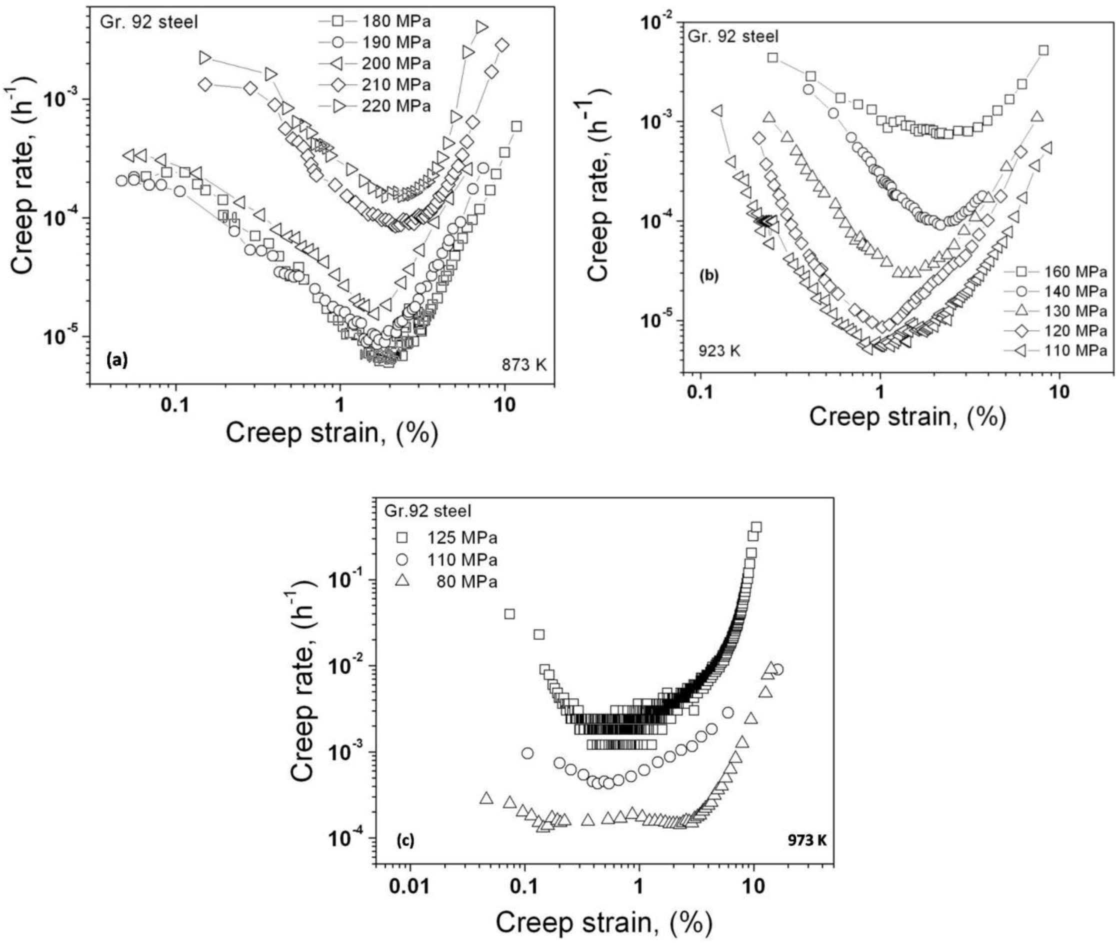

Fig. 6.4 Variation of creep rate with creep strain (%) of Gr.92 steel at (a) 873 K (600 °C), (b) 923 K (650 °C) and (c) 973 K (700 °C) over stress range of 80 MPa to 220 MPa.

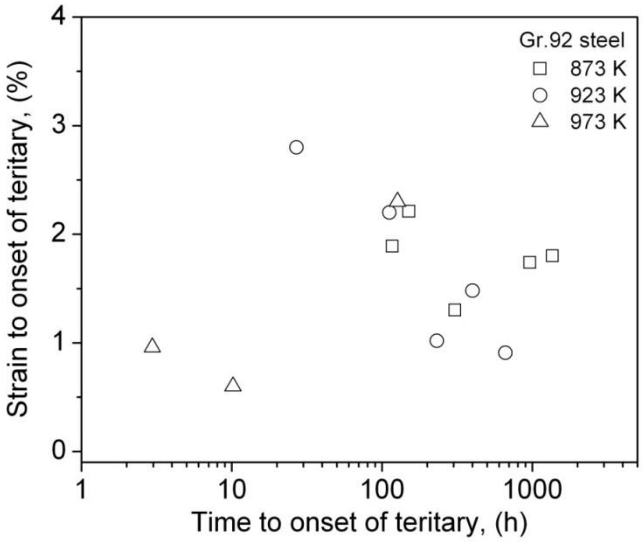

Fig. 6.5 Variation of strain to onset of tertiary creep with time to onset of tertiary creep regime of Gr.92 steel at 873 K (600 °C), 923 K (650 °C) and 973 K (700 °C).

6.2.3 Stress and temperature dependence of minimum creep rate

The variation of minimum creep rate ($\dot{\epsilon}_{min}$) with applied stress at 873, 923 and 973 K are shown in Fig. 6.6. The variation of minimum creep rate ($\dot{\epsilon}_{min}$) with applied stress (σ) followed Norton's power law of creep as $\dot{\epsilon}_{min} = A\sigma^n$, where *A* is a constant, *n* is the stress exponent of the matrix. The variation in *n* value is found to represent the change in creep deformation mechanisms in the materials; *n* =1 for Harper-Dorn creep where the dislocation density is invariant with stress and *n*=3 corresponds to the dislocation glide controlled by the rate of migration of solute atoms that are attached to the moving dislocations (solute-drag creep). *n*=5 corresponds to creep by dislocation climb controlled process. This is generally observed in materials which show sub-grain structure formation and power law breakdown (PLB) behaviour. When creep deformation occurs under constant microstructure a value of *n*=8 is observed under dislocation climb controlled creep. PLB occurs due to excess vacancy generation at higher stresses, and cross slip and obstacle controlled glide [140]. In the present investigation, stress exponent values of 15.1, 12.3 and 5.8 have been observed at 873 K, 923 K and 973 K respectively (Table 6.1). *n* value for this steel does not change with stress in the investigated stress range. However, significant breakdown of stress exponent under longer creep exposure (> 10000 h) in P92 steel at 923 K has been reported [135]. The obtained *n* values are higher than the diffusion controlled dislocation based creep deformation models [107,140]. *n* values of 12 and 13 have been reported in literature in P92 type steels at 923 K [141]. A decrease in *n* value with increase in test temperatures occurred in the steel due to extensive microstructural changes at higher test temperatures such as formation (Laves phase) and coarsening of precipitates (Laves phase, $M_{23}C_6$). Also, a decrease in coherency strain between MX precipitates and matrix results in lower stress dependence of minimum creep rate [78,107,130,141,142]. The σ and temperature (*T*) dependencies of creep rate of pure metals and single phase alloys are generally described by Bird-Mukherjee-Dorn (BMD) relationship as [105],

$$\frac{\dot{\epsilon}kT}{D_o\mu b} = A\left(\frac{\sigma}{\mu}\right)^n \exp(-\frac{Q_c}{RT})$$

where $D=D_0 \exp(-Q_c/RT)$) is the diffusion coefficient, D_0 is the frequency factor, Q_c is the activation energy for creep deformation, R is the gas constant, T is the temperature in Kelvin, μ is the shear modulus, b is the burgers vector, k is the Boltzmann constant, n is the stress exponent, A is a dimensionless constant. The creep parameters n and Q are used to identify the operating creep mechanisms. From the slope of the Arrhenius plot $\ln(\dot{\epsilon}_{\min})$ versus $1/T$, Q_c was evaluated at constant stress (Fig. 6.7) as 619.6 kJ/mole which is comparable to the reported activation energy for Fe with various Cr concentrations [106]. Also, the Q_c evaluated from the present investigation is comparable with the reported energy values of 510 kJ/mole and 510 to 621 kJ/mole for ferritic steels [5,107]. The observed values of n and Q_c are high compared to those for the solid solution Fe-based single phase alloys because of strong interaction between precipitates and mobile dislocations, which is generally described by threshold stress [105,107,113] and is discussed in the next section.

6.2.3.1 Threshold stress and true creep activation energy

In order to understand the interactions between precipitates and mobile dislocations in P92 steel, threshold stress (σ_{th}) has been evaluated. Threshold stress for a specific creep mechanism is generally defined as the stress below which creep deformation does not occur by that mechanism. Hence, an effective stress has been considered as responsible for creep deformation instead of applied stress for alloys strengthened by particles or precipitates [26]. The threshold stress (σ_{th}) can be determined using the modified version of Mukherjee-Bird-Dorn creep equation as [105,107,113],

$$\dot{\epsilon}_{min} = A\left(\frac{\sigma_a - \sigma_{th}}{\mu}\right)^n \exp(-\frac{Q_c}{kT})$$

Stress exponent value about 4, and similar activation energy for creep (Q_C) and lattice self diffusion (Q_D) have been observed in pure metals [105,107]. The threshold stress is evaluated from strain rate ($\dot{\epsilon}^{1/4}$) versus applied stress plot, where a value of 4 has been used for the stress exponent of the matrix (Fig. 6.8). The intercepts on the stress axis at zero strain rate provides the σ_{th} at various temperatures; values of 138, 83 and 30 MPa were obtained at 873, 923 and 973 K respectively. It is significant to note that the threshold stress decreases with increase in temperature due to the increase in precipitates size and decrease in dislocation density on high temperature exposure.

The variation of $\dot{\epsilon}_{\min}$ with effective stress normalized by shear modulus $((\sigma_{a}- \sigma_{th})/\mu)$ is shown in Fig. 6.9. Stress exponent values of 3.54, 3.13 and 3.90 were obtained at 873, 923 and 973 K respectively. The true creep activation energy (Q_c) from the $\ln(\dot{\epsilon}_{\min})$ versus $1/T$ plot was evaluated at constant normalized stress $((\sigma_a-\sigma_{th})/\mu)$ of 4.91×10^{-4} as shown in Fig. 6.10. A value of Q_c 244 kJ/mole has been obtained from the slope of the Arrhenius plot. This value is similar to the activation energy for self diffusion of α - iron, 241 kJ/mole [104]. True activation energy value of 244 kJ/mole has been reported for creep deformation of precipitation strengthened Fe-19Cr steel [107]. Fig. 6.11 shows the variation of minimum creep rate normalized by creep activation energy with effective stress normalized by shear modulus, where the values for different temperatures collapse into a single line and slope, which is rationalized with matrix stress exponent of 4 and creep activation energy 244.1 kJ/mole [105].

6.2.3.2 Creep mechanisms

The following creep mechanisms were considered to explain the existence of threshold stress in precipitation strengthened metals: (i) detachment of dislocations from precipitates, (ii) shearing of precipitates, (iii) bypassing of precipitates by Orowan dislocation looping and (iv) dislocation climb over precipitates [107,142]. The detachment of dislocations from precipitates is not likely where the coherent precipitates exist in the matrix. This mechanism is not considered in the steel since the precipitates (MX and $M_{23}C_6$) exist in high degree of coherency with the matrix [78,130,141,142]. Shearing of precipitates is another possible mechanism, and precipitates shearing stress can be evaluated as given below [107],

$$\sigma_{\mathrm{sh}} = \frac{0.81M\gamma}{2b}\left(\frac{3\pi\varphi}{8}\right)^{1/2}$$

where M = 2.9 is the mean orientation factor for bcc matrix, b = 0.248 nm is the burgers vector, φ is the volume fraction of precipitates, γ is the particle-matrix interface energy. The interface energy is given as, $\gamma = \frac{\mu b\theta(A - ln\theta)}{4\pi(1-v)}$, where μ is the shear modulus of the matrix (61.6, 59.3 and 57.0 GPa at 873, 923 and 973 K respectively), θ is the misorientation angle, A is 0.45, v is the Poisson ratio (0.3). The interface energy has been evaluated from the above equation by considering misorientation angle 1.5 deg at different temperatures. The interface energy was about 0.11 J/m^2. The energy of interface does not change significantly with temperature, whereas it changes significantly with misorientation angle. A value of about 0.75 J/m^2 for the interface energy has been reported in the literature [106]. The shearing stress was evaluated for P92 steel using φ=0.23% for MX and 0.8 % for $M_{23}C_6$. The shearing stresses for precipitates were evaluated as 283, 273 and 264 MPa for MX and 513, 495 and 477 MPa for $M_{23}C_6$ at 873, 923 and 973 K respectively. The shearing stress values were higher than the threshold stress in the steel, hence the precipitates shearing mechanism was excluded. The Orowan dislocation looping stress is given by [107],

$$\sigma_{or} = \frac{M\ 0.4\ \mu b}{\pi\sqrt{(1-v)}} \frac{\ln\left(2\sqrt{\frac{2}{3}}(R)/b\right)}{\lambda}$$

where R is the radius of precipitate, λ is the distance between the precipitates, M, μ, b and v are same as mentioned previously. The precipitates size was measured from the FEG-SEM and TEM micrographs. The precipitates in the size ranges about 30 nm were considered as MX, and those about 50 nm and above were considered as $M_{23}C_6$. The inter-particle average distance was ~ 175 nm. The Orowan stress at different temperatures was estimated as 177, 170 and 163 MPa for MX (MX type of precipitate is mainly considered in this investigation which is generally maximum inside the laths region), and 197, 189 and 182 MPa for $M_{23}C_6$ at 873, 923 and 973 K respectively. These values are higher than the observed threshold stress in the steel, and hence, dislocation looping of precipitates has not been considered as creep deformation mechanism in the steel. The climb of dislocations is another possible creep mechanism, which generally occurs at stresses below that required for dislocation looping around the precipitate. The threshold stress arises due to increase in dislocation length during climb over the precipitates. Magnitude of threshold stress is found to change with the geometry of the dislocation climbing event [143]. Threshold stress normalized with Orowan stress ranges about 0.03 - 0.06 for general climb and 0.4 - 0.7 for local climb of dislocations [107]. A true activation energy value of 244 kJ/mole has been obtained in the steel, which is comparable to the self diffusion of the α-Fe 241 kJ/mole. The threshold stress normalized by Orowan looping stress values of 0.77, 0.48 and 0.18 have been obtained at 873, 923 and 973 K respectively. The obtained values of σ_{th}/σ_{or} ~ 0.18 - 0.77 and creep activation energy 244.1 kJ/mole demonstrate the occurrence of creep deformation by lattice diffusion assisted localised climb of dislocations at 873 K and 923 K, and transformation towards lattice diffusion assisted general climb of dislocation at 973 K in P92 steel.

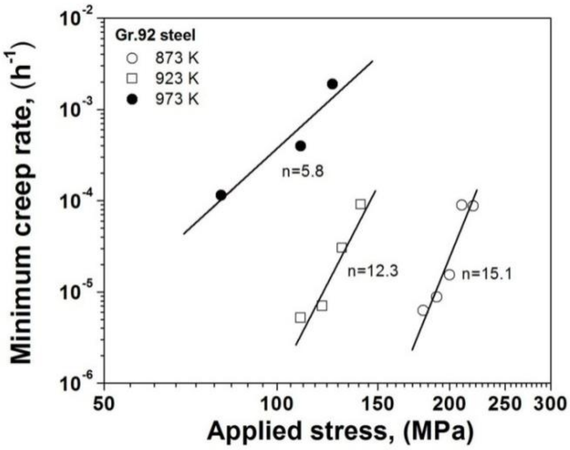

Fig. 6.6 Variation of minimum creep rate with applied stress of Gr.92 steel at 873 K (600 °C), 923 K (650 °C) and 973 K (700 °C).

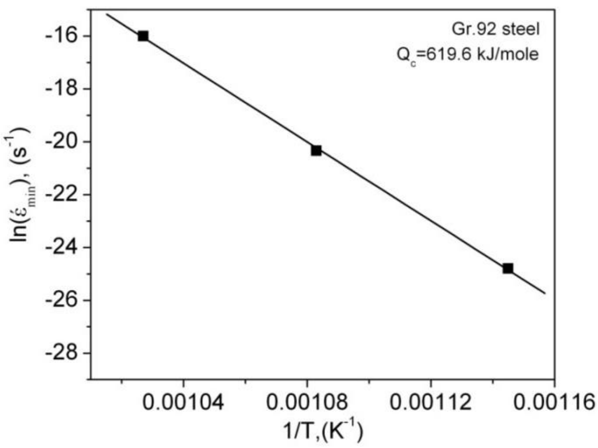

Fig. 6.7 Arrhenius plot of temperature dependence of minimum creep rate.

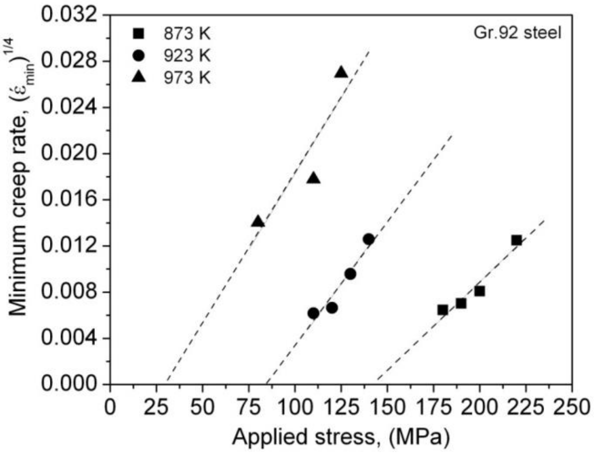

Fig. 6.8 Variation of minimum creep rate $(\acute{\varepsilon}_{min})^{1/4}$ with applied stress (σ_a) to obtain threshold stress at 873 K (600 °C), 923 K (650 °C) and 973 K (700 °C).

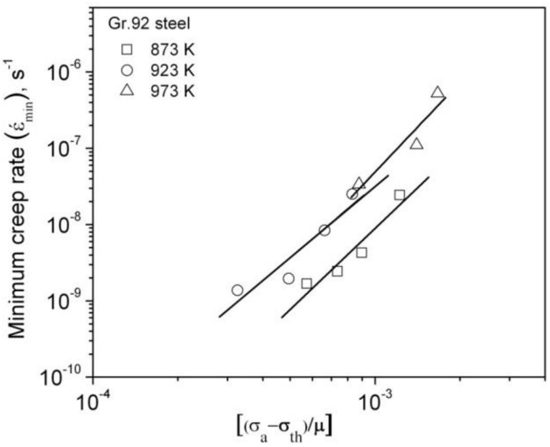

Fig. 6.9 Variation of minimum creep rate with normalized effective stress by shear modulus $[\sigma_a-\sigma_{th}]/\mu$ for P92 steel at 873 K (600 °C), 923 K (650 °C) and 973 K (700 °C).

Table 6.1 The values of stress coefficients and stress exponents for stress dependence minimum creep rate and rupture life of P92 steel.

Temperature, K	$\dot{\epsilon}_{min} = A\sigma^{n}$		$t_r = A_1\sigma^{-n_1}$	
	A	n	A_1	n_1
873	3.84×10^{-40}	15.1	1.54×10^{38}	15.3
923	3.28×10^{-31}	12.3	5.75×10^{22}	9.4
973	8.62×10^{-16}	5.8	5.75×10^{15}	6.9

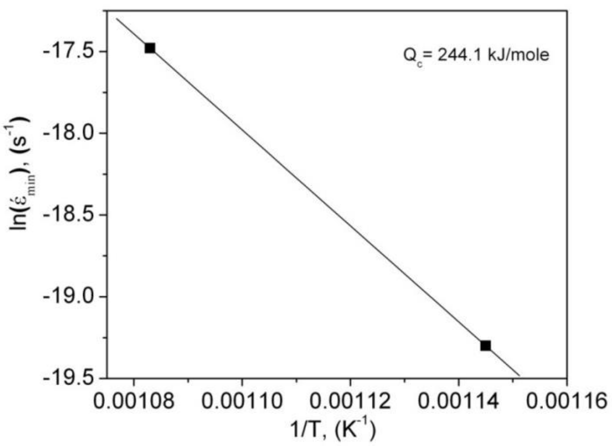

Fig. 6.10 Arrhenius plot of temperature dependence of threshold stress compensated minimum creep rate.

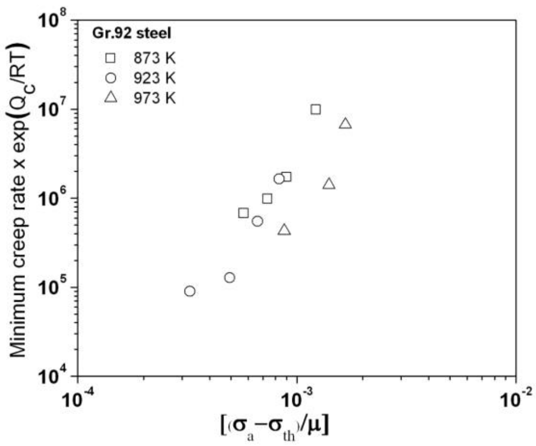

Fig. 6.11 Variation of normalized minimum creep rate by activation energy with effective stress by shear modulus.

6.2.4 Creep rupture life and ductility

The variation of creep rupture life with applied stress at various temperatures is shown in Fig. 6.12. The rupture life (t_r) decreases with increase in applied stress (σ_a) and test temperature. This variation obeyed the power law of creep similar to the variation of minimum creep rate with applied stress as $t_r = A_1\sigma^{-n_1}$, where A_1 is the stress coefficient and n_1 is the stress exponent. n_1 values of 15.3, 9.4 and 6.9 have been obtained at 873, 923 and 973 K respectively. The stress exponent does not vary within the investigated applied stress range. The creep rupture life with applied stress and test temperature is expressed as [133, 144], $t_r = A_1\sigma^{-n_1}\exp(\frac{Q_{c1}}{RT})$, where Q_{c1} is the apparent activation energy for creep rupture life, R is the gas constant, T is the temperature in K. The apparent activation energy for creep rupture of 599 kJ/mole has been obtained in this steel (Fig. 6.13) which is in close agreement with the apparent activation energy value of 624 kJ/mole for creep rupture reported for 9% Cr ferritic steels [133,144]. The breakdown of creep strength with decreasing applied stress has not been noticed in the investigated range of stress. However, the breakdown of creep strength under lower stress (> 10000 h creep exposure) regime has been reported in grade 92 steel and grade 91 steels due to significant modifications in the microstructural constituents of the steels, where change in stress exponent and activation energy also have been reported [144]. The breakdown of creep strength occurs early at higher temperatures [16]. The change in creep strength of Gr.91 steel has been observed around 50000 h at 923 K, and it is not evident up to 100000 h at 873 K [106]. The observed value of n and n_1 in the present investigation confirms a close correlation between the mechanism of creep deformation and rupture processes.

The variations of reduction in area (%) and elongation (%) with rupture life are shown in Fig. 6.14. The reduction in area decreased with increasing t_r at all test temperatures, and the decrement occurred earlier at higher test temperatures (Fig. 6.14 (a)). Also, the reduction in area (%) increased with increase in temperature. The coarsening of various phases (Laves, $M_{23}C_6$) led to decrease in reduction in area under lower applied stress. The elongation (%) varied between 15 to 20 %, and no systematic change has been observed in the investigated duration at various temperatures (Fig. 6.14 (b)). However, elongation (%) showed a small increasing tendency with increase in creep exposure. The stress enhanced recovery and coarsening of precipitates might have led to increased elongation (%) with creep exposure. Enhanced softening and precipitation in the stressed region have been reported earlier in modified 9Cr-1Mo and P92 steels [78,104,130].

SEM fractographs of creep ruptured specimens at various stress and test temperatures are shown in Fig. 6.15. Transgranular ductile (dimple) mode of fracture has been observed in all test conditions. However, changes in size and number density of dimples were observed. At low applied stress, extensive coalescence of micro-voids resulted in larger number density of dimples (Fig. 6.15(b)). The numbers of smaller dimples were more at high stress level and low temperature (Fig. 6.15(c) and (d)). The brittle mode of fracture accompanied by low reduction in area and hardness have been reported under long term creep exposure (>10000 h) in P92 steel [144]. However, significant degradation in rupture ductility has been reported only after ~25000 h at 923 K and above in P91 steel [115]. Laves phase (Fe_2W) has been observed at prior-austenite and subgrain boundaries under SEM-BSE mode (Fig. 6.16). Presence of Laves phase is confirmed from the BSE mode SEM image in which the tungsten rich Laves phase appeared as bright phase because of its higher average atomic number [81]. Creep cavities were associated with Laves phase. The large incoherent precipitates cause decohesion at the interface. The stress required for decohesion is lower. Cavitation occurs in the steel due to increase in stress concentration at the particles, which impede the motion of dislocations. Subsequent increase in localized stress at the particle-matrix interface, which experiences the excess localized plastic deformation led to micro-cracks.

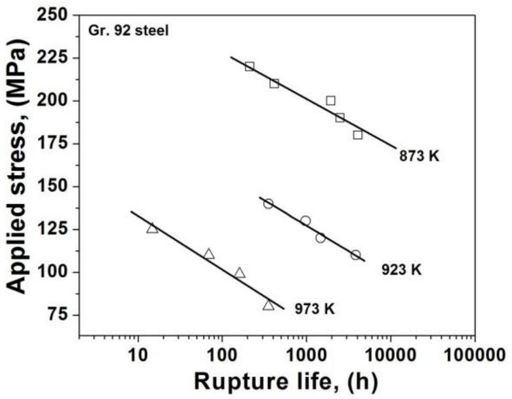

Fig. 6.12 Variation of creep rupture life with applied stress at 873 K (600 °C), 923 K (650 °C) and 973 K (700 °C).

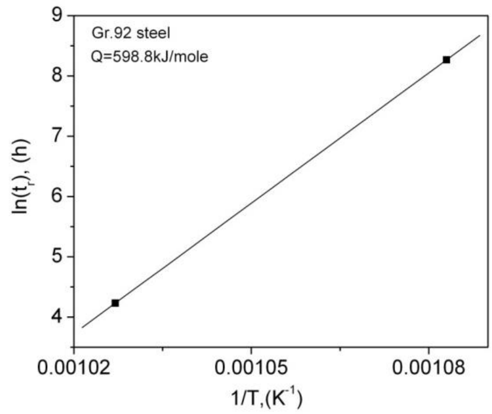

Fig. 6.13 Arrhenius plot of temperature dependence of creep rupture life.

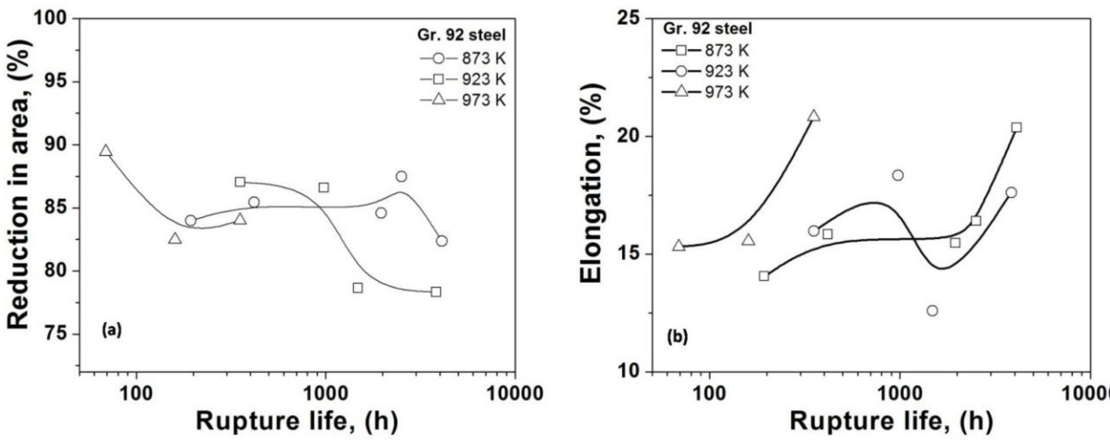

Fig. 6.14 Variation of (a) reduction in area (%), and (b) elongation (%) with rupture life at 873 K (600 °C), 923 K (650 °C) and 973 K (700 °C).

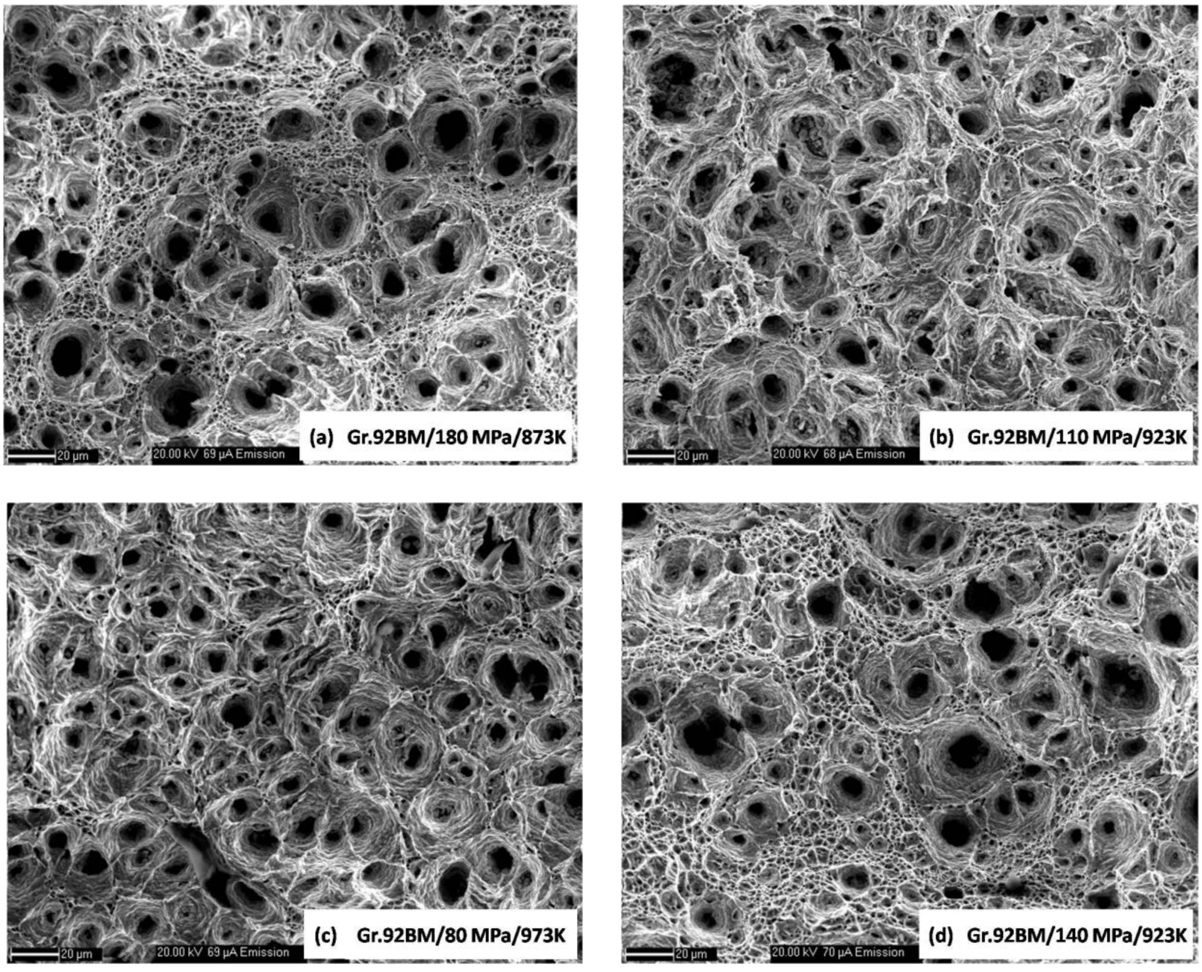

Fig. 6.15 Fracture surface of creep ruptured specimen at various temperature and stress.

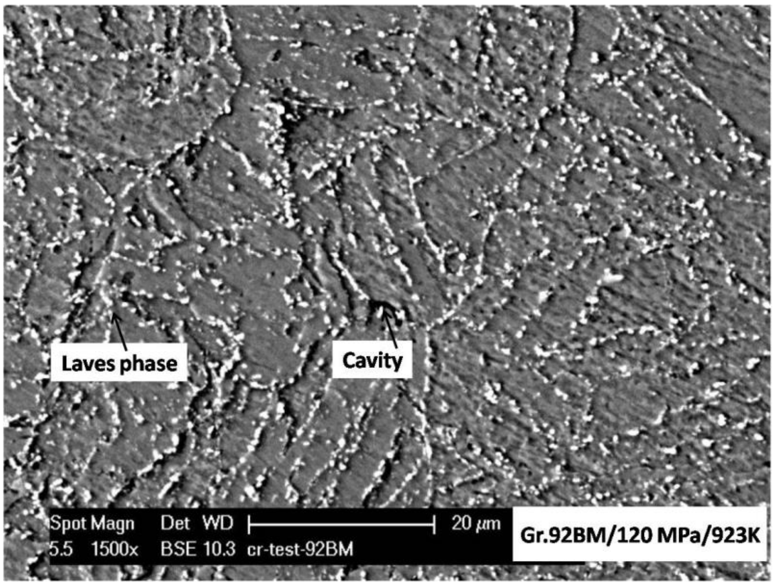

Fig. 6.16 SEM-BSE micrograph of Gr.92 steel creep ruptured at 923 K (650 °C) and 120 MPa depicting the presence of Laves phase and creep cavities.

6.2.5 Creep rate-rupture life relationships

The minimum creep rate and rupture life are related by the Monkman-Grant (MG) equation as [2,31],

$$\dot{\epsilon}_{min}^{\alpha} \cdot t_r = C_{\mathrm{MG}}$$

where $\dot{\epsilon}_{min}$ is the minimum creep rate, t_r is the rupture time, α is a constant close to unity and C_{MG} is a Monkman-Grant constant. For materials which fail under intergranular fracture and experience more secondary stage of creep deformation, $\dot{\epsilon}_{min} x\, t_r$ is a measure of strain to failure, and α and C are independent of test temperature and applied stress [5]. Monkman-Grant relationship has been modified by Dobes and Milika [5,145] for the materials which generally exhibit larger tertiary creep deformation and shorter secondary creep deformation regime as,

$$\dot{\epsilon}_{min}^{\alpha} \cdot \frac{t_r}{\varepsilon_f} = C_{\mathrm{MMG}}$$

where ϵ_f is the strain to failure, C_{MMG} is the modified Monkman-Grant constant. The variation of t_r and normalized rupture time by strain to failure (t_r/ε_r) with $\dot{\epsilon}_{min}$ are shown in Fig. 6.17. P92 steel obeyed the Monkman and modified Monkman-Grant relationship. The value of C_{MG} and C_{MMG} are 0.029 and 0.237 respectively (Fig. 6.17). Low values of C_{MG} and C_{MMG} confirms that major part of creep strain is accumulated in the tertiary creep regime. The validity of MG and MMG relationships in the steel shows the existence of close relationship between the creep deformation and fracture mechanisms. The time to onset of tertiary stage (t_{ot}) of deformation has been obtained from the time at which creep rate accelerates from minimum or steady state creep rate. The variation of t_{ot} with t_r (Fig. 6.18) followed a linear relationships as $t_{ot} = f.t_r$, where f is a constant. The value of f was about 0.248, which clearly demonstrates that this steel spent maximum (~75% of t_r) time in the tertiary stage of creep deformation. The extensive creep strain accumulation (lower values of C_{MG} and C_{MMG}) and larger creeping duration in the tertiary stage of deformation have been observed in the steel. Similar behaviour has been reported in various 9 wt.% Cr ferritic steels [5].

Based on the continuum damage mechanics (CDM) approach, creep damage tolerance factor (λ) has been defined as the ratio of strain to failure to Monkman-Grant ductility (MGD) as [5,145],

$$\lambda = \frac{\varepsilon_f}{\dot{\epsilon}\ t_r} = 1/C_{\mathrm{MMG}}$$

Creep damage occurs by loss of cross section (external-necking and internal-cavities) and changes in the microstructural constituents such as coarsening of precipitates and substructure, and decrease in dislocation density [5,145]. The creep damage tolerance factor has been used to assess the creep damage mode, whose value ranges from 1 to 20 for various structural materials. The value of λ=1 indicates for the materials possess low creep strain, high value of λ demonstrates the ability of materials to withstand strain concentrations without local cracking [5]. The value of λ in the range of 1.5 to 2.5 indicates that the damage occurs due to growth of cavities and higher than 2.5< λ >5 indicates necking dominated creep damage. The value of λ=5 and above indicates damages by decrease in dislocation density, and coarsening of precipitates and sub-grain structure. Creep damage tolerance factor values of 4 and 5 have been reported for grade 91 steel [5]. The creep damage tolerance factor λ=6 was observed in the present investigation (Fig. 6.19). This indicates the microstructure evolution such as coarsening of $M_{23}C_6$ precipitates which formed during tempering, formation and coarsening of Laves phase (Fe_2W), sub-grain coarsening and decrease in dislocation density coupled with limited cavity formation have contributed to damage in P92 steel.

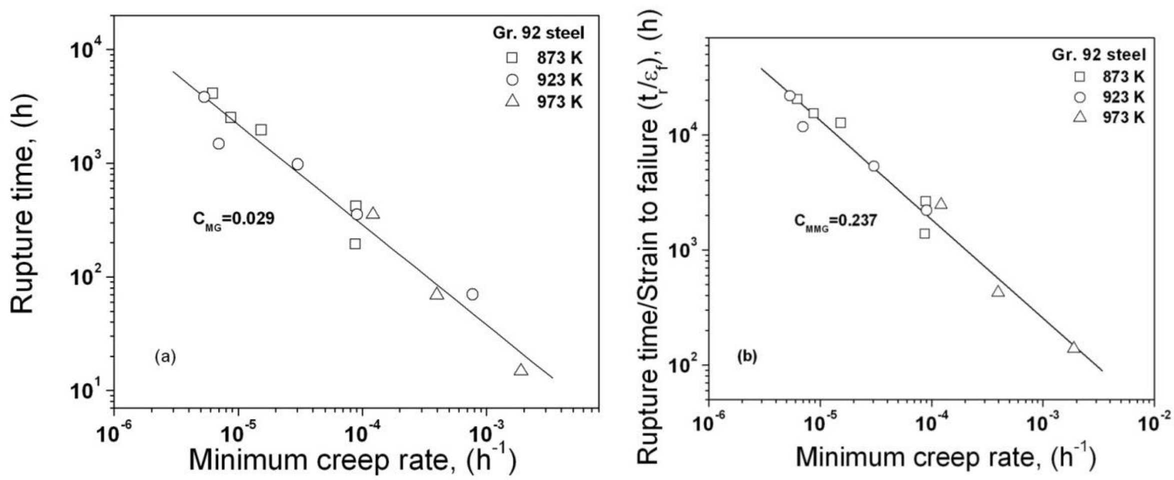

Fig. 6.17 Variation of (a) rupture time with minimum creep rate and (b) normalized rupture time by rupture strain with minimum creep rate at 873 K (600 °C), 923 K (650 °C) and 973 K (700 °C).

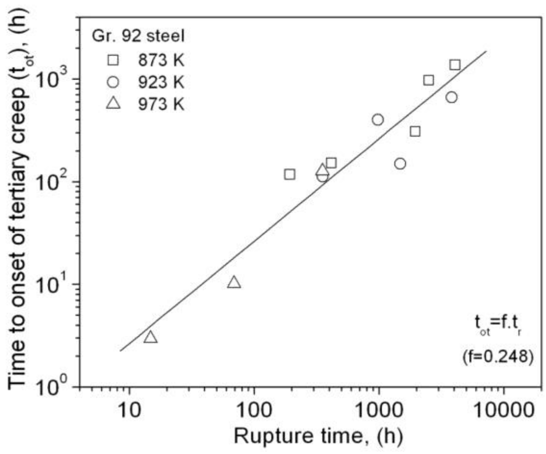

Fig. 6.18 Variation of time to onset of tertiary with rupture time of Gr.92 steel at 873 K (600 °C), 923 K (650 °C) and 973 K (700 °C).

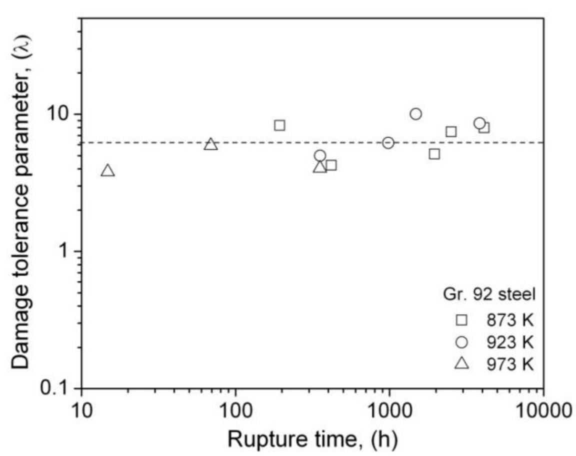

Fig. 6.19 Variation of damage parameter with rupture time of Gr.92 steel at 873 K (600 °C), 923 K (650 °C) and 973 K (700 °C).

6.3 P92 steel weld joint

In order to study the type IV cracking behaviour of the P92 steel weld joint, creep tests have been conducted at 923 K on specimens extracted from P92 weld joints fabricated by Narrow Gap-TIG (NG-TIG) welding process. Detailed metallographic analysis of the creep ruptured specimens has been performed to gain an insight into the operating failure mechanism based on the evolution of precipitates and cavitation under creep. Creep rupture behaviour of NG-TIG and A-TIG weld joints have been compared. The details of the investigations and the results are presented in the following sections.

6.3.1 Microstructure and hardness of the weld joint

Microstructure details of P92 steel in the normalized and tempered (NT) condition has been given in section 6.2. The plates were edge prepared with groove angle of 15° and butt welded using narrow-gap TIG welding process using 1.2 mm diameter filler wire. Macrograph of NG-TIG weld joint depicting weld metal, HAZ and base metal is shown in

Fig. 6.20. The optical micrographs observed at different regions across the joint such as CGHAZ, FGHAZ, ICHAZ and base metal are shown in Fig. 6.21(a-d). The prior-austenite grain size at different regions of HAZ depicts the different peak temperatures experienced during weld thermal cycle, which influenced the dissolution and coarsening of precipitates in addition to austenite transformation under weld heating cycle [3,10,146]. The PAG size decreased from fusion boundary to base metal with a predominant dip at the ICHAZ region which is close to unaffected base metal of the joint (Fig. 6.22). The dissolution of precipitates (MX and $M_{23}C_6$) in the steel adjacent to fusion boundary during weld heating cycle led to coarsening of austenite grains (Fig. 6.21(a)). The presence of MX precipitates (that remain undissolved due to the lower temperature experienced) resists the mobility of austenite grain boundary, which assists to form fine grains (FGHAZ) between CGHAZ and ICHAZ region (Fig. 6.21(b)). Finer PAGs were observed in the ICHAZ (Fig. 6.21(c)) which undergoes the partial transformation to austenite and predominant coarsening of $M_{23}C_6$ precipitates upon heating between Ac_3 and Ac_1 temperature regime [71,130,146]. Microstructure of the unaffected base metal is presented in (Fig. 6.21(d)). The average PAG size of the CGHAZ, FGHAZ, ICHAZ and base metal were 27±5 μm, 11±3 μm, 8±2 μm and 21±5 μm respectively. PAG size influences the type-IV cracking behaviour in addition to other microstructural constituents in the 9-12% Cr ferritic steel weld joints [91].

SEM SE and BSE mode micrographs observed at the different regions of weld joint are shown in Fig. 6.23. The PAG, packet, block and lath boundaries were decorated by $M_{23}C_6$ precipitates. MX precipitates were observed predominantly in the intra-lath region, which are relatively finer in comparison with $M_{23}C_6$ precipitates. Laves phase was not observed in the pre-creep condition of weld joint (Fig. 6.23(b,d,f,h,j)) [71,81]. The $M_{23}C_6$ precipitates were coarser in the ICHAZ (164 nm), compared to those in the weld metal (110 nm), CGHAZ (135 nm), FGHAZ (140 nm) and base metal (154 nm) (Fig. 6.24). The dissolution of $M_{23}C_6$

precipitates during welding and subsequent formation of $M_{23}C_6$ precipitates during PWHT results in finer $M_{23}C_6$ precipitates in the CGHAZ (Fig.7.23(c)) and FGHAZ (Fig. 6.23(e)) as compared to ICHAZ (Fig. 6.23(g)) and BM (Fig. 6.23(i)). During welding as well as PWHT predominant coarsening of $M_{23}C_6$ precipitates occurs in the ICHAZ region than in other regions. $M_{23}C_6$ precipitates formed in the BM during tempering coarsen under PWHT. TEM micrographs observed in the CGHAZ, FGHAZ and ICHAZ regions are shown in Fig. 6.25. Coarser $M_{23}C_6$ precipitates and subgrain formation with decrease in dislocation density were predominantly noticed in the ICHAZ (Fig. 6.25(c)) as compared to CGHAZ (Fig. 6.25(a)) and FGHAZ (Fig. 6.25(b)) regions due to weld thermal cycle. The finer precipitates effectively pin the boundaries and dislocations, which delay the recovery of dislocation structure in comparison with the coarser precipitates. The $M_{23}C_6$ and MX precipitates were analyzed by energy dispersive spectroscopy (EDS) (Fig. 6.26). MX [V(C,N)] is thermally more stable than $M_{23}C_6$ and Laves phase (Fig. 6.26(b)). About 8 to 12 wt. % tungsten was found to be present in the $M_{23}C_6$ carbide in P92 steel (Fig. 6.26(a)), which led to decrease in the $M_{23}C_6$ precipitate coarsening under weld thermal cycle and creep due to lower mobility of the constituent elements. In the ICHAZ region, the boundaries were relatively free from fine $M_{23}C_6$ precipitates due to partial transformation to austenite upon heating and formation of new boundaries during weld thermal cycle, which led to reduction in boundary strengthening.

The variation of hardness with distance across the weld joint is shown in Fig. 6.27. A decrease in the hardness from the weld metal (about 300 VHN) to the base metal (240 VHN) with a dip in the ICHAZ region (about 210 VHN) was observed. The hardness of the CGHAZ and FGHAZ was about 270 VHN and 220 VHN respectively. The decrease in hardness from the weld metal through HAZ indicates the decrease in austenisation temperature and reduced dissolution of precipitates/increase in coarsening of precipitates during weld heating cycle. The coarsening of $M_{23}C_6$ precipitates and tendency of sub-grain formation with reduction in dislocation density results in lower hardness at the ICHAZ and FGHAZ in comparison with its adjacent regions. The predominant loss of hardness in the ICHAZ as compared to other regions in the steel weld joint has been attributed to the coarsening of $M_{23}C_6$ precipitates reducing their effectiveness in strengthening along with loss of carbon and alloying elements reducing the solid solution strengthening, loss of precipitates at the boundaries and sub-grain formation with reduction in dislocation density (Fig. 6.25(c)). The steels with lower hardness in the pre-creep condition are reported [81,146] to have lower creep rupture life.

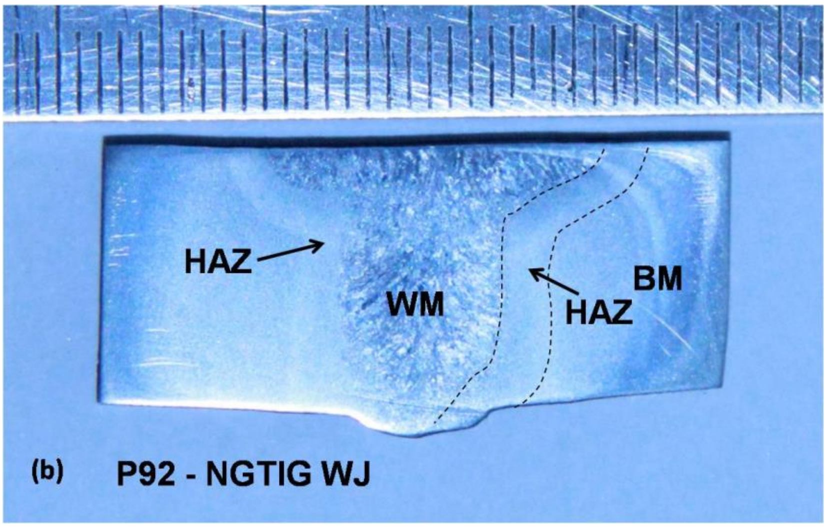

Fig. 6.20 Macrograph of P92 steel NG-TIG weld joint.

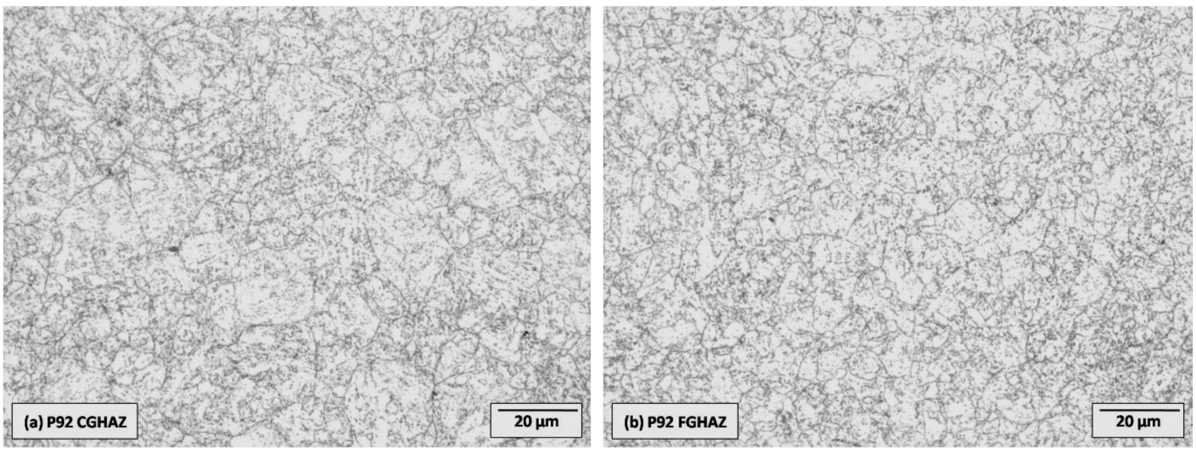

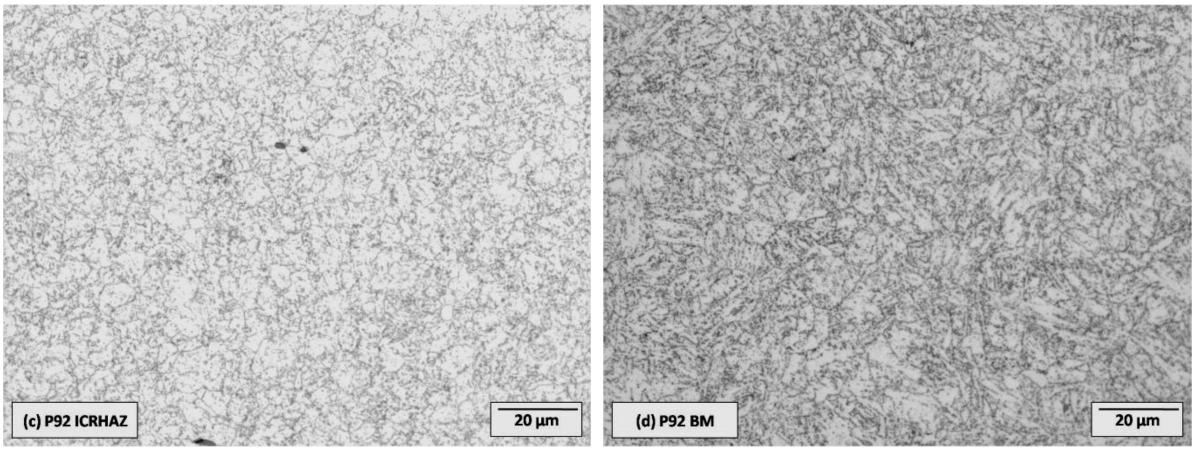

Fig. 6.21 Optical microstructure observed across the HAZ (a) CGHAZ, (b) FGHAZ, (c) ICHAZ and (d) base metal of P92 steel NG-TIG weld joint.

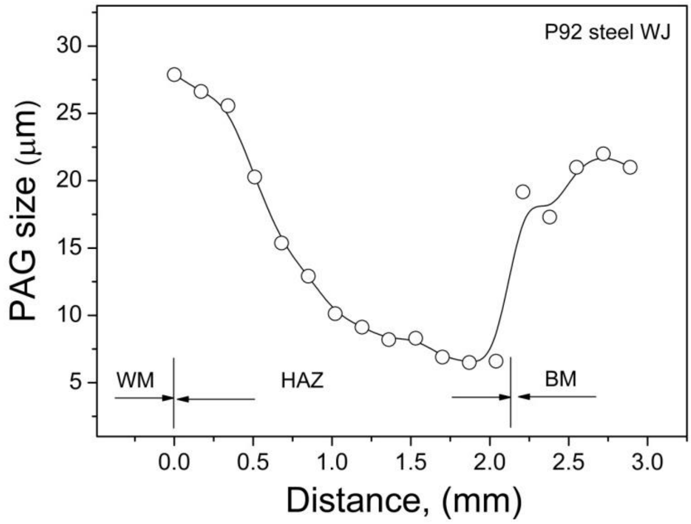

Fig. 6.22 Variation of PAG size with distance across the NG-TIG weld joint of P92 steel.

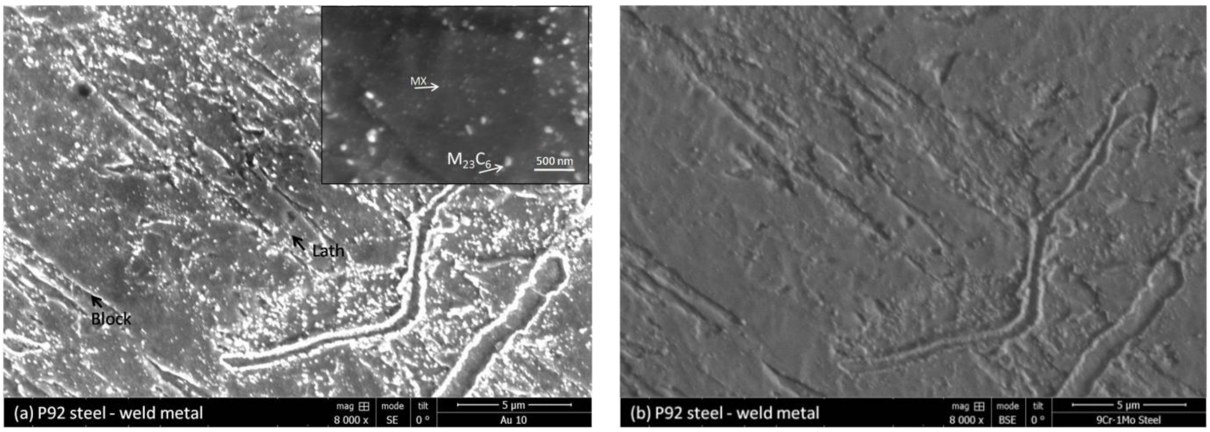

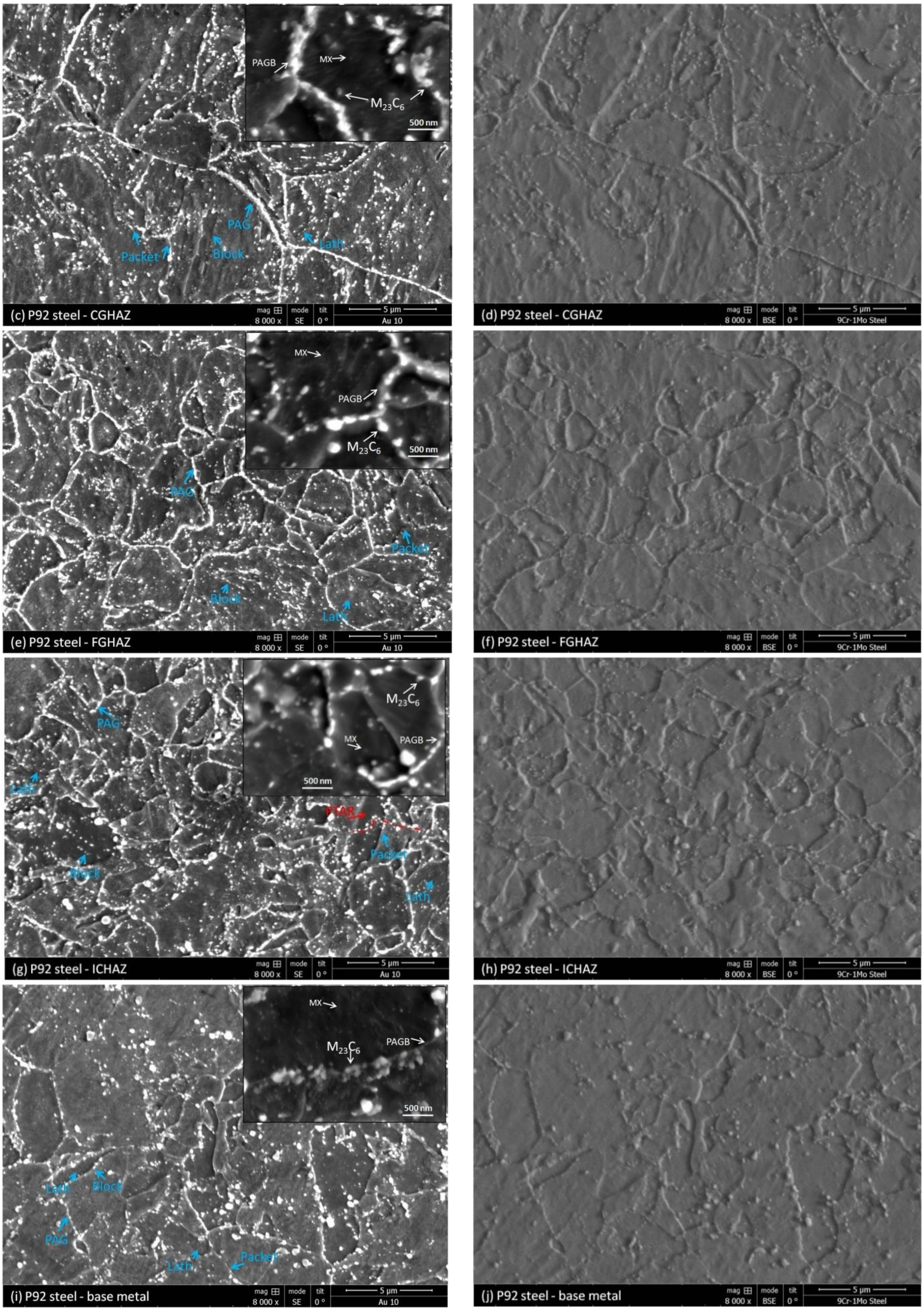

Fig. 6.23 SEM SE/BSE mode microstructures observed across the NG-TIG weld joint of P92 steel (a, b) WM, (c, d) CGHAZ, (e, f) FGHAZ, (g,h) ICHAZ and (i, j) base metal.

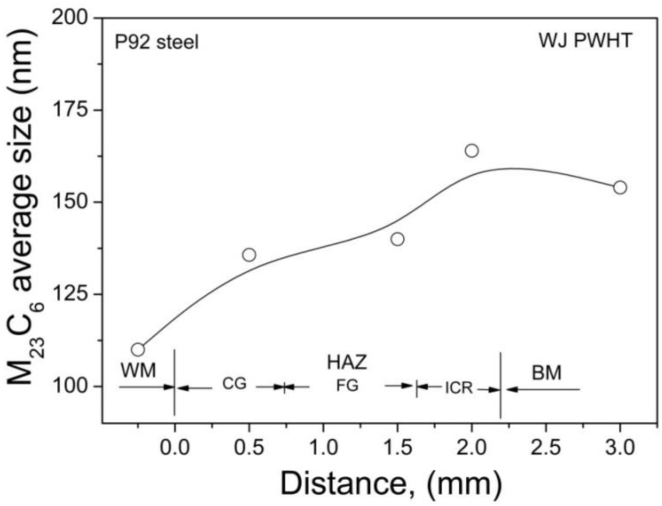

Fig. 6.24 Variation of $M_{23}C_6$ average precipitate size with distance across the NG-TIG weld joint of P92 steel.

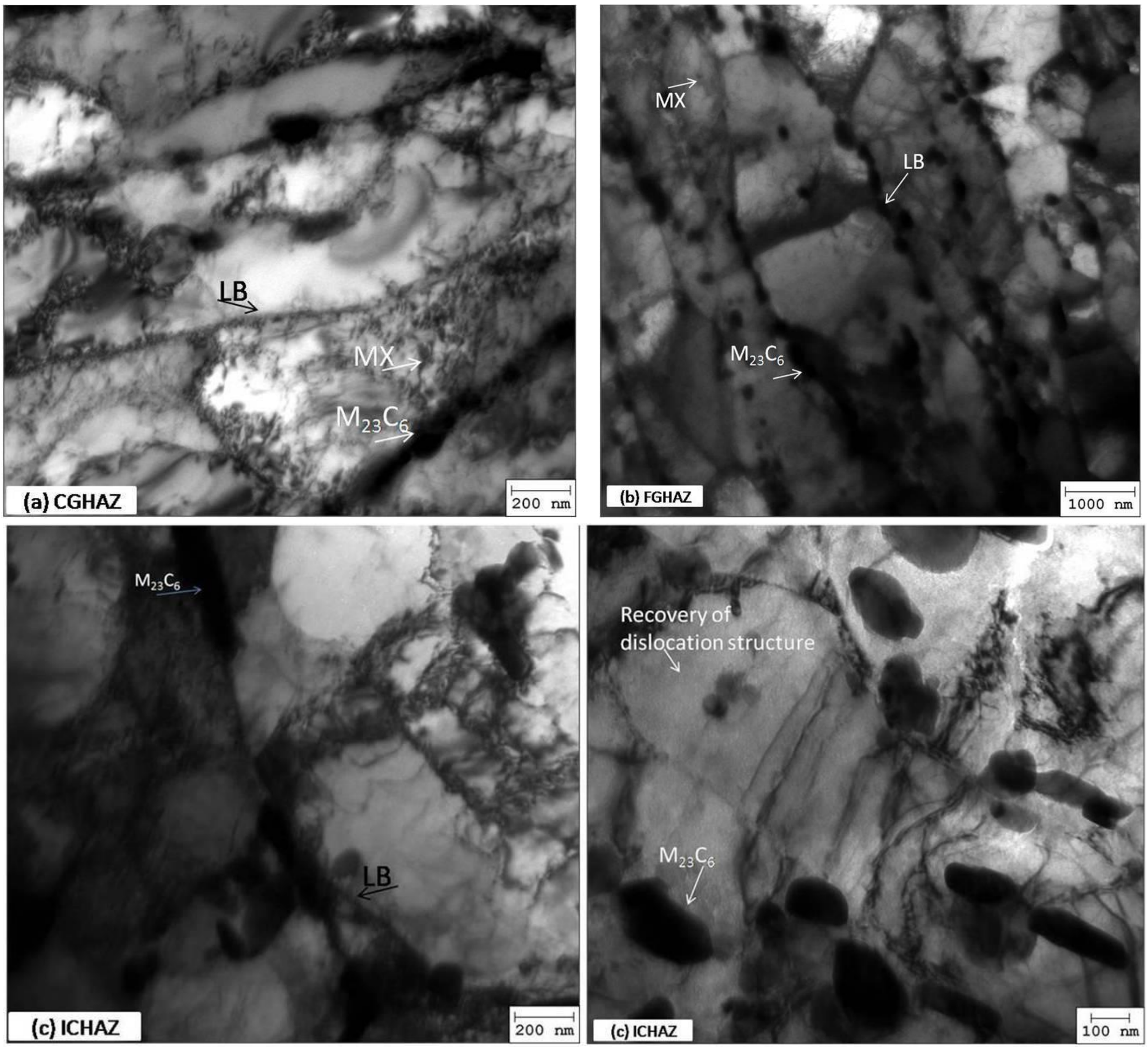

Fig. 6.25 TEM micrographs of (a) CGHAZ, (b) FGHAZ and (c) ICHAZ of P92 steel weld joint depicting the lath boundary (LB), $M_{23}C_6$ and MX precipitates.

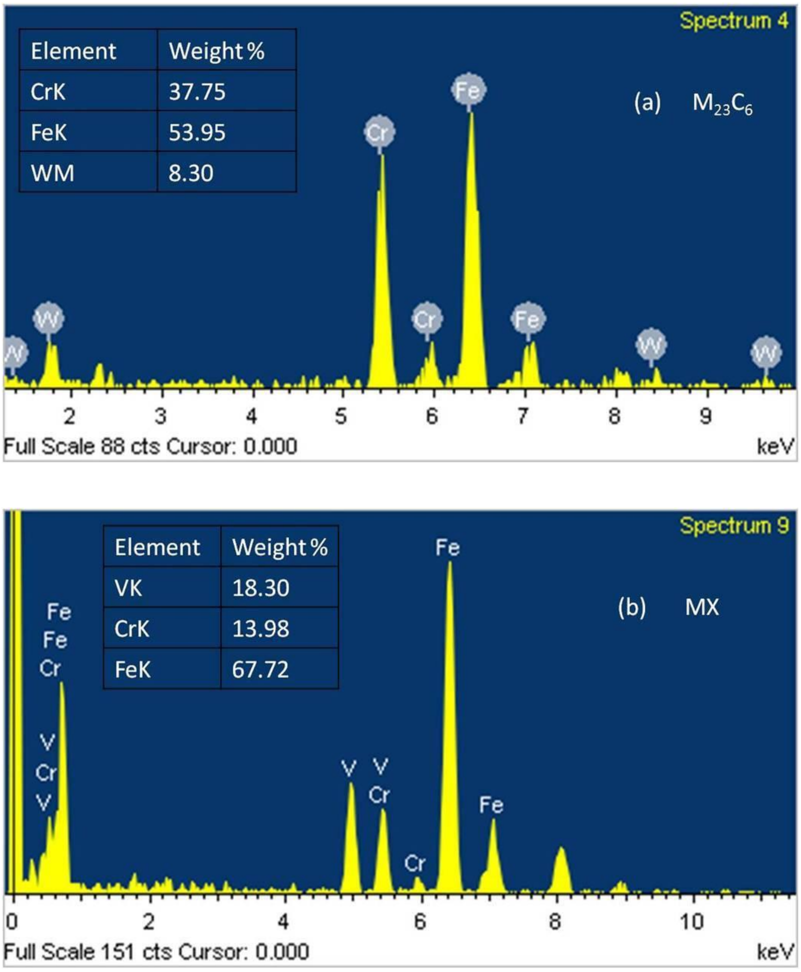

Fig. 6.26. EDS spectra of (a) $M_{23}C_6$ and (b) MX precipitates observed in the P92 steel NG-TIG joint.

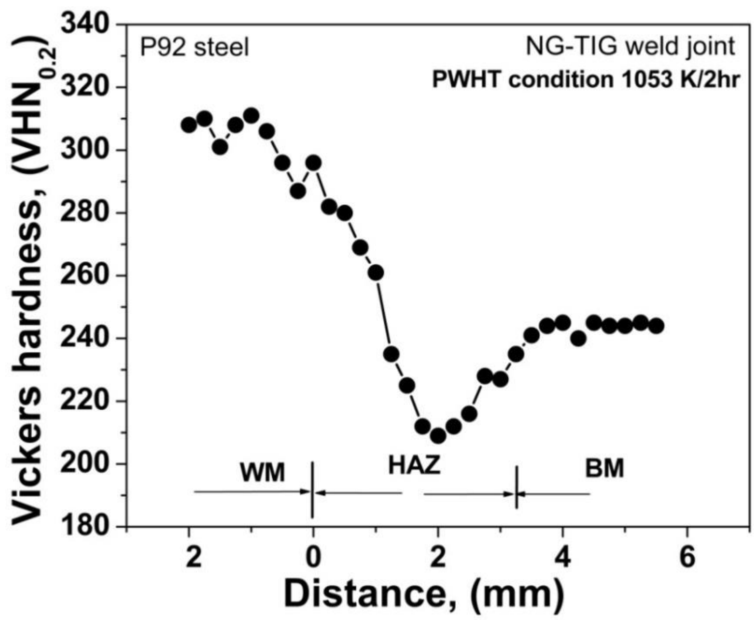

Fig. 6.27 Variation of hardness with distance across the NG-TIG weld joint of P92 steel.

6.3.2 Creep behaviour of the weld joint

The creep curves of P92 steel weld joint at 923 K over a stress range of 100 MPa to 140 MPa are shown in Fig. 6.28. The creep curves of the base metal and the joint at 110 MPa are presented in Fig. 6.29(a). The base metal and the weld joint (Fig. 6.29(a)) exhibit clear primary, secondary and accelerating tertiary creep regimes. Lower creep strain accumulation has been observed in the weld joint than in the base metal. The plot of creep rate with time (logarithmic scale) for the base metal and weld joint at 110 MPa are shown in Fig. 6.29(b). The creep rate decreased with creep exposure to minimum value followed by accelerated increase with no predominant secondary creep regime. In the transient regime, the weld joint possessed relatively lower creep rate as compared to the base metal. This is due to the constraints imposed by adjacent stronger regions and localized deformation at the particular zone in the weld joint and subsequent strain calculation based on the entire gauge length. However, the tertiary creep in the weld joint initiated early as compared to the base metal. The time spent in the tertiary creep regime was higher than the time spent in the transient regime similar to that observed in the base metal. The continuous changes in the microstructural constituents of the tempered martensite ferritic steels with the creep exposure has been considered to result in absence of predominant steady state creep regime [25]. The inhomogeneous deformation along the weld results in a mechanical notch at the soft region (ICHAZ/FGHAZ) which imposes a local deformation constraint leading to early onset of tertiary creep.

The variation of t_r of base metal and weld joint with σ_a at 923 K is shown in Fig. 6.30. The base metal and weld joint show comparable lives at high stress level (>130 MPa). The weld joint displays lower rupture life in comparison with the base metal under lower applied stress (130 MPa and below). The difference in t_r between base metal and weld joint significantly increased with decreasing applied stress. The loss of creep rupture strength of weld joint under long term exposure occurs due to changes in the microstructural constituents (coarsening of precipitate, reduction in dislocation density, softening of matrix by loss of solution strengthening elements) and internal creep cavitation damage in the localized region (FGHAZ). Higher maximum principal stress and higher triaxial state of stress in the FGHAZ due to constraints imposed on it by the adjacent regions, results in significant reduction in creep rupture life of the joint [147]. Premature creep failures of the steel weld joints fabricated by different welding techniques in comparison with base metal in the 9Cr ferritic steel have been reported by various researchers [147-156]. The creep rupture life of P92 steel NG-TIG weld joint were comparable to that of the joint prepared using submerged arc welding (SAW) process which has generally been used for joining of thick sections [156,157]. NG-TIG weld joint exhibited lower creep rupture strength than the activated TIG (A-TIG) joint [81]. Higher creep rupture strengths of P92 steel NG-TIG weld joint than those fabricated using RPEB1 [156] and MMAW [157] processes have been reported.

The variation of elongation (%) and reduction in area (%) with rupture life of base metal and weld joint are shown in Fig. 6.31(a) and (b). Comparable elongation (%) and reduction in area (%) were observed in the base metal and weld joint at high stress levels where the rupture took place in the base metal of the joint, where the deformation of narrow HAZ was mechanically constrained but no localized cavitation took place. The elongation (%) and reduction in area (%) of the weld joint decreased drastically under lower stress level (increase in creep exposure period) where fracture occurred in the HAZ of the joint. The extensive localized creep cavitation damage and deformation at the HAZ led to loss of creep ductility with increase in creep exposure. The transition from ductile mode of creep rupture associated with diffusive deformation at higher stress to the significant reduction in ductility associated with extensive localized deformation under lower stress have been evidently seen in the ruptured specimens (Fig. 6.31(c)). Initially, all the components of the specimens *viz* BM, WM, CGHAZ, FGHAZ and ICHAZ deform according to their creep resistance. The FGHAZ and ICHAZ deform more and a local stress triaxiality develops. At higher stresses, this stress triaxiality restricts further deformation in these regions despite of their lower creep resistance. Continued deformation leads to failure in the BM. At low stresses, on the other hand, sufficient time is available for the microstructural changes (as discussed section 6.3.3) to take place and further weaken the ICHAZ and FGHAZ regions and render them more prone to cavitation, by presence of cavity nucleation sites as well as adequate strain to cause the nucleation and growth aided by the stress triaxiality. The rupture ductility of NG-TIG joint is comparable with A-TIG joint [81]. SEM investigation performed on the fracture surface of crept specimens revealed ductile mode of failure with predominant dimple features at high stress level, whereas intergranular Type IV creep failure (less ductile and dimpled) under low stress level have been observed in the weld joint (Fig. 6.32). It is significant to note that such reduction in ductility due to localized deformation and internal cavitation under long creep exposure does not lead to significant external dimensional change under service, and can lead to catastrophic failure if dimensional change is the parameter considered for service extension. However, the internal damage examination of the material may assist significantly in predicting component life, which will be discussed in subsequent sections. Low ductility creep failures at HAZ have been reported earlier on P92 steel weld joint at applied stresses of 120 MPa and below at 923 K [71,148,158]. In the present study too, the premature low ductility failure in the HAZ at 923 K has been observed for applied stresses of 120 MPa and below.

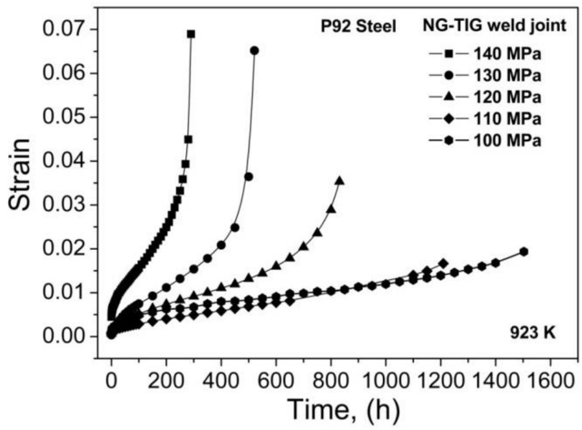

Fig. 6.28 Creep curves of P92 steel NG-TIG weld joint at 923K.

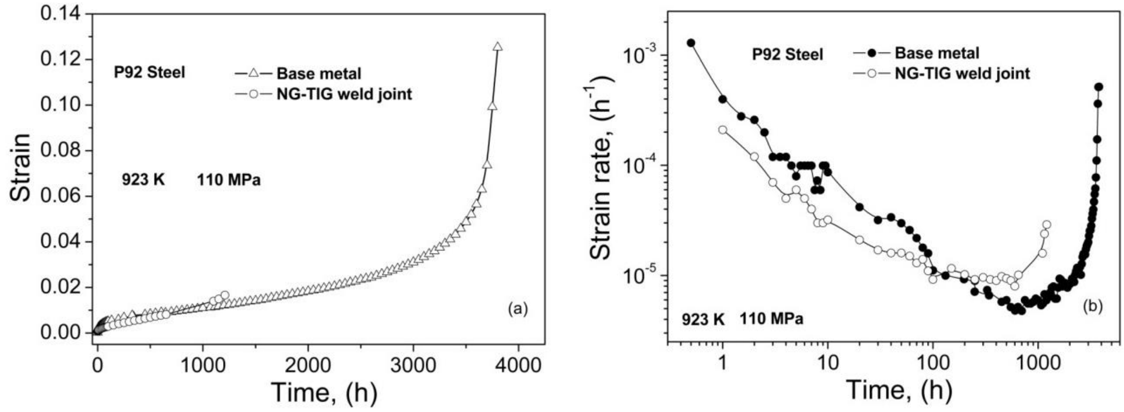

Fig. 6.29 (a) creep strain and (b) creep strain rate with time curves of P92 steel base metal and NG-TIG weld joint at 923 K and 110 MPa applied stress.

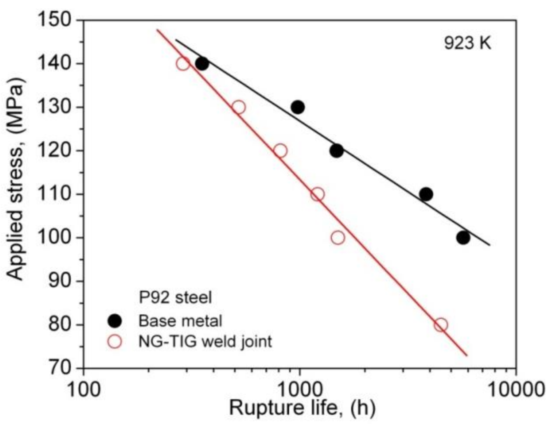

Fig. 6.30 Variation of creep rupture life with applied stress of base metal and NG-TIG weld joint at 923K.

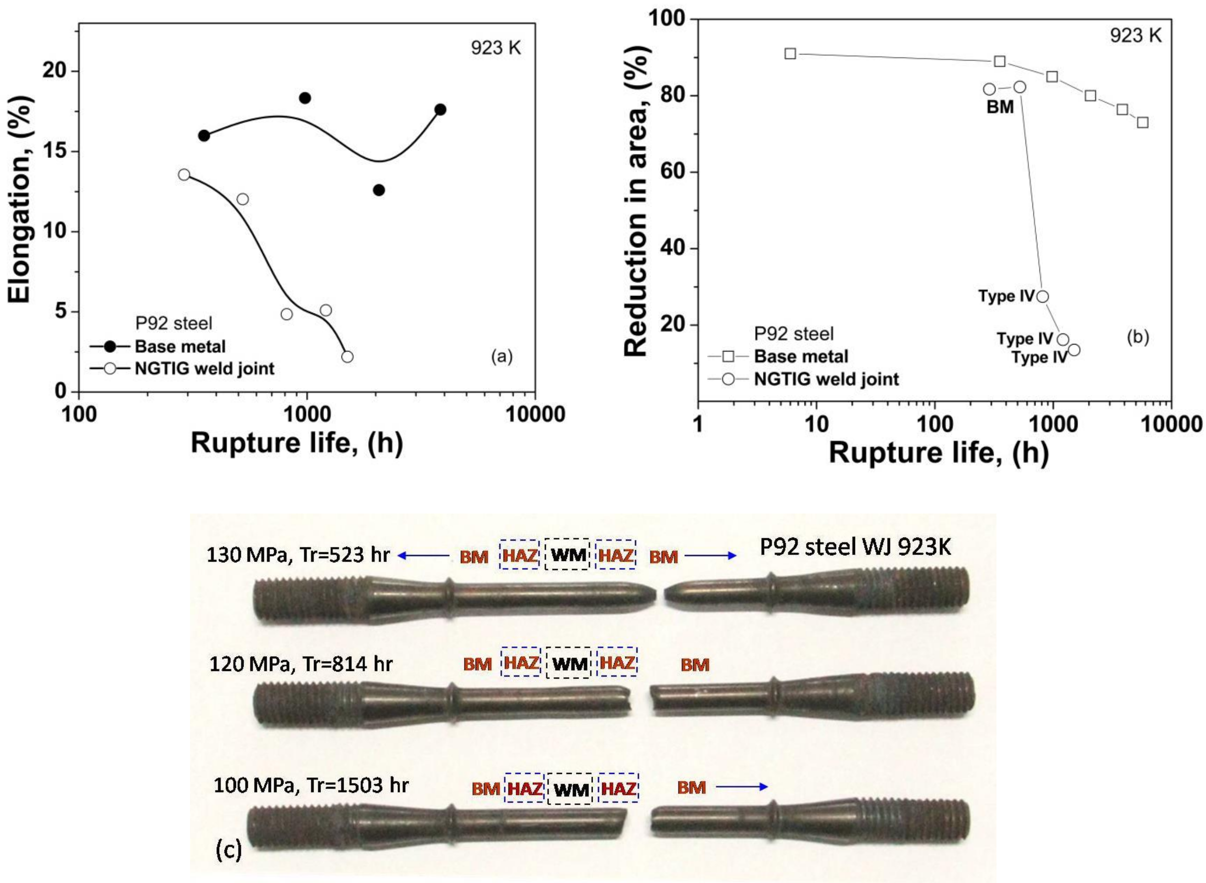

Fig. 6.31 (a) variation of elongation (%) and (b) reduction in area (%) with rupture life of base metal and NG-TIG weld joint at 923 K, (c) creep tested at 923 K specimen depicting the transition of fracture location from base metal to the outer edge of HAZ with reduction in ductility.

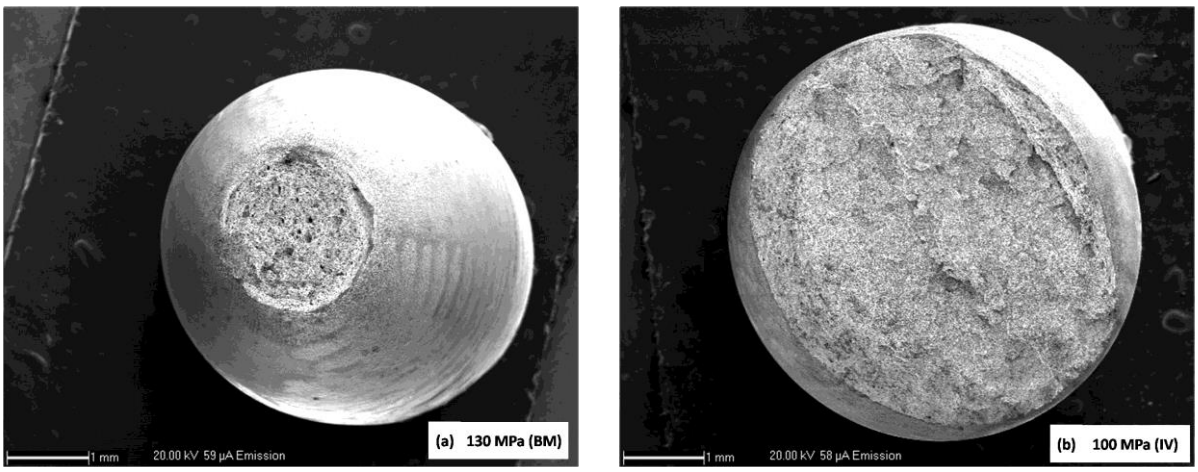

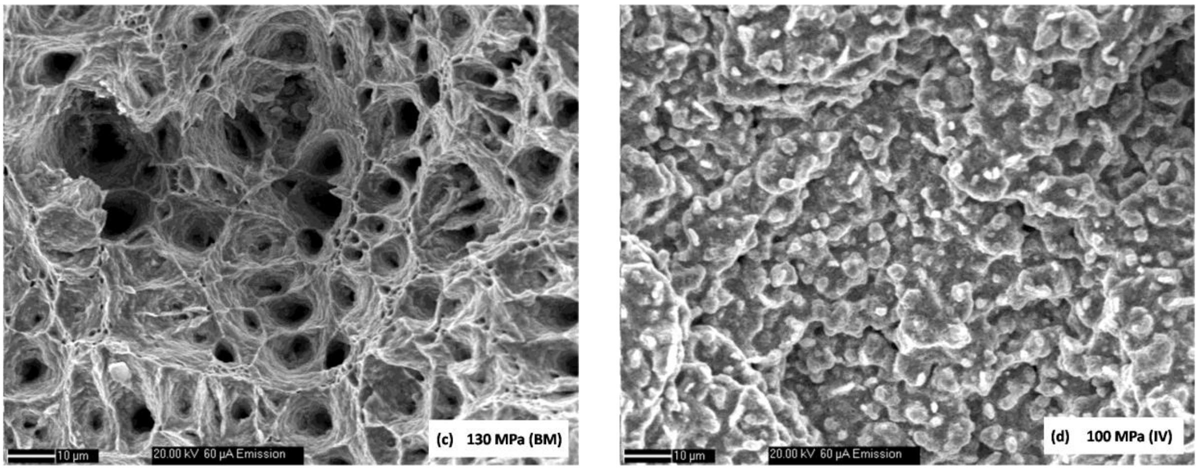

Fig. 6.32 Fracture surface of NG-TIG weld joint creep exposed at 923K at (a, c) 130 MPa and (b,d) 100 MPa.

6.3.3 Creep damage in the weld joint: Correlation with microstructure

In order to identify the reasons for the behaviour observed in the previous sections, optical metallography and hardness studies were carried out. The optical macrographs of the surface and mid-section across the intact side of the weld joint exposed to creep at 923 K and 110 MPa weld joint are shown in Fig. 6.33. Examination of the surface macrostructure revealed no cavitation damage in the joint (Fig. 6.33(a)). The mid-thickness section of the weld joint exhibited significant creep cavitation (Fig. 6.33(b)). Examination of the different constituents of the weld joint revealed predominant creep cavitation in the mid-section of the weld joint, and cavities were significantly localized in the FGHAZ of the joint (Fig. 6.34(a)). Significantly less creep cavitation was observed in the weld metal, CGHAZ and base metal (Fig. 6.34). The predominant localized creep cavitation in the mid-section than on the surface region of the weld joint is due to change from plane stress condition at surface to the plane strain condition (increased triaxial stress state) at mid-section. Extensive cavitation in the FGHAZ (Fig. 6.34(b)) at mid-section of the joint is attributed to the deformation constraint imposed by adjacent stronger constituents of weld joint and increased triaxial stress state. Complex state of stress (triaxiality) promotes the cavity growth and coalescence of cavities leads to formation of cracks in the FGHAZ, in addition to contributions towards accelerated changes in microstructural constituents [91]. The average creep cavity size was higher in the FGHAZ than the adjacent constituents of the weld joint (Fig. 6.34(c)). Extensive creep voids formation in the plate mid-thickness region than in the surface of the weld joint and localized creep damage at the outer edge of HAZ due to higher triaxial stress state have been reported in T/P91 and P92 steel weld joints [30-34]. Creep cavitation damage was higher in NG-TIG joint as compared to A-TIG joint, due to the higher deformation constraint on the FGHAZ in the NG-TIG joint due to mixed HAZ regions [81].

In order to identify the possible precipitates present in the steel, the equilibrium phases in P92 steel has been predicted using thermo-calc program. The predicted equilibrium phase diagram is shown in Fig. 6.35. It is observed that the phases such as VX and NbX do not dissolve up to 1353 K and 1573 K respectively, while $M_{23}C_6$ precipitates do not dissolve up to 1123 K. The Laves phase present is shown in line 6 in Fig. 6.35, clearly indicating that the phase is present up to 923 K and is lesser stable than VX, NbX and $M_{23}C_6$ precipitates. The presence of tungsten in the material increases the stability of $M_{23}C_6$ in P92 steel as compared to P91 steel [25,158,159]. The formation of relatively less stable Laves phase has been found to influence more on the degradation of creep strength of P92 steel by rapid coarsening and decrease in tungsten content in the matrix, reducing the contribution to solid solution strengthening [28,78,150]. The Laves phase precipitation increases with creep exposure time by consuming tungsten from supersaturated solid solution [25]. Coarsening of Laves phase and $M_{23}C_6$ precipitates leads to decrease in the pinning strength of the boundaries [78].

SEM SE and BSE mode micrographs examined at different locations of weld joint such as WM, CGHAZ, FGHAZ, ICHAZ and BM in the creep exposed (at 923 K and 110 MPa) specimen are shown in Figs. 6.36 and 6.37. The PAG and sub-grain boundaries were decorated by $M_{23}C_6$ precipitates and Laves phase particles. Coarsening of $M_{23}C_6$ precipitates in the different constituents of the joint under creep exposure was found to be less extensive compared to that of Laves phase. Presence of tungsten in $M_{23}C_6$ precipitate reduces the coarsening kinetics of precipitate under creep due to retardation of the diffusion of its constituents in presence of tungsten [159]. The variation of precipitate size (Laves phase + $M_{23}C_6$) with distance from weld metal to base metal is shown in Fig. 6.38(a). The average sizes of precipitates in different regions of HAZ and base metal at the surface of specimen were comparable (CGHAZ=183 nm, FGHAZ=187 nm, ICHAZ=178 nm and BM=189 nm). The weld metal has shown enhanced precipitation of $M_{23}C_6$ finer in size compared to the other regions (Fig.6.36). The average size of the precipitates observed across the joint in different regions at mid-section of the specimen were comparable to that observed across the surface of specimen (Fig. 6.38(a)) except in FGHAZ. An enhanced coarsening in the mid-section of the specimen as compared to the surface region in the FGHAZ has been noticed in the present investigation (Fig. 6.38(a)). This can be attributed to higher deformation constraint and triaxiality which led to increased coarsening kinetics of the precipitates. Higher triaxiality in the softer region of the joint has been earlier reported by other researchers too [23,24,33,160]. High density of fine $M_{23}C_6$ carbides helps reducing the instability of the martensitic sub-structure under creep and delays the onset of tertiary due to microstructural instability. The increase in creep rupture strength of Gr.92 steel is considered to be due to the higher resistance to recovery of dislocation lath structure in the presence of solid solution strengthener tungsten [3,78,130, 150,159,161].

Coarser bright precipitates were observed in various boundaries (PAG, packet and block) in the steel (Figs. 6.36 and 6.37), which were identified as Laves phase (higher tungsten content) from the Energy Dispersive spectroscopy (EDS) spectrum. BSE mode SEM micrographs have been used to identify the tungsten rich Laves phase which appeared as a bright phase because of its higher average atomic number [8,10,35]. Laves phase formation across the weld joint in the grain and sub-grain boundaries at the expense of tungsten in solid solution in the matrix was found to become more predominant with increased creep exposure [71,146,148]. The Laves phase observed at different locations in the surface and mid-section of the joint is shown in Figs. 6.36 and 6.37. Variation of size and area fraction (%) of Laves phase in different regions from weld metal to base metal is shown in Fig. 6.38(b, c). Laves phase observed at the surface of the specimen is coarser in the WM and FGHAZ region (Fig. 6.38(b)) than in the other regions being largest in the WM. However, the number density of Laves phase particles in WM was significantly lower than the FGHAZ. Laves phase size increased at mid-section than the surface of the specimen except in ICHAZ, which has low dislocation density in the pre-creep condition. The localized increase in state of stress (triaxial) in addition to the finer grain size and high dislocation density in the FGHAZ than the ICHAZ resulted in enhanced precipitation of Laves phase both at the surface and mid-section of the specimen in the joint.

TEM micrograph from FGHAZ in the creep exposed condition shows extensive tungsten rich Laves phase and subgrain formation with reduction in dislocation density (Fig. 6.39 (a)). The creep cavities were associated with Laves phase in the FGHAZ (Figs. 6.37(e,f) and 6.40). The deformation mismatch at the particle-matrix interface enhanced by the loss of strength in the FGHAZ due to reduction in solid solution strengthening from tungsten by Laves phase formation led to increased cavitation in the FGHAZ region. Further, cavitation damage is accelerated by localized increase in triaxial state of stress in the region. Extensive cavitation leading to Type IV cracking observed in the FGHAZ of the P92 steel NG-TIG weld joint is presented in Figs. 6.33, 6.34, 6.37 and 6.40.

Variation of hardness across the weld joint in creep exposed condition is shown in Fig. 6.41(a). Hardness across the weld joint reduced from weld metal to base metal with a significant dip in the FGHAZ. General reduction in hardness is not significant in ICHAZ due to strengthening from formation of fine Laves phase compensating for loss of W. Higher dislocation density in general, enhances the formation and coarsening of precipitates [25]. The shift in hardness dip from ICHAZ in the pre-creep condition to FGHAZ under creep exposure clearly depicts the role of fine grain size and high dislocation density for enhanced diffusion of tungsten from the matrix to form Laves phase precipitate. The reduction in solid solution strengthener tungsten in the matrix due to formation of chunky Laves phase particles and recovery of dislocation lath structure with creep exposure (Fig. 6.39(b)) results in considerable reduction in hardness in FGHAZ.

6.3.4 Weld strength factor

The presence of weld in the components reduces its long term creep strength significantly. The reduction in creep rupture strength of the weld joint of Fe-9Cr ferritic steels in comparison with its base metal is a major concern in safety as well as economy of the high temperature plants. The following factors are considered responsible for the reduced creep strength of the weld joints; (i) changes in the microstructural constituents during weld thermal cycle (welding process, parameters) and its influence on mechanical properties, (ii) heterogeneous mechanical properties across the different constituents of the weld joint induced by microstructural constituents and its influence on adjacent regions in the steel weld joint, (iii) changes in mechanical constraints across the weld joint due to weld geometry (thickness of the joint, HAZ width and orientation, weld groove angle). Creep design of welded components accounts for this by introducing a weld strength factor (WSF), which is defined as the ratio of the uniaxial creep rupture strength of the weld joint to that of the base metal at the same rupture life [81,91]. This factor has been used with base metal to calculate allowable design stress for the welded component [68,114,148,]. The variation of WSF for NG-TIG weld joint of P92 steel with creep rupture life at 923 K presented in Fig. 6.41(b) clearly shows the loss of creep rupture strength of the joint with increase in creep exposure time. A 41% loss of creep rupture strength of the joint (WSF about 0.59) compared to the base metal (at 923 K for 10^5 h) has been predicted in this investigation. WSF about 0.77 for 5000 h at 923 K has been observed in the joint. WSF about 0.85 for 1000 h at 923 K has been reported by Sklenicka et al [148]. WSF about 0.49 for 50000 h at 923 K has been reported by Mohyla et al [157]. A WSF of ~0.53 at 923 K under long term creep testing has been reported for Gr.92 steel joint by Jonathan Parker et al [68].

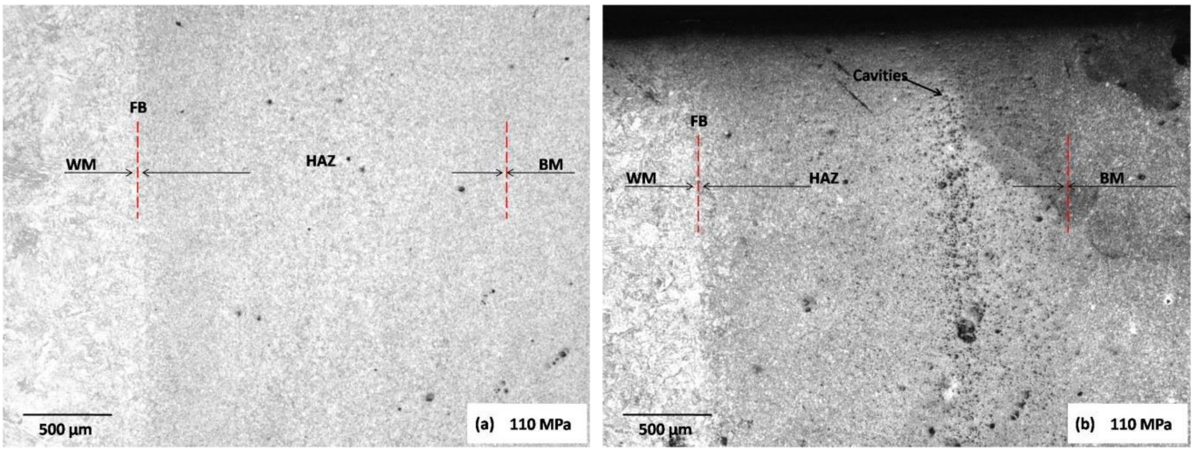

Fig. 6.33 Optical macrostructure of P92 steel NG-TIG weld joint creep exposed at 923K and 110 MPa depicting (a) very less or no creep cavitation at surface and (b) predominant cavitation at mid-section (d/2) of the specimen.

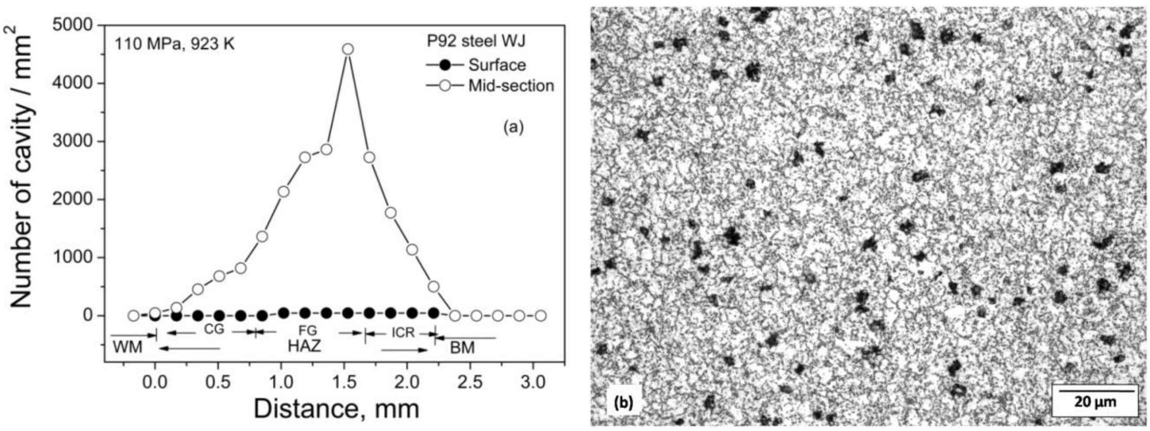

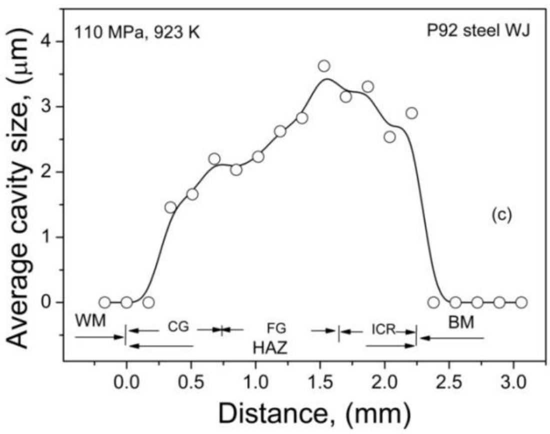

Fig. 6.34 Variation of creep cavity density (number/area) with distance across the P92 steel NG-TIG weld joint creep exposed at 923K and 110 MPa (a) surface and mid-section of the specimen, and (b) optical micrograph depicting extensive creep cavitation in the FGHAZ region of mid- section, (c) creep cavity average size with distance across the mid-section of NG-TIG weld joint of P92 steel.

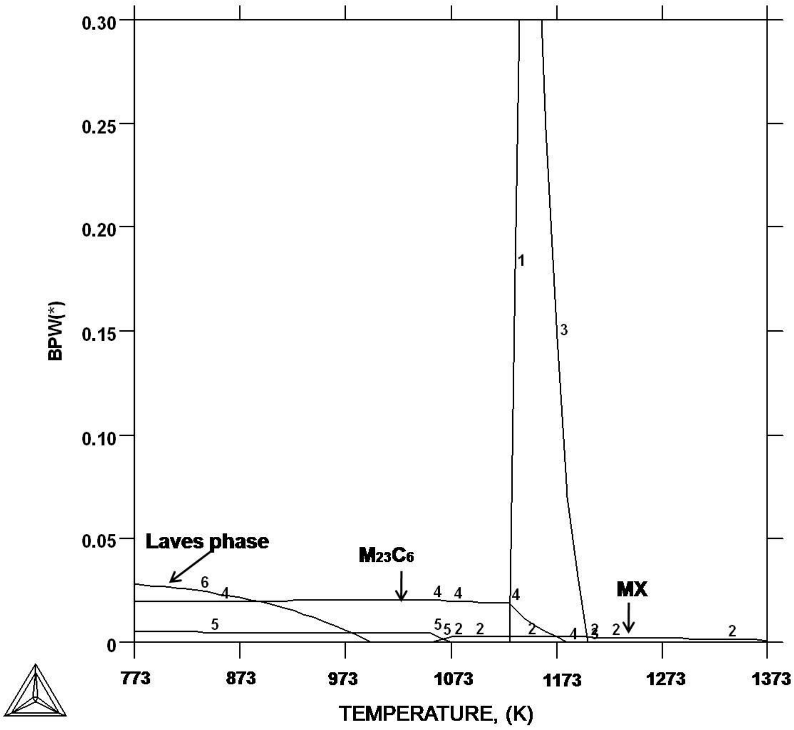

Fig. 6.35 Predicted equilibrium phases in P92 steel using thermo-calc program showing the amount of various precipitates with the temperature.

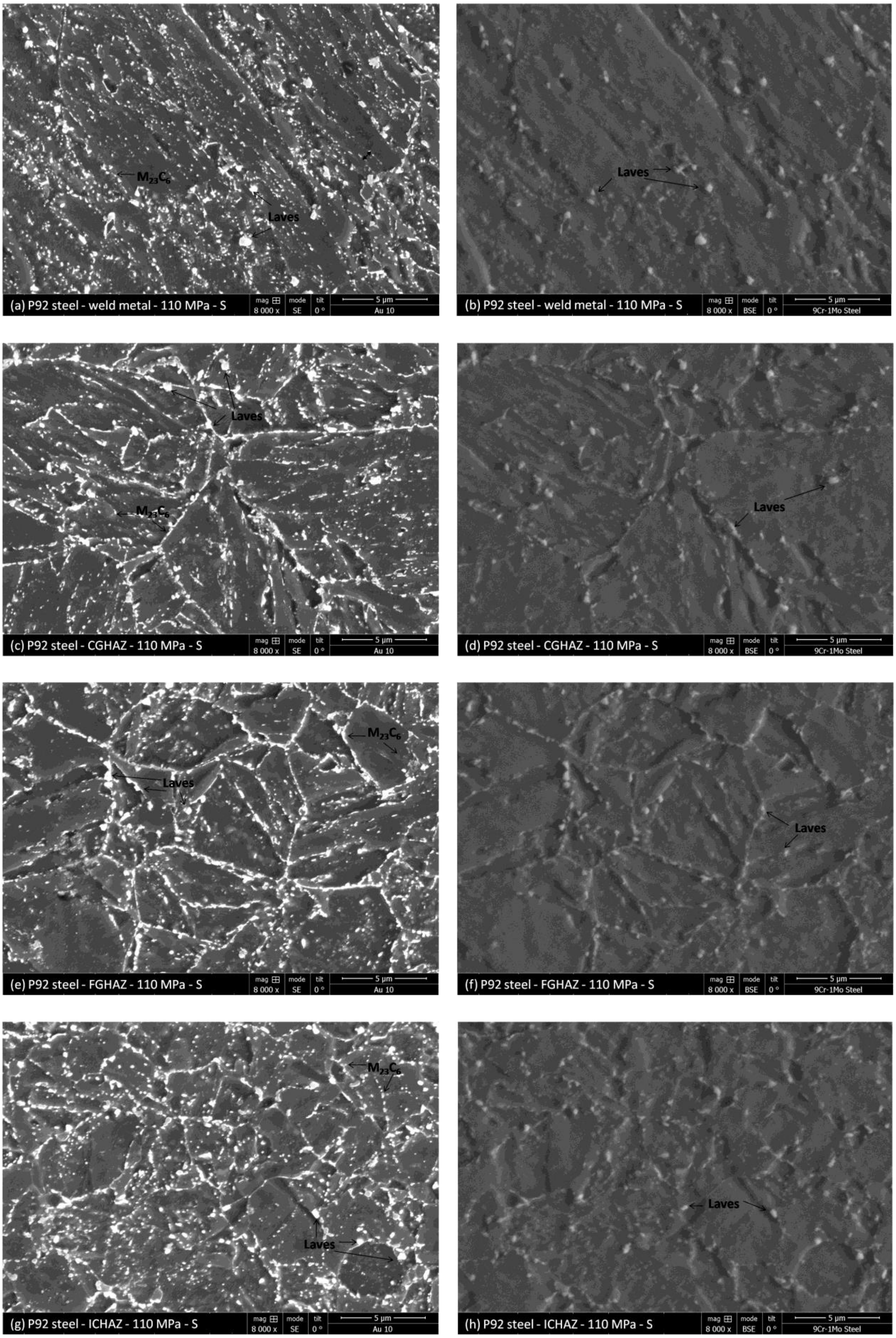
$M_{23}C_6$
Laves
(a) P92 steel - weld metal - 110 MPa - S
Laves
(b) P92 steel - weld metal - 110 MPa - S
Laves
$M_{23}C_6$
(c) P92 steel - CGHAZ - 110 MPa - S
Laves
(d) P92 steel - CGHAZ - 110 MPa - S
$M_{23}C_6$
Laves
(e) P92 steel - FGHAZ - 110 MPa - S
Laves
(f) P92 steel - FGHAZ - 110 MPa - S
$M_{23}C_6$
Laves
(g) P92 steel - ICHAZ - 110 MPa - S
Laves
(h) P92 steel - ICHAZ - 110 MPa - S

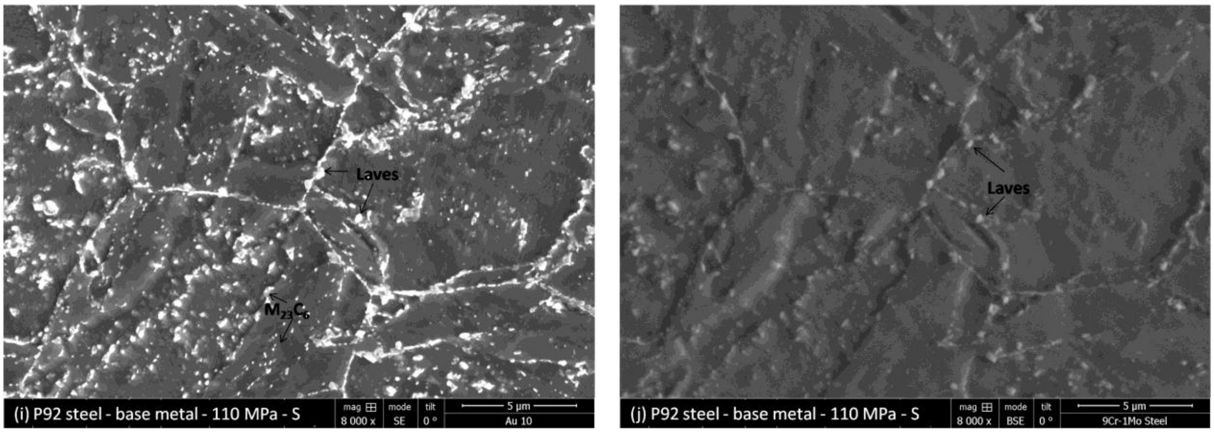

Fig. 6.36 SEM SE/BSE mode microstructures observed across the surface of P92 steel NG-TIG weld joint creep exposed at 923K and 110 MPa stress (a, b) WM, (c,d) CGHAZ, (e,f) FGHAZ, (g,h) ICHAZ and (i,j) base metal.

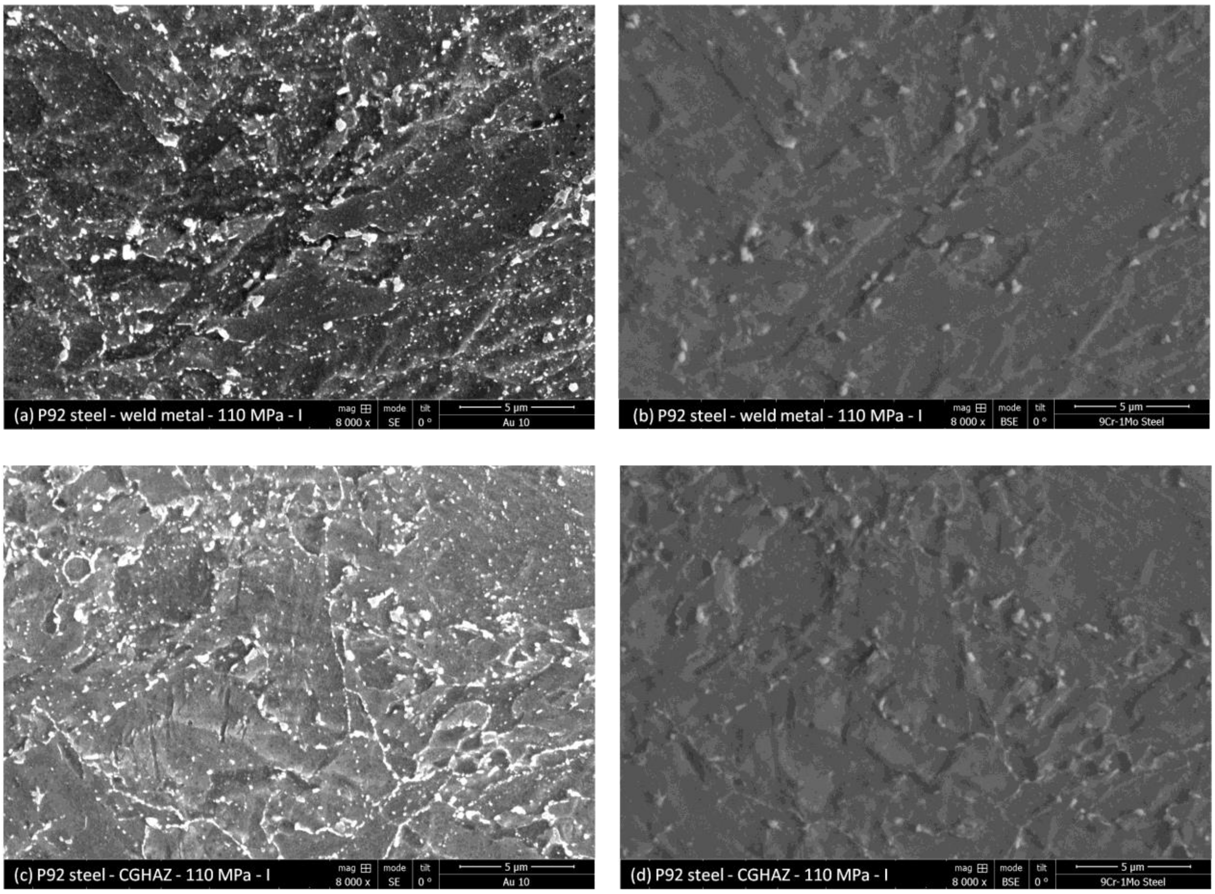

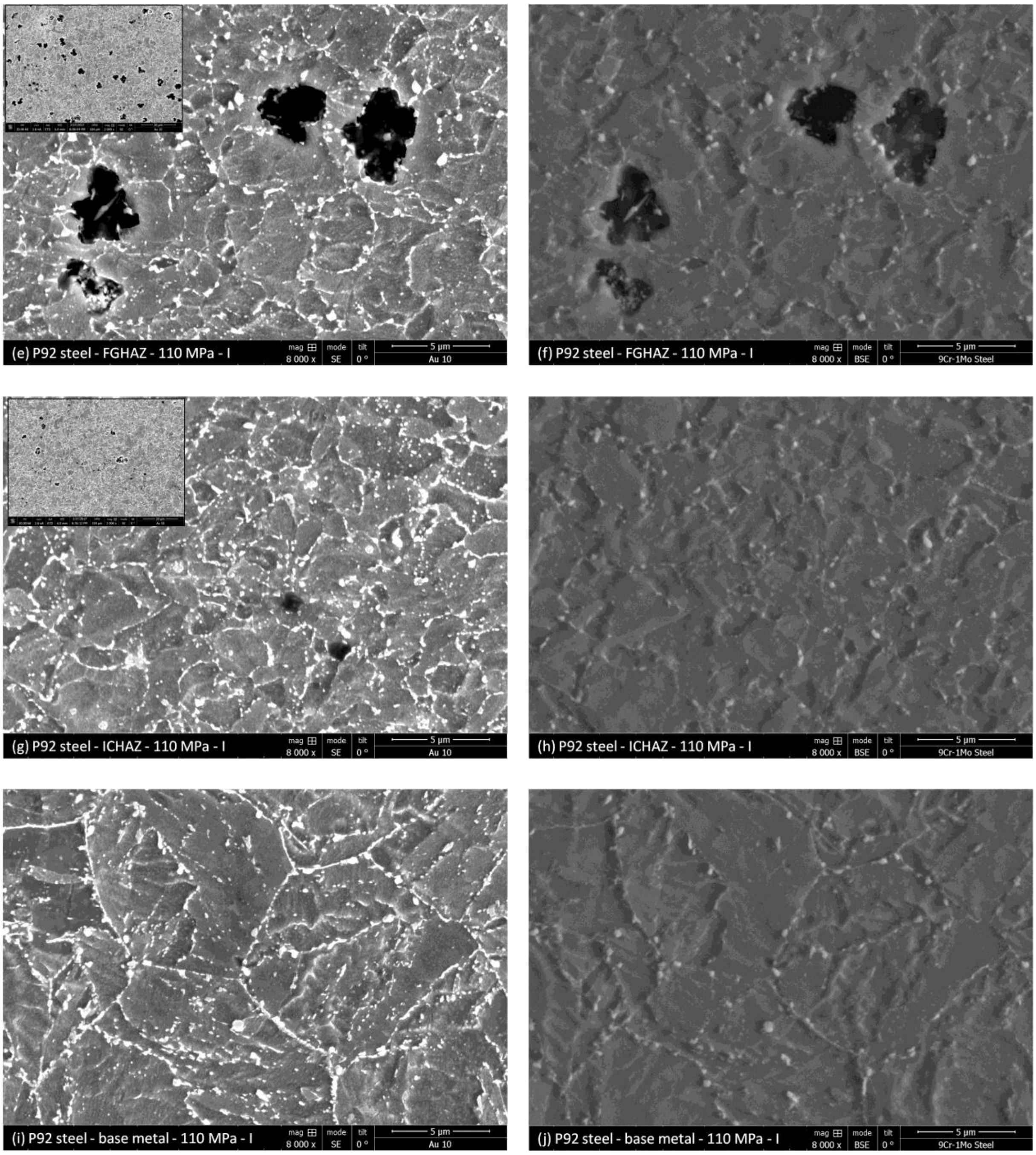

Fig. 6.37 SEM SE/BSE mode microstructures observed across the mid-section of P92 steel NG-TIG weld joint creep exposed at 923K and 110 MPa stress (a, b) WM, (c, d) CGHAZ, (e, f) FGHAZ, (g,h) ICHAZ and (i, j) base metal.

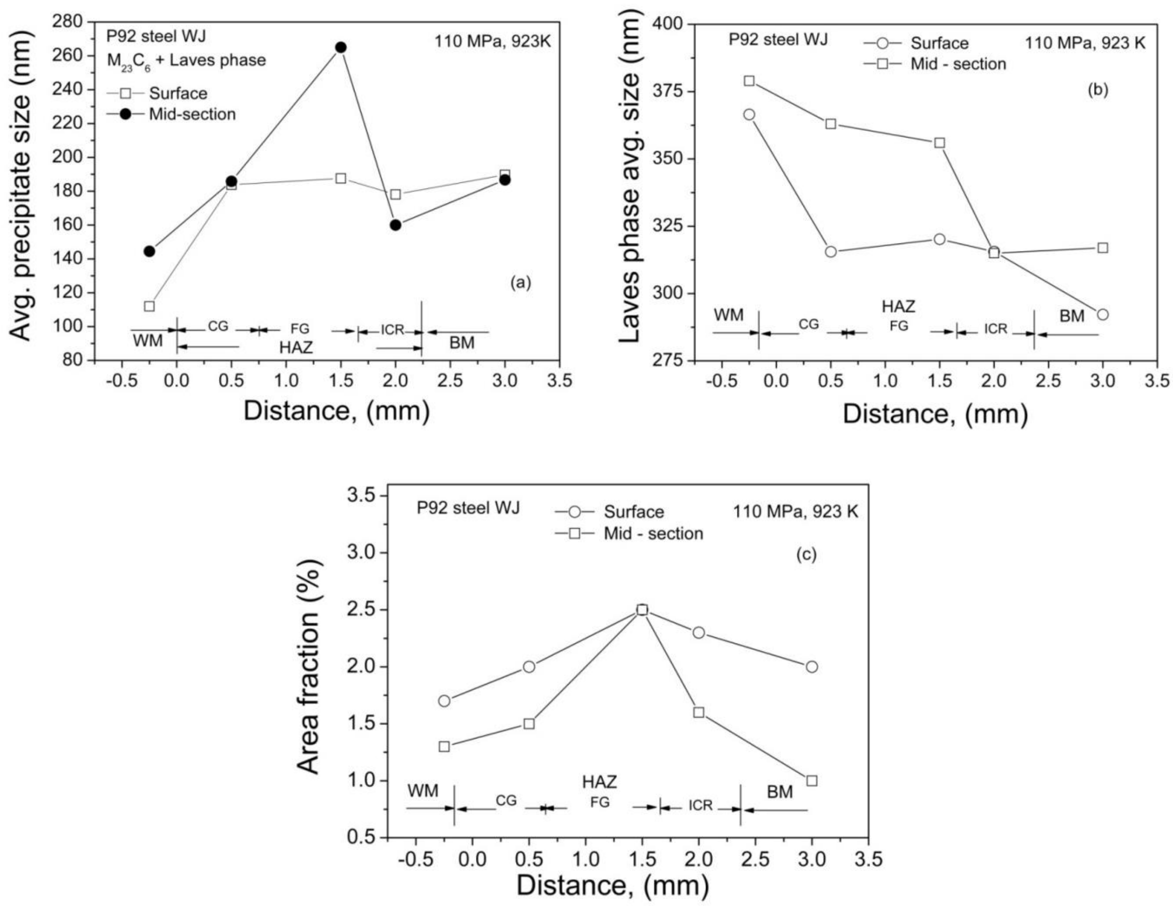

Fig. 6.38 (a) variation of average precipitate size with distance, Laves phase (b) average precipitate size and (c) area fraction (%) across the NG-TIG weld joint of P92 steel at surface and mid-section of specimen.

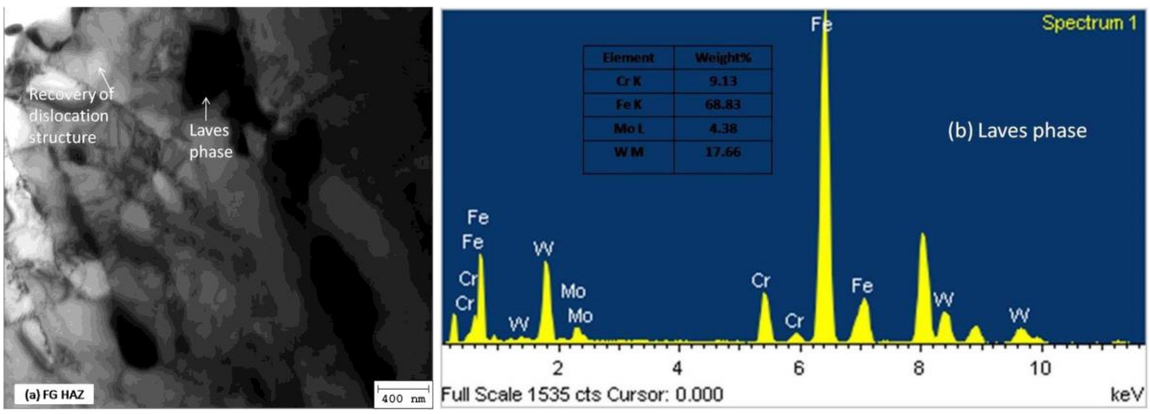

Fig. 6.39 (a) TEM micrograph depicting the recovered dislocation structure and Laves phase in the FGHAZ, (b) EDS spectra of Laves phase (Fe_2W) precipitate observed in the FGHAZ of creep exposed P92 steel NGTIG weld joint at 923 K and 110 MPa.

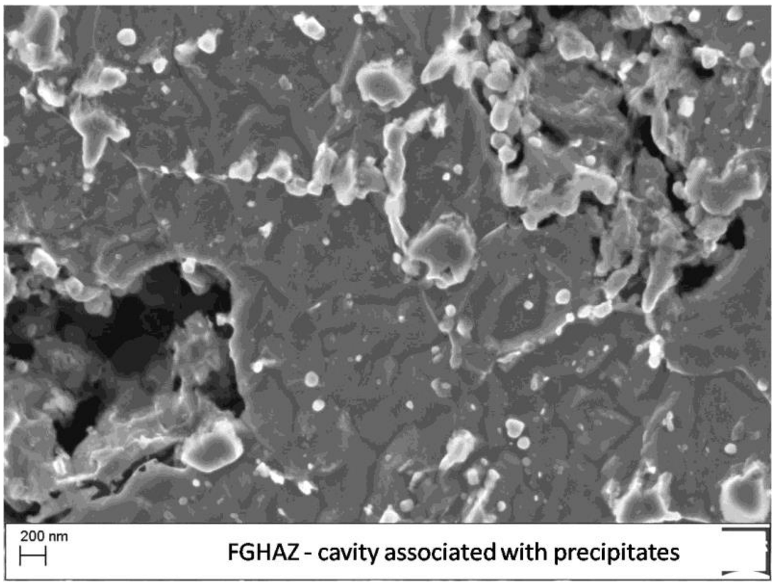

Fig. 6.40 SEM micrograph observed in the FGHAZ of creep exposed P92 steel NG-TIG weld joint at 923 K and 110 MPa stress depicting the creep cavity associated with precipitates.

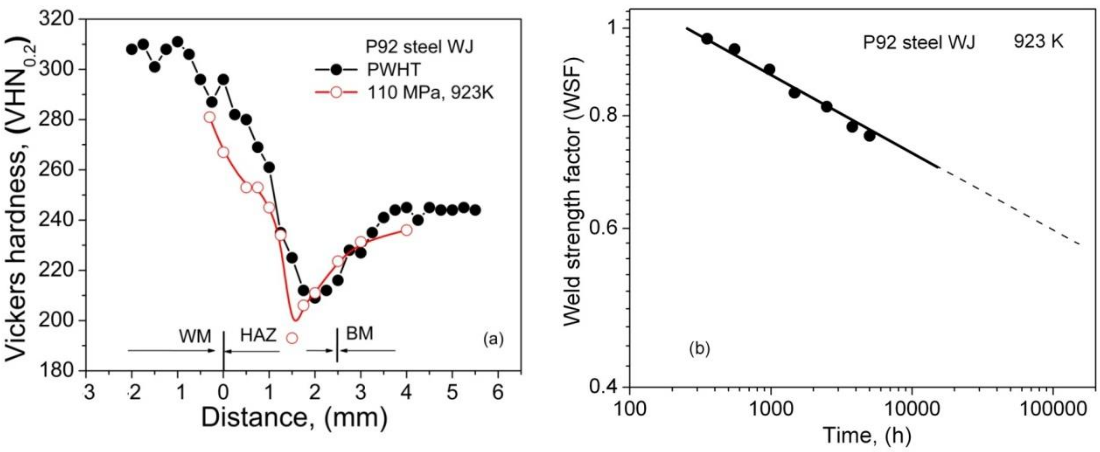

Fig. 6.41 Variation of (a) hardness with distance across the mid-section of creep exposed P92 steel NG-TIG weld joint at 923K and 110 MPa, (b) weld strength factor (WSF) with time of P92 steel NG-TIG weld joint at 923 K.

6.3.5 Microstructure and mechanical properties of HAZ regions

In order to have a better insight to the creep cracking behaviour of the joint, different microstructural constituents of HAZ in the joint have been simulated using isothermal heat treatments at temperatures chosen based on peak temperature experienced by these regions during welding. Steel blanks have been heated to 1448, 1331, 1203, 1173, 1163 and 1133 K for 5 minutes then oil quenched in order to simulate the CGHAZ near weld metal to ICHAZ near base metal respectively. The steel blanks were subjected to heat treatment at 1053 K for 2 hours to simulate the PWHT.

6.3.5.1 Microstructure, hardness and tensile properties

Optical micrographs of HAZ in the weld joint and simulated at different temperatures (1148, 1203 and 1133 K) are shown in Fig. 6.42. The microstructures across the HAZ of the joint and simulated HAZs of the joint were comparable. The grain size of the simulated CGHAZ, FGHAZ and ICHAZ were 25 µm, 11 µm and 6 µm respectively. The simulated grain size of the HAZ microstructural constituents was comparable to the weld joint HAZ constituents at particular temperature region of the weld thermal cycle. SEM micrographs of simulated HAZ regions are shown in Fig. 6.43. Coarser precipitates were observed in the samples heat treated at 1133 to 1173 K as compared to those at 1203-1448 K. TEM micrographs of region simulated at different temperatures are shown in Fig. 6.44. Coarsening of $M_{23}C_6$ precipitates and subgrain formation with decrease in dislocation density have been noticed in the intercritical temperature (1163 K) as compared to that of 1448 K and base metal. The hardness variations across the weld joint and in comparison with those of simulated constituents of the HAZs are shown in Fig. 6.45. The hardness of the simulated microstructural constituents of HAZ was comparable with the different HAZ constituents hardness across the weld joint. A decrease in grain size from 25 to 6 µm and hardness from 290 – 204 VHN has been observed from the simulated CGHAZ to the ICHAZ and this is comparable to the corresponding regions in the actual weld joint. The decrease in hardness in the ICHAZ is due to the coarsening of the $M_{23}C_6$ precipitate and sub-grain formation with lower dislocation density.

The tensile properties of the different simulated constituents are determined at 923 K. The yield stress of the base metal, and simulated CGHAZ, FGHAZ and ICHAZ were 372 MPa, 308 MPa, 240 MPa, 238 MPa respectively at 923 K. The ultimate tensile strength of the base metal, and simulated CGHAZ, FGHAZ and ICHAZ were 384 MPa, 319 MPa, 262 MPa, 246 MPa respectively. It is significant to note that the strength of the ICHAZ and FGHAZ were lower than the base metal and CGHAZ, where hardness measurements on actual weld joint also showed similar behaviour.

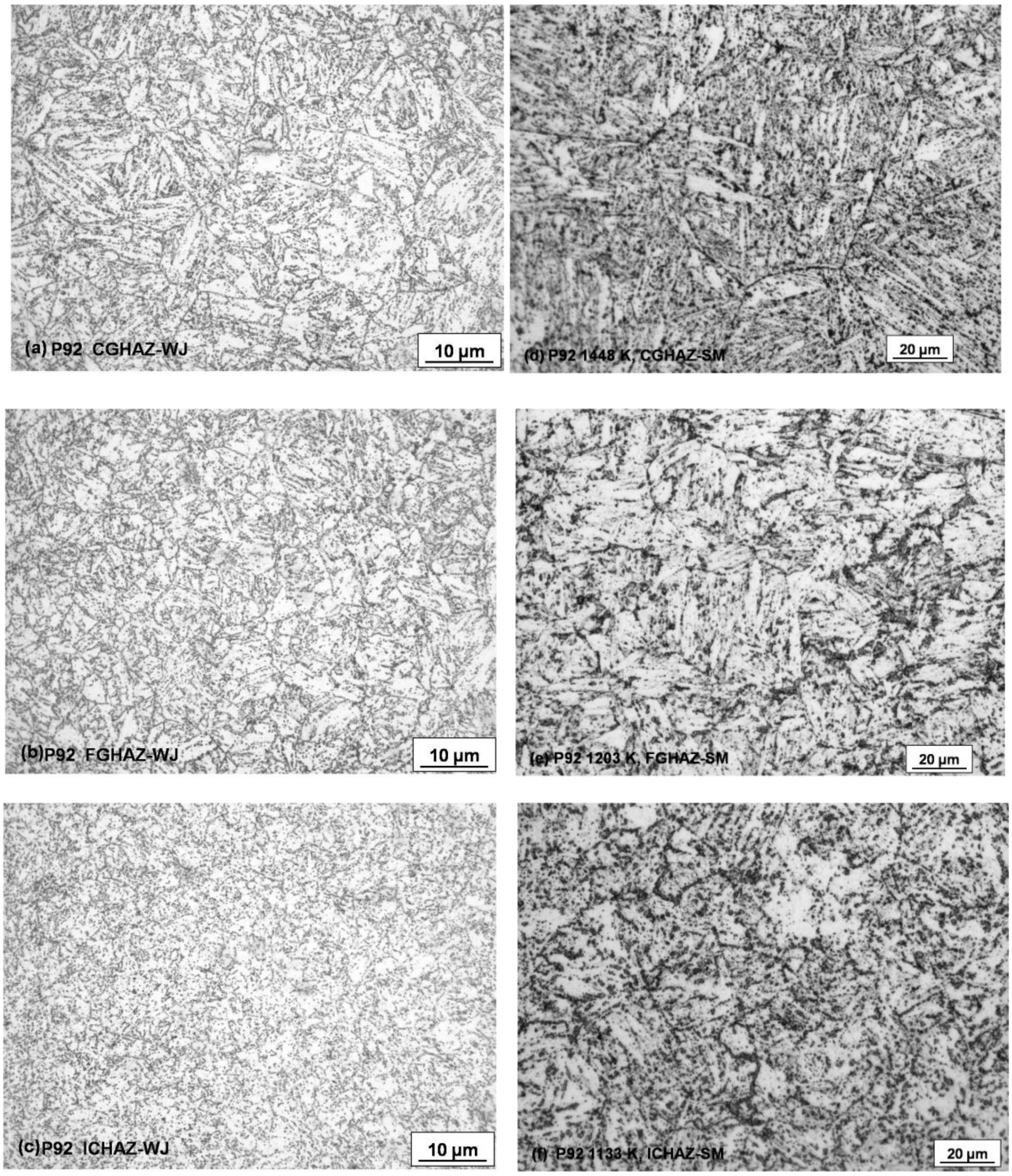

Fig. 6.42 Variations of microstructures across the HAZ of weld joint of P92 ferritic steel (a) CGHAZ, (b) FGHAZ, (c) ICHAZ and simulated (d) CGHAZ, (e) FGHAZ, (f) ICHAZ.

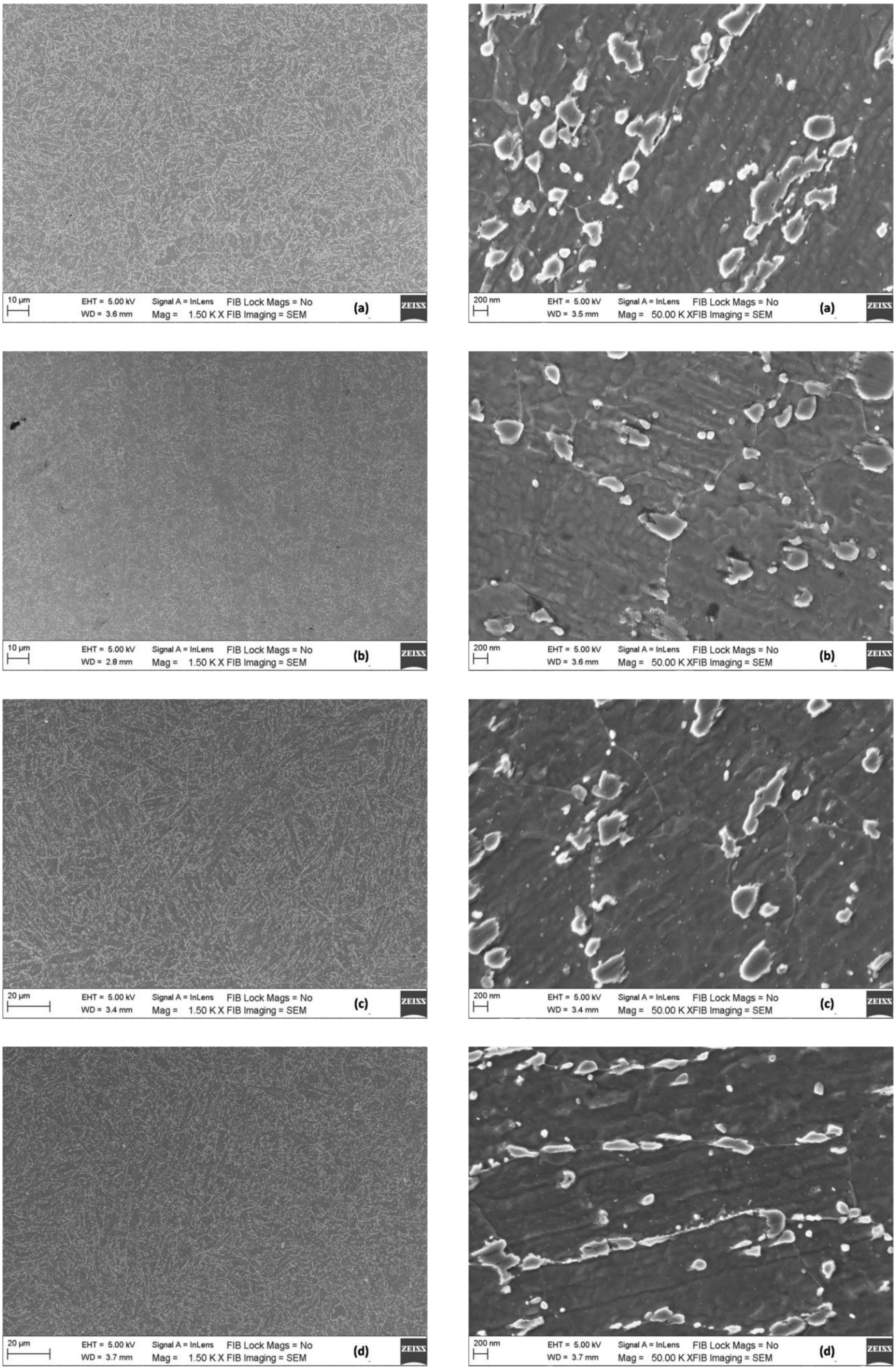
10 µm
EHT = 5.00 kV
WD = 3.6 mm
Signal A = InLens
Mag = 1.50 K X
FIB Lock Mags = No
FIB Imaging = SEM
(a)
ZEISS
200 nm
EHT = 5.00 kV
WD = 3.5 mm
Signal A = InLens
Mag = 50.00 K X
FIB Lock Mags = No
FIB Imaging = SEM
(a)
ZEISS
10 µm
EHT = 5.00 kV
WD = 2.8 mm
Signal A = InLens
Mag = 1.50 K X
FIB Lock Mags = No
FIB Imaging = SEM
(b)
ZEISS
200 nm
EHT = 5.00 kV
WD = 3.6 mm
Signal A = InLens
Mag = 50.00 K X
FIB Lock Mags = No
FIB Imaging = SEM
(b)
ZEISS
20 µm
EHT = 5.00 kV
WD = 3.4 mm
Signal A = InLens
Mag = 1.50 K X
FIB Lock Mags = No
FIB Imaging = SEM
(c)
ZEISS
200 nm
EHT = 5.00 kV
WD = 3.4 mm
Signal A = InLens
Mag = 50.00 K X
FIB Lock Mags = No
FIB Imaging = SEM
(c)
ZEISS
20 µm
EHT = 5.00 kV
WD = 3.7 mm
Signal A = InLens
Mag = 1.50 K X
FIB Lock Mags = No
FIB Imaging = SEM
(d)
ZEISS
200 nm
EHT = 5.00 kV
WD = 3.7 mm
Signal A = InLens
Mag = 50.00 K X
FIB Lock Mags = No
FIB Imaging = SEM
(d)
ZEISS

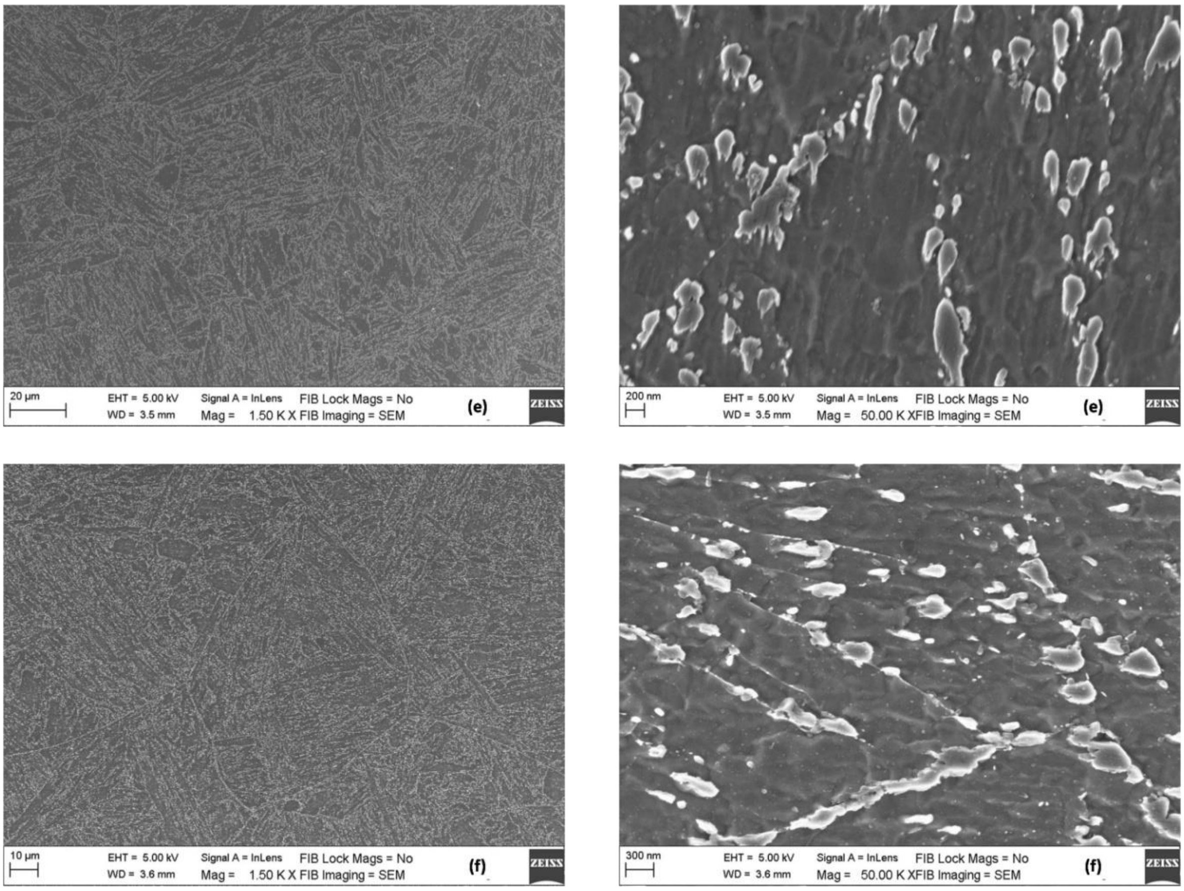

Fig. 6.43 Microstructures across the simulated HAZ of P92 steel (a) 860, (b) 890, (c) 900, (d) 930, (e) 1050 and (f) 1175 °C depicting variation in PAG, lath and precipiates size.

(a) (b)

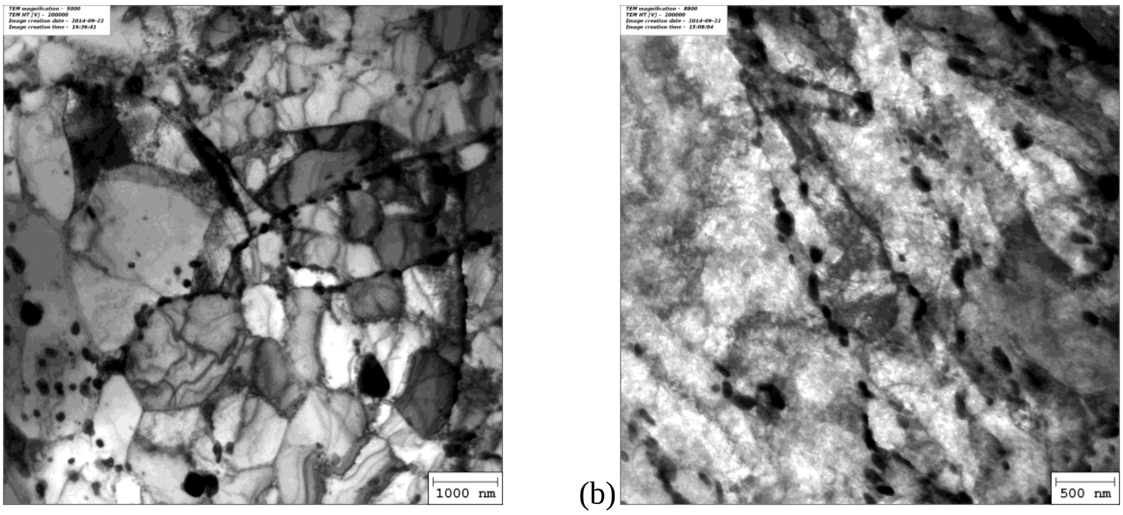

Fig. 6.44 TEM micrographs of simuluated HAZ of P92 steel (a) 890 and (b) 1175 °C.

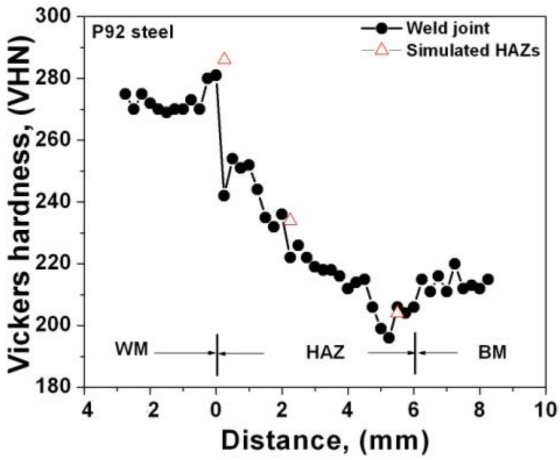

Fig. 6.45 Variations of hardness across the weld joint and simulated HAZs (CGHAZ, FGHAZ, ICHAZ) of P92 ferritic steel.

6.3.5.2 Creep deformation and rupture behaviour of HAZs

The creep curves of different simulated HAZs at 923 K are shown in Fig. 6.46 along with that for the joint. The creep curves exhibited primary creep regime followed by an apparent steady state creep deformation and an accelerating tertiary creep regime as in base metal. The variations of creep rate with creep exposure time for different constituents of the HAZs are compared in Fig. 6.46. The weld joint exhibited comparable minimum creep rate as in the simulated FGHAZ and ICHAZ. The tertiary stage of creep deformation was found to initiate much early in the ICHAZ of the joint than the weld joint.

Under long term creep exposure, the rupture life of FGHAZ was found to lower than the ICHAZ (Fig. 6.47(a)). This is in line with degradation/creep failure found to shift from ICHAZ to FGHAZ in the joint significantly. The variations of rupture life with applied stress for the base, A-TIG weld joint and simulated HAZ of the joint at 923 K are shown in Fig. 6.47(b-c). In both the base metal and weld joint, the variation of creep rupture life with stress showed a two-slope behaviour. The weld joint had significantly lower creep rupture life than the base metal for applied stresses lower than around 120 MPa. The rupture life of the simulated constituents of HAZs displayed significant differences among them. The rupture life of the simulated FGHAZ and ICHAZ were significantly lower than the simulated CGHAZ of the joint and was comparable to the rupture life of the weld joint (Fig. 6.47). It may be recalled from section 6.3.3 that extensive microstructural changes and creep cavitation in selected constituents of the joint were considered to be responsible for the early onset of tertiary stage of creep deformation in the weld joint. Also, hardness and metallographic investigation of the creep exposed joint revealed that creep failure of the joint under relatively lower applied stress occurred in the FGHAZ, even though the ICHAZ has lower hardness (Fig. 6.45). The rupture ductility (reduction in area percentage) of the joint and simulated zones is shown in Fig. 6.47(c). The shift in failure location from base metal to FGHAZ with increase in rupture life (decrease in applied stress) was accompanied with the drastic reduction in rupture ductility in the weld joint. The weld joint, base metal and simulated ICHAZ, FGHAZ are comparable in terms of rupture ductility *i.e.,* reduction in area.

Microstructure investigation across the creep exposed weld joint revealed precipitation of Laves phase in all regions across the joint. The precipitate was identified as Fe_2W and was relatively extensive in the FGHAZ in the weld joint (Fig. 6.48). Under low stress regime the Laves phase size was higher in FGHAZ than the adjacent region of the weld joint. Creep cavities were found to be associated with Laves phase and extensively in the FGHAZ of the joint, where fracture occurred in the weld joint. Similarly, the investigation on simulated HAZs show that more extensive creep cavitation occurred in the FGHAZ than the ICHAZ and CGHAZ (Fig. 6.49) at 130 MPa stress. The cavities were larger (~12 μm) in the simulated FGHAZ than the 5 μm observed in the (FGHAZ) of weld joint. Thus, it is confirmed that the localized creep deformation and cavitation are responsible for the premature Type IV failure of the components associated with weld joint under low stress and at high temperature.

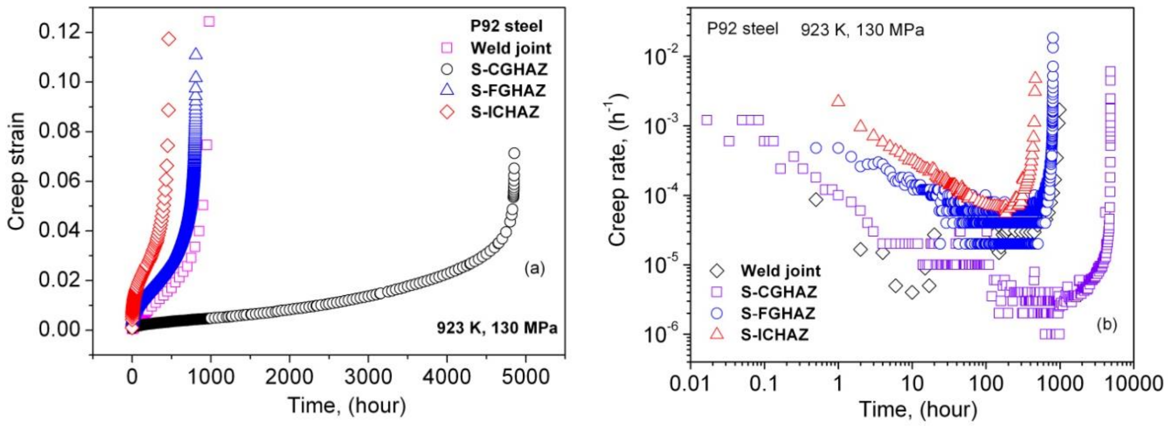

Fig. 6.46 Creep curves of simulated microstructures of HAZ of the P92 steel joint at 923 K.

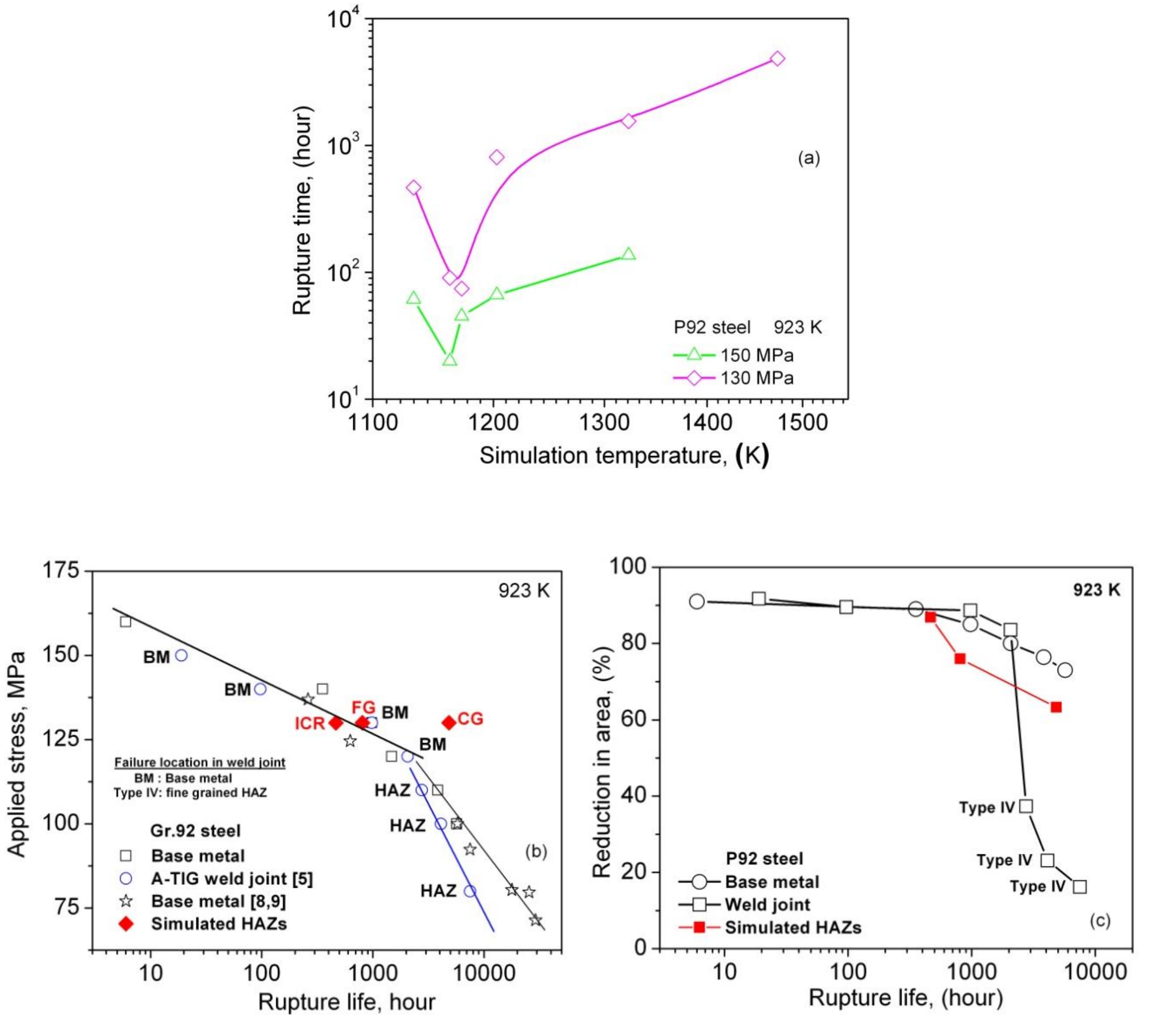

Fig. 6.47 Variations of (a) rupture life of simulated regions of HAZ, (b) rupture life with applied stress and (c) reduction in area (%) with rupture life for base metal, weld joint and simulated HAZs of P92 steel at 923 K.

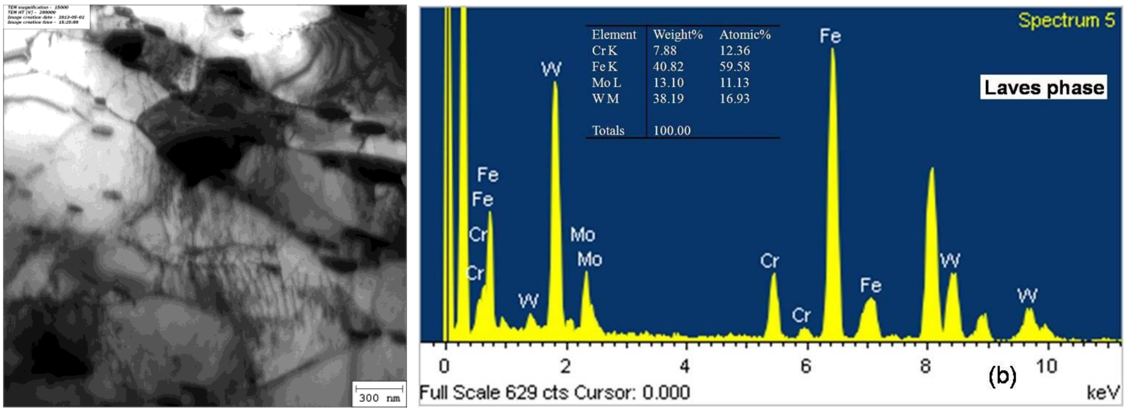

Fig. 6.48 TEM micrographs of creep ruptured FGHAZ of P92 steel weld joint showing extensive Laves phase precipitation at 923 K and 100 MPa.

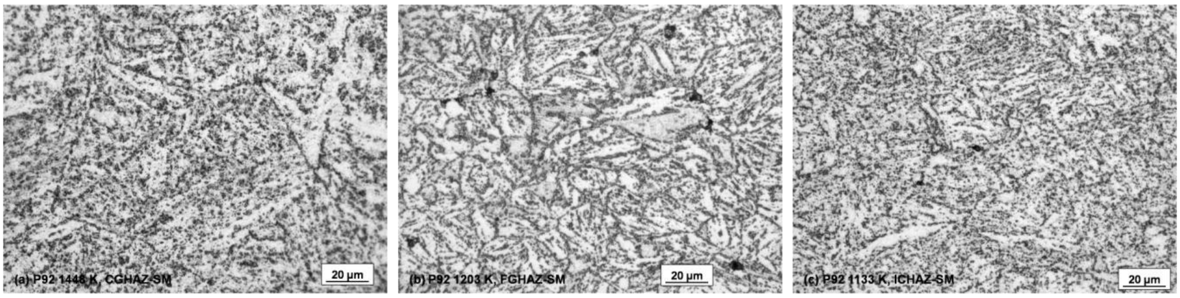

Fig. 6.49 Variations of creep cavities in the simulated microstructures HAZ of P92 steel at 923 K and 130 MPa, (a) CGHAZ, (b) FGHAZ, (c) ICHAZ.

6.4 Conclusions

Following conclusions have been drawn based on the investigations performed on creep deformation and rupture behaviour of P92 steel and its weld joint made from NG-TIG, and HAZ regions of weld joint at different temperatures (873 to 923 K) and over a stress range of 220 to 80 MPa.

i) The stress dependence of minimum creep rate obeyed Norton's power law with higher apparent stress exponents of 5.8 to 15.2 and activation energy value of 619 kJ/mole.

ii) The threshold stress values of 137.5 MPa, 83.3 MPa and 29.7 MPa were obtained at 873 K, 923 K and 973 K respectively.

iii) The threshold stress compensated true stress exponent of 4 and true activation energy of 244 kJ/mole, as well as threshold stress normalised by Orowan stress in the range 0.18-0.77 confirm that the rate controlling phenomenon of creep deformation in the steel is lattice diffusion assisted localised climb of dislocations over the precipitates.

iv) The apparent stress exponents of 6.9 to 15.3 and apparent activation energy value of 598.8 kJ/mole obtained for creep rupture indicates that creep deformation and rupture in P92 steel are controlled by the same mechanism.

v) The steel obeyed Monkman-Grant and modified Monkman-Grant relationships.

vi) Creep damage tolerance factor of 6 in the steel demonstrates that the microstructural degradation such as coarsening of precipitates and subgrain structure is the dominant damage mechanism in the steel.

vii) Creep rupture life of the NG-TIG weld joint was lower than the base metal; the difference in creep rupture life between the base metal and weld joint increased significantly with decrease in applied stress.

viii) The failure location in the NG-TIG weld joint was found to change from the base metal at high stress to the fine grain (FG) HAZ (Type IV cracking) under lower stress level.

ix) Extensive Laves phase formation with significant loss of solution strengthening from tungsten under creep exposure led to reduction in hardness and extensive cavitation in the FGHAZ resulting in premature type IV failure of the weld joint.

x) Coarsening of precipitates was predominant in the mid-section due to complex state of stress than at the surface of the specimen.

xi) A weld strength factor about 0.59 has been evaluated for 10^5 hour at 923 K in the steel.

CHAPTER 7

Effect of Geometry on Type IV Cracking of Weld Joints

7.1 Introduction

From the work reported in the previous chapters, it is clear that failure due to type IV cracking occurs by cavitation in the fine grain or intercritical region of HAZ. The orientation of this region with respect to the applied stress is expected to be an important factor in deciding the extent of cracking in this region. This aspect is examined in the present chapter, by studying the effects of stress axis of the cross-weld specimen with respect to welding fusion-line on type IV cracking behaviour. P91 steel weld joint with different groove angles and specimens fabricated in different orientations from the P92 steel weld joint were used in this study. The influence of groove angles on stress distribution across the P91 steel weld joints analyzed using the Finite Element Method has been presented.

7.2 Weld groove angle

P91 steel weld joints having different bevel angles, viz., 35°, 45° and 60° (included or groove angles of 70°, 90° and 120°) were prepared using TIG welding process and its creep behaviour has been discussed in this section. The edge preparation of plates for weld pads, base metal and filler metal compositions, heat treatment and welding process parameters are given in chapter 2.

7.2.1 Microstructure, hardness across the weld joints

Microstructure observed across the P91 steel TIG weld joint (bevel angle 35°) are shown in Fig. 7.1. Weld metal possessed dendrite structure, delta ferrite was not observed in the weld metal and fusion boundary. Adjacent to the weld metal region, coarse grain (CGHAZ), fine grain (FGHAZ) and intercritical (ICHAZ) HAZ regions were observed towards the unaffected base metal. Width of the different regions across the HAZ in the 35° joint are 1.0, 1.4 and 0.9 mm for CGHAZ, FGHAZ and ICHAZ respectively. HAZ width in the 35°, 45° joints were about ~3.3 mm and 60° joint was about ~ 4 mm. The increase in HAZ width with increase in groove angle is due to increased number of weld passes required to fill the weld groove leading to repeated thermal cycles experienced by the weld and HAZ. The width of the HAZ in the single-pass A-TIG joint having 0° groove angle was 8.3 mm (Fig. 3.13(a)). Average PAG size of CGHAZ, FGHAZ and ICHAZ in the 35° joint were 40, 14 and 8 µm respectively. Similar PAG sizes in different regions of HAZ have been observed across the weld joints with all groove angles. Coarser $M_{23}C_6$ precipitates in ICHAZ were observed than the other regions in the weld joint (Fig. 7.2). $M_{23}C_6$ precipitates average size was higher in the ICHAZ of the 60° joint due to more repeated thermal cycles than the ICHAZ of other joints. $M_{23}C_6$ precipitates size in the ICHAZ of single pass joint with 0° bevel angle was comparable with those in 35° joint. Hardness decreased from weld metal to base metal with a dip in the ICHAZ in all the joints. Hardness values in the ICHAZ in the weld joint having different bevel angles were comparable in spite of the variations in the $M_{23}C_6$ precipitate size. However, A-TIG weld joint (Fig. 3.13) has shown relatively lower hardness as compared to other bevel joints.

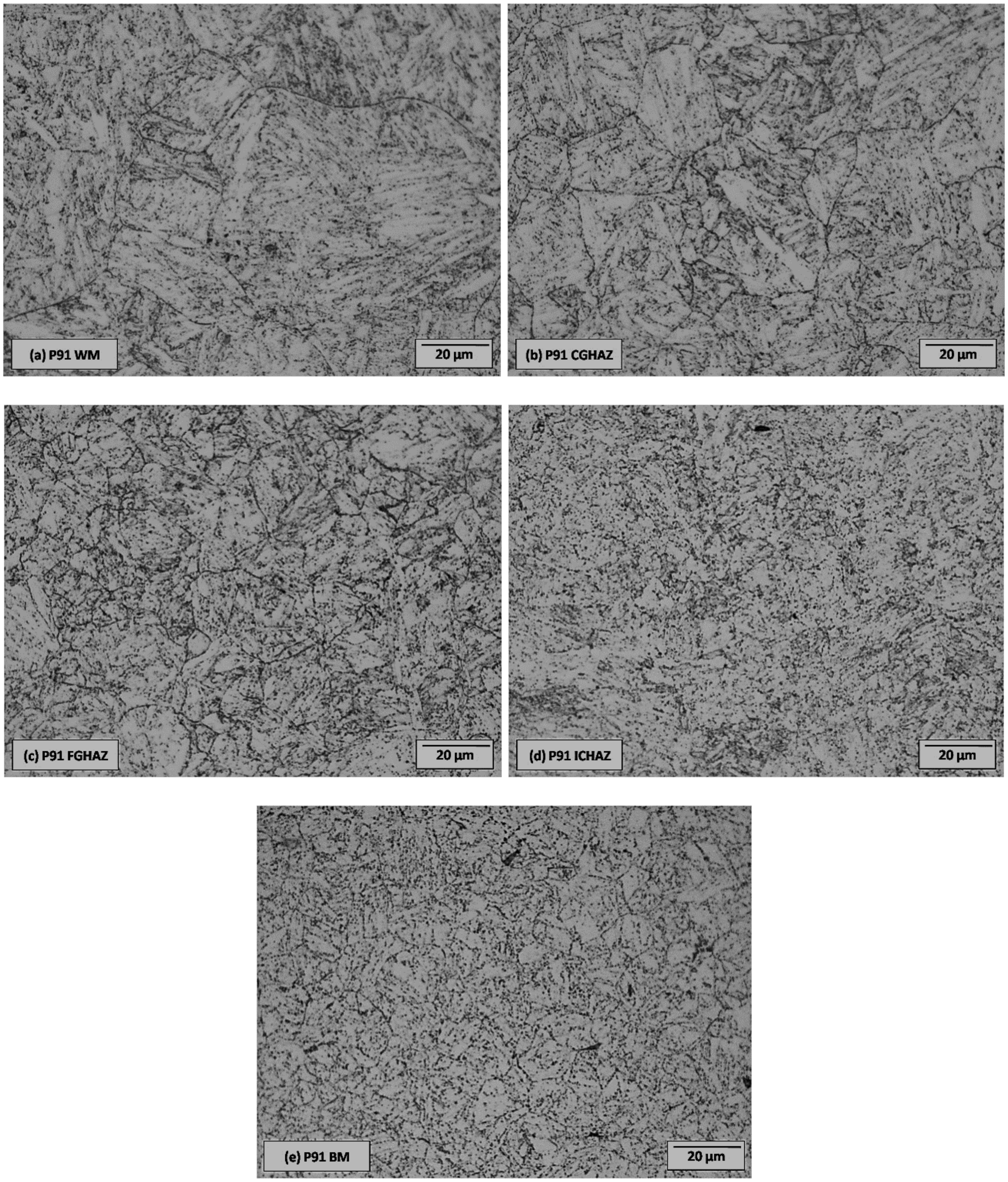

Fig. 7.1 Microstructure across the P91 steel TIG weld joint (bevel angle 35°) (a) WM, (b) CGHAZ, (c) FGHAZ, (d) ICHAZ and (e) BM.

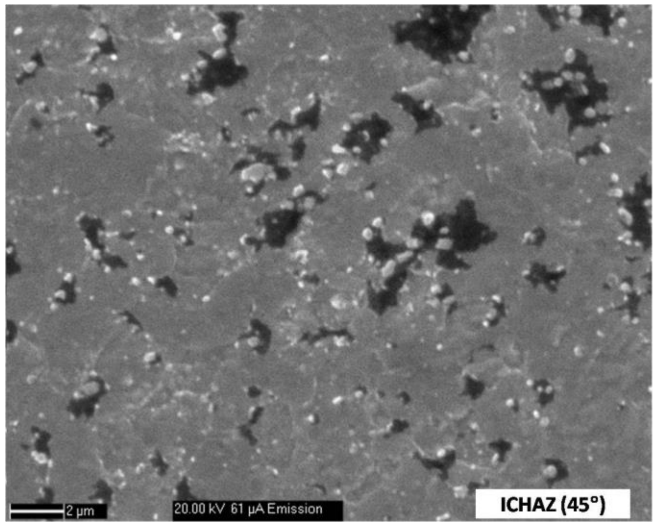

Fig. 7.2 SEM micrograph of ICHAZ in 45° bevel angle joint.

7.2.2 Rupture behaviour and microstructure of creep exposed weld joints

The creep rupture life (t_r) variation of specimens from joints with different bevel angles are shown in Fig. 7.3. Creep rupture life of the weld joint is found to decrease with increase in bevel angles. The joint with 35° bevel angle (70° included or groove angle) shows t_r higher by a factor of 1.6 and 2.5 respectively than the joints made with 45° and 60° bevel angles (90° and 120° included or groove angle). The joint made from 60° bevel angle exhibited the lowest t_r life. The EB/A-TIG joint of 0° bevel angle exhibited the highest t_r than the V-groove joints having different bevel angles (by a factor of ~2.5 with respect to the t_r of 35° joint which was the highest among the V groove joints). The significant decrease in rupture life in the joint having higher groove angle can be attributed to two factors; (i) microstructural damage in the HAZ by more number of repeated weld thermal cycles during welding and (ii) alteration in the state of stress at the ICHAZ of the joint, which is constrained by the adjacent stronger regions. Parker [68] has reported higher t_r in weld joint of groove angle 10° than in the 30° groove angle joint of P91 steel. In the present investigation, a wider range of bevel angles have been employed. Weld joints of 0°, 35°, 45° bevel angles fractured in the type IV region (Fig. 7.4(a-c)), whereas the 60° weld joint experienced fracture across the near HAZ to unaffected BM region (Fig. 7.4(d)). Francis et al [163] have reported an increase in t_r with increase in pre-heat temperature and reduction in joint preparation angle based on neural network prediction, and also showed that the influence of heat input on type IV cracking is relatively low compared to pre-heat temperature and joint angle.

Creep ductility was significantly lower in the joints that failed in the type IV region as compared to BM and the weld joint with 60° bevel angle. The % reduction in area (RA) of the weld joint decreased with decrease in bevel angle (Fig. 7.5). Significant decrease in RA has been observed in the joints with 0°, 35° and 45° bevel angles as compared to the 60° joint. However, the reduction in area of 0° and 35° joints were comparable. The microstructure of the 35° weld joint crept at 60 MPa and 923 K is shown in Fig. 7.6. Localized creep deformation and cavitation in the ICHAZ were observed in the weld joints that ruptured in the type IV region (Fig. 7.4 and 7.6). The predominant creep cavitation was observed in the ICHAZ than the other regions in the weld joint. Creep cavitation damage was extensive in the mid-section of the specimen than the surface of the joint due to the increased triaxial state of stress in the mid-section. The extent of cavitation damage was higher in the joint with lower bevel angles 0° and 35° (Fig. 7.7). Creep cavitation, in terms of both size and number density, was lesser in the joint having 45° than those with 0° and 35°. Creep damage in the 0° and 35° joints was comparable; these have undergone longer creep exposure too. The critical size of the cavity for type IV fracture is about ~30 μm, which has been obtained from the intact side of the HAZ and type IV fractured region of the weld joint (Fig. 7.7). Alteration in state of stress by the groove angle of the weld joint has been examined in electron beam weld (EBW), laser weld (LW) and TIG weld joints of P122 steel

[160]. It has been concluded that the reduction in HAZ width or groove angle of the joint led to improvement in creep rupture life [160]. Siefert et al have reported that in a weld joint, the region possessing higher angle has shown higher damage than the regions having lower angle [8]. In Figs. 7.7 and 7.8, predominant recovered structure from martensitic lath structure is evident at the cavitated region in the ICHAZ. Kimura et al [14,115] have reported that the internal stresses at the vicinity of PAG boundaries are higher than the interior of the grain. Higher grain boundary area led to increase the rate of recovery of subgrain lath structure [65]. It is clear from Fig. 7.7 that there is a significant decrease in cavitation in the ICHAZ with increasing bevel angle. In spite of this, and the fact that failure occurred in this region for all the specimens (except that from 60° bevel angle joint), the rupture life t_r decreased with increasing bevel angle.

The occurrence of creep fracture across the HAZ to BM in the 60° bevel angle joint is due to (i) extensive microstructural change in the ICHAZ during welding and (ii) reduction in deformation constraint due to change in the orientation of stress axis with respect to HAZ. Coarse $M_{23}C_6$ precipitates were observed in the ICHAZ of the creep exposed weld joints and it was predominant in the joint having 0°, 35° and 45° than the 60° (Fig. 7.8). The size of $M_{23}C_6$ precipitates in the joints with 0° and 35° bevel angles were comparable. The 0° bevel angle joint was single pass, and did not experience repeated thermal cycles. However, it experienced longer creep exposure due to the fine precipitates and less recovery of the martensitic structure and presence of unmixed regions of HAZ. The multi-pass joints that experienced more weld thermal cycles resulted in coarser $M_{23}C_6$ precipitates (35° and 45°) and heterogeneity due to mixed regions of HAZ in the joints. Precipitate coarsening under creep exposure was less in the 60° bevel joint as compared to other joints (Fig. 7.8). Although HAZ orientation moves towards stress axis of the specimen with increasing the bevel angle which led to change in the constraint towards the BM region, the microstructural damage (coarsening of precipitates and recovered martensitic structure) which occurred during multiple weld thermal cycle precludes the advantage derived from HAZ orientation with respect to stress axis, this resulted in earlier failure than the single pass joint having unmixed regions. This effect is evident in the weld joint having 60° bevel angle. The variation of hardness in the crept weld joints having different bevel angles with distance across is shown in Fig. 7.9. The hardness decreased from WM to BM with a dip in the ICHAZ in all the joints. The fracture is evidently seen at the region where lower hardness was observed in the joints. However, joint having 60° bevel angle was fractured across near HAZ to BM.

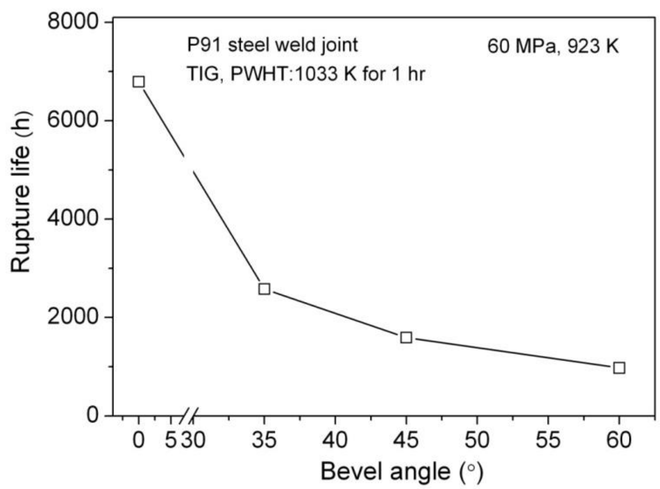

Fig. 7.3 Variation of creep rupture life of the weld joints with the bevel angle.

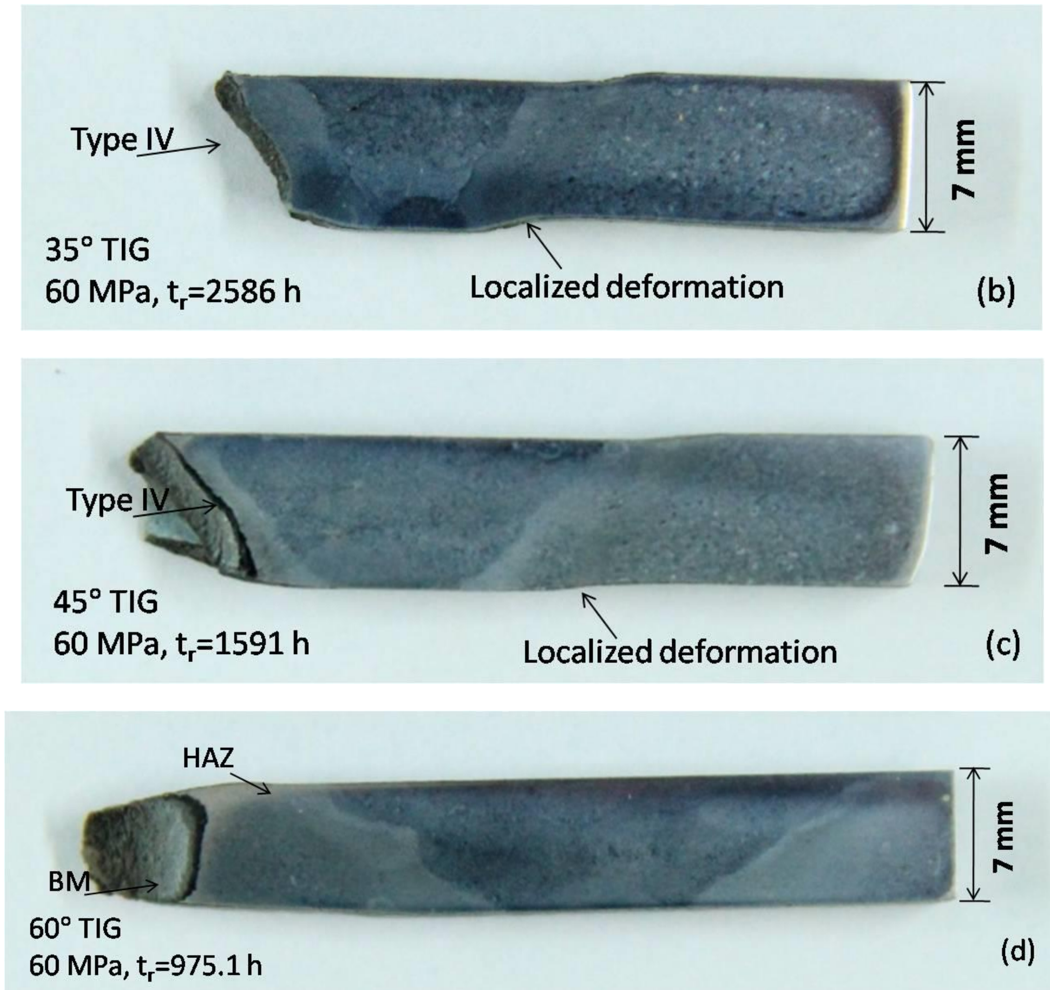

Fig. 7.4 Specimens of joints with different groove angles creep ruptured at 60 MPa and 923 K.

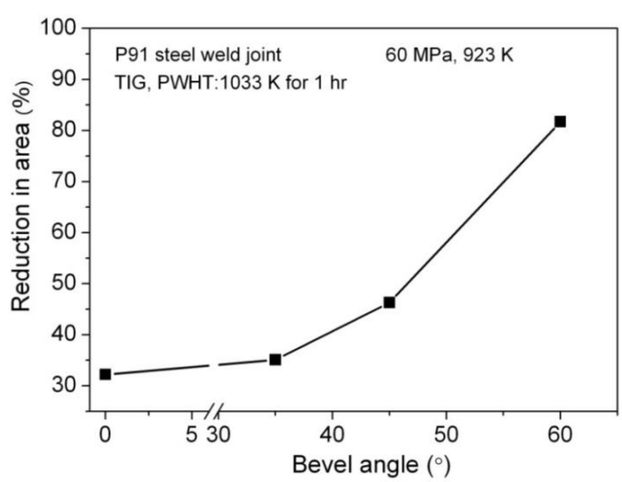

Fig. 7.5 Reduction in area (%) of joints with different bevel angles at 60 MPa and 923 K.

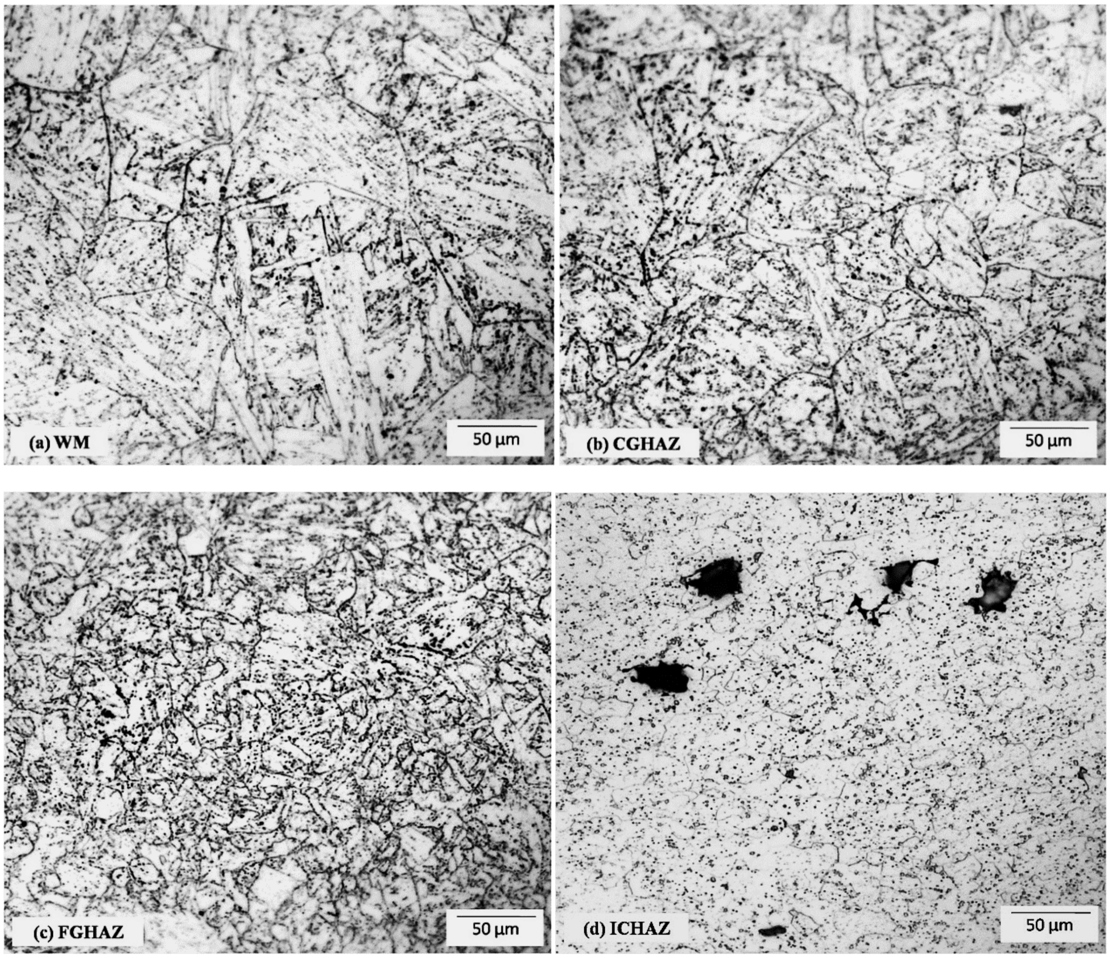

Fig. 7.6 Microstructure in different regions of crept P91 steel weld joint having 35° bevel (70° groove) angle at 60 MPa and 923 K.

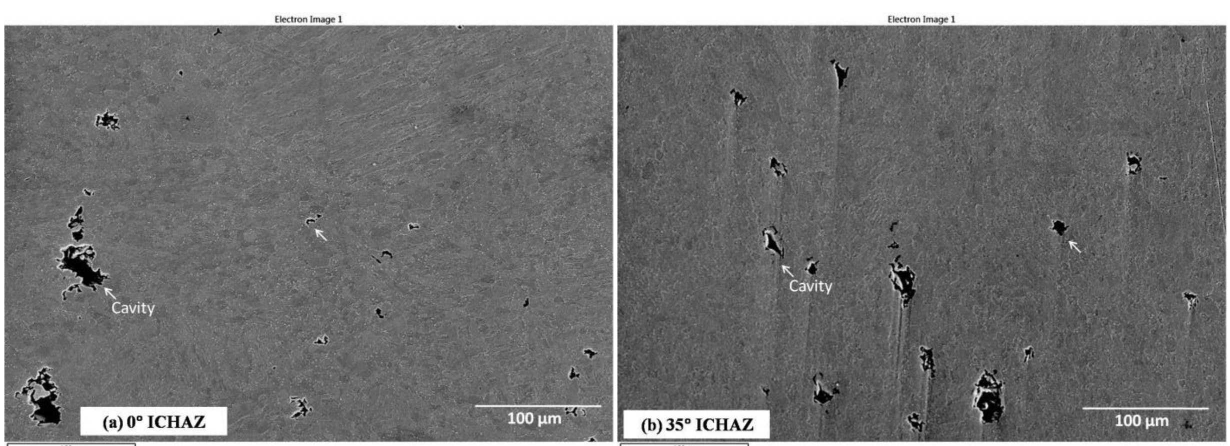

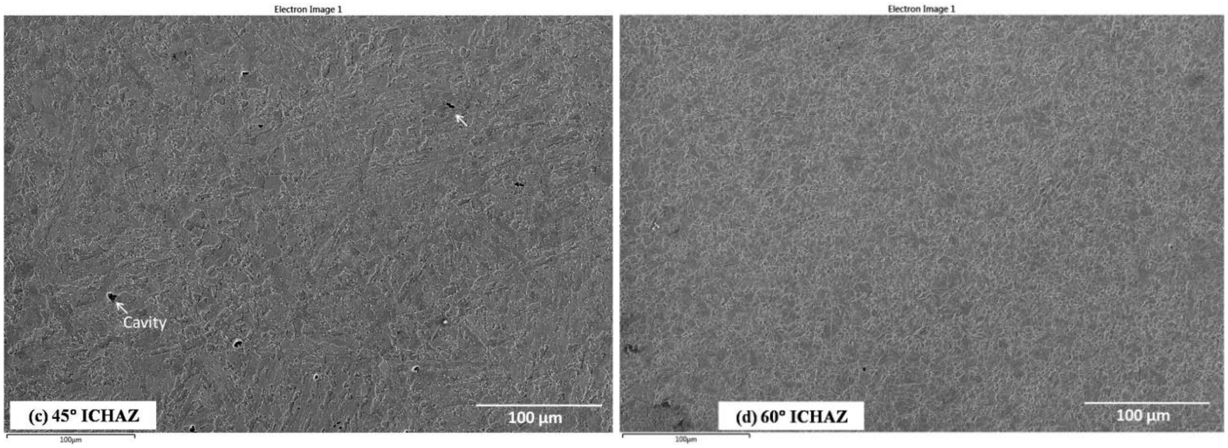

Fig. 7.7 The ICHAZ of crept weld joints specimen (60 MPa and 923 K) from different bevel angles (a) 0°, (b) 35°, (c) 45° and (d) 60° showing different extents of cavitation.

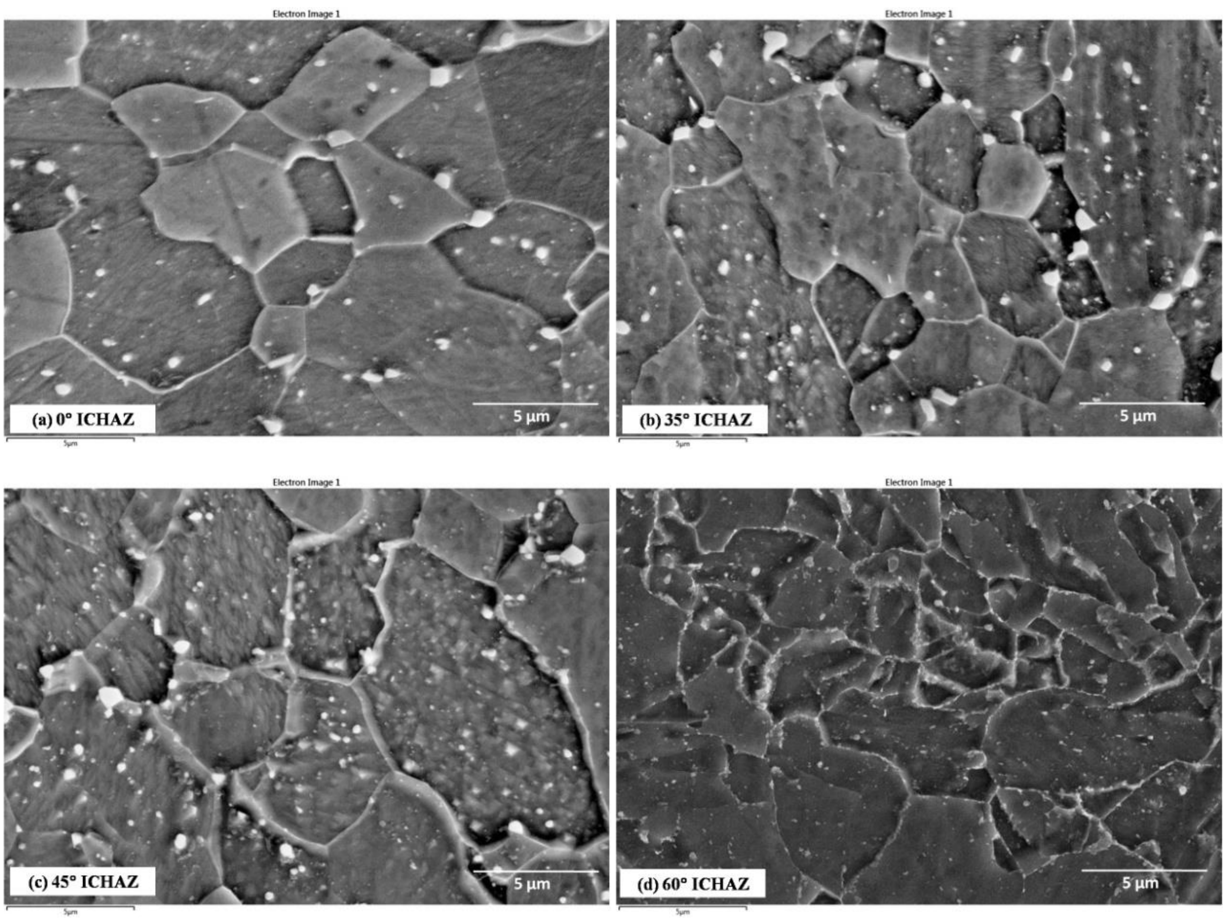

Fig. 7.8 SEM micrographs of ICHAZ of the weld joints crept at 923 K and 60 MPa (a) 0°, (b) 35°, (c) 45° and (d) 60° bevel angles.

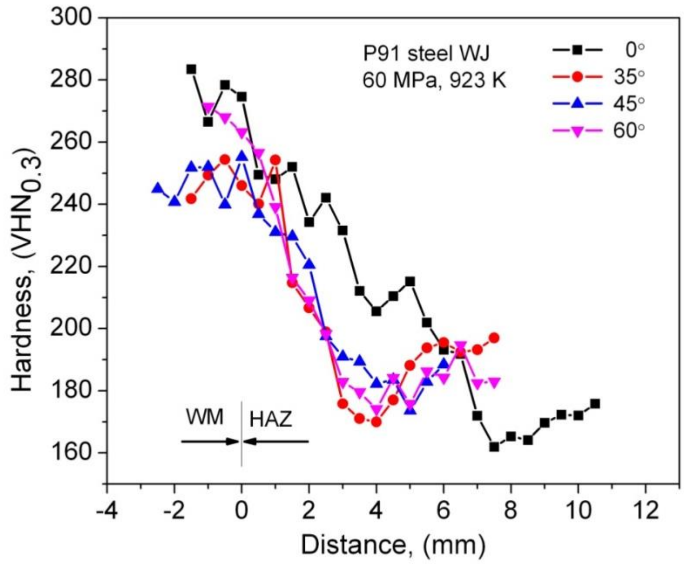

Fig. 7.9 Variation of hardness across the weld joints having different groove angles at 60 MPa and 923 K.

The joint having 35° has exhibited higher t_r than those with higher bevel angles due to less microstructural damage since the weld thermal cycles are limited. Thus, the V-groove joints having bevel angle of 35° or lower value (0°) is preferred to have better creep rupture strength of the components with weld joints.

7.2.3 Finite element analysis of weld joints

Two dimensional elastic-creep FEM analysis of P91 weld joints having 35° and 60° bevel angles using the elastic and creep properties of WM, CGHAZ, FGHAZ, ICHAZ and BM were carried out to study the variations in distribution of principal stress, hydrostatic stress, Von-Mises and stress triaxiality with groove angle. The details are presented in the following sections.

7.2.3.1 Material Properties

The Norton's power law of creep constitutive equation ($\dot{\epsilon}_{min} = A\sigma^n$) was employed for the analysis. The creep properties of different HAZ regions were obtained from tests conducted on furnace simulated specimens, i.e., blanks were exposed to different peak temperatures to obtain the microstructure of various regions in the HAZ (details are given in section 2.3.2). All-weld specimens extracted from the weld joint were tested to derive the weld metal creep properties. The material properties at 923 K used in the FEM analysis are given in Table 7.1. Young's modulus and Poisson's ratio of 160 GPa and 0.33 respectively were used in the analysis. The FEM analysis was carried out with an applied stress of 60 MPa for 35° and 60° bevel angled joints.

Table 7.1 Materials constants for P91 steel WM, BM, and simulated HAZ regions obtained from uniaxial creep at 923 K.

Weld joint regions	A (MPa^{-n} h^{-1})	n
WM	$3.0\text{x}10^{-22}$	10.2
CGHAZ	$3.2\text{x}10^{-21}$	10.5
FGHAZ	$5.3\text{x}10^{-18}$	8.17
ICHAZ	$3.0\text{x}10^{-16}$	6.5
BM	$7.2\text{x}10^{-17}$	7.3

7.2.3.2 Results

The distribution of maximum principal stress, hydrostatic stress, Von-Mises stress and triaxiality factor contours for the weld joints having 35° and 60° bevel angles are shown in Fig. 7.10. Higher maximum principal stress, hydrostatic stress and triaxiality factor were observed in the ICHAZ as compared to other regions in the 35° bevel angle weld joint. This led to premature type IV cracking in the ICHAZ (Fig. 7.4). However, maximum principal stress in the ICHAZ of 60° bevel angle joint was higher than that in the 35° joint. Hydrostatic stresses observed in the both the joints were comparable. The triaxiality factor was relatively lower in the ICHAZ of the 60° bevel angle joint as compared to the 35° bevel joint, but the base metal region possessed relatively higher value than the joint having 35° bevel angle this led to premature failure of the 60° bevel angle joint adjacent to the HAZ across BM. The lower maximum principal stress and Von-Mises stress in the ICHAZ in the lower bevel angle led to increase the creep rupture life of the weld joint (Fig. 7.10). Similar observations have been reported for P92 steel weld joint based on numerical analysis [164]. It may be recalled that extensive cavity formation and growth have been observed in the ICHAZ of 0° and 35° bevel joints, whereas in the case of 45° bevel joint smaller size cavities were observed (ref. the earlier Fig. 7.7). This can be attributed to the relatively higher maximum principal stress in 45° bevel joint aiding cavity nucleation, but their growth is reduced due to lesser triaxiality in the ICHAZ as observed in the FEM with increase in bevel angles, Figs. 7.7 and 7.10.

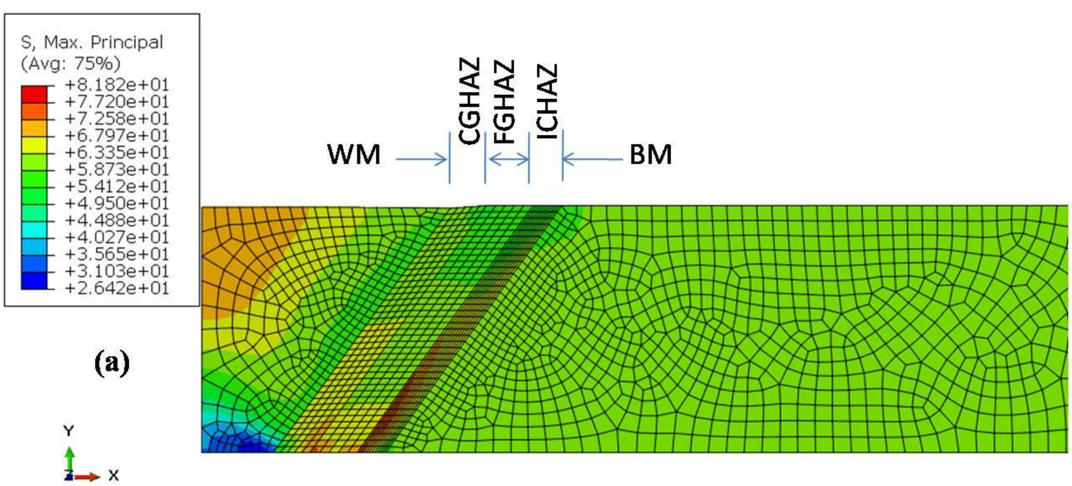

(a)

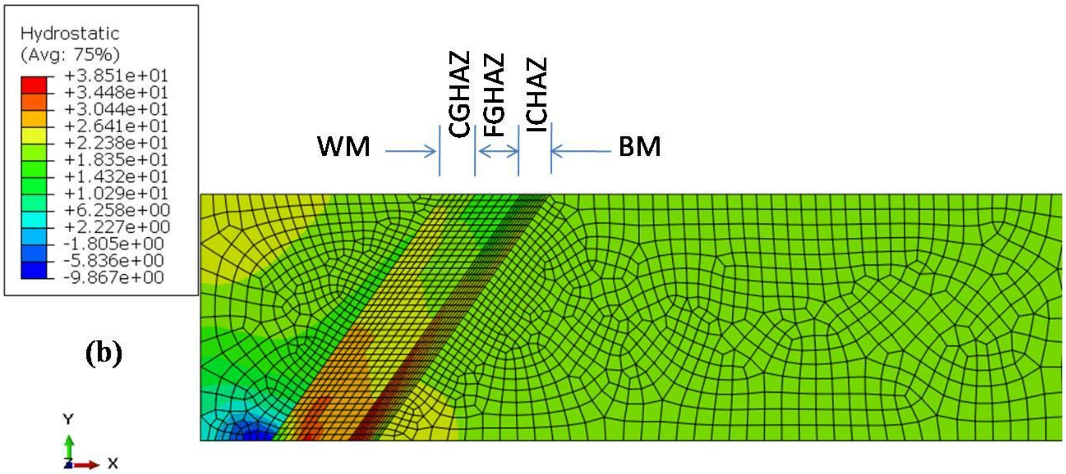
Hydrostatic
(Avg: 75%)
+3.851e+01
+3.448e+01
+3.044e+01
+2.641e+01
+2.238e+01
+1.835e+01
+1.432e+01
+1.029e+01
+6.258e+00
+2.227e+00
-1.805e+00
-5.836e+00
-9.867e+00
WM
CGHAZ
FGHAZ
ICHAZ
BM
Y
X

(b)

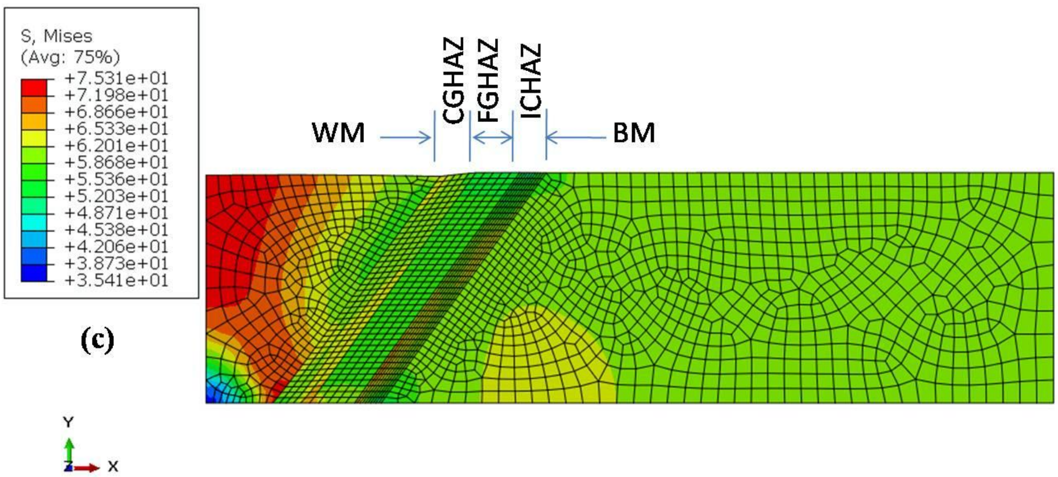
S, Mises
(Avg: 75%)
+7.531e+01
+7.198e+01
+6.866e+01
+6.533e+01
+6.201e+01
+5.868e+01
+5.536e+01
+5.203e+01
+4.871e+01
+4.538e+01
+4.206e+01
+3.873e+01
+3.541e+01
WM
CGHAZ
FGHAZ
ICHAZ
BM
Y
X

(c)

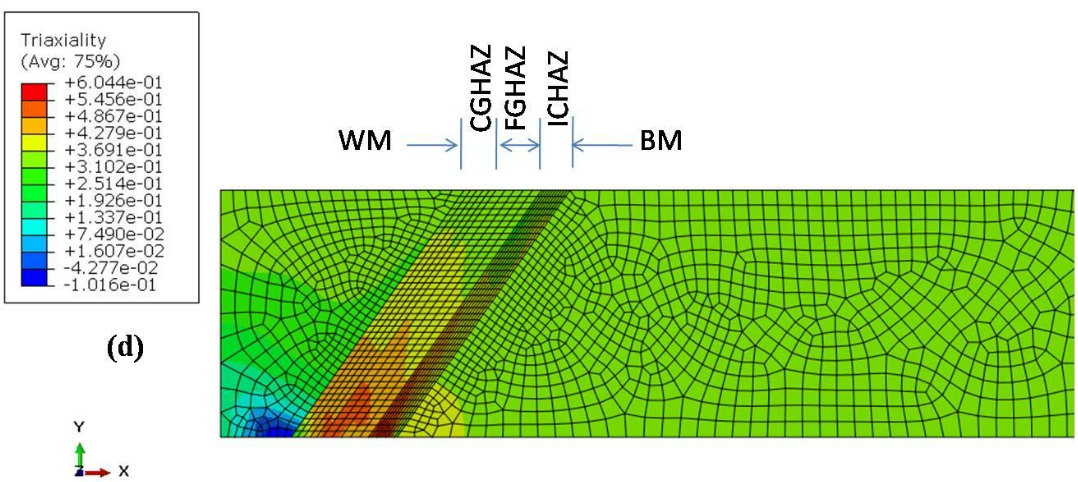
Triaxiality
(Avg: 75%)
+6.044e-01
+5.456e-01
+4.867e-01
+4.279e-01
+3.691e-01
+3.102e-01
+2.514e-01
+1.926e-01
+1.337e-01
+7.490e-02
+1.607e-02
-4.277e-02
-1.016e-01
WM
CGHAZ
FGHAZ
ICHAZ
BM
Y
X

(d)

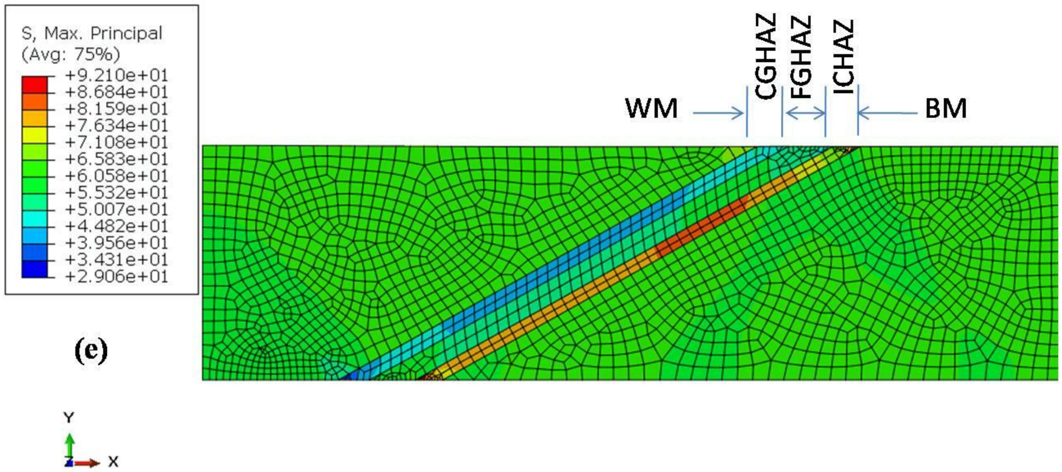
S, Max. Principal
(Avg: 75%)
+9.210e+01
+8.684e+01
+8.159e+01
+7.634e+01
+7.108e+01
+6.583e+01
+6.058e+01
+5.532e+01
+5.007e+01
+4.482e+01
+3.956e+01
+3.431e+01
+2.906e+01
CGHAZ
FGHAZ
ICHAZ
WM
BM
Y
X

(e)

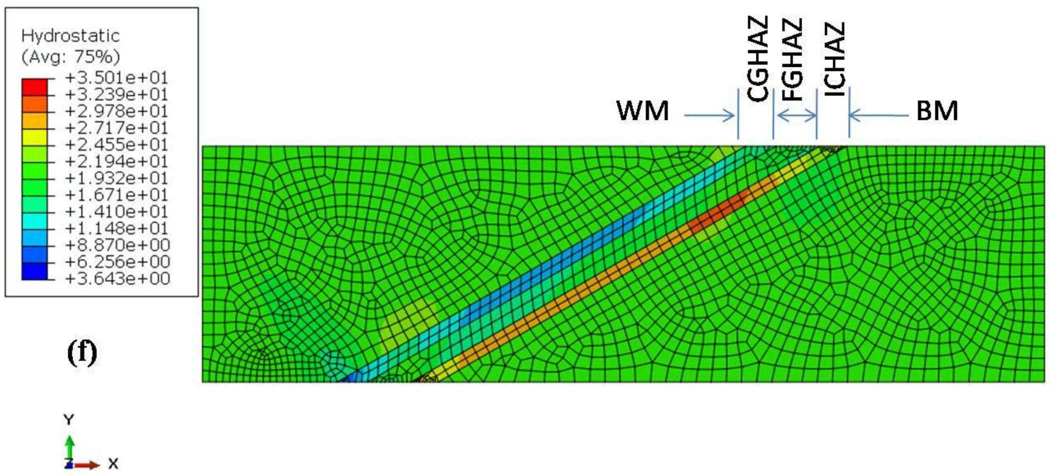
Hydrostatic
(Avg: 75%)
+3.501e+01
+3.239e+01
+2.978e+01
+2.717e+01
+2.455e+01
+2.194e+01
+1.932e+01
+1.671e+01
+1.410e+01
+1.148e+01
+8.870e+00
+6.256e+00
+3.643e+00
CGHAZ
FGHAZ
ICHAZ
WM
BM
Y
X

(f)

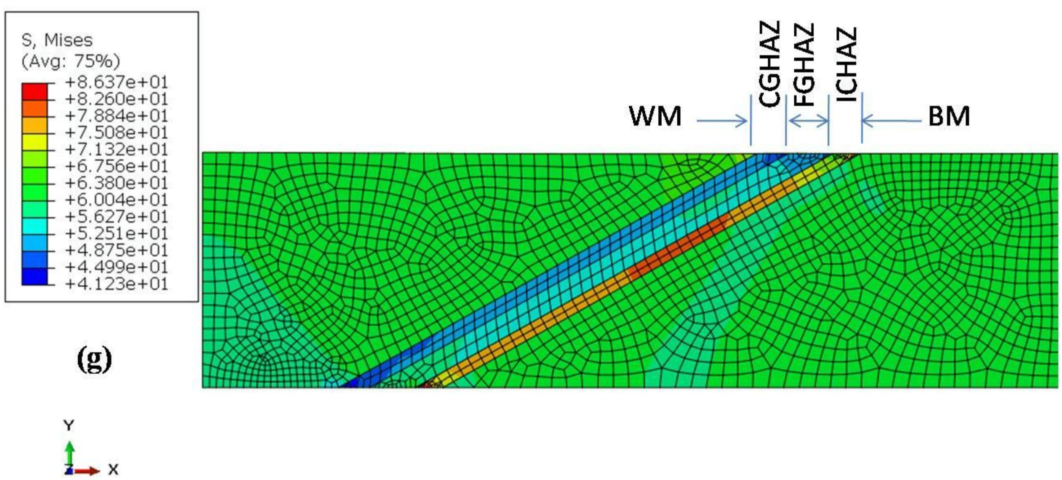
S, Mises
(Avg: 75%)
+8.637e+01
+8.260e+01
+7.884e+01
+7.508e+01
+7.132e+01
+6.756e+01
+6.380e+01
+6.004e+01
+5.627e+01
+5.251e+01
+4.875e+01
+4.499e+01
+4.123e+01
CGHAZ
FGHAZ
ICHAZ
WM
BM
Y
X

(g)

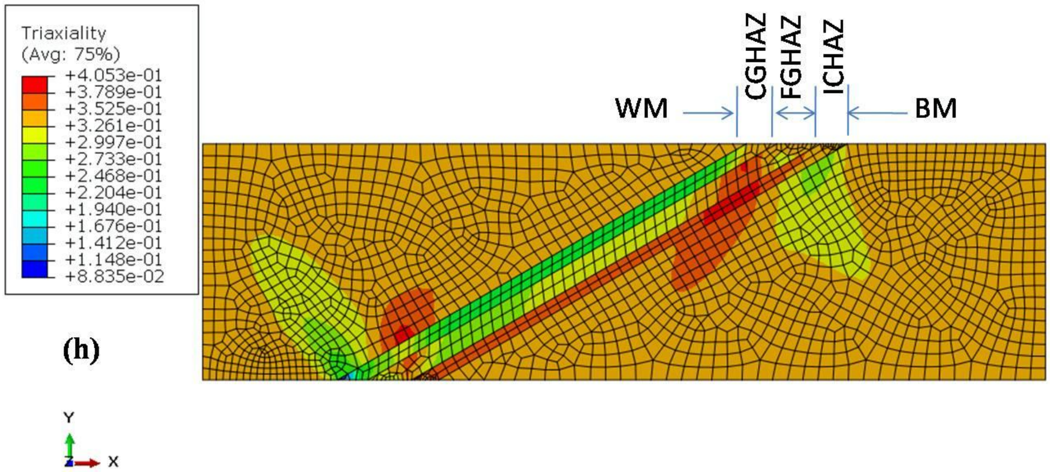

Fig. 7.10. Distribution of maximum principal stress, hydrostatic stress, Von-Mises stress and triaxiality contours for the weld joints having 35° (a, b, c, d) and 60° (e, f, g, h) bevel angles.

7.3 Effect of HAZ orientation

It is seen from the previous sections on the effect of groove angle on the type IV cracking that the differences in the number of passes affect the microstructure and make the interpretation of results difficult, especially to identify quantitatively the contributions from constraints/triaxiality and the microstructure. Therefore, a study was taken up by varying the specimen orientation in an NG-TIG joint of P92 steel. This steel was chosen since thick plates were welded using NG-TIG procedure. P92 steel weld joint fabricated using NG-TIG process is shown in Fig. 2.6. The microstructures across the NG-TIG weld joint are shown in Figs. 6.20 and 6.23. In order to understand the effects of weld joint orientation with respect to applied stress, specimens were extracted at different orientations (Fig. 2.6). These specimens were creep tested at 923 K and 110 MPa applied stress. Variation in t_r with orientation of the specimen is shown in Fig. 7.11. The specimen having 90° stress axis with respect to weld direction/HAZ exhibited lowest t_r. It is observed that t_r increased with decreasing angle between the WJ/HAZ and the stress axis, which can be attributed to the decreased constraint effect on FGHAZ/ICHAZ with decreasing orientation angle. Reduction in area and elongation (%) for different orientations are given in Fig. 7.12. The specimens in which the HAZ was at 90°, 60° and 45° with the stress axis with HAZ fractured in the type IV region with significant decrease in creep ductility. On the other hand, the specimen in which the HAZ was at 30° and 20° with the stress axis fractured across the fusion line to BM and had higher ductility. The higher ductility observed in the 30° and 20° specimens can be ascribed to reduction in deformation constraint in the outer edge of HAZ (FGHAZ/ICHAZ) and shifting of deformation constraint predominantly towards BM.

Creep ruptured specimens having different orientations are shown in Fig. 7.13(a). It is evident that the orientation of the fracture surface matches with that of the HAZ/fusion line angle. Specimen having 20° has experienced predominant crack propagation through the BM although crack was noticed to pass-through the HAZ (Fig. 7.13(e)). Deformation was localized in the FGHAZ, and the deformation was significantly lowered in the type IV susceptible regime for specimens in other orientations (90°, 60° and 45°) (Fig. 7.13 (a-d)). Optical micrographs of the crept joint of 60° orientation are shown in Fig. 7.14. Extensive localized creep cavitation was observed in the FGHAZ as compared to other regions in the weld joint. The creep cavitation in the FGHAZ was predominant in the 90° specimen and reduced with decrease in the specimen orientation from 60° to 45° presumably due to reduction in deformation constraint in the FGHAZ. Both, size and number density of creep cavities reduced with decreasing orientation angles (Fig. 7.15). Under lower orientation angle (30° and 20°), the creep damage occurs across the HAZ to BM. Microstructure observed in the FGHAZ of the specimens having different orientations is shown in Fig. 7.15(b, d and f). The extent of coarsening of $M_{23}C_6$ and Laves phase precipitates in the FGHAZ was comparable in all the specimens, despite the difference in t_r by a factor of ~2. The t_r data at 110 MPa/923 K for specimens with different orientations along with the variation of rupture life of NG-TIG weld joint have been shown in Fig. 7.16(a). Weld strength factors for specimens of different orientations and those for NG-TIG weld joint have been shown in Fig. 7.16(b). The WSF is found to increase with decreasing orientation angle due to decrease in constraint effect on the FGHAZ/ICHAZ. Hence, minimization of the orientation angle between the stress axis and weld joint fusion line/HAZ is recommended in order to increase the life of the welded components for high temperature applications made of steels that are susceptible to Type IV cracking.

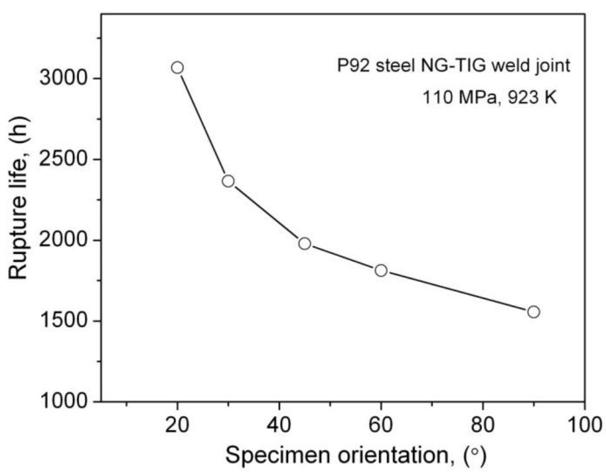

Fig. 7.11 Creep rupture life with specimen orientations of P92 steel NG-TIG weld joint at 923 K and 110 MPa.

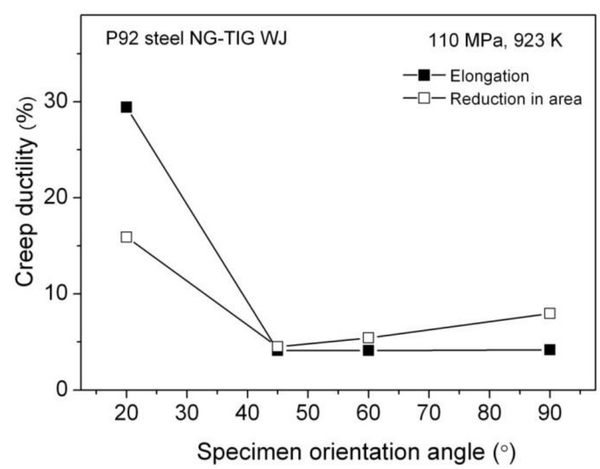

Fig. 7.12 Creep ductility (elongation and reduction in area (%)) with specimen orientations of P92 steel NG-TIG joint at 923 K and 110 MPa.

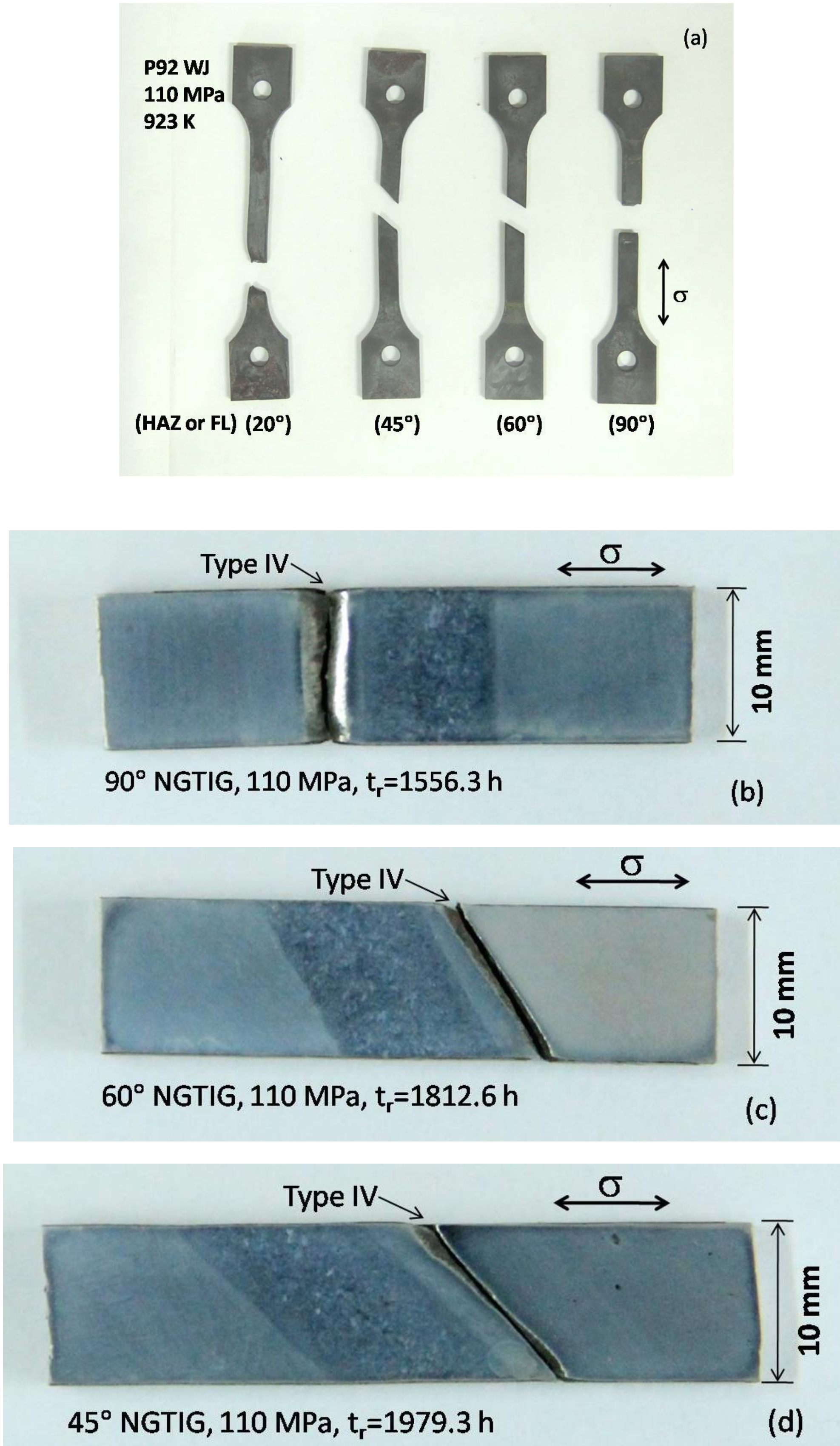
(a)
P92 WJ
110 MPa
923 K
σ
(HAZ or FL) (20°)
(45°)
(60°)
(90°)
Type IV
σ
10 mm
90° NGTIG, 110 MPa, tr=1556.3 h
(b)
Type IV
σ
10 mm
60° NGTIG, 110 MPa, tr=1812.6 h
(c)
Type IV
σ
10 mm
45° NGTIG, 110 MPa, tr=1979.3 h
(d)

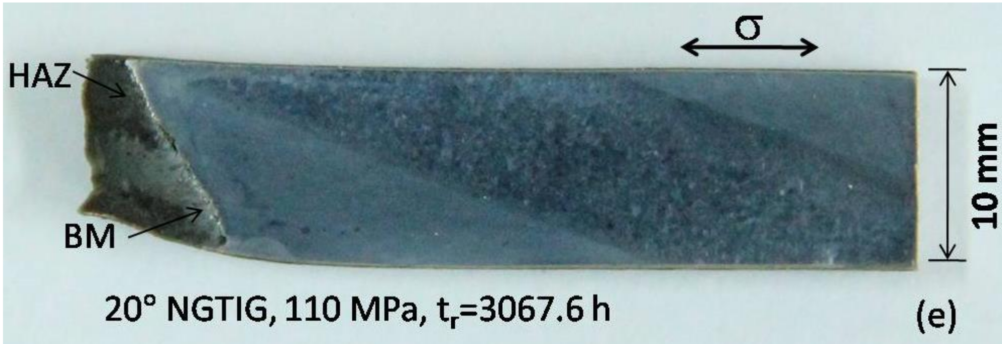

Fig. 7.13 (a) Creep ruptured specimens having different FL/HAZ orientation with stress axis, (b) 90°, (c) 60°, (d) 45° and (e) 20° at 923 K and 110 MPa.

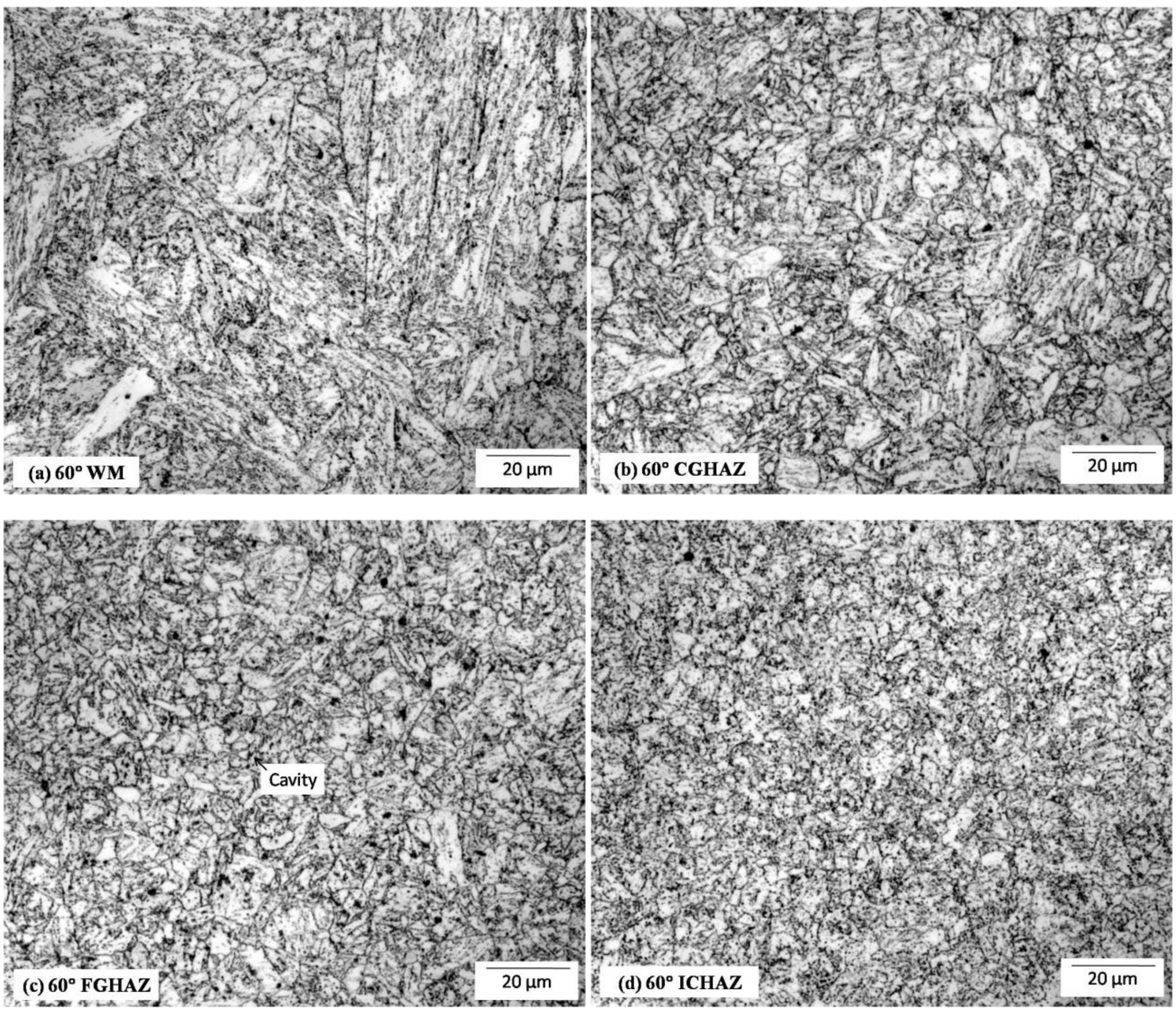

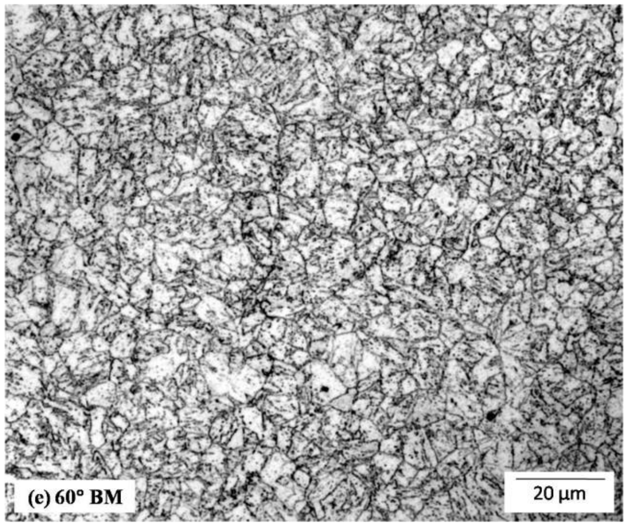

Fig. 7.14 Microstructure of P92 weld joint specimen with the fusion line/HAZ at 60° to the stress axis, crept at 923 K and 110 MPa (a) WM, (b) CGHAZ, (c) FGHAZ, (d) ICHAZ and (e) BM.

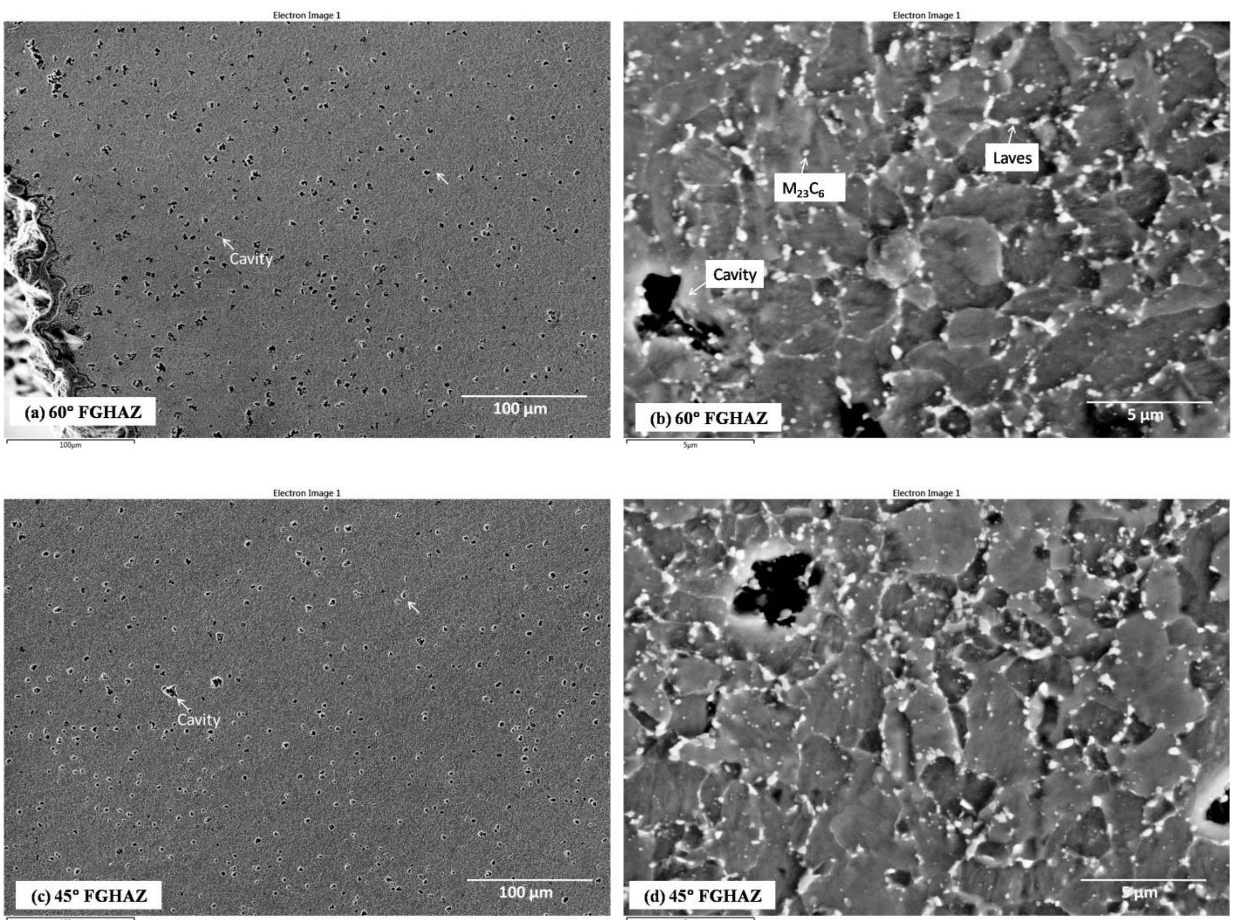

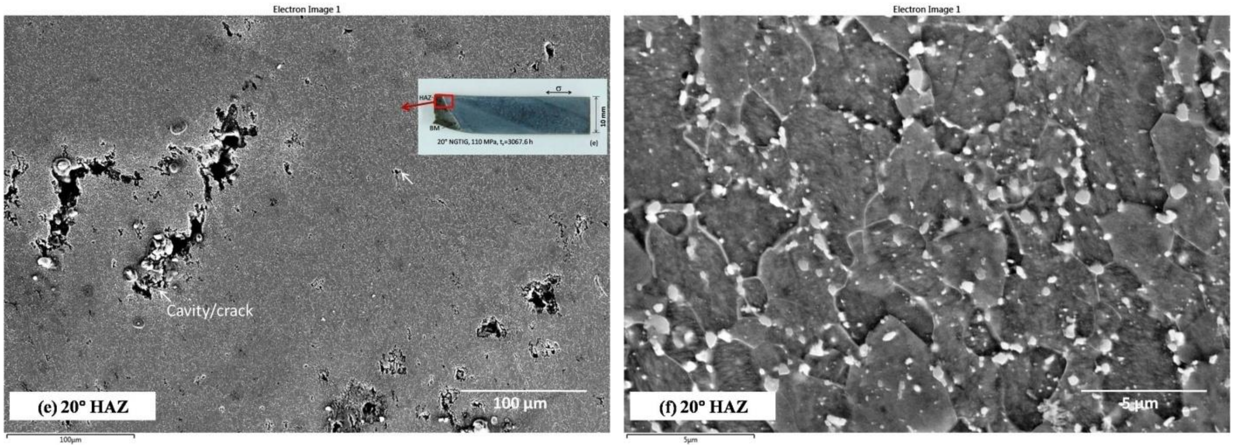

Fig. 7.15 FGHAZ of weld joint from different specimen orientations with stress axis (a) 60°, (b) 45°and (c) 20° at 923 K and 110 MPa.

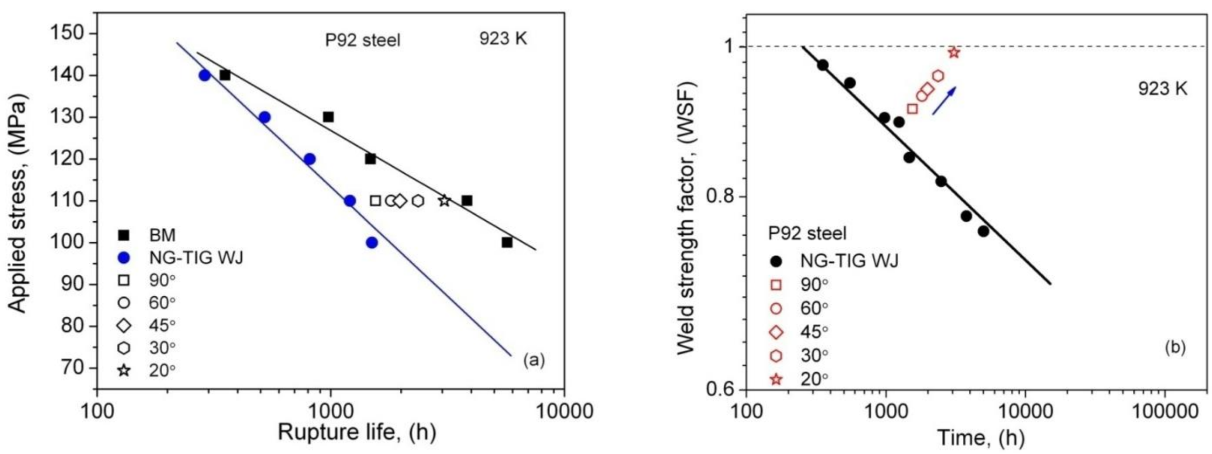

Fig. 7.16 (a) Rupture life of P92 steel weld joint at different conditions with applied stress, (b) weld strength factor for P92 steel weld joint in different conditions at 923 K.

7.4 Conclusions

The effect of orientation of the HAZ with respect to the stress axis of the cross-weld specimen on the type IV cracking behaviour has been studied by changing (i) the weld bevel angle in P91 joint and (ii) the orientation of the specimen in an NG-TIG joint of P92 steel with nearly 0 degree bevel angle.

In the case of P91 steel joint with different bevel angles, in addition to the orientation, the number of weld thermal cycles are different, leading to changes in the initial microstructure of the HAZ region. A bevel angle of 35° is found to be better than higher bevel angles from the point of view of longer life for the P91 weld joint, due to the limited microstructural damage through limited number of weld thermal cycles. At the same time, there will be the beneficial effect of reducing the maximum principal stress and Von-Mises stress in the ICHAZ. 0° bevel single pass A-TIG weld joint exhibited significantly higher creep rupture life due to reduced microstructural damage in the HAZ. The weld joint having lower bevel angle is preferred to have better creep rupture strength of the components associated with weld joints.

Specimen orientation influenced the creep rupture life of the P92 NG-TIG joint significantly. Creep cavitation damage in the FGHAZ of weld joint decreased with decrease in the angle between stress axis of the specimen and the weld fusion line/HAZ. Size of the precipitates in the FGHAZ region of the specimens in different orientations crept at 923 K under 110 MPa were comparable despite the difference in t_r by a factor of nearly 2. The weld strength factor is found to increase with decreasing orientation angle due to decrease in constraint effect on the FGHAZ/ICHAZ. Hence, minimization of the orientation angle between stress axis and weld joint fusion line/HAZ is recommended for improved life of the components of this steel with multi-pass joints operating at high temperature.

REFERENCES

[1] R.L. Klueh and D. R. Harries, High chromium ferritic and martensitic steels for nuclear applications, ASTM, 2001, ISBN 0-8031-2090-7.

[2] R. L. Klueh, Elevated temperature ferritic and martensitic steels and their application to future nuclear reactors, International Materials Reviews, 2005, Vol. 50(5), 287-312.

[3] Kouichi Maruyama, Kota Sawada, Jun-ichi Koike, Strengthening mechanisms of creep resistant tempered martensitic steel, ISIJ International, Vol. 41 (2001), No. 6, pp. 641-653.

[4] Fujio Abe, Precipitate design for creep strengthening of 9% Cr tempered martensitic steel for ultra-supercritical power plants, Science and technology of advanced materials, 9 (2008), 013002 (pp 15).

[5] Triratna Shrestha, Mehdi Basirat, Indrajit Charit, Gabriel P. Potirniche, Karl K. Rink, Creep rupture behavior of Grade 91 steel, Materials Science and Engineering A 565 (2013) 382-391.

[6] J. Hald, Microstructure and long-term creep properties of 9–12% Cr steels, International Journal of Pressure Vessels and Piping 85 (2008) 30-37.

[7] F. Abe, M. Taneike, K. Sawada, Alloy design of creep resistant 9Cr steel using a dispersion of nano-sized carbonitrides, International Journal of Pressure Vessels and Piping 84 (2007) 3-12.

[8] J. A. Siefert, J. D. Parker, Evaluation of the creep cavitation behavior in grade 91 steels, International journal of pressure vessels and piping, 138, 2018, 31-44.

[9] D. J. Abson, J. S. Rothwell, Review of type Iv cracking of weldments in 9-12%Cr creep strength enhanced ferritic steels, International Materials Reviews, 2013, Vol. 58(8), 437-473.

[10] J. Parker, Guidelines and Specifications for High-Reliability Fossil Power Plants, Electric Power Research Institute, Technical report, 1023199, 2011.

[11] J. A. Francis, W. Mazur, H. K. D. H. Bhadeshia, Type IV cracking in ferritic power plant steels, Materials Science and Technology, 2006, Vol. 22 (12), P: 1387-1395.

[12] S. A. David, J. A. Siefert, Z. Feng, Welding and weldability of candidate ferritic alloys for future advanced ultrasupercritical fossil power plants, Science and technology of welding and joining, 2013, 18(8), 631-651.

[13] ASME SA-335/SA355M, Section II, Part A, Specification for seamless ferritic alloy steel pipe for high-temperature service, 2010.

[14] K. Kimura, Y. Toda, H. Kushima, K. Sawada, Creep strength of high chromium steel with ferrite matrix, International Journal of Pressure Vessels and Piping 87 (2010), 282-288.

[15] Carl D Lundin et al., A literature review on characteristics of high temperature ferritic Cr-Mo steels and weldments, WRC Bulletin 454.

[16] K. Sawada et al., Microstructural change of 9% Cr-welded joints after long-term creep, Materials Science and Engineering A 527 (2010) 1417-1426.

[17] K. Sawada et al., Z-phase formation during creep and aging in 9-12 %Cr heat resistant steels, ISI International, Volume 46 (2006), No 5, p 769-775.

[18] K. Sawada et al., Effect of tempering temperature on Z-phase formation and creep strength in 9Cr-1Mo-V-Nb-N steel, Materials Science and Engineering A 480 (2008) 558-563.

[19] K. Sawada et al., Microstructural degradation of Gr.91 steel during creep under low stress, Materials Science and Engineering A 528 (2011) 5511-5518.

[20] J. A. Francis et al., Type IV cracking in ferritic power plant steels, Materials Science and Technology, Volume 22, No 22, 2006, p1387-1395.

[21] Masayoshi Yamazaki, et al., Creep rupture properties of welded joints of heat resistant steels, Journal of Power and Energy System, Volume 2, No.4, 2008, p 1140-1148.

[22] M.E. Kassner et al., Creep cavitation in metals, International Journal of Plasticity 19 (2003) 1715–1748.

[23] Takashi Watanabe et al., Creep damage evaluation of 9Cr-1Mo-V-Nb steel welded joints showing Type IV fracture, International Journal of Pressure Vessels and Piping 83 (2006) 63 - 71.

[24] Yongkui Li et al., Evaluation of creep damage in heat affected zone of thick welded joint for modified 9Cr-1Mo steel, International Journal of Pressure Vessels and Piping 86 (2009) 585-592.

[25] K. Laha et al., Characterization of microstructure across the heat affected zone of the modified 9Cr-1Mo weld joint to understand its role in promoting Type IV cracking, Metallurgical and Materials Transactions A, 2007, 38A, 58-68.

[26] S. Spigarelli et al., Analysis of the creep behaviour of modified P91 (9Cr--1Mo-NbV) welds, Materials and Design 23, (2002) 54.

[27] Takashi Ogata et al., Damage characterisation of a P91 steel weldment under uniaxial and multi axial creep, Materials Science and Engineering A, 510-511 (2009) 238-243.

[28] S. K. Albert et al., Variation in the Type IV cracking behaviour of a high Cr steel weld with post weld heat treatment, International Journal of Pressure Vessels and Piping 80 (2003) 405 - 413.

[29] Fujio Abe et al., Suppression of Type IV fracture and improvement of creep strength of 9Cr steel welded joints by boron addition, International Journal of Pressure Vessels and Piping, 84 (2007) 44-52.

[30] V. Gaffard et al., High temperature creep flow and damage properties of 9Cr1MoNbV steels: base metal and weldment, Nuclear Engineering and Design 235 (2005) 2547-2562.

[31] K. S. Chandravathi et al., Microstructure and tensile properties of modified 9Cr-1Mo steel (grade 91), Materials Science and Technology, Volume 17, 2001, 559-565.

[32] K. Laha et al., A comparison of creep rupture strength of ferritic/austenitic dissimilar weld joints of different grades of Cr-Mo ferritic steels, Metallurgical and Materials Transactions A, 43A, 2012, 1174-1186.

[33] D. J. Smith et al., Type IV creep cavity accumulation and failure in steel welds, International Journal of Pressure Vessels and Piping 80 (2003) 617-627.

[34] J. C. Vaillant et al., T/P23, 24, 911 and 92: New grades for advanced coal-fired power plants - properties and experience, International Journal of Pressure Vessels and Piping 85 (2008) 38-46.

[35] S. Kunimitsu et al., Effect of thermo-mechanical treatment on toughness of 9Cr-W ferritic-martensitic steels during aging, Journal of Nuclear Materials, 179-181 (1991) 689-692.

[36] A. Aghajani et al., On the effect of long-term creep on the microstructure of a 12% chromium tempered martensitic ferritic steel, Acta Materialia 57 (2009) 5093-5106.

[37] Dr.-Ing Peter Seliger et al., Creep-rupture strength of welded joints made of X10CrMoVNb9-1 (P91), Welding and Cutting, Issue 4/2002, p 11-16.

[38] Ahmed Shibli et al., Some aspects of plant and research experience in the use of new high strength martensitic steel P91, International Journal of Pressure Vessels and Piping, 84 (2007) 114-122.

[39] C. R. Das et al., Effect of prior microstructure on microstructure and mechanical properties of modified 9Cr-1Mo steel weld joints, Materials Science and Engineering A, 477 (2008) 185-192.

[40] Yan Zhang, Changes in Microstructure and Mechanical Properties of P91 Weld Metal during Creep, PhD thesis, The University of Nottingham, 2009.

[41] J. Vivas, C. Capdevila, E. Altstadt, M. Houska, D. San-Martín, Importance of austenitization temperature and ausforming on creep strength in 9Cr ferritic/martensitic steel, Scripta Materialia 153 (2018) 14-18.

[42] Hilmar Kjartansson Danielsen, John Hald, Behaviour of Z phase in 9–12%Cr steels, Energy Materials: Materials Science and Engineering for Energy Systems, 2006, 1(1):49-57.

[43] G. Gupta and G. S. Was, Interpretation of improved creep properties of a 9Cr-1Mo-Nb-V (T91) Steel by Grain Boundary Engineering, TMS Lett., 2, 71, 2005.

[44] R. Viswanathan, Damage mechanisms and life assessment of high temperature components, ASM international, US, 1989.

[45] B. Neubauer and U. Wedel, Rest life estimation of creeping components by means of replicas, in Advances in life prediction methods, D.A, Woodford and J.R. Whitehead Eds. ASME, New York, 1983, 307- 314.

[46] M.E. Kassner and M.T.P. Prado, Fundamental of creep in metals and alloys, Elsevier, 2004.

[47] H.J. Frost and M.F. Ashby, Deformation mechanism maps, Pergamon Press, 1982.

[48] M.F. Ashby, C. Gandhi and D.M.R. Taplin, Fracture mechanism maps and their construction for FCC metals and alloys, Acta Met., 27 (1979) 699- 729.

[49] S.H. Goods and L.M. Brown, The nucleation of cavities by plastic deformation, Acta Met., 27 (1979) 1- 15.

[50] W.D. Nix, Mechanisms and controlling factors in creep fracture, Mater. Sci. Engg. A, 103 (1988) 103-110.

[51] M.E. Kassner and M.T.P. Prado, Fundamental of creep in metals and alloys, Elsevier, 2004.

[52] R. Raj and M.F. Ashby, Intergranular fracture at elevated temperature, Acta Met., 23 (1975) 653- 666.

[53] H. Cerjak, I. Holzer, P. Mayr, et al, Pro. 5th Int. Conf. on Advances in materials technology, Marco Island, FL, USA, October 2007, 627.

[54] C.R. Das, S.K. Albert, J. Swaminathan, et al, Transition of Crack from Type IV to Type II Resulting from Improved Utilization of Boron in the Modified 9Cr-1Mo Steel Weldment, Metallurgical and Materials Transactions A, 2012, 43A, 3724-3741.

[55] J. Baral, J. Swaminathan, D. Chakrabarti, R.N. Ghosh, Effect of welding on creep damage evolution in P91B steel, Journal of Nuclear Materials, (2017), 490, 333-343.

[56] F. Abe , M. Tabuchi , M. Kondo, H. Okada, Suppression of Type IV fracture in welded joints of advanced ferritic power plant steels - effect of boron and nitrogen, Materials at High Temperatures, 2006, 23(3/4), 145-154.

[57] Y.J. Li, D. Ponge, P. Choi, D. Raabe, Segregation of boron at prior austenite grain boundaries in a quenched martensitic steel studied by atom probe tomography, Scripta Materialia, 2015, 96, 13-16.

[58] R.L. Klueh, N. Hashimoto, P.J. Maziasz, New nano-particle-strengthened ferritic/martensitic steels by conventional thermo-mechanical treatment, Journal of Nuclear Materials, 2007, 367-370, 48-53.

[59] S. Hollner, B. Fournier, J. Le Pendu, T. Cozzika, I. Tournié, J.-C. Brachet, A. Pineau, High-temperature mechanical properties improvement on modified 9Cr–1Mo martensitic steel through thermomechanical treatments, Journal of Nuclear Materials, 2010, vol.405, pp.101-108.

[60] L. Tan, D.T. Hoelzer, J.T. Busby, M.A. Sokolov, R.L. Klueh, Microstructure control for high strength 9Cr ferritic–martensitic steels, Journal of Nuclear Materials,2012, vol.422, pp. 45-50.

[61] L. Tan, Y. Yang, J.T. Busby, Effects of alloying elements and thermomechanical treatment on 9Cr Reduced Activation Ferritic–Martensitic (RAFM) steels, Journal of Nuclear Materials, 2013, vol.442, pp.S13-S17.

[62] L. Tan, J.T. Busby, P.J. Maziasz, Y. Yamamoto, Effect of thermomechanical treatment on 9Cr ferritic-martensitic steels, Journal of Nuclear Materials, 2013, 441, 713-717.

[63] Benjamin A. Shassere, Yukinori Yamamoto, Sudarsanam Suresh Babu, Toward improving the type IV cracking resistance in Cr-Mo steel weld through thermo-mechanical processing, Metall. Mater. Trans. A, 2016, vol. 47A, pp. 2188-2200.

[64] M. Song, C. Sun, Z. Fan, Y. Chen, R. Zhu, K.Y. Yu, K.T. Hartwig, H. Wang, X. Zhang, A roadmap for tailoring the strength and ductility of ferritic/martensitic T91 steel via thermo-mechanical treatment, Acta Materialia, 2016,vol.112, pp.361-377.

[65] O.E.El-Desoky, M.E.Abd El-Azim, M.R.ElKossy, Analysis of creep behavior of welded joints of P91 steel at 600°C, International Journal of Pressure Vessels and Piping, 2019, 171, 2019, 145-152.

[66] Bin Wang, Zhenyu Liu, Xiaoguang Zhou, Guodong Wang, R.D.K. Misra, Precipitation behavior of nanoscale cementite in 0.17% carbon steel during ultra fast cooling (UFC) and thermomechanical treatment (TMT), Materials Science and Engineering A, 2013, vol.588, pp.167-174.

[67] J. Hoffmann, M. Rieth, L. Commin, P. Fernández, M. Roldán, Improvement of reduced activation 9%Cr steels by ausforming, Nuclear Materials and Energy, 2016, vol.6, pp. 12-17.

[68] Jonathan Parker, Factors affecting Type IV creep damage in Grade 91 steel welds, Materials Science and Engineering A, 2013, 578, 430-437.

[69] Jonathan Parker, Steve Brett, Creep performance of a grade 91 header, International Journal of Pressure Vessels and Piping, 2013, 111-112, p.82-88.

[70] Wang Xue, Pan Qian-gang, Liu Zhi-jun, Zeng Hui-qiang, Tao Yong-shun, Creep rupture behaviour of P92 steel weldment, Engineering Failure Analysis, 2011, 18, 186-191.

[71] Wang Xue, Pan Qian-gang, Ren Yao-yao, Shang Wei, Zeng Hui-qiang, Liu Hong, Materials Science and Engineering A, 2012, 552, 493-501.

[72] S. Huysmans, J. Vekeman, Challenging weld repair of grade 91 tubing by avoiding PWHT, Energy Materials-Materials Science and Engineering for Energy Systems, 2009,4(2),76-83.

[73] ABAQUS finite element software, V6.14, Dassault Systemes, 2014.

[74] C.R. Calladine, Time-scales for redistribution of stress in creep of structures, Proc. Royal Soc. Lond., 1969, A309, 363-375.

[75] Yiyu Wang, Rangasayee Kannan, Leijun Li, Characterization of as-welded microstructure of heat-affected zone in modified 9Cr-1Mo-V-Nb steel weldment, Materials Characterization, Vol. 118, 2016, P:225-234.

[76] Jian Xu, Xiangyu Zhong, Tetsuo Shoji, Tadashi Tatsuki, Yuji Matsumura, Makoto Nakashima, Characterizations of the Microstructure of 9Cr-1Mo Steel Weld Joint After Long-Term Service in a Supercritical Fossil Power Plant, Metallurgical and Materials Transactions A, Vol.49A, 2019, P:123-132.

[77] K. Laha, K.S. Chandravathi, P. Parameswaran, K. Bhanu Sankara Rao, Type IV Cracking Susceptibility in Weld Joints of Different Grades of Cr-Mo Ferritic Steel, Metallurgical and Materials Transactions A, Vol.40(2), 2009, P:386-397.

[78] Irina Fedorova, Alla Kipelova, Andrey Belyakov, and Rustam Kaibyshev, Microstructure evolution in an advanced 9 pct Cr martensitic steel during creep at 923 K, Metallurgical and Materials Transactions A, vol. 44A, 2013, pp. 128-135.

[79] M. E. Abd El-Azim, O. H. Ibrahim, O. E. El-Desoky, Long term creep behaviour of welded joints of P91 steel at 650°C, Materials Science and Engineering A 560, 2013, P:678-684.

[80] T. Sakthivel, K. Laha, M. Vasudevan, M. Koteswara Rao and S. Panneer Selvi, Type IV cracking behaviour of modified 9Cr-1Mo steel weld joints, Materials at High Temperatures, 2016, 33(2), 137-153.

[81] T. Sakthivel, M. Vasudevan, K. Laha, P. Parameswaran, K.S. Chandravathi, S. Panneer Selvi, V. Maduraimuthu, M.D. Mathew, Creep rupture behavior of 9Cr-1.8W-0.5Mo-VNb (ASME grade 92) ferritic steel weld joint, Materials Science and Engineering A, Vol.591, 2014, 111-120.

[82] V. Maduraimuthu, M. Vasudevan, V. Muthupandi, A.K. Bhaduri, T. Jayakumar, Effect of activated flux on the microstructure, mechanical properties, and residual stresses of modified 9Cr-1Mo steel weld joints, Metallurgical and Materials Transactions B, Volume 43B (2012) 123-132.

[83] T. Sakthivel, M. Vasudevan, K. Laha, P. Parameswaran, K.S. Chandravathi, M.D. Mathew, A.K. Bhaduri, Comparison of creep rupture behaviour of type 316L(N) austenitic stainless steel joints welded by TIG and activated TIG welding processes, Materials Science and Engineering A 528, 2011, P:6971-69.

[84] Rishi Pamnani, V.Karthik, T. Jayakumar, et al, Evaluation of mechanical properties across micro alloyed HSLA steel weld joints using Automated Ball Indentation, Materials Science and Engineering: A, 2016, 651, 214-223.

[85] Peishan Zhou, Bin Wang, Liang Wang, Yiwen Hu, Luo Zhou, Effect of welding heat input on grain boundary evolution and toughness properties in CGHAZ of X90 pipeline steel, Materials Science and Engineering A, Vol.722, 2018, P:112-121.

[86] Fujimitsu Masuyama, Effect of specimen size and shape on creep rupture behavior of creep strength enhanced ferritic steel welds, International Journal of Pressure Vessels and Piping, 87 (2010) 617-623.

[87] Aritra Sarkar, Manmath Kumar Dash, A. Nagesha, Arup Dasgupta, M. Okazaki, EBSD based studies on various modes of cyclic deformation at 923K in a type 316LN stainless steel, Materials Science and Engineering A 723, 2018, P:229-237.

[88] H.Y.Yu, J.C.M. Li, Computer simulation of impression creep by the finite element method, Journal of Materials Science, 12 (1977), P:2214-2222.

[89] Hiromichi Hongo, Masaaki Tabuchi, Takashi Watanabe, Type IV creep damage behavior in Gr.91 steel welded joints, Metallurgical and Materials Transactions A, Volume 43A, 2012, 1163-1173.

[90] J. D. Parker, J. A. Siefert, Evaluation of options for weld repair of Grade 91 piping and components: metallographic characterization, Science and Technology of Welding and Joining, Vol.18, No.6, 2013, 507-517.

[91] L. Esposito, Type IV creep cracking of welded joints: numerical study of the grain size effect in HAZ, Procedia Structural Integrity 2 (2016) 919-926.

[92] Toshiaki Horiuchi, Masaaki Igarashi, Fujio Abe, lmproved utilization of added B in 9Cr heat-resistant steels containing W, ISIJ International, Vol. 42 (2002), Supplement, pp. S67-S71.

[93] Bo Xiao, Lianyong Xu, Lei Zhao, Hongyang Jing, Yu Zhang, Creep properties, creep deformation behavior, and microstructural evolution of 9Cr-3W-3Co-1CuVNbB martensite ferritic steel, Materials Science and Engineering: A 711 (2018), P: 434-447.

[94] I. Fedorova, F. Liu, F.B. Grumsen, Y. Cao, O.V. Mishin, J. Hald, Fine (Cr, Fe)2B borides on grain boundaries in a 10Cr-0.01B martensitic steel, Scripta Materialia, 156 (2018) 124-128.

[95] F. Abe, H. Semba, T. Sakuraya, Effect of boron on microstructure and creep Deformation behavior of tempered martensitic 9Cr steel, Materials Science Forum, Vols. 539-543, 2007, pp 2982-2987.

[96] Fujio Abe, Effect of Boron on Microstructure and Creep Strength of Advanced Ferritic Power Plant Steels, Procedia Engineering 10 (2011) 94–99.

[97] J. Takahashi, K. Ishikawa, K. Kawakami, M. Fujioka, N. Kubota, Atomic-scale study on segregation behavior at austenite grain boundaries in boron- and molybdenum-added steels, Acta Materialia, Vol. 133 (2017), P:41-54.

[98] E. Tkachev, A. Belyakov, R. Kaibyshev, Creep behavior and microstructural evolution of a 9%Cr steel with high B and low N contents, Materials Science and Engineering A 725 (2018) 228-241.

[99] K.S. Chandravathi, K. Laha, P. Parameswaran, M.D. Mathew, Effect of microstructure on the critical strain to onset of serrated flow in modified 9Cre1Mo steel, International Journal of Pressure Vessels and Piping 89 (2012) 162-169.

[100] P. Rodriguez, Serrated plastic flow, Bull. Mater. Sci., Vol.6, No.4, 1984, 653-663.

[101] T. Sakthivel, K. Laha, M. Nandagopal and M. D. Mathew, Influence of temperature on tensile flow and work hardening behaviour of modified 9Cr-1Mo steel, Materials at High Temperatures, 2014, Vol.31, No.1, 60-68.

[102] Kouichi Maruyama, Kota Sawada, Jun-ichi Koike, Strengthening mechanisms of creep resistant tempered martensitic steel, ISIJ International, Vol. 41 (2001), No. 6, pp. 641-653

[103] Hyeong Min Heo, Eun Hee Jeong, Sung Ho Kim, Jong Ryoul Kim, Comparison between effect of B and N on the microstructure of modified 9Cr-2W steel during aging and creep, Materials Science and Engineering A 670 (2016) 106-111.

[104] H. Ghassemi-Armaki, R.P. Chen, K. Maruyama, M. Igarashi. Contribution of recovery mechanisms of microstructure during long-term creep of Gr.91 steels Journal of Nuclear Materials, 2013, vol. 433, pp. 23-29.

[105] Triratna Shrestha, Mehdi Basirat, Indrajit Charit, Gabriel P. Potirniche, Karl K. Rink, Uttara Sahaym: Journal of Nuclear Materials, 2012, vol. 423, pp. 110-119.

[106] K. Maruyama, H. Ghassemi Armaki, R.P.Chen, K.Yoshimi, M. Yoshizawa, M. Igarashi, Cr concentration dependence of overestimation of long term creep life in strength enhanced high Cr ferritic steels, International Journal of Pressure Vessels and Piping, 2010, vol. 87, P:276-281.

[107] Nhon Q. Vo, Christian H. Liebscher, Michael J.S. Rawlings, Mark Asta, David C. Dunand, Creep properties and microstructure of a precipitation-strengthened ferritic Fe–Al–Ni–Cr alloy, Acta Materialia, 2014, 71, 89-99.

[108] B. Ule, A. Nagode, A model based creep equation for 9Cr-1Mo-0.2V (P91 type) steel, Material Science and Technology, 2007,Vol.23,No.11, P:1367-1374.

[109] Feng-Shi Yin, Li-Qian Tian, Bing Xue, Xue-Bo Jiang, Li Zhou, Effect of carbon content on microstructure and mechanical properties of 9 to 12 pct Cr ferritic/martensitic heat-resistant steels, Metallurgical and Materials Transactions A, Vol.43A, 2012, 2203-2209.

[110] M.F. Ashby, B.F. Dyson, in: S.R. Valluri, et al., (Eds.), Advances in Fracture Research, vol. 1, Pergamon Press, Oxford, 1984pp. 3–30.

[111] N. Dudova, A. Plotnikova, D. Molodov, A. Belyakov, R. Kaibyshev, Structural changes of tempered martensitic 9%Cr-2%W-3%Co steel during creep at 650°C, Materials Science and Engineering A 534 (2012), 632-639.

[112] Abdullah S. Alomari, N. Kumar, K.L. Murty, Creep behavior and microstructural evolution of a Fe-20Cr-25Ni (mass percent) austenitic stainless steel (alloy709) at elevated temperatures, Metallurgical and Materials Transactions A, Vol.50A, 2019, 641-654.

[113] S. Spigarelli, Microstructure-based assessment of creep rupture strength in 9Cr steels International Journal of Pressure Vessels and Piping, 2013, vol. 101, pp. 64-71.

[114] RCC MR Design code, Section1, Sub section Z, 2002. French Society for Design and Construction Rules for Nuclear Island components.

[115] K. Kimura, H. Kushima, K. Sawada, Long-term creep deformation property of modified 9Cr–1Mo steel, Materials Science and Engineering A 510–511 (2009) 58-63.

[116] Erin M. Haney, France Dalle, Maxime Sauzay, Ludovic Vincent, Ivan Tournie, Lucien Allais, Benjamin Fournier, Macroscopic results of long-term creep on a modified 9Cr-1Mo steel (T91), Materials Science and Engineering A 510–511 (2009) 99-103.

[117] Hyeong Min Heo, Eun Hee Jeong, Sung Ho Kim, Jong Ryoul Kim, Comparison between effect of B and N on the microstructure of modified 9Cr-2W steel during aging and creep, Materials Science and Engineering A 670 (2016) 106-111.

[118] Eun Hee Jeong, Jun Hwan Kim, Sung Ho Kim, Young Do Kim, Influence of B and N on the microstructural characteristics and high-temperature strength of 9Cr-2W steel during an aging treatment, Materials Science and Engineering: A700 (2017), P:701-706.

[119] Genichi Shigesato, Taishi Fujishrio, Takuya Hara, Grain boundary segregation behavior of boron in low-alloy steel, Metallurgical and Materials Transactions A, 2014, Vol.45A, 1876-1882.

[120] K. S. Chandravathi, K. Laha, Norio Shinya, M. D. Mathew, Effects of boron and cerium on creep rupture properties of modified 9Cr-1Mo steel and its weld joint, Procedia Engineering 55 (2013) 433 – 437.

[121] Dong Jun Mun, Eun Joo Shin, Young Won Choi, Jae Sang Lee, Yang Mo Koo, Effects of cooling rate, austenitizing temperature and austenite deformation on the transformation behavior of high-strength boron steel, Materials Science and Engineering A 545 (2012) 214-224.

[122] Masaaki Tabuchi, Hiromichi Hongo, Yukio Takahashi, Effect of boron on microstructures and creep properties of weld joint for high Cr heat resisting steels, Journal of the Society of Materials Science, Japan, Vol. 58, No. 2, 2009, pp. 108-114.

[123] Rui Wu, Rolf Sandstrom, Facredin Seitisleam, Influence of extra coarse grains on the creep properties of 9 percent CrMoV (P91) steel weldment, Journal of Engineering Materials and Technology, Vol.126, 2004, 87-94.

[124] T.C. Totemeier, H. Tian, J.A. Simpson, Effect of normalization temperature on the creep strength of modified 9Cr-1Mo steel, Metall. Mater. Trans. A,2006, 37A, 1519-1525.

[125] M. Zhang, Y.H. Wang, C.L. Zheng, F.C. Zhang, T.S. Wang, Austenite deformation behavior and the effect of ausforming process on martensite starting temperature and ausformed martensite microstructure in medium-carbon Si–Al-rich alloy steel, Materials Science and Engineering A, 2014, 596, 9-14.

[126] T.S. Wang, M. Zhang, Y.H. Wang, J. Yang, F.C. Zhang, Martensitic transformation behaviour of deformed supercooled austenite, Scripta Materialia, 2013, 68, 162-165.

[127] Hong-Seok Yang, H.K.D.H. Bhadeshia, Austenite grain size and the martensite-start temperature, Scripta Materialia, 2009, 60, 493-495.

[128] R. Lagneborg, B. Bergman, The stress/creep rate behaviour of precipitation-hardened alloys, Metal Science, 1976, 10(1).

[129] Zhiqiang Xu, Yinzhong Shen, Zhongxia Shang, Chuqiao Zhang, Xi Huang, Precipitate phases in ferritic/martensitic steel P92 after thermomechanical treatment, Journal of Nuclear Materials, 2018, 509, 355-365.

[130] Valeriy Dudko, Andrey Belyakov, Dmitri Molodov, Rustam Kaibyshev, Microstructure evolution and pinning of boundaries by precipitates in a 9 pct Cr heat resistant steel during creep, Metall. Mater. Trans. A, 2013, 44A, 162-172.

[131] Shengzhi Li, ZumratEliniyaz, Feng Sun, Yinzhong Shen, Lanting Zhang, Aidang Shan, Effect of thermo-mechanical treatment on microstructure and mechanical properties of P92 heat resistant steel, Materials Science and Engineering A, 2013, 559, 882-888.

[132] Manabu Tamura, Takuya Kumagai, Kazuhisa Sakai, Kei Shinozuka, HisaoEsaka, A new approach to improve creep resistance of high Cr martensitic steel, Journal of Nuclear Materials, 2011, 417, 29-32.

[133] T. Sakthivel, P. Shruti, P. Parameswaran, G. V. S. Nageswara Rao, K. Laha, T. Srinivasa Rao, Enhancement in Creep Strength of Modified 9CR–1MO Steel Through Thermo-Mechanical Treatment, Trans. Indian Inst. Met, DOI 10.1007/s12666-016-0902-z.

[134] P. Fernandez, J. Hoffmann, M. Rieth, M. Roldan, A. Gomez-Herrero, TEM characterization on new 9% Cr advanced steels thermomechanical treated after tempering, Journal of Nuclear Materials, 2018, 500, 1-10.

[135] P. J. Ennis, A. Zielinska-Lipiec, O. Wachter, and A. Czyrska-Filemonowicz: Acta Materialia, 1997, vol. 45, pp. 4901-4907.

[136] S.S. Wang, D.L. Peng, L. Chang, and X.D. Hui: Materials and Design, 2013, vol. 50, pp. 174-180.

[137] I. Fedorova, A. Belyakov, P. Kozlov, V. Skorobogatykh, I. Shenkova, and R. Kaibyshev: Materials Science and Engineering A, 2014, vol. 615, pp. 153-163.

[138] O. Prat, J. Garcia, D. Rojas, G. Sauthoff, and G. Inden: Intermetallics, 2013, vol. 32, pp.362-372.

[139] A. Kostka, K.-G. Tak, R.J. Hellmig, Y. Estrin, and G. Eggeler: Acta Materialia, 2007, vol. 55, pp. 539-550.

[140] Oleg D. Sherby, Eric M. Taleff: Materials Science and Engineering A, 2002, vol. 322, pp. 89-99.

[141] K. Sawada, K. Kubo, and F. Abe: Materials Science and Engineering A, 2001, vol. 319-321, pp. 784-787.

[142] Fujio Abe: Materials Science and Engineering A, 2001, vol. 319-321, pp. 770–773.

[143] J Čadek: Creep in Metallic materials, Elsevier, 1988.

[144] Jae Seung Lee, Hassan Ghassemi Armaki, Kouichi Maruyama, Taro Muraki, and Hitoshi Asahi: Materials Science and Engineering A, 2006, vol. 428, pp. 270-275.

[145] B. F. Dyson and T. B. Gibbons: Acta Materialia, 1987, vol.35, pp. 2355.

[146] X. Xu, G. D. West, J.A. Sifert, J.D.Parker, R. C. Thomson, Metallurgical and Materials Transactions A, Volume 48A (2017) 5396-5414.

[147] Lei Zhao, Hongyang Jing, Lianyong Xu, Junchao An, Guanchun Xiao, Materials and Design 34 (2012) 566-575.

[148] V. Sklenička, K. Kuchařová, M. Svobodová, M. Kvapilová, P. Král, L. Horváth, Materials Characterization 119 (2016) 1-12.

[149] K. Sawada, H. Hongo, T. Watanabe, M. Tabuchi, Materials Characterization 61 (2010) 1097-1102.

[150] H. Naoi, M. Ohgami, S. Araki, T. Ogawa, H. Yasuda, H. Masumoto, and T. Fujita, Development of High-Strength Ferritic Steel NF616 for Boiler Tubes, Nippon Steel Technical Report, No. 50 (1991), pp 7-13.

[151] M. Ohgami, H. Mimura, H. Naoi, T. Ikemoto, S. Kinbara, T. Fujita, Nippon Steel Technical Report, No.72 (1997), pp 59-64.

[152] Y. Hasegawa, H. Morimoto, Proc. of Creep and Fracture of Engineering Materials and Structures (Creep2012), The Japan Institute of Metals, (2012) B38.

[153] Mariya Yurechko, Carsten Schroer, Aleksandr Skrypnik, Olaf Wedemeyer, Jürgen Konys, Journal of Nuclear Materials 432 (2013) 78–86.

[154] M. Yoshizawa, M. Igarashi, K. Moriguchi, A. Iseda, Hassan Ghassemi Armaki, K. Maruyama, Materials Science and Engineering A 510–511 (2009) 162–168.

[155] Y. Hasegawa, M. Ohgami, Y. Okamura, Advanced Heat Resistant Steels for Power Generation, ed. By R. Viswanathan and J Nutting, The University Press, Cambridge (1999), 655.

[156] Nick Bagshaw, Chris Punshon, John Rothwell, Development of welding P92 pipes using the reduced pressure electron beam welding process for a study of creep performance, Proceedings of the ASME symposium on elevated temperature application of materials for fossil, nuclear, and petrochemical Industries, March 25-27, 2014, ETAM2014-1010.

[157] P. Mohyla, Z. Kubon, R. Cep, I. Samardzic, Evaluation of creep properties of steel P92 and its weld joint, Metalurgija 53 (2014) 2, 175-178.

[158] P.J. Ennis, A.Zielinska-Lipiec, A. Czyrska-Filemonowicz, Materials Science and Technology, 2000, 16, 1226-1232.

[159] Fujio Abe, Materials Science and Engineering A, 2001,319-321, 770-773.

[160] S. K. Albert, M. Tabuchi, H. Hongo, T. Watanabe, K. Kubo and M. Matsui, Journal, Science and Technology of Welding and Joining , 2005, 10,149-157.

[161] P. J. Ennis, A. Zielinska-Lipiec, O. Wachter, A. Czyrska-Filemonowicz, Acta Materialia, 1997,45(12), 4901-4907.

[162] X. Xu, G.D.West, J.A.Siefert, J.D.Parker, R.C.Thomson, Metall. Mater. Trans. A, 2017, 48A, 5396-5414.

[163] J. A. Francis, G. M. D. Cantin , W. Mazur,H. K. D. H. Bhadeshi, Science and Technology of Welding and Joining, 2009,14(5), 436-442.

[164] Lei Zhao, Hongyang Jing, Lianyong Xu, Junchao An, Guangchun Xiao, Materials and Design, 2012, 34, 566-575.

Thesis Highlights

Name of the Student: T. SAKTHIVEL

Name of the CI/OCC: IGCAR **Enrolment No.: ENGG02201304008**

Thesis Title: ***Effect of geometry, composition and thermomechanical treatment on the Type IV cracking during creep in advanced 9Cr ferritic steels weld joint***

Discipline: Engineering Sciences **Sub-Area of Discipline: Metallurgy**

Date of viva voce: 09-02-2021

[1] The factors leading to higher rate of deformation in the ICHAZ region than the other regions in the single-pass A-TIG weld joint are the following: (i) lower content of low misorientation angle and coincidence site lattice (CSL) boundaries, (ii) finer grain size, (iii) enhanced heterogeneity in microstructures by a combination of recovered and deformed structure in the martensite, (iv) coarser $M_{23}C_6$ precipitates, and (v) boundaries devoid of precipitates. Activated TIG (A-TIG) welding is preferred to fabricate the components in order to achieve resistance against Type IV cracking; TIG welding is preferred to SMAW in the case of thick components requiring multi-pass welding.

[2] P91BN steels containing boron with controlled nitrogen content resulted in finer martensite lath width than in the P91 steel. The time spent in each creep regime increased significantly in P91BN steels as compared to P91 steel. Sluggish coarsening of $M_{23}C_6$ and finer MX precipitates significantly delayed the recovery of dislocation structure and migration of boundaries in P91BN steel than in P91 steel. From the point of view of rupture life of P91BN steel and its weld joint, the combination of 60 ppm boron with controlled (110 ppm) nitrogen content is optimum at 873 K as compared to other combinations of B and N examined in this study.

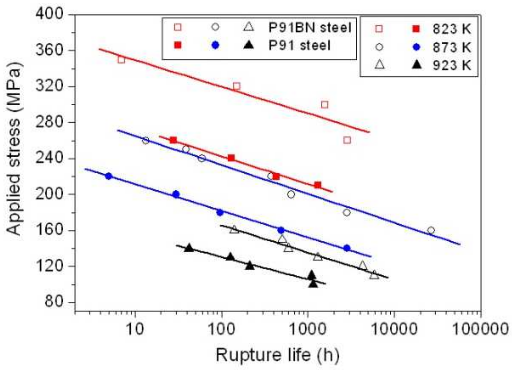

Figure 1 : Effect of boron

[3] Thermo-mechanical treatment (TMT) processing of modified 9Cr-1Mo steel (P91) leads to refined microstructure of the steel. The degree of TMT deformation is important since high levels of deformation leads to ferrite formation. The thermo-mechanical processing of modified 9Cr-1Mo steel led to enhanced type IV cracking resistance significantly.

[4] Creep rupture life of the P92 steel NG-TIG weld joint was lower than the base metal. Extensive Laves phase formation accompanied by significant loss of solution strengthening from tungsten under creep exposure led to premature type IV failure of the weld joint in the FGHAZ.

[5] Apart from refinement of microstructural constituents (reduction in coarsening of $M_{23}C_6$ and enhanced MX precipitation) favorable for long term stability of microstructure to obtain better creep life of the base and weld joint, enhancement of the type IV cracking resistance of the steel joint can be obtained from joint having lower bevel angle, less heterogeneity across the weld joint, moving the orientation of stress axis in a joint to reduce the angle between fusion line/HAZ and stress axis.

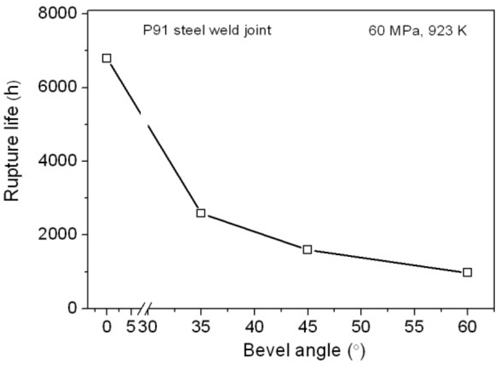

Figure 2: Influence of bevel angle